REPORT 88001_1

AD-A283 597

A Collection of Publications Under the ONR Contract

"EVOLUTION OF A COLLECTION OF BUBBLES WITH APPLICATION TO WAKES, BUBBLE SCREENS, AND CLOUD NOISE"

DYNAFLOW, INC.

Contract No. N00014-89-C-0025 ONR

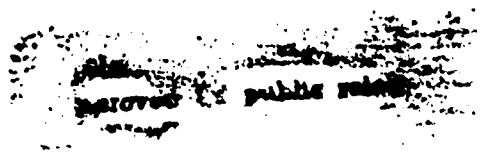

DYNAFLOW, INC.
Research & Development in Applied Sciences

7210 Pindell School Road, Fulton, Maryland 20759 Tel: (301) 604-3688 - Fax:(301) 604-3689

A Collection of Publications Under the ONR Contract

"EVOLUTION OF A COLLECTION OF BUBBLES WITH APPLICATION TO WAKES, BUBBLE SCREENS, AND CLOUD NOISE"

DYNAFLOW, INC.

Contract No. N00014-89-C-0025 ONR

FINAL LETTER CONTRACT REPORT
Contract N00014-89-0025

Principal Investigator: Georges L. CHAHINE

a Foreword

This report contains copies or reprints of publications made under contract No. N00014-89-C-0025 funded by the Office of Naval Research, Fluid Dynamics Program under the technical monitoring of Dr. Edwin Rood.

It is intended to document the technical achievements accomplished under this contract. In reverse order of dates, the following documents are included:

1. G.L. CHAHINE, "Bubble Dynamics and Cavitation Inception in Non-Uniform Flow Fields," to appear in *Proceedings of the Twentieth ONR Symposium on Naval Hydrodynamics"*, Santa Barbara, CA, August 1994..

2. G.L. CHAHINE, "Bubble Interactions with Vortices," in "Vortex Flows," S. GREEN, ed., *to be published by Kluwer Academic,* 1994.

3. G.L. CHAHINE, "Cavitation Dynamics at Microscale Level," *Journal of Heart Valve Disease*, vol. 3, 1993.

4. G. DESGRESS DU LOU, T. SARAZIN, AND G.L. CHAHINE, "Viscous Interaction Between Bubble and Line Vortex," DYNAFLOW, INC. *Technical Report, 6.002_15*, 1993.

5. Y.L. GUERRIER, "The Motion of a Spherical Body Below a Free Surface," DYNAFLOW, INC. *Technical Report, 6.002_14*, 1993.

6. A. VAN DER BEKEN, R. DURAISWAMI, AND G.L. CHAHINE,"Study of Jet Instability Formation on Free Surfaces," DYNAFLOW, INC. *Technical Report, 6-002-13,* 1993.

7. S. ZHANG, J. DUNCAN, AND G.L. CHAHINE, "The Final Stage of the Collapse of a Cavitation Bubble Near a Rigid Wall," *J. Fluid Mech.*, vol. 257, 1993.

8. G. L. CHAHINE, E. DELEPOULLE, AND P. HAUWAERT, "Study of the Interaction Between a Bubble and a Vortical Structure," Proceedings *Cavitation and Multiphase Flow Forum, New York,* 1993.

9. M. REBUT AND G.L. CHAHINE, "Asymptotic Study of Bubble Dynamics in a Nonuniform Potential Flow," in *Proceedings, ASME Cavitation and Multiphase Flow Forum,* Los Angeles, 1992.

10. R.DURAISWAMI AND G.L. CHAHINE, "Analytical study of the interaction a gas bubble and a line vortex," in *Proceedings ASME Cavitation and Multiphase Flow Forum,* Los Angeles, 1992.

11. G.L. CHAHINE, R. DURAISWAMI, AND M. REBUT, "Analytical and Numerical Study of Large Bubble/Bubble and Bubble/Flow Interactions," *Proceedings of the Nineteenth ONR Symposium on Naval Hydrodynamics"*, Seoul, S. Korea, 1992.

12. J.B. VILLE AND G.L. CHAHINE, "Asymptotic Study of Bubble Dynamics in a Slightly Compressible flow," DYNAFLOW, INC. *Technical Report, 6.002_12*, 1992.

13. L. MAUDUIT AND G.L. CHAHINE, "Asymptotic Study of Bubble Cloud Dynamics in the Proximity of a Body in Potential Flow," DYNAFLOW, INC. *Technical Report, 6.002_11*, 1992.

14. G.L. CHAHINE, R. DURAISWAMI, AND A.N. LAKSHMINARASIMHA, "Dynamical Interactions in a Bubble Cloud," *ASME J. Fluids Engg.*, vol. 114, 1992.

15. G.L. CHAHINE, "Dynamics of the Interaction of Non-Spherical Cavities," in *"Mathematical Approaches in Hydrodynamics, (ed. T. Miloh), SIAM*, PHILADELPHIA, PP. 51-67, 1991.

b Summary

The primary focus of the work conducted under this contract is the investigation of the mechanism of interaction between bubbles and underlying flows, and of the mutual interaction of bubbles. The tools developed and the knowledge gained will be useful to us and other researchers and engineers to model and understand the problem of cavitation inception in various circumstances. This is of relevance to Navy applications where cavitation and bubble dynamics can generate noise, adversely affect the flow, or negatively impact on the performance. Our main emphasis during this research program was to develop a description of the dynamics of strong interactions on the microscale level (the dynamics of bubble nuclei) and its implications on the macroscale level (cavitation inception, emitted noise).

Since the fine and precise modeling of the overall phenomenon of cavitation is very complicated, and understanding of many of its aspects has confounded scientists and engineers, we concentrated attention on some relatively simple but practically important flow situations, so that the basic physics of the problem could be understood. This understanding of the fundamental mechanisms is essential to the understanding of more complicated flows involving bubbles, and allow one to justify or discount assumptions made in other studies of more complex flow situations. We have sought to achieve this goal by using numerical, analytical, and experimental methods.

Tools which we used and/or developed in this study, and in the computer programs that have resulted, are based on Matched Asymptotic expansions, axisymmetric and 3-D Boundary Element Methods (BEM) , and Vortex Element Methods. In addition, in order to study viscous flow / bubble interactions a simple finite difference code coupled with a Runge-Kutta model was developed for the axisymmetric problem of bubble / vortex viscous flow interaction.

In this letter report we will not go into the details of our results. These are described in the various publications (listed in Appendix A) that arose from work on this contract (copies of the most relevant publications are attached). Instead we will concentrate here on some aspects of the results, and their implications on future fundamental and/or numerical work and on applications.

c Bubble Flow Interaction

This section relates to the dynamics of bubble nuclei (cavitation inception) in boundary layers, shear layers and in vortex flows. After developing the method of approach, particular attention was given to bubble behavior in vortical flows and close to a boundaries. In all cases single and multiple bubble dynamics were considered. Whenever possible comparison was made with existing experimental evidence or with small scale experiments conducted in parallel at DYNAFLOW. Specific areas which we have addressed are:

- Interaction between multiple bubbles (cloud cavitation)
- Influence of shear and vortical flows on single and multiple bubbles (cavitation inception in boundary layers and trailing vortices)
- The description of large bubble deformation near a submerged body (bubble dynamics near head forms, also applicable to underwater explosion bubble dynamics)
- Development of an asymptotic model of a cavitating bubbly flow.
- Bubble capture and behavior in a vortex flow (bubble capture, cavitation, and vortex flow modification)

c.1 Bubbles in vortex line-flow

c.1.1 Bubble capture and deformation in a line vortex flow

To study bubble capture and interaction with the viscous flow field of a vortex line or a vortex ring, a model where the interaction is restricted to the constraint that no additional vorticity is generated by the bubble dynamics led to the following results:

1. Criteria for bubble capture, and for large bubble deformations during bubble interaction with a vortex line flow were obtained.
2. Two key parameters on the bubble / vortex interaction appear to be the ratio between bubble size and "viscous core" size, and the ratio between ambient pressure and the pressure drop at the vortex center due to the circulation in the vortex.

3. Prior to bubble capture by the vortex and its centering on the vortex axis, the strongest shear effects on the bubble occur in the region close the vortex core edge.

4. During strong bubble dynamics (as in cavitation inception conditions) bubble deviation from spherical shape during bubble growth can be very significant, leading eventually to jet formation and bubble splitting, and thus to sound emission very close to the inception region.

5. In strong vortices, such as in a tip vortex, deviation from sphericity occurs even for the smallest conceivable bubble sizes.

6. Once the bubble is on the axis, it tends to elongate significantly if the ratio between its characteristic size and the viscous core radius is large. It then tends to subdivide into a string of elongated bubbles along the axis.

7. The model was extended to the case of multiple bubbles in the vortex flow, and was able to capture both inter-bubble and bubble-flow interactions.

Extension to a two-phase flow field

With a view towards large scale bubble flow simulations, the above approach was implemented in an asymptotic approach which has the advantage of being much less constraining computationally both on time and memory, at the expense of restraining solutions to small bubble deformations. The method of *matched asymptotic expansions* was used, the small parameter ϵ in these expansions being the ratio of the original bubble radius and the distance between the bubble and the nearest line vortex. Analytical developments up to and including $O(\epsilon^2)$ were made. The results were then expressed in terms of a series of ordinary differential equations (in time) for the coefficients of the bubble shape function (in terms of spherical harmonics).

Experimental validation

A series of *experiments* on the interaction of spark generated bubbles and cavitating and non-cavitating vortex rings was performed in order to confront the codes. A vortex ring was generated in a Plexiglas chamber maintained at pressures below the ambient. A spark generated bubble was formed at various distances away from the ring, and high speed movies,video recordings and transient pressures in the liquid were recorded. A series of *numerical simulations* were also performed with the BEM program in the same conditions and showed better than expected

agreement with the experiment despite the modeling assumptions of inviscid liquid away from a thin viscous core, and despite neglect of vortex ring behavior modification due to the presence of the bubble.

c.1.2 Elongated bubble full interaction with a viscous line vortex flow

As a first step towards a full bubble / viscous flow interaction study, the following simplified problem of cavitation inception in a line vortex was addressed. The dynamics of an infinitely elongated (cylindrical) bubble was considered in a vortex line flow field. The Navier Stokes equations were then solved in this axisymmetric two-dimensional case. The bubble dynamics was obtained in terms of a second order differential equation, similar to the Rayleigh Plesset, but which is restricted to a cylindrical geometry, and contains a term which is an integral of the angular velocities in the flow. This term constitutes the coupling with the viscous flow. The viscous flow is then obtained, using a finite difference scheme, by resolution of a diffusion equation (reduced NS equations) whose coefficients depend on the bubble characteristics. The results of this study are as follows:

1. Starting from an imposed Rankine vortex flow field (sharp change in the slope of the velocity profile, $\partial u_\theta / \partial r$, between the viscous and the inviscid parts), one observes that a smoother profile is rapidly established.

2. The position, r_c, and the amplitude of maximum tangential velocity, $u_{\theta\,\max}$, strongly depend on the bubble dynamics:

   - r_c increases during the bubble growth and significantly decreases during collapse.
   - $u_{\theta\,\max}$ decreases during the bubble growth, and significantly increases during collapse.

3. Vorticity concentrates near the axis, stretches during bubble collapse, and decays and diffuses with time and during bubble growth due to viscous diffusion.

4. This results in a moderated bubble collapse and growth (compared to the idealized case where the viscous basic flow is assumed independent of time) when viscous effects are fully accounted for in the bubble/flow interactions.

c.2 Bubble behavior in a shear layer near a flat plate

c.2.1 Asymptotic Analysis

During this contract we have studied bubbles in shear flows by means of the method of matched asymptotic expansions, and by means of BEM simulations. A treatment of the behavior of a bubble in a general potential flow was developed, under the assumption that the bubble size was smaller than the characteristic length scale associated with the external flow. Equations up to and including the $O(\epsilon^2)$ were developed.

The resulting equations were then specialized for the case of the flow past a semi-infinite bluff body (the Schiebe half body). The equations obtained were then integrated, and showed some interesting features. The formation of the reentrant jet was shown to be due to both a combination of the presence of the wall and of the shear flow. In fact, the presence of the wall (in terms of an image of the bubble) does not appear but at order ϵ^2, the main effect of the wall at the leading order being its imposition of a shear velocity field.

c.2.2 Numerical Simulation

A systematic numerical study of bubble behavior near a flat plate was conducted, using high definition bubble discretization. This showed interesting results on bubble behavior during its growth and collapse near a wall. For an increasing ratio, τ, between the shear flow velocity at the bubble center level (shear flow is zero at wall and increases linearly away from it) and the bubble characteristic Rayleigh velocity the following is observed:

1. For increased values of τ, the bubble deforms and elongates more and more during its growth.

2. For small values of τ, the re-entering jet deviates from the perpendicular direction to the plate with increasing values of τ.

3. For larger values of τ, the re-entering jet formation is totally modified and the bubble tends to cut itself into two bubbles.

4. An interesting lifting effect is observed with increasing values of τ. The bubble centroid is seen to move further and further away from the wall with increasing values of τ. This is probably due to an interaction between the wall shear flow and the effective rotation of the bubble with time.

c.3 Multiple Bubble Dynamics

The focus of our study on multiple bubble dynamics has been both computational and analytical. The computational part of the study involved the simulation of various multiple bubble dynamics problems. Full simulations of clouds subject to step changes in the pressure were performed. The BEM simulations were compared with the predictions of an analytical treatment based on the method of matched asymptotic expansions, with the small parameter chosen to be the ratio of characteristic bubble size and characteristic inter-bubble distance. As would be expected, the two methods predict similar solutions for small values of ϵ, but diverge when the value of ϵ is increased. These comparisons serve to provide a means of mutual validation of the analytical technique and the numerical algorithm. A series of numerical experiments were then performed to bring out various features of the dynamics of bubbles. The following conclusions were brought out.

1. Multibubble effects result in a cumulative pressure build-up.

2. Pressure much higher than due to summation of the pressures due to the individual bubbles are obtained. However, overestimates of these pressures are obtained with the asymptotic approach.

3. While growth of a cloud of very close bubbles does not deviate much from the case of weak interactions, collapse of a cloud proceeds in a very directive way. Bubbles on the outer shell of a cloud collapse first, leading to a propagation of the collapse front towards the inside of the cloud.

4. Most striking are screening influences of the bubbles – outer members of the cloud respond in a manner markedly different from the ones on the inside of the cloud.

An asymptotic analysis was also performed to study the effect of compressibility on the dynamics of a bubble cloud. This analysis, similar to that used by other workers to study single spherical bubble dynamics, replaces the Rayleigh-Plesset equation by a Keller-Herring (or other compressible equations). However, the analysis is complicated by the appearance of two small parameters – the Mach number and the ratio ϵ of typical bubble size to inter bubble distance. Corrections due to the compressibility were obtained. The analysis was performed up to ϵ^3, and for the first order in Mach number.

d A New BEM Technique for Study of Liquid-Liquid Impact

While the BEM programs developed during the conduct of this study are much more efficient than other methods used to simulate free surface problems, they suffered from a major breakdown when the bubble surface became multi-connected (penetration and touchdown of a re-entering jet). This affected for instance our simulations in the case of strong interactions between multiple bubbles. In this case, the validity of the simulation is controlled by the shortest period of the bubbles in the cloud. As soon as the shape of that bubble becomes multi-connected the method fails and the computation stops. Thus a key extension of the simulations, is determining the bubble dynamics beyond the point where bubble splitting, or reentrant jet penetration and touch-down occurs. This is also interesting because the collapsing bubbles *are themselves capable of forming vortical structures* following the non spherical collapse. This issue is one of both practical and theoretical significance. Practically, these structures appear to be associated with cavitation damage. Fundamentally, this highlights a mechanism by which a flow that starts off being potential is later on able to develop vorticity by the collapse of various pieces of the boundary onto each other.

Equations for the further flow were developed. The key feature of the methods is that the surfaces formed by the touching parts of the bubble are treated as material vortex sheets. This enables us to treat the problem with the boundary element method. A BEM program capable of simulating bubble collapse past the touchdown point for axisymmetric geometries was developed. This technique is presently being implemented in the 3-D code.

e BEM algorithm improvement for free-surface flow

Since the BEM programs developed deal essentially with the large deformation of free surfaces (here mainly bubble interfaces), these same codes can be used after some adjustments to more conventional free surface flows. During this contract, we applied these technique to study high velocity jets that develop from the movement of a free surface suddenly generated when the bottom of an empty cylinder open at both end is suddenly raised from the bottom of a container full of water. The results correlated reasonably well with those observed experimentally using high speed photography. Similarly, the flow due to a droplet impact on a free surface and to bubble dynamics below a free surface were studied in small students projects.

f Conclusions and Future Plans

The above described work forms the basis of our on-going development of a powerful free surface large nonlinear motion codes including vortical effects and two-phase flows. By combining all the various tools described above, a large simulation code to run on supercomputers or parallel machines is now conceivable. Most of the fundamental issues have been worked out under this contract and other IR&D parallel efforts. Similarly, we are presently coupling a Vortex Element Method with the BEM codes described above to study vortical flows / bubbly flows interactions. We are also coupling our BEM code with a finite element (shell) method provided by Laurence Livermore National Laboratories to study fluid structure interaction. We hope to be able to achieve such a useful tool in the near future, in order to take advantage of the ever-improving hardware computational capabilities.

A List of Publications

1 Papers Published in Refereed Journals

1. G.L. CHAHINE AND R. DURAISWAMI "Dynamical Interactions in a Bubble Cloud," *ASME J. Fluids Engg.*, vol. 114, pp. 680-686, (1992).

2. G.L. CHAHINE, G.S. FREDERICK, AND R.D. BATEMAN, "Propeller Tip Vortex Cavitation Suppression Using Selective Polymer Injections," *ASME J. Fluids Engg.*, vol. 115, (1993).

3. S. ZHANG, J. DUNCAN AND G.L. CHAHINE, "Dynamics of a bubble past the point of collapse," *J. Fluid Mech.*, vol. 257, pp. 147-181, (1993).

4. G.L. CHAHINE, "Cavitation Dynamics at Microscale Level," *Journal of Heart Valve Disease*, vol. 3, (1993).

2 Books, or Chapters of Books

1. G.L. CHAHINE, "Dynamics of the interaction of non-spherical Cavities," in "Mathematical Approaches in Hydrodynamics," (ed. T.MILOH), *SIAM, Philadelphia*, pp. 51-67, (1991).

2. G.L. CHAHINE, "Bubble Interactions with Vortices," in "Vortex Flows," S. GREEN, ed., *to be published by Kluwer Academic,* (1993).

3. G.L. CHAHINE, K.M. KALUMUCK, AND R. DURAISWAMI, "Coupling of a Fluids BEM Code with a Structures FEM code for Fluid Structure Interaction," in "Boundary Elements 15, Vol.2: Stress Analysis" C.A. BREBBIA AND J.J. RENCIS ED., *Elsevier Applied Science*, (1993).

4. G.L. CHAHINE, "Dynamique des Bulles Non-Sphériques," *Chapter to appear in* " CAVITATION", EDITOR: J.P. FRANC, France (1994).

A.1 Technical Reports, Non Refereed Papers

1. G.L. CHAHINE, R. DURAISWAMI, AND A.N. LAKSHMINARASIMHA, "Dynamical Interactions in a Bubble Cloud," Proceedings ASME Cavitation and Multiphase Flow Forum, Portland, pp.49-54. 1991

2. G.L. CHAHINE, K. WENK, S. GUPTA, AND P. ELMORE "Bubble Formation Following Drop Impact at a Free Surface," Proceedings ASME Cavitation and Multiphase Flow Forum, Portland, pp. 63-69. 1991

3. G.L. CHAHINE, G.S. FREDERICK, AND R.D. BATEMAN, "Propeller Tip Vortex Cavitation Suppression Using Selective Polymer Injections," DYNAFLOW, INC. Technical Report 91001_1.

4. M. REBUT AND G.L. CHAHINE "Asymptotic Study of Bubble Dynamics in a Nonuniform Potential Flow," in *Proceedings, ASME Cavitation and Multiphase Flow Forum, Los Angeles 1992.*

5. R.DURAISWAMI AND G.L. CHAHINE "Analytical study of the interaction a gas bubble and a line vortex," in *Proceedings ASME Cavitation and Multiphase Flow Forum, Los Angeles, 1992.*

6. K. KALUMUCK AND G.L. CHAHINE "Large Reynolds Number Cavitating Vortex Ring Propagation and Scaling," in *Proceedings ASME Cavitation and Multiphase Flow Forum, Los Angeles, 1992.*

7. S. ZHANG, J. DUNCAN AND G.L. CHAHINE, "Dynamics of a bubble past the point of collapse," *ASME Cavitation and Multiphase Flow Forum*, Los Angeles, 1992.

8. R. DURAISWAMI AND G.L. CHAHINE, "Bubble Nuclei Size Determination via an Inverse Acoustic Scattering Technique," DYNAFLOW, INC. Technical Report 92004-1.

9. E. DELEPOULLE, and P. HAUWAERT, "Experimental and Numerical Study of the Interaction Between a Bubble and a Vortex Ring," DYNAFLOW Technical Report 6.002-10, 1991.

10. L. MAUDUIT and G. L. CHAHINE, "Asymptotic Study of Bubble Cloud Dynamics in a Slightly Compressible Fluid," DYNAFLOW Technical Report 6.002-11, July 1992.

11. J-B. VILLE AND G.L. CHAHINE, "Asymptotic Study of Bubble Dynamics in the Proximity of a Body in Potential Flow," DYNAFLOW Technical Report 6.002-12, July 1992.

12. M. MORGAN, D. ROQUELET, and G.L. CHAHINE, "Cavitation Bubble Behavior in Vortical Structures," Technical Report 6.002-13, October 1992.

13. G.L. CHAHINE, R. DURAISWAMI, AND M. REBUT, "Analytical and Numerical Study of Large Bubble/Bubble and Bubble/Flow Interactions," *Nineteenth ONR Symposium on Naval Hydrodynamics, Seoul, S. Korea*"

14. G.L. CHAHINE, G.S. FREDERICK, AND R.D. BATEMAN, "Propeller Tip Vortex Cavitation Suppression Using Selective Polymer Injections," presented at the *2nd International Symposium on Propeller and Cavitation, Hangzhou, China*

15. G. L. CHAHINE AND R. DURAISWAMI, "*Boundary Element Method for Calculating 2-D and 3-D Underwater Explosion Bubble Behavior in Free Water and Near Structures,*" NSWC Ship Structures and Protection Department Research and Development Report NSWCDD/TR-93/44, September 1993.

16. G. L. CHAHINE, E. DELEPOULLE, AND P. HAUWAERT, "Experimental and Numerical Study of the Interaction Between a Bubble and a Vortex Ring," Proceedings *Cavitation and Multiphase Flow Forum*, ed. O. Furuya, FED vol. 153, *ASME, New York*, (1993).

17. R. DURAISWAMI, "A Pseudospectral Mapping Technique for the Accurate Simulation of Viscous Flows in Complex Geometries," NASA Phase I SBIR final report, also DYNAFLOW, INC. *Technical Report 93004-1nasa.*

18. R. DURAISWAMI, C.J. GRAY, AND G.L. CHAHINE, *"A User Manual for the Axisymmetric Boundary Element Bubble Dynamics Code 2DYNAFS-PC,"* DYNAFLOW, INC. Manual 2DYNAFS-PC-β1, March 1993.

19. R. DURAISWAMI, "Bubble Nuclei Measurement via an Inverse Acoustic Scattering Technique," Proceedings *Cavitation and Multiphase Flow Forum*, ed. O. Furuya, FED vol. 153, pp. 67-74, *ASME, New York*, (1993).

20. K.M. KALUMUCK AND G.L. CHAHINE, "The Influence of Cavitation on Submerged Water Jet Velocity and Spreading," Proceedings *Cavitation and Multiphase Flow Forum*, ed. O. Furuya, FED vol. 153, *ASME, New York*, (1993).

21. A VAN DER BEKEN, R. DURAISWAMI, AND G.L. CHAHINE,"Study of Jet Instability Formation on Free Surfaces," DYNAFLOW, INC. *Technical Report, 6-002-13,* (1993).

A.2 Presentations

1. R. DURAISWAMI AND G.L. CHAHINE, "Multiple Bubble Interactions in a Slightly Compressible Liquid: Asymptotic Analysis." presented at International Conference on Industrial and Applied Mathematics, Washington D.C. July 1991

2. G.L. CHAHINE AND A.N. LAKSHMINARASIMHA, "Large Free Surface Deformations using a 3D Boundary Element Method," presented at International Conference on Industrial and Applied Mathematics, Washington D.C. July 1991.

3. R. DURAISWAMI AND A. PROSPERETTI, "Effective Equations for Sound Propagation in Fogs," presented at International Conference on Industrial and Applied Mathematics, Washington D.C. July 1991.

4. G.L. CHAHINE, R. DURAISWAMI, AND A.N. LAKSHMINARASIMHA, "Dynamical Interactions in a Bubble Cloud," ASME Cavitation and Multiphase Flow Forum, Portland, 1991.

5. G.L. CHAHINE, K. WENK, S. GUPTA, AND P. ELMORE "Bubble Formation Following Drop Impact at a Free Surface," ASME Cavitation and Multiphase Flow Forum, Portland, 1991.

6. G. L. CHAHINE, E. DELEPOULLE, AND P. HAUWAERT, "Experimental and Numerical Study of the Interaction Between a Bubble and a Vortex Ring," Proceedings *Cavitation and Multiphase Flow Forum, Washington D.C., June*, (1993).

7. R. DURAISWAMI, "Bubble Nuclei Measurement via an Inverse Acoustic Scattering Technique," Proceedings *Cavitation and Multiphase Flow Forum, Washington D.C., June*, (1993).

8. K.M. KALUMUCK AND G.L. CHAHINE, "The Influence of Cavitation on Submerged Water Jet Velocity and Spreading," Proceedings *Cavitation and Multiphase Flow Forum, Washington D.C., June*, (1993).

9. G.L. CHAHINE, K.M. KALUMUCK, AND R. DURAISWAMI, "Coupling of a Fluids BEM Code with a Structures FEM code for Fluid |Structure Interaction," *Boundary Element 15, Worcester Polytechnic Institute, Worcester, MA, August,* (1993).

10. K.M. KALUMUCK, G.L. CHAHINE, AND G.S. FREDERICK,"The Influence of Ambient Pressure and Nozzle Shape on Submerged Water Jet Velocity and Spreading," *7th American Water Jet Technology Conference, Seattle, August* 1993.

11. G.L. CHAHINE, "Bubble Interactions with Shear Flows," *IUTAM meeting on Bubble Dynamics and Interface Phenomena, Birmingham*, September 1993.

B Lists of Honors/Awards

1. Dr. Chahine was an organizer of the IUTAM meeting on Bubble Dynamics and Interface Phenomena, and presented an invited talk. This meeting was held at Birmingham in September 1993.

2. The Knapp Award for the best paper in Multiphase Flow in the ASME Journal of Fluids Engineering in 1992, was awarded to Dr. Chahine and Dr. Duraiswami,

3. Dr. Chahine was awarded a travel award by AGARD to lecture in France in 1992, 1993 and 1994.

To be Presented at the Twentieth ONR Symposium, Santa Barbara, CA, August 1994.

BUBBLE DYNAMICS AND CAVITATION INCEPTION IN NON-UNIFORM FLOW FIELDS

Georges L. Chahine
DYNAFLOW, INC.
7210 Pindell School Road
Fulton, Maryland 20759

ABSTRACT

The study of cavitation inception in non-uniform flow fields requires complex and sophisticated methods. These need to account for the interaction between the nuclei and the underlying flow, often in the neighborhood of walls, in shear layers, in separated regions, and in turbulent flow fields. This paper describes our contributions towards the development of techniques for the study of fully 3D bubble/bubble and bubble/flow interactions. With the advent of fast and affordable computers such techniques have become more and more practical, and can be effectively used as tools for the description of large scale bubble/vortical flow field interaction simulations.

INTRODUCTION

In order to achieve a cavitation free design of a submerged body such as a propeller, or to test a scale model in a laboratory environment, it is necessary to establish criteria for cavitation inception and to define scaling parameters between models and full scale. The traditional cavitation number based on the engineering definition of cavitation inception: *a liquid flow experiences cavitation if the local pressure drops below the liquid vapor pressure* is obviously not always adequate. A large number of studies over the years have aimed to replace this criterion with a more adequate one based on spherical bubble dynamics, following introduction of the concept of *critical pressure* to replace *vapor pressure*. In fact, cavitation very seldom occurs under the format of spherical bubble growth and collapse. Cavitation inception appears in several forms [1, 2], the most recognized being :

(a) Explosive growth of individual bubbles,

(b) Sudden appearance of transient cavities or "flashes" on boundaries,

(c) Sudden appearance of attached partial cavities, or sheet cavities,

(d) Explosive growth of bubble clouds and attached cavities or a vibrating surface.

(e) Sudden appearance of rotating filaments, or vortex cavitation.

Upon further scrutiny, all of these forms can be related to the explosive growth of *pre-existing* nuclei in the liquid when subjected to pressure drops generated by various forms of local pressure disturbances. These are either acoustically imposed pressure variations, uniform pressure drops due to local liquid accelerations, or strongly non-uniform pressure fields due to streamwise or transverse large vortical structures. The presence of nuclei or *weak spots* in the liquid is therefore, essential for cavitation inception to occur. Indeed, a pure liquid free of nuclei can sustain very large tensions, in the hundreds of atmospheres, before a cavity can be generated through separation of the liquid molecules. Any fundamental analysis of cavitation inception has to start from the observation that, any real liquid contains nuclei which when subjected to variations in the local ambient pressure will respond dynamically by oscillating and eventually *growing explosively* (i.e. *cavitate*).

In most real flow conditions which involve non-uniform flow fields the conditions leading to cavitation inception involve subjection of the cavitation nuclei not only to significant pressure drops, but also to equally significant pressure and/or velocity gradients. The spherical model, despite all the help it has provided over the years, fails to address these conditions because it assumes that the bubble follows the flow, and that its size remains smaller than the length scales of the pressure and velocity fluctuations. However, detailed and precise observations of flow fields in even the most simplified flow conditions (hemispherical body, simple two-dimensional blades, linear tip vortices, vortex rings, submerged jets, etc.) show that the velocity and pressure fluctuations in these flow fields are on the scale of strong eddies of the same size as the microbubbles present in the liquid. These observations gain further importance

when one notices that all laboratory scale model experiments are inevitably done under conditions in which the eddies and the bubbles are not scaled in the same proportions (if bubbles are scaled at all). The study of bubble dynamics in non-uniform flow fields then stands out as being as fundamental and important as spherical bubbles have been for the past decades.

In this paper we describe our efforts towards the understanding of this problem and complement our contribution at the previous symposium [3]. To do so we consider three fundamental problems of relevance to real flow field configurations: 1. bubble dynamics in the boundary layer of a flat wall, 2. bubble dynamics in the boundary layer of a head-form, and 3. Bubble dynamics in a vortical flow field. This should enable one to deduce criteria for cavitation inception accounting for large bubble deformation and splitting. In addition, in the case of the bubble dynamics in a vortex flow, we present schemes to model flow modification by the bubble dynamics.

SOLUTION METHOD

One of the numerical methods that has proven to be very efficient in solving the types of free boundary problems associated with bubble dynamics is the Boundary Element Method. Several investigators [4, 5, 6, 7] used this method in the solution of axisymmetric problems of bubble growth and collapse near boundaries. This method was extended to three-dimensional bubble dynamics problems by Chahine *et al.* [8, 9]. We describe here the model, then apply it to various cases of bubbles in a vortical flow. More analytical methods such as those we presented at the previous ONR Symposium [3], give very good insight into the dynamics but are limited to small bubble/flow field interactions.

Statement of the problem

Let us consider the dynamics of bubbles oscillating in a non-uniform flow field ("*basic flow*") of velocity $\mathbf{V}_o$ that is known (or determined by the problem solution) and which satisfies the incompressible Navier Stokes equations:

$$\frac{\partial \mathbf{V}_o}{\partial t} + \mathbf{V}_o \cdot \nabla \mathbf{V}_o = -\frac{1}{\rho}\nabla P_o + \nu \nabla^2 \mathbf{V}_o \,. \quad (1)$$

Without any additional assumptions, in the presence of oscillating bubbles the resulting velocity field, given by $\mathbf{V}$, also satisfies the incompressible Navier Stokes equation:

$$\frac{\partial \mathbf{V}}{\partial t} + \mathbf{V} \cdot \nabla \mathbf{V} = -\frac{1}{\rho}\nabla P + \nu \nabla^2 \mathbf{V} \,. \quad (2)$$

Let us then define the ***bubble flow*** velocity and pressure variables, $\mathbf{V}_b$ and P_b, as follows:

$$\mathbf{V}_b = \mathbf{V} - \mathbf{V}_o, \qquad P_b = P - P_o. \quad (3)$$

We now consider the case where, because we are interested in cavitation bubbles with high but subsonic bubble wall velocities, the "***bubble flow***" field is potential.

$$\mathbf{V}_b = \nabla \Phi_b, \qquad \nabla^2 \Phi_b = 0, \quad (4)$$

We now subtract (1) from (2) accounting for (4) to obtain

$$\nabla \Psi = \mathbf{V}_b \times (\nabla \times \mathbf{V}_o), \quad (5)$$

$$\Psi = \frac{\partial \Phi_b}{\partial t} + \frac{1}{2} \mid \mathbf{V}_b \mid^2 + \mathbf{V}_o \cdot \mathbf{V}_b + \frac{P_b}{\rho}. \quad (6)$$

This equation, once integrated, is to replace the classical unsteady Bernoulli equation.

The assumption of potential "***bubble flow***" may imply that no new vorticity can be generated by the bubble behavior with the chosen model. However, if we allow the basic flow to interact with the bubble dynamics and be modified by it in a unrestricted and rotational manner, as done later below, we can recover generation and modification of vorticity by the presence and dynamics of the bubble.

For the particular cases considered in this paper, the following integrations can be made. In the case of a flat wall boundary layer flow such that all velocity vectors are parallel to the wall, and depend only on the distance to the wall, $\mathbf{V}_o = f(z).\mathbf{e}_x$, where $\mathbf{e}_x$ is the unit vector in the flow direction, and $\mathbf{e}_z$ is the unit vector in the direction perpendicular to the wall, Equation (6) becomes:

$$\Psi = \textit{constant in the } \mathbf{e}_y \textit{ direction}. \quad (7)$$

For the case where the basic flow field is composed of linear vortices of axis direction, $\mathbf{e}_z$, $\mathbf{V}_o = V_\theta.\mathbf{e}_\theta$, with V_θ the tangential velocity, Equation (6) becomes:

$$\Psi = \textit{constant in the } \mathbf{e}_z \textit{ direction} \,. \quad (8)$$

Bubble Flow Equations

As stated above, we consider the cases where the presence of bubbles in the flow has significant effects, that is cases where bubble volume variations are not negligible. This implies large but subsonic bubble wall velocities. Therefore, we consider a ***bubble flow*** that is potential.

The solution must satisfy initial conditions and boundary conditions at infinity, at the bubbles walls and at the boundaries of any nearby bodies. At all moving or fixed surfaces (such as a bubble surface or a nearby boundary) an identity between fluid velocities normal to the boundary and the normal velocity of the boundary itself is to be satisfied:

$$\nabla\Phi_b \cdot \mathbf{n} = \mathbf{V_s} \cdot \mathbf{n}, \tag{9}$$

where $\mathbf{n}$ is the local unit vector normal to the bubble surface and $\mathbf{V_s}$ is the local velocity vector of the moving surface.

The bubble is assumed to contain noncondensible gas of partial pressure, P_g, and vapor of the surrounding liquid of partial pressure, P_v. Vaporization of the liquid occurs at a fast enough rate so that the vapor pressure may be assumed to remain constant throughout the simulation and equal to the equilibrium vapor pressure at the liquid ambient temperature. In contrast, since time scales associated with gas diffusion are very large, the amount of noncondensible gas inside the bubbles remains constant and the gas pressure is assumed to satisfy the polytropic relation,

$$P_g \mathcal{V}^k = constant, \tag{10}$$

where $\mathcal{V}$ is the bubble volume and k the polytropic constant, with $k = 1$ for isothermal behavior and $k = c_p/c_v$ for adiabatic conditions.

The pressure in the liquid at the bubble surface, P_L, is obtained at any time from the following pressure balance equation:

$$P_L = P_v + P_{g_0}\left(\frac{\mathcal{V}_o}{\mathcal{V}}\right)^k - C\gamma, \tag{11}$$

where P_{g_0} and $\mathcal{V}_o$ are the initial gas pressure and volume respectively, γ is the surface tension, C is the local curvature of the bubble, and $\mathcal{V}$ is the instantaneous value of the bubble volume. In the numerical procedure P_{g_0} and $\mathcal{V}_0$ are given quantities at $t = 0$.

3-D Boundary Integral Method

In order to render possible the simulation of single or multiple bubble behavior in complex geometry and flow configurations including the full non-linear boundary conditions, a three-dimensional Boundary Element Method was developed and implemented [8, 9, 10, 11]. This method was chosen because of its computational efficiency. By considering only the boundaries of the fluid domain it reduces the dimension of the problem by one. This method provides a solution of the Laplace equation (4) in terms of Green's equation, which provides Φ_b^P anywhere in the domain of the fluid (field points P) if the velocity potential, Φ_b , and its normal derivatives are known on the fluid boundaries (points M),

$$\int_s \left[\frac{-\partial\Phi_b}{\partial n}\frac{1}{|\mathbf{MP}|} + \Phi_b\frac{\partial}{\partial n}\frac{1}{|\mathbf{MP}|}\right] ds = \Omega\Phi_b^P, \tag{12}$$

where Ω is the solid angle under which P sees the fluid. $\Omega = 4\pi$ if P is a point in the fluid; $\Omega = 2\pi$ if P is a point on a smooth surface, and $\Omega < 4\pi$ if P is a point at a sharp corner of the surface.

If the field point is selected to be on the surface of any of the bubbles or on the surface of the nearby boundaries, then a closed set of equations can be obtained and used at each time step to solve for values of $\partial\Phi_b/\partial n$ (or Φ_b) assuming that all values of Φ_b (or $\partial\Phi_b/\partial n$) are known at the preceding step.

Discretization

To solve Equation (12) numerically, it is necessary to discretize each bubble into panels, perform the integration over each panel, and then sum up the contributions to complete the integration over the entire bubble surface. To do this, the initially spherical bubbles are discretized into geodesic shapes using flat, triangular panels. To evaluate the integrals over any particular panel, a linear variation of the potential and its normal derivative over this panel is assumed. In this manner, both Φ_b and $\partial\Phi_b/\partial n$ are continuous over the bubble surface, and are expressed as a function of the values at the three nodes which delimit a particular panel.

Equation (12) then becomes a set of N equations (N is the number of discretization nodes) of index i of the type:

$$\sum_{j=1}^{N} A_{ij}\frac{\partial\Phi_{b,j}}{\partial n} = \sum_{j=1}^{N} B_{ij}\Phi_{b,j} - \Omega\Phi_{b,i}, \tag{13}$$

where the matrices A_{ij} and B_{ij} are the discrete equivalent of the integrals in (12).

Curvature and tangential velocity computations

In order to proceed with the computation of the bubble dynamics several quantities appearing in the above boundary conditions need to be evaluated at each time step. The bubble volume presents no particular difficulty, while the unit normal vector, the local surface curvature, and the local tangential velocity at the bubble interface need further development. In order to compute the curvature of the bubble surface, a three-dimensional local bubble surface

fit, $f(x,y,z) = 0$, is first computed. The unit normal at a node can then be expressed as:

$$\mathbf{n} = \pm \frac{\nabla f}{|\nabla f|}, \tag{14}$$

with the appropriate sign chosen to insure that the normals are always directed towards the fluid. The local curvature is then computed using

$$\mathcal{C} = \nabla \cdot \mathbf{n}. \tag{15}$$

To obtain the total fluid velocity at any point on the surface of the bubble, the tangential velocity, $\mathbf{V}_t$, must be computed at each node in addition to the normal velocity, $\mathbf{V}_n = \partial\Phi_b/\partial n\ \mathbf{n}$. This is also done using a local surface fit to the velocity potential, $\Phi_l = h(x,y,z)$. Taking the gradient of this function at the considered node, and eliminating any normal component of velocity appearing in this gradient gives a good approximation for $\mathbf{V}_t$:

$$\mathbf{V}_t = \mathbf{n} \times (\nabla\Phi_l \times \mathbf{n}). \tag{16}$$

Time stepping

The basic procedure can then be summarized as follows. With the problem initialized and the velocity potential known over the surface of the bubble, an updated value of $\partial\Phi_b/\partial n$ can be obtained by performing the integrations in (12) and solving the corresponding matrix equation (13). $D\Phi_b/Dt$ is then computed using the "modified" Bernoulli equation (7) or (8). Using an appropriate time step all values of Φ_b on the bubble surface can then be updated using Φ_b at the preceding time step and,

$$\frac{D\Phi_b}{Dt} = \frac{\partial\Phi_b}{\partial t} + \left(\frac{\partial\Phi_b}{\partial n}\mathbf{n} + \mathbf{V_t}\right) \cdot \nabla\Phi_b. \tag{17}$$

In the results presented below the time step, dt, is based on the ratio between the length of the smallest panel side, l_{min} and the largest node velocity, V_{max}. This choice limits the motion of any node to a fraction of the smallest panel side. It has the great advantage of constantly adapting the time step, by refining it at the end of the collapse – where l_{min} becomes very small and V_{max} very large – and by increasing it during the slow bubble size variation period. New coordinate positions of the nodes are then obtained using the displacement:

$$d\mathbf{M} = \left(\frac{\partial\Phi_b}{\partial n}\mathbf{n} + V_t\mathbf{e}_t + \mathbf{V}_o\right) dt, \tag{18}$$

where $\mathbf{n}$ and $\mathbf{e}_t$ are the unit normal and tangential vectors. This time stepping procedure is repeated throughout the bubble growth and collapse, resulting in a shape history of the bubble.

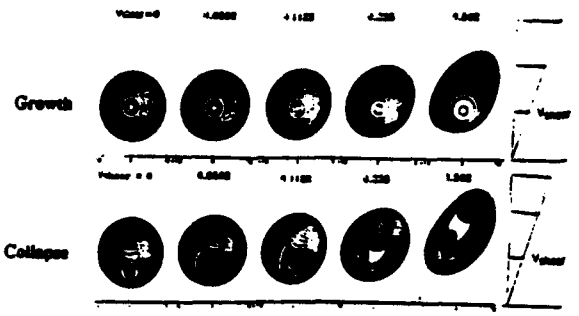

Figure 1: Influence of a linear shear velocity on the collapse of a bubble near a solid wall. V_{shear} is normalized with the Rayleigh velocity $\sqrt{(\Delta P/\rho)}$.

The developed code and method were validated using comparisons with known results in the literature for spherical or axisymmetric bubble configurations. Convergence of the 2-D and 3-D model were then established for cases of interest using increased numbers of grid points. Such detailed comparisons can be found in [12].

BUBBLE COLLAPSE NEAR A FLAT WALL IN A SHEAR FLOW

In most previously published studies of bubble dynamics near solid walls, the wall was considered rigid and infinite, and the liquid quiescent in the absence of the bubble. The only asymmetry in the problem is then due to the presence of the infinite wall, and the bubble behaves axisymetrically. In this case, the bubble forms a reentering jet perpendicular to the plate during the collapse phase. Such a model has been extensively used by many authors both for experimental and analytical/numerical studies mainly aimed at studying erosion due to cavitation bubbles, and was justified in the absence of more advanced techniques. It is however, obvious that this configuration is rarely encountered in practical cavitating flow fields.

Figure 1 shows the results obtained with a relatively simple model for the wall flow using our BEM code **3DynaFS**. The velocity is assumed to vary linearly from a value, V_{shear} at a distance R_{max} from the wall to zero at the wall. The *"basic"* pressure, P_{amb}, is assumed constant across the shear layer and is an input of the problem as is the initial gas

pressure inside the bubble, P_{go}. The bubble center is located at a distance L from the wall. The bubble behavior strongly depends on the parameter, $\epsilon = R_{max}/L$, characterising wall proximity, and on a shear parameter, χ, ratio between the shear velocity, V_{shear} , and a characteristic bubble dynamics velocity: $\chi = V_{shear}/\sqrt{\Delta P/\rho}$.

Figure 1 shows selected bubble contours of the bubble during its growth and collapse. These are cross cuts of the 3-D bubble shapes obtained along the plane of symmetry (perpendicular to the wall and parallel to the flow direction). The presence of shear is clearly apparent during the bubble growth: downstream bubble points move away from the initial bubble center much faster than upstream points. This follows the simple intuitive reasoning that each point on the bubble surface moves with a velocity composed of the velocity it would have in absence of shear plus the local velocity of the *"basic flow"*. For instance the farthest upstream bubble points sees its undisturbed growth velocities increased by V_{shear} while the farthest downstream point has its velocity decreased by V_{shear}. The opposite is true during the collapse phase. As can be seen by comparing the various cases of increasing χ in Figure 1 "stretching" of the bubble in the flow direction increases with the shear intensity.

During the bubble collapse an even more significant effect of the presence of shear on the bubble dynamics can be seen. The formation and development of the reentering jet seems to be very dramatically modified. Even when the shear velocity is very small, the jet is very much delayed and weakened in comparison with the case of the absence of shear. Let us note that in the absence of a *"basic flow"* the jet is directed towards the wall, and that in the other extreme case, i.e. no wall and uniform flow, the reentering jet is directed upstream. For a finite value of χ one would expect a jet angled towards the wall and upstream.

For increased values of χ, the bubble deformation and elongation is enhanced during the growth. During collapse for small values of χ, the re-entering jet is deviated for increasing values of χ from the perpendicular to the plate. For larger values of χ, the re-entering jet formation is totally modified and the bubble tends to cut itself into two bubbles. In addition, an interesting lifting effect is observed. The bubble centroid is seen to move further and further away from the wall with increasing values of χ. This is probably due to an interaction between the wall shear flow and the bubble rotation.

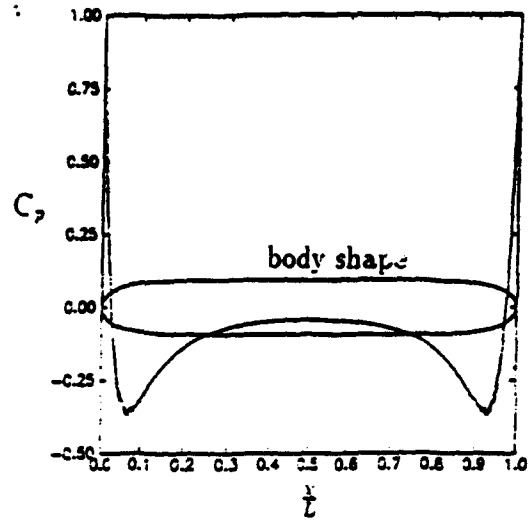

Figure 2: The hemispherical Rankine body shape used in the simulations and the corresponding pressure coefficient, c_p, distribution.

BUBBLE DYNAMICS NEAR A HEMISPHERICAL BODY

Cavitation on hemispherical bodies has been studied for a long time. The Schiebe body for instance has been used in various laboratories for studying cavitation scaling effects. More recently, an extensive program for the study of cavitation inception for various Schiebe body sizes was conducted at Caltech and in the Large Cavitation Tunnel (LCC) in Memphis [13, 14]. Very interesting observations of bubble behavior on these headforms were made. These observations indicated strong interaction between the bubbles and the boundary layer on the headform. Large deviations from spherical bubble shapes were observed, including bubble splitting and breakup, formation of a weak reentering jet during bubble growth, and formation of long 'secondary cavitation' or a trail behind the bubble. We present in this section a numerical simulation of these effects using the methods described above. The objective here is not to reproduce all the characteristics of the experimental studies, but to observe which characteristics can be captured by the present solution method.

To do so, the flow field around the Schiebe body was simulated using a very elongated Rankine oval closed body. Figure 2 shows the hemispherical body shape and the corresponding pressure distribution along the body. One can clearly observe the presence of a very sharp pressure drop at the upstream body at location $x/L = 0.05$, followed by a pressure rise which is maintained until the downstream location, $x/L = .95$, where a second symmetric pressure drop is present. The *"basic flow"* for the problem here is defined as that due to the superposition of

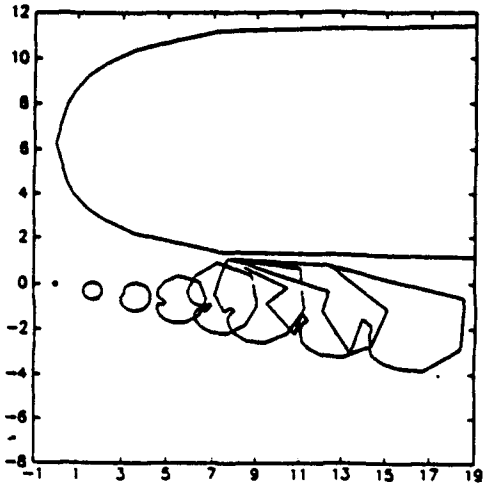

Figure 3: Simulation of the behavior of a bubble near a hemispherical Rankine body shape showing formation of indentation and trail.

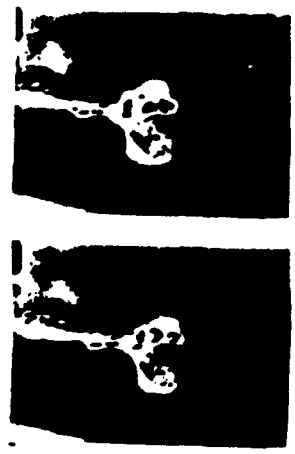

Figure 4: Bubble behavior in the boundary layer of a cambered lifting surface showing the formation of a long trail behind the bubble (from [15])

a uniform flow, V_∞, and two sources of intensity Q. To maintain the body shape for various values of the uniform flow velocity, the ratio V_∞/Q was maintained constant. In order to account for the presence of a boundary layer on the body, this inviscid flow field was modified arbitrarily in the neighborhood of the hemispherical body shape, in such a way that the velocity was decreased linearly to zero on the body.

In the following figures, the selected Rankine body had a radius of 4 inches, and a length of 55 inches. In the simulations we have conducted the bubble sizes were varied from 10 to 1000μm, and the flow velocities from 0 to 20 m/s. The cases presented here are selected because they reproduce many of the characteristics of the experimental observations in [13, 14]. Figure 3 shows bubble contours at various times, and illustrates clearly several key experimental observations: the formation of an indentation on the bubble top while the bubble is being convected downstream by the hemispherical body, the formation of a wedge shape on the downstream portion of the bubble, the lifting of this portion of the bubble from the wall, and the formation of a 'trail' behind the bubble during its motion.

The indentation appears due to the opposing effects on the upstream bubble portion of the basic flow and the bubble growth velocity. This bubble portion moves away the least from the initial bubble center. With time due to the presence of the shear, as in the flat wall case, this bubble region rolls away from the body into the flow direction and, then, encounters a pressure rise which enhances the motion of the indentation towards the body wall. On the other hand, the bubble points that penetrate the simulated 'boundary layer' of the body, find themselves quasi-trapped in that layer. As a result, these points lag behind the rest of the bubble and a bubble 'trail' appears. With the simple model used here, this trail differs from that in the experiments by the fact that it issues from the center part of the bubble and not from its side. This could also be a scaling effect, in the sense of differing ratios between the bubble and the body sizes. Figure 4 taken from observations on a lifting surface [15] shows a trail which resembles very much those obtained by the present numerical simulations.

Figure 5 shows the case of a bubble where the rolling motion of the bubble points is not strong enough for the reentering point to relocate itself above the wall. Instead, the indentation occurs early on in the downstream portion of the bubble leading to a fission of the bubble and the formation of a long trail.

Figure 6 shows the case where fission of the front of the bubble is very obvious. This case resembles very much to the experimental observations, and precedes bubble collapse and rebound.

BUBBLE /VORTEX INTERACTIONS

A fundamental aspect of cavitation in turbulent flows, and in boundary and shear layer flows concerns the interaction between bubbles and vortices. A simple example is that of a 'tip vortex' cavitation on propellers and three-dimensional airfoils. The interaction between bubbles and vortex flows is in fact of relevance to several fluid engineering problems involving submerged jets, flows behind constrictions and orifices, in wakes and in separated flow areas.

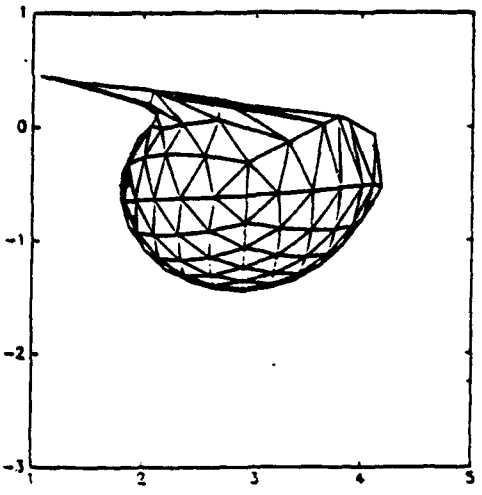

Figure 5: 3-D view of the bubble shape near a hemispherical Rankine body shape after formation of a trail.

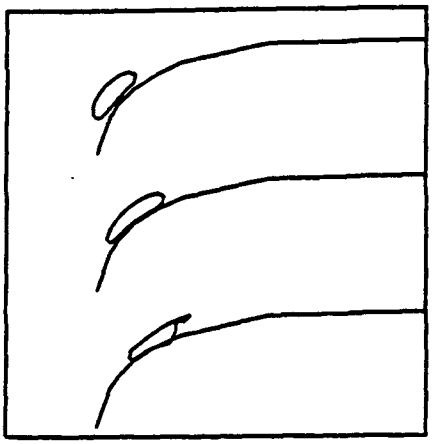

Figure 6: Bubble end splitting near a hemispherical Rankine body shape.

Mechanistic Description

When a bubble approaches a region of high vorticity in a liquid, it is accelerated towards the center of rotation due to the highly asymmetric pressure field. On its path the bubble experiences a decreasing ambient pressure which leads to an increase in its volume. Simultaneously, since the non uniformity of the pressure field increases with proximity to the vortex axis, bubble shape deformation increases.

Over the last decade several investigators have addressed the phenomenon of bubble capture by a vortex [16, 18, 19]. These studies made the simplifying assumption that the bubble, even though able to undergo volume changes, remains spherical. In addition, the type of interactions they considered was one-sided, since they did not consider vortex flow modification by the presence and behavior of the bubble. More recently we considered a broader approach where bubble deformation and motion were coupled while neglecting flow field modification by the bubble presence [10, 20]. This study showed that the pressure gradient across the bubble can lead to significant departure from bubble sphericity, and led to the suggestion that the deformation and later splitting of the bubble during its motion towards the vortex center is, in addition to its volume change, a main source of noise in tip vortex cavitation. This appears to explain the reason for the location of tip vortex noise at cavitation inception very close to the blade [22], and is in agreement with recent observations by [23] about bubble capture in tip vortex cavitation.

One can distinguish three phases in the interactive dynamics of bubbles and vortices: a) bubble capture by the vortex, b) interaction between the vortex and the bubble, c) dynamics of bubbles elongated only on the vortex axis. We consider these aspects below.

Order of magnitude considerations

In order to discuss the problem of bubble capture and behavior in a line vortex let us consider a Rankine vortex flow field. We define Γ as the vortex line circulation, and u_θ the only non-zero velocity component. For distances r smaller than R_c, the radius of the viscous core, the flow has a solid body rotation behavior while for distances r larger than R_c the flow behaves as an ideal inviscid irrotional vortex:

$$u_\theta = \frac{\Gamma r}{2\pi R_c^2}, \quad r \le R_c; \quad u_\theta = \frac{\Gamma}{2\pi r}; \quad r \ge R_c. \quad (19)$$

For such a flow the pressure field, $p(r)$, is known. Its value and the corresponding pressure gradient are

given by the following normalized expressions.

$$\begin{aligned} \bar{p}(\bar{r}) &= 1-\Omega/\bar{r}^2; \quad \partial\bar{p}/\partial\bar{r} = 2\Omega/\bar{r}^3; \quad \bar{r} \geq 1, \\ \bar{p}(\bar{r}) &= 1-\Omega\left(2-\bar{r}^2\right); \quad \partial\bar{p}/\partial\bar{r} = 2\Omega\bar{r}; \quad \bar{r} \leq 1 \end{aligned} \tag{20}$$

with

$$\bar{r} = r/R_c; \quad \bar{p}(\bar{r}) = p(r)/p_\infty. \tag{21}$$

The parameter , Ω, defined as

$$\Omega = \frac{1}{2}\rho\left(\frac{\Gamma}{2\pi R_c}\right)^2/p_\infty \ , \tag{22}$$

characterizes the intensity of the pressure drop due to the rotation relative to the ambient pressure, p_∞.

The pressure gradient steepens in the inviscid region when the viscous core is approached, achieves its maximum at $\bar{r} = 1$, and levels off in the viscous core close to the vortex axis. In this pressure field, the bubble experiences a higher pressure on its right side than on its left side, the difference being greater the larger the bubble is. Similarly, the bubble is 'sheared', since fluid particles on the bubble/liquid interface experience different velocities. The type of shearing action depends on the position of the bubble relative to the viscous core/inviscid fluid boundary, R_c. If the bubble is fully immersed in the inviscid region of the flow, fluid particles on its left side will experience larger velocities, while if it is fully immersed in the solid body rotation region of the flow, fluid particles on its right side will experience larger velocities. The most complex situation is when the bubble is partly in the viscous core and partly in the inviscid region.

The degree of bubble shape deviation from sphericity is a function of the relative orders of magnitude of the pressure gradient, the bubble wall acceleration due to volume change, and surface tension forces. An evaluation of the bubble wall acceleration can be obtained from a characteristic bubble radius, R_b, and from the Rayleigh time, τ_R, time needed for an empty bubble to collapse from its radius R_b to 0, under the influence of the pressure outside the bubble. If we take for characteristic outside local pressure the pressure at $r = R_c$, the characteristic bubble wall acceleration, γ_{growth}, is :

$$\gamma_{growth}|_{r=R_c} \simeq p_\infty(1-\Omega)/\rho R_b \tag{23}$$

This value is to be compared with the acceleration force $\gamma_{gradient}$ due to the pressure gradients expressed in (20):

$$\gamma_{gradient}|_{r=R_c} \simeq 2\Omega p_\infty/\rho R_c, \tag{24}$$

The ratio between these two accelerations is:

$$\left.\frac{\gamma_{gradient}}{\gamma_{growth}}\right|_{r=R_c} = \frac{2R_b}{R_c}\cdot\frac{\Omega}{1-\Omega} \tag{25}$$

This expression underlines the importance between the ratio of characteristic bubble size R_b, to viscous core size R_c . Keeping the surface tension parameter the same, the larger the ratio (25) is, the more important bubble deformation will be. *This remark has important implications concerning scale effects where R_b and R_c do not increase in the same proportion between model and full scale*, since in most practical cases bubble distributions and sizes are uncontrolled and typically cannot be scaled much, while sizes of the vortical regions depend on the selected geometry and velocity scales.

The ratio (25) is only an indication of the relative importance of bubble growth and slip forces at a given position. In fact the relative importance of these competing forces changes during the bubble capture process. For instance, the acceleration of the bubble toward the vortex axis increases with its proximity to the viscous core while the growth rate tends toward a constant value (decreasing pressure gradient). This indicates that strong deformation becomes predominant relative to volume change when either the bubble is very close to the axis or when Ω becomes large.

Another important physical factor which affects bubble shape is the surface tension. A normalized value of this pressure can be obtained as a ratio of the surface tension pressure and either the pressure difference between the inside and the outside of the bubble, or the amplitude of the variations of the local pressures (pressure gradients) around the bubble. The first number, W_{e_1}, is given by:

$$W_{e_1} = R_b\left[p_i - p_\infty(1-\Omega)\right]/\gamma, \tag{26}$$

where p_i is the pressure inside the bubble. The second number, W_{e_2}, is given by:

$$W_{e_2} = R_b\left(\partial p/\partial r\right)/\left(\gamma/R_b\right), \tag{27}$$

which can be written for $r = R_c$:

$$W_{e_2} = W_{e_1}\frac{2\Omega}{p_i/p_\infty - (1-\Omega)}\frac{R_b}{R_c}. \tag{28}$$

For small values of either of these two numbers, surface tension forces are predominant and prevent bubble distortion and deviation from sphericity. Expressions (28) shows that this is possible only if Ω is small and if R_b is much smaller than R_c. Therefore, as for the discussion on the acceleration forces, one should expect larger bubble deformations for strong vortex circulations and large bubbles.

Bubble capture by a vortex

Despite several significant contributions to the study of bubble capture by a vortex, to our knowledge no complete approach has yet been undertaken. The complexity of the full problem due to bubble deformation during its capture has led the various contributors to neglect one or several of the factors in play, and therefore to only investigate the influence of a limited set of parameters.

The order of magnitude of the bubble capture time by the vortex can be easily obtained [16, 17] if one considers, the case where the rate of change of the bubble volume is negligible relative to the other terms. In this case, the distance between the sphere center and the vortex center, $\zeta(t)$, is given by:

$$\bar{\zeta}(\bar{t}) \simeq \sqrt{1 + (\overline{v_{\theta o}}^2 - 3)\,\bar{t}^2} \leq \sqrt{1 - 3\bar{t}^2}, \qquad (29)$$

where ζ is normalized with the initial bubble position, ζ_o, time is normalized with $(2\pi\zeta_o^2/\Gamma)$, and $\bar{v}_{\theta o}$ is the initial bubble tangential velocity normalized by $(\Gamma/2\pi\zeta_o)$.

The capture time, T_c, for a bubble initially at rest in the fluid ($\overline{v_{\theta o}} = 0$) is therefore of the order:

$$\bar{t}_c \simeq \sqrt{\frac{1}{3}}; \qquad or \qquad T_c \simeq \frac{2\pi\zeta_o^2}{\Gamma\sqrt{3}}. \qquad (30)$$

In fact, for a sphere, only viscous friction forces are responsible for bubble entrainment with the flow. The characteristic time of viscous effects, or the time needed by the bubble to be entrained by the flow is

$$T_\nu = a_o^2/\nu. \qquad (31)$$

The qualitative nature of the capture depends on the relative size between T_c and T_ν.

If $T_c \gg T_\nu$ the capture time is too long, viscous effects are predominant, and the bubble is entrained by the liquid and it swirls around the vortex while approaching the center very slowly.

If $T_c \ll T_\nu$ the opposite situation occurs. Viscous effects are very slow to take effect and the bubble is practically sucked into the vortex and moves towards its center almost in a purely radial fashion.

Finally, for $T_c \approx T_\nu$ entrainment by the liquid and attraction towards the center of the vortex occur on the same time scale. Therefore, the bubble approaches the axis in a spiral fashion.

The above reasoning allows one to define a "*violent capture radius*" around the vortex which is bubble radius dependent. A bubble of radius a_o will be sucked in by the vortex if it is within the radial distance $R_{capture}$:

$$R_{capture} = a_o \left(\frac{\Gamma\sqrt{3}}{2\pi\nu}\right)^{\frac{1}{2}}. \qquad (32)$$

This implies for a tip vortex flow field, for instance, that only nuclei present in a small 'window' are rapidly attracted by the vortex and strongly interact with it, which explains difficulty in observing with some precision tip vortex cavitation inception events.

Numerical Results: Large bubble growth rate, low surface tension

As expected from the discussion presented above numerical simulations using the fully three-dimensional numerical code **3DynaFS** reveal potential for strong bubble deformation during capture by a vortex. The numerical results indicate that this is the case for a very wide range of bubble sizes and initial values of the pressure difference between the inside and the outside of the bubble.

Figure 7 shows bubble behavior in the case where the ratio between the pressure inside the bubble and the ambient pressure is significantly large. $p_i/p_\infty \simeq 584$. This would be the case where the bubble in equilibrium in a high ambient pressure environment is suddenly subjected to the flow field of a vortex, as for instance when a propeller tip vortex suddenly captures a cavitation bubble [23, 24]. In a Cartesian system of coordinates, the bubble is initially centered at (0,0,0), and the line vortex is parallel to the Z axis, at $\overline{X} = X/R_{max} = 2R_{max}$ is the maximum size the bubble would have if allowed to grow under the same pressure difference in an infinite medium). The core size is $4R_{max}$. With this geometry the bubble center remains in the plane $Z = 0$.

Figure 7*a* gives a projected view of the bubble in the XOY plane at different instants. The observer is looking down on the XOY plane from very far on the Z axis. The bubble is seen spiraling around the vortex axis while approaching it. At the same time, due to the presence of the pressure gradient, the bubble strongly deforms and a reentering jet is formed directed towards the vortex axis, indicating the presence of a much larger dynamic pressure on the bubble side opposite to the vortex axis.

Figure 7*b* shows a projected view of the same bubble in the YOZ plane seen from the OX axis. Here some moderate elongation of the bubble is observed along the axis of the vortex as well as a very distinct side view of the re-entrant jet. *This result is totally contrary to the usually held belief that bubbles*

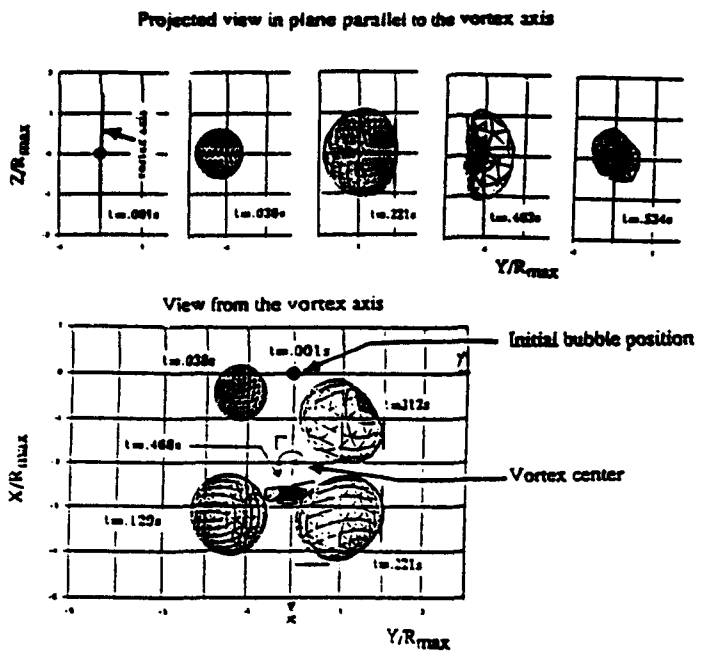

Figure 7: 3D bubble shapes at various times. Bubble initially at the origin of coordinate and vortex at $X = 2R_{max}$. $\Omega = 0.474$, $p_i/p_\infty = 584.3$, $R_c/R_{max} = 4$. Projected view a) in the XOY plane; b) in the XOZ plane.

constantly grow during their capture until they reach the axis and elongate along it.

Figure 8 shows in the XOY plane perpendicular to the vortex axis the motion of two particular points on the bubble, A and B, initially along OY. Also shown is the motion of the midpoint, C. While C seems to follows a path similar to the classical logarithmic spiral, A and B can follow more complicated paths, even moving away from the vortex axis at some point in time for case (b) where the vortex axis was initially at $X = 1$.

Small growth rate and surface tension

Figure 9 considers the influence of bubble size on bubble behavior during the capture process. In all three cases shown in the figure a ratio between the pressures inside and outside the bubble equal to one is considered, $p_i/p_\infty = 1$. In all cases, the viscous core radius is chosen to be $R_c = 2.2\ mm$, while the initial distance between the vortex center and the center of each bubble is chosen to be $\zeta_o \simeq 1.5R_c = 3.2\ mm$. The dimensions shown are normalized with the initial bubble radius for each case. The circulation in the vortex is chosen to correspond to a practical value for the case of a tip

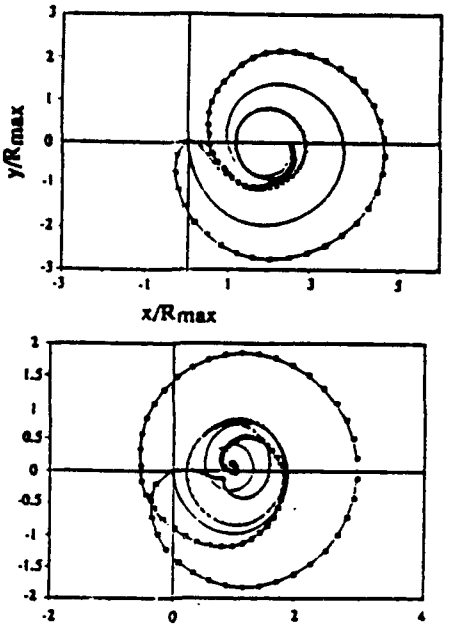

Figure 8: Motion of points A and B initially on axis OX, and mid point C, versus times. $\Omega = 0.474$, $p_i/p_\infty = 584.3$, $a_c/R_{max} = 4$. Vortex at a) $X = 2R_{max}$; b) $X = R_{max}$.

vortex behind a foil, such as in the experiments described in [23, 24], $\Gamma = 0.152\ m^2/s$. Three bubble sizes are considered: 10 μm, 100 μm and 1000 μm. As expected, bubble deformation increases with the bubble size. The deformation is small for a_o=10 μm, becomes very significant for a_o=100 μm, and is extremely important for a_o=1000 μm. In all cases, the bubbles, while remaining in the inviscid region, are seen to be sheared very strongly by the flow. The smaller bubbles appear to deform in the expected way in a shear flow. The larger bubble case (a_o=1000 μm) shows extreme bubble elongation and wrapping around the viscous core region.

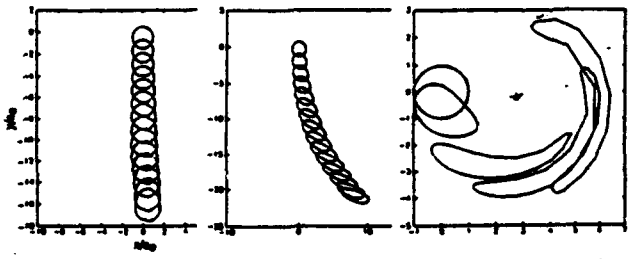

Figure 9: Bubble contours at various times. $\Gamma = 0.1527 m^2/s$, $p_i = p_\infty$, $a_c = 2.2mm$, vortex at $X = 3.2mm$, with a_o = a) 10μm. b) 100μm. c) 1000μm.

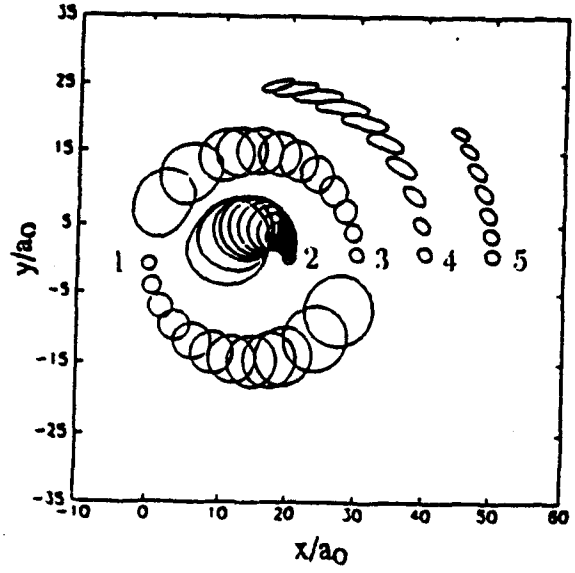

Figure 10: Behavior of 5 bubbles in a vortex line flow - Contour shapes at various times. The vortex line is perpendicular to the page and centered on $Y = 1.5mm$. $R_c = 2.2mm$, $\Gamma = 0.1573m^2/s$. $\Omega = 0.872$. All bubbles have $a_0 = 100\mu m$.

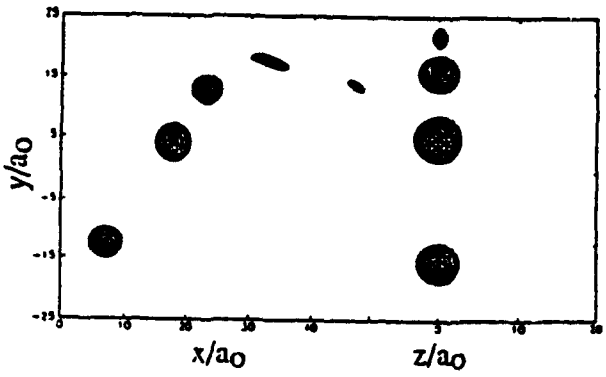

Figure 11: 3D bubble shapes in the vortex line flow field of Figure 8 before collapse of buble No. 1. View from a) OZ axis, b) OX axis.

Multiple Bubbles

One of the key question that one needs to address in the practical studies of bubble/vortical field interaction is how does a distribution of bubbles modify the flow field. In order to address such a problem the program **3DynaFS** is being modified for effective implementation on a supercomputer. Indeed one of the difficulties of such a study is the required large number of discretization points which prevents significant runs on typical memory and speed limited computers. Some preliminary multibubble interactions were considered in [27, 26]

Figure 10 shows the case of a 5-bubble configuration. This run has the advantage of including both vortex/bubble and bubble/bubble interactions. All five bubbles are chosen such that in absence of the vortex flow field, the pressures inside and outside each of them is the same and equal to 0.74 atm, $p_i/p_\infty = 1$. The viscous core radius and the circulation are again chosen to be in the same ranges as those in the experiments described in [23, 24]. The viscous core is chosen to be $R_c = 2.2mm$, while $\Gamma = 0.1573\ m^2/s$, $\Omega = 0.872$. The initial bubble centers are selected to be on OY axis at $Y = 0, 2, 3, 4$ and 5 mm. The vortex line is parallel to OX axis and is centered on $Y = 1.5\ mm$. As a result, bubbles No. 1, 2 and 3 are initially located in the viscous core, while bubbles No. 4 and 5 are located in the inviscid flow region. All five bubbles considered have an initial radius of 100 μm. Figure 10 shows contours of the bubbles as they rotate around the vortex axis at various times. This figure clearly shows the presence of a non-uniform flow field. Indeed Bubble No. 3 which is the closer to the region of highest angular velocity of the *"basic flow"* is seen to swirl around the vortex center at the fastest rate, while Bubble No. 2, which is the closest to the vortex center is seen to practically rotate around itself. Similarly, the highest shear is seen to occur close to the viscous core edge where the pressure gradients and their variations are steeper.

Since all bubbles were chosen to have the same initial radius and internal pressure, the natural period of oscillation of each of the selected bubbles increases with the proximity to the vortex axis. As a result, the farthest bubble from the axis, Bubble No. 5, collapses first while stretching and deforming.

Figure 11 shows two thee-dimensional views of the bubbles before the collapse of bubble No. 1. These views enable one to have a better idea of the bubble shape deformation and elongation during the capture phenomenon. Similar experimented observations were seen in [24].

Bubble on vortex axis

Let us consider now the case where the bubble is captured by the vortex and placed at its axis. Such a problem was considered earlier in [21] for an elongated bubble. Unfortunately, that study neglected an essential element of vortex dynamics: i.e. the

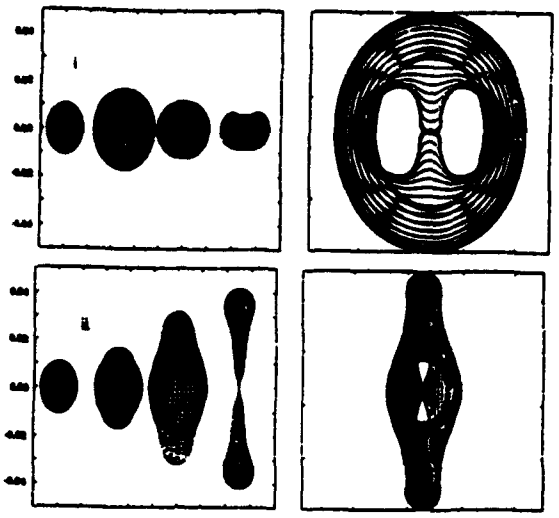

Figure 12: Comparison between the contours of an elongated bubble during its collapse in the absence and in the presence of swirl. Initial elongation ratio of 3. $p_\infty/p_i = 3.27$. a) No swirl. b) $\Omega = 0.56$. $R_c/R_{max} = 3$.

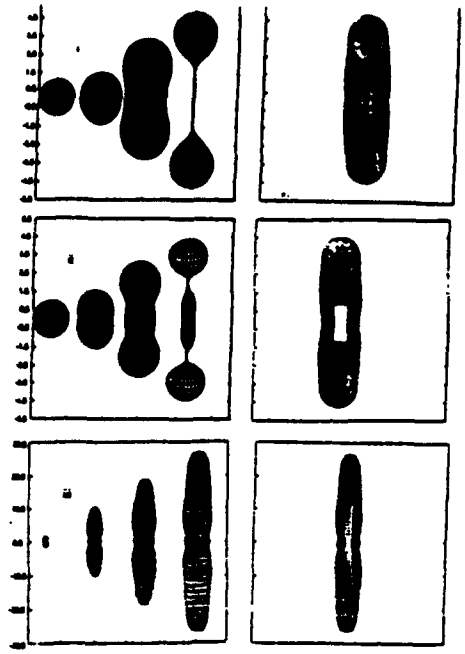

Figure 13: Bubble dynamics on the axis of a vortex line. Left side shows 3D shapes at selected times. Right side shows bubble contours at increasing times. $\Gamma = 0.005m^2/s$. $R_o = 100\mu m$. a)$p_i/p_\infty = 2$, $R_c/R_o = 1$. b) $p_i/p_\infty = 2$. $R_c/R_o = 1$. c) $p_i/p_\infty = 1$, $R_c/R_o = 0.57$.

presence of an azimuthal velocity, and a strong jet which initiated at both extreme points of the bubble along the axis of symmetry was obtained. As shown in Figure 12*a* such a behavior is reproduced using the program **2DynaFS** when the vortex flow field is neglected. However, the opposite effect is in general obtained when the rotation in the vortex flow is included. Figure 12*b* illustrates this for particular values of Ω and the normalized core radius, $\overline{R_c} = R_c/R_{max}$.

In both cases shown in Figures 12*a* and 12*b* the initial length to radius bubble elongation ratio was three. It is clear from the comparison that the swirl flow has a conclusive effect on the bubble dynamics. Bubble surface portions away from the vortex axis experience much higher pressures than bubble surface portions on and close to the vortex axis, and therefore move much faster during the collapse phase generating, instead of the sharp jets on the axis as in Figure 12*a*, a constriction in the mid-section of the bubble. This generates an hourglass shaped bubble which then separates into two tear-shaped bubbles.

In the following figure 13$a-c$, various configurations of initially spherical bubble dynamics are studied. The initial internal pressures inside the bubbles are taken to be larger than the pressure on the vortex axis, and the bubbles are left free to adapt to this pressure difference. The figures show that the bubble behavior depends significantly for a given value of the swirl parameter, Ω. on the normalized core radius $\overline{R_c}$, ratio of R_c to R_{max}. In all cases where R_{max} is larger than R_c it appears that the ***bubble tends to adapt to the vortex tube of radius*** R_c. This could lead to various bubble shapes as shown in the following figures ending up with a very elongated bubble with a wavy surface for large values of R_{max}/R_c.

Figures 13$a-c$ show bubble contours at various times during growth and collapse for increasing values of the core radius. R_c, and decreasing values of p_i/p_∞. Also shown are selected 3D shapes of the bubbles at various times. It is apparent from these figures, that during the initial phase of the bubble growth, radial velocities are large enough to overcome centrifugal forces and the bubble first grows almost spherically. Later on. the bubble shape starts to depart from spherical and to adapt to the pressure field. The bubble then elongates along the axis of rotation. Once the bubble has exceeded its equilibrium volume, bubble surface portions away from the axis – high pressure areas – start to collapse, or to return rapidly towards the vortex axis. To the contrary, points near the vortex axis do not experience rising pressures during their motion, are not forced back towards their initial position, and continue to elongate along the axis. As a result, a constriction appears in the mid-section of the bubble. The bub-

ble can then separate into two or more tear-shaped bubbles. It is conjectured that this splitting of the bubbles is a main contributor to cavitation inception noise. This behavior is very similar to that observed for bubble growth and collapse between two plates [15], which results in the formation of a vortex line!

Keeping Ω constant while reducing the core size R_c has the effect of steepening the radial pressure gradient along the bubble surface and increasing the rotation speed inside the viscous core. This enhances the deviation of the bubble shape from a sphere, and increases the centrifugal force on the fluid particles closer to the vortex axis. This has the consequence of increasing the elongation rate of the bubble and results in more and more complex dynamic shapes of the elongated bubbles. The bubble can then become subdivided into three, four or more satellite bubbles during the collapse. The elongated and wavy shapes obtained have been observed on cavitation on the axis of the vortex formed in a vortex tube [26].

Observation of the elongated bubble dimension variations with time are very revealing [10, 26]. Normalizing lengths by R_{max} and time by the Rayleigh time based on R_{max} and the pressure difference between P_{∞} and the pressure on the vortex axis, one finds that the bubble length along the rotation axis strongly depends on Ω. However, the bubble cross-section radius closely follows the classical Rayleigh model and is very little dependent on Ω. Variations of Ω between 0.1 and 0.94 modify the normalized bubble period by less than 10 percent. One should notice, however, that bubble period is here defined as the time needed for the bubble to subdivide into two secondary bubbles.

More realistic vortex line model

While the Rankine model is very helpful to study the fundamentals of bubble/vortex interactions, it does not allow one to capture other features such as flow and bubble motion along the axis of rotation. In [28] we conducted a study where a Burgers vortex line flow field was considered.

$$u_r = -Cr, \quad u_z = Cz$$

$$u_\theta = \frac{\Gamma}{2\pi r}\left[1 - \exp\left(\frac{-r^2}{4\delta^2}\right)\right], \qquad (33)$$

where C is a constant, and δ is the viscous core radius. The pressure distribution can then be obtained by solving the momentum equation:

$$p(r,z,t) = p_\infty - 2\rho C^2 z^2 - 2\rho C^2 \delta^2 X^2 - B/2X^2 + B\left[\exp(-X^2) - \exp(-2X^2)/2\right]/X^2 + B\left[E_i(-X^2) - E_i(-2X^2)\right], \qquad (34)$$

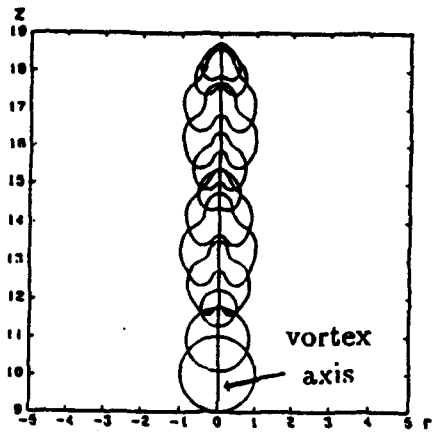

Figure 14: Bubble dynamics on the axis of a viscous line vortex. Contour shapes versus time. Basic field obtained using a viscous flow solver with viscous diffusion along x and r. Viscous core size $1mm$, initial bubble size $100\mu m$.

with $B = \rho\Gamma/2\pi\delta$ and $X = r/2\delta$. This flow and pressure field were used to study bubble dynamics on the vortex axis. When the bubble in initially centered at the origin of coordinates it has again a symmetric behavior. However, a much faster bubble elongation with time is then seen, but here again the bubble cross section does not exceed the core size.

Figure 14 show an example of bubble behavior in an even more realistic vortex line flow field. In this case the flow field of the vortex line is obtained by solving the viscous flow field due to an imposed Rankine vortex flow plus a uniform axial velocity at $z = 0$. This is to simulate the diffusion of a vortex line generated at the tip of a three-dimensional foil. The commercial Navier Stokes solver Fidap was then used at the Ecole Navale at Brest to obtain the diffusion of such a flow along the z axis, and included an axial flow at $z = 0$. The resulting flow field was then used as a basic flow to study 3-D bubble behavior using **3DynaFS**. In this case pressure gradients along the vortex axis are important enough to produce a reentering jet along the vortex axis while the bubble is entrained along the vortex line by the z component of the flow.

Experimental validation study

In order to validate the numerical studies on bubble vortex interactions, a fundamental experiment was conducted. This consisted of the controlled observation of the interaction between a vortex ring and a bubble. The results of the experiment were

then compared with those obtained with 3DynaFS described above [25, 26]. The vortex ring was generated in a Plexiglas tank using a cylinder equipped with a 2.5 *cm* radius piston. The cylinder had a sharp lip exit to enhance the roll up of the fluid vortex generated at the lip. This results in a vortex ring with a diameter slightly larger than that of the cylinder. A spark generated bubble was produced where desired in the vortex ring flow field. The interaction between the generated ring and bubble was then observed using high speed photography. A triggering line allowed one to synchronize the departure of the piston and the triggering of the spark generator using pressure transducers to precisely detect the vortex ring motion.

Both the experimental observations and the numerical computations showed very similar behaviors. The results of these comparisons can be found in [25, 26]. Bubble shearing and splitting along the flow direction appears common. This can be qualitatively understood by considering the velocity and pressure fields around the bubble. The motion of each point on the surface of the bubble is the result of the combination of the underlying fluid velocity and of the velocity due to the bubble growth or collapse. The effect of the underlying fluid flow is usually small during initial bubble growth and later bubble collapse phases due to the large bubble wall velocity during these phases, but becomes most important at the end of the growth where bubble wall velocities reach a minimum. For a bubble in a uniform flow, the presence of the underlying flow reflects on the bubble shape during the growth by a larger extension of the bubble in the downstream direction and by a flattening of the bubble shape in the upstream direction. Later on due to inertia, the downstream bubble part that has extended further collapses faster forming a reentering jet directed upstream.

When the flow is not uniform, a similar phenomenon occurs but is stronger on one side of the bubble than on the other due to the typical asymmetry of a shear flow. In addition, the fact that the underlying shear flow becomes at some point during the bubble history stronger than the local bubble wall velocity creates the opportunity of a jet generated by the underlying flow, which can be opposite to the one described above and directed downstream. This leads to the formation of a constriction all around the bubble with a tendency for bubble splitting.

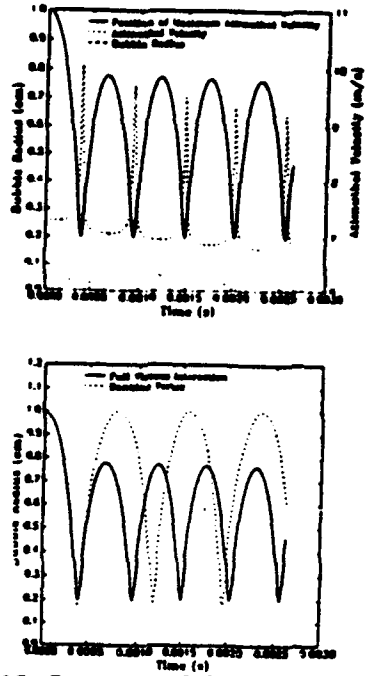

Figure 15: Dynamics of the interaction between a cylindrical bubble and a line vortex. $\Gamma = 0.5\ m^2/s$. $P_{go} = 5 \times 10^3 Pa$, $P_\infty = 1.3 \times 10^5 Pa$. a) Bubble radius. value of maximum azimuthal velocity $u_{\theta\,max}$, and position of $R_{\theta\,max}$. b) Bubble radius versus time with and without viscous interaction.

FULL VISCOUS INTERACTION BETWEEN A CYLINDRICAL BUBBLE AND A LINE VORTEX

One weakness of the numerical approach presented above is the fact that, while the influence of the flow on the bubble was fully accounted for, the modification of the flow by the bubble presence and dynamics was restricted to the case where the "bubble flow" was potential. In the present section, we will remove this restriction in the simple case of the interaction between a cylindrical bubble and a line vortex. This corresponds to cases where the line vortex has the central part of its viscous core gaseous or vaporous. Such an analysis is important to determine criteria for unstable bubble growth (cavitation inception), and to describe how bubble dynamics affects the viscous flow itself. To do so, we consider the case where an axisymmetric elongated bubble of initial radius a_o is located on the axis of a fully viscous line vortex. For illustration, we consider the case where, at $t = 0$, the vortex line is a Rankine vortex. From there on, the vortex diffuses with time and interacts fully with the bubble. The generated flow satisfies the axisymmetric incompressible Navier-Stokes equations.

Denoting the radius of the bubble as $a(t)$, and its time derivative, $\dot{a}(t)$, the continuity equation leads to:

$$u_r = a(t)\,\dot{a}(t)/r. \qquad (35)$$

Replacing u_r by its expression in the momentum equations one obtains:

$$\frac{1}{r}\left(a\,\ddot{a} + \dot{a}^2 - u_\theta^2\right) - \frac{a^2\,\dot{a}^2}{r^3} = -\frac{1}{\rho}\frac{\partial p}{\partial r}, \qquad (36)$$

$$\frac{\partial u_\theta}{\partial t} + \frac{a\,\dot{a}}{r}\left(\frac{\partial u_\theta}{\partial r} + \frac{u_\theta}{r}\right) = \nu\frac{\partial}{\partial r}\left(\frac{1}{r}\frac{\partial}{\partial r}(r u_\theta)\right), \qquad (37)$$

This set of coupled equations allows one to describe both the bubble dynamics and the flow field modification accounting for two-way interaction.

Method of Solution

In order to obtain a differential Equation for the bubble radius variations, similar to the Rayleigh Plesset Equation, Equation (36) is integrated between $r = a(t)$ and a very large radial distance, $r = R_{inf}$, beyond which the vortex flow is assumed to be inviscid (vortex line of circulation Γ). This leads to an integral term containing u_θ^2. In order to obtain this term, a space and time integration of Equation (37) is needed. This is obtained using a Crank-Nicholson finite difference integration scheme. To do so, the domain of integration is made time independent using the variable change,

$$s = r/a(t). \qquad (38)$$

The integration region becomes for all times $[1; s_{inf}]$, with $R_{inf}(t) = a(t)s_{inf}$. Equation 37 becomes:

$$\frac{D\overline{u_\theta}}{Dt} = -\frac{s}{\bar{a}}\frac{\dot{\bar{a}}}{\bar{a}}\frac{\partial\overline{u_\theta}}{\partial s} - \frac{\dot{\bar{a}}}{s\bar{a}}\frac{\partial\overline{u_\theta}}{\partial s} - \frac{\dot{\bar{a}}}{s^2\bar{a}}\overline{u_\theta} + \frac{1}{R_e}\frac{1}{\bar{a}^2}\left(\frac{\partial^2\overline{u_\theta}}{\partial s^2} + \frac{1}{s}\frac{\partial\overline{u_\theta}}{\partial s} - \frac{\overline{u_\theta}}{s^2}\right) \qquad (39)$$

with

$$\bar{a} = \frac{a}{a_0}, \quad \bar{t} = \frac{t}{a_0}\sqrt{\frac{P_\infty}{\rho}}, \quad R_e = \frac{a_0}{\nu}\sqrt{\frac{P_\infty}{\rho}}. \qquad (40)$$

Similarly, Equation (36) becomes:

$$\bar{a}\,\ddot{\bar{a}} + \dot{\bar{a}}^2 = \frac{\dot{\bar{a}}^2}{2\ln s_{inf}}\left[\frac{-1}{s_{inf}^2} + 1\right] + \frac{1}{\ln s_{inf}}\int_1^{s_{inf}}\frac{\overline{u_\theta}^2}{s}ds - \frac{1}{\ln s_{inf}}\left[1 - \left(\frac{\bar{\Gamma}}{2\pi\bar{a}s_{inf}}\right)^2 - \overline{p_v} + \overline{p_{g_0}}\left(\frac{1}{\bar{a}}\right)^{2k}\right] - \frac{1}{\ln s_{inf}}\left[\frac{1}{W_e\bar{a}} - \frac{2\,\dot{\bar{a}}}{R_e\bar{a}}\right] \qquad (41)$$

with

$$\bar{\Gamma} = \frac{\Gamma}{a_0}\sqrt{\frac{P_\infty}{\rho}}, \quad W_e = \frac{a_0 P_\infty}{\sigma}. \qquad (42)$$

Initial and Boundary Conditions

The initial conditions considered are as follows. For the bubble,

$$a(0) = a_0, \qquad \dot{a}(0) = 0. \qquad (43)$$

For the line vortex, the equation at $t = 0$, is that of a Rankine vortex. In addition, the following boundary condition is imposed at the bubble interface:

$$P(a) = p_v + p_{g_0}\left(\frac{a_0}{a}\right)^{2k} - \frac{\sigma}{a} + 2\mu\frac{\partial u_r(a)}{\partial r}, \qquad (44)$$

where μ is the dynamic viscosity, and the gas compression law is given by:

$$p_g = p_{g_0}\left(\frac{a_0}{a}\right)^{2k}. \qquad (45)$$

To close the problem, the following condition is imposed on the pressure at the distance, R_{inf} :

$$P(R_{inf}) = p_\infty - 2\rho\left(\frac{\Gamma}{2\pi s_{inf}a(t)}\right)^2. \qquad (46)$$

Some Preliminary Results

Figures 15*a* and 15*b* illustrate both the bubble/vortex flow field interaction and a case where there is a need to include this full interaction in the dynamics. In these two figures, the bubble has an initial radius of $1mm$, while the viscous core of the vortex has an initial radius of $1cm$. The initial circulation in the vortex is $0.5\ m^2/s$, and the initial pressure in the bubble is $5\times10^3 Pa$, while the ambient pressure is $1.3\times10^5 Pa$. Therefore, the bubble starts its dynamics by collapsing. Figure 15*a* shows simultaneously three characteristic quantities of the problem versus time. The first quantity is the bubble radius versus time, while the other two quantities are the radial position, $R_{\theta\,max}$, of the maximum azimuthal velocity, $u_{\theta\,max}$, and the value of this velocity. In the previous sections, these two last quantities remained constant with time. A very important first result very clearly shown in Figure 15*a* is that both the position of $R_{\theta\,max}$, and the value of $u_{\theta\,max}$, both directly depend on the variation of $a(t)$. The viscous core (of radius $R_{\theta\,max}$) is seen to decrease with

the bubble radius during bubble collapse, and to increase with the bubble radius during bubble growth. This tendency of the viscous core to get displaced with the bubble wall, corresponds to intuition, but is proven numerically to our knowledge for the first time here and in [28].

Viscous effects appear more prominently when following the bubble dynamics over more than a single period of oscillation. Both maximum values of $R_{\theta\,max}$ and $u_{\theta\,max}$ are seen to decrease with time. Through conservation of momentum, the azimuthal velocity follows an tendency opposite to the core size. As the bubble wall moves inward the viscous core shrinks, simultaneously increasing the tangential velocity to a maximum when the bubble reaches maximum size. As the bubble grows again, the core expands and the tangential velocity decelerates to a minimum at the maximum bubble radius. When the fluid particles are pulled in towards the vortex axis they accelerate tangentially. This is similar to the phenomenon of vortex stretching .

Figure 15*b* shows the importance of the inclusion of full viscous flow / bubble interaction in the dynamics. The figure shows also the case where the underlying flow field is forced to remain that of a Rankine vortex. In that case, the bubble oscillations are repeatable with time, and no viscous decay of the amplitude of the oscillations are visible. To the contrary when the underlying flow is modified through viscous diffusion and interaction with the bubble, the bubble radius oscillations decays very much after the first collapse, and the flow field characteristics are modified as described in Figure 15*a*.

Figures 16*a* and 16*b* show, respectively, the influence on the problem dynamics of the initial gas pressure inside the bubble, P_{go}, and the ratio of initial core radius to initial bubble radius, R_c/a_o. For an initial pressure on the vortex axis of $7\times10^5 Pa$, Figure 16*a* shows the dynamics of the bubble and the viscous core size when the initial pressure in the bubble decreases from $5\times10^5 Pa$ to $1.5\times10^5 Pa$. For $P_{go} = 5\times10^5 Pa$ the bubble collapse is very weak, and the core radius is seen to follow the bubble wall oscillations. For all three other smaller values of P_{go} starting from $P_{go} = 4\times10^5 Pa$ the bubble collapse is strong enough to result in a full collapse of the viscous core which practically disappears (maximum azimuthal velocity at the bubble wall) during the later phases of the bubble collapse. This is followed by a much stronger rebound of the viscous core than the bubble rebound.

Figure 16*b* shows a behavior similar to the previous figure when the ratio, R_c/a_o, increases. Here again a strong core collapse and rebound is observed

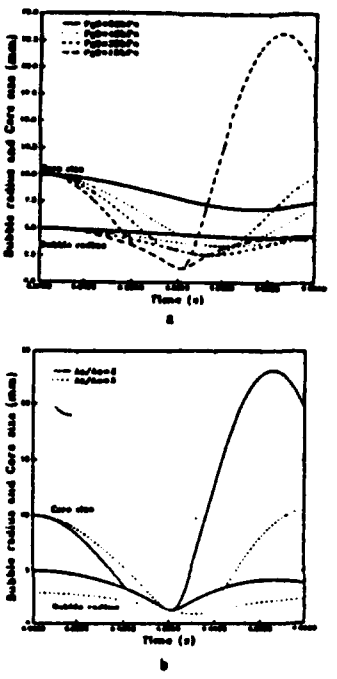

Figure 16: Dynamics of the interaction between a cylindrical bubble and a line vortex. $P_{axis} = 7\times10^5 Pa$. a) Influence of the initial bubble pressure, P_{go}, on bubble radius and position of $R_{\theta\,max}$. $R_c/a_o = 2$. b)Influence of R_c/a_o on the bubble radius and position of $R_{\theta\,max}$. $P_{go} = 1.5\times10^5 Pa$.

when the initial distance between the bubble wall and the core radius is decreased.

The case of initial bubble growth instead of collapse is not shown here because it presents the same character as observed in the rebound cases in the above figures.

INTERACTION BETWEEN A BUBBLE AND A VORTICAL FLOW

In order to extend the methods presented above to the more general case of the interaction between a bubble and a general rotational field, the BEM method was coupled to a vortex element method. With this approach the *basic vortical flow* is represented by a distribution of three-dimensional vortex elements, and if need be, by the addition of a potential component. The procedure then is to track in time both the bubble free surface motion and the vortex elements motion. By doing so, one is able to obtain not only the bubble motion and deformation, but also the vorticity distribution variation with time. Modification of the vortical field by the presence of the bubbles is thus an outcome of the interaction method.

The above is based on the basic principle that any arbitrary basic flow field may be decomposed

into a potential part, ϕ_o, and a rotational part, A :

$$\mathbf{u} = \mathbf{u}_\phi + \mathbf{u}_\omega = \nabla\phi_o + \nabla \times \mathbf{A}. \qquad (47)$$

The rotational part of the velocity $\mathbf{u}_\omega$ derives from the vector potential A which satisfies

$$\nabla^2 \mathbf{A} = -\omega, \qquad (48)$$

where ω is the vorticity. The velocity is obtained by the Biot-Savart law:

$$\mathbf{u}_\omega(\mathbf{x}) = \frac{-1}{4\pi} \int \frac{(\mathbf{x}-\mathbf{y}) \times \omega(\mathbf{y})}{|\mathbf{x}-\mathbf{y}|^3}\, d\mathbf{y}. \qquad (49)$$

For numerical simulation, the vorticity field is discretized using a desingularized representation of vorticity [29, 30, 31].

$$\omega(\mathbf{x},0) = \sum_{i=0}^{N} \omega_i f_\delta(\mathbf{x}-\chi_i)\, dV_i \qquad (50)$$

where χ_i are the centers of the vortex elements,and f_δ is a spherical rapidly decaying core function or mollifier [29], which is chosen to be

$$f_\delta(r) = \frac{3}{4\pi\delta^3} e^{-\frac{r^3}{\delta^3}} \qquad (51)$$

following [31]. With the discretized vorticity distributed over vortex elements, we may also write $dV_i = dA_i \times d\chi_i$,and hence

$$\omega_i dV_i = \Gamma_i d\chi_i \qquad (52)$$

where Γ_i is the elementary circulation associated with the i-th line element. By virtue of Kelvin and Helmholtz theorems Γ_i remains invariant in time, and the elements follow the local velocity field enabling stretching and tilting of the elements. The change in the vorticity is represented by a change in the line element $d\chi_i$. The discretized velocity expression is:

$$\mathbf{u}_\omega(\mathbf{x}) = \sum_{i=0}^{N} \frac{1}{4\pi} \Gamma_i \frac{(\mathbf{x}-\chi_i) \times d\chi_i}{|\mathbf{x}-\chi_i|^3} \kappa\left(\frac{\mathbf{x}-\chi_i}{\delta}\right),$$

$$\kappa = 1 - e^{-r^3}. \qquad (53)$$

The element positions are updated by the velocities at their end points

$$\chi_i(t+dt) = \chi_i(t) + \mathbf{u}(\chi_i, t)dt. \qquad (54)$$

The convergence of this vortex method was proven in [32]. The procedure is as follows. For a given vorticity distribution in the flow field of interest, a geometric distribution of three-dimensional vortex elements is selected. In the examples below a Gaussian distribution is selected. The inverse problem of (50) is then solved to obtain the values of the elementary circulations, Γ_i, associated with each finite line element. With the knowledge of this initial vortex element distribution, and the initial bubble discretization, one can proceed with the time stepping to solve the problem. The influence of all bubble panels and all vortex elements on the bubble and vortex nodes are computed. This allows determination of the new values of the velocity on all the bubble nodes. Knowing all values of Φ_b and $\partial\Phi_b/\partial n$ on the boundaries one can deduce the velocity anywhere, and in particular at all nodes of the vortex elements whose position can then be updated using (54).

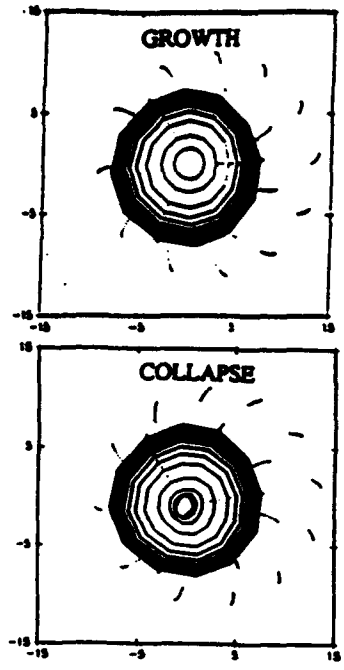

Figure 17: Interaction between a bubble and a finite thickness line vortex represented by 3D vortex elements. Crosscut in the plane of symmetry z=0. Note motion of the vortex line points close to the bubble deviate significantly from a pure circular motion as away from the bubble.

The case of a finite thickness line vortex was considered and represented with 18 vortex lines discretized into 3D elements. One can then obtain as shown in Figure 17 both the bubble and the vortex line deformations. Figure 17 shows the intersection at various times during bubble growth and collapse between the plane $z = 0$ and the bubble and the vortex elements. This shows both bubble and vortex elements motion with time. Note that the motion of the vortex line point close to the bubble deviate sig-

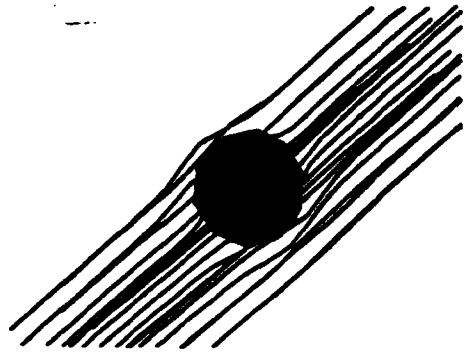

Figure 18: Interaction between a bubble and a finite thickness line vortex represented by 3D vortex elements. 3D view at maximum bubble size of the bubble and vortex line shapes

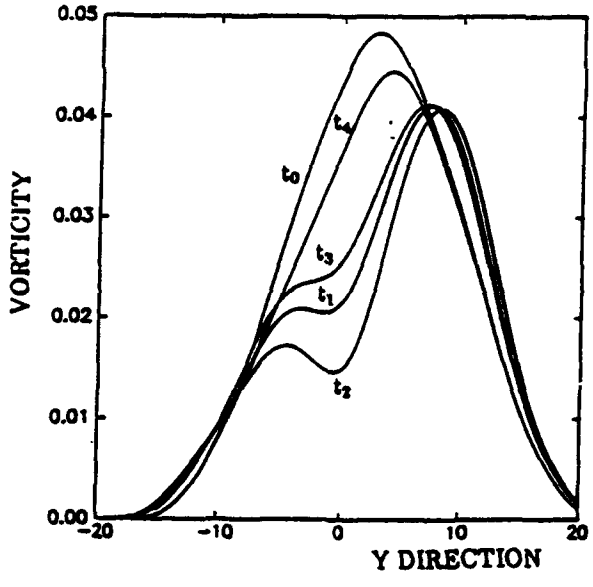

Figure 19: Vorticity distribution modification along the OY axis during bubble oscillation in a finite thickness line vortex represented by 3D vortex elements.

nificantly from a pure circular motion. Those away from it just rotate around the central point due their mutual interaction and to the symmetry of the distribution. Figure 18 shows a 3D snapshot of the bubble and vortex line shapes for the example of a bubble immersed in the vortical field. Figure 19 shows how the vorticity distribution along the OY axis has been modified by the dynamics and presence of the bubble. It is apparent in this case that very significant redistribution of the vortex field is possible during the bubble motion.

The above example is shown as an illustration of the method being developed. More detailed descriptions and a more extensive analysis are in preparation [33].

CONCLUSIONS

The study of bubble dynamics in non-uniform flow fields is complex but essential to any real attempt to study bubble dynamics in realistic flow conditions. Due to the difficulties involved in both experimental and analytical approaches, the trend is to address the problems by a two-pronged effort involving numerical and experimental simulations. This is made possible by the development of advanced high speed computers which render direct numerical simulations possible in reasonable amounts of time. The studies presented above addressed various aspects of the problem, namely bubble behavior in the vicinity of boundaries, bubble capture by a vortex and bubble dynamics in a vortical flow field. The most interesting development is the capability to study the influence of the bubble's presence on the vortical field itself. Our attempts in this direction were briefly presented and are presently very actively being pursued. It is hoped that a matching between a flow solver, at least in the vortical region, and a bubble dynamics solver such as **2DynaFS** or **3DynaFS** will enable one to describe with some acceptable accuracy the full interaction between the bubbles and the vortical flow field. This is of great importance since it would allow the user to understand the mechanics involved thus enabling one to manipulate the phenomena for technological advantage in applications such as, in ship wakes, bubble drag reduction, or cavitation inception delay.

ACKNOWLEDGMENTS

We are grateful for the support of the Office of Naval Research, under Contract N00014-89-C-0025 monitored by Dr. Edwin Rood. The author would like to acknowledge the contributions of colleagues at DYNAFLOW, INC. especially Drs. Kausik Sarkar,

Ramani Duraiswami and Kenneth Kalumuck. The author would also like to thank Drs. J.Y. Billard and P. Cerrutti from the Ecole Navale for providing the viscous flow vortex results and for the significant contribution of their students while at DYNAFLOW to several aspects of this study.

References

[1] Rood, E. P., 1991, "*Review - Mechanisms of Cavitation Inception,*" Journal of Fluids Engineering, Vol 113, June.

[2] Rood, E. P., 1992, "*Cavitation Inception Research - Focus and Direction*", Report on the Advisory Council on Cavitation Events, ONR meeting, Memphis, TN, May 20th, 1992.

[3] Chahine, G.L., Duraiswami, R., Rebut, M., 1992, "*Analytical and Numerical Study of Large Bubble/Bubble and Bubble/Flow Interactions,*" Proc. 19th ONR Symposium on Naval Hydrodynamics, Seoul, S. Korea.

[4] Guerri, L., Lucca, G., and Prosperetti, A., 1981, "*A Numerical Method for the Dynamics of Non-Spherical Cavitation Bubbles,*" Proc. 2nd Int. Coll. on Drops and Bubbles, JPL Publication 82-7, Monterey, CA.

[5] Blake, J. R., Taib, B.B. and Doherty, G., 1986, "*Transient Cavities Near Boundaries. Part I. Rigid Boundary,*" Journal of Fluid Mechanics, vol. 170, pp. 479-497.

[6] Blake, J. R, and Gibson, D. C., 1987, "*Cavitation Bubbles Near Boundaries,* " Annual Review Fluid Mechanics., Vol. 19, pp. 99-123.

[7] Wilkerson, S.,1989, "*Boundary Integral Technique for Explosion Bubble Collapse Analysis,*" ASME Energy Sources Technology Conference and Exhibition, Houston Tx.

[8] Chahine, G.L., Perdue, T.O., and Tucker, C.B., 1988, "*Interaction Between an Underwater Explosion and a Solid Submerged Structure,*" DYNAFLOW, INC. Technical Report 89001-1.

[9] G.L. Chahine and T.O. Perdue, 1989a, "*Simulation of the Three-Dimensional Behavior of an Unsteady Large Bubble Near a Structure,*" in "*Drops and Bubbles*" edited by T.G. Wang, A.I.P. Conference Proceedings, 197, 169-187.

[10] Chahine, G.L.,1990a, "*Nonspherical Bubble Dynamics in a Line Vortex,*" in Proceedings of the ASME Cavitation and Multiphase Flow Forum, Toronto, FED- Vol. 98, pp. 121-127.

[11] Chahine, G.L., 1990b, "*Numerical Modeling of the Dynamic Behavior of Bubbles in Nonuniform Flow Fields*" ASME Symposium on Numerical Methods for Multiphase Flows, Toronto, FED-Vol. 91, pp 57-65.

[12] Chahine, G.L., Duraiswami, R., 1993, "*Boundary Element Method for Calculating 2-D and 3-D Underwater Explosion Bubble Behavior in Free Water and Near Structures,*" Naval Surface Warfare Center, Dahlgren Division, White Oak Detachment, Report NSWCDD/TR-93/44.

[13] Ceccio, S.L., Brennen, C.E., 1991, "*Observation of the dynamics and acoustics of travelling bubble cavitation,*" Journal of Fluid Mechanics, vol., 233, 633-660.

[14] Dechizelle, Y.K., Ceccio, S.L., Brennen, C.E., Shen, Y., 1992 "*Cavitation Scaling Experiments with Headforms: Bubble Acoustics*", Proceedings Second Internatinoal Symposium on Propeller and Cavitation, Hangzhou, China.

[15] Chahine, G.L., 1979, "*Etude Locale du Phénomène de Cavitation -Analyse des Facteurs Regissant la Dynamique des Interfaces,*" Doctorat D'Etat Es-Sciences Thesis, Universite Pierre et Marie Curie.

[16] Bovis, A.G., 1980a, "*Asymptotic Study of Tip Vortex Cavitation*", ASME Cavitation and Polyphase Flow Forum, New Orleans, pp. 19-21.

[17] Bovis, A.G., 1980b, "*Etude Asymptotique du Phénomène de Cavitation. Cavités nonsphériques,*" Thèse de Docteur Ingénieur. Université Pierre et Marie CURIE, Paris.

[18] Latorre, R., 1982, "*TVC Noise Envelope - An approach to Tip Vortex Cavitation Noise Scaling*", Journal of Ship Research, Vol. 26, No. 1, pp. 65-75.

[19] Ligneul, P. and Latorre R., 1989, "*Study of the Capture and Noise of Spherical Nuclei in the Presence of the Tip Vortex of Hydrofoils and Propellers*", Acustica Vol. 68.

[20] Chahine, G.L., Duraiswami, R., 1992, "*Analytical Study of a Gas Bubble in the Flow Field of a Line Vortex,*" Proceedings, ASME Cavitation and Multiphase Flow Forum, Los Angeles.

[21] Crespo A., Castro F., Manuel, F., and Hernandez J., 1990, "*Dynamics of an Elongated Bubble*

During Collapse", Journal of Fluids Engineering, Vol 112, 232-237.

[22] Higuchi, H., Arndt, R.E.A. and Rogers, M.F., 1989, *"Characteristics of Tip Vortex Cavitation Noise"*, Journal of Fluids Engineering, Vol. 111, No 4, pp. 495-502.

[23] Maines, B.H., and Arndt, R.E.A., 1993, *"Bubble Dynamics of Cavitation Inception in a Wing Tip Vortex"*, ASME Cavitation and Multiphase Flow Forum, Washington D.C., FED-Vol. 153, pp. 93-99.

[24] Green, S.I., 1991, *"Correlating Single Phase Flow Measurements with Observations of Trailing Vortex Cavitation"*, Journal of Fluids Engineering, Vol. 113, No 1, pp. 125-130.

[25] Chahine, G.L., Delepoule, E., and Hauwaert, P., 1993a, *"Study of the Interaction Between a Bubble and a Vortical Structure*, "1993 ASME Cavitation and Multiphase Flow Forum, Washington D.C., FED-Vol. 153, pp. 39-47.

[26] Chahine, G.L., 1994, *"Bubble Interactions with Vortices,"* in *Fluid Vortices* Ed. Sheldon Green to be published by Kluwer Academic.

[27] Chahine, G.L., 1991, *"Dynamics of the Interaction of Non-Spherical Cavities,"* in *"Mathematical Approaches in Hydrodynamics,"* ed. T. Miloh, SIAM, Philadelphia.

[28] Desgrees du Lou, G., Sarasin, T. and Chahine, G.L., 1993, *"Viscous Interaction Between Bubble and Line Vortex,"* DYNAFLOW, INC. Technical Report 6.002-15.

[29] Leonard, A., 1985, *"Computing Three- Dimensional Incompressible Flows with Vortex Elements,"* Ann. Rev. Fluid Mech., 17, 523-559.

[30] Sarpkaya, T., 1989, *"Computational Methods with Vortices— The 1988 Freeman Scholar Lecture,"* J. Fluids Engg., 111, 5-52.

[31] Knio, O. M., and Ghoniem, A. F., 1990, *"Numerical Study of a Three-Dimensional Vortex Method,"* J. Comp. Phys., 86, 75-106.

[32] Beal, J. T., and Majda, A., 1985, *"Higher Order Accurate Vortex Methods with Explicit Velocity Kernels,"* J. Comp. Phys., 58, 188-208.

[33] Sarkar, K., and Chahine, G.L., 1994, *"A Coupled Three-Dimensional Boundary Element-Vortex Method for Vortical Flows-Bubble Interactions"*, DYNAFLOW, INC. Technical Report 6.002-20 (in preparation).

To be published by Kluwer Academic, 1994.

Chapter 19

BUBBLE INTERACTIONS WITH VORTICES

Georges L. Chahine[1]
DYNAFLOW, Inc.
7210, Pindell School Road
Fulton Maryland 20759

Abstract

The understanding of the fundamental mechanisms involved in the interaction between bubbles and vortices is of relevance to many important engineering applications. Classical assumptions of bubble sphericity and decoupling between bubble and flow behavior prevent one from capturing essential elements of the interaction. Bubble motion and deformation are seen to be of great importance for most bubbles in the size spectrum. In this chapter studies on bubble capture by a vortex, bubble motion and deformation during that capture, and bubble behavior once the bubble is on the vortex axis are described. Flow field modifications once the bubble is on the vortex axis are also briefly considered. The most promising approach appears to consist of a coupling between a boundary element method to describe the bubble behavior and a viscous flow solver to describe the basic flow.

19.1. INTRODUCTION

The simultaneous presence of bubbles and vortices is typical of many high velocity turbulent flows. Spectacular examples can be observed with propellers, where at high rotational speeds the helicoidal tip vortices formed at the tip of each blade 'cavitate' and become sites of bubble concentration and fluid vaporization into what is termed 'tip vortex cavities' (see photograph in Figure 19.1*a*). This phenomenon is addressed in more detail in Chapter 17. While for practical reasons engineers tend to superficially address the fundamental problem – by stating, for example, that cavity formation in the vortex will occur if the pressure on the center line drops in the monophase model below the liquid vapor pressure–, a closer look at the fundamental processes at work reveals that the actual phenomenon is rather very complex and very poorly understood. Questions such as how does a microscopic bubble behave in the presence of the vortex ..., or how and to what extent the presence of bubbles modifies the flow field of the vortex ... have, at this point, only preliminary answers or no answers at all. The interaction between bubbles and vortex flows is in fact of relevance to several fluid engineering problems. Important examples include cavitation in shear layers, boundary

[1] also Research Professor, The Johns Hopkins University, Baltimore, MD

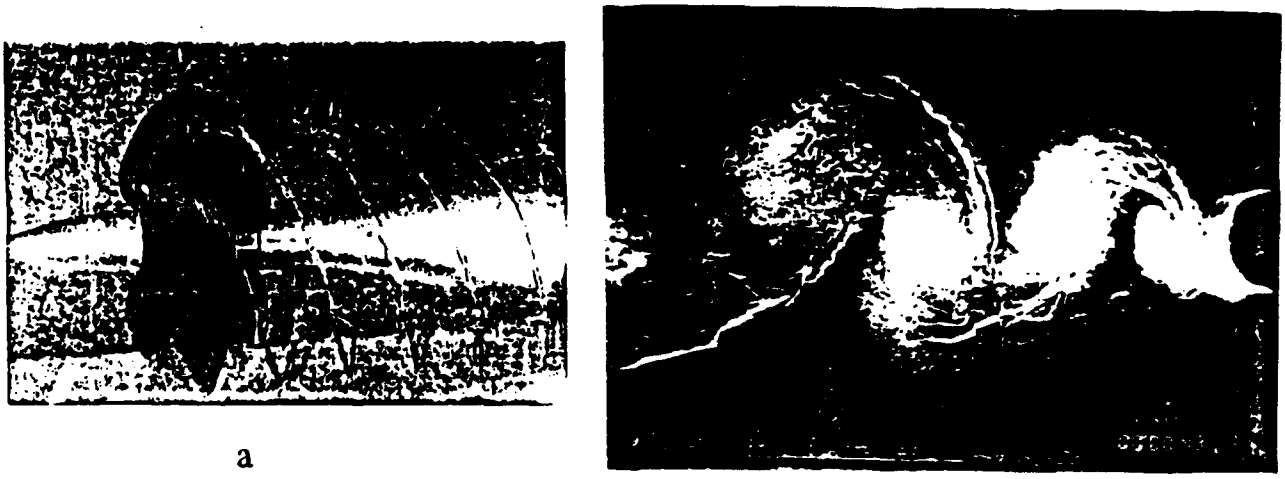

a b

Fig. 19.1. *Practical examples of bubbles and vortices. a) Tip vortex cavitation on a propeller (Chahine et al., 1993b), b) Vortex cavitation in the separated region behind a cylinder (courtesy cc. J.Y Billard, Ecole Navale, Brest, France).*

layers, tip vortex cavitation, bubbles in the shear layer of submerged jets, cavitation behind orifices, bubbles in separated flow areas (see Figure 19.1*b*), microbubbles in boundary layers, ...etc. In the above mentioned flows, bubbles are held responsible for dramatic effects such as noise generation, materials erosion, and bubble drag reduction. These effects, experimentally observed and widely accepted, are not yet completely understood. Therefore, a satisfactory control of the deleterious effects is not presently possible.

This chapter will try to highlight the problems, present some proposed explanations and methods for solution, and provide some preliminarily confirmed results. However, it does not claim to answer all the complex and presently unanswered questions, and likely fails to address some of the problems that will appear to be important in some configurations in future research.

19.1.1. Mechanistic Description When a bubble approaches a region of high vorticity in a liquid, it is accelerated towards the center of the vortex. The asymmetric pressure field pushes the bubble towards the vortex axis while it is swirling. On its path the bubble experiences a decreasing ambient pressure which can lead to an increase in the bubble size. Simultaneously, since the non uniformity of the pressure field around the bubble increases with proximity to the vortex axis, bubble shape deformation increases. An explosive bubble growth is provoked if the pressure in the vortex field drops below the bubble '*critical pressure*', p_c. For a bubble of radius r_o in static equilibrium when the ambient pressure is P_o, this pressure is defined as the pressure below which an equilibrium bubble radius does not exist. In cavitation studies within the assumption of an isothermal law of behavior of the gas included in the bubble

(see Section 19.4.1, Equation (19.37)) this pressure is defined by[2]

$$p_c = P_v - \frac{4\sigma}{3r_c}, \tag{19.1}$$

where σ is the surface tension parameter, and r_c is the '*critical radius*' given by

$$r_c = \left[\frac{3r_o^3}{2\sigma}\left(P_o - P_v + \frac{2\sigma}{r_o}\right)\right]^{1/2}, \tag{19.2}$$

where P_v is the liquid vapor pressure (see for example Hammitt 1980).

Over the last decade several investigators have addressed the phenomenon of bubble capture by a vortex (Bovis, 1980a,b; Latorre, 1982; Ligneul, 1989; Ligneul and Latorre, 1989). However, these studies made the strong simplifying assumption that the bubble, even though able to undergo volume changes, remains spherical. In addition, the type of interactions they considered was one-sided, since they did not consider vortex flow modification by the presence and behavior of the bubble. More recently, Chahine (1990) considered a broader approach where bubble deformation and motion were coupled while neglecting flow field modification by the bubble presence. This study showed that the pressure gradient across the bubble can lead to significant departure from bubble sphericity, and led to the suggestion that the deformation and later splitting of the bubble during its motion towards the vortex center is, in addition to its volume change, the main source of noise in vortex cavitation. This appears to explain the reason for the location of tip vortex noise at cavitation inception very close to the blade (Higuchi *et al*, 1989), and is in agreement with recent observations by Arndt and Maines (1993) about bubble capture in tip vortex cavitation. We will consider the details of such approaches in the following sections.

One can distinguish three phases in the interactive dynamics of bubbles and vortices: a) bubble capture by the vortex, b) interaction between the vortex and an initially quasi-spherical bubble on its axis, c) dynamics of elongated bubbles on the vortex axis. After some phenomenological and order of magnitude considerations of the phenomena at hand, we will consider each of the three phases and the method of solution proposed for their study.

19.2. ORDER OF MAGNITUDE CONSIDERATIONS

In order to analyze the problem of bubble capture and behavior in a line vortex let us consider as an example the Rankine vortex flow field described in Section 1.1. We adopt a notation consistent with that section, denoting Γ the vortex circulation, and u_θ the only non-zero velocity component. However, in order to avoid potential confusion with the bubble radius definitions later, we will use R_c for the radius of the viscous core (R is used in section 1.1). For distances r smaller than R_c the flow has a solid body rotation behavior (velocities vary as r), while for distances r larger than R_c the flow behaves as in an ideal inviscid irrotational vortex (velocities vary as $1/r$). The expression of the velocity is given in Equation (1.1.14). For such a flow the pressure field is known and its value $p(r)$ is given by Equation (1.1.16). A key parameter which appears in the pressure expression is the "*swirl parameter*", Ω, defined as

[2] This is obtained by considering Equation (19.38), writing $V = \frac{4}{3}\pi r_b^3$ and $V_0 = \frac{4}{3}\pi r_0^3$, and solving for the minimum of the function $P_L(r)$.

$$\Omega = \frac{\frac{1}{2}\rho(\frac{\Gamma}{2\pi R_c})^2}{p_\infty}, \tag{19.3}$$

which characterizes the intensity of the pressure drop due to the rotation relative to the ambient pressure, p_∞. To illustrate the importance of this parameter, we normalize the pressure with p_∞, to obtain the following normalized expressions for the pressure and the pressure gradient:

$$\begin{aligned} &\overline{p}(\overline{r}) = 1 - \frac{\Omega}{\overline{r}^2}; \qquad \frac{\partial \overline{p}}{\partial \overline{r}} = \frac{2\Omega}{\overline{r}^3}; \qquad \overline{r} \geq 1, \\ &\overline{p}(\overline{r}) = 1 - \Omega\left(2 - \overline{r}^2\right); \qquad \frac{\partial \overline{p}}{\partial \overline{r}} = 2\Omega\overline{r}; \qquad \overline{r} \leq 1, \end{aligned} \tag{19.4}$$

with

$$\overline{r} = \frac{r}{R_c}; \qquad \overline{p}(\overline{r}) = \frac{p(r)}{p_\infty}. \tag{19.5}$$

Note that the pressure on the vortex axis is $(1-2\Omega)$ and goes to zero when Ω approaches 1/2.

As seen in Figure 1.1.5 the pressure gradient steepens in the inviscid region when the viscous core is approached, achieves its maximum at $\overline{r} = 1$, and levels off in the viscous core close to the vortex axis. If a bubble is subjected to the pressure field shown in the figure, it will experience a higher liquid pressure on its right side than on its left side, the difference being greater the larger the bubble is. Similarly, the bubble is 'sheared', since fluid particles on the bubble / liquid interface experience different velocities. The type of shearing action depends on the position of the bubble relative to the viscous core / inviscid fluid boundary, R_c. If the bubble is fully immersed in the inviscid region of the flow, fluid particles on its left side will experience larger velocities, while if it is fully immersed in the solid body rotation region of the flow fluid particles on its right side will experience larger velocities. The most complex situation is when the bubble is partly in the viscous core and partly in the inviscid region. In that case, it is expected that the bubble behavior will be vortex flow model dependent, since in fact the sharp separation between the two regions is purely mathematical, and is a very schematic representation of the physical reality.

Due to the pressure and velocity gradients the bubble is accelerated toward the axis while somewhat growing and deforming. Therefore, depending on its size and position, the bubble experiences a pressure variation along its surface and a slip velocity relative to the surrounding fluid. This results in some degree of bubble shape deviation from sphericity. The importance of this deviation is a function of the relative orders of magnitude of the pressure gradient, the bubble wall acceleration due to volume change, and surface tension forces.

An evaluation of the bubble wall acceleration can be obtained from a characteristic bubble radius, R_b, and from the Rayleigh time, τ_R, time needed for a empty bubble to collapse from its radius R_b to 0, under the influence of the pressure outside the bubble (Rayleigh, 1917). For the present problem let's take for characteristic outside local pressure the pressure at $r = R_c$, that is $(\overline{p} = 1 - \Omega)$ as the typical local ambient pressure, the Rayleigh time is then:

$$\tau_R = R_b\sqrt{\frac{\rho}{p_\infty(1-\Omega)}}. \tag{19.6}$$

The characteristic bubble wall acceleration, γ_{growth}, at $r = R_c$ is then:

$$\gamma_{growth}\big|_{r=R_c} \simeq \frac{R_b}{\tau_R^2} \simeq \frac{p_\infty(1-\Omega)}{\rho R_b} \tag{19.7}$$

This value is to be compared with the acceleration force $\gamma_{gradient}$ due to the pressure gradients expressed in (19.4):

$$\gamma_{gradient} \simeq \frac{1}{\rho}\frac{\partial P}{\partial r},$$

$$\gamma_{gradient}\big|_{r=R_c} \simeq \frac{2\Omega p_\infty}{\rho R_c}, \tag{19.8}$$

The ratio between these two accelerations can be evaluated, for instance at $r = R_c$, to yield the simple expression:

$$\left.\frac{\gamma_{gradient}}{\gamma_{growth}}\right|_{r=R_c} = \frac{2R_b}{R_c}\cdot\frac{\Omega}{1-\Omega} \tag{19.9}$$

This expression underlines the relative importance between the characteristic bubble size R_b, and the viscous core size R_c . Keeping the surface tension parameter the same (see discussion on the Weber number below), the larger the ratio (19.9) is, the more important bubble deformation will be. *This remark has important implications concerning scale effects where R_b and R_c do not increase in the same proportion between scale and model*, since in most practical cases bubble distributions and sizes are uncontrolled and typically cannot be scaled much, while the size of the vortical regions depend on the selected geometry and velocity scales.

The ratio (19.9) is only an indication of the relative importance of bubble growth and slip forces at a given position. In fact the relative importance of these competing forces changes during the bubble capture process. For instance, the acceleration of the bubble toward the vortex axis increases with its proximity to the viscous core while the growth rate tends toward a constant value (decreasing pressure gradient). This indicates that strong deformation becomes predominant relative to volume change when either the bubble is very close to the axis or the vortex circulation (the "*swirl parameter*", Ω) becomes large.

Another important physical factor which affects bubble shape is the surface tension. A normalized value of the corresponding pressure, a Weber number, can be constructed by combining the surface tension pressure (coefficient, σ) with either the pressure difference between the inside and the outside of the bubble, or the amplitude of the variations of the local pressures (pressure gradients) around the bubble. The first number. W_{e_1}, is given by:

$$W_{e_1} = \frac{p_i - p_\infty(1-\Omega)}{\sigma/R_b}, \tag{19.10}$$

where p_i is the pressure inside the bubble. The second number, W_{e_2}, is given by:

$$W_{e_2} = R_b\frac{\partial p/\partial r}{\sigma/R_b}, \tag{19.11}$$

which can be written for $r = R_c$:

$$W_{e_2} = 2\Omega\left(\frac{p_\infty}{\sigma/R_b}\right)\left(\frac{R_b}{R_c}\right) = W_{e_1}\frac{2\Omega}{\overline{p_i} - (1-\Omega)}\cdot\frac{R_b}{R_c}. \tag{19.12}$$

For small values of either of these two numbers tension forces are predominant and prevent bubble distortion and deviation from sphericity. Expressions (19.12) shows that this is possible only if Ω is small and if R_b is much smaller than R_c. Therefore, as for the discussion on the acceleration forces, one should expect larger bubble deformations for stronger vortex circulations and larger bubbles.

19.3. BUBBLE CAPTURE BY A VORTEX

Despite several significant contributions to the study of bubble capture in a vortex, to our knowledge, no complete approach has yet been undertaken. While the overall approach, in terms of the investigation of the bubble motion has several similarities to the problem of the interaction between vortices and solid particles (see Chapter 20), the bubbles, unlike solid particles, will deform and change volume while interacting with the vortex flow field. The complexity of the problem has led the various contributors to neglect one or several of the factors in play, and therefore to only investigate the influence of a limited set of parameters. The first approaches to the problem were attempted independently at about the same time by Bovis (1980a), and Latorre (1980). While both studies accounted for volume change during bubble motion, the basic assumptions and effects taken into account were quite different. Bovis (1980a,b) considered the case where the flow velocities in the vortex flow are large enough to justify the assumptions of inviscid potential flow. This simplification, valid for instance in tip vortex cavitation where very large tangential velocities come into play, and when the bubble is not too close to the vortex axis, allows one to consider other important effects. For instance, one can then consider in a consistent fashion important phenomena such as the modification of the vortex flow by the presence of the bubble and the volume change and shape deformation of the bubble (Duraiswami and Chahine, 1991). On the other hand, Latorre (1980) and in following studies (Ligneul and Latorre, 1989), in a more pragmatic approach, considered real fluid effects to determine the bubble motion equation, neglecting bubble shape deformation and modification of the flow by the bubble behavior. They coupled these equations with a spherical bubble dynamics model to deduce noise emission in tip vortex cavitation.

In the potential flow approach, the expression of the modified flow field due to the presence of a spherical bubble is based on Weiss' theorem (see Milne-Thomson, 1968). In a spherical system of coordinates centered at the sphere center, if the undisturbed potential flow in absence of the sphere of radius a, is $\Phi_0(r,\theta,\phi)$,the velocity potential of the modified flow due to the presence of the fixed sphere is $\Phi(r,\theta,\phi)$ given by the equation:

$$\Phi(r,\theta,\phi) = \Phi_0(r,\theta,\phi) + \frac{1}{a}\int_0^{a^2/r^2} x\frac{\partial\Phi_0(x,\theta,\phi)}{\partial x}dx. \tag{19.13}$$

Using the notations in Figure 19.2, the expression of the velocity potential of the vortex flow is:

$$\Phi_0(r,\theta,\phi) = \frac{\Gamma}{2\pi}\tan^{-1}\frac{r\sin\theta\sin\phi}{\zeta(t)+r\sin\theta\cos\phi}, \tag{19.14}$$

where Γ is the vortex circulation and $\zeta(t)$ is the instantaneous distance between the vortex and the bubble center.

Similarly, the expression of the velocity potential of the flow due to the bubble radius time

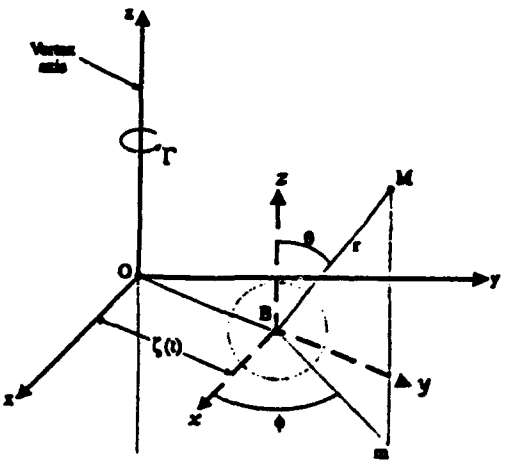

Fig. 19.2. *Sketch of the geometric quantities involved in the analytical description of bubble capture in a vortex line.*

variations, $\overset{\circ}{a}(t)$, is

$$\Phi_b(r,\theta,\phi) = -\frac{a^2(t)\,\overset{\circ}{a}(t)}{r}, \tag{19.15}$$

where $\circ$ indicates time differentiation. If we account for a relative velocity $(\mathbf{V}-\mathbf{V_B})$ between the spherical bubble and the fluid the modified bubble velocity potential becomes:

$$\Phi_b(r,\theta,\phi) = -\frac{a^2(t)\,\overset{\circ}{a}(t)}{r} - \frac{a^3(t)}{2r^3}\mathbf{r}\cdot(\mathbf{V}-\mathbf{V_B}), \tag{19.16}$$

where $\mathbf{V(t)}$ and $\mathbf{V_B(t)}$ are the instantaneous fluid and bubble center velocities. The absolute velocity potential in the fixed coordinate system attached to the vortex, Φ_a, which accounts for bubble motion and radius variations is then:

$$\Phi_a = \Phi_0 - \frac{a^2\,\overset{\circ}{a}}{r} - \frac{a^3(t)}{2r^3}\mathbf{r}\cdot(\mathbf{V}-\mathbf{V_B}) + \frac{1}{a}\int_0^{a^2/r^2} x\frac{\partial\Phi_0(x,\theta,\phi)}{\partial x}dx. \tag{19.17}$$

The equation of motion of the sphere can now be obtained by using Bernoulli's equation and integrating the pressure over the surface of the sphere. The resulting force leads to the following dynamic equation:

$$\frac{4}{3}\pi a^3\rho_b\frac{d\mathbf{V_B}}{dt} = \rho\iint_S\left[\frac{\partial\Phi_a}{\partial t} + \frac{|\nabla\Phi_a|^2}{2}\right]\mathbf{n}ds, \tag{19.18}$$

where ρ and ρ_b are the liquid and bubble content density, a the bubble radius, $\mathbf{n}$ the normal vector to the bubble surface, and $d\mathbf{V_B}/dt$ the bubble acceleration. The evaluation of the expression (19.18) in the general case is rather complex. A simplified asymptotic expression can however be obtained when the radius of the bubble is small relative to the distance from the vortex axis,

$$\epsilon = \frac{a_0}{\zeta_0} \ll 1. \tag{19.19}$$

The expression of the two nondimensional components of the acceleration are then:

$$\left(\frac{\rho_b}{\rho}+\frac{1}{2}\right)\frac{d\overline{V_{br}}}{d\bar{t}} = -\frac{3}{2\bar{\zeta}^3} + \left(\frac{\rho_b}{\rho}+\frac{1}{2}\right)\frac{\overline{V_{b\theta}^2}}{\bar{\zeta}} - \frac{\overline{V_{br}}\dot{\bar{a}}}{\bar{a}}, \tag{19.20}$$

$$\frac{d\overline{V_{b\theta}}}{d\bar{t}} = -\frac{\overline{V_{b\theta}V_{br}}}{\bar{\zeta}} + \dot{\bar{a}}\left(\frac{3}{\bar{\zeta}} - \frac{2\overline{V_{b\theta}}}{\bar{a}}\right), \tag{19.21}$$

where the velocities are normalized by the tangential velocity at the location ζ_o of the center of the bubble at $t = 0$, and time by the ratio between the distance ζ_o, and that characteristic velocity,

$$\overline{V_i} = V_i \;/\; \frac{\Gamma}{2\pi\zeta_o},$$

$$\bar{t} = t \;/\; \frac{2\pi\zeta_o^2}{\Gamma}. \tag{19.22}$$

Similarly, ζ is normalized with the initial position, $\bar{\zeta} = \zeta/\,\zeta_o$. Note that $V_{br} = d\zeta/dt$, and that for a bubble ρ_b/ρ is negligible. The third component along ϕ is obviously zero due to the symmetry of the problem (see Darrozes and Chahine, 1983, for further discussions and derivations of the above equations).

In the studies of Ligneul and Latorre (1989) the bubble equation (19.18) is replaced by an empirical force balance equation first given by Johnson and Hsieh (1966):

$$\frac{d\mathbf{V_B}}{dt} = 3(\mathbf{V}-\mathbf{V_B})\frac{\dot{a}}{a} - \frac{3\nabla p}{\rho} + \frac{C_d}{4a}|\mathbf{V}-\mathbf{V_B}|, \tag{19.23}$$

where C_d is a viscous drag coefficient. The first two terms on the right hand side come from inviscid flow considerations and are therefore included more formally and more accurately in Equation (19.18). The first term which results directly from the integration in (19.18) of the third term in Equation (19.17). It reflects the fact that any slip velocity between the bubble center and the surrounding fluid increases with an increase of the bubble wall velocity and a decrease of the bubble radius. Therefore, the bubble center decelerates during bubble growth and accelerates very much during the bubble collapse where both $\dot{a}$ and a^{-1} are very large. The second term is in fact an acceleration term of the relative or slip velocity, $(\mathbf{V}-\mathbf{V_B})$, whose expression has been often debated in the multiphase flow community (Van Wijngaarden, 1980). The third term is a viscous drag term where the drag coefficient C_d depends on the Reynolds number of the relative flow, R_{e_b}. Ligneul and Latorre (1989) used the expression:

$$C_d = \frac{24}{R_{e_b}}\left[1 + 0.197R_{e_b}^{0.63} + 2.6\times10^{-4}R_{e_b}^{1.38}\right]; \qquad \text{with} \quad R_{e_b} = \frac{2a|\mathbf{V}-\mathbf{V_B}|}{\nu} \tag{19.24}$$

Other authors add a memory term (Basset term) which accounts for the full history of the slip velocity through an integration between 0 and t. Based on equation (19.23) the equations of motion of the bubble become for a Rankine vortex of viscous core radius, R_c:

$$\frac{dV_{br}}{dt} = \zeta V_{b\theta}^2 - 3V_{br}\left[\frac{\dot{a}}{a} + \frac{C_d|\delta V|}{4a}\right] - \frac{3\Gamma^2}{4\pi^2R_c^2}f_1\left(\frac{\zeta}{R_c}\right);$$

(19.25)
$$\zeta\frac{dV_{b_\theta}}{dt} = -2\dot{\zeta}V_{b\theta} + 3\xi\left[\frac{\dot{a}}{a} + \frac{C_d|\delta V|}{4a}\right];$$

$$\frac{dV_{bz}}{dt} = -3z\left[\frac{\dot{a}}{a} + \frac{C_d|\delta V|}{4a}\right],$$

with

$$|\delta V| = \left(V_{br}^2 + V_{b_\theta}^2 + V_{bz}^2\right)^{\frac{1}{2}},$$

(19.26)
$$f_1 = \frac{\zeta}{R_c}, \quad \xi = \frac{\Gamma\zeta}{2\pi R_c^2} - \zeta\frac{dV_{b_\theta}}{dt}; \qquad \zeta \le R_c,$$

$$f_1 = \frac{\zeta^3}{R_c^3}, \quad \xi = \frac{\Gamma}{2\pi\zeta} - \zeta\frac{dV_{b_\theta}}{dt}; \qquad \zeta \ge R_c.$$

Both approaches (Bovis, 1980a, Latorre, 1980) used the spherical bubble dynamics equation – known as Rayleigh Plesset Equation (Plesset, 1948) – to determine the bubble radius variation with time:

(19.27)
$$\rho\left(a\ddot{a} + \frac{3}{2}\dot{a}^2\right) - 4\mu\frac{\dot{a}}{a} = -P_\infty(t) + P_v + P_{go}\left(\frac{a_o}{a}\right)^{3k} - 2\frac{\gamma}{a},$$

where μ is the dynamic viscosity, P_{go} the initial gas pressure with k the polytropic gas constant, P_v the vapor pressure, and γ the surface tension coefficient. Assumptions leading to this equation are described further in Section 19.4.1.

19.3.1. Capture Time In order to get an idea about the characteristic time for bubble capture by the vortex let us consider equations (19.20) and (19.21). If one considers – for an order of magnitude evaluation– the case where the rate of change of the bubble volume is negligible relative to the other terms, then the two equations of motion degenerate to:

$$\mathcal{M}\frac{d\overline{V_{br}}}{dt} = -\frac{3}{2\overline{\zeta}^3} + \mathcal{M}\frac{\overline{V_{b\theta}^2}}{\overline{\zeta}},$$

(19.28)
$$\frac{d\overline{V_{b\theta}}}{dt} = -\frac{\overline{V_{b\theta}V_{br}}}{\overline{\zeta}},$$

where

(19.29)
$$\mathcal{M} = \frac{\rho_b}{\rho} + \frac{1}{2}.$$

Equations (19.28) can be integrated to give the position of the non deforming bubble relative to the vortex axis versus time. Using $d\zeta/dt$ as an intermediary variable to express d/dt as $d/d\zeta \cdot d\zeta/dt$, and assuming that the bubble center has no initial radial velocity ($v_{r_o} = 0$), while the initial tangential velocity is v_{θ_o}, Equation (19.28) leads to:

(19.30)
$$\overline{V_{b\theta}}(t) = \frac{\overline{v_{\theta_o}}}{\overline{\zeta}(\bar{t})}, \qquad \text{and} \qquad \overline{\zeta}(\bar{t}) = \left[1 + \left(\overline{v_{\theta_o}}^2 - \frac{3}{2\mathcal{M}}\right)\bar{t}^2\right]^{1/2}.$$

Equation 19.30 is very instructive in terms of the motion of a particle of density ρ_b in a vortex flow field. Depending on the sign of $\left(\overline{v_{\theta_o}}^2 - \frac{3}{2\mathcal{M}}\right)$the particle will be attracted or

repelled by the vortex. This term in fact expresses a balance between inertial (centrifugal) and pressure forces. For bubbles entrained in the flow field of the vortex, v_{θ_o} is between 0 and 1, and $\mathcal{M}$ is very close to $\frac{1}{2}$, since $\rho_b/\rho \ll 1$. As a result

$$\bar{\zeta}(\bar{t}) \simeq \sqrt{1 + (\overline{v_{\theta_o}}^2 - 3)\bar{t}^2} \leq \sqrt{1 - 3\bar{t}^2}. \tag{19.31}$$

The capture time, T_c, for a bubble initially at rest in the fluid ($\overline{v_{\theta_o}}(0) = 0$) is therefore

$$\bar{t}_c = \sqrt{\frac{1}{3}}; \quad \text{or} \quad T_c = \frac{2\pi\zeta_o^2}{\Gamma\sqrt{3}}. \tag{19.32}$$

In fact, for a sphere, only viscous effects can be responsible for bubble entrainment with the flow, since with the inviscid model Equations (19.18) clearly indicate that only radial forces on the sphere are non-zero. In the presence of viscosity friction forces enable entrainment of the bubble with the fluid. The characteristic time of viscous effects, or the order of magnitude of the time needed for the bubble to be entrained in the flow being

$$T_\nu = \frac{a_o^2}{\nu}, \tag{19.33}$$

the qualitative nature of the capture depends on the relative size between T_c and T_ν.

If $T_c \gg T_\nu$ the capture time is too long, viscous effects are strong enough for the bubble to be entrained relatively rapidly by the liquid and it starts swirling around the vortex. It approaches the vortex axis little by little but very slowly.

If $T_c \ll T_\nu$ the opposite situation occurs: viscous effects are very slow to take effect and the bubble is practically sucked into the vortex moving towards its center almost in a purely radial fashion.

Finally, for $T_c \approx T_\nu$ entrainment by the liquid and attraction towards the center of the vortex occur on the same time scale. Therefore, the bubble approaches the axis in a spiral fashion. The above reasoning allows one to define a "*violent capture radius*" around the vortex which is bubble radius dependent. A bubble of radius a_o will be sucked in by the vortex if it is within the radial distance $R_{capture}$:

$$R_{capture} = a_o \sqrt{\frac{\Gamma\sqrt{3}}{2\pi\nu}}. \tag{19.34}$$

19.4. NUMERICAL STUDY

Due to the difficulty of the problem at hand and to the improved performance of high speed computers, numerical methods offer presently the best hope for solutions. Coupled with guidance from analytical, experimental and order of magnitude or phenomenological studies, a numerical approach can enable minimization of the number of physical phenomena to take into account. One of the numerical methods that has proven to be very efficient in solving the type of free boundary problem associated with bubble dynamics is the Boundary Element Method. Among others, Guerri *et al.* (1981), Blake *et al.* (1986, 1987), and Wilkerson (1989)

used this method in the solution of axisymmetric problems of bubble growth and collapse near boundaries. This method was extended to three-dimensional bubble dynamics problems by Chahine *et al.* (1988, 1989). We describe here the model, then apply it to the case of bubbles in a vortex flow.

19.4.1. Bubble Flow Equations Let us consider the cases where the presence of a bubble in the flow has significant effects, that is cases where bubble volume time variations are not negligible. This implies large but subsonic bubble wall velocities. Therefore, one can neglect viscosity and compressibility effects on the bubble dynamics. These assumptions, classical in cavitation bubble dynamics studies, result in a flow that is potential, (velocity potential, Φ), and which satisfies the Laplace equation,

$$\nabla^2\Phi = 0. \tag{19.35}$$

The solution must in addition satisfy initial conditions and boundary conditions at infinity, at the bubble walls and at the boundaries of any nearby bodies.

At all moving or fixed surfaces (such as a bubble surface or a nearby boundary) an identity between fluid velocities normal to the boundary and the normal velocity of the boundary itself is to be satisfied:

$$\nabla\Phi \cdot \mathbf{n} = \mathbf{V}_s \cdot \mathbf{n}, \tag{19.36}$$

where $\mathbf{n}$ is the local unit vector normal to the bubble surface and $\mathbf{V}_s$ is the local velocity vector of the moving surface.

The bubble is assumed to contain noncondensible gas as well as vapor of the surrounding liquid. The pressure within the bubble is considered to be the sum of the partial pressures of the noncondensible gases, P_g , and that of the liquid vapor, P_v. Vaporization of the liquid is assumed to occur at a fast enough rate so that the vapor pressure may be assumed to remain constant throughout the simulation and equal to the equilibrium vapor pressure at the liquid ambient temperature. In contrast, since time scales associated with gas diffusion are much larger, the amount of noncondensible gas inside the bubbles is assumed to remain constant and the gas is assumed to satisfy the polytropic relation,

$$P_g \mathcal{V}^k = constant, \tag{19.37}$$

where $\mathcal{V}$ is the bubble volume and k the polytropic constant, with $k = 1$ for isothermal behavior and $k = c_p/c_v$ for adiabatic conditions.

The pressure in the liquid at the bubble surface, P_L , is obtained at any time from the following pressure balance equation:

$$P_L = P_v + P_{g_0}\left(\frac{\mathcal{V}_0}{\mathcal{V}}\right)^k - C\sigma, \tag{19.38}$$

where P_{g_0} and $\mathcal{V}_0$ are the initial gas pressure and volume respectively, σ is the surface tension, C is the local curvature of the bubble, and $\mathcal{V}$ is the instantaneous value of the bubble volume. In the numerical procedure P_{g_0} and $\mathcal{V}_0$ are known quantities at $t = 0$.

19.4.2. Boundary Integral Method for Three-Dimensional Bubble Dynamics In order to render possible the simulation of single or multiple bubble behavior in complex

geometry and flow configurations including the full non-linear boundary conditions, a three-dimensional Boundary Element Method was developed and implemented by Chahine *et al.* (1988-1991). The Boundary Element Method was chosen here because of its computational efficiency. By considering only the boundaries of the fluid domain it reduces the dimension of the problem by one. This method is based on Green's equation which provides Φ anywhere in the domain of the fluid (field points P) if the velocity potential, Φ , and its normal derivatives are known on the fluid boundaries (points M), and if Φ satisfies the Laplace equation:

$$\iint_s \left[-\frac{\partial \Phi}{\partial n} \frac{1}{|\,\mathbf{MP}\,|} + \Phi \frac{\partial}{\partial n} \left(\frac{1}{|\,\mathbf{MP}\,|} \right) \right] ds = a\pi\Phi(P), \tag{19.39}$$

where $a\pi = \Omega$ is the solid angle under which P sees the fluid.

a = 4, if P is a point in the fluid,

a = 2, if P is a point on a smooth surface, and

a < 4, if P is a point at a sharp corner of the surface.

If the field point is selected to be on the surface of any of the bubbles or on the surface of the nearby boundaries, then a closed set of equations can be obtained and used at each time step to solve for values of $\partial\Phi/\partial n$ (or Φ) assuming that all values of Φ (or $\partial\Phi/\partial n$) are known at the preceding step.

To solve Equation (19.39) numerically, it is necessary to discretize each bubble into panels, perform the integration over each panel, and then sum up the contributions to complete the integration over the entire bubble surface. To do this, the initially spherical bubbles are discretized into a geodesic shape using flat, triangular panels. This discretization of a bubble shape is described in Chahine *et al.* (1988 and 1993c). Equation (19.39) then becomes a set of N equations (N is the number of discretization nodes) of index i of the type:

$$\sum_{j=1}^{N} \left(A_{ij} \frac{\partial \Phi_j}{\partial n} \right) = \sum_{j=1}^{N} (B_{ij}\Phi_j) - a\pi\Phi_i; \qquad i = 1, .., N \tag{19.40}$$

where A_{ij} and B_{ij} are elements of matrices which are the discrete equivalent of the integrals given in Equation (19.39).

To evaluate the integrals in (19.39) over any particular panel, a linear variation of the potential and its normal derivative over the panel is assumed. In this manner, both Φ and $\partial\Phi/\partial n$ are continuous over the bubble surface, and are expressed as a function of the values at the three nodes which delimit a particular panel. Obviously higher order descriptions are conceivable, and would probably improve accuracy at the expense of additional analytical effort and numerical computation time. The two integrals in (19.39) are then evaluated analytically. The resulting expressions, too long to present here, can be found in Chahine *et al.* (1988).

In order to proceed with the computation of the bubble dynamics several quantities appearing in the above boundary conditions need to be evaluated at each time step. The bubble volume presents no particular difficulty, while the unit normal vector, the local surface curvature, and the local tangential velocity at the bubble interface need further development. In order to compute the curvature of the bubble surface a three-dimensional local bubble surface fit, $f(x, y, z) = 0$, is first computed. The unit normal at a node can then be expressed

as:

$$\mathbf{n} = \pm \frac{\nabla f}{|\nabla f|}, \tag{19.41}$$

with the appropriate sign chosen to insure that the normal is always directed towards the fluid. The local curvature is then computed using

$$\mathcal{C} = \nabla \cdot \mathbf{n}. \tag{19.42}$$

To obtain the total fluid velocity at any point on the surface of the bubble, the tangential velocity, $\mathbf{V_t}$, must be computed at each node in addition to the normal velocity, $\mathbf{V_n} = \partial\Phi/\partial n$ $\mathbf{n}$. This is also done using a local surface fit to the velocity potential, $\Phi_l = h(x, y, z)$. Taking the gradient of this function at the considered node, and eliminating any normal component of velocity appearing in this gradient gives a good approximation for the tangential velocity

$$\mathbf{V_t} = \mathbf{n} \times (\nabla \Phi_l \times \mathbf{n}). \tag{19.43}$$

The basic procedure can then be summarized as follows. With the problem initialized and the velocity potential known over the surface of the bubble, an updated value of $\partial\Phi/\partial n$ can be obtained by performing the integrations in (19.39) and solving the corresponding matrix equation (19.40). $D\Phi/Dt$ is then computed using a "modified" Bernoulli equation (see Equation (19.51) below). Using an appropriate time step all values of Φ on the bubble surface can then be updated using Φ at the preceding time step and $D\Phi/Dt$,

$$\frac{D\Phi}{Dt} = \frac{\partial \Phi}{\partial t} + \left(\frac{\partial \Phi}{\partial n} \mathbf{n} + \mathbf{V_t} \right) \cdot \nabla \Phi. \tag{19.44}$$

In the results presented below the time step, dt, was based on the ratio between the length of the smaller panel side, l_{min} and the highest node velocity, V_{max}. This choice limits the motion of any node to a fraction of the smallest panel side. It has the great advantage of constantly adapting the time step, by refining it at the end of the collapse – where l_{min} becomes very small and V_{max} very large – and by increasing it during the slow bubble size variation period. New coordinate positions of the nodes are then obtained using the displacement:

$$d\mathbf{M} = \left(\frac{\partial \Phi}{\partial n} \mathbf{n} + V_t \mathbf{e_t} + \mathbf{V_o} \right) dt, \tag{19.45}$$

where $\mathbf{n}$ and $\mathbf{e_t}$ are the unit normal and tangential vectors. This time stepping procedure is repeated throughout the bubble growth and collapse, resulting in a shape history of the bubble.

19.4.3. Pressure / Velocity Potential Relation Let us consider the case of a bubble growing and collapsing in a nonuniform flow field ("*basic flow*") of velocity $\mathbf{V_0}$ that is known and satisfies the Navier Stokes equations:

$$\frac{\partial \mathbf{V_0}}{\partial t} + \mathbf{V_0} \cdot \nabla \mathbf{V_0} = -\frac{1}{\rho} \nabla P_0 + \nu \nabla^2 \mathbf{V_0} \, . \tag{19.46}$$

Also assume that in presence of the oscillating bubbles, the resulting velocity field, given by $\mathbf{V}$, also satisfies the incompressible Navier Stokes equation:

$$\frac{\partial \mathbf{V}}{\partial t} + \mathbf{V} \cdot \nabla \mathbf{V} = -\frac{1}{\rho} \nabla P + \nu \nabla^2 \mathbf{V} \,. \tag{19.47}$$

Both $\mathbf{V}$ and $\mathbf{V}_0$ also satisfy the continuity equation. We can now define bubble flow velocity and pressure variables, $\mathbf{V}_b$ and P_b, as follows:

$$\mathbf{V}_b = \mathbf{V} - \mathbf{V}_0, \qquad P_b = P - P_0. \tag{19.48}$$

If we consider the case where "*bubble flow*" field is potential[3] :

$$\mathbf{V}_b = \nabla \Phi_b, \qquad \nabla^2 \Phi_b = 0, \tag{19.49}$$

and subtract (19.46) from (19.47) accounting for (19.49) we obtain

$$\nabla \Psi = \nabla \left[\frac{\partial \Phi_b}{\partial t} + \frac{1}{2} \mid \mathbf{V}_b \mid^2 + \mathbf{V}_0 \cdot \mathbf{V}_b + \frac{P_b}{\rho} \right] = \mathbf{V}_b \times (\nabla \times \mathbf{V}_0). \tag{19.50}$$

The assumption of *potential "bubble flow"* implies that, even though the basic flow is allowed to interact with the bubble dynamics and be modified by it, no new vorticity can be generated by the bubble behavior with the chosen model. Equation (19.50) can be integrated to obtain an equation similar to the classical unsteady Bernoulli equation. For the particular case of the Rankine vortex Equation (19.51) can be written in cylindrical coordinates, when the "bubble flow" does not have any $\mathbf{e}_\theta$ components:

$$\frac{\partial \Psi}{\partial r} = 0, \qquad \frac{1}{r} \frac{\partial \Psi}{\partial \theta} = 2V_b, \qquad \frac{\partial \Psi}{\partial z} = 0.$$

In this case the Bernoulli equation is to be replaced by:

$$\frac{\partial \Phi_b}{\partial t} + \frac{1}{2} \mid \mathbf{V}_b \mid^2 + \frac{P - P_0}{\rho} = \textit{constant in any radial direction.} \tag{19.51}$$

Accounting for at-infinity conditions, the pressure in the liquid at the bubble wall, P_L, given by (19.51) is related to Φ_b and the pressure field in the Rankine vortex P_0 by:

$$\left[\frac{P_L}{\rho} = \frac{P_0}{\rho} - \frac{\partial \Phi_b}{\partial t} - \frac{1}{2} \mid \mathbf{V}_b \mid^2 \right]_{\textit{at bubble wall}} . \tag{19.52}$$

19.4.4. Specialization to Axisymmetric Problems In axisymmetric problems, the physical variables (velocity potential and pressure) are independent of the angular coordinate. Thus the angular coordinate only enters the formulation through the argument of the Green's function in Equation (19.39)

$$G(\mathrm{MP}) = 1/ \mid \mathrm{MP} \mid . \tag{19.53}$$

The integration of these dependent quantities can be explicitly carried out. Let C represent the trace of the geometry under consideration in a meridian plane. Let r, θ, z be the cylindrical

[3] This is obviously a simplifying assumption which needs to be removed in future research on the subject. Section 19.8 presents a first step in that direction.

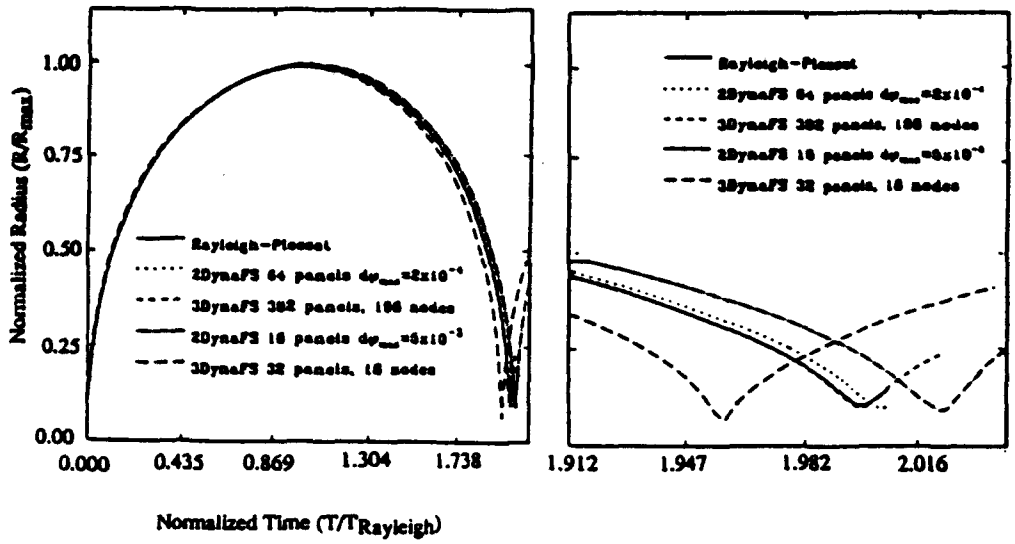

Fig. 19.3. *Comparison between Rayleigh-Plesset solution and the axisymmetric BEM code* **2DynaFS** *and the 3D BEM code* **3DynaFS**. *Computations started with an initial bubble pressure 584 times larger than the ambient pressure. a) Over bubble period. b) End of collapse.*

coordinates of point M, running point on the boundary, and without loss of generality we select the coordinates of P to be $(R, 0, Z)$. The integral equation (19.39)can then be written

$$\phi(R,0,Z) = \int_C \phi(r,z) r \frac{\partial}{\partial n_M}\left(\int_0^{2\pi} G d\theta\right) ds_M - \int_C \frac{\partial \phi}{\partial n_M} r \int_0^{2\pi} G d\theta \, ds_M \tag{19.54}$$

In writing the above expression the fact that the normal to an axisymmetric surface is independent of the angular coordinate has been used. Thus, integration over the angular variable is reduced to evaluation of one integral

$$I = \int_0^{2\pi} G(r,\theta,z;R,Z) d\theta = -\frac{1}{4\pi}\int_0^{2\pi} \frac{d\theta}{\sqrt{R^2 + r^2 - 2rR\cos\theta + (Z-z)^2}}, \tag{19.55}$$

which is nothing but the *complete elliptic integral of the first kind*, $K(m)$, with

$$m = \frac{4rR}{A}; \qquad A = \sqrt{(R+r)^2 + (Z-z)^2}. \tag{19.56}$$

The equation for the potential may then be written as:

$$2\pi\phi(R,Z) = -\int_C \phi(r,z) r \frac{\partial}{\partial n_M}\left(\frac{4K(m)}{\sqrt{A}}\right) ds_M + \int_C \frac{\partial \phi}{\partial n_M}(r,z) \frac{4K(m)}{\sqrt{A}} r ds_M. \tag{19.57}$$

Further details of the method can be found in Taib (1985).

19.5. NUMERICAL RESULTS AND DISCUSSION

19.5.1. Validation of Numerical Codes The use of the Boundary Element Method to study axisymmetric bubble dynamics has been validated by the various authors quoted earlier. This has included both comparisons with a quasi-analytical solution for spherical

bubbles – Rayleigh-Plesset Equation (19.27) – and experimental validation for the relatively simple cases of spherical and axisymmetric bubble collapse near flat solid walls. Figures 19.3*a* and 19.3*b* show comparative results between the codes used below (axisymmetric **2DynaFS** and fully three-dimensional **3DynaFS**) and the semi-analytical results.

Comparison of the results of the 3D code used in the examples shown below against previously published and confirmed results in the literature for the relatively simple cases have been very favorable. For spherical bubbles, comparison with the Rayleigh-Plesset "exact" solution revealed that numerical errors for a "coarse" discretization of a 102-node bubble (not shown in the above figures) was about 2 percent of the achieved maximum radius, but was very small, 0.03 percent, of the bubble period. The error on the maximum radius was less than 0.14 percent for a discretized bubble of 162 nodes (320 panels), and dropped to 0.05 percent for 252 nodes (500 panels). Comparisons were also made with studies of axisymmetric bubble collapse available in the literature (Guerri, *et al*, 1981, Blake *et al*, 1986, 1987), and have shown, for the coarse discretization, differences with these studies on the bubble period of the order of 1 percent. Finally, comparison with actual test results of the complex three-dimensional behavior of a large bubble collapse in a gravity field near a cylinder shows very satisfactory results, (Chahine, 1988, 1991). The observed difference in the period was shown to be related to the confinement of the experimental bubble in a cylindrical container.

19.5.2. Bubble Capture

Large bubble growth rate, low surface tension case As expected from the mechanistic considerations analysis presented in Sections 19.1.1 and 19.1.2 numerical simulations using the fully three-dimensional numerical approach reveal potential for strong bubble deformation during capture by a vortex. The numerical results indicate that this is the case for a very wide range of bubble sizes and initial values of the pressure difference between the inside and the outside of the bubble.

Figure 19.4 shows three-dimensional bubble behavior in the case where the ratio between the pressure inside the bubble and the ambient pressure is significantly large, $p_i/p_\infty = 584.3$. This would be the case where the bubble in equilibrium in a high ambient pressure environment is suddenly subjected to the flow field of a vortex, as for instance when a propeller tip vortex suddenly captures a cavitation bubble (see Maines and Arndt, 1993, and Green, 1991). In a Cartesian system of coordinates, $OXYZ$, the bubble is initially centered at (0,0,0), and the line vortex is located parallel to the Z axis, at $\overline{X} = X/R_{max} = 2$ (two times the maximum size, R_{max}, the considered bubble would have if allowed to grow under the same pressure difference in an infinite medium). The core size considered here is $4R_{max}$. With this geometry the bubble center remains in the plane $Z = 0$.

Figure 19.4*a* gives a projected view of the bubble in the XOY plane at different instants. The observer is looking down on the XOY plane from very far on the Z axis. The bubble is seen spiraling around the vortex axis (perpendicular to the figure) while approaching it. At the same time, due to the presence of the pressure gradient, the bubble strongly deforms and a reentrant jet is formed directed towards the axis of the vortex, thus indicating the presence of a much larger dynamic pressure on the bubble side opposite to the vortex axis.

Figure 19.4*b* shows projected view of the same bubble in the YOZ plane seen from the OX axis. Here some moderate elongation of the bubble is observed along the axis of the vortex

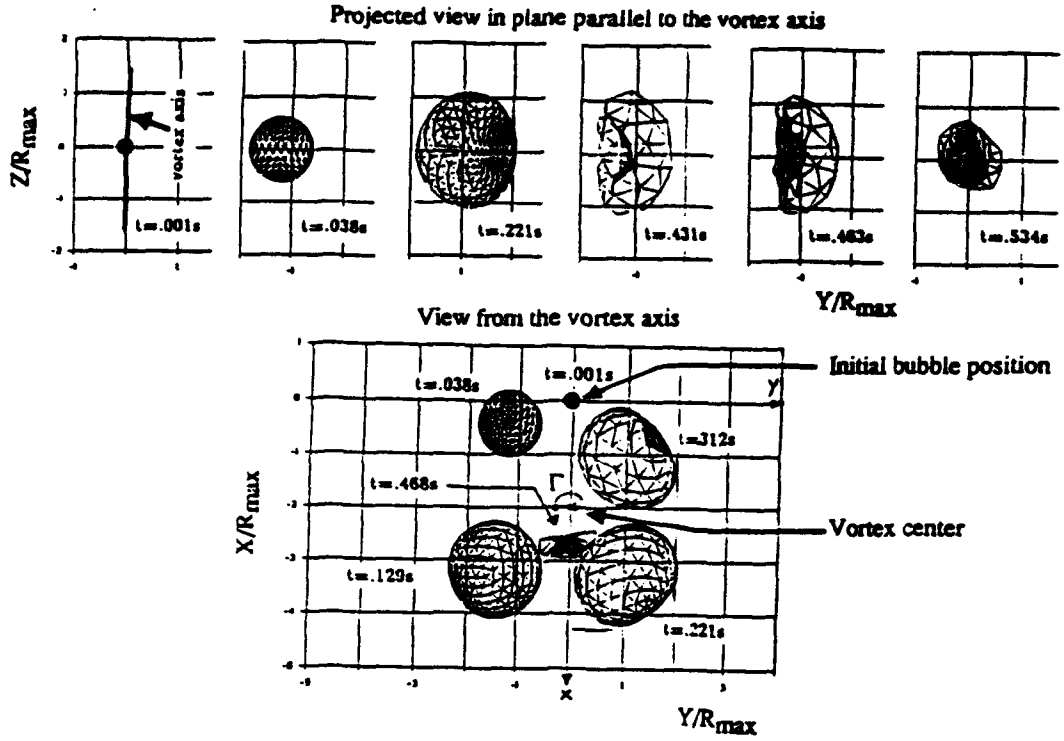

Fig. 19.4. *3D bubble shapes at various times. Bubble initially at the origin of the cartesien coordinate system, and vortex at* $X = 2R_{max}$. $\Omega = 0.474$, $p_i/p_\infty = 584.3$, $R_c/R_{max} = 4$. *Projected view a) in the* XOY *plane; b) in the* XOZ *plane.*

as well as a very distinct side view of the re-entrant jet. *This result is totally contrary to the usually held belief that bubbles constantly grow during their capture until they reach the axis and elongate along it.*

Figure 19.5 shows in the XOY plane perpendicular to the vortex axis the motion of two particular points on the bubble, A and B, initially along OY. Also shown is the motion of the midpoint, C. While C seems to follows a path similar to the classical logarithmic spiral, A and B can follow more complicated paths, even moving away from the vortex axis at some point in time for case (b) where the vortex axis was initially at $X = 1$.

Small growth rate and surface tension Figure 19.6 considers the influence of bubble size on bubble behavior during the capture process. In all three cases shown in the figure a ratio between the pressures inside and outside the bubble equal to one is considered, $p_i/p_\infty = 1$. In all cases, the viscous core radius is chosen to be $R_c = 2.2\ mm$, while the initial distance between the vortex center and the center of each bubble is chosen to be $\zeta_o \simeq 1.5R_c = 3.2\ mm$. The dimensions shown are normalized values with the initial bubble radius for each case. The circulation in the vortex is chosen to correspond to a practical value for the case of a tip vortex behind a foil, such as that used in the experiments described by Maines and Arndt (1993) and Green (1991), $\Gamma = 0.152\ m^2/s$. Three bubble sizes are considered: 10 μm, 100 μm and 1000 μm. As expected, bubble deformation increases with the bubble size. The deformation is small for a_o=10 μm, becomes very significant for a_o=100 μm, and is extremely important for a_o=1000 μm. In all cases, the bubbles while remaining in the inviscid region, are seen to be sheared very strongly by the flow. The smaller bubbles appear to deform in the expected way

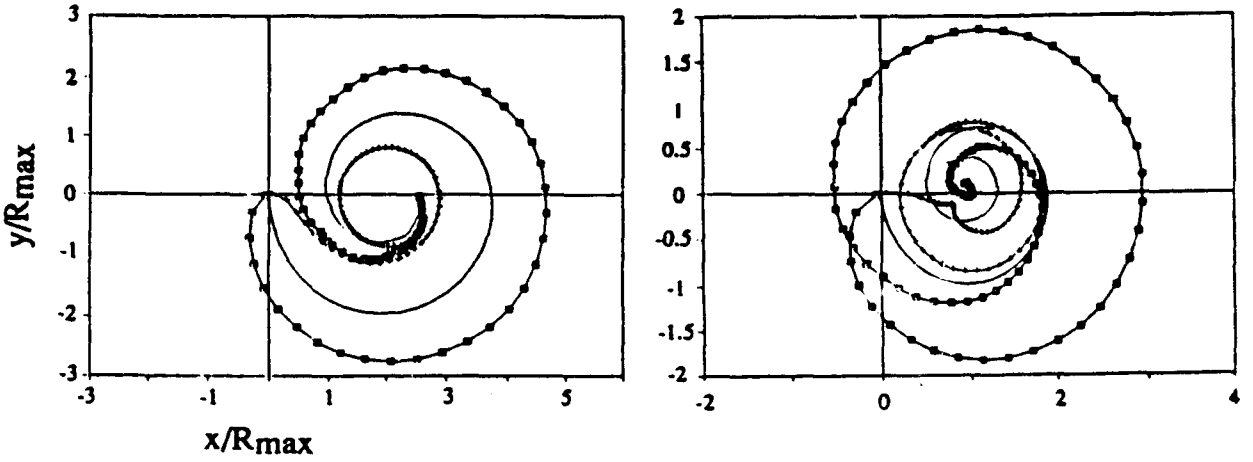

Fig. 19.5. *Motion of the two points initially on axis OX, A and B, and the mid point C between A and B, versus times.* Ω = 0.474, $p_i/p_\infty = 584.3$, $a_c/R_{max} = 4$. *Vortex located at a)* $X = 2R_{max}$; *b)* $X = R_{max}$.

in a shear flow. The computations were stopped when significant bubble shape deformations necessitated finer time steps. The larger bubble case (a_o=1000 μm) shows extreme bubble elongation and wrapping around the viscous core region.

19.5.3. Multiple Bubbles One of the key question that one needs to address in bubble/vortex interaction practical studies is how does a distribution of bubbles modify the flow field in a vortex line. In order to address such a problem the program **3DynaFS** is being modified for effective implementation on a supercomputer. Indeed one of the difficulties of such a study is the required large number of discretization points which prevents significant runs on typical memory and speed limited computers. Figure 19.7 shows a case run in the case of a field of bubbles in absence of a vortex field on a Cray machine. In the figure case two planes of symmetry were assumed to minimize computation times. In the presence of a vortex line use of such a symmetry is not warranted since, due to various rates of rotation of each bubble in the vortex field, the symmetry is not preserved during the bubble motion. In addition, due to the high shear rates that bubbles can experience, a relatively large number of discretization points is needed to describe each bubble.

Figure 19.8 shows the case of a 5-bubble configuration. This run has the advantage of including both vortex / bubble and bubble / bubble interactions. All five bubbles are chosen such that in absence of the vortex flow field, the pressures inside and outside each bubble are the same and equal to 0.74 atm, $p_i/p_\infty = 1$. The viscous core radius and the circulation are again chosen to be in the same ranges as those in the experiments described by Maines and Arndt (1993), and Green (1991). The viscous core is chosen to be $R_c = 2.2mm$, while $\Gamma = 0.1573\ m^2/s$, $\Omega = 0.872$. The initial bubble centers are selected to be on OY axis at the coordinates: $Y = 0, 2, 3, 4$ and 5 mm. The vortex line is parallel to OX axis and is centered on $Y = 1.5\ mm$. As a result, bubbles No. 1, 2 and 3 are initially located in the viscous core, while bubbles No. 4 and 5 are located in the inviscid flow region. All five bubbles considered have an initial radius of 100 μm. Figure 19.8 shows contours of the bubbles as they rotate around the vortex axis at various times This figure clearly shows the presence of a nonuniform

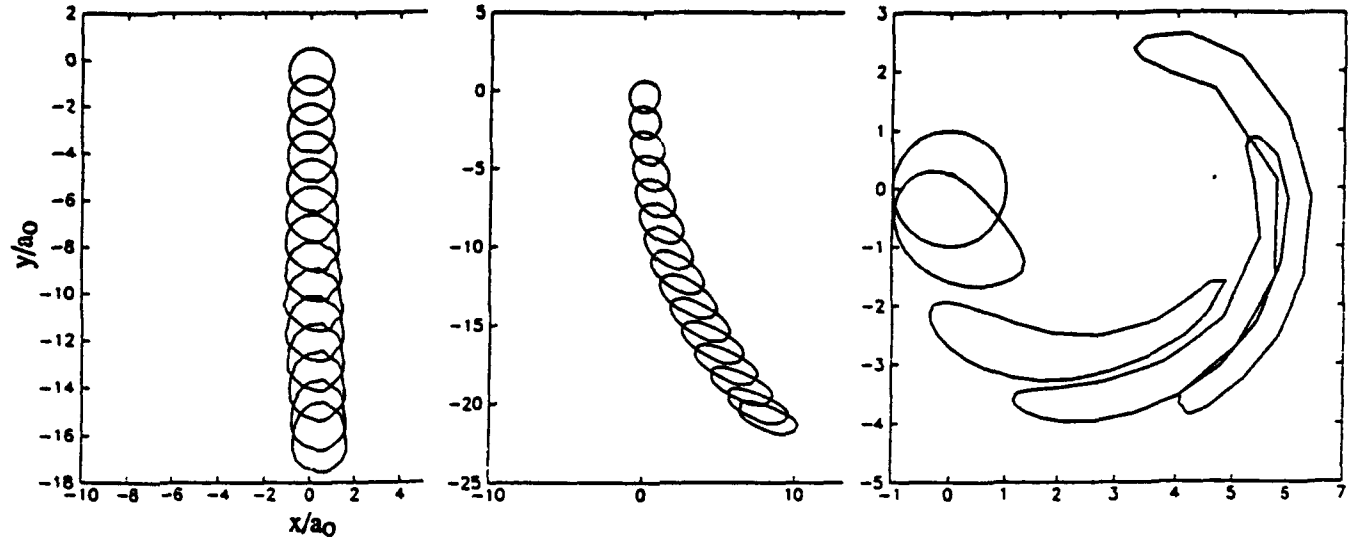

Fig. 19.6. *Bubble contours at various times.* $\Gamma = 0.1527m^2/s$, $p_i/p_\infty = 1$, $a_c = 2.2mm$, *vortex located at* $X = 3.2mm$, *with* $a_o =$ *a)* $10\mu m$, *b)* $100\mu m$, *c)* $1000\mu m$.

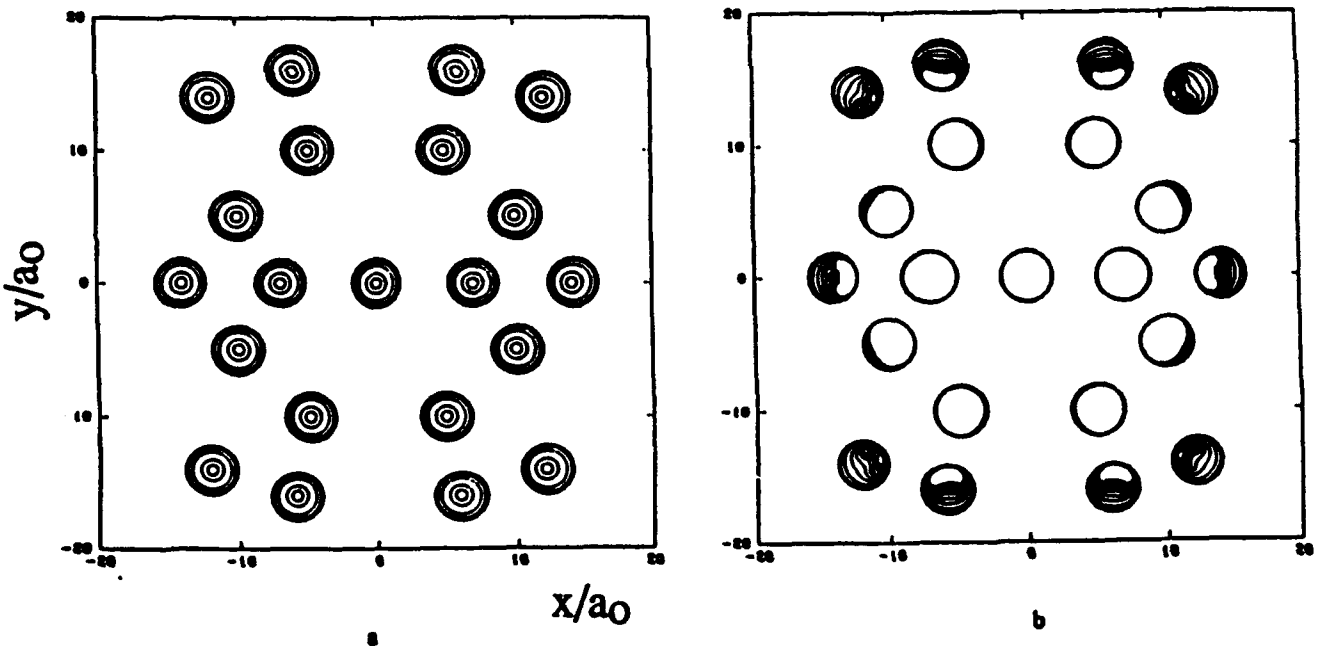

Fig. 19.7. ***Simulation of the dynamical interactions between a cloud of 21 bubbles using*** **3DynaFS** ***on a Cray. Two planes of symmetry are used. Each bubble has 102 nodes and 200 panels. a) Growth. b) Collapse.***

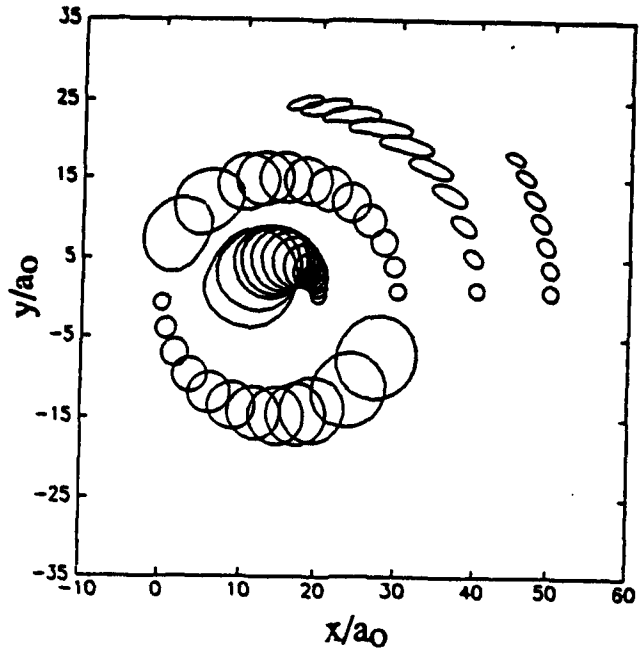

Fig. 19.8. *Dynamical behavior of 5 bubbles in a vortex line flow - Bubble contours at various times. The vortex line is perpendicular to the page and centered on* $Y = 1.5mm$. $R_c = 2.2mm$, $\Gamma = 0.1573m^2/s$. $\Omega = 0.872$. *All bubbles have* $a_0 = 100\mu m$.

flow field. Indeed, Bubble No. 3 which is the closer to the region of highest angular velocity of the *"basic flow"* is seen to swirl around the vortex center at the fastest rate, while Bubble No. 2, which is the closest to the vortex center is seen to practically rotate around itself. Similarly, the highest shear is seen to occur close to the viscous core edge where the pressure gradients and their variations are steeper.

Since all bubbles were chosen to have the same initial radius and internal pressure, the natural period of oscillation of each of the selected bubbles increases with the proximity to the vortex axis. As a result, the farthest bubble from the axis, Bubble No. 5, collapses first while stretching and deforming. In order to be able to continue the computation following break up of a bubble, that bubble was removed and the computation was continued with the bubbles left.

Figure 19.9 shows two thee-dimensional views of the bubbles before the collapse of bubble No. 1. These views enable one to have a better idea of the bubble shape deformation and elongation during the capture phenomenon.

Figure 19.10, courtesy of Sheldon Green, is an unpublished photo of a bubble in the viscous core of the trailing vortex of a NACA 66-209 hydrofoil (see Green,1991, for details of the experiment). The photograph is a double exposure, the time of separation between the two pictures being 150 μs. The three bubble shapes in the top of the figure are aligned along the axis of the vortex. The diameter of these shapes is of the order or 200 μm. The bottom two shapes are those of the same bubble at two instants 150 μs, and illustrate very clearly the large deformations of the bubble during its capture by the vortex. As in the numerical simulations presented above, this behavior appears to be related to the large shear stresses experienced by the bubble while approaching the vortex axis. In the first of the two pictures the bubble is very elongated due to shear, while 150 μs later, it appears to have grown in

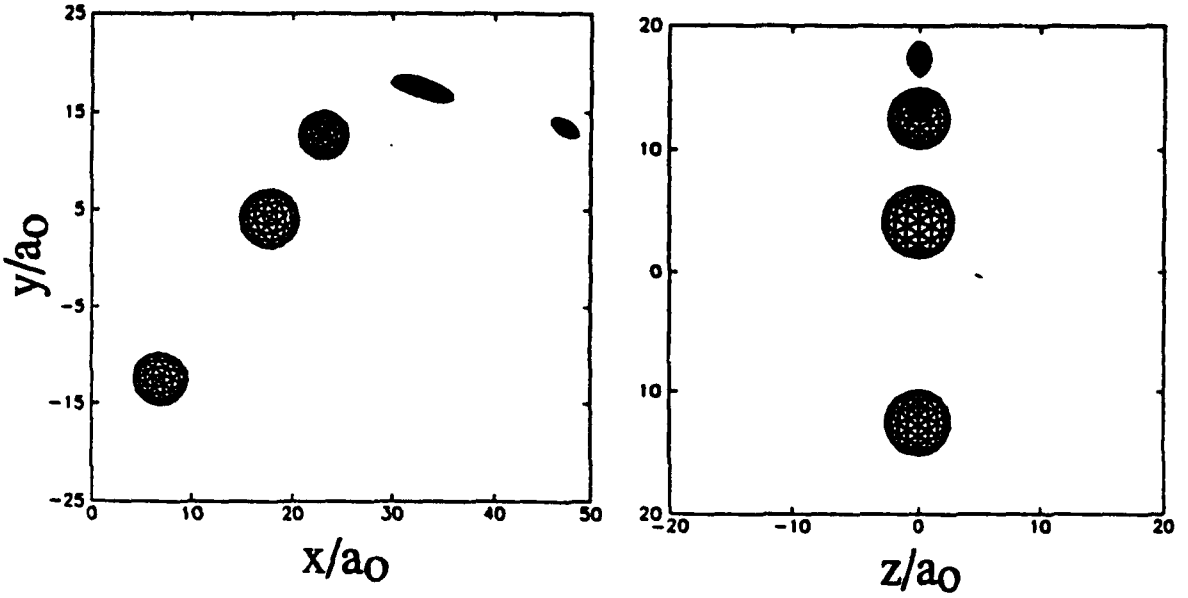

Fig. 19.9. *3D bubble shapes in the vortex line flow field of Figure 8 before collapse of buble No. 1. View from a) OZ axis, b) OX axis.*

size – due to the pressure drop in the vortex,– while conserving a strong deformation on its downstream surface.

19.5.4. Bubble on Vortex Axis Let us consider now the case where the bubble is placed at the vortex axis at $t = 0$ and starts to grow due to the excess between the internal pressure and the local ambient pressure. Such a problem was considered earlier by Crespo *et al* (1990) who studied the dynamics of an elongated bubble. Unfortunately, his model neglected essential elements in the bubble / line vortex dynamics: i.e. the presence of an azimuthal velocity flow field, a rotational and viscous flow, and a pressure "well" on the axis. Crespo obtained a strong jet which initiated at both extreme points of the bubble along the axis of symmetry. As shown in Figure 19.11*a* such a behavior is reproduced using the program **2DynaFS** when the vortex flow field is neglected. However, the opposite effect is in general obtained when the rotation in the vortex flow is included. Figure 19.11*b* illustrates this for particular values of the circulation, Γ, (or the swirl parameter, Ω) and the normalized core radius, $\overline{R_c} = R_c/R_{max}$. Modifications in the results when Ω and $\overline{R_c}$ are changed are discussed in the following paragraph.

In both cases shown in Figures 19.11*a* and 19.11*b* the initial bubble shape elongation ratio, bubble length to radius, was three. It is clear from the comparison that the swirl flow has a conclusive effect on the bubble dynamics. Bubble surface portions away from the vortex axis experience much higher pressures than bubble surface portions on and close to the vortex axis, and therefore move much faster during the collapse phase generating, instead of the sharp jets on the axis as in Figure 10*a*, a constriction in the mid-section of the bubble. This generates an hourglass shaped bubble which then separates into two tear-shaped bubbles.

In the following figures 19.12*a* – *c*, the dynamics of initially spherical bubble positioned at $t = 0$ on the vortex axis are studied. The initial internal pressures inside the bubbles are taken to be larger than the pressure on the vortex axis, and the bubbles are left free to adapt to this pressure difference. The figures strongly indicate that the bubble behavior depends significantly for a given value of the swirl parameter, Ω, on the normalized core radius $\overline{R_c}$,

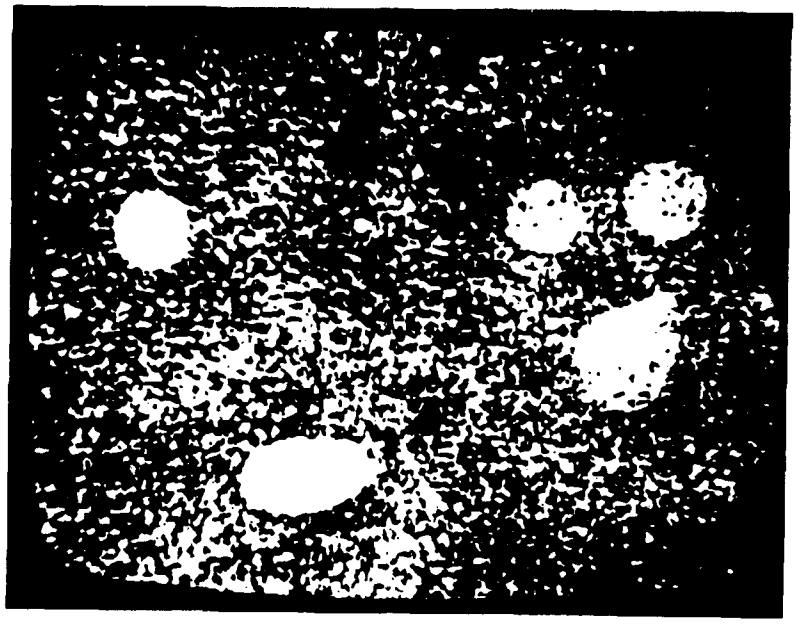

Fig. 19.10. *Double exposure photo of a bubble in the viscous core of the trailing vortex of a NACA 66-209 hydrofoil (see Green, 1991). Time of separation between two exposures =150 μs. Scale 190 μm./cm.* $R_e = 6.810^5$, $\Gamma = 0.232m^2/s$. *Courtesy of Sheldon Green.*

ratio of R_c to R_{max}, the maximum radius the bubble would achieve if it was in an infinite medium with an ambient pressure equal to that on the vortex axis. In all cases where the bubble maximum radius, R_{max} is larger than R_c it appears that the bubble tends to adapt to the vortex tube of radius R_c. This could lead to various bubble shapes as shown in the following figures ending up with a very elongated bubble with a wavy surface for large values of R_{max}/R_c.

Figures 19.12a – c show bubble contours at various times during growth and collapse for increasing values of the core radius, R_c, and decreasing values of p_i/p_∞. Also shown are selected 3D shapes of the bubbles at various times which have the advantage of being much more descriptive. It is apparent from these figures, that during the initial phase of the bubble growth, radial velocities are large enough to overcome centrifugal forces and the bubble first grows almost spherically. Later on, the bubble shape starts to depart from spherical and to adapt to the pressure field. The bubble then elongates along the axis of rotation. Once the bubble has exceeded its equilibrium volume, bubble surface portions away from the axis – high pressure areas – start to collapse, or to return rapidly towards the vortex axis. To the contrary, points near the vortex axis do not experience rising pressures during their motion, are not forced back towards their initial position, and continue to elongate along the axis. As a result, a constriction appears in the mid-section of the bubble. The bubble can then separate into two or more tear-shaped bubbles. It is conjectured that this splitting of the bubbles is a main contributor to cavitation inception noise. This behavior is very similar to that observed for bubble growth and collapse between two plates (Chahine, 1989), which results in the formation of a vortex line! (see Figure 19.12).

Keeping Ω constant while reducing the core size R_c has the effect of steepening the radial pressure gradient along the bubble surface and increasing the rotation speed inside the viscous core. This enhances the deviation of the bubble shape from a sphere, and increases the

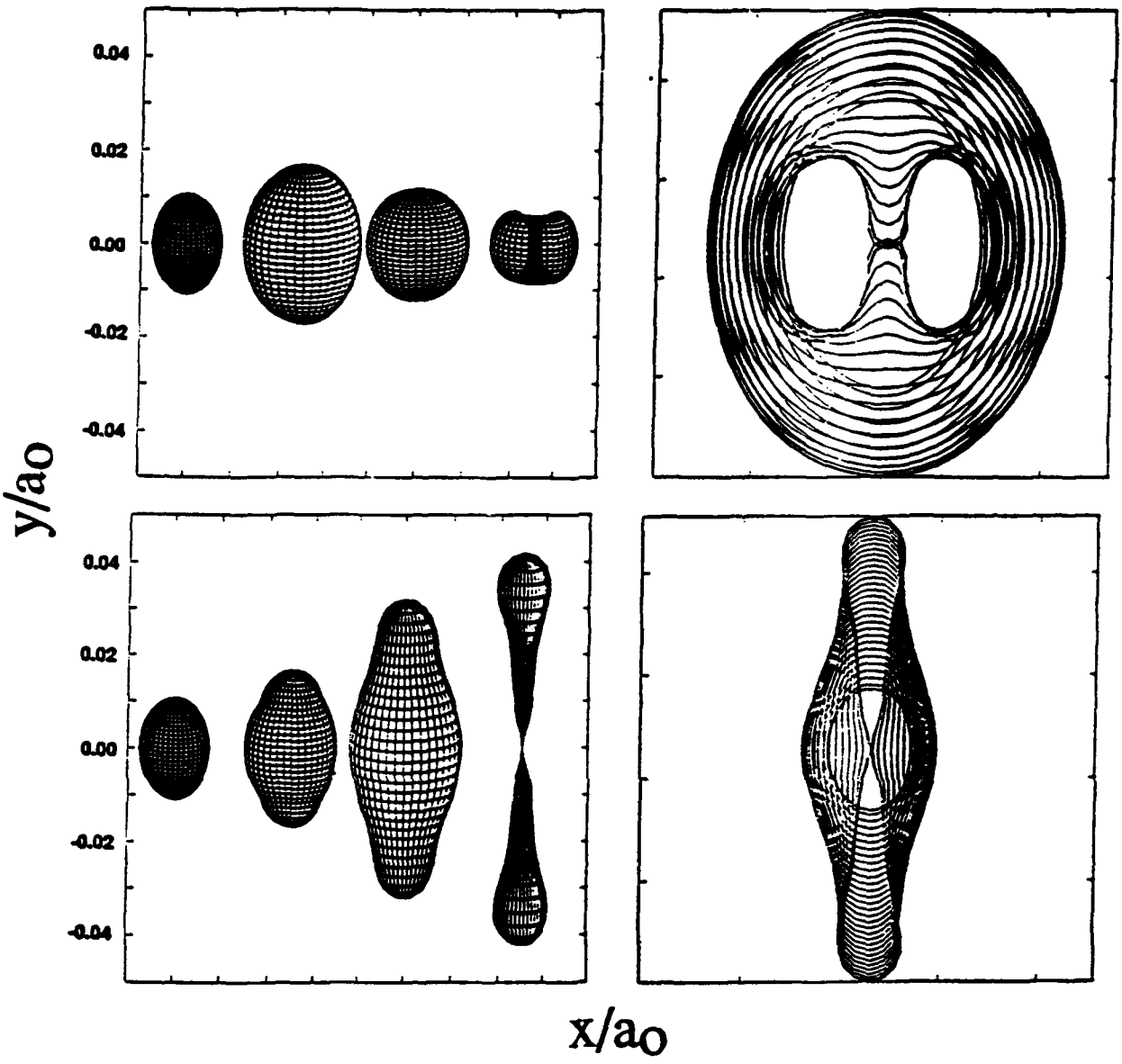

Fig. 19.11. *Comparison between the contours of an elongated bubble during its collapse in the absence and in the presence of swirl. Initial elongation ratio of 3.* $p_\infty/p_i = 3.27$. *a) No swirl. b)* $\Omega = 0.56$. $R_c/R_{max} = 3$.

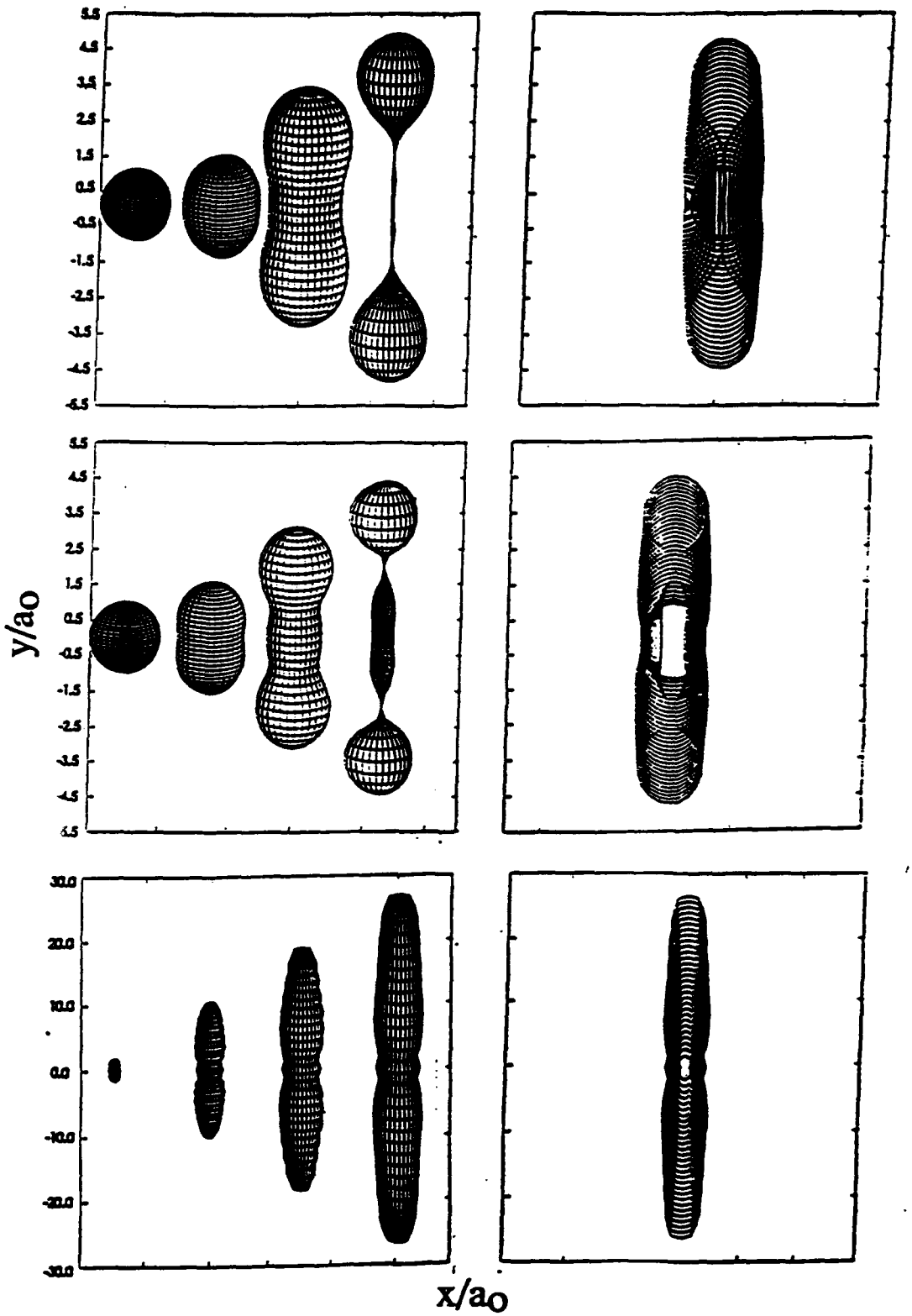

Fig. 19.12. *Bubble dynamics on the axis of a vortex line. Left side shows 3D shapes at selected times. Right side shows bubble contours at increasing times.* $\Gamma = 0.005m^2/s$, $R_o = 100\mu m$. *a)* $p_i/p_\infty = 2$, $R_c/R_o = 1$, *b)* $p_i/p_\infty = 2$, $R_c/R_o = 1$, *c)* $p_i/p_\infty = 1$, $R_c/R_o = 0.57$.

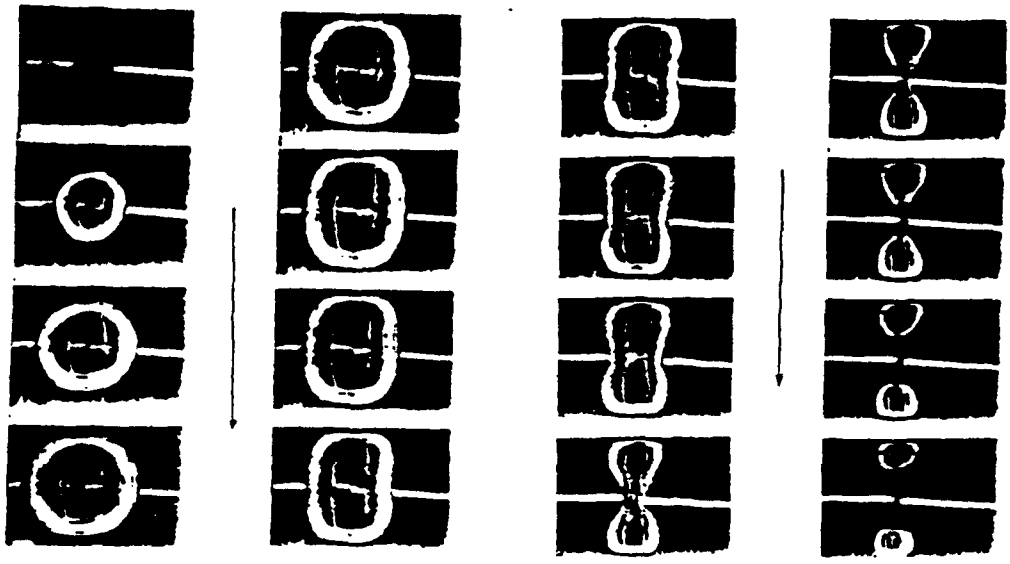

Fig. 19.13. *Bubble collapse between two solid parallel plates resulting in the formation of an hourglass shaped bubble and a line vortex perpendicular to the two plates.*

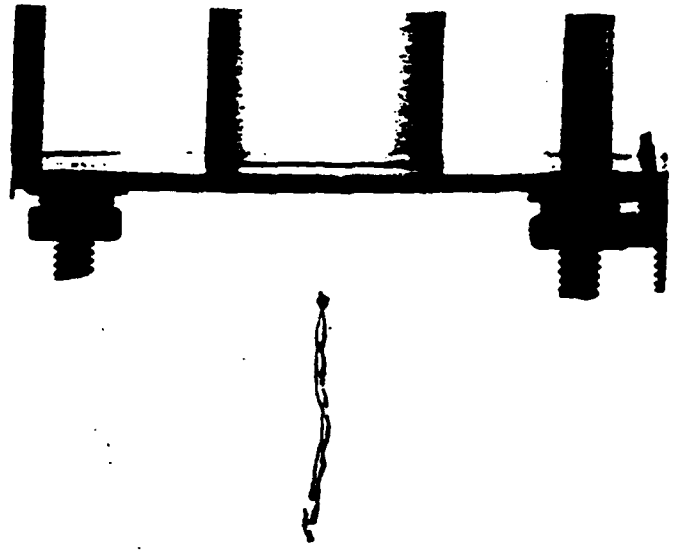

Fig. 19.14. *Cavitation bubble shapes observed at the exit of a vortex tube.*

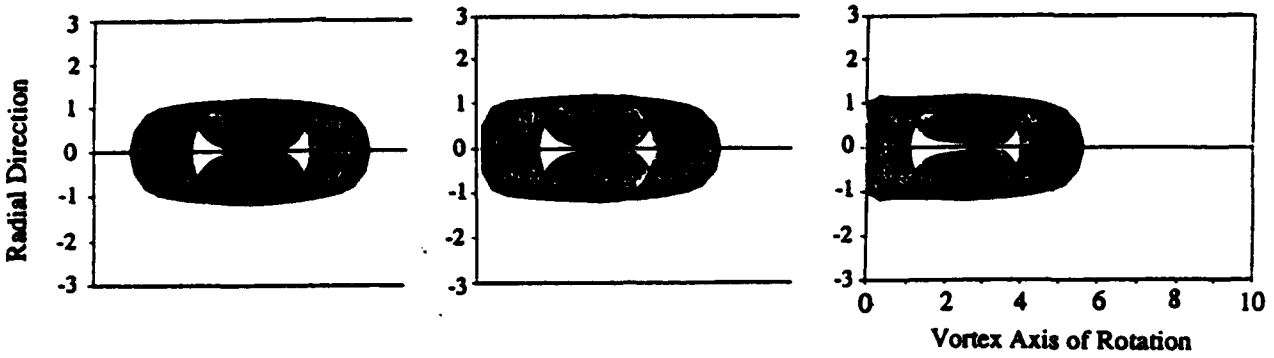

Fig. 19.15. *Influence of solid wall distance on bubble collapse in a line vortex.* $\Omega = .475$, $p_i/p_\infty = 584$, $a_c = 1.18$. L/R_{max} = *a) 4; b) 3; c) 2.5.*

centrifugal force on the fluid particles closer to the vortex axis. This has the consequence of increasing the elongation rate of the bubble and results in more and more complex dynamic shapes of the elongated bubbles. The bubble can then become subdivided into three, four or more satellite bubbles during the collapse. The elongated and wavy shapes obtained have been observed in unpublished tests that we have conducted on cavitation on the axis of the vortex formed in a vortex tube (see Figure 19.14).

19.5.5. Bubble on Vortex Axis Near a Wall The series of Figures 19.15$a-c$ show the collapse of a bubble trapped in a line vortex perpendicular to a solid wall at various distances from this wall. The boundary is at $y = 0$ and its distance to the initial bubble center, L, is normalized with R_{max}. The presence of the wall is accounted for by the incorporation of an image bubble. The uneventful growth phase ends with the elongated spheroid shaped contours shown at the center of each figure. Then, the overall bubble behavior appears to be similar to that in absence of the wall; namely, bubble elongation along the axis followed by a splitting into two bubbles. The presence of the wall is felt by an asymmetry between the two secondary bubbles. In all cases, computation was stopped at bubble splitting. A special treatment to the bubble shape discretization needs to be done after that point (panel removal) and is being implemented. It is speculated, based on previous bubble dynamics observations, that very strong jets bringing back the two pointed tips (in the splitting region) of the two secondary bubbles inside each bubble will be generated. This phenomenon is expected to be stronger for the secondary bubble close to the wall since that bubble has a much more elongated tip.

Figure 19.16 shows the influence of the circulation parameter, Ω, on the bubble behavior for fixed values of the core radius and the distance to the wall. This figure contains significant information on the scaling of bubble behavior in a vortex flow. Three characteristic dimensions of the bubble are shown as a function of time. These are the bubble radius along the plane perpendicular to the line vortex, R_n, and the distances between the initial bubble center and the two extreme points on the vortex axis, $Z_n(1)$ and $Z_n(100)$. Figure 19.16 shows time variation of these three quantities normalized with R_{max}. Time is normalized with the

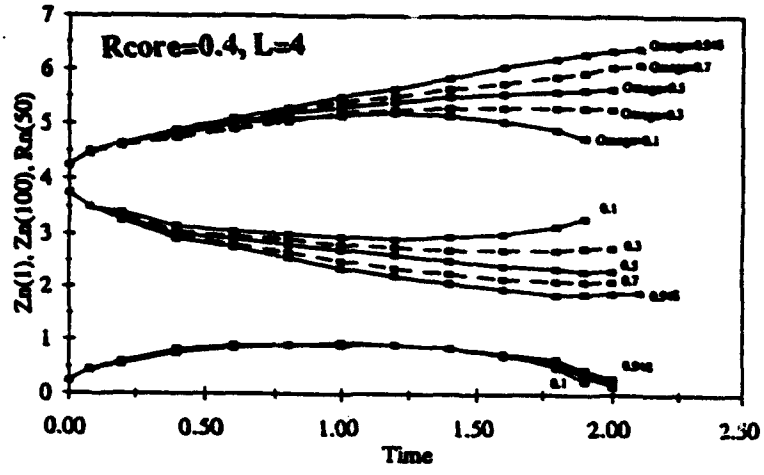

Fig. 19.16. *Influence of* Ω *on the motion of bubble axial and longitudinal dimensions versus time for a bubble trapped in a line vortex perpendicular to a solid wall. Distances are normalized with* R_{max} *and times are normalized with Rayleigh time.* $p_i/p_\infty = 584$, $a_c/R_{max} = 0.4$, $L/R_{max} = 4$.

Rayleigh time based on R_{max} and the pressure difference between P_{go} and the pressure on the vortex axis. It is apparent from this figure that R_n follows the classical Rayleigh model. Variations of Ω between 0.1 and 0.94 modify the normalized bubble period by less than 10 percent. One should notice, however, that bubble period is here defined as the time needed for the bubble to subdivide into two secondary bubbles, and that no bubble surface instability, as described earlier, occurred in that case. Bubble elongation, on the other hand, depends strongly on Ω, as can be seen from the Z_n curves. The elongation of the bubble part close to the wall is seen to be affected for large values of Ω.

19.6. VALIDATION STUDY: BUBBLE / VORTEX RING INTERACTION.

19.6.1. Experimental Study In order to validate the numerical studies on bubble / vortex interactions, a fundamental experimental and numerical study was conducted. This consisted of the controlled observation of the interaction between a vortex ring and a bubble. The results of the experiment were then compared with those obtained with the 3D free surface dynamics numerical code **3DynaFS** described above (Chahine et al, 1993).

A vortex ring was generated in a Plexiglas tank using a cylinder equipped with a 2.5 *cm* radius piston. The cylinder has an sharp lip exit to enhance the roll up of the fluid vortex generated at the lip. This results in a vortex ring with a diameter slightly larger than that of the cylinder (Kalumuck and Chahine, 1990). The water in the tank is degassed using a vacuum pump and a spark generated bubble is produced using two tungsten electrodes submerged in the tank which can be manipulated from outside the tank to be placed where desired. The spark is produced by discharging during a very short time period ($\simeq 10^{-4}s$) a high voltage (6000 volts) from a series of capacitors. The interaction between the generated ring and bubble was then observed. A spark generating the bubble has the advantage of simulating cavitation bubbles and allowing one to choose precisely when and where the bubble is generated, which is essential to coordinating the positions of the bubble and the ring, and the starting time of a high speed camera. A triggering line allows one to synchronize the departure of the piston and

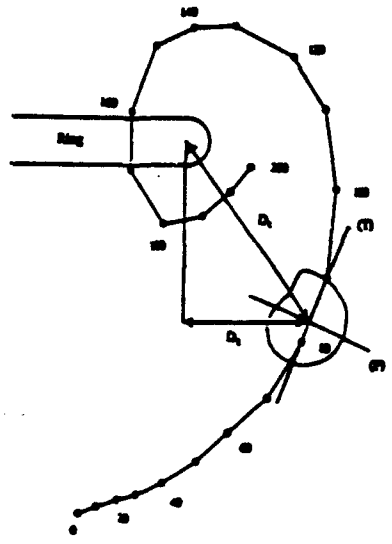

Fig. 19.17. *Particle trajectory around the ring viscous core.*

the triggering of the spark generator using pressure transducers to precisely detect the vortex ring motion. As the piston starts to move down, a pressure pulse is created in the tank by the fluid impulsive motion. This is detected by the transducer probe and amplified to trigger a delay generator. The output signal (a very short pulse) then triggers the spark generator. Visualization was performed using a HYCAM II high speed camera capable of 11,000 frames per second.

On several of the motion pictures taken very small gas bubbles were present under the piston. The visualization of the motion of these bubbles allows one to observe their trajectory around the vortex ring. The existence of a "viscous core" was apparent from the velocity profile obtained by tracing the microbubbles' motion, whether or not the vortex ring was cavitating. For the cavitating cases, the "viscous core" surrounded the vaporous/gaseous core. A typical trajectory of the small bubbles is shown in Figure 19.17. Also shown in this figure is a sketch of a bubble and the particle trajectory line (T). Figure 19.17 also shows the geometric characteristics of the bubble/ring positions. D_1 is the distance between the bubble center and the viscous core center when the bubble is at its maximum volume and has the equivalent maximum radius R_{max}. D_2 is the horizontal distance between the bubble and the center of the viscous core. The normalized quantities $\overline{D_1} = D_1/R_{max}$ and $\overline{D_2} = D_2/R_{max}$ characterize the bubble / vortex ring interactions. As expected, it is observed that smaller $\overline{D_1}$ and $\overline{D_2}$ correspond to stronger interactions and larger bubble deformations.

Figure 19.18*a* – *c* drawn in the ring reference frame shows the bubble motion and deformation with time for three selected cases of increasing bubble/shear interaction. The electrodes position shown on each graph is the one at the instant of the spark generation. The vortex ring side view indicates the position of the reference frame.

As can be seen from the pictures in Figure 19.19*a* ($\overline{D_1} = 2.16$, $\overline{D_2} = 0$, $V_{ring} = 0.28m/s$) and from the contours in Figure 19.20*a* , the bubble remains practically spherical during its growth. The interaction is weak due to the relatively large distance between the bubble and the ring, and also due to the relatively small circulation of the ring. The first collapse is too fast, and no significant deformation of the bubble is seen until the rebound when a reentrant jet appears on the bottom face of the bubble followed after the rebound by an outgoing

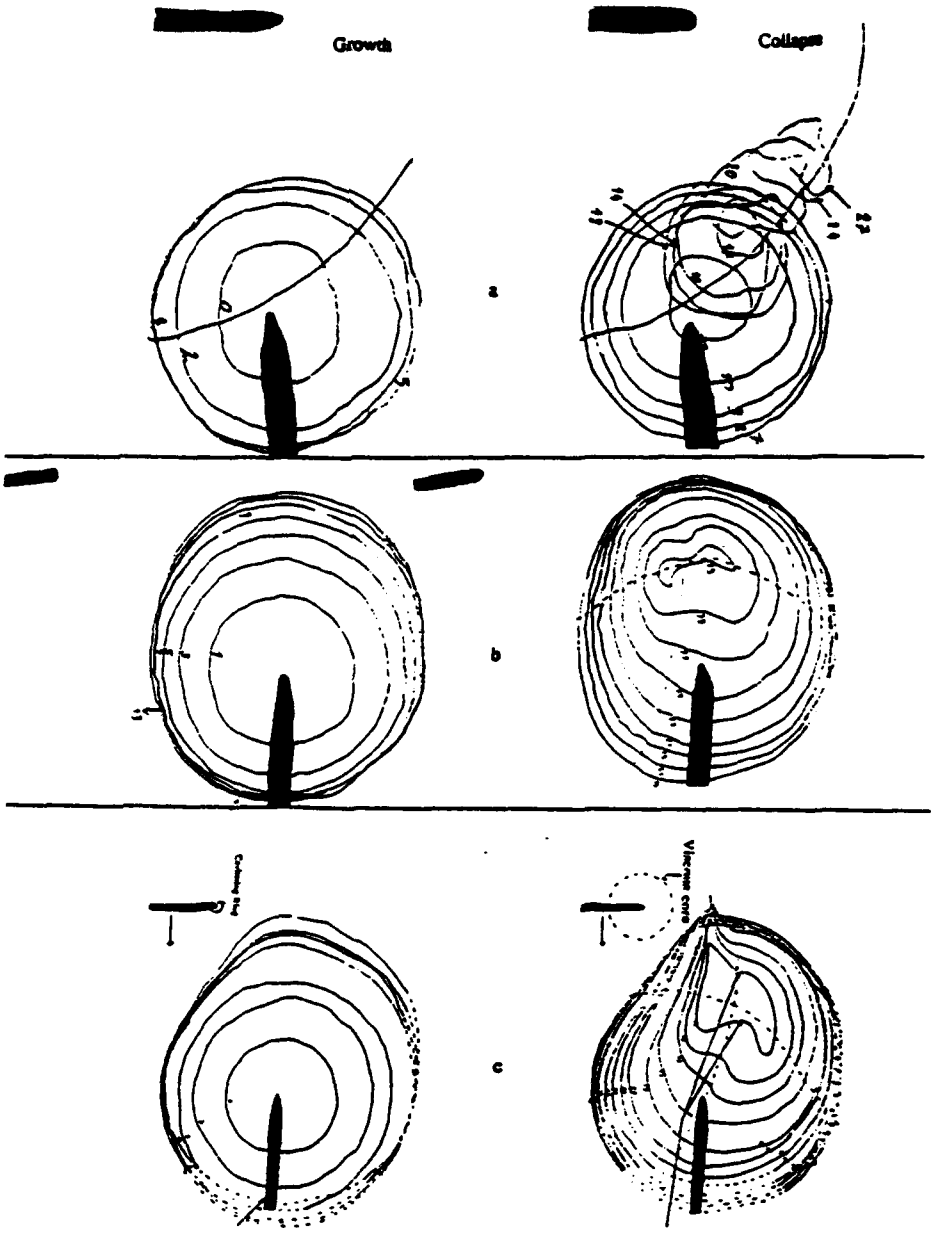

Fig. 19.18. *Bubble contours at various times from High Speed sequences of Figure 19.19. a)* $\overline{D_1} = 2.16$, $\overline{D_2} = 0$, $V_{ring} = 0.28m/s$, *b)* $\overline{D_1} = 2.38$, $\overline{D_2} = 1.5$, $V_{ring} = 0.78m/s$, *c)* $\overline{D_1} = 1.1$, $\overline{D_2} = 0.37$, $V_{ring} = 0.82m/s$.

jet on the top face. It appears that during the first bubble oscillation period the bubble translation velocity is smaller than the vortex generated fluid velocity. The bubble therefore sees a flow moving upward. The jet direction (including the reentrant and the outside jet) is on a pathline of shear flow, and the bubble motion after the collapse follows a particle path line while oscillating and cutting itself in two.

In Figure 19.19*b* ($\overline{D_1} = 2.38$, $\overline{D_2} = 1.5$, $V_{ring} = 0.78m/s$) the bubble first grows spherically, then it starts to stretch into an ovoid shape: the bottom face is less curved and the top face more curved than in the spherical case. Here the distance $\overline{D_1}$ is not too different from the previous case but the circulation in the vortex ring is about three times larger. When the bubble volume decreases, the stretching due to the shearing action becomes more pronounced and a constriction along the bubble periphery appears along the pathlines (T). The bubble then rebounds with a dumbbell shape.

In Figure 19.19*c* ($\overline{D_1} = 1.1$, $\overline{D_2} = 0.37$, $V_{ring} = 0.82m/s$) the bubble appears to be stretched more and more in the pathlines' direction during its growth, with the top region more stretched than the bottom one, and the top right part growing more than the left one. When the bubble collapses, its left side continues to be sheared by the flow into a pathline direction and a 'beak' forms at the top left part and becomes more pronounced once the volume of the bubble starts to decrease. Then, there is a constriction all around the bubble which appears first on the top face of the bubble. The bubble then cuts itself in two and rebounds as two side-by-side very distorted bubbles (or bubble clouds). The left one then touches the cavitating ring and splits again into two parts. The deformations of the bubble are more significant in this case than in the two previous cases, because the bubble is closer to the center of the ring core and experiences a strong shear flow. In addition, there appears to be a "venturi effect" between the bubble and the viscous core that further increases the stretching of the left part of the bubble

Within the margin of errors of the measurements, comparison of the time variation of the average radius of each bubble shows no significant effect of the presence of shear on the bubble period. However, indications of a lengthening effect of the bubble period can be seen on the characteristic distances between the bubble 'center' and the two upstream and downstream points along a particle pathline (direction (T)) . This effect however seems small in the cases presented here and should be investigated further.

Physical explanations The observations made above can be qualitatively understood by considering the velocity and pressure fields around the bubble. The motion of each point on the surface of the bubble is the result of the combination of the underlying (shear) fluid velocity and of the velocity due to the bubble growth or collapse. The effect of the underlying fluid flow (whose characteristic speed is about $2m/s$) is minor during initial bubble growth and later bubble collapse phases, but becomes most important at the end of the growth and at the beginning of the collapse where bubble wall velocities reach a minimum. Indeed, right after the spark generation, the speed of each point of the bubble surface is very high (about $40m/s$). It then decreases to zero at about the maximum radius, and then increases during the bubble collapse. For a bubble in a uniform flow, the existence of the flow reflects on the bubble shape by a larger bubble growth in the downstream direction and by a flattening of the bubble shape in the upstream direction. Later on due to inertia, the downstream part that has extended further collapses faster forming a reentrant jet directed upstream in the

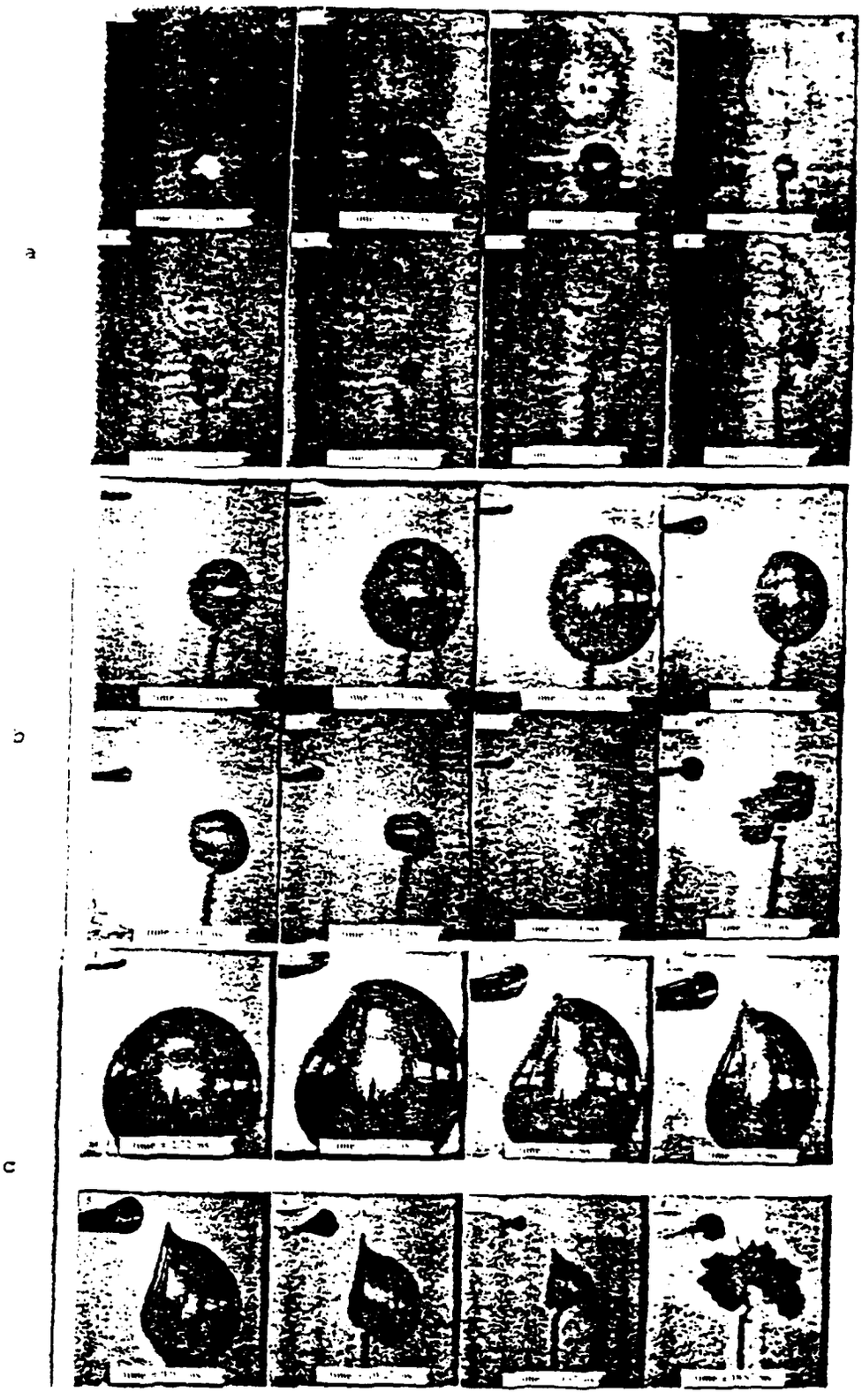

Fig. 19.19. *High Speed Movie sequences of bubble / vortex ring interaction.* a) $\overline{D_1} = 2.16$, $\overline{D_2} = 0$, $V_{ring} = 0.28m/s$, b) $\overline{D_1} = 2.38$, $\overline{D_2} = 1.5$, $V_{ring} = 0.78m/s$, c) $\overline{D_1} = 1.1$, $\overline{D_2} = 0.37$, $V_{ring} = 0.82m/s$.

plane of symmetry of the bubble.

When the flow is not uniform, a similar phenomenon occurs but is stronger on one side of the bubble than on the other due to the typical asymmetry of a shear flow. In addition, the possibility that the underlying shear flow becomes at some point during the bubble history stronger than the bubble wall velocity creates the possibility of a jet generated by the underlying flow, which can be opposite to the one described above and directed downstream. In the case of the figures shown here, the velocity profile seen by the bubble decreases from left to right. When the bubble starts to grow, the speed of each point is much more important than the velocity of the fluid flow: the bubble is therefore almost spherical. Then, when the speed of each point decreases, the influence of the fluid flow increases. The top part of the bubble grows more than without the presence of the basic flow and, due to the shear, the left part grows more than the right one. In addition, the top face is more stretched than the bottom face because on the top face the speeds add up, while they subtract on the bottom. The opposite is true during the collapse where velocities add up on the bottom part of the bubble and subtract on the top.

As the fluid flow moves upward in the case shown in the figure, the reentrant jet is expected to appear on the top face. However, due to the strong shear, the left part of the bubble is prevented from collapsing forcing a compensating middle of the bubble constriction all along the bubble, with a tendency to form reentrant jets on both ends of the bubble along the pathline. This constricted shape of the bubble is similar to that obtained with a bubble collapsing between two walls.

19.6.2. Numerical Modeling In order to model the bubble/shear flow interaction described above, the Boundary Element Method (BEM) code described above, **3DynaFS**, was used. The flow field of the moving vortex ring was modeled using the following classical expression for the velocity potential at the point M produced by a vortex ring ($\mathcal{R}$):

$$\phi(M) = -\frac{\Gamma}{4\Pi} \iint_{S_R} \frac{\mathbf{e_t} \cdot \mathbf{PM}}{|\mathbf{PM}|^2} ds_P, \tag{19.58}$$

where S_R is any surface limited by the ring vortex ring line ($\mathcal{R}$), and $\mathbf{e}_t$ is the tangential direction along ($\mathcal{R}$). This enables one to determine the velocity and pressure field outside of the viscous core region of the vortex ring.

Figure 19.20c shows simulations for these same experimental conditions as in Figure 19c with $\Gamma = 0.12m^2/s$, while Figures 19.20a and 19.20b show the same conditions but for $\Gamma = 0.25m^2/s$ and $\Gamma = 0.10m^2/s$. As in the experiment Figure 19.20c shows elongation of the left side of the bubble in the shear flow direction. The formation of a beak at the end of the bubble growth is also evident but not as pronounced as in the experiment. Later a constriction in the bubble shape along the fluid pathline is also apparent. The overall comparison between this numerical modeling and the experiment is encouraging. However, the strong shearing effect on the beak preventing the bubble top from collapsing from the left side is not as strongly reproduced in the numerical simulation. This is most probably due to the fact that the simulation neglected the vortex *bubble* ring behavior and did not include any modification of the flow due to the growth of the ring bubble near the spark-generated bubble creating the venturi effect we mentioned earlier.

At the smaller circulations the tendency of the bubble to elongate and then cut itself into

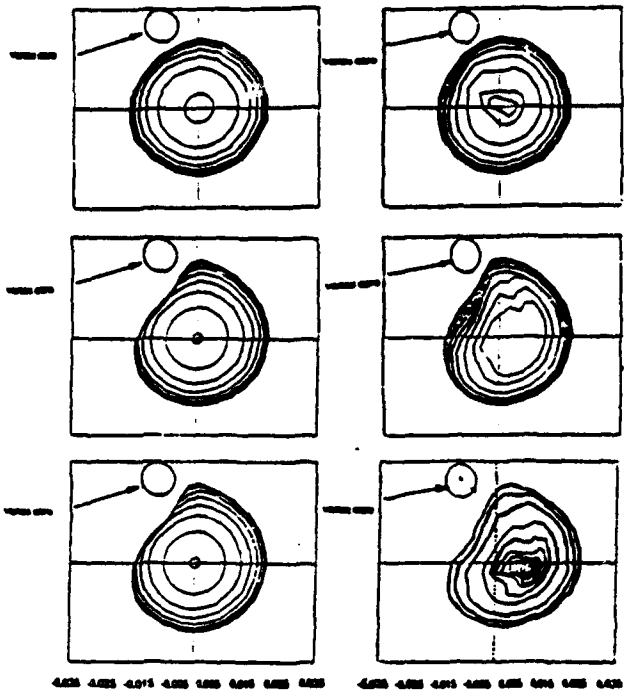

Fig. 19.20. *Numerical simulations of bubble / vortex ring interaction..* $\overline{D_1} = 1.1$, $\overline{D_2} = 0.37$, $V_{ring} = 0.82m/s.$; $\Gamma =$ *a)* $0.025m^2/s$; *b)* $0.10m^2/s$; *c)* $0.12m^2/s$ *which corresponds to Figure 19.18c.*

two is also clearly apparent as in the experiments.

19.7. OTHER RELEVANT STUDIES

One other relevant aspect of bubble / vortex interactions concerns the case where the gaseous phase or cavitation is so developed that the vortex center is filled with gas or vapor. The dynamics of such cavities have been considered in the particular cases of cavitating vortex rings and well developed tip vortices. As for the studies presented above, various simplifying assumptions were made by the various authors in order to address these problems. For the sake of brevity we will not consider these studies here. However, we refer the readers to the following publications on cavitating vortex rings (Chahine and Genoux, 1983, Genoux and Chahine 1984, Chahine and Kalumuck, 1988 and Kalumuck and Chahine, 1990). Concerning elongated developed tip vortices, the readers can consult the following publications (Bovis, 1980a, Ligneul and Latorre, 1989, and Ligneul, 1989).

19.8. FULL VISCOUS INTERACTION BETWEEN A CYLINDRICAL BUBBLE AND A LINE VORTEX

One weakness of the numerical approaches presented above is the fact that, while the influence of the flow on the bubble was fully accounted for, the modification of the flow by the bubble's presence and dynamics was restricted to the case where the "bubble flow" was potential (see Section 19.4.3). In the present section, we will remove this restriction in the simple but interesting case of the interaction between a cylindrical bubble and a line vortex. This corresponds to cases such as described in the previous section, where the line vortex has the central part of its viscous core gaseous or vaporous. As illustrated below, such an analysis is important to determine criteria for unstable bubble growth (cavitation inception), and

to describe how bubble dynamics affects the viscous flow itself. To do so, we consider the case where an axisymmetric elongated bubble of initial radius a_o is located on the axis of a fully viscous line vortex. For illustration, we consider the case where, at $t = 0$, the vortex line is a Rankine vortex. From there on, the vortex diffuses with time and interacts fully with the bubble. The generated flow satisfies the axisymmetric incompressible Navier-Stokes' equations in cylindrical coordinates. With all derivatives with respect to z and θ being null, the continuity and momentum equations reduce to:

$$\frac{1}{r}\frac{\partial}{\partial r}(r\rho u_r) = 0. \tag{19.59}$$

$$\frac{\partial u_r}{\partial t} + u_r\frac{\partial u_r}{\partial r} - \frac{u_\theta{}^2}{r} = \frac{-1}{\rho}\frac{\partial p}{\partial r} + \nu\frac{\partial}{\partial r}\left[\frac{1}{r}\frac{\partial}{dr}(ru_r)\right], \tag{19.60}$$

$$\frac{\partial u_\theta}{\partial t} + u_r\frac{\partial u_\theta}{\partial r} + \frac{u_r u_\theta}{r} = \nu\frac{\partial}{\partial r}\left[\frac{1}{r}\frac{\partial}{\partial r}(ru_\theta)\right], \tag{19.61}$$

Denoting the radius of the bubble as $a(t)$, and its time derivative, $\mathring{a}(t)$, the continuity equation leads to:

$$u_r = \frac{a(t)\,\mathring{a}(t)}{r}. \tag{19.62}$$

Replacing u_r by its expression in 19.60 and 19.61 one obtains:

$$\frac{1}{r}\left[a\,\mathring{\mathring{a}} + \mathring{a}^2 - u_\theta^2 - \frac{a^2\,\mathring{a}^2}{r^2}\right] = -\frac{1}{\rho}\frac{\partial p}{\partial r}, \tag{19.63}$$

$$\frac{\partial u_\theta}{\partial t} + \frac{a\,\mathring{a}}{r}\left(\frac{\partial u_\theta}{\partial r} + \frac{u_\theta}{r}\right) = \nu\frac{\partial}{\partial r}\left[\frac{1}{r}\frac{\partial}{\partial r}(ru_\theta)\right], \tag{19.64}$$

This set of coupled equations allows one to describe both the bubble dynamics and flow field modification with time accounting for the interaction with the bubble.

19.8.1. Method of Solution In order to obtain a differential Equation for the bubble radius variations, similar to the Rayleigh Plesset Equation (19.27), Equation (19.63) is integrated between $r = a(t)$ and a very large radial distance $r = R_{inf}$, beyond which the vortex flow is assumed to be inviscid, and that due to a line vortex of circulation Γ. This leads to an integral term containing u_θ^2. In order to obtain this term, a space and time integration of Equation (19.64) is needed. This is obtained using a Crank-Nicholson finite difference integration scheme of the partial differential equation (19.64). To do so, the domain of integration is made time independent using the variable change,

$$s = \frac{r}{a(t)}. \tag{19.65}$$

The integration region becomes for all times $[1; s_{\inf}]$, with $R_{inf}(t) = a(t)s_{inf}$. With a, $\mathring{a}$ known at a given time step through the solution of Equation 19.63, Equation 19.64 becomes:

$$\frac{D\overline{u_\theta}}{D\bar{t}} = -\frac{s\,\dot{\bar{a}}}{\bar{a}}\frac{\partial \overline{u_\theta}}{\partial s} - \frac{\dot{\bar{a}}}{s\bar{a}}\frac{\partial \overline{u_\theta}}{\partial s} - \frac{\dot{\bar{a}}}{s^2\bar{a}}\overline{u_\theta} + \frac{1}{R_e}\frac{1}{\bar{a}^2}\left(\frac{\partial^2 \overline{u_\theta}}{\partial s^2} + \frac{1}{s}\frac{\partial \overline{u_\theta}}{\partial s} - \frac{\overline{u_\theta}}{s^2}\right) \tag{19.66}$$

with

$$\bar{a} = \frac{a}{a_0}, \quad \bar{t} = \frac{t}{a_0}\sqrt{\frac{P_\infty}{\rho}}, \quad \overline{u_\theta} = u_\theta\sqrt{\frac{P_\infty}{\rho}}, \quad R_e = \frac{a_0}{\nu}\sqrt{\frac{P_\infty}{\rho}}, \quad \bar{r} = \frac{r}{a_0}. \tag{19.67}$$

Similarly, Equation (19.63) becomes:

$$\bar{a}\,\ddot{\bar{a}} + \dot{\bar{a}}^2 = \frac{\dot{\bar{a}}^2}{2\ln(s_{\inf})}\left[-\frac{1}{s_{\inf}^2} + 1\right] + \frac{1}{\ln(s_{\inf})}\int_1^{s_{\inf}} \frac{\overline{u_\theta}^2}{s}ds +$$

$$-\frac{1}{\ln(s_{\inf})}\left[1 - \left(\frac{\bar{\Gamma}}{2\pi\bar{a}s_{\inf}}\right)^2 - \overline{p_v} + \overline{p_{go}}\left(\frac{1}{\bar{a}}\right)^{2k} - \frac{1}{W_e\bar{a}} - \frac{2\,\dot{\bar{a}}}{R_e\bar{a}}\right], \tag{19.68}$$

with

$$\bar{\Gamma} = \frac{\Gamma}{a_o}\sqrt{\frac{P_\infty}{\rho}}, \quad \overline{p_v} = \frac{p_v}{p_\infty}, \quad \overline{p_g} = \frac{p_g}{p_\infty}, \quad W_e = \frac{a_o P_\infty}{\sigma}. \tag{19.69}$$

19.8.2. Initial and Boundary Conditions The initial conditions considered are as follows. For the bubble,

$$a(0) = a_o, \qquad \dot{a}\,(0) = 0. \tag{19.70}$$

For the line vortex, the equation at $t = 0$, is that of a Rankine vortex as described in Section (1.1.14), with

$$u_r(r, t = 0) = 0. \tag{19.71}$$

In addition, the following boundary condition, similar to Equation (19.38), is imposed at the bubble interface:

$$P(a) = p_v + p_{g_o}\left(\frac{a_o}{a}\right)^{2k} - \frac{\sigma}{a} + 2\mu\frac{\partial u_r(a)}{\partial r}, \tag{19.72}$$

where μ is the dynamic viscosity, and the gas compression law is given by:

$$p_g = p_{g_o}\left(\frac{a_o}{a}\right)^{2k}. \tag{19.73}$$

In addition, the following 'at-infinity' condition is imposed on the pressure at the distance, R_{inf} :

$$P(R_{\inf}) = p_\infty - 2\rho\left(\frac{\Gamma}{2\pi s_{\inf}a(t)}\right)^2. \tag{19.74}$$

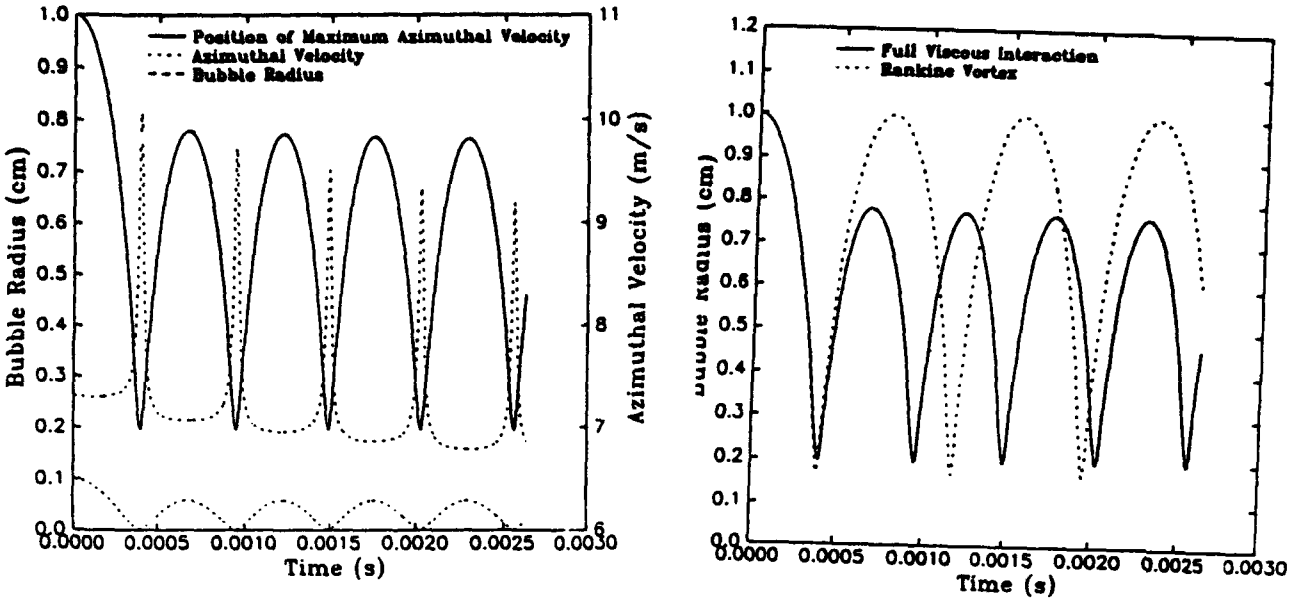

Fig. 19.21. *Dynamics of the interaction between a cylindrical bubble and a line vortex.* $\Gamma = 0.5\ m^2/s$, $P_{go} = 5\times10^3 Pa$, $P_\infty = 1.3\times10^5 Pa$. a) Bubble radius, value of maximum azimuthal velocity $u_{\theta\,\max}$, and position of $R_{\theta\,\max}$. b) Bubble radius versus time with and without viscous interaction.

19.8.3. Some Preliminary Results Figures 19.21*a* and 19.21*b* illustrate both the bubble / vortex flow field interaction and a case where there is a need to include this full interaction in the dynamics. In these two figures, the bubble has an initial radius of $1mm$, while the viscous core of the vortex has an initial radius of $1cm$. The initial circulation in the vortex is $0.5\ m^2/s$, and the initial pressure in the bubble is $5\times10^3 Pa$, while the ambient pressure is $1.3\times10^5 Pa$. Therefore, the bubble starts its dynamics by collapsing. Figure 19.21*a* shows simultaneously three characteristic quantities of the problem versus time. The first quantity is the bubble radius versus time, while the other two quantities are the radial position, $R_{\theta\,\max}$, of the maximum azimuthal velocity, $u_{\theta\,\max}$, and the value of this velocity. In the previous sections, these two last quantities remained constant with time. A very important first result very clearly shown in Figure 19.21*a* is that both the position of $R_{\theta\,\max}$, and the value of $u_{\theta\,\max}$, both directly depend on the variation of $a(t)$. The viscous core (of radius $R_{\theta\,\max}$) is seen to decrease with the bubble radius during bubble collapse, and to increase with the bubble radius during bubble growth. This tendency of the viscous core to get displaced with the bubble wall, corresponds to intuition, but is proven numerically to our knowledge for the first time here and in Desgrees du Lou *et al.*, 1993.

Viscous effects appear more prominently when following the bubble dynamics over more than a single period of oscillation. Both maximum values of $R_{\theta\,\max}$ and $u_{\theta\,\max}$ are seen to decrease with time. Through conservation of momentum, the azimuthal velocity follows an tendency opposite to the core size. As the bubble wall moves inward the viscous core shrinks, simultaneously increasing the tangential velocity to a maximum when the bubble reaches maximum size. As the bubble grows again, the core expands and the tangential velocity decelerates to a minimum at the maximum bubble radius. When the fluid particles are pulled in towards the vortex axis they accelerate tangentially. This is similar to the phenomenon of

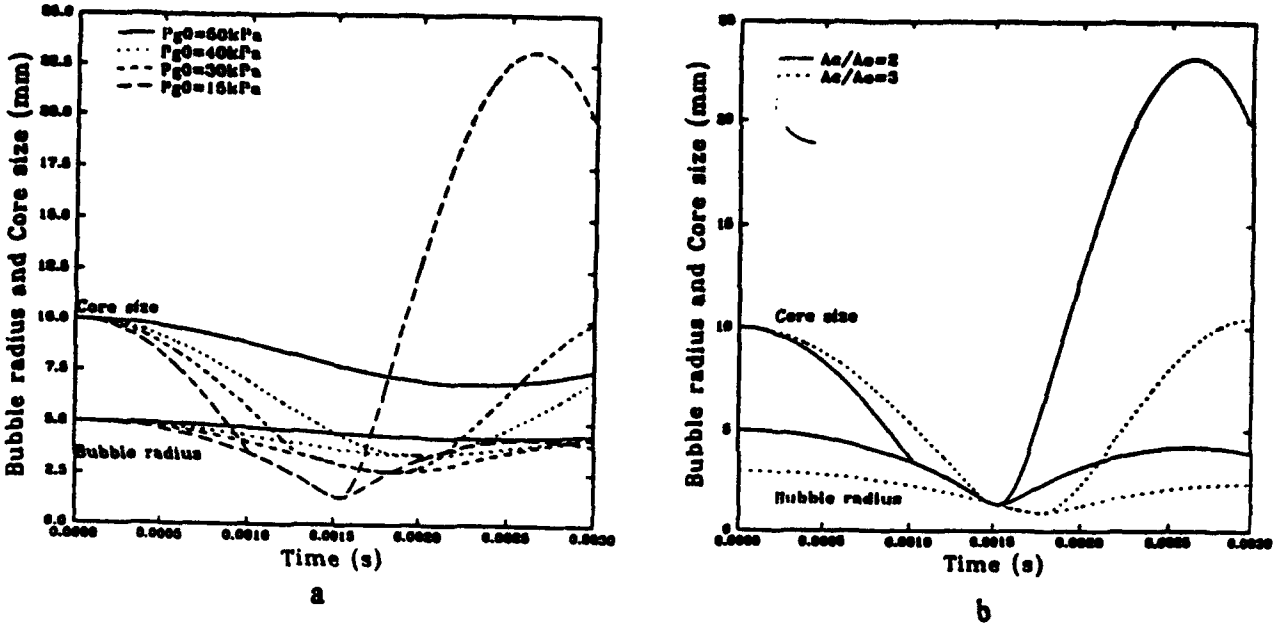

Fig. 19.22. *Dynamics of the interaction between a cylindrical bubble and a line vortex.* $P_{axis} = 7\times10^5 Pa$. *a) Influence of the initial bubble pressure,* P_{go}, *on bubble radius and position of* $R_{\theta max}$. $R_c/a_o = 2$. *b)Influence of* R_c/a_o *on the bubble radius and position of* $R_{\theta max}$. $P_{go} = 1.5\times10^5 Pa$.

vortex stretching .

Figure 19.21*b* shows the importance of the inclusion of full viscous flow / bubble interaction in the dynamics. One graph in the figure considers the case where the underlying flow field is forced to remain that of a Rankine vortex. In that case, as apparent in the figure, the bubble oscillations are repeatable with time, and no viscous decay of the amplitude of the oscillations are visible. To the contrary when the underlying flow is modified through viscous diffusion and interaction with the bubble, the bubble radius oscillations decays very much after the first collapse, and the flow field characteristics are modified as described in Figure 19.21*a*.

Figures 19.22*a* and 19.21*b* show, respectively, the influence on the dynamics of the initial gas pressure inside the bubble, P_{go}, and the ratio of initial core radius to initial bubble radius, R_c/a_o. For an initial pressure on the vortex axis of $7\times10^5 Pa$, Figure 19.22*a* shows the dynamics of the bubble and the viscous core size when the initial pressure in the bubble decreases from $5\times10^5 Pa$ to $1.5\times10^5 Pa$. For $P_{go} = 5\times10^5 Pa$ the bubble collapse is very weak, and the core radius is seen to follow the bubble wall oscillations. For all three other larger values of P_{go} starting from $P_{go} = 4\times10^5 Pa$ the bubble collapse is strong enough to entrain a full collapse of the viscous core which practically disappears (maximum azimuthal velocity at the bubble wall) during the later phases of the bubble collapse. This is followed by a much stronger rebound of the viscous core than the bubble rebound.

Figure 19.22*b* shows a behavior similar to the previous figure when the ratio, R_c/a_o, increases. Here again a strong core collapse and rebound is observed when the initial distance between the bubble wall and the core radius is decreased.

trend is to address the problems by a two-pronged effort involving numerical and experimental simulations. This is made possible by the development of advanced high speed computers which render direct numerical simulations possible in reasonable amounts of time. The studies presented above addressed various aspects of the problem, namely bubble capture by the vortex and bubble dynamics in the vortex flow field. Very much lacking and presently a subject of active work at our research center is the influence of the bubble's presence on the vortex behavior. It is hoped that a matching between a viscous solver, at least in the vortex viscous core region, and a bubble dynamics solver such as **2DynaFS** or **3DynaFS** would enable one to describe with some acceptable accuracy the full interaction between the bubbles and the vortex flow field. This is of great importance since it would enable the user to understand the mechanics involved thus enabling one to manipulate the phenomena for technological advantage such as is bubble drag reduction or cavitation inception delay.

19.10. ACKNOWLEDGMENTS

This study was partially supported by the Office of Naval Research, Contract N00014-89-C-0025. The author would like to acknowledge the contributions of colleagues at DYNAFLOW, INC. especially Dr. Ramani Duraiswami and Dr. Kenneth Kalumuck for their help with the BEM code, and their review of and suggestions for the manuscript. Special thanks to Prof. Sheldon Green and Dr. Jean-Yves Billard for providing pictures to illustrate the text, and to the following ex-students at the Ecole Navale de Brest for their contributions to part of this study: Eric Delepoule, Pierre Hauwaert, Thomas Sarazin and Guillaume Desgrees du Lou. Many thanks also to the Numerical Aerodynamic Simulation (NAS) Systems Division at NASA Ames Research Center for grant of supercomputer time.

19.11. REFERENCES

Blake, J. R., Taib, B.B. and Doherty, G., 1986, "*Transient Cavities Near Boundaries. Part I. Rigid Boundary,*" Journal of Fluid Mechanics, vol. 170, pp. 479-497.

Blake, J. R, and Gibson, D. C., 1987, *"Cavitation Bubbles Near Boundaries, "* Annual Review Fluid Mechanics., Vol. 19, pp. 99-123.

Bovis, A.G., 1980a, *"Asymptotic Study of Tip Vortex Cavitation"*, ASME Cavitation and Polyphase Flow Forum, New Orleans, pp. 19-21.

Bovis, A.G., 1980b, "*Etude Asymptotique du Phénomène de Cavitation. Cavités non-sphériques,*" Thèse de Docteur Ingénieur. Université Pierre et Marie CURIE, Paris.

Chahine, G.L., and Genoux, Ph., 1983, "*Collapse of a Cavitating Vortex Ring,*" Journal of Fluids Engineering, Vol. 105, 400-405.

Chahine, G.L., Perdue, T.O., and Tucker, C.B., 1988, *"Interaction Between an Underwater Explosion and a Solid Submerged Structure,"* DYNAFLOW, INC. Technical Report 89001-1.

Chahine, G.L., and Kalumuck, K.M., Frederick, G.S., and Watson, R.E., 1988 "*Development of a Directed Underwater Destructive Vortex Bubble Ring,*" Ttacor Hydronautics Inc. Technical Report, 88018-1.

G.L. Chahine and T.O. Perdue, 1989a, "*Simulation of Three-Dimensional Behavior of an Unsteady Large Bubble Near a Structure,*" in "*Drops and Bubbles*" edited by T.G. Wang, A.I.P. Conference Proceedings, 197, 169-187.

Chahine, G.L., 1989b,"*A Numerical Model for Three-Dimensional Bubble Dynamics in Complex Configurations,*" 22nd. American Towing Tank Conference, St. Johns, Newfound-

land, Canada.

Chahine, G.L.,1990a, "*Nonspherical Bubble Dynamics in a Line Vortex,*" in Proceedings of the ASME Cavitation and Multiphase Flow Forum, Toronto, FED- Vol. 98, pp. 121-127.

Chahine, G.L., 1990b, "*Numerical Modeling of the Dynamic Behavior of Bubbles in Nonuniform Flow Fields*" ASME Symposium on Numerical Methods for Multiphase Flows, Toronto, FED-Vol. 91, pp 57-65.

Chahine, G.L., 1991, "*Dynamics of the Interaction of Non-Spherical Cavities,*" in *"Mathematical Approaches in Hydrodynamics,"* ed. T. Miloh, SIAM, Philadelphia.

Chahine, G.L., Delepoule, E., and Hauwaert, P., 1993a, "*Study of the Interaction Between a Bubble and a Vortical Structure*, "1993 ASME Cavitation and Multiphase Flow Forum, Washington D.C., FED-Vol 153, pp. 39-47.

Chahine, G.L., Frederick, G.F., and Bateman, R.D., 1993b, "*Propeller Tip Vortex Cavitation Suppression Using Selective Polymer Injection,*" Journal of Fluids Engineering, Vol. 115, pp. 497-504.

Chahine, G.L., Duraiswami, R., 1993c, "*Boundary Element Method for Calculating 2-D and 3-D Underwater Explosion Bubble Behavior in Free Water and Near Structures,*" Naval Surface Warfare Center, Dahlgren Division, White Oak Detachment, Report NSWCDD/TR-93/44.

Crespo A., Castro F., Manuel, F., and Hernandez J., 1990, *"Dynamics of an Elongated Bubble During Collapse"*, Journal of Fluids Engineering, Vol 112, 232-237.

Darrozes, J.S., and Chahine, G.L., 1983, "*Les Recherches sur le Phénomène de Cavitation à l'Ecole Nationale Supérieure des Techniques Avancées,*" Sciences et Techniques de l'Armement, 1er Fascicule, 173 pages, Imprimerie Nationale, Paris.

Desgrees du Lou, G., Sarazin, T. and Chahine, G.L., 1993, "*Viscous Interaction Between Bubble and Line Vortex,*" DYNAFLOW, INC. Technical Report 6.002-15.

Genoux, Ph., and Chahine, G.L., 1983, "*Collapse of a Toroidal Bubble near a Solid Wall,*" ASME Cavitation and Multiphase Flow Forum, New Orleans, pp. 69-72.

Guerri, L., Lucca, G., and Prosperetti, A., 1981, *"A Numerical Method for the Dynamics of Non-Spherical Cavitation Bubbles,"* Proc. 2nd Int. Coll. on Drops and Bubbles, JPL Publication 82-7, Monterey, CA.

Green, S.I.,"*Correlating Single Phase Flow Measurements with Observations of Trailing Vortex Cavitation*", Journal of Fluids Engineering, Vol. 113, No 1, pp. 125-130.

Higuchi, H., Arndt, R.E.A. and Rogers, M.F., 1989, *"Characteristics of Tip Vortex Cavitation Noise"*, Journal of Fluids Engineering, Vol. 111, No 4, pp. 495-502.

Johnson, V.E., Jr. and Hsieh, T.,1966, "*The influence of Trajectories of Gas Nuclei on Cavitation Inception*", Proc. 6th Symposium of Naval Hydrodynamics, pp. 163-179.

Hammitt, F.G., 1980, "*Cavitation and Multiphase Flow Phenomena*", Mc. Graw-Hill Inc. N.Y.

Kalumuck, K. M. and Chahine, G.L., 1990, "*Cavitating Vortex Ring Formation and Dynamics.*' ASME Cavitation and Multiphase Flow Forum, Toronto, FED, Vol 98, pp.43-49.

Kezios, P. and Schowalter, W.R., 1986, "*Rapid Growth and Collapse of single Bubbles in Polymer Solutions Undergoing Shear,*" Phys. Fluids 29 (10), 3172-3181.

Latorre, R., 1980, *"Study of Tip Vortex Cavitation Noise from Foils"*, International Shipbuilding Progress, 676-685.

Latorre, R., 1982, *"TVC Noise Envelope - An approach to Tip Vortex Cavitation Noise Scaling"*, Journal of Ship Research, Vol. 26, No. 1, pp. 65-75.

Ligneul, P. and Latorre R., 1989, *"Study of the Capture and Noise of Spherical Nuclei in the Presence of the Tip Vortex of Hydrofoils and Propellers"*, Acustica Vol. 68.

Ligneul, P., 1989, *"Theoretical Tip Vortex Inception Threshold"*, Eur. J. Mech., B/Fluids, 8, no. 6, 495-521.

Maines, B.H., and Arndt, R.E.A., 1993, *"Bubble Dynamics of Cavitation Inception in a Wing Tip Vortex"*, ASME Cavitation and Multiphase Flow Forum, Washington D.C., FED-Vol 153, pp. 93-99.

Milne-Thomson, 1968, *"Theoretical Hydrodynamics"*, 5th Edition, the McMillan company, New York.

Plesset, M.S., 1948, *"Dynamics of Cavitation Bubbles"*, Journal of Applied Mechanics, Trans. ASME, 16, 228-231.

Rayleigh, Lord., 1918, *"On the Pressure Developed in a Liquid during collapse of a Spherical Cavity"*, Phil. Mag., 34, 94-98.

Taib, B.B., 1985, *"Boundary Integral Method Applied to Cavitation Bubble Dynamics,"* Ph. D. Thesis, University of Wollongong, Australia.

Wilkerson, S.,1989, *"Boundary Integral Technique for Explosion Bubble Collapse Analysis,"* ASME Energy Sources Technology Conference and Exhibition, Houston Tx.

Van Wijngaarden, L., 1980, *"Sound and Shock Waves in Bubbly Liquids,"* in Cavitation and Inhomogeneities in Underwater Acoustics, Ed. W. Lauterborn, Springer-Verlag, Berlin. pp. 127-140.

Cavitation Dynamics at Microscale Level

Georges L. Chahine

Dynaflow, Inc., Fulton, Maryland and John Hopkins University, Baltimore

Cavitation in a liquid is known for its deleterious effects, namely erosion, noise and loss of performance. In a mechanical heart valve, stresses generated by cavitation could lead to catastrophic failure. These deleterious effects are directly connected to the dynamics of pre-existing microscopic nuclei in the liquid medium. To highlight this, a selective review of the dynamics of the bubbles at the microscopic levels is considered here; the various aspects of the problem are highlighted and briefly addressed; new areas of research in non-spherical and bubble cloud dynamics are then considered. The importance of the inclusion of these collective and non-uniform flow effects in the dynamics of bubbles in a realistic cavitating flow field is also elucidated.

The Journal of Heart Valve Disease 1994;3 (Suppl. I): S 102-116

Cavitation and bubble dynamics have been the subject of extensive research since the early works of Besant (1) and Lord Rayleigh (2). The phenomenon has been studied mostly for hydrodynamic applications, where its presence is associated with deleterious effects; i.e. performance deterioration, material erosion, and noise generation. More recently, cavitation has been studied for useful purposes including sound generation, cutting, drilling, cleaning, enhancement of mixing and chemical reactions, emulsification, etc. (3-8).

This article studies the damaging effects of cavitation on implants such as mechanical heart valves, and its negative effects on biological cells and tissue in vivo. In both these cases stresses generated by cavitation lead to undesirable effects; in a mechanical heart valve, failure of the valve could result from the development of cracks, while cells could be damaged or induced to collect around bubbles.

This presentation does not intend to be a complete and inclusive review of the phenomenon of cavitation. Instead it will consider some aspects of the subject relevant to cavitation erosion from a microscopic point of view of the bubble dynamics. Our aim is to give an overview of the problem areas where significant knowledge has been accumulated and to discuss important aspects of the dynamics which either have not yet been addressed properly or are the subject of on-going intensive research.

Address for correspondence:
Georges L. Chahine, Dynaflow Inc., 7210 Pindell School Road, Fulton, Maryland 20759, USA

Cavitation inception

Background

Despite a large number of investigations and publications on the subject - including several well documented books and review articles (6-9) - the fundamentals of cavitation remain relatively poorly understood. In order to achieve a cavitation-free design of a submerged body (such as a valve, propeller, etc.), or to simulate cavitation and test a model scale in a laboratory environment, it is necessary to establish criteria for cavitation inception, and to define scaling parameters between model and full scale. From talking to engineers and practitioners of fields where cavitation is a problem, the most commonly used definition of cavitation is based on an over-simplification that serves the purpose in most engineering cases but could lead to erroneous conclusions if used to explain or model new problems areas. This traditional engineering definition is that a liquid flow experiences cavitation if the local pressure drops below the liquid vapor pressure, p_v.

Definition of the cavitation number

A dimensional analysis of the flow around an obstacle (e.g. foil or a valve) of streamwise and transverse characteristic length scales, L and W, shows that the pressure, p_M, at any point M, can be written as a function, $\mathcal{F}$, of the following variables:

$$p_M = \mathcal{F}\,(P_\infty, \alpha, L, W, \rho, V_\infty, \mu), \qquad (1)$$

where α is the incidence angle of the flow relative to the obstacle, P_∞ and V_∞ are the characteristic pressure and

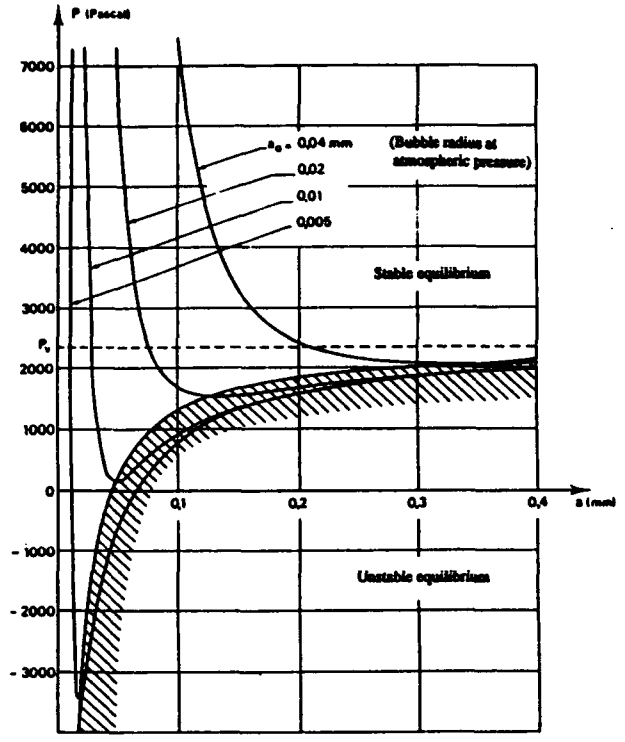

Figure 1: Curves of bubble static equilibrium.

velocity of the flow, respectively, and ρ and μ are the liquid density and kinematic viscosity, respectively. Based on the above engineering definition of cavitation, from a cavitation inception standpoint, any pressure, p_M, in the liquid flow is important only in terms of the pressure difference, p_M - p_v, since the liquid cavitates when $p_M = p_v$. In this case, Equation (1) becomes at the inception of cavitation:

$$\frac{P_\infty - P_v}{1/2\,\rho V_\infty^2} = \mathcal{F}\left(\alpha, \frac{W}{L}, \frac{\rho V_\infty L}{\mu}\right), \quad \text{or} \quad \sigma = \mathcal{F}(\alpha, \mathcal{G}, \mathcal{R}_e). \quad (2)$$

$\mathcal{R}_e$ is the Reynolds number, $\mathcal{G}$ is a geometric characteristic (shape parameter) of the obstacle, and σ is the "cavitation number" defined as:

$$\sigma = \frac{p_\infty - p_v}{1/2\,\rho V_\infty^2} \quad (3)$$

Scaling various cavitation experiments or a model configuration to a full scale configuration is obtained by conserving σ.

Presence of cavitation nuclei

The above definition of cavitation inception is only true in static conditions when the liquid is in contact with its vapor through the presence of a large free surface. For the more common condition of a liquid in a flow, or in a biological application, liquid vaporization can only occur through the presence of "micro free surfaces" or microbubbles, also called "cavitation nuclei". Indeed, a pure liquid free of nuclei can sustain very large tensions, measured in hundreds of atmospheres, before a cavity can be generated through separation of the liquid molecules. Therefore, any fundamental analysis of cavitation inception has to start from the observation that any real liquid contains nuclei which when subjected to variations in the local ambient pressure will respond dynamically by oscillating and eventually growing explosively (i.e. cavitate). A more precise definition is presented in the next section.

Cavitation inception appears under several forms, the most recognized being (14):

(a) Explosive growth of individual bubbles,
(b) Sudden appearance of transient cavities or "flashes" on boundaries,
(c) Sudden appearance of attached partial cavities, or sheet cavities,
(d) Explosive growth of bubble clouds, behind attached cavities or a vibrating surface.
(e) Sudden appearance of rotating filaments, or vortex cavitation.

Upon further analysis, all these forms can be related to the explosive growth of pre-existing nuclei in the liquid when subjected to pressure drops generated by various forms of local pressure disturbances. These are either acoustically imposed pressure variations (ultrasound applications), uniform pressure drops due to local liquid accelerations, or strongly non-uniform pressure fields due to streamwise or transverse large vortical structures. The presence of nuclei or weak spots in the liquid is therefore essential for cavitation inception to occur when the local pressure in the liquid drops below some critical value, p_c, which is addressed next.

Bubble static equilibrium

The first level of sophistication for the definition of a cavitation inception criterion is based on the concept of static equilibrium of a bubble in a liquid. The criterion predominantly used is based on a spherical bubble model, even though it applies only to a limited number of the cavitation forms listed above. In this model, the bubble is assumed to contain non condensable gas of partial pressure, P_g, and vapor of the liquid of partial pressure, p_v (6-9). Therefore, at any point M on the bubble surface, the balance between the internal pressure, the liquid pressure, and surface tension can be written:

$$P_{L_0} = p_v + P_{g_0} - \frac{2\gamma}{R_0}, \quad (4)$$

where P_{L_0} is the pressure in the liquid, γ is the surface tension parameter, and R_0 is the bubble radius.

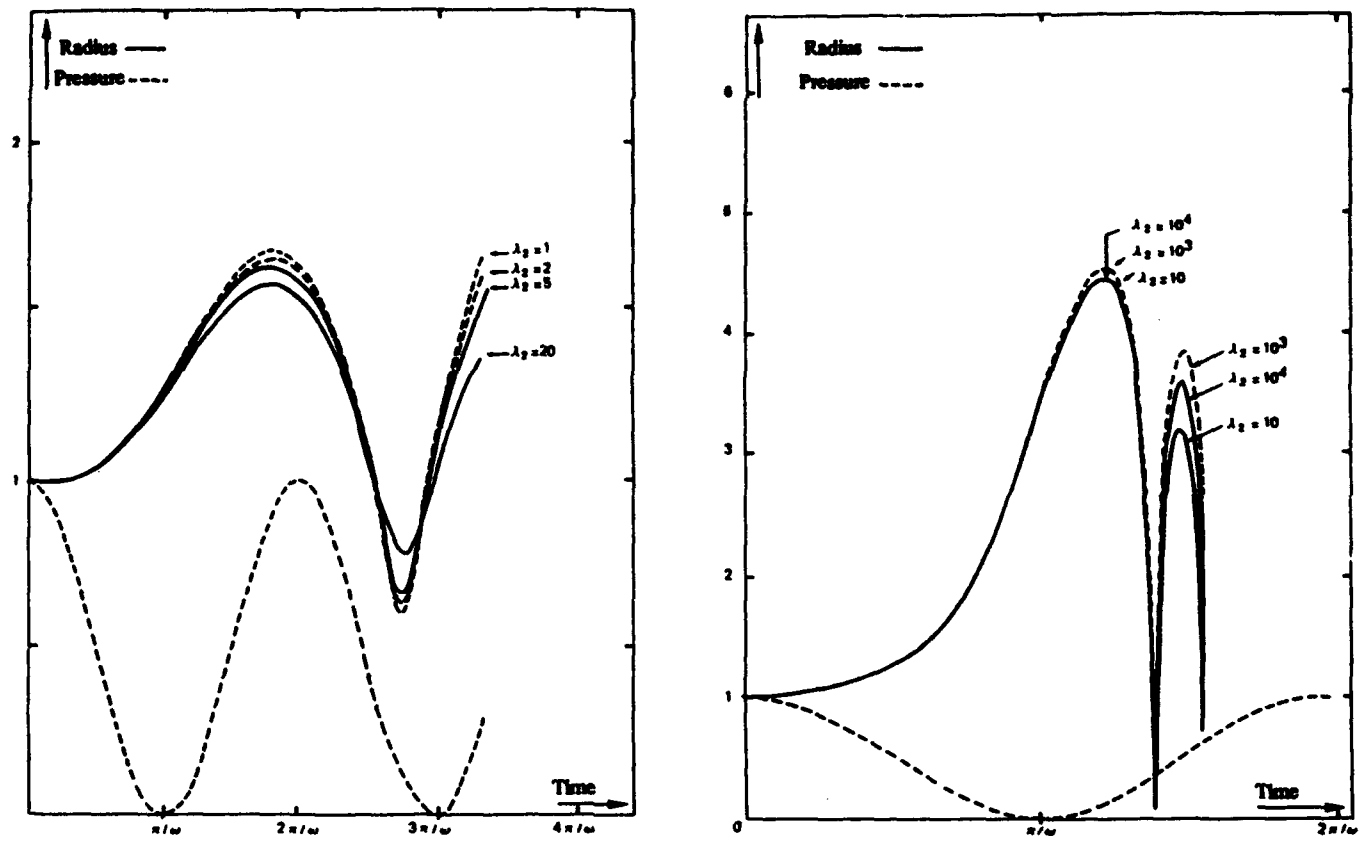

Figure 2: Influence of viscoelastic properties on spherical bubble dynamics. λ_1 and λ_2 correspond to Newtonian fluid. a) Bubble oscillations case; $\lambda_1 = 2$. b) Bubble collapse case; $\lambda_1 = 10^3$. Reprinted from (10).

If the liquid ambient pressure changes very slowly, the bubble radius will change accordingly to adapt to the new value. This is accompanied by a modification of the pressure inside the bubble. The vaporization of the liquid at the bubble-liquid interface occurs very fast relative to the time scale of the bubble dynamics, so that the liquid and the vapor can be considered in equilibrium at every instant, and the partial pressure of the vapor in the bubble is always constant. On the other hand, gas diffusion occurs over a much longer time scale, so that the amount of gas inside the bubble remains constant. This results in a gas partial pressure which varies with the bubble volume. Since we are interested in a quasi-steady equilibrium, P_g is considered to follow an isothermal compression law, and is related to the reference value, P_{go}, and to the new bubble radius R, through:

$$P_g = Pg_o\left(\frac{R_o}{R}\right)^3. \qquad (5)$$

The dynamic equation at the bubble wall becomes:

$$P_L(R) = P_v + P_{g_o}\left(\frac{R_o}{R}\right)^3 - \frac{2\gamma}{R}, \qquad (6)$$

where the notation, $P_L(R)$, is meant to associate the liquid pressure, P_L, to the bubble radius, R.

An understanding of the bubble stable equilibrium can be obtained by considering the curve, $P_L(R)$. As illustrated in Figure 1, this curve has a minimum below which there is no equilibrium bubble radius. Only the left side branch of the curve corresponds to a stable equilibrium.

If the pressure in the flow field drops below the minimum of the curve, or critical pressure, p_c, an explosive bubble growth (cavitation) is provoked. This provides an improved definition for cavitation inception which depends on the size of the nuclei. The "critical pressure" is obtained by solving for the minimum of $P_L(R)$, using Equation (6) and can be expressed as:

$$p_c = p_v - \frac{4\gamma}{3r_c}, \qquad (7)$$

where γ is the surface tension parameter, and r_c is the "critical radius" given by:

$$r_c = \left[\frac{3R_o^3}{2\gamma}\left(P_{Lo} - p_v + \frac{2\gamma}{R_o}\right)\right]^{1/2}. \qquad (8)$$

For a given ambient pressure, P_{Lo}, any bubble larger

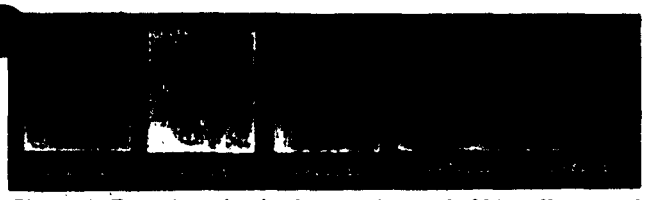

Figure 3: Emission of a shock wave during bubble collapse and rebound. Reprinted from (13).

than r_c will cavitate. This definition is much more accurate than the engineering definition, but lacks consideration of any dynamic or non-spherical effects, which can be predominant in some situations.

This new definition of cavitation inception highlights the fact that a correct scaling of the cavitation phenomenon has to account not only for the conservation of the parameters shown in Equation (2), but also for the nuclei size distribution between the model and the full scale.

Spherical bubble dynamics

Newtonian incompressible model - Rayleigh-Plesset equation

The most commonly used bubble dynamics model is based on the assumption of a spherical bubble in an incompressible liquid. In this case, the radial velocity of the liquid, u_r, at a distance, r, from the bubble center, is directly related to the bubble wall velocity through the continuity, or mass conservation equation:

$$ur = \dot{R}(t)\left[\frac{R(t)}{r}\right]^2, \qquad (9)$$

where $R(t)$ is the bubble radius at time t, and $\dot{R}(t)$ is the bubble wall velocity. This equation accounts for the kinematic condition at the bubble wall - i.e. the velocity of the bubble wall is identical to the liquid velocity at this wall. This obviously neglects any flow (mass transfer) across the bubble interface. A second boundary condition at the bubble wall, which is dynamic, expresses the balance of the normal stresses at the wall. For a Newtonian fluid it can be written:

$$P_L(R) + 4\mu\frac{\dot{R}}{R} = P_i - \frac{2\gamma}{R}, \qquad (10)$$

where $P_L(R)$ is the pressure in the liquid at the bubble wall, P_i the pressure inside the bubble, γ the surface tension, and μ the kinematic viscosity. As above, the bubble contains vapor of the liquid at the constant partial pressure, p_v, and non-condensable gas at the partial pressure, P_g, which is related to the reference value P_{go} through:

$$P_g = P_{go}\left(\frac{\mathcal{V}_o}{\mathcal{V}}\right)^k, \qquad (11)$$

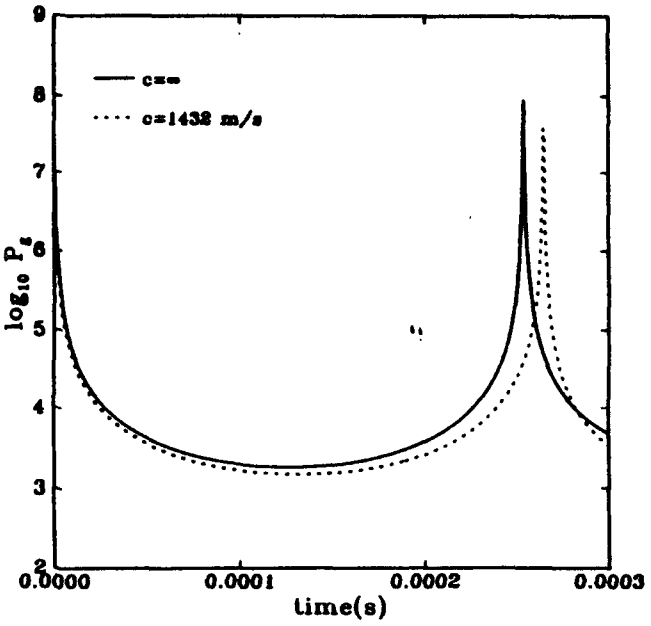

Figure 4: Gas pressure inside the bubble as a function of time for a bubble subjected to a sudden pressure drop. Comparison between an incompressible medium case (c=[infinity]) and a compressible medium.

where the constant k is between 1.0 (isothermal) and c_p/c_v (adiabatic), and V_o and V are the reference and instantaneous values of the bubble volume respectively.

The pressure balance at the bubble interface then becomes:

$$P_L(M) = P_v + P_{go}\left(\frac{R_o}{R}\right)^{3k} - \frac{2\gamma}{R} - 4\mu\frac{\dot{R}}{R}. \qquad (12)$$

A number of effects such as gas diffusion or heat transfer have been neglected in the above equation, and are usually unimportant in the case of a growing and collapsing bubble in a cold liquid. For an oscillating bubble, however, rectified diffusion can be very important.

If we replace Equation (9) in the liquid momentum equation, integrate that equation between the radius of the bubble and infinity where the imposed pressure is $P_\infty(t)$, and account for Equation (11), we obtain the well known Rayleigh-Plesset (RP) Equation (2,9) where dots denote time derivatives:

$$\rho\left[R\ddot{R} + \frac{3}{2}\dot{R}^2\right] + 4\mu\frac{\dot{R}}{R} = P_{go}\left(\frac{R_o}{R}\right)^{3k} + P_v - P_\infty(t) - \frac{2\gamma}{R}. \qquad (13)$$

This differential equation describes the bubble radius versus time when the time variations of P_∞ are known. Integration of this equation enables one to obtain conditions for bubble oscillations, or rapid bubble growth and collapse. In addition, this equation provides the necessary input to compute the pressure generated

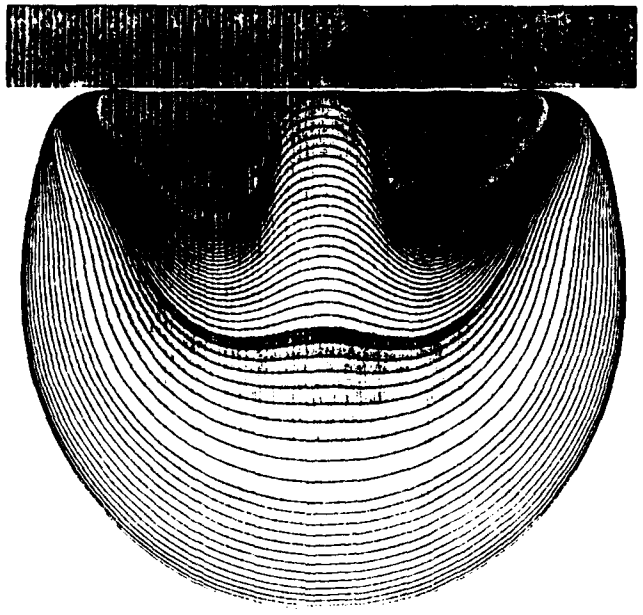

Figure 5: Numerical simulation of bubble collapse near a solid wall using 2DynaFS. Bubble contours at various times during collapse.

during bubble collapse. These pressures can be very large. They decrease with an increase in the amount of initial gas in the bubble. They will be considered as reference values in comparison with other models in the following sections.

Viscoelastic liquid: modified RP equation

When the liquid in which cavitation occurs does not have Newtonian properties, the above RP dynamics equation must be modified to account for a non-linear stress-strain relationship. This is the case for instance in blood flow, or in hydrodynamics when polymer additives are used to reduce drag. The question is then to evaluate to what extent accounting for the fluid's non-Newtonian behavior is important from the cavitation view point. In previous studies (10-12), we considered theoretically (10), and experimentally the behavior of spherical and non-spherical (11,12) bubbles in a viscoelastic fluid medium. The equation of state of the fluid was taken to be a general 3-parameter Oldroyd model such that the stress-strain relationship (σ and e are the stress and strain tensors) is given by:

$$\sigma_{ij}^{D} + \tau_g \frac{d\sigma_{ij}^{D}}{dt} = 2\mu \left(e_{ij}^{D} + \theta_g \frac{de_{ij}^{D}}{dt} \right) \qquad (14)$$

where τ_g, $\tau\eta_g$, and μ are characteristic relaxation times and the dynamic viscosity of the non-Newtonian fluid. For a spherical bubble this fluid behavior shows up in both the momentum equation:

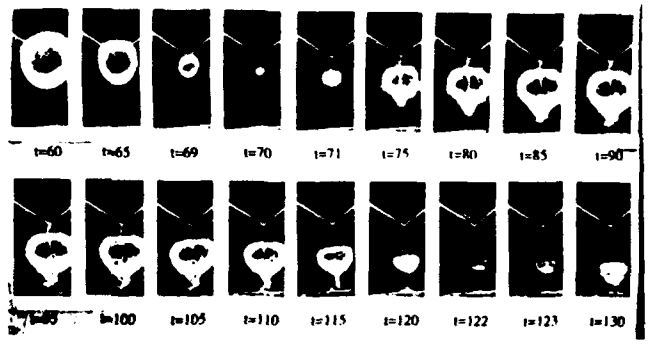

Figure 6: High speed photographs of bubble collapse near a solid wall using a spark-generated bubble.

$$\rho \left[\frac{\partial u}{\partial t} + u \frac{\partial u}{\partial r} \right] = - \frac{\partial p}{\partial r} + \frac{\partial \sigma_{rr}^{D}}{\partial r} + \frac{3\sigma_{rr}^{D}}{r}, \qquad (15)$$

where the last two terms have replaced the more conventional viscous terms, and in the stress balance equation at the bubble interface, which becomes:

$$P_L(M) = P_{go} \left(\frac{R_o}{R} \right)^{3k} + P_v - \frac{2\gamma}{R} - \sigma_{rr}^{D}. \qquad (16)$$

Finally, for an incompressible isolated bubble the differential equation describing the bubble radius versus time becomes:

$$\rho \left[R\ddot{R} + \frac{3}{2}\dot{R}^2 \right] = P_{go} \left(\frac{R_o}{R} \right)^{3k} + P_v - \frac{2\gamma}{R_o} - P_\infty(t) - 4\mu \left[\frac{\theta_g}{\tau_g} \frac{\dot{R}}{R} - \frac{\theta_g - \tau_g}{\tau_g^2} \int_0^t e^{(\alpha - t)/\tau_g} \times \frac{R^2(\alpha)\dot{R}(\alpha)}{R^3(\alpha) - R^3(t)} \log \frac{R^3(\alpha)}{R^3(t)} \, d\alpha \right]. \qquad (17)$$

Figure 2 shows a comparison between the oscillation and collapse of a spherical bubble in a viscoelastic liquid and water. Negligible effects are seen for a strong bubble collapse unless for very large unrealistic values of $\lambda_1 = \tau_g \rho\sigma^2/64\mu^3$ and $\lambda_2 = \tau\eta_g \rho\sigma^2/64\mu^3$. Viscoelastic effects appear less negligible for weaker bubble oscillations, and when several bubble periods are considered (10). Experimental results relative to the viscoelastic effects are presented below.

Influence of liquid compressibility

Even though generally neglected in bubble dynamics studies, compressibility of the liquid medium can become important when the speed of the bubble wall during collapse or rebound approaches the sound speed in the liquid. This is illustrated in Figure 3, where shock waves are emitted at bubble collapse (13). In order to model the liquid compressibility, an equation

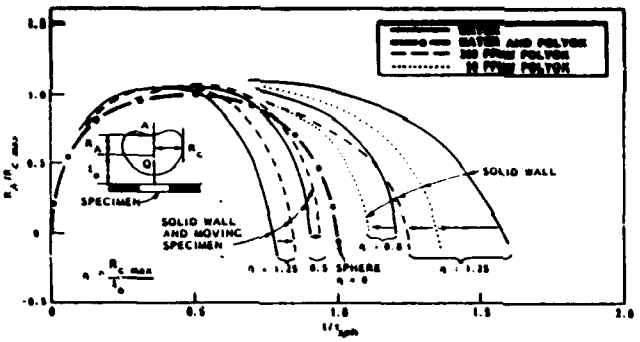

Figure 7: Motion of the re-entering jet point in the presence of a moving and rigid solid wall. Influence of the addition of a polymer solution. Reprinted from (12).

of state of the liquid is introduced. For instance, for water the following Tait equation (6-8) is used:

$$\frac{p+B}{p_\infty+B}=\left(\frac{\rho}{\rho_\infty}\right)^n, \qquad (18)$$

in which B and n are constants depending upon the liquid, with values of 3000 atmospheres and 7.25, respectively, for water. The model that has been shown to be the most precise, was proposed by Gilmore (15), and is based on the Kirkwood-Bethe (16) hypothesis. This hypothesis states that the disturbance of any fluid property propagates along an outgoing characteristic of velocity of propagation of $u + c$, the sum of the local velocity of the fluid and the sound speed. In this case the equation of motion of the bubble wall can be written:

$$R\ddot{R}\left(1-\frac{\dot{R}}{c}\right)+\frac{3}{2}\dot{R}^2\left(1-\frac{\dot{R}}{3c}\right)$$

$$=H\left(1+\frac{\dot{R}}{c}\right)+\frac{R}{c}\frac{dH}{dt}\left(1-\frac{\dot{R}}{c}\right) \qquad (19)$$

where c is the sound speed at the bubble wall. H is the difference between the enthalpy at the bubble wall and at infinity, and with an isentropic liquid compression assumption is defined as:

$$H(p)=\int_{p_\infty}^{p} dh=\int_{p_\infty}^{p}\frac{dp}{\rho}. \qquad (20)$$

The pressure in the liquid is then given by the following equation at a given location r:

$$p(r)=(p_\infty+B)\left[\left(\frac{y}{r}-\frac{u^2}{2}\right)\left(\frac{n-1}{n}\frac{\rho_\infty}{\rho_\infty+B}\right)+1\right]^{n/(n-1)}-B. \qquad (21)$$

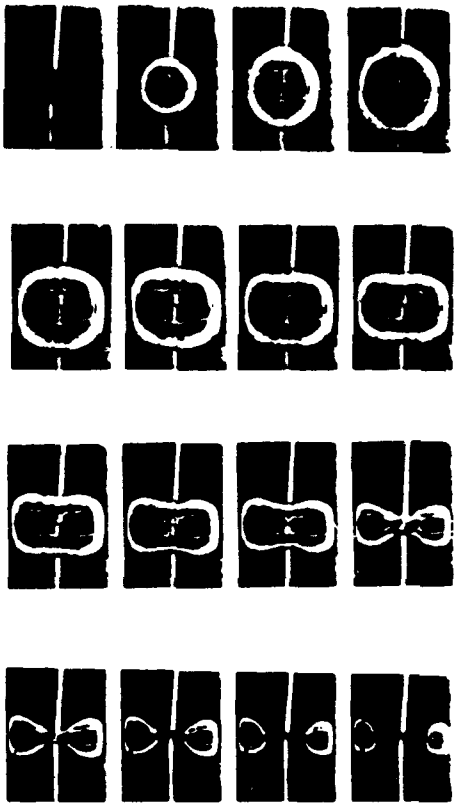

Figure 8: High speed photography observation of bubble dynamics between two solid walls.

The velocity of the fluid along the characteristic surface is given by:

$$\frac{du}{dt}=\frac{1}{c-u}\left[(c+u)\frac{y}{r^2}-2\frac{c^2u}{r}\right], \qquad (22)$$

with $y = (h - u^2/2)/r$. Using as the initial condition the velocity and radius of the bubble wall, the above equation can be used to compute the velocity along the characteristic. Equation (20) then gives the corresponding pressures.

The former expressions reduce to the incompressible ones as the quantity $\dot{R}/c$ drops below 0.2. In general a slightly compressible model can be used to replace the Rayleigh-Plesset equation with the Keller-Herring equation (8):

$$\rho\left[\left(1-\frac{\dot{R}}{c}\right)R\ddot{R}+\frac{3}{2}\left(1-\frac{\dot{R}}{3c}\right)\dot{R}^2\right]$$

$$=\frac{1}{\rho}\left(1+\frac{\dot{R}}{c}+\frac{R}{c}\frac{d}{dt}\right)[P_L-p_\infty], \qquad (23)$$

where:

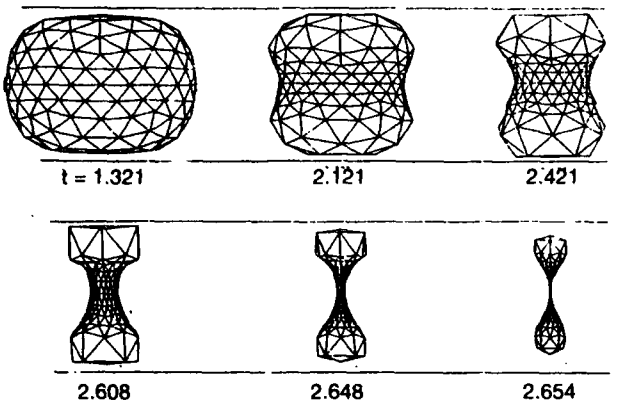

Figure 9: Numerical simulation using 3DynaFS of bubble dynamics between two solid walls.

$$P_L = P_{g0}\left(\frac{R_0}{R}\right)^{3k} + P_v - \frac{2\sigma}{R}. \qquad (24)$$

Figure 4 compares the pressures in the bubble when compressibility is taken into account and when it is not for a particular case of a spherical bubble collapse. Both an increase in the bubble period and a decrease in the maximum bubble pressure can be observed when a finite sound speed in the water is considered.

Non-spherical bubble dynamics

Introduction

In most practical applications where cavitation occurs, bubbles are seldom isolated or spherical. This is the case, for instance, in biological applications when blood flows in and out of the heart through a heart valve. During closure of the valve, flow separation and increased velocities can induce bubble nuclei explosive growth followed in the higher pressure regions by bubble collapse. Fortunately, with the recent advent of modern computational, experimental, and analytical techniques, the often-neglected bubble flow and bubble boundary interaction and deformation effects can be addressed. To do so, we developed a numerical method which accounts for strong bubble/bubble and bubble/flow interactions. This method has been used to date to study interaction between bubbles, bubbles and nearby rigid or deformable/movable boundaries, and bubble behavior in non-uniform flows when the underlying flow is viscous. Two particular shear flow cases of relevance to cavitation in separated flows are briefly considered here; a boundary layer flow near a flat wall and the flow field of a line vortex.

Shear and boundary interactions are probably important for flow around heart valves. In both cases significant modifications of the bubble dynamics are associated with the presence of the shear and its combined effects with nearby boundaries.

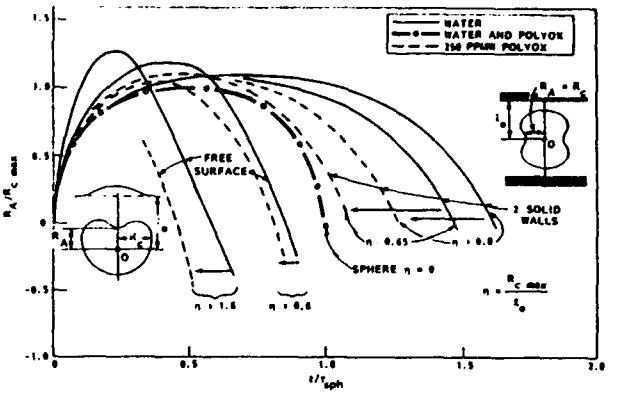

Figure 10: Motion of the re-entering jet point in the presence of two solid walls or free surface. Influence of the addition of a polymer solution. Reprinted from (12).

Bubble dynamics model: numerical boundary element method

For cavitation bubbles, large but subsonic bubble wall velocities are involved and, as a result, viscous and compressible effects in the liquid can be neglected. This results in a flow due to bubble dynamics that is potential (velocity potential, ϕ_b), and which satisfies the Laplace equation:

$$\nabla^2\phi_b = 0 \qquad (25)$$

Boundary conditions are such that at all moving or fixed surfaces in the flow field an identity between fluid velocities normal to the boundary and the normal velocity of the boundary itself is to be satisfied. The bubble is assumed to contain non-condensable gas as well as vapor of the surrounding liquid, as above.

The three-dimensional Boundary Element Method developed (**3DynaFS**, with an axisymmetric version **2DynaFS** (17-19)) uses Green's equation to determine a solution to the Laplace equation. If the velocity potential, ϕ_b, and its normal derivatives are known on the fluid boundaries (points M), and ϕ_b satisfies the Laplace equation, then ϕ_b can be determined at any point P in the fluid domain using:

$$\int\int_S \left[-\frac{\partial\phi_b}{\partial n}\frac{1}{|MP|} + \phi_b\frac{\partial}{\partial n}\left(\frac{1}{|MP|}\right)\right] dS = \alpha\pi\phi_b(P), \qquad (26)$$

$a\pi = \Omega$ is the solid angle under which P sees the fluid. The advantage of this integral representation is that it effectively reduces by one the dimension of the problem. If P is selected to be on the boundary of the fluid domain, then a closed system of equations is obtained and used at each time step to solve for values of $\delta\phi_b/n$ (or ϕ_b), assuming that all values of ϕ_b (or $\delta\phi_b/n$) are known at the preceding time step.

To solve Equation (26) numerically, the initially

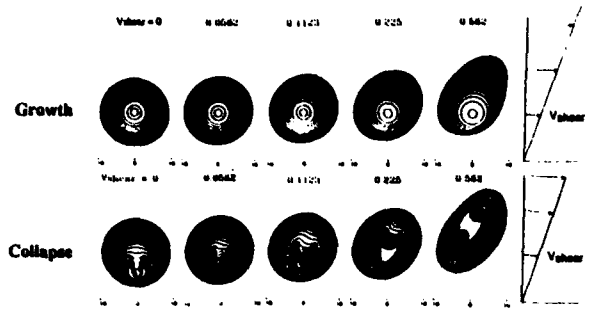

Figure 11: Influence of the presence of a linear shear velocity on the collapse of a bubble near a solid wall. V_{shear} is normalized with the Rayleigh velocity $\sqrt{\Delta P/\rho}$.

spherical bubble is discretized into a geodesic shape with flat, triangular panels. To evaluate the integrals in Equation (26) over any particular panel, linear variations of the potential and its normal derivative over the panel are assumed.

With the problem initialized and the velocity potential known over the surface of the bubble, an updated value of $\delta\phi_b/\delta n$ can be obtained by performing the integrations expressed above and solving the corresponding matrix equation. The unsteady Bernoulli equation can then be used to solve for $D\phi_b/Dt$, the total material derivative of δ_b while following a particular node during its motion. Using an appropriate time step, all values of ϕ_b on the bubble surface and all node positions can be updated. This time-stepping procedure is repeated throughout the bubble oscillation period, resulting in a shape history of the bubbles. The details of the numerics are described in a report by Chahine et al. (17).

Presence of a basic flow

To study bubble dynamics in a non-uniform flow field, the following model was used. Denoting the velocity of the non-uniform "basic flow" as V_o, and the resulting velocity field in the presence of oscillating bubbles as V_1, we defined the "bubble flow" velocity and pressure variables, V_b and P_b, as:

$$\mathbf{V}_b = \mathbf{V}_1 - \mathbf{V}_o, \qquad P_b = P_1 - P_0. \tag{27}$$

By noticing that, for cavitating flows, this "bubble flow" field can be considered to be a potential model, we were able to use a method similar to the one described in the previous section to study the dynamics. We then obtained the following modified Bernoulli equation (18,19,23):

$$\nabla\left[\frac{\delta\phi_b}{\delta t} + \frac{1}{2}|\mathbf{V}_b|^2 + \mathbf{V}_o\cdot\mathbf{V}_b + \frac{P_b}{\rho}\right] = \mathbf{V}_b\times(\nabla\times\mathbf{V}_o). \tag{28}$$

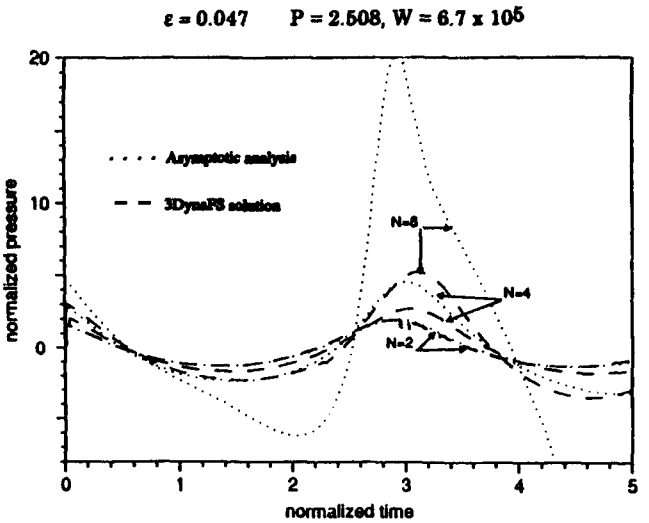

Figure 12: Comparison of the pressures at the cloud center predicted by 3DynaFS and the asymptotic analysis code. $\varepsilon = R_{max}/l_0 = 0.047$. Pressures are normalized by maximum value for isolated bubble. Reprinted from (24).

For cavitation in a line vortex, Equation (28) becomes (18):

$$\frac{\delta\phi_b}{\delta t} + \frac{1}{2}|\mathbf{V}_b|^2 + \frac{P_b}{\rho}$$

= constant along a radial direction. (29)

In the case of a flat wall boundary layer flow such that all velocity vectors are parallel to the wall (unit direction, e_x), and depend only on the distance, z, to the wall, $V_o = f(z).e_x$, Equation (28) becomes (19):

$$\frac{\partial\phi_b}{\delta t} + \frac{1}{2}|\mathbf{V}_b|^2 + \mathbf{V}_o\cdot\mathbf{V}_b + \frac{P_b}{\rho}$$

= constant along the *y* direction. (30)

These two expressions were used in conjunction with the numerical model described above to conduct the simulations shown below.

Interaction with a nearby deformable structure

To study bubble interaction with deformable structures, the above described BEM codes were coupled to existing solid mechanics/structural dynamics codes, Nike3D and Nike2D, developed by Lawrence Livermore National Laboratories. These codes have the ability to include complex material and structure properties. The coupling between the two sets of codes is achieved through the dynamic condition at the boundaries of the deformable boundary. At these boundaries, the pressure from the liquid obtained through solution of the BEM liquid problem is used as the input or driving force for the structural model. The resulting

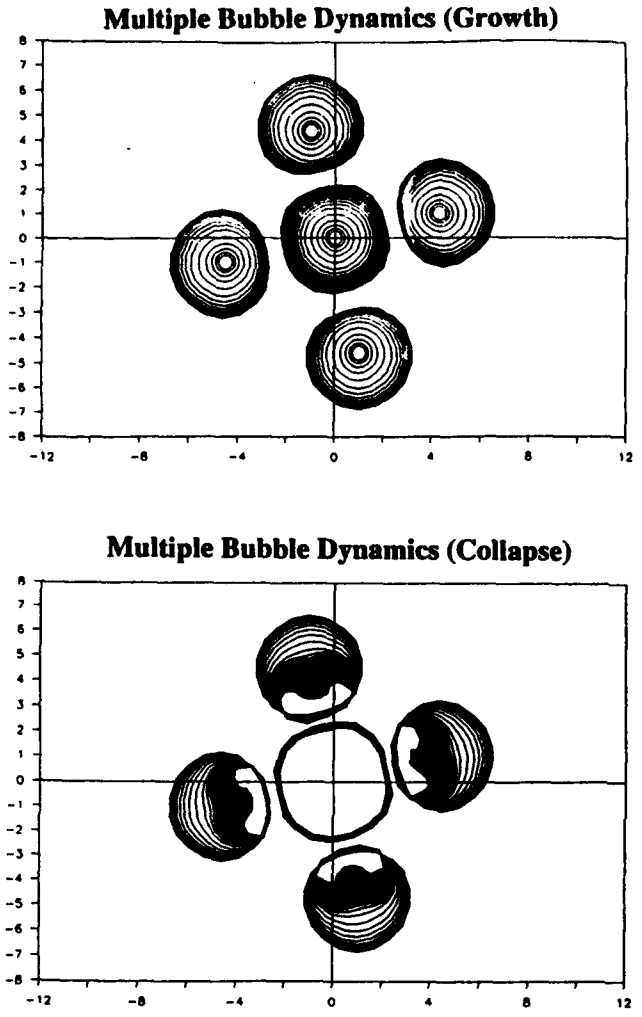

Figure 13: Growth and collapse of five bubbles having the same initial size and internal pressure. Influence of the initial bubble geometry distribution on dynamics. $\varepsilon = 0.474$, $P_{go}/P_{amb} = 283$. *Reprinted from (23).*

motion of the structure is then fed back into the BEM code to calculate the fluid motion at each time step, as described above. The velocity and position of each node are transferred to the fluid model. This coupling results in a fully interactive calculation (26).

Illustrative numerical results and experimental observations: spark-generated bubbles

In all the experiments reported here vapor bubbles (with some non-condensable gas) were generated in water by discharging a capacitor across a pair of platinum or tungsten electrodes for a very brief period of time. The generators used were capable of capacitor charge up to 10 kV. Such a system has been widely used by various authors for bubble dynamics studies, and the validity of the analogy between the collapse of the bubbles it produces and cavitation bubbles has

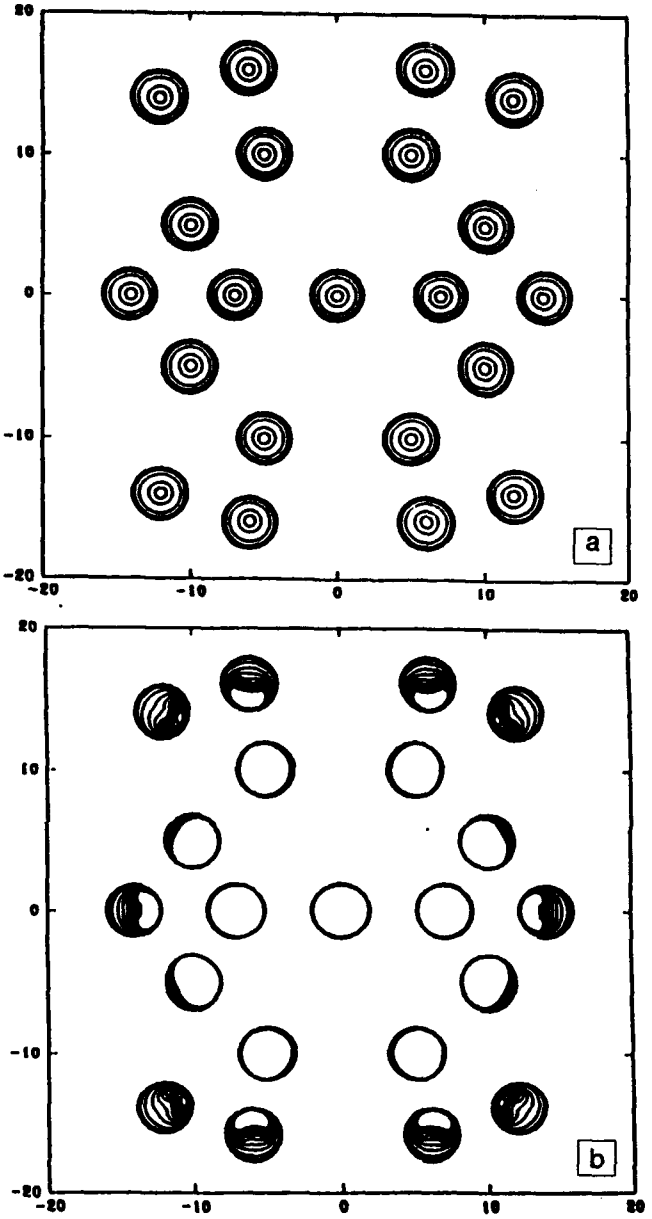

Figure 14: Simulation of the dynamic interactions between a cloud of 21 bubbles using 3DynaFS on a Cray. Two planes of symmetry are used; each bubble has 102 nodes and 200 panels. a) Growth. b) Collapse.

been established (7). The electrodes were mounted in a large vessel which was hermetically sealed and connected to a vacuum pump. Lowering the ambient pressure was used for degasing and, when desired, for increasing the bubble size, thus slowing down the phenomena observed. This enabled the use of a moderate framing rate high-speed camera, a HYCAM, whose maximum capability was 10,000 frames per second.

Behavior near a solid wall

The physical mechanisms by which bubble collapse

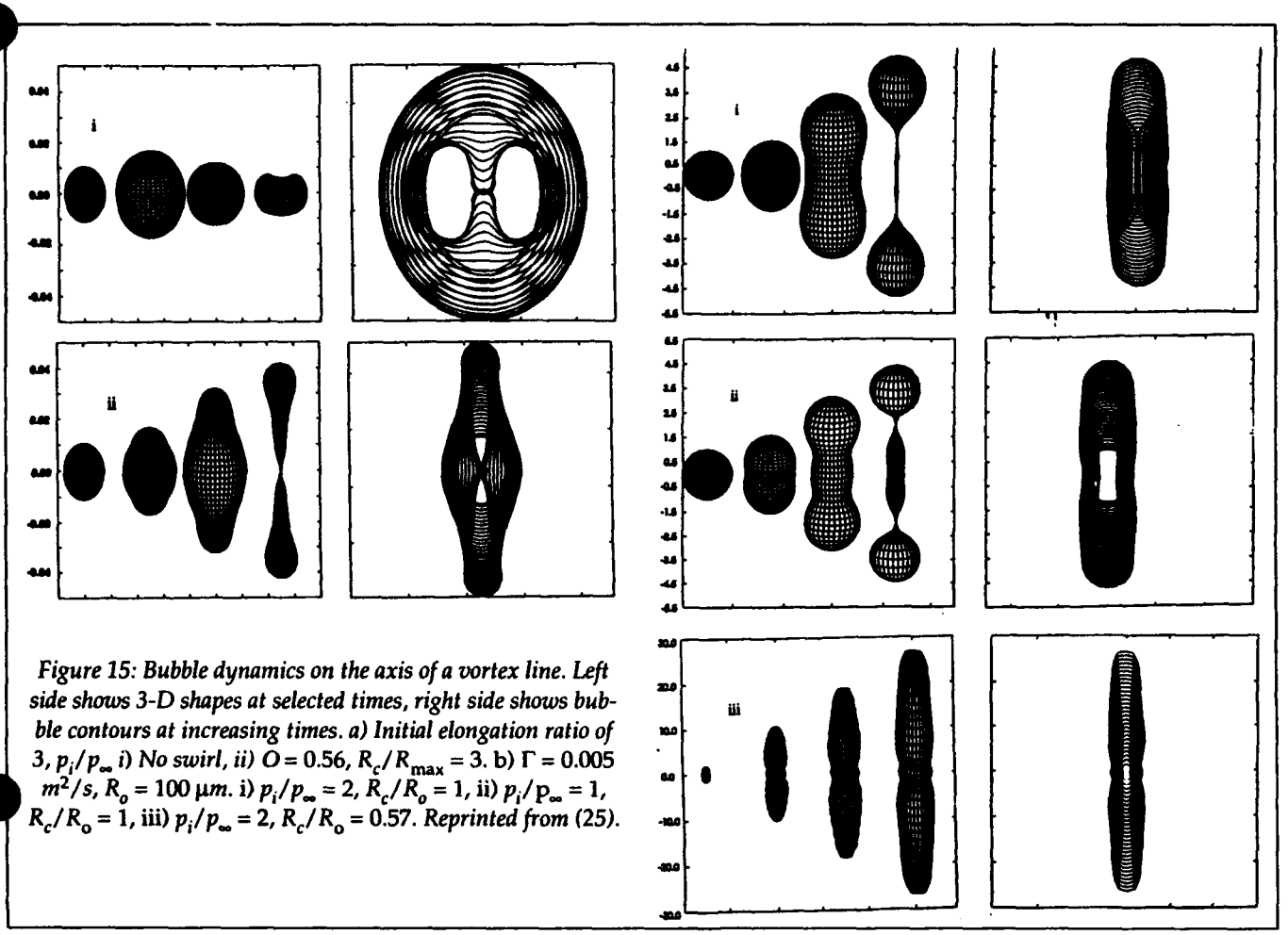

Figure 15: Bubble dynamics on the axis of a vortex line. Left side shows 3-D shapes at selected times, right side shows bubble contours at increasing times. a) Initial elongation ratio of 3, p_i/p_∞ i) No swirl, ii) $O = 0.56$, $R_c/R_{max} = 3$. b) $\Gamma = 0.005$ m^2/s, $R_o = 100\ \mu m$. i) $p_i/p_\infty = 2$, $R_c/R_o = 1$, ii) $p_i/p_\infty = 1$, $R_c/R_o = 1$, iii) $p_i/p_\infty = 2$, $R_c/R_o = 0.57$. Reprinted from (25).

near a solid wall causes material erosion have been the subject of controversy for a long time. Indeed, a shock wave can be generated at bubble collapse (Fig. 2). In addition, bubble collapse near a solid surface proceeds with the formation of a damaging microjet. During its implosion the bubble first elongates perpendicular to the wall, then the side away from it flattens and a re-entering region is formed initiating a microjet which can pierce the bubble and hit the wall. Figure 5 shows a numerical simulation of this collapse using 2DynaFS. Very beautiful pictures of the phenomenon were taken by Lauterborn (20) who generated the bubbles using a laser. Figure 6 presents some of our high speed photographs using the spark generated bubbles (21).

Influence of fluid properties on the bubble behavior

Drag-reducing polymers are known to greatly reduce the cavitation inception index for several types of flows. The onset of cavitation is also delayed in acoustic cavitation in a stagnant fluid (16). In addition, cavitation erosion has been reported to be greatly modified (in both directions) with additives. Experimental (1) and theoretical (2,21) studies on a spherical bubble growth and collapse have shown no significant differences between a Newtonian and a viscoelastic fluid. This conclusion was supported by our high-speed photographic observations of spark-generated bubbles in an unbounded fluid (4).

However, these observations showed that a Polyox WSR 301 solution has a noticeable influence on non-spherical bubble dynamics near solid walls, compared to a liquid having the same viscosity (water + glycerin). The effect of the presence of the additives is to bring the bubble behavior closer to that of a spherical cavity. In order to compare bubble behavior in water and in a viscoelastic liquid, diluted polymer solutions of Polyox were used in the set up described above. In the first series of tests (11), a cylindrical aluminium specimen, used to record the damage due to the implosion, was fitted under the electrodes in a hole drilled in a Plexiglas plate. It was observed later, while analyzing the motion pictures, that this specimen, not being tight enough in the hole, was being slightly sucked up towards the bubble during its growth and then returned after the implosion.

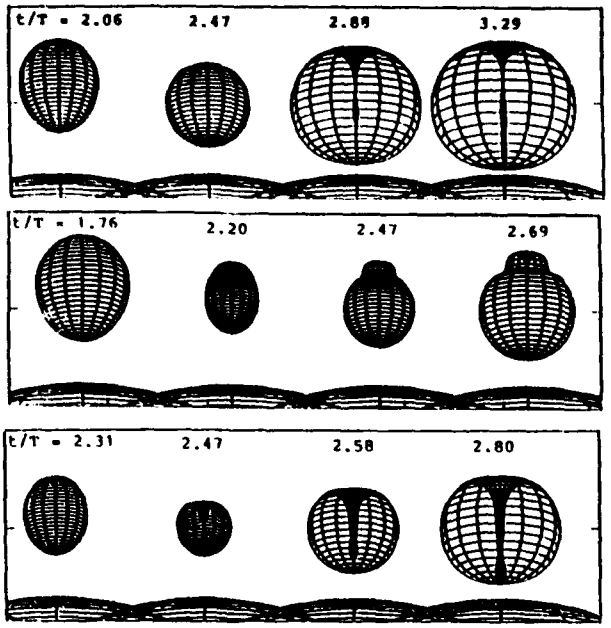

Figure 16: Comparison of calculated bubble collapse contours using 2DynaFS and Nike2D. Top to bottom: fixed, rigidly moving, and deforming structure. Reprinted from (26).

This was in fact fortunate since it allowed the study of the influence of wall motion on the bubble dynamics. In that case the curves $R_A/R_{Cmax} = f(t/\tau_{sph})$(see Figure 7 also for definitions), where τ_{sph} is the period of oscillation of the spherical bubble obtained in the same conditions show that the period of oscillation of the bubble decreases when $\varepsilon = R_{Cmax}/l_o$ increases. This behavior, comparable to that near a free surface, is the opposite of what happens near a fixed solid wall.

The experiment was then repeated with a fixed wall. The lengthening effect on the bubble life was verified and increased with ε (Fig. 7). In both cases described above, the bubble was violently attracted towards the wall during its successive collapses and rebounds.

In the presence of polymer additives the following observations were made. In the vicinity of the moving solid wall, for the same ε, the addition of a 250 ppm of Polyox delayed the creation of the microjet thus increasing the bubble lifetime and moving the curves $R_A = f(t)$ toward the spherical case curve. Near a fixed solid wall the apparently opposite effect (shortening of the period of oscillation) in the presence of polymers was also seen to reduce the differences between the considered case (given ε) and the spherical case (11,12). This seems to indicate a stabilizing effect on bubble departure from sphericity due to the presence of the viscoelastic fluid. However, as shown in Figure 10, the opposite effect was observed in the presence of a free surface (12).

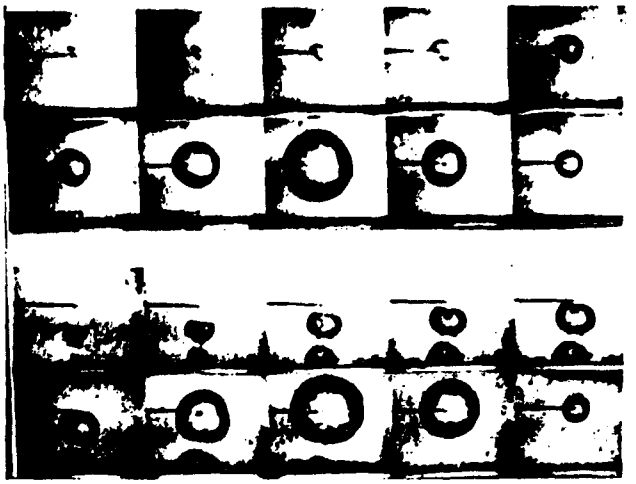

Figure 17: Collapse of spark-generated bubbles below a plate. a) Rigid 0.475 in. Plexiglas plate. b) Flexible 0.125 in. nylon plate.

Behavior between two solid walls

The collapse of bubbles between two solid walls is interesting from the practical view point of cavitation in confined areas. The large deformations involved are also of interest from the fundamental dynamics point of view. When $\varepsilon < 1$, a bubble at equal distance from the walls first elongates parallel to the walls (direction of most freedom) during its growth, then perpendicularly when the implosion starts. Later the bubble constricts in the medium plane of symmetry and splits in two parts. This is observed experimentally in Figure 8 and simulated numerically in Figure 9 using the code 3DynaFS. Later on each of the two bubbles formed collapses with the formation of a microjet directed to the closer wall. When $\varepsilon \geq 1$, the bubble behaves as a cylindrical cavity until the final stages of collapse where it constricts and splits in two parts (7,9).

Quantitatively the presence of the two walls augments the bubble lifetime significantly. This lengthening effect increases dramatically with ε (Figure 10). When ε is approximately equal to 0.7 the period increases by 50% (compared to only 7% in the presence of a single wall) and when ε is approximately equal to 2 it is doubled.

In the presence of polymer additives a shortening of the period of oscillation tends, as for the single wall, to reduce the differences between the considered case and the spherical case.

Bubble collapse near a flat wall in a shear flow

While most numerical simulations and experimental observations of fundamental bubble dynamics have been made in a quiescent liquid near an infinite wall, it is obvious that cavitating bubbles most often occur in a

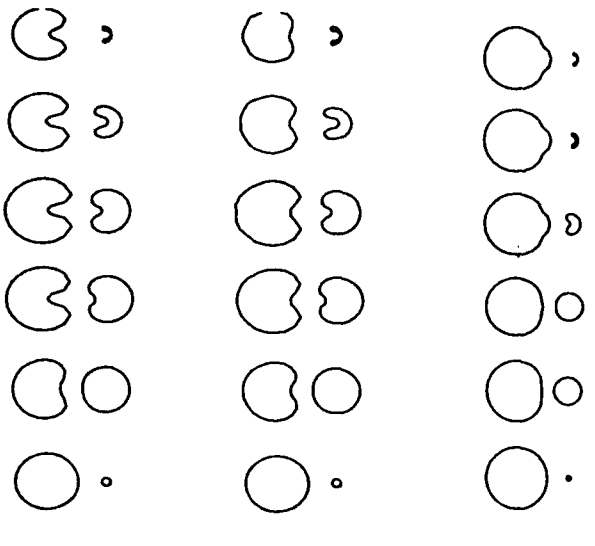

Figure 18: Simulation of the growth and collapse of a bubble near a globule. Bubble and globule shapes versus time. Indices 1 and 2 are for bubble and globule respectively. a) $R_{max1} = R_{max2}$, $\sigma_1 = \sigma_2 = 0.77$ *N/m*, $k_1 = 1.25$, $k_2 = 10$. b) $R_{max1} = R_{max2}$, $\sigma_1 = 0.77$ N/m, $\sigma_2 = 10^4$ *N/m*, $k_1 = 1.25$, $k_2 = 10$. c) $R_{max1} = 2R_{max2}$, $\sigma_1 = \sigma_2 = 0.77$ N^2/s, $k_1 = 1.25$, $k_2 = 10$.

flow with a slip velocity between the bubble and the liquid. These effects can be simulated numerically using 3DynaFS. Figure 11 illustrates the results of bubble behavior near a flat plate in the presence of a shear flow. The shear flow is such that $V_o = 0$ at the wall and grows linearly away from it to attain V_{shear} at the location of the bubble center. The figure shows interesting results for bubble behavior during bubble growth and collapse.

For an increasing ratio, $\tau = V_{shear}/\sqrt{\Delta_{P/\rho}}$ between the shear flow velocity and the characteristic bubble collapse velocity, the bubble deforms and elongates more and more during its growth. For small values of τ, the re-entering jet is deviated from the perpendicular to the plate with increasing values of τ. For larger values of τ, the re-entering jet formation is totally modified and the bubble tends to cut itself into a toroidal bubble. With increasing values of τ, an interesting lifting effect is observed, and the bubble centroid is seen to move further and further away from the wall. This results from an interaction between the shear flow and the rotation imparted to the bubble.

Interaction between multiple bubbles

In a cavitating flow field bubbles are seldom isolated, so there is a need for simulation tools for multibubble interactions. The first model we developed was based on matched asymptotic expansions (22). This model explained the fact that collective bubble dynamics can generate pressures much higher than expected from the simple addition of single bubble effects. This explains the very high erosion rates observed when cloud cavitation occurs. However, this model diverged when the number of bubbles increased or when the bubble spacing decreased. Using the BEM method, these limitations can be removed and more realistic and accurate results obtained. Figure 12 compares the results obtained with 3DynaFS with those using an asymptotic approach (22,24). Note that the asymptotic approach is already an improvement over most previous studies, which totally neglected the interactions. The bubble cloud is subjected to a sudden pressure drop, and cloud configurations of 1, 2, 4 and 8 bubbles are considered.

For the 2-bubble case the bubble centers are separated by a distance l_0, and the initial gas pressure in each bubble is such that the bubble would achieve a maximum radius $R_{max} = R_{b0} = 0.047l_0$ if isolated. The four-bubble configuration considers similar bubbles centered on the corners of a square with sides of dimension l_0. Finally, the eight bubbles are located on the corners of a cube of side l_0. The figure presents the variations with time of the pressure measured at the "cloud center" normalized by that obtained with an isolated bubble. As expected, the asymptotic approach gives a very good approximation for a small number of bubbles, N. However, the pressures predicted by the asymptotic analysis are seen to become much higher than the more accurate 3D results for an increasing value of N. Similar results are observed when the cloud void fraction or the ratio, $\epsilon\pi = r_{b0}/l_0$, increases (24). This result qualifies earlier conclusions about extremely large pressures generated by a bubble cloud collapse.

Figure 13 illustrates another important effect due to asymmetries in a bubble cloud configuration. It considers an asymmetric five bubble configuration. All bubbles have the same initial radius and internal pressure, and are initially spherical and located in the same plane. The most visible effect is that observed on the center bubble; its growth is initially similar to that of the other bubbles, but it ends up being the least deformed. Later on, as the collapse proceeds with the development of a re-entrant jet directed towards the central bubble, this bubble appears to be shielded by the rest of the cloud. Its period is at least double that of the other bubbles. Very similar effects are seen when the number of bubbles is increased. Figure 14 shows a 21-bubble configuration, where again growth occurs without too much interference between the bubbles. However, collapse proceeds from the outer bubble shells towards the inside, indicating a cloud period of oscillation much larger than that of individual bubbles, as predicted by cloud cavitation models (8).

Bubble dynamics on the axis of a vortex

Let us now consider the case where the bubble is

placed at the axis of a vortex line at $t = 0$ and starts to grow due to the excess between the internal pressure and the local ambient pressure. During the growth phase the bubble elongates along the vortex axis, then starts its collapse from a significantly elongated shape (25). As shown in Figure 15a, this elongation is not the key parameter to the subsequent bubble behavior. If the rotation velocity is neglected, the collapse would proceed as for elongated bubbles with two opposing jets formed at the bubble points along the axis (Fig. 14). However, the opposite effect with a radial jet forming is in general obtained when the rotation in the vortex flow is included. The bottom of Figure 14a illustrates this for particular values of the vortex circulation, Γ, and the normalized viscous core radius, $R_c = R_c/R_{max}$.

In Figure 15b, the initial pressures inside the bubbles are taken to be larger than the pressure on the vortex axis, and the bubbles are left free to adapt to this pressure difference. For a given value of the circulation (normalized parameter, [equ 30]), the bubble behavior strongly depends on the ratio of the core radius R_c to R_{max}. In all cases where R_{max} is larger than R_c, it appears that the bubble tends to adapt to the vortex tube of radius R_c. This could lead to various bubble shapes, as shown in Figure 15b, ending up with a very elongated bubble with a wavy surface for large values of R_{max}/R_c. The figure shows bubble contours at various times during growth and collapse for various values of the core radius, R_c, and the ratio of the initial bubble and ambient pressures. Also shown are selected 3D shapes of the bubbles at various times which have the advantage of being much more descriptive.

It is apparent from these figures that during the initial phase of bubble growth, radial velocities are large enough to overcome centrifugal forces and the bubble first grows almost spherically. Later on, the bubble shape starts to depart from the spherical and adapts to the pressure field. The bubble then elongates along the axis of rotation. Once the bubble has exceeded its equilibrium volume, bubble surface portions away from the axis - high pressure areas - start to collapse, or to return rapidly towards the vortex axis.

On the other hand, points near the vortex axis do not experience rising pressures during their motion, and are not forced back towards their initial position, thus continuing to elongate along the axis. As a result, a constriction appears in the mid-section of the bubble. The bubble can then separate into two or more tear-shaped bubbles. It is conjectured that this splitting of the bubbles is a main contributor to cavitation inception noise which can be used as a means of detecting cavitation.

Bubble collapse near deformable bodies

This section illustrates the importance of accounting for the motion and deformation of a nearby body in the study of bubble dynamics. This has been illustrated indirectly in the above experiments, where the motion of an impacted sample significantly modified the history of the jet point. Figure 16 shows the behavior of a large bubble near a spherical structure. Three characteristic interaction cases are considered (26). In the first case the sphere is rigid and does not move or deform. In that case, as for a bubble collapsing near an infinite wall, the bubble collapse proceeds with the formation of a re-entering jet perpendicular to the sphere. In the second case, the sphere is allowed to move rigidly in response to the bubble pressure field. A very significant modification of the bubble behavior is observed, leading to a constriction of the bubble top prior to the formation of the re-entering jet. Finally, in the third case, a full coupling between the structure motion and deformation and the bubble behavior is considered using the coupled 2DynaFS and Nike2D codes. In that case, a bubble behavior between the above two cases is observed. A re-entering jet is still formed, but it is wider and slower than that achieved in the presence of a rigid sphere. However, the pressure felt by the deforming structure is larger (26).

Figures 17a and 17b compare the experimental observations of large spark-generated bubble behavior near a solid and a flexible plate. In both cases, a relatively large bubble is generated through a reduced ambient pressure in the bubble chamber, and the bubbles are spark-generated below horizontal plates. In Figure 17a, the plate is made of thick Plexiglas (0.475 inch), while in Figure 17b, the plate is made of thin (0.125 in) pliable plastic. The bubbles are generated under identical conditions and would have the same radius if in an infinite medium. The difference in the behavior of the two bubbles is, however, very obvious. Two important characteristics of the rigid wall case are the formation of a bubble re-entering jet directly towards the plate, and the reflection of an expansion wave at the plate wall which creates a secondary bubble from minute air bubbles trapped under the plate (Fig. 17a).

In the flexible wall case shown in Figure 17b, the re-entering jet is practically eliminated, and the bubble collapses almost spherically without moving towards the plate. Due to some asymmetry in the plate position relative to the bubble, a small motion sideways and away from the plate is observed. The formation and growth of a bubble layer near the solid plate is replaced in the flexible plate case with a very fine sheet of tiny bubbles which move away from the plate. This again illustrates the importance of nearby wall motion and deformation on bubble dynamics.

Bubble collapse near simulated cells

The last example presented in this communication concerns the behavior of a bubble near simulated blood

cells. Undesirable effects of cavitation using ultrasound have been reported in the literature (8). The negative effects of cavitating bubbles on nearby cells are explained by the impact of re-entering jets on the cells and by the generation of large stresses on the cell. Without trying to simulate accurately the cell globule, we have considered the interaction of a growing and collapsing bubble and a nearby spherical globule with a very high surface tension and/or a very low compressibility content. The bubble behavior near such a simulated cell is seen to depend on the size ratio between the bubble and the globule.

In most cases, as in Figures 18a and b, the cell acts as a nearby free surface and tends to repel the re-entering jet formed during the bubble collapse. This jet moves away from the globule. However, it appears that the globule is seen subjected to very high stresses leading to a sharp intrusion of the fluid in the globule and a potential rupture of the globule interface. Figure 18c shows a second configuration where the globule is much larger than the bubble, in which case the globule is stretched in a different fashion.

Conclusions

We have reviewed various aspects of cavitation inception and highlighted the potential for error in scaling if the proper definition is not used. For instance, the concept of nuclei distribution in the cavitating medium, often not addressed, can be a source of serious scaling problems. A few models for bubble growth and collapse were then presented, including the effects of a non-Newtonian fluid which are of relevance to biological applications. The importance of non-spherical bubble dynamics was then addressed as this is very common in any conditions where cavitation erosion occurs. The influence of relative liquid bubble flow, multibubble interactions and the presence of non-uniform flow fields were then briefly considered. Finally, the importance of the inclusion of the motion and deformation of the nearby boundaries or cells was highlighted.

While this communication addressed a host of problems, showing some particular solutions, it was not able to give definite general conclusions. It did, however, highlight the fact that the study of cavitation is much more complex than usually thought. Simplified, commonly used models (spherical and axisymmetric) can lead to simplified answers. However, these results are only good in very limited conditions, and risk results that can be in error by orders of magnitudes. Fortunately, with recent advances in computational techniques and computers, detailed simulations of particular conditions are becoming more and more within reach.

Acknowledgements

Major parts of this paper are based on work supported by the Office of Naval Research, Contract N00014-89-C-0025. The author would like to acknowledge the contributions of several colleagues at Dynaflow, particularly Drs. Ramani Duraiswami and Kenneth Kalumuck.

References

1. Besant WH. Hydrostatics and hydrodynamics. Cambridge University Press, London, 1859:Art. 158
2. Lord Rayleigh. On the pressure developed in a liquid during collapse of a spherical cavity. Phil Mag 1917;34:94-98
3. Brown B, Goodman JE. High intensity ultrasonics - industrial applications. Ilife Books ltd., London, 1965
4. Chahine GL, Johnson VE Jr. Mechanics and applications of self-resonating cavitating jets. ASME International Symposium on Jets and Cavities, WAM, Miami, Florida, 1985;FED-Vol.31:21-35
5. Chahine GL, Johnson VE Jr, Lindenmuth WT, Frederick GS. The use of self-resonating cavitating water jets for underwater sound generation. J Acoustical Soc Am 1985;77-1:113-126
6. Knapp RT, Daily JW, Hammitt FG. Cavitation. McGraw Hill Book Co., NY, 1970
7. Hammitt FG. Cavitation and multiphase flow phenomena. McGraw-Hill International Book Co., NY, 1980
8. Young FR. Cavitation. McGraw Hill Book Co., NY, 1989
9. Plesset MS, Prosperetti A. Bubble dynamics and cavitation. Ann Rev Fluid Mech 1977;9:145-185
10. Chahine GL. Etude asymptotique et experimentale des oscillations et du collapse des bulles de cavitation. Docteur Ingenieur Thesis, Universite Paris VI, Pierre et Marie Curie, 1974
11. Chahine GL, Fruman DH. Dilute polymer solution effects on bubble growth and collapse. Physics of Fluids 1979;22(7):1406-1407
12. Chahine GL. Experimental and asymptotic study of non-spherical bubble collapse. Appl Scientific Res 1982;38:187-197
13. Alloncle AP, Dufresne D. Visualization of laser induced vapor bubbles and pressure waves. Proceedings, IUTAM Symposium on Bubble Dynamics and Interface Phenomena, Birmingham, 6-9 Sept. 1993;(in press)
14. Rood EP. Cavitation Inception Research - Focus and Direction. Report on the "Advisory Council on Cavitation Events" ONR meeting on May 20th 1992 in Memphis TN.
15. Gilmore FR. The growth and collapse of a spherical bubble in a viscous compressible liquid. California

Institute of Technology Report 26-4, California, 1952
16. Cole RH. Underwater explosions. Dover Publications, 1948
17. Chahine GL, Perdue TO, Tucker CB. Interaction between an underwater explosion and a solid submerged body. Dynaflow, Inc. Technical Report, 89001-1, Sep. 1988
18. Chahine GL. Nonspherical bubble dynamics in a line vortex. Proceedings of ASME 1990 Cavitation and Multiphase Flow Forum, Toronto, Canada, 1990;FED-Vol.98:121-127
19. Chahine GL. Numerical modelling of the dynamic behavior of bubbles in nonuniform flow fields. ASME symposium on numerical methods for multiphase flows, Toronto, Canada, 1990;FED-Vol.91:57-65
20. Lauterborn W. Cavitation and coherent optics. In: Lauterborn W (ed). Cavitation and inhomogeneities in underwater acoustics. Springer Verlag, 1980:3-13
21. Chahine GL. Etude locale du phenomene de cavitation. Analyse des facteurs regissant la dynamique des interfaces. Docteur d'Etates-Sciences Thesis, Université Pierre et Marie Curie, April, 1979
22. Chahine GL. Cloud cavitation: theory. 14th Symposium on Naval Hydrodynamics, Ann Arbor, Michigan, National Academy Press, Washington, DC, 1983:165-195
23. Chahine GL. Dynamics of the interaction of nonspherical cavities. In: Miloh T (ed). Mathematical approaches in hydrodynamics. SIAM, Philadelphia, 1991:51-68
24. Chahine GL, Duraiswami R. Dynamical interactions in a multi-bubble cloud. ASME, J Fluids Eng 1992;114:680-687
25. Chahine GL. Bubble interaction with vortices. In: Green S (ed). Fluid vortices Kluwer Academic Publishers 1994:(in press)
26. Chahine GL, Kalumuck KM, Duraiswami R. Coupling of a fluid's BEM code with a structural FEM code for fluid-structure interaction simulation. Boundary Element XV, Vol.1. Stress Analysis. Brebbia CA Rencis JJ (eds). CMP, Elsevier, 1993:581-597

Discussion

Swanson:

This photography is to be commended. One of the things that I would like to point out specifically is that in the very last series there were a number of rebounds for those bubbles. As the bubbles collapse, the generated jet does all those damages. These are the prettiest pictures I have seen in a long time.

Chahine:

Thank you.

Israelachvili:

How do you know that the damage is not caused by the spark? I would like to show some pictures given to me by Professor Ellis before he died. These pictures show that the shock waves at the inception are as strong as they are when they collapse.

Chahine:

The subject of what generates the erosion, the shock or the re-entering jet, is very old as we saw from Professor Ellis' picture. I think that it is a combination of both effects and depending upon the bubble distance from the wall and what configuration is used it is one rather than the other. For example, in an underwater explosion it would be much more the shock. However, we have been working on instances where it is the jet that is much more erosive than the shock.

Regnault:

Maybe you can clear up a few concerns or questions I have about cavitation. You defined cavitation as the expansion of nuclei bubbles and the recollapse of those as opposed to the generation of vapor without a nuclei. Is that correct?

Chahine:

I have no doubt in my mind that it is practically impossible to generate vapor out of no nuclei. I think maybe 95% of the cavitation community would agree.

Regnault:

In the case of cavitation in the body where we would have a large amount of dissolved gases, would you say that the drawing out of dissolved gases from the bloodstream then the recollapse of these bubbles would be the source for cavitation bubbles?

Chahine:

No, I think there is a confusion between dissolved gases and gases that are in suspension as nuclei. In the first set, the molecules of the gas are mixed with the molecules of the water. The characteristic time for these dissolved gases to go into the nuclei is very long. That is not what I am talking about. I am talking about actual microscopic bubbles that are already present in the liquid, very different from the dissolved gases in the bloodstream.

VISCOUS INTERACTION BETWEEN BUBBLE AND LINE VORTEX

G. Desgress du Lou
T. Sarazin
G. L. Chahine

October 1993

DYNAFLOW, INC.
7210 Pindell School Road
Fulton, MD 20759

VISCOUS INTERACTION

BETWEEN

BUBBLE AND LINE VORTEX.

MM.: **DESGREES du LOU** et **SARAZIN**, midshipmen, E.N.91.

Jury : President: M.**MICHEL**, Directeur de recherches au CNRS.

Members: M.**CHAHINE**, Docteur ès sciences,
Project Manager,
M.**BILLARD**, capitaine de frégate,
Docteur ès sciences,
Project Pilot,
M.**CERRUTI**,
Professor at the Naval Academy,
M.**MICHEL**, Agrégé,
Professor at the Naval Academy,
Head of the language department.

Our study consisted in analysing the interaction between a bubble and a vortex flow. Therefore, we tried to use more physically realistic vortex models, and we highlighted the effects of a fully viscous interaction.

Statement of work:

Theory: The theoretical part aims at showing the effects of the interaction on bubble behaviour and on the vortex flow behaviour.

A first approach examine the 2D axisymmetric interaction, considering that the fluid is perfect.

In a more general chapter, we take a fully viscous interaction into account.

Results: Two vortex models lead to realistic evolutions of the bubble and of the vortex flow, with the influence of an axial velocity.

A 1D model shows, for the first time, that the interaction seems to be non linear.

Synthesis and conclusion: We propose a matching of the two solutions for an axisymmetric and finite bubble, which would lead to understand the non linear viscous interaction, taking the axial flow of the vortex into account.

Acknowledgements

We would like to thank Dynaflow Inc. and all its team.
They enabled us to accomplish this study in the best conditions.
We would like to thank especially our project manager, G.L. CHAHINE,
and our project pilot, capitaine de frégate BILLARD.

Contents

NOMENCLATURE

a bubble radius.
a_o initial bubble radius.
A_c Rankine's core radius.
C Burgers constant.
c local curvature on the bubble surface.
$\frac{D}{Dt}$ Lagrangian or material derivative.
dt time step.
g gravity field.
j number of the time step.
k polytropic constant for PV^k =constant.
P pressure field.
P_{g_o} initial partial gas pressure in the bubble.
P_l pressure in the liquid.
P_s pressure at O, the stagnation point of the initial Burgers vortex.
P_v partial vapor pressure.
P_∞ pressure at infinity.
Re Reynolds number
s variable: $s = r/a$.
$\overline{T}$ stress tensor.
t time.
U velocity field: $\mathbf{U} = U_r \vec{e}_r + U_\theta \vec{e}_\theta + U_z \vec{e}_z$
V bubble volume.
V_o initial bubble volume.
We Weber number
δ Burgers core radius.
δ_o initial Burgers core radius.
Γ circulation of the fluid.
μ dynamic viscosity coefficient.
ν cinematic viscosity coefficient.
Φ velocity potential.
ρ fluid density.
σ surface tension.
ω vorticity.

INTRODUCTION

The presence and dynamics of bubbles in a flow field can have significant effects of relevance to engineering applications of great importance. These effects include erosion, noise generation, damping of acoustic signals, degradation of performances. This has instigated a great interest in the study of the problem, especially in high vorticity regions. These regions can be found at the tip of propellers' blades or in swirl chambers for example. The presence of cavities in such a tip vortex can have significant effects on the behavior of the flow and on its characteristics, in relation to transportation and exchanges of energy. These effects cannot be understood without adressing complicated, but nonetheless fundamental phenomena associated with the interactions and the motion of the bubble. The complexity of the general physical and mathematical problem can be approached by making assumptions, which simplify the problem. Then, once the problem has been posed, we solve it by using computational methods. In the first approach, we consider a bubble in a vortex, taking an axial velocity into account, where the vorticity is due to the initial flow. Thus the interaction is linearized, considering the addition of the flow generated by the bubble with the initial "basic flow". In a parallel approach, a fully viscous interaction between the bubble and the flow is considered. The viscous solver is one-dimensional as we look at an infinitely long cavity such as one can find on the axis of a tip-vortex behind a propeller. In the third part we try to propose a solution to the matching of the two methods, so that the interaction between the vortex flow and the bubble may be fully understood.

1. Generalities.

1.1. Cavitation.Bubble dynamics.

The variations of the pressure field in a fluid containing nuclei (cavitation germs) may produce large cavities of gas and liquid vapor, in other words bubbles.

The dynamics of these bubbles in respect to the flow around them is a complex problem which has been solved in different cases.

The cavity, submitted to forces may also be deformed, rebound or collapse; in accordance to the ambiant med...

1.2. Vorticity. Vortex models

The whole of this study is axisymmetric. Figure 1 shows the referential we are using.

A newtonian fluid in motion can rotate about itself. To measure this effect, we use a vector quantity named vorticity: defined by

$$\omega = \nabla \times U,$$

which physically coresponds to the angular velocity of two line segments in the fluid mutually normal to n. (See figure2)

Figure (2) is an intuitive illustration of vorticity. The cross represents two lines of fluid particles. At time step one the cross has right angles. It is then convected in the fluid. At time step two the cross has changed it angles. We have observed the rate of change of the angle between these two segments. This angular velocity corresponds to vorticity.

1.2.1. The vorticity equation.

The momentum equation, written in an inertial frame of reference is:

$$\frac{DU}{Dt} = \frac{\partial U}{\partial t} + (U.\nabla U) = -\frac{\nabla P}{\rho} + \frac{\nabla T}{\rho} + g\,. \qquad (1.1)$$

Replacing $(\mathbf{U}.\nabla)\mathbf{U}$ by $\nabla((\mathbf{U}.\mathbf{U})/2) - \mathbf{U}\times\omega$,
and taking the curl of equation (3.25) leads to:

$$\frac{D\omega}{Dt} = -\omega(\nabla\mathbf{U}) + (\nabla\omega)\mathbf{U} + \frac{1}{\rho^2}\nabla\rho\times\nabla P - \frac{1}{\rho^2}\nabla\rho\times\left(\nabla\overline{T}\right) + \frac{1}{\rho}\nabla\times\left(\nabla\overline{T}\right) + \nabla\times\mathbf{g}\,.$$

If we consider the flow of a Newtonian fluid of constant density and viscosity, with only potential body forces, the vorticity equation becomes

$$\frac{D\omega}{Dt} = \omega(\nabla\mathbf{U}) + \nu\nabla^2\omega\,. \tag{1.2}$$

This equation has the form of a convection-diffusion equation, like a thermal diffusion equation, and characterizes the diffusion of vorticity due to the action of viscosity.

A fluid vortex is a region of concentrated vorticity and a vortex line is a line everywhere tangeant to the local vorticity vector.

Different models of vortex flows have been given through the years. We will describe two of them here.

1.2.2. Rankine vortex.

This is probably one of the most basic axisymmetric vortex flows. It consists in a rotating core of very viscous fluid and an outer region where the fluid is assumed to be perfect .

Mathematically, the expression of the velocity components amounts to:

$$u_\theta = \frac{\Gamma}{2\pi Ac^2}r,\quad r \le Ac.$$

$$u_\theta = \frac{\Gamma}{2\pi r},\quad r \ge Ac.$$

$$u_z = 0$$

1.2.3. Burgers vortex.

BURGERS (1948) solved equation (3.26), demonstrating the vorticity enhancement by stretching. A vortex in an incompressible, Newtonian, body force free fluid must satisfy the vorticity equation.

If the vortex is axisymmetric, aligned with the z-direction, and placed in a uniaxial straining field along its length, then $U_z = 2Cz$, where C is the Burgers constant.

The continuity equation dictates the presence of a radial influx of fluid:

$$U_r = -Cr$$

and equation (3.26) has the following solution:

$$U_z = 2Cz,$$

$$U_r = -Cr,$$

$$U_\theta = \frac{\Gamma}{2\pi r}\left[1 - \exp\left(-\frac{r^2}{4\delta^2}\right)\right] \text{ ,(see figure (3))}$$

$$\text{and } \omega_z = \frac{\Gamma}{\pi\delta^2} exp(-\frac{r^2}{4\delta^2});$$

$$\text{where } \quad \delta^2 = \frac{\nu}{C} + \left(\delta_o^2 - \frac{\nu}{C}\right) exp(-Ct).$$

δ may be defined to be the vortex core radius at any time t, and δ_o the initial vortex core radius.

Figure (4) describes the evolution of δ in time versus C.

At $t = 0$, and for $C = 0$, we find the formulation used by some researchers:

$$U_z = U_r = 0 \ ,$$

$$U_\theta = \frac{\Gamma}{2\pi}\left[1 - \exp\left(\frac{-r^2}{4\delta_o^2}\right)\right] \tag{1.3}$$

One should note however, that this particular expression (at t=0) cannot be considered to hold at all times since (1.3) taken to be true at all times does not satisfy the general equation (3.25).

1.2.4. Diffusion of vorticity in a viscous fluid.

The code described in chapter 3 (see figure (5))enables us to observe the effect of viscosity on a Rankine vortex flow. We insert a cylinder of constant radius in the vortex . According to the transport of momentum principle, the vorticity spreads out and diffuses in the medium. Another illustration of viscosity would be Couette's experiment: he takes one cylinder which he inserts into a larger whollow cylinder. He then pours fluid in between these cylinders and has the inside one start spinning. Through viscosity the second one also starts spinning around a little while later.

1.2.5. Viscous interaction between bubbles and flows.

The understanding of the interaction phenomena remains up to now one-sided. The effects of the flow on the bubble has been instigated in several of studies. Recent studies have shown that in a region of high vorticities the bubble is accelerated to the axis of the vortex. On its way the variations of ambient pressure deforms it and once on the axis the bubble can split into elongated bubbles. The effects of the bubble on the flow are yet to be fully understood. Phenomenas related to viscosity should enable us to find leads to consistent explanations. In the following chapters we will deal with both sides of the interaction theoretically and numerically, restricting the study to cases where the bubble is on the axis.

2. 2D-analysis of Burgers vortex.

2.1. Vortex without bubble.

2.1.1. Discussion.

This model is only valid near the axis of the vortex, since U_r and U_z increase linearly with r and z. Unlike Rankine's vortex, it does not present any discontinuity, and is physically more realistic, according to experimental studies.

- For $C > 0$, if δ_o is less than $\sqrt{\nu/C}$, δ will increase in time, viscous diffusion being predominant.

  On the other hand, if δ_o is greater than $\sqrt{\nu/C}$ (the asymptotic value of δ), it will decrease in time. $\omega_z(r=0)$ will then increase in time, which occurs with vortex stretching and compression.

- If $C \leq 0$, δ increases whithout bound.

2.1.2. Calculation of the pressure distribution.

Replacing U_z and U_r in the Navier-Stokes equation by their Burgers vortex expressions leads to:

$$\frac{\partial P}{\partial r} = -\rho C^2 r + \rho \frac{U_\theta^2}{r} , \tag{2.1}$$

$$\frac{\partial P}{\partial z} = -4\rho C^2 z , \tag{2.2}$$

and, because of the axisymmetry,

$$\frac{\partial P}{\partial \theta} = 0 . \tag{2.3}$$

- Equation (2.2) implies that $P(r,z,t) = -2\rho C^2 z^2 + F(r,t)$.
- To solve equation (2.1), we set $X = r/2\delta$, and $A = (\Gamma/2\pi)^2 \rho/8\delta^3$.

$\rho U_\theta^2/r$ becomes

$$\frac{\rho U_\theta^2}{r} = \frac{A}{X^3} - 2\frac{A}{X^3}\exp\left(-X^2\right) + \frac{A}{X^3}\exp\left(-2X^2\right) .$$

So we integrate:

$$\int \frac{\exp(-X^2)}{X^3} dX = -\frac{1}{2}X^{-2}\exp(-X^2) - \frac{1}{2}E_i(-X^2)$$

and

$$\int \frac{\exp(-2X^2)}{X^3} dX = -\frac{1}{2}X^{-2}\exp(-2X^2) - E_i(-2X^2)$$

(integration by parts, and change of variable $u = X^2$)
where Ei is the **Exponential integral:**

$$E_i(ax) = \int_x^\infty \frac{\exp(-at)}{t} dt$$

We set $B = 2A\delta$, and we get

$$P(r,z,t) = -2\rho C^2\delta^2X^2 - \frac{B}{2X^2} + \frac{B}{X^2}\exp(-X^2) - \frac{B}{2X^2}\exp(-2X^2) + B\left(E_i(-X^2) - E_i(-2X^2)\right) + G(z,t)\ .$$

- For the boundary conditions, a TAYLOR's series expansion indicates that the point O(r=0,z=0) is a stagnation point, where the pressure is P_o.

Thus we finally have

$$\begin{aligned} P(r,z,t) = P_o &- 2\rho C^2z^2 - 2\rho C^2\delta^2X^2 - \frac{B}{2X^2} \\ &+ \frac{B}{X^2}\left(\exp(-X^2) - \tfrac{1}{2}\exp(-2X^2)\right) \\ &+ B\left(E_i(-X^2) - E_i(-2X^2)\right) \end{aligned} \qquad (2.4)$$

$$where\ \ B = \frac{\rho\Gamma}{4\pi\delta}\ and\ X = \frac{r}{2\delta}\ .$$

(see figures (6),(7),(8))

2.2. Bubble in a Burgers vortex.

2.2.1. Navier Stokes equations.

Let's consider the case of a bubble growing and collapsing in a known flow field. Let the isolated Burgers vortex constitute this basic flow, $\mathbf{U}_o$, P_o; it satisfies the Navier Stokes equation:

$$\frac{\partial \mathbf{U}_o}{\partial t} + \mathbf{U}_o.\nabla\mathbf{U}_o = -\frac{1}{\rho}\nabla P_o + \nu\nabla^2\mathbf{U}_o\ . \qquad (2.5)$$

In presence of an oscillating bubble, the resulting velocity field, given by $\mathbf{U}$, also satisfies the Navier Stokes equation:

$$\frac{\partial \mathbf{U}}{\partial t} + \mathbf{U}.\nabla\mathbf{U} = -\frac{1}{\rho}\nabla P + \nu\nabla^2\mathbf{U}\ . \qquad (2.6)$$

Both $\mathbf{U}_o$ and $\mathbf{U}$ also satisfy the continuity equation:

$$\nabla.\mathbf{U}_o = \nabla.\mathbf{U} = 0\ .$$

Since we are interested in the modification of the basic flow by the presence of the bubble, it is convenient to define the "bubble flow" velocity and pressure variables, $\mathbf{U}_b$ and P_b, as follows:

$$\boxed{\mathbf{U}_b = \mathbf{U} - \mathbf{U}_o, \qquad P_b = P - P_o\ .}$$

If we assume that the "bubble flow" is potential,

$$\boxed{\mathbf{U}_b = \nabla\Phi_b}\ . \tag{2.7}$$

where Φ_b is the reduced or bubble potential.
Because of continuity, Φ_b satisfies Laplace's equation:

$$\nabla^2\Phi_b = 0\ .$$

We now substract equation (2.5) from equation (2.6), taking equation (2.7) into account, and we obtain

$$\nabla\left[\frac{\partial\Phi_b}{\partial t} + \frac{1}{2}|\mathbf{U}_b|^2 + \mathbf{U}_o.\mathbf{U}_b + \frac{P_b}{\rho}\right] = \mathbf{U}_b \times (\nabla \times \mathbf{U}_o) \tag{2.8}$$

The assumption of potential "bubble flow" implies that, as the basic flow interacts with the bubble dynamics, and is modified by it,
the bubble cannot generate any new vorticity. An attempt to remove this constraint is undertaken in chapter 3.

Equation (2.8) is now to be integrated at any point within the liquid, to obtain an equation similar to the classical unsteady Bernoulli equation.

The component of $\mathbf{U}_b$ in the $\vec{e_\theta}$ direction must be zero, because the contribution in this direction of the velocity field can only come from the axisymetric basic flow; so we get

$$\frac{\partial \Phi_b}{\partial t} + \frac{1}{2}(\nabla \Phi_b)^2 - Cr\frac{\partial \Phi_b}{\partial r} + 2Cz\frac{\partial \Phi_b}{\partial z} + \frac{P_b}{\rho} = \text{Constant in any direction.}$$

Very far from the bubble, the pressure tends towards the basic pressure, so the constant is zero.

At the bubble surface: the pressure in the liquid balances with the surface tension and the pressure in the bubble, so we know there the "bubble pressure":

$$P_b = P_l - P_o = P_v + P_{go}(\frac{V_o}{V})^k - c\sigma - P_o \ ,$$

and so

$$\frac{\partial \Phi_b}{\partial t} + \frac{1}{2}(\nabla \Phi_b)^2 - Cr\frac{\partial \Phi_b}{\partial r} + 2Cz\frac{\partial \Phi_b}{\partial z} + \frac{Pv + P_{go}\left(\frac{V_o}{V}\right)^k - c\sigma}{\rho} = \frac{P_o}{\rho} \ . \qquad (2.9)$$

2.2.2. Non-dimensionalization.

We normalize all variables as follow: lengths are non-dimensionalized by R_{max}, the maximum radius the bubble would achieve if isolated in the absence of flow, and pressures by P_∞ the initial pressure at the stagnation point (r=0).

According to the Rayleigh-Plesset equation, the program estimates a value of R_{max}, considering the case of a single bubble in an infinite fluid.

Thus, the time scale is normalized by its characteristic time, the Rayleigh time whose value is

$$T_{Rayleigh} = R_{max}\sqrt{\frac{\rho}{P_\infty}} \ .$$

This leads to a new non-dimensionalized form of equation (2.9) used in the axisymmetric Fortran code:

$$\frac{D\overline{\Phi}_b}{D\overline{t}} = \overline{P}_o + \frac{1}{2}\left(\frac{\partial \overline{\Phi}_b}{\partial \overline{r}}\right)^2 + \frac{1}{2}\left(\frac{\partial \overline{\Phi}_b}{\partial \overline{z}}\right)^2 - \left(\overline{P}_v + \overline{P}_{g_o}\left(\frac{V_o}{V}\right)^k - \overline{c\sigma}\right) \ , \qquad (2.10)$$

where

$$\overline{P}_o = 1 - \frac{\overline{C}^2\overline{r}^2}{2} - 2\overline{C}^2\overline{z}^2 + \frac{\overline{B}}{\overline{X}^2}\left(\exp\left(-\overline{X}^2\right) - \frac{1}{2}\exp\left(-2\overline{X}^2\right)\right) + \overline{B}\left(\mathrm{Ei}(-\overline{X}^2) - \mathrm{Ei}(-2\overline{X}^2)\right) ,$$

$$\overline{B} = \sqrt{\frac{\rho}{P_o}}\frac{\Gamma}{4\pi\delta} ,$$

$$\overline{X} = \frac{\overline{r}}{2\overline{\delta}} ,$$

$$\overline{\delta}^2 = \frac{\overline{t}}{\overline{C}} + \left(\overline{\delta}_o^2 - \frac{\overline{t}}{\overline{C}}\right) exp\left(-\overline{C}\overline{t}\right) ,$$

In all the following, we now consider each variable as non-dimensionalized.

2.2.3. The Boundary Element Method.

This method was developed by DYNAFLOW in the code 2DynaFs that we had to modify. This program considers closed surfaces such as bubbles in an infinite domain of fluid. We had to adapt it to take a "basic flow" interacting with a bubble into account. We now sum up the main steps tc implement the method for an axisymmetric problem.

In order to calculate the time evolution of the bubble surface, the axisymetric Boundary Elements Method is used, which reduces the dimension of the problem by one. This method is based on Green's identity, which provides Φ_b anywhere in the fluid, if this potential or its normal derivatives are known on the bubble surface.

Implementation. Considering the fact that Φ_b satisfies Laplace's equation, and defining the bubble boundary by S, we can write the following expression for the potential at any point x in the field

$$\Phi_b(x) = \int_s [\Phi_b(y)\nabla_y G(x,y) - G(x,y)\nabla_y \Phi_b(y)] . n_y dS , \qquad (2.11)$$

where y is the variable of integration of the bubble surface and G is the Green's function for the Laplace operator, explicitly given by

$$G(x,y) = -\frac{1}{4\pi}\frac{1}{|x-y|} .$$

As we consider an axisymmetric problem, the only function which can depend on θ is the mathematical Green's function (all physical quantities are independent of the angular coordinate). Let us define the trace of the bubble surface in a

meridional plan by C. We select this plan to be $\theta = 0$ in our cylindrical system of coordinates. Let the coordinate of the point x in the plan $\theta = 0$ be $(R, 0, Z)$, and the coordinates of the variable of integration be (r, θ, z). As the normal to the bubble surface has no components along the angular coordinate, the integral equation (2.11) becomes:

$$\Phi_b(R,Z) = \int_C \left[r\Phi_b(r,z) \frac{\partial}{\partial n} \int_0^{2\pi} G(x,y)d\theta \right] dS - \int_C \left[r \frac{\partial \Phi_b(r,z)}{\partial n} \int_0^{2\pi} G(x,y)d\theta \right] dS$$

Thus the integration over the angular variable is reduced to the integral

$$I = \int_0^{2\pi} G(r,\theta,z,R,Z)d\theta \ .$$

Replacing the Green's function by its expression, and using the substitutions

$$A = (R+r)^2 + (Z-z)^2, m = \frac{4rR}{A}, x = \cos(\frac{\theta}{2}),$$

we get

$$I = \frac{4}{\sqrt{A}} K(m).$$

where

$$K(m) = \frac{-1}{4\pi} \int_0^1 \frac{dx}{\sqrt{(1-mx^2)(1-x^2)}} \ .$$

is the complete elliptic integral of the first kind.
The equation for the potential can then be cast in the form

$$2\pi\Phi_b(R,Z) = -\int_c [r\Phi_b(r,z)h(r,z,R,Z]\,dS + \int_c \left[r \frac{\partial \Phi_b(r,z)}{\partial n} g(r,z,R,Z) \right] dS \tag{2.12}$$

where $g(r,z,r,Z) = K(m)/\sqrt{A}$, and $h(r,z,R,Z) = n_r \partial g/\partial r + n_z \partial g/\partial z$,
$n_r = dz/dS$, and $n_z = -dr/dS$

To solve equation (2.12) , we discretize the geometry of the contour of the bubble into N panels. We assume that the potential Φ_b is distributed linearly over each panel, while $\partial\Phi_b/\partial n$ is assumed to be constant over each panel. Equation (2.12) then becomes a set of N equations of index i of the type:

$$2\pi\Phi_{bi} = -\sum_{j=1}^{N}\left(\widetilde{B_{ij}}\Phi_{bj}\right) + \sum_{j=1}^{N}\left(\widetilde{A_{ij}}\frac{\partial\Phi_{bj}}{\partial n}\right) ,$$

which can be rewritten as

$$\sum_{j=1}^{N}(B_{ij}\Phi_{bj}) = \sum_{j=1}^{N}\left(A_{ij}\frac{\partial\Phi_{bj}}{\partial n}\right) , \tag{2.13}$$

where A_{ij} and B_{ij} are the discrete equivalent of the integrals given in equation (2.12).

So we perform the integration over each panel, using a Gaussian quadrature, and sum up the contributions to complete the integration over the entire contour of the bubble surface.

Time stepping To advance the points on the bubble surface, we assume that they move with the fluid at velocity $\nabla\Phi_b + U_o$. The normal "bubble velocity" $\left(\frac{\partial\Phi_b}{\partial n}\right)$ is known from the solution of the integral equations, while the tangencial "bubble velocity" is obtained by differenciation of $\Phi_b(c)$ (c is the arc length parameter along C). The nodes N_i are then advanced according to

$$\mathbf{ON}_i' = \mathbf{ON}_i + (\nabla\Phi_b + \mathbf{U}_o)dt .$$

To advance the potential, we need $\frac{D\Phi_b}{Dt}$, which is given by equation (2.10).

The time step dt is determined as

$$dt = \frac{(d\Phi_b)_{max}}{1 + 0.5V_m^2} ,$$

where V_m is the maximum velocity obtained at time t. That ensures that smaller time steps are chosen when rapid changes in the potential occur, while larger one are chosen for less rapid changes.

Results

The results related to this study are in chapter 4.1 to 4.2.

3. Problem formulation

Results of 2DynFs with a Burgers Vortex (see chapter 4.1), have shown that the bubble in a vortex flow can be elongated in such a way that the ratio of the

bubble's radius over its length can be very large. In that case if we are near the bubble and far from its ends, we may assume that it is infinitely long.

This element allows us to use an axisymmetric model of an elongated bubble in a fully viscous flow.

To solve the interaction between the bubble motion and the flow into account, without making any assumptions on the flow being potential or not, a starting point can be the Navier Stokes equations applied to the model. Once determined, the equations will have to be solved numerically.

3.1. Model definition

Figure (8) shows the model we are studying. The bubble is infinitely long. It is located on the axis of a Rankine vortex flow. The fluid is viscous. Cylindrical coordinates are used for all variables. The symmetry of the figure shows that as long as the axial flow is considered to be constant the problem we are dealing with is one-dimensional and located from the bubble wall out along the r-axis.

3.2. General equations

To study the problem we start from the Navier-Stokes' Equations, so we can fully determine the interaction between the bubble and the flow. Cylindrical coordinates used due to the geometry of the problem.

The Navier-Stokes equation are written:

$$\nabla U = 0,$$

$$\frac{DU}{Dt} = -\frac{\nabla p}{\rho} + \frac{\nabla \overline{T}}{\rho} + g,$$

where $\overline{T}$ is the stress tensor. In cylindrical coordinates they can be written:

$$div U = 0 \Leftrightarrow \frac{1}{r}\frac{\partial}{\partial r}(r\rho u_r) + \frac{1}{r}\frac{\partial}{\partial \theta}(\rho u_\theta) + \frac{\partial}{\partial z}(\rho u_z) = 0. \tag{3.1}$$

$$\frac{\partial u_r}{\partial t} + u_r\frac{\partial u_r}{\partial r} + \frac{u_\theta}{r}\frac{\partial u_r}{\partial \theta} - \frac{{u_\theta}^2}{r} + u_z\frac{\partial u_r}{\partial z} =$$

$$= -\frac{1}{\rho}\frac{\partial p}{\partial r} + \nu\frac{\partial}{dr}\left[\frac{1}{r}\frac{\partial}{dr}(ru_r)\right] + \nu\left(\frac{1}{r^2}\frac{\partial^2 u_r}{\partial \theta^2} - \frac{2}{r^2}\frac{\partial u_\theta}{\partial \theta} + \frac{\partial^2 u_r}{\partial z^2}\right), \tag{3.2}$$

$$\frac{\partial u_\theta}{\partial t} + u_r \frac{\partial u_\theta}{\partial r} + \frac{u_\theta}{r}\frac{\partial u_\theta}{\partial \theta} + \frac{u_r u_\theta}{r} + u_z \frac{\partial u_\theta}{\partial z} =$$

$$= -\frac{1}{\rho r}\frac{\partial p}{\partial \theta} + \nu \frac{\partial}{dr}\left[\frac{1}{r}\frac{\partial}{dr}(r u_\theta)\right] + \nu\left(\frac{1}{r^2}\frac{\partial^2 u_\theta}{\partial \theta^2} + \frac{2}{r^2}\frac{\partial u_r}{\partial \theta} + \frac{\partial^2 u_\theta}{\partial z^2}\right), \qquad (3.3)$$

$$\frac{\partial u_z}{\partial t} + u_r \frac{\partial u_z}{\partial r} + \frac{u_\theta}{r}\frac{\partial u_z}{\partial \theta} + u_z \frac{\partial u_z}{\partial z} =$$

$$= g - \frac{1}{\rho}\frac{\partial p}{\partial z} + \nu \frac{1}{r}\frac{\partial}{dr}\left[r\frac{\partial}{dr}(u_z)\right] + \frac{\partial^2 u_z}{\partial z^2} + \nu\left(\frac{1}{r^2}\frac{\partial^2 u_z}{\partial \theta^2} + \frac{\partial^2 u_z}{\partial z^2}\right), \qquad (3.4)$$

3.3. Geometrical considerations

The bubble is infinitely long and axisymmetric, so all variables are independent of θ and z :

$$\frac{\partial u_r}{\partial z} = 0,\ \frac{\partial u_\theta}{\partial z} = 0,\ \frac{\partial u_z}{\partial z} = 0,\ \frac{\partial p}{\partial z} = 0.$$

$$\frac{\partial u_r}{\partial \theta} = 0,\ \frac{\partial u_\theta}{\partial \theta} = 0,\ \frac{\partial u_z}{\partial \theta} = 0,\ \frac{\partial p}{\partial \theta} = 0.$$

3.4. Axisymetric formulation

The axial flow is assumed constant along the r-axis. This slug axial flow has no consequences on the bubble dynamics. It corresponds to an axial translation of the referential.

So we assume:

$$u_z = 0.$$

The general equations become (3.1), (3.3), (3.2), (3.3) and (3.4)

$$\frac{1}{r}\frac{\partial}{\partial r}(r\rho u_r) = 0. \qquad (3.5)$$

$$\frac{\partial u_r}{\partial t} + u_r \frac{\partial u_r}{\partial r} - \frac{u_\theta^2}{r} = \frac{-1}{\rho}\frac{\partial p}{\partial r} + \nu \frac{\partial}{dr}\left[\frac{1}{r}\frac{\partial}{dr}(r u_r)\right], \qquad (3.6)$$

$$\frac{\partial u_\theta}{\partial t} + u_r \frac{\partial u_\theta}{\partial r} + \frac{u_r u_\theta}{r} = \nu \frac{\partial}{dr}\left[\frac{1}{r}\frac{\partial}{dr}(r u_\theta)\right], \tag{3.7}$$

The radius of the bubble is $a(t)$; and its time derivative versus time $\dot{a}(t)$ also represents the radial velocity of the bubble wall. We can integrate Equation (3.5) over $[a(t), r]$ and write

$$\int_{a(t)}^{r} \frac{\partial}{\partial r}(r \rho u_r)\, dr = 0, \tag{3.8}$$

which leads to

$$r u_r = a(t)\, \dot{a}(t). \tag{3.9}$$

This continuity equation gives us a straight forward connection between the flow and the bubble behaviour.

By replacing the radial velocity in (3.6) (3.7) by the expression given in (3.9) and knowing that

$$\frac{\partial}{\partial t}\left(\frac{a\,\dot{a}}{r}\right) = \frac{1}{r}\,\dot{a}^2 + \frac{a}{r}\,\ddot{a},$$

$$\frac{\partial}{\partial r}\left(\frac{a\,\dot{a}}{r}\right) = -\frac{a\,\dot{a}}{r^2},$$

$$\frac{\partial}{dr}(r u_r) = \frac{\partial}{dr}\left(r\frac{a\,\dot{a}}{r}\right) = 0,$$

the Navier-stokes equations now become:

$$\frac{1}{r}\,\dot{a}^2 + \frac{a}{r}\,\ddot{a} - \frac{a^2}{r^3}(\dot{a})^2 - \frac{u_\theta^2}{r} = \frac{-1}{\rho}\frac{\partial p}{\partial r}, \tag{3.10}$$

$$\frac{\partial u_\theta}{\partial t} + \frac{a}{r}\,\dot{a}\,\frac{\partial u_\theta}{\partial r} + \frac{a}{r}\,\dot{a}\,\frac{u_\theta}{r} = \nu \frac{\partial}{dr}\left[\frac{1}{r}\frac{\partial}{dr}(r u_\theta)\right], \tag{3.11}$$

We end up with a set of coupled equations that describes the whole region of our particular vortex flow, in the presence of an interacting bubble.

3.5. Initial conditions and boundary conditions

3.5.1. Initial conditions

Bubble dynamics under water are controlled by the difference between the pressure inside the bubble and the ambient pressure. The initial conditions are simply stated as a prescribed initial bubble size and internal pressure and the value of the ambient pressure.

The initial radius of the bubble is

$$a(0) = a_o, \tag{3.12}$$

and its initial rate of growth

$$\dot{a}\,(0) = 0. \tag{3.13}$$

The initial vortex flow in which the bubble is located is based on the axisymmetry of the problem and the fact that we are interested in viscous vortex flows. The radial component must be zero due to the continuity equation (3.9) and initial conditions (3.13)

$$(u_r(r))_{t=0} = 0.$$

The Rankine flow described in chapter (1) can be used as an initial condition.

3.5.2. boundary conditions

The cavity contains non condensible gas of partial pressure P_g which follows a polytropic law $p_g = p_{g_o}\left(\frac{a_o}{a}\right)^{2k}$ and liquid vapor of partial pressure p_v, which balance the external stresses on the bubble surface and the pressures due to the surface tension σ through the equation:

$$P(a) = p_v + p_{g_o}\left(\frac{a_o}{a}\right)^{2k} - \frac{\sigma}{a} + 2\mu\frac{\partial u_r(a)}{\partial r},$$

with

$$2\mu\frac{\partial u_r(a)}{\partial r} = -2\rho\nu\frac{a\,\dot{a}}{r^2},$$

and the pressure at the infinity remains constant and equal to the ambient pressure

$$p_\infty = const.$$

3.5.3. Non-dimensionalization

The problem will be non-dimensionalized in order to keep the parameters of the same order.

The scale chosen for the length is the initial bubble radius, a_o.

Density is normalized by ρ and the pressure is non dimensionalized by the ambient pressure p_∞

The different scales for velocity, time and acceleration are given by:

$$\text{velocity: } U \sim \left(\frac{p_\infty}{\rho}\right)^{\frac{1}{2}},$$

$$\text{time: } T_r \sim a_o \left(\frac{\rho}{p_\infty}\right)^{\frac{1}{2}},$$

where T_r is the Rayleigh time for a bubble in a fluid in the absence of gravity.

$$\text{acceleration: } \tilde{A} \sim \frac{p_\infty}{\rho a_o}.$$

The normalized equations are written, where the bars denote nondimensional variables.

$$\overline{u_r} = \frac{\overline{a}(t)\,\dot{\overline{a}}(t)}{\overline{r}}. \tag{3.14}$$

$$\frac{1}{\overline{r}}\dot{\overline{a}}^2 + \frac{\overline{a}}{\overline{r}}\ddot{\overline{a}} - \frac{\overline{a}^2}{\overline{r}^3}(\dot{\overline{a}})^2 - \frac{\overline{u_\theta}^2}{\overline{r}} = -\frac{\partial \overline{p}}{\partial \overline{r}}, \tag{3.15}$$

$$\frac{\partial \overline{u_\theta}}{\partial \overline{t}} + \frac{\overline{a}}{\overline{r}}\dot{\overline{a}}\frac{\partial \overline{u_\theta}}{\partial \overline{r}} + \frac{\overline{a}}{\overline{r}}\dot{\overline{a}}\frac{\overline{u_\theta}}{\overline{r}} = \frac{1}{Re}\frac{\partial}{d\overline{r}}\left[\frac{1}{\overline{r}}\frac{\partial}{d\overline{r}}(\overline{r}\overline{u_\theta})\right], \tag{3.16}$$

where Re the Reynolds number is defined as:

$$Re = \frac{a_o}{\nu}\sqrt{\frac{p_\infty}{\rho}}$$

The nondimensionalized boundary condition on the bubble surface is:

$$\overline{P(a)} = \overline{p_v} + \overline{p_{g_o}}\left(\frac{1}{\overline{a}}\right)^{2k} - \frac{1}{We\overline{a}} - \frac{2\dot{\overline{a}}}{Re\overline{a}} \tag{3.17}$$

where

$$\overline{p_v} = \frac{p_v}{p_\infty}$$

$$\overline{p_{g_o}} = \frac{p_{g_o}}{p_\infty}$$

and We is the Weber number:

$$We = \frac{a_o p_\infty}{\sigma}$$

3.5.4. Discussion on the integration boundaries. Change of variables.

The problem will be solved once the equations have been integrated. The choice of the region over which we integrate the equations is relevant in this case because one of the boundaries - the bubble surface - is in motion.

The initial integration region is

$$[a(t); +\infty].$$

If we make the change of variable

$$s = \frac{r}{a(t)},$$

the integration region becomes for all times

$$[1; +\infty].$$

We may also encounter problems on the left boundary: $+\infty$.

The terms in $\frac{1}{r}$ of equations (3.15) and (3.16) once integrated out to infinity will diverge like $\ln(r)$.

To avoid this problem we limit the integration region to a maximum distance, the domain then becomes:

$$[1; s_{max}],$$

with

$$s_{max} = \frac{r_{max}}{a(t)}.$$

In our case we will assume that far distances larger than s_{max} from the bubble the flow is once again potential. This means that the region we are now studying is separated into two domains: the viscous region on one side, a potential extending to infinity on the border of which the pressure is:

$$P(r_{max}) = p_\infty - 2\rho\left(\frac{\Gamma}{2\pi r_{max}}\right)^2,$$

or

$$\overline{P}(s_{max}) = 1 - \left(\frac{\overline{\Gamma}}{2\pi s_{max}\overline{a}(t)}\right)^2,$$

where the circulation Γ is expressed non dimensionally

$$\overline{\Gamma} = \Gamma\frac{1}{a_o}\sqrt{\frac{\rho}{p_\infty}},$$

Use of the variable s has implications on the time and space derivatives. For a point P in the transformed domain $[1; s_{max}]$ time variations of all the quantities are in fact made in the real domain while following a particle moving at the speed $\dot{a}(t)$ Therefore time changes of quantities (such as u_θ) can be written:

$$\frac{D\overline{u_\theta}}{D\overline{t}} = \frac{\partial\overline{u_\theta}}{\partial s}\frac{\partial s}{\partial\overline{t}} + \frac{\partial\overline{u_\theta}}{\partial\overline{t}} = -\frac{s}{\overline{a}}\dot{\overline{a}}\frac{\partial\overline{u_\theta}}{\partial s} + \frac{\partial\overline{u_\theta}}{\partial\overline{t}},$$

In addition expressions of derivatives relative to s can be obtained as follows:

$$\frac{\partial s}{\partial\overline{t}} = \frac{\partial s}{\partial\overline{a}}\dot{\overline{a}} = -\frac{s}{\overline{a}}\dot{\overline{a}},$$

$$\frac{\partial\overline{u_\theta}}{\partial\overline{r}} = \frac{1}{a}\frac{\partial\overline{u_\theta}}{\partial s}, \frac{\partial^2\overline{u_\theta}}{\partial\overline{r}^2} = \frac{1}{a^2}\frac{\partial\overline{u_\theta}^2}{\partial s^2},$$

$$\frac{\partial}{d\overline{r}}\left(\frac{1}{\overline{r}}\frac{\partial}{d\overline{r}}(\overline{r}\overline{u_\theta})\right) = \frac{1}{a^2}\frac{\partial}{ds}\left(\frac{1}{s}\frac{\partial}{ds}(s\overline{u_\theta})\right) = \frac{1}{a^2}\left(\frac{\partial^2\overline{u_\theta}}{\partial s^2} + \frac{1}{s}\frac{\partial\overline{u_\theta}}{\partial s} - \frac{\overline{u_\theta}}{s^2}\right),$$

Equations (3.14), (3.15), and (3.16) become

$$\overline{u_r} = \frac{\dot{\overline{a}}(t)}{s}, \tag{3.18}$$

$$\frac{1}{s\overline{a}}\,\dot{\overline{a}}^2+\frac{1}{s}\,\ddot{\overline{a}}-\frac{1}{s^3\overline{a}}(\dot{\overline{a}})^2-\frac{\overline{u_\theta}^2}{s\overline{a}}=-\frac{1}{\overline{a}}\frac{\partial \overline{p}}{\partial s}. \tag{3.19}$$

$$\frac{D\overline{u_\theta}}{D\overline{t}}+\frac{s}{\overline{a}}\,\dot{\overline{a}}\,\frac{\partial \overline{u_\theta}}{\partial s}+\frac{1}{s\overline{a}}\,\dot{\overline{a}}\,\frac{\partial \overline{u_\theta}}{\partial s}+\frac{1}{s^2\overline{a}}\,\dot{\overline{a}}\,u_\theta=\frac{1}{Re}\frac{1}{\overline{a}^2}\left(\frac{\partial^2\overline{u_\theta}}{\partial s^2}+\frac{1}{s}\frac{\partial \overline{u_\theta}}{\partial s}-\frac{\overline{u_\theta}}{s^2}\right), \tag{3.20}$$

By isolating $\frac{D\overline{u_\theta}}{D\overline{t}}$ in equation (3.20) it becomes:

$$\frac{D\overline{u_\theta}}{D\overline{t}}=-\frac{s}{\overline{a}}\,\dot{\overline{a}}\,\frac{\partial \overline{u_\theta}}{\partial s}-\frac{1}{s\overline{a}}\,\dot{\overline{a}}\,\frac{\partial \overline{u_\theta}}{\partial s}-\frac{1}{s^2\overline{a}}\,\dot{\overline{a}}\,u_\theta+\frac{1}{Re}\frac{1}{\overline{a}^2}\left(\frac{\partial^2\overline{u_\theta}}{\partial s^2}+\frac{1}{s}\frac{\partial \overline{u_\theta}}{\partial s}-\frac{\overline{u_\theta}}{s^2}\right) \tag{3.21}$$

Equation (3.21) shows us that if we know $\overline{a}$, $\dot{\overline{a}}$ we have a partial differential equation for u_θ that we can solve numerically as a function of s.

Equation (3.19) can then be solved to provide the bubble dynamics and the pressure field along the axis.

Elongated bubble dynamics.

Equation (3.19) can be expressed as a differential equation of the form

$$\ddot{\overline{a}}=Rk(a,\dot{\overline{a}},t),$$

where Rk is a function.

By integrating this equation along $[1;s_{max}]$ one can obtain the bubble radius evolution in time.

We integrate (3.19) from the bubble's surface to s_{max}:

$$\left(\frac{1}{\overline{a}}\,\dot{\overline{a}}^2+\ddot{\overline{a}}\right)[\ln(s)]_1^{s_{max}}-\frac{1}{\overline{a}}(\dot{\overline{a}})^2\left[-\frac{1}{2s^2}\right]_1^{s_{max}}-\frac{1}{\overline{a}}\int_1^{s_{max}}\frac{\overline{u_\theta}^2}{s}ds$$

$$=-\frac{1}{\overline{a}}\int_1^{s_{max}}\frac{\partial \overline{p}}{\partial s}ds,$$

and by isolating $\ddot{\overline{a}}$ the equation becomes:

$$\ddot{\overline{a}}=-\frac{1}{\overline{a}}\,\dot{\overline{a}}^2+\frac{1}{\overline{a}\ln(s_{max})}(\dot{\overline{a}})^2\left[-\frac{1}{2s^2}\right]_1^{s_{max}}+\frac{1}{\overline{a}\ln(s_{max})}\int_1^{s_{max}}\frac{\overline{u_\theta}^2}{s}ds$$

$$-\frac{1}{\overline{a}\ln(s_{max})}\int_1^{s_{max}}\frac{\partial \overline{p}}{\partial s}ds.$$

But we also have

$$\int_1^{s_{max}} \frac{\partial \overline{p}}{\partial s} ds = \overline{p}(s_{max}) - \overline{p}(1),$$

because the pressure at that boundary is that of a potential vortex flow:

$$\overline{p}(s_{max}) = \frac{p_{s_{max}}}{p_\infty} = 1 - \left[\frac{\Gamma}{2\pi \overline{a} s_{max}}\right]^2,$$

and (3.17) gives us information on the pressure at the bubble surface

$$\overline{p}(s_{max}) - \overline{P(1)} = \overline{p}(s_{max}) - \overline{p_v} + \overline{p_{og}} \left(\frac{1}{\overline{a}}\right)^{2k} - \frac{1}{We\overline{a}} - \frac{2\dot{\overline{a}}}{Re\overline{a}},$$

so the equation is finally written:

$$\ddot{\overline{a}} = -\frac{1}{\overline{a}} \dot{\overline{a}}^2 + \frac{1}{\overline{a}\ln(s_{max})}(\dot{\overline{a}})^2 \left[-\frac{1}{2s_{max}^2} + \frac{1}{2}\right] + \frac{1}{\overline{a}\ln(s_{max})} Q$$

$$- \frac{1}{\overline{a}\ln(s_{max})} \left[1 - \left(\frac{\Gamma}{2\pi \overline{a} s_{max}}\right)^2 - \overline{p_v} + \overline{p_{og}} \left(\frac{1}{\overline{a}}\right)^{2k} - \frac{1}{We\overline{a}} - \frac{2\dot{\overline{a}}}{Re\overline{a}}\right], \qquad (3.22)$$

with

$$Q = \int_1^{s_{max}} \frac{\overline{u_\theta}^2}{s} ds. \qquad (3.23)$$

Equation (3.22) can easily be solved numerically as described below.

Second set of information: Pressure field along the s-axis.

By integrating (3.17) over $[s_{max}; s]$ we will obtain the pressure at any point of the s-axis:

The integration gives us:

$$\frac{1}{\overline{a}} \dot{\overline{a}}^2 [\ln(s)]_{s_{max}}^{s} + \ddot{\overline{a}} [\ln(s)]_{s_{max}}^{s} - \frac{1}{\overline{a}}(\dot{\overline{a}})^2 \left[-\frac{1}{2s^2}\right]_{s_{max}}^{s} - \frac{1}{\overline{a}} \int_{s_{max}}^{s} \frac{\overline{u_\theta}^2}{s} ds$$

$$= -\frac{1}{\overline{a}} \int_{s_{max}}^{s} \frac{\partial \overline{p}}{\partial s} ds,$$

but we also have

$$\int_{s_{max}}^{s} \frac{\partial \overline{p}}{\partial s} ds = \overline{p}(s) - \overline{p}(s_{max}) = \overline{p}(s) - \left[1 - \left(\frac{\Gamma}{2\pi \overline{a} s_{max}}\right)^2\right],$$

so the expression becomes

$$\left(\frac{1}{\overline{a}}\dot{\overline{a}}^2 + \ddot{\overline{a}}\right)[\ln(s)]_{s_{max}}^{s} - \frac{1}{\overline{a}}(\dot{\overline{a}})^2\left[-\frac{1}{2s^2}\right]_{s_{max}}^{s} - \frac{1}{\overline{a}}\int_{s_{max}}^{s} \frac{\overline{u_\theta}^2}{s} ds$$

$$= -\frac{1}{\overline{a}}\left(\overline{p}(s) - \left[1 - \left(\frac{\Gamma}{2\pi \overline{a} s_{max}}\right)^2\right]\right),$$

and the pressure field along the s-axis is finally described by

$$\begin{aligned}\overline{p}(s) = 1 - &- \left(\tfrac{\Gamma}{2\pi \overline{a} s_{max}}\right)^2 - \dot{\overline{a}}^2 [\ln(s)]_{s_{max}}^{s} - \ddot{\overline{a}}\,\overline{a}\,[\ln(s)]_{s_{max}}^{s} \\ &+ (\dot{\overline{a}})^2\left[-\tfrac{1}{2s^2}\right]_{s_{max}}^{s} + \int_{s_{max}}^{s} \tfrac{\overline{u_\theta}^2}{s} ds.\end{aligned} \tag{3.24}$$

So the final set of equations we possess to solve our problem is:

$$\frac{D\overline{u_\theta}}{Dt} = -\frac{s}{\overline{a}}\dot{\overline{a}}\frac{\partial \overline{u_\theta}}{\partial s} - \frac{1}{s\overline{a}}\dot{\overline{a}}\frac{\partial \overline{u_\theta}}{\partial s} - \frac{1}{s^2\overline{a}}\dot{\overline{a}}\,\overline{u_\theta} + \frac{1}{Re}\frac{1}{\overline{a}^2}\left(\frac{\partial^2 \overline{u_\theta}}{\partial s^2} + \frac{1}{s}\frac{\partial \overline{u_\theta}}{\partial s} - \frac{\overline{u_\theta}}{s^2}\right), \tag{3.25}$$

$$\ddot{\overline{a}} = -\frac{1}{\overline{a}}\dot{\overline{a}}^2 + \frac{1}{\overline{a}\ln(s_{max})}(\dot{\overline{a}})^2\left[-\frac{1}{2s_{max}^2} + \frac{1}{2}\right] + \frac{1}{\overline{a}\ln(s_{max})}Q$$

$$-\frac{1}{\overline{a}\ln(s_{max})}\left[1 - - \left(\frac{\Gamma}{2\pi \overline{a} s_{max}}\right)^2 - \overline{p_v} + \overline{p_{vg}}\left(\frac{1}{\overline{a}}\right)^{2k} - \frac{\sigma}{a_\infty p_\infty \overline{a}}\right], \tag{3.26}$$

$$\begin{aligned}\overline{p}(s) = 1 - &\left(\tfrac{\Gamma}{2\pi \overline{a} s_{max}}\right)^2 - \dot{\overline{a}}^2 [\ln(s)]_{s_{max}}^{s} - \ddot{\overline{a}}\,\overline{a}\,[\ln(s)]_{s_{max}}^{s} \\ &+ (\dot{\overline{a}})^2\left[-\tfrac{1}{2s^2}\right]_{s_{max}}^{s} + \int_{s_{max}}^{s} \tfrac{\overline{u_\theta}^2}{s} ds.\end{aligned} \tag{3.27}$$

Each of these equations are adapted to numerical solutions.

3.6. Method of solution

3.6.1. Discretization

The gridding of the s-axis is a basic linear discretization using a constant grid-step, ds.

$$s_i = 1 + ids \; ; \; i = 1, n$$

The parameters are discretized in time or space and both if required . The time and space stepping is given by:

$$(\lambda)_i^{j+1} = (\lambda)_i^j + dt\frac{\partial \lambda}{\partial t}$$

$$(\lambda)_{i+1}^j = (\lambda)_i^j + ds\frac{\partial \lambda}{\partial s}$$

with

$$\lambda = \overline{u_\theta} \text{ or } \overline{p} \text{ and dt being the time step}$$

and

$$(\alpha)_{j+1} = (\alpha)_j + dt\frac{\partial \alpha}{\partial t}$$

with

$$\alpha = \overline{a} \text{ or } \dot{\overline{a}} \text{ or } \ddot{\overline{a}}$$

3.6.2. Numerical tools available

Equation (3.25) is a partial differential equation of one form of a combined advection-diffusion equation:

$$\frac{D\overline{u_\theta}}{Dt} = A\overline{u_\theta} + B\frac{\partial \overline{u_\theta}}{\partial s} + C\frac{\partial^2 \overline{u_\theta}}{\partial s^2}$$

The numerical method used to solve this type of equation is typically a Crank-Nicholson's method. It can be expressed by:

$$\left(\frac{D\overline{u_\theta}}{Dt}\right)_i^j = \frac{\overline{u_\theta}_i^j - \overline{u_\theta}_i^{j-1}}{dt} = \frac{1}{2}\left(F\left(\overline{u_\theta}_i^j\right) + F\left(\overline{u_\theta}_i^{j-1}\right)\right). \qquad (3.28)$$

In our case at time step j, F is the function:

$$(F(X))_j = \left(-\frac{1}{\overline{s}^2\overline{a_j}}\dot{\overline{a}_j}\right)X + \left(-\frac{\overline{s}}{\overline{a_j}}\dot{\overline{a}_j} - \frac{1}{\overline{s}\overline{a_j}}\dot{\overline{a}_j} + \frac{1}{Re\overline{s}}\frac{1}{\overline{a_j}^2}\right)\frac{\partial X}{\partial s} + \frac{1}{Re}\frac{1}{\overline{a_j}^2}\frac{\partial^2 X}{\partial s^2}.$$

Both left and right hand sides of equation (3.28) are centered at time step $(j-\frac{1}{2})$ so the method is second order accurate in time.

The character of this scheme is semi-implicit. The right hand side of equation (3.28) has terms of time step j and of time step $j-1$.

To calculate the spatial derivatives we use centered differences which can be written:.

$$\left(\frac{\partial \overline{u_\theta}}{\partial s}\right)_i^j = \frac{\overline{u_\theta}_{i+1}^j - \overline{u_\theta}_{i-1}^j}{2ds},$$

$$\left(\frac{\partial^2 \overline{u_\theta}}{\partial s^2}\right)_i^j = \frac{\overline{u_\theta}_{i+1}^j + \overline{u_\theta}_{i-1}^j - 2\overline{u_\theta}_i^j}{ds^2}$$

By replacing the discretized expression of the derivatives in the developed form of (3.28) we obtain a set of simultanous linear equations that fortunatly forms a tridiagonal system.

By grouping the terms according to their time step in (3.28) we get:

$$f(i)\overline{u_\theta}_{i-1}^j + g(i)\overline{u_\theta}_i^j + h(i)\overline{u_\theta}_{i+1}^j = f_1(i)\overline{u_\theta}_{i-1}^{j-1} + g_1(i)\overline{u_\theta}_i^{j-1} + h_1(i)\overline{u_\theta}_{i+1}^{j-1},$$
$$i = 1, 2 \ldots n-1$$

(the values of the variables at time-step j are placed on the left and those of time-step $j-1$ on the right hand side of the equation)

In a matrix form this can be written

$$\begin{pmatrix} g(1) & h(1) & 0 & 0 & 0 \\ f(2) & g(2) & h(2) & 0 & 0 \\ 0 & . & . & . & 0 \\ 0 & 0 & . & . & .0 \\ 0 & 0 & 0 & f(n) & g(n) \end{pmatrix} \begin{pmatrix} u_{\theta_1}^j \\ . \\ . \\ . \\ u_{\theta n}^j \end{pmatrix} = \begin{pmatrix} g_1(1) & h_1(1) & 0 & 0 & 0 \\ f_1(2) & g_1(2) & h_1(2) & 0 & 0 \\ 0 & . & . & . & 0 \\ 0 & 0 & . & . & .0 \\ 0 & 0 & 0 & f_1 n) & g_1(n) \end{pmatrix} \begin{pmatrix} u_{\theta_1}^{j-1} \\ . \\ . \\ . \\ u_{\theta n}^{j-1} \end{pmatrix}$$

The only unknowns here are $(u_\theta)_{i=1,n}^j$. The right hand side only contains information from the previous time-step $(j-1)$ and the matrix on the left hand

side needs information on the bubble dynamics at time step (j). This will have a consequence in the logical order needed to solve our problem.

To solve this matrix equation we use an algorithm given for tridiagonal matrix equations.

Equation (3.26) as an ordinary differential equation.

$$\ddot{\overline{a}} = Rk\left(\overline{a}, \dot{\overline{a}}, t\right),$$

with

$$Rk\left(\overline{a}, \dot{\overline{a}}, t\right) = -\frac{1}{\overline{a}}\dot{\overline{a}}^2 + \frac{1}{\overline{a}\ln(s_{max})}(\dot{\overline{a}})^2\left[-\frac{1}{2s_{max}} + \frac{1}{2}\right] + \frac{1}{\overline{a}\ln(s_{max})}Q$$

$$-\frac{1}{\overline{a}\ln(s_{max})}\left[1 - \left(\frac{\overline{\Gamma}}{2\pi\overline{a}s_{max}}\right)^2 - \overline{p_v} + \overline{p_{og}}\left(\frac{1}{\overline{a}}\right)^{2k} - \frac{1}{We\overline{a}} - \frac{2\dot{\overline{a}}}{Re\overline{a}}\right],$$

can be reduced to the study of a set of first order differential equations

$$\dot{\overline{a}} = \overline{b},$$

$$\dot{\overline{b}} = Rk\left(\overline{a}, \dot{\overline{a}}, t\right).$$

hello

The numerical solution chosen to solve this set of equation is the most used **fourth order Runge-Kutta method.** At each time step the derivative is evaluated four times: the initial point, twice at trial mid-poinnts and at a trial end point. These derivatives then give us the final value of the function

The 4^{th} order Runge Kutta scheme is the following:

$$\begin{aligned} k_1 &= dtRk'(t, b_j), \\ k_2 &= dtRk'(t + \tfrac{dt}{2}, b_j + \tfrac{k_1}{2}), \\ k_3 &= dtRk'(t + \tfrac{dt}{2}, b_j + \tfrac{k_2}{2}), \\ k_4 &= dtRk'(t + dt, b_j + k_3), \end{aligned}$$

with k_1, k_2, k_3, k_4 corresponding to the four evaluations of the derivatives we obtain

$$b_{j+1} = b_{j+1} + \frac{k_1}{6} + \frac{k_2}{3} + \frac{k_3}{3} + \frac{k_4}{6}.$$

In our case we will also have to evaluate (3.23) at each time-step. A basic trapezoidal method was used:

$$Q^j = \left(\int_1^{s_{max}} \frac{\overline{u_\theta}^2}{s} ds \right)^j = \sum_{i=2}^{n} \left[\frac{\left(\overline{u_\theta}_i^j\right)^2}{\overline{s}_i} + \frac{\left(\overline{u_\theta}_{i+1}^j\right)^2}{\overline{s}_{i+1}} \right] \frac{ds}{2}$$

3.7. Algorithm of solution

By contrast with equation (3.25) in which the semi implicit method used implie that we need information on the bubble dynamics of the current time step to determine the unknown $\left(\overline{u_\theta}_i^j\right)$, equation (3.26) only needs the initial conditions of the bubble dynamics and the initial flow. Thus (3.26) will be delt with before (3.25).

At this point a flow chart is needed to show the algorithm :see figure(9)

3.8. Description of the code

The program solves the Navier Stokes Equations for an infinitely elongated bubble in a viscous vortex. The input allows the user to specify the following parameters:

$$\frac{A_c}{a_o},$$

$$\frac{\Gamma}{a_o \sqrt{\frac{p_{go}}{\rho}}},$$

and

$$\frac{p_{go}}{p_{axis}}.$$

The Reynolds number and the Weber number are automatically calculated in the program.

3.8.1. Convergence study

Numerical methods need a test on the convergence. This is to check stability and convergence due to accumulating errors. The scheme applied here is to reduce the time step and grid size simultanously, keeping a constant ratio between them. Figure (10) illustrates the scheme. Each curve is related to a different timestep and grid size. As the latter decrease the curves converge to a smooth curve.

Between dt=0.002 and 0.001 the difference in the curves was undetectable. For running the tries that are studied in capter 4 we chose 0.001 as a time step and 0.01 as a grid size.

3.8.2. Varying time steps and grid size in time.

The runs that we made showed that in some conditions a too sudden bubble collapse could stop the code from running due to large errors.In other cases when the bubble wall velocity is at very low the time step could then have been increased to speed up the execution. A variable time step scheme still has to be implemented on the code. It would shrink the time step in cases of high rates of growth and keep the ratio between the time step and the grid size constant.

3.8.3. Case of the axial flow.

The study has been neglecting the axial flow.We could observe the Navier-Stokes equations now with the axial flow:

$$u_{z\neq 0}, \frac{\partial u_r}{\partial z} \neq 0, \ \frac{\partial u\theta}{\partial z} \neq 0$$

$$\frac{Du_r}{Dt} + u_r\frac{\partial u_r}{\partial r} - \frac{u_\theta{}^2}{r} + u_z\frac{\partial u_r}{\partial z} = \frac{-1}{\rho}\frac{\partial p}{\partial r} + \nu\frac{\partial}{dr}\left[\frac{1}{r}\frac{\partial}{dr}(ru_r)\right] + \frac{\partial^2 u_r}{\partial z^2}$$

$$\frac{Du_\theta}{Dt} + u_r\frac{\partial u_\theta}{\partial r} + \frac{u_r u_\theta}{r} + u_z\frac{\partial u_\theta}{\partial z} = \nu\frac{\partial}{dr}\left[\frac{1}{r}\frac{\partial}{dr}(ru_\theta)\right] + \frac{\partial^2 u_\theta}{\partial z^2}$$

$$\frac{Du_z}{Dt} + u_r\frac{\partial u_z}{\partial r} + \frac{u_r u_\theta}{r} + u_z\frac{\partial u_z}{\partial z} = \frac{-1}{\rho}\frac{\partial p}{\partial z} + \nu\frac{1}{r}\frac{\partial}{dr}\left[r\frac{\partial}{dr}(u_z)\right] + \frac{\partial^2 u_z}{\partial z^2}$$

and the continuity equation

$$divU = 0 \Leftrightarrow \frac{1}{r}\frac{\partial}{\partial r}(r\rho u_r) + \frac{\partial}{\partial z}(\rho u_z) = 0$$

The assumptions on axisymetry remain valid but the problem has gained one dimension in its geometry.

4. Results analysis.

This chapter sums up the results obtained from the two methods develloped in the two previous chapters. The shortage of time has a considerable impact on the range of parameters we were able to study. This needs to be taken into account when reading any conclusions concerning the results.

4.1. 2D bubble in Burgers flow.

For each run, the value of the initial radius of the bubble was equal to 10^{-2} m, the value of the initial core radius was $5 \cdot 10^{-2}$, and the initial pressure inside the bubble was $5 \cdot 10^5$ Pa, while our reference pressure, P_∞, was 10^5 Pa.

The first set of trials that we conducted aimed at determining the infuence of C, the Burgers constant, on the flow, and as a result on the evolution of the bubble, while the vorticity diffusion is only due to the evolution of δ in time.

We may define by T the "top point" of the bubble, moving on the z-axis, for z positive if the bubble is centered on O. B is the "bottom point" of the bubble, moving on the z-axis as well, where z is negative if the bubble is centered. Let I be the "side point", moving on the r-axis during the evolution of the bubble. (see figure(11)).

4.1.1. Strong basic velocities.

Let us consider the case where C is positive (this is the most physical case). According to the formulation of the vortex core radius, the variation of δ in time should lead to two physical cases: either the bubble is within the viscous core ($a(t) < \delta(t)$), or the bubble radius is greater than the vortex core radius. If C is strong enough, we can observe the variation of δ in time. But in this case, we also notice that U_r and U_z cannot be neglected. Thus if C is of the order of magnitude of 1, a bubble in the vortex is submitted to these velocities, and is very quickly stretched to become an elongated cylinder along the z-axis. The ratio $\frac{OT}{OI}$ can even reach 10^3 before the bubble divides into two elongated bubbles, which then move along the z-direction.

The more C increases, the quicker the bubble is stretched and subdivides, and δ has no time to change (we cannot observe any vorticity diffusion), and so has no influence on the deformations of the bubble, because of the collapsing speed, which depends more on U_r and U_z than on U_θ.

So the resulting velocity and pressure field are mostly due to the basic flow, which is hardly modified by the "bubble potential". It means we cannot define any region of interaction dominated by the bubble dynamics. A large number of trials showed this was still true while $C > 10^{-2}$.

4.1.2. Strong interaction of the bubble with a low velocity field.

This case deals with trials performed with a small Burgers constant. The previous subsection leads to run the code with lower Burgers velocities, when C is less than 10^{-3}.

If the initial pressure inside the bubble is greater than the pressure in the liquid near its boundary, the bubble has time to grow, and we then can define a zone where it has a real influence on the basic flow, in terms of pressure and of velocities.

Bubble on the axis. When the bubble is centered on the axis and in the initial conditions shown figure(12), it first grows up to twice its initial volume, and then collapses (see figures 13). During the second growth, we can observe an elongation, but only such as the ratio OT/OI reaches 2.

We must notice the presence of a stagnation point, where the "bubble velocity" cancels the basic velocity. It means there is a stagnation ring around the bubble. G, the stagnation point in the plane $\theta = 0$, is moving

- on the r-axis when the bubble grows (figure (14)),
- on the bubble surface when the distance of the side point from the origin is decreasing while the distance of the top point from the origin increases (figure (15)),
- and on the z-axis during the collapse (figure (16)).

The analysis of the resulting pressure distribution leads to considerations about the location of the highest pressure points: during the first period of the bubble, we notice, around the bubble, the presence of a high pressure ring, whose intersection with the plane $\theta = 0$ is the point H (see figure (17)). The distance between H and the surface of the bubble varies in the same way as the distance between the bubble surface and the stagnation point. This evolution first shows a short unsteady period right after the begining of the growth, after which H oscillates

around a medium position in an almost steady pressure distribution, until the pressure in the bubble reaches its peak. It occurs at time 4 on the drawing , and the highest pressure point in the liquid is then at the bubble surface.

The explanation comes from the continuity at the bubble surface, where the pressure in the bubble, and the surface tension balance the pressure in the liquid. This implies that the pressure in the liquid near the bubble must follow the pressure inside the bubble. The growth of the bubble, due to a low pressure zone near the boundary implies that the highest pressure point is near the bubble at the begining, and then moves, because the pressure in the bubble decreases. At the end of the collapse, the pressure increases in all the liquid, because of the peak in the bubble.

Thus point H characterizes the bound between the "bubble" or the basic flow predominance: beyond H, the resulting flow may be considered as following a displaced Burgers distribution still depending on the interaction; within H, the bubble flow is predominant.

Bubble moving on the z-axis. Figure(18) illustrates the evolution of the caracteristic points in this case. With the same initial conditions as the previous case, except for the location of the bubble, which is now initially off-centered on the z-axis at $Z_o > 0$. During the growth of the bubble, the z coordinate of the stagnation point follows the center of the bubble (figure(19)), moving on the z-axis. As the high pressure point is far from the bubble, it does not present any particular evolution due to the non symmetrical evolution of the bubble. Figure (20, 21, 22) describe the velocity field evolution in time. (t=4,5,6,7).

4.1.3. Intermediate interaction and stretching.

The case of $C = 10^{-3}$ is an intermediate case where the bubble is quickly stretched along the z-direction (figure (23)), while the side point oscillates as in the previous case. The bubble has time to grow and to collapse during its elongation. As the distance of the top and the bottom points from the origin always increase in time, the stagnation point remains on the r-axis, moving between the bubble surface and its maximum value (figure (24) to (27)).

The highest pressure point remains close to the elongated bubble; it means that the Burgers pressure distribution, as the velocity field, is modified only near the axis at the bubble surface, where it is influenced by the bubble dynamics.

4.2. A more realistic vortex.

As the 2D-axisymmetric code runs with any basic flow, it becomes more interesting to deal with a physically more realistic model of the vortex. That is what we did, considering the results obtained with a Navier Stokes solver (FIDAP) using as boundary conditions a Rankine Vortex and a uniform axial velocity at $x = 0$, and allowing the vortex to decay with distance x increasing, sent to Dynaflow by the "LABORATOIRE D'HYDRODYNAMIQUE DE L'ECOLE NAVALE". Figures (28) to (33) describe the results in absence of a bubble. This flow is used as a basic flow. We modified the axisymmetric code so it could read in the Fidap output file each time the axisymmetric code needed the basic flow. Since Fidap uses a predefined fixed grid, as the bubble is in motion, the basic flow at each node was calculated by linear interpolation.

In this case, the results show that the bubble has more complicated deformations than in a classical Rankine or Burgers case. These deformations are characteristic of a bubble moving with a lower speed than the fluid. The consequence is a reentrant jet moving downstream in the direction of the z-axis when the bubble collapses. Figures (34) and (35) show the evolution of the three characteristic points of the bubble, and its deformation in time.

4.3. 1D viscous solver.

Our interest lies in the interaction between the bubble and the flow. Therefore we will analyze data related to the bubble motion:

-bubble radius and velocity,
-bubble collapse period and amplitude,
and related to the flow:
-flow field,
-magnitude of the maximum tangential velocity and of the velocity.
-motion of the core radius.

4.3.1. Physical parameters.

The physical parameters modified for each run of the code are

$$\frac{A_c}{a_o}, \frac{\Gamma}{a_o\sqrt{\frac{2p_\infty}{\rho}}}, \frac{p_{g_o}}{p_{static}}.$$

The ratio of the initial core radius and the initial bubble radius relates information on the influence of the size of the viscous core on the bubble.

The circulation ratio gives us the effect of the swirl's strength on the bubble dynamics.

The ratio between initial gas pressure in the bubble and the initial pressure on the axis determines its reaction to the ambient medium.

4.3.2. Evidence of the interaction.

To show some evidence of the interaction between the bubble and the viscous vortex we considered two cases: one where we forced the flow not to interact and another where the flow was interacting. Figure (36) illustrates the differences in the bubble dynamics anf figure (37) shows how the flow is modified by the bubble.

Analysis of the interactiv bubble. In figures (36) and (37) the initial pressure inside the bubble is lower than the outside pressure, therefore the bubble starts by collapsing. As the bubble wall moves inward the viscous core shrinks, simultanously enhancing the tangential velocity to a maximum when the bubble rebounds. As the bubble grows again the core expands and the tangential velocity decelerates to a minimum before the bubble collapses a second time. When the fluid particles are pulled towards in towards the vortex axis they accelerate tangentially. This is similar to the phenomenon of vortex stretching . As the core is compressed the stream of vortex lines is also compresed so the vorticities are stretched and the swirl around the bubble becomes stronger.

The fact that the core moves is a relation between the diffusion through viscosity and the bubble motion. It has been observed that in physics transfers of matter, energy and momentum always tend to bring the material towards an equilibrium. In our case the bubble is growing inside the fluid; the velocity being non-uniform along the r-axis, tangential components of the local stress appear in the fluid. The layers of fluid around the bubble have different tangential velocities

$$\frac{\partial u_\theta}{\partial r} \neq 0.$$

This derivative is related to the shear through the expression:

$$\sigma_1 = \nu \frac{\partial u_\theta}{\partial r}$$

where σ_1 is the stress tensor.

The growth of the bubble adds a radial velocity to the layers of fluid, so they move back, which explains why the core is expanding. But as the distance between one fluid particle and the axis of the swirl increases its tangential velocity drops. This is due to conservation of the total momentum in the fluid.

On a larger time scale viscosity also has an effect on the field. This effect is illustrated by a constant decrease of the peaks of $u_{\theta_{max}}$ in time and can be related to the diffusion effect quoted in chapter 1.

Thus a viscous interaction is taking place between the bubble and the flow. Now we need to determine a criteria on the different physical parameters that tells us in which conditions the viscous interaction is most likely to be relevant.

4.3.3. Parameter analysis

This set of results allows us to find out which parameters we should vary to bring out the key elements on the viscous interaction between the bubble and the flow.

a. Circulation

By changing the circulation of the vortex, we simultanously change the initial tangential velocity in the fluid and the pressure on the axis. In this case when analysing the results we would need to find out which of the parameters Γ or $\frac{p_\infty}{\rho_{vap}}$ are acting most in the behaviour of the interacting bubble.

Figure (38) illustrates the drop of the initial pressure on the axis due to an increasing circulation. The bubble experiences growth in one case ($\Gamma = 0.6$) and collapses in the other ($\Gamma = 0.1$).

Figure (39) shows the interaction of the bubbles with the vortex is shown as we plotted the size of the viscous core and the bubble radius on the same graphic. We can observe (see figur (39)) that the viscous core practically vanishes at bubble collapse.

Figure (40) shows that the absolute pressure at collapse (curve 1) reaches 7 atmospheres.

The tangential velocity is modified at each collapse as we explained in 4.3.2. When the bubble grows from its initial value the effect on the magnitude of u_θ is less apparent (see figure(41)).

b. Changing $\frac{A_c}{a_0}$ by modifying A_c.

The modification of the core radius influences the initial pressure on the axis. The two cases in Figure(42) and Figure(43) show a bubble collapsing and a bubble growing from their initial positions and the motion of the viscous core with the bubble. A growing bubble generates a pressure drop around it (see figure(44)).

This pressure drop seems to increase the size of the core and decreases the magnitude of the tangential velocity. A collapsing bubble sees a pressure increase around it, which compresses the viscous core and increases the bubble velocity.

It is still too early to make conclusions on the interaction laws of a bubble and a viscous vortex. These first results have shown that the physical parameters we can modify to find an interaction criteria are:

$$\frac{p_{g_o}}{p_{axis}}$$

and

$$\frac{A_c}{a_o}$$

(by changing a_o only).

The caracteristics that seem most relevant to our study are: the bubble radius vs. time and the ratio of the core size over the bubble radius vs. time.

These two caracteristics give us information on bubble behaviour and simultanously of the effect it has on the viscous flow.

c. Varying parameter: $\frac{p_{g_o}}{p_{axis}}$

The case of a very strong collapse for $\frac{p_{g_o}}{p_{axis}} = \frac{5}{7}10^{-1}$ on figure(45) has a relevant influence on the size of the viscous core (figure(46)). At the rebound (t=2.1) the core size increases as much as 8.5 times the initial buble radius and stops growing as the bubble motion decelerates. For less sudden collapses $\left(\frac{p_{g_o}}{p_{axis}} = 0.4\right)$ the core interacts with the bubble in the same way as in previously shown collapses. In the case of an initial gas pressure inside the bubble close to that on the axis , the small variations of bubble radius in time (figure(47))have hardly any influence on the core. Let p_{g_o} be three times that of the pressure on the axis. The bubble then grows and collapses at a given period (figure(48)), the core behaves like the bubble: it grows and decreases with time.

A first conclusion would be that the influence of the bubble on the viscous core is diminished as $\frac{p_{g_o}}{p_{axis}}$ nears 1.

d. Varying parameter: $\frac{A_c}{a_o}$ where a_o is being modified.

Looking at the ratio of the core radius and the bubble radius can teach us how the interaction between the bubble and the core is modified when one size is small compared to the other.

In this study, we do not investigate initial bubble sizes larger than core sizes.

Figures (49) and (50) show the evolution of the interaction when the ratio $\frac{A_c}{a_o}$ is halfed. The period of rebounds of the bubble is decreasing; It seems that the

closer the high tagential velocities are to the bubble($u_{\theta_{max}}$ corresponds to the core boundary) the collapse nd the rebound of the bubble occur.

The amplitude of the core size variations increases with the ratio $\frac{A_s}{a_o}$. In figures (51) and (52), as the ratio $\frac{A_s}{a_o}$ decreases the period of rebounds still decreases, but by measuring the amplitude of the bubble motion, we observe that between $a_o = 1mm$ and $a_o = 7mm$, the trend in the amplitude variations has changed. Figure (53) shows this non linear phenomena.We see that the bubble radius minima vs. time is increasing and then decreasing.

The only conclusion we can make at this point of the experiments is that the interaction between the bubble and the viscous vortex flow around it seems to be non-linear.

5. Synthesis

In the two previous chapters we studied the interaction between a bubble and a viscous vortex flow from two points of view: one makes the assumption that a basic flow around the bubble is modified linearly by a flow created by the bubble through the equation:

$$U = U_o + U_{basic},$$

and the second uses a viscous solver.

5.1. Matching the solutions.

In order to match these two solutions: a viscous solver should be coupled to the code 2DynaFs.We would need to extend the viscous solver to the case where the axial flow is taken fully into account. Then the bubble studied would both be axisymmetric and finite.

2DynaFs showed that the bubble on the vortex axis elongated before splitting up. The infinitely elongated bubble viscous solver enables us to illustrate the viscous interaction with the vortex in a region far from the ends of that same bubble. The stretching of vorticity and the motion of the core radius related to the bubble dynamics only occurs in particular domains of the physical parameters. Outside these areas we can always implement 2DynaFs without the viscous solver. In the regions where viscous interaction is strong, we would need a 2D (Axisymmetric) viscous solver. So the cases where the bubble generates a potential flow in absence of shear flow could then be complemented by adding the effects of viscosity.

CONCLUSION

Significant results have been obtained in this parallel study of bubble and flow interaction. On one side the influence of C (Burger's vortex), and mostly of u_z on the bubble motion, interesting results concerning FIDAP's vortex flow and its interaction with the bubble were obtained. On the other side the effects of viscous interaction on bubble behaviour and vortex flow behaviour were highlighted for the first time.

The general problem of bubble and flow interaction, especially the viscous interaction point of view which still needs to be develloped in 2D or even 3D, remains a domain not yet fully understood. Step by step and from various directions we get closer to the resolution of the problem. In our case we decided to take one approach from the point of view of the flow by studying bubble motion with new vortex models containing axial flows and which were more realistic physically. The other approach tried to take bearings from the point of view of the bubble and of the flow simultanously in a simple 1D model of fully viscous interactions.

Further studies, experimental as well as numerical, should enable the understanding of bubble and flow interaction in a near future.

Bibliography

1. J.S. Darrozes, G.L. Chahine, "Les recherches sur le phenomene de cavitation effectuees a l'Ecole Nationale Superieur Des Techniques Avancees.' Extrait de Sciences et Techniques de l'armement, Memorial de l'Artillerie francaise, Paris, imprimerie nationale, 1983.

2. Frederick G. Hammit, "Cavitation and Multiphase Flow Phenomena", McGraw-Hill Inc. , 1980.

3. G.K Batchelor, "An Introduction to FLUID DYNAMICS", Cambridge University Press, 1967.

4. J.S Darrozes, "Mecanique des fluides incompressibles, tomel", Ecole Nationale Superieur de Techniques Avancees, 1975.

5. P. Ligneul, "Theoretical tip vortex cavitation inception threshold", European Journal of Mechanics, B/FLUIDS, Vol 8, Number 6, 1989.

6. Ramani Duraiswami and G.L. Chahine," Analytical study of a gas bubble in the flow field of a line vortex", Dynaflow Inc.

7. P. Ligneul, "Study Of Nuclei Distribution And Vortex Diffusion Influence On Nuclei Capture By A Tip Vortex And Nuclei Capture Noise", ASME 1986.

8. A. Bovis, "Some results on cavitation induced by trailing vortex flows", Euromech, Sept. 1981.

9. G.L Chahine, P.F Genoux, Han Lieh Liu, Virgil E. Johnson," Analytical and experimental study of self resonating water jets: Nozzle Jet and Wall Jet interactions.

10. S.H Crandall, "Engineering Analysis", McGraw-Hill,1956.

11. A. Bovis, "Etude asymptotique du phenomene de cavitation: cavites non spheriques", These,1980.

12. G.L Chahine,"Etude locale du phenomene de cavitation, analyse des facteurs regissant la dynamique des interfaces",Rapport de recherche 116, Ecole Nationale Superieur des Techniques Avancees, Avril 1976.

13. W.F. Ames,"Numerical methods for partial differential equations", Academic Press,1977.

14. P.J. Roache,"Computational Fluid Dynamics", Hermosa Publishers,1976.

Figure 1

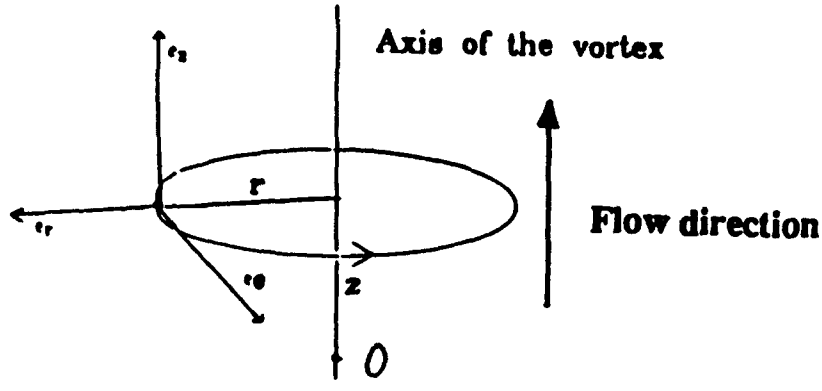

CYLINDRICAL COORDINATES

Figure 2

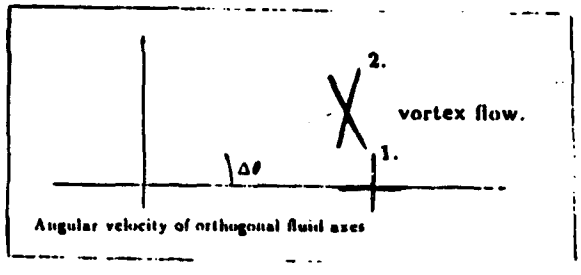

illustration of vorticity

BURGERS VORTEX WITHOUT BUBBLE

Figure 3

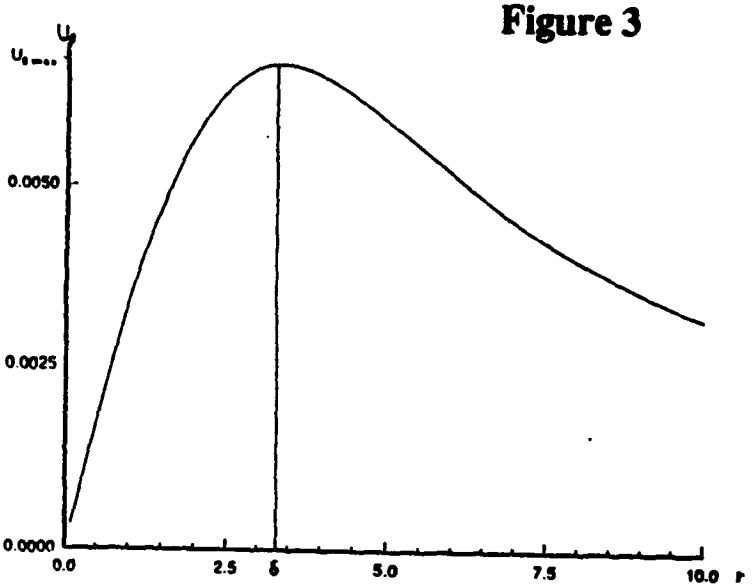

U_θ VERSUS r

Figure 4

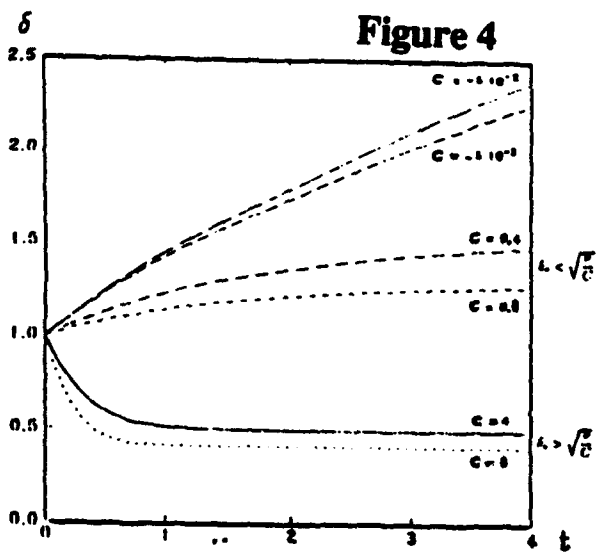

$\delta(t)$ versus C

Figure 5

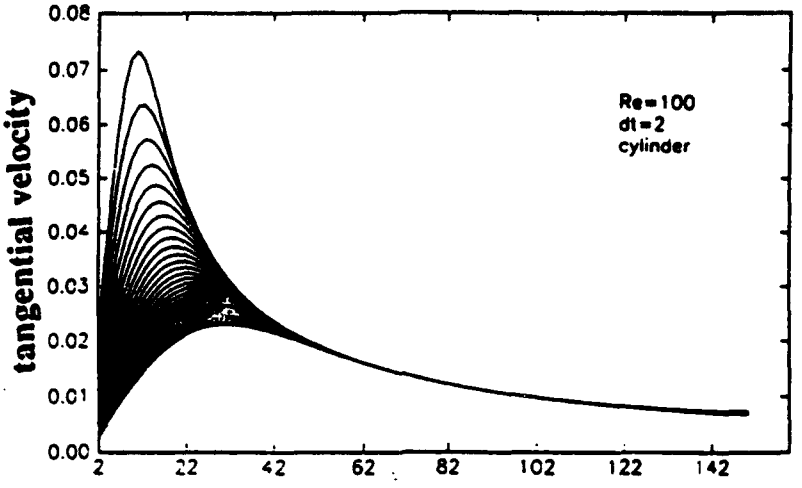

tangential velocity vs r

BURGERS PRESSURE DISTRIBUTION

Figure 6

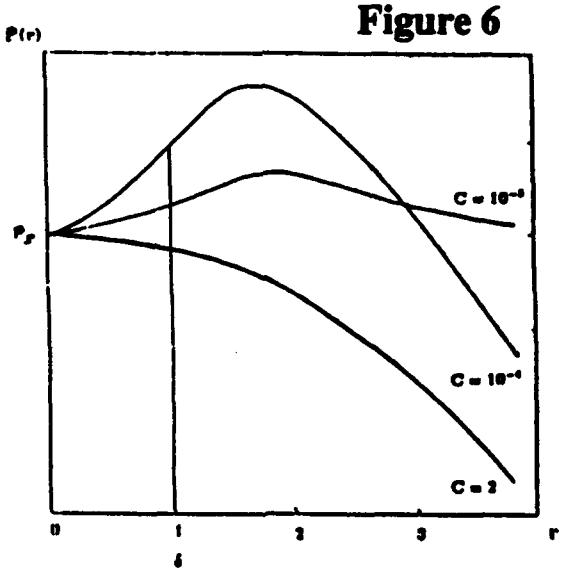

P(r) VERSUS G AT Z CONSTANT

Figure 7

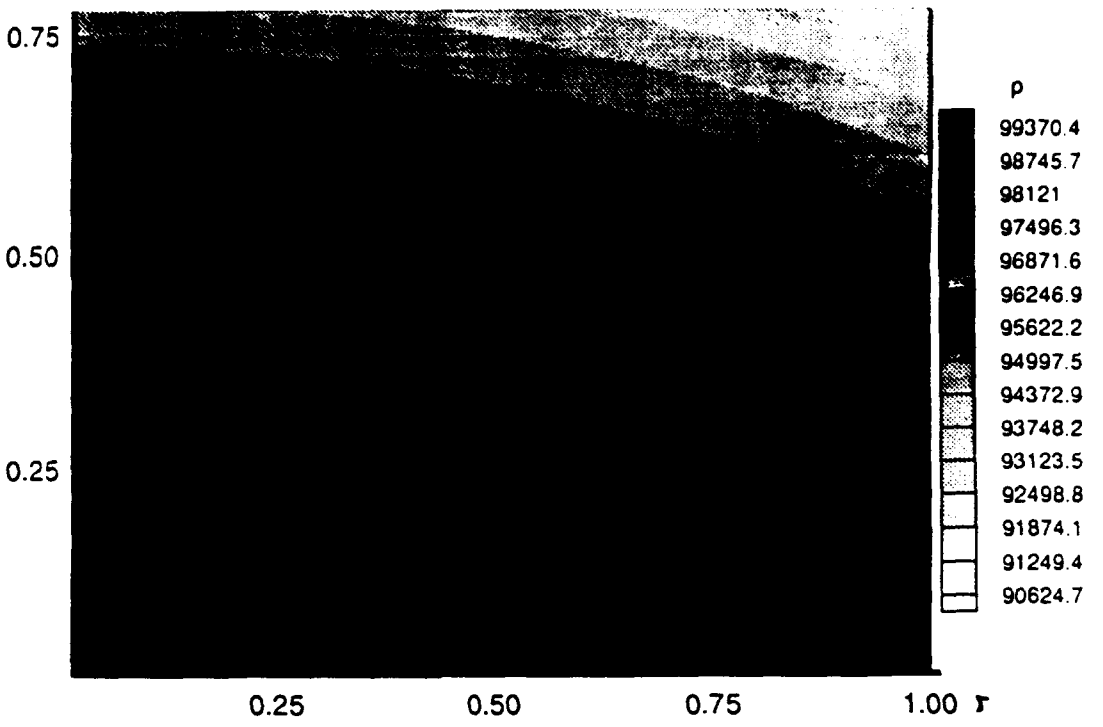

PRESSURE DISTRIBUTION: C=2.

Figure 8

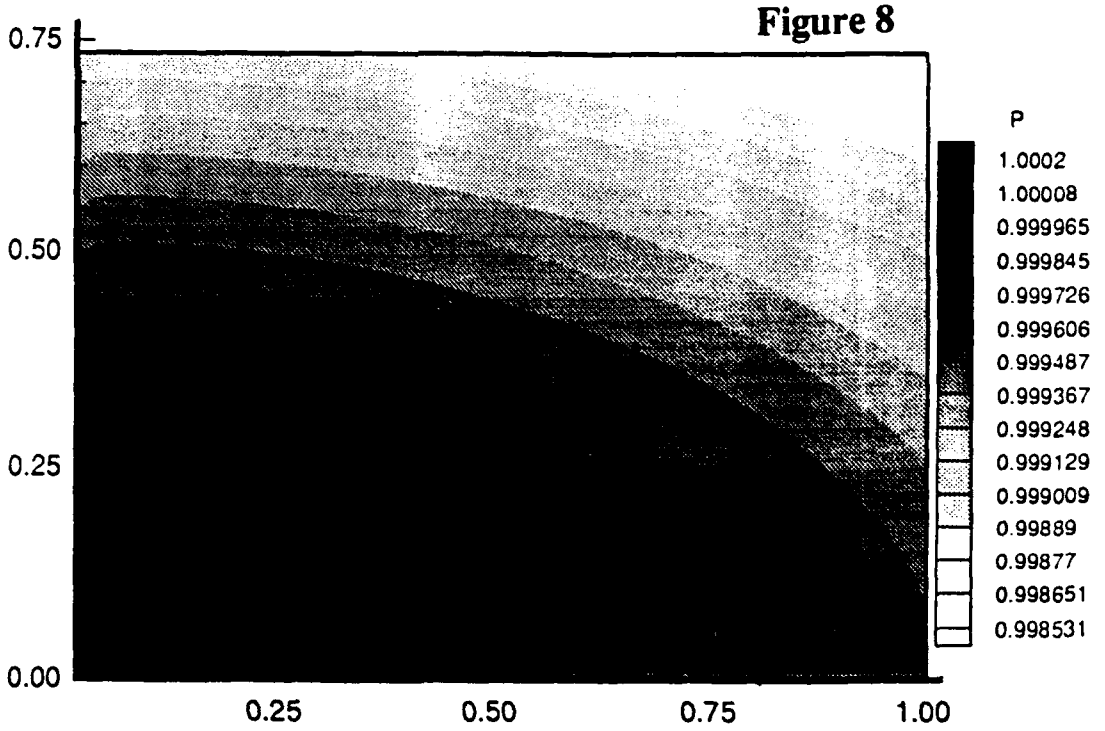

PRESSURE DISTRIBUTION: $C=10^{-4}$

Figure 9
1D Viscous solver, Flow Chart

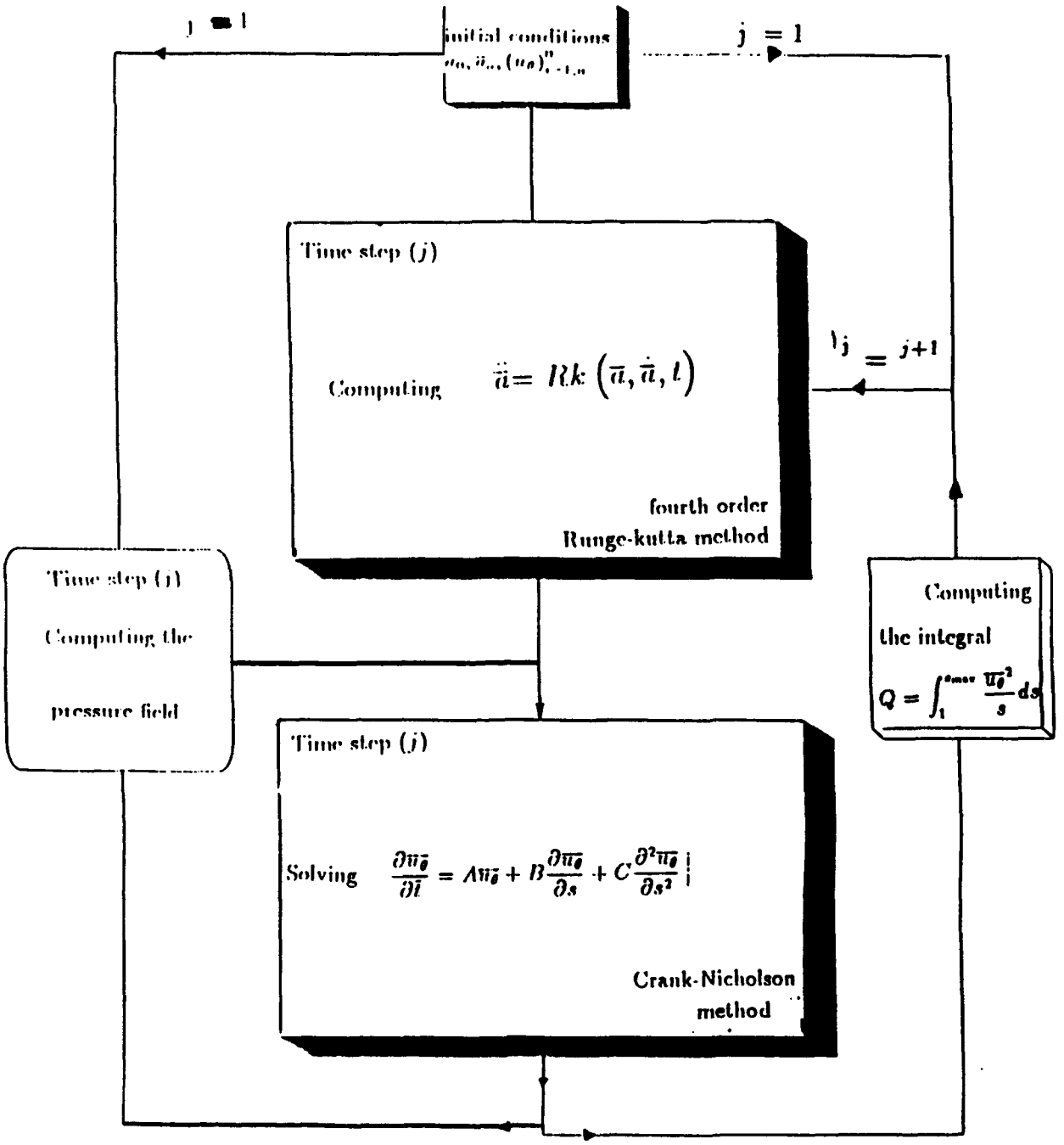

Figure 10

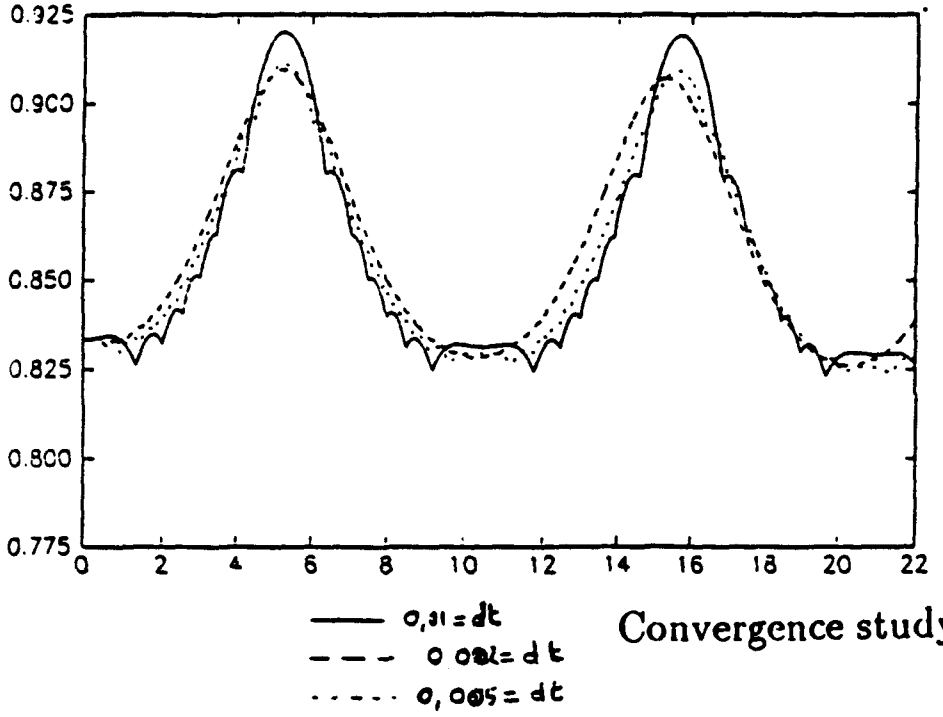

Convergence study

Figure 11

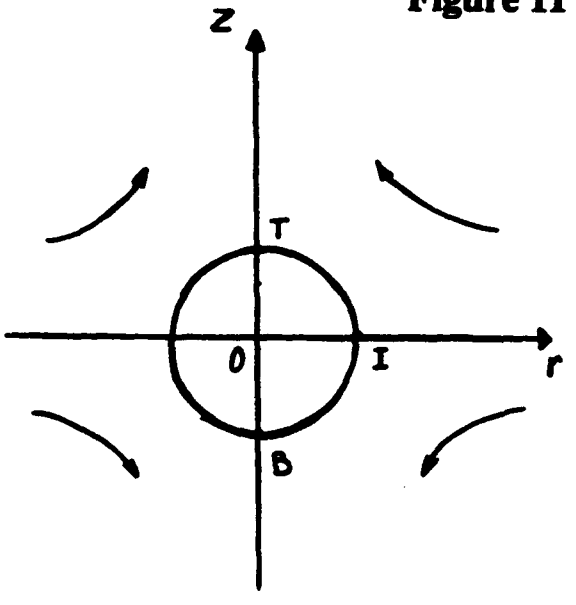

THE CHARACTERISTIC POINTS

CASE OF C=10 :STRONG INTERACTION BETWEEN THE BUBBLE AND THE FLOW

Figure 12

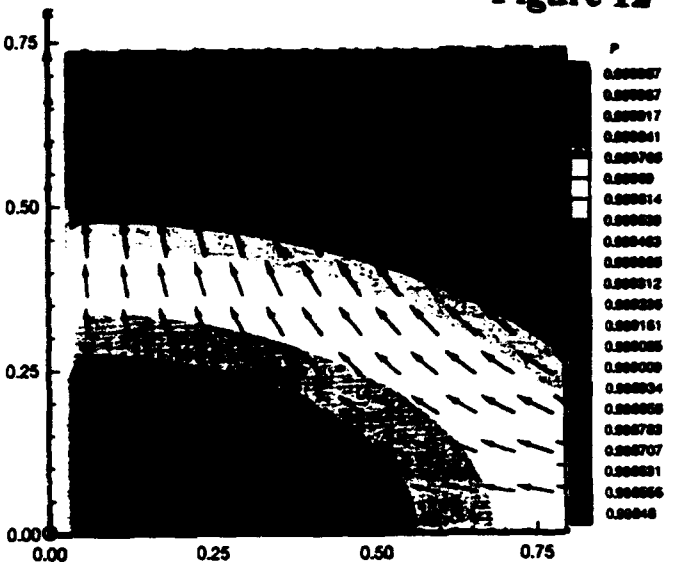

T=0 : BUBBLE IN THE BURGERS VORTEX.
PRESSURE AND VELOCITY FIELDS

Figure 13

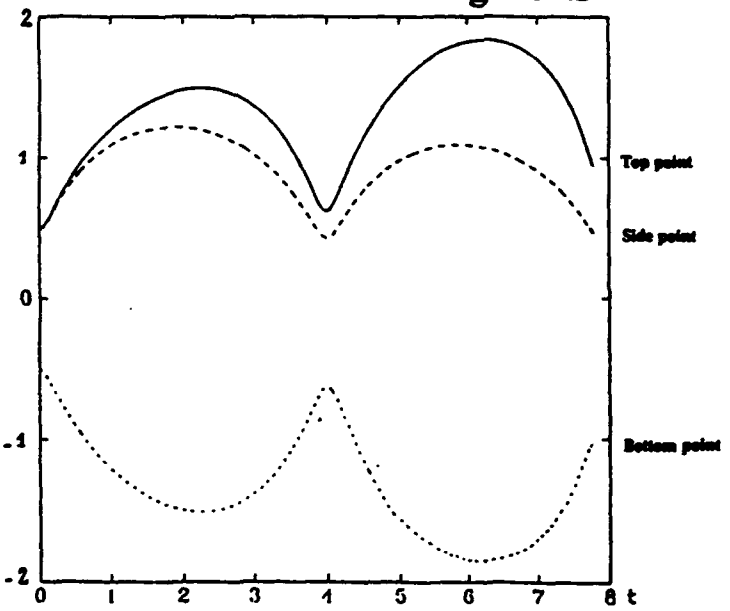

EVOLUTION OF THE CHARACTERISTIC POINTS VERSUS TIME.

Figure 14

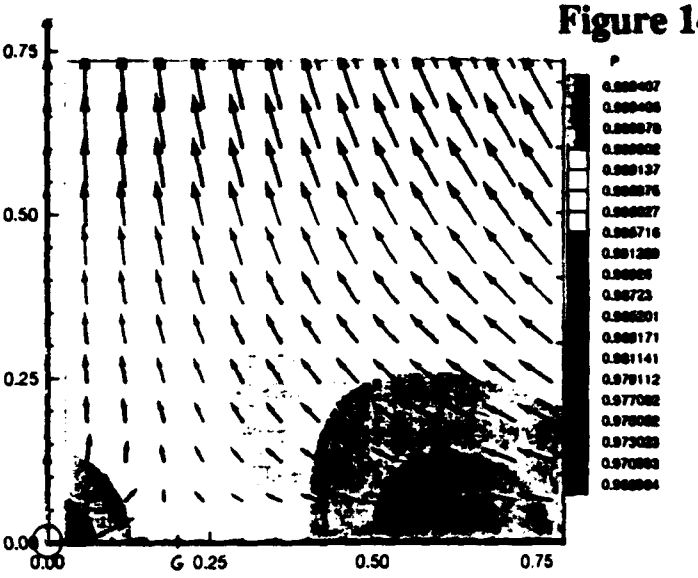

T=1 : BUBBLE GROWS.

Figure 15

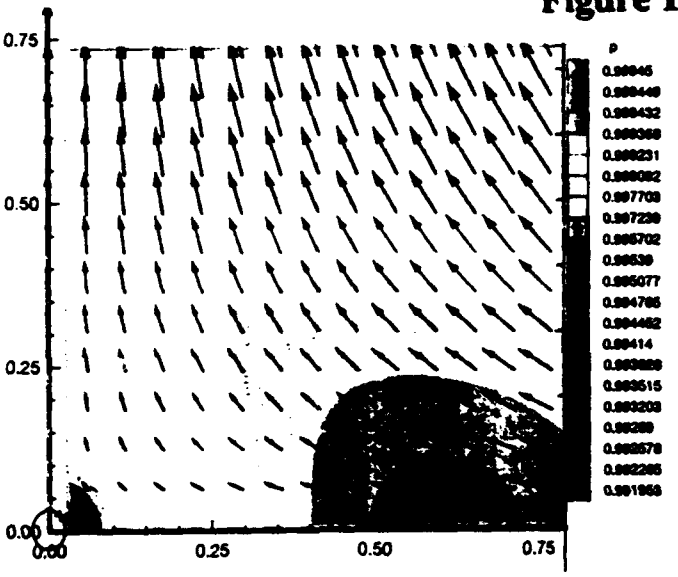

T=2 : BUBBLE BEGINS TO COLLAPSE.

Figure 16

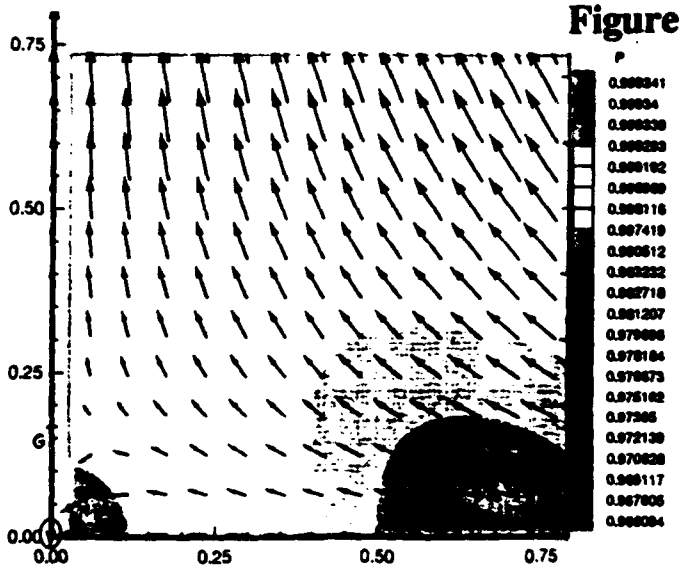

T=3.5 : BUBBLE IS COLLAPSING.

PRESSURE AND VELOCITY FIELDS

CASE OF C=10^{-4}:STRONG INTERACTION BETWEEN THE BUBBLE AND THE FLOW

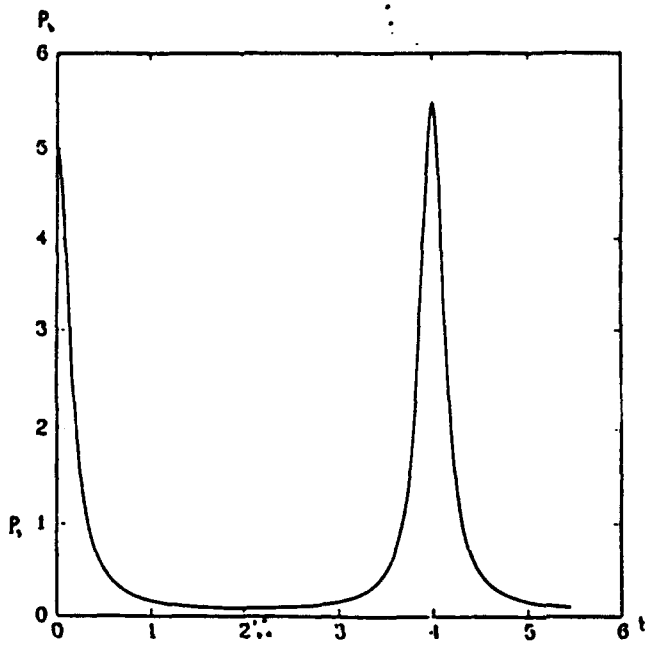

PRESSURE IN THE BUBBLE VERSUS TIME.

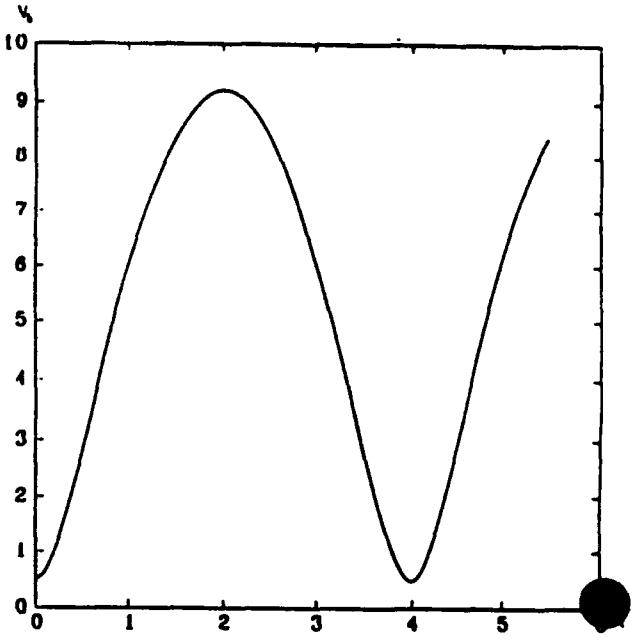

VOLUME OF THE BUBBLE VERSUS TIME.

Figure 17

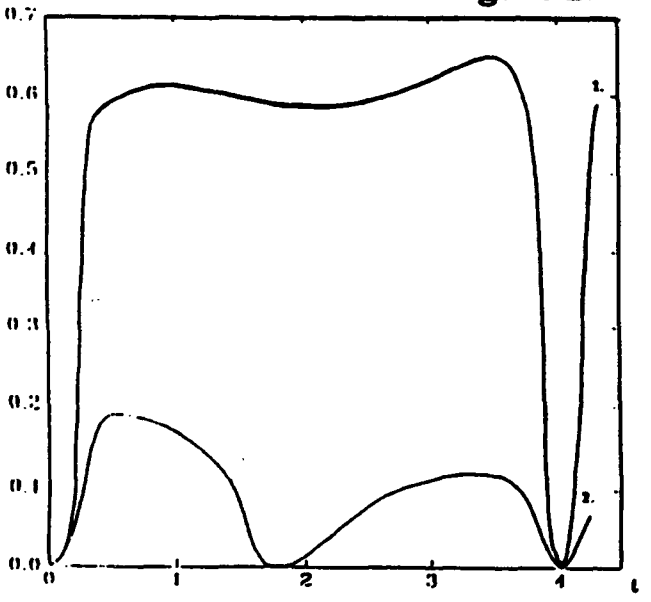

1- Distance between H and the bubble surface.
2- Distance between G and the bubble surface.

MOVING OF H AND G VERSUS TIME

BUBBLE MOVING ON THE Z-AXIS ($C=10^{-4}$)

Figure 18

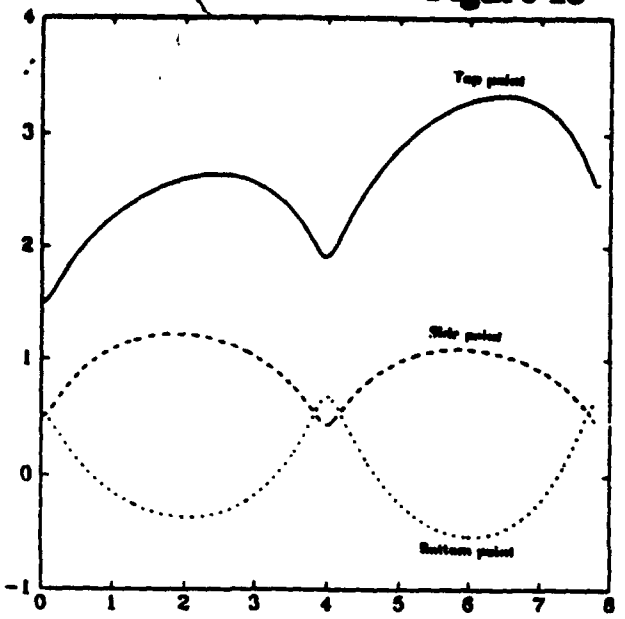

EVOLUTION OF THE CHARACTERISTIC POINTS VERSUS TIME.

VELOCITY FIELD

Figure 19

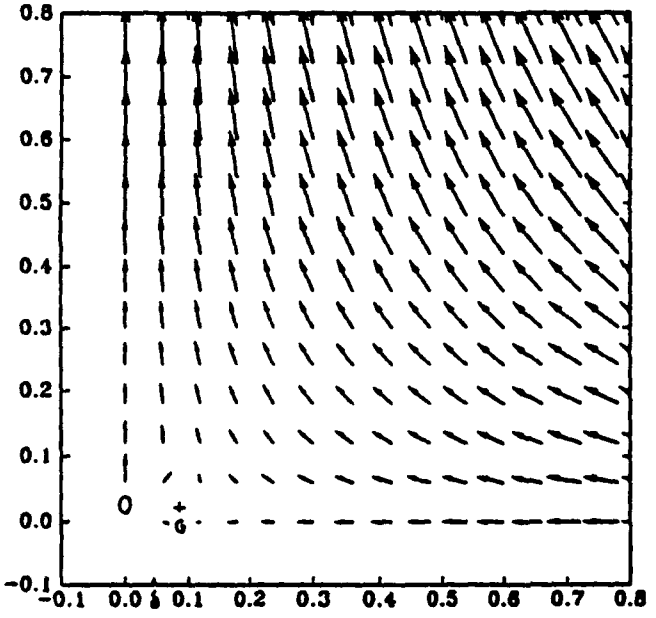

T=4

VELOCITY FIELD

Figure 20

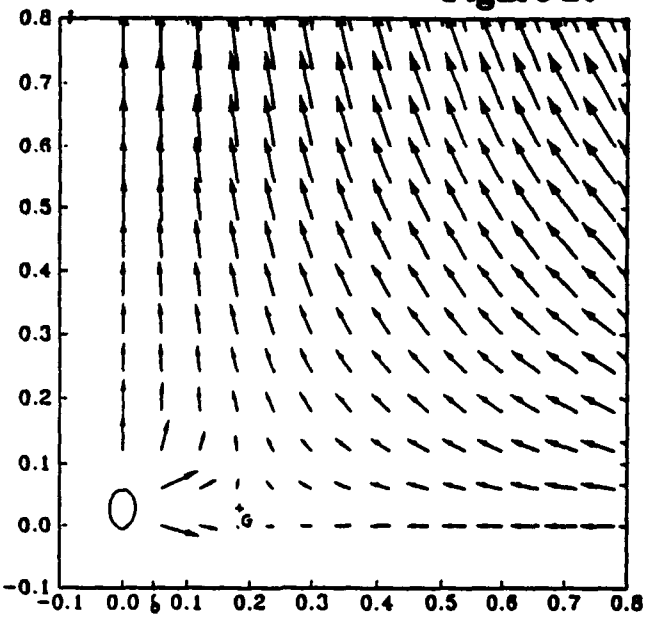

T=5

Figure 21

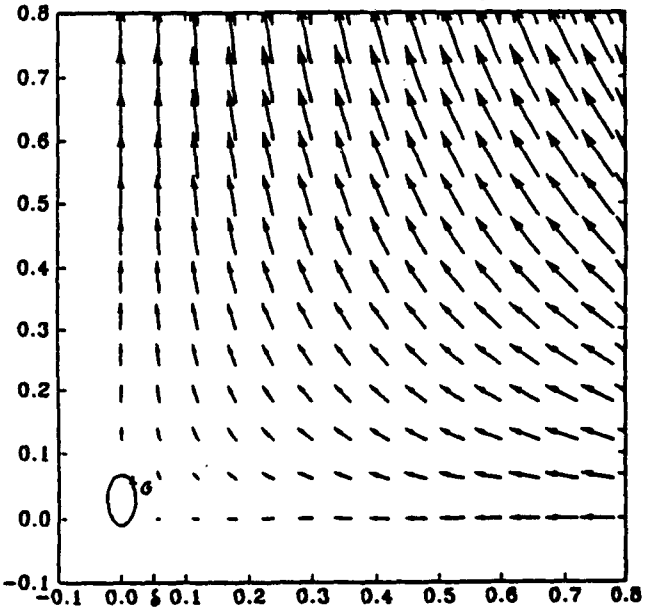

T=6

VELOCITY FIELD

Figure 22

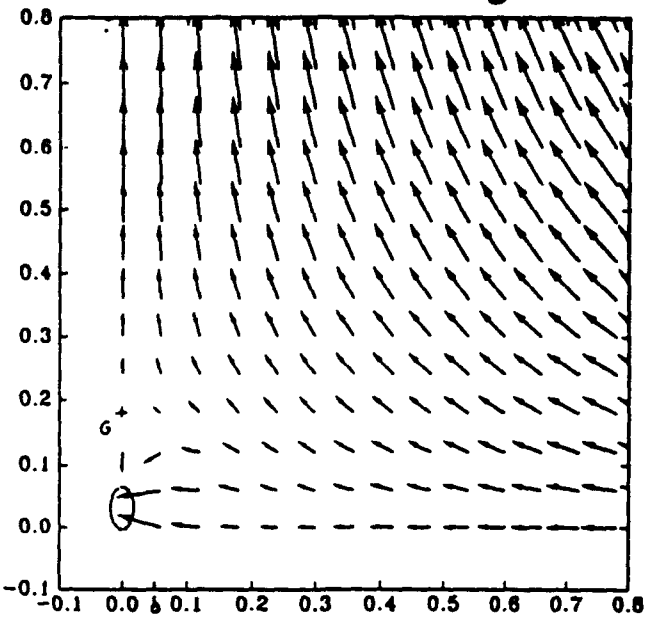

T=7

CASE OF C=10^{-3}:INTERMEDIATE INTERACTION

Figure 23

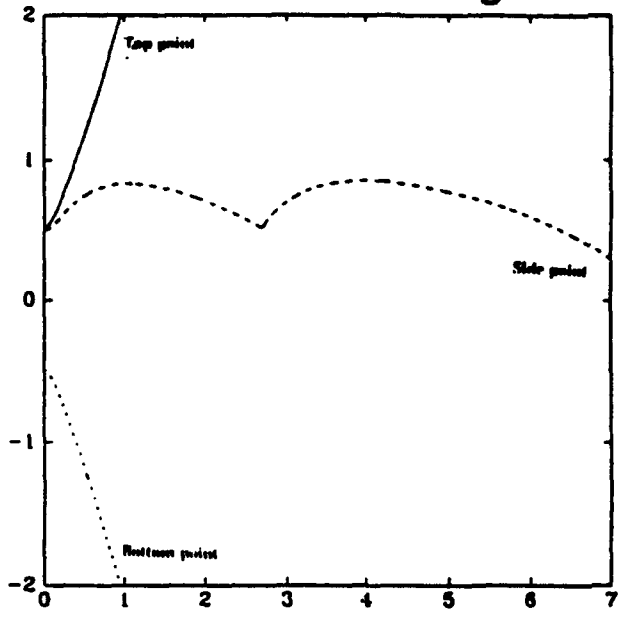

EVOLUTION OF THE CHARACTERISTIC POINTS VERSUS TIME.

VELOCITY FIELD

Figure 24

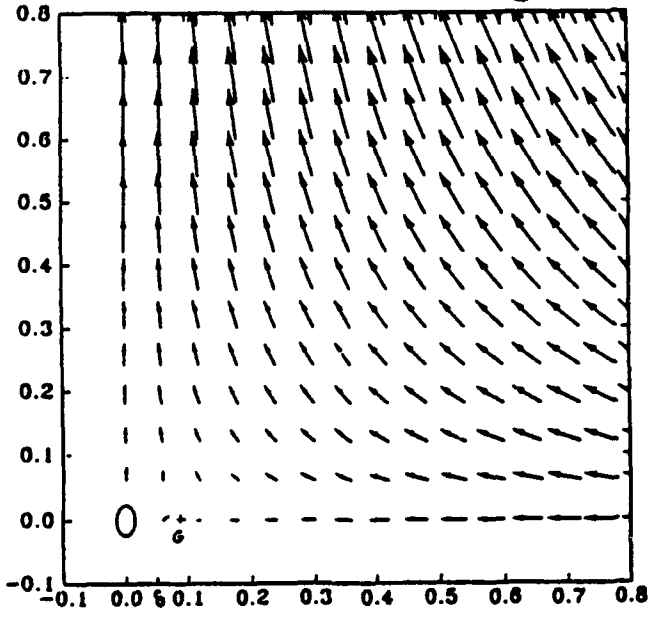

T=0.5

VELOCITY FIELD

Figure 25

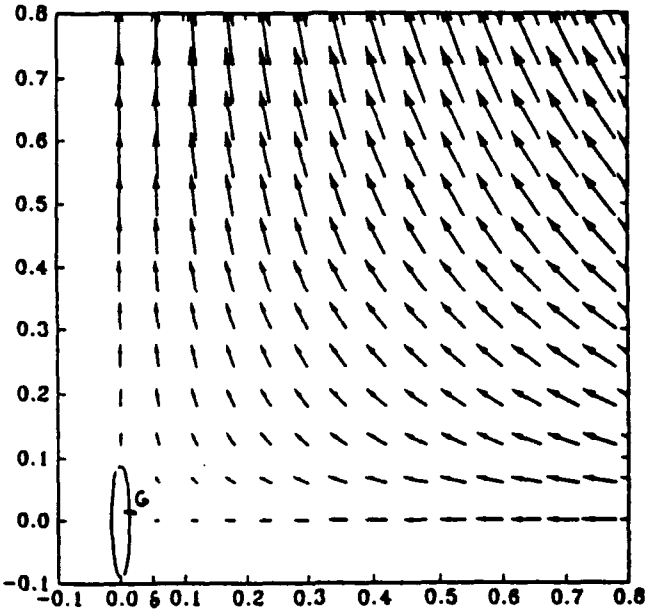

T=2

Figure 26

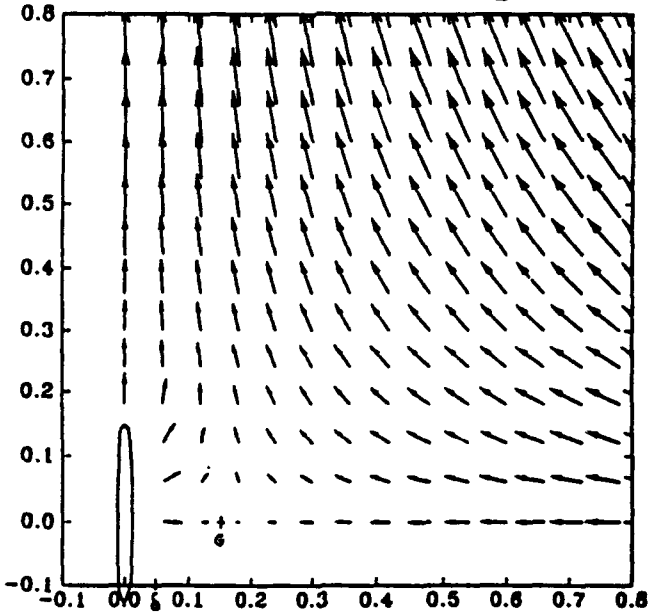

T=2.8

VELOCITY FIELD **Figure 27**

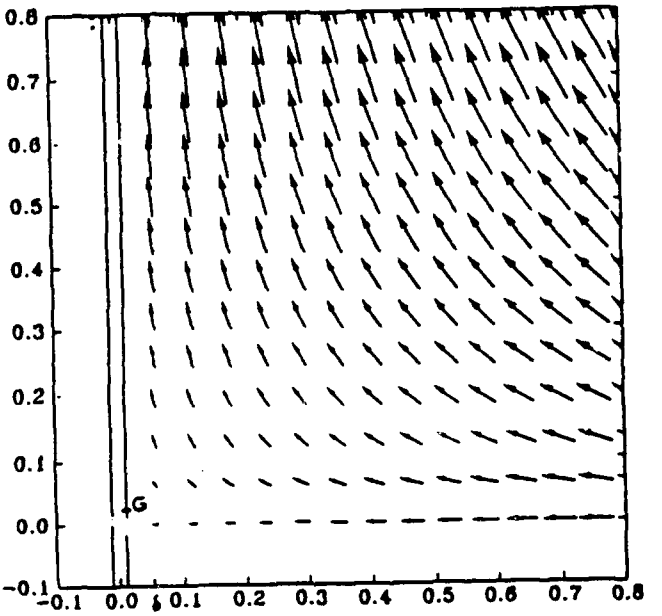

T=6

Figure 28

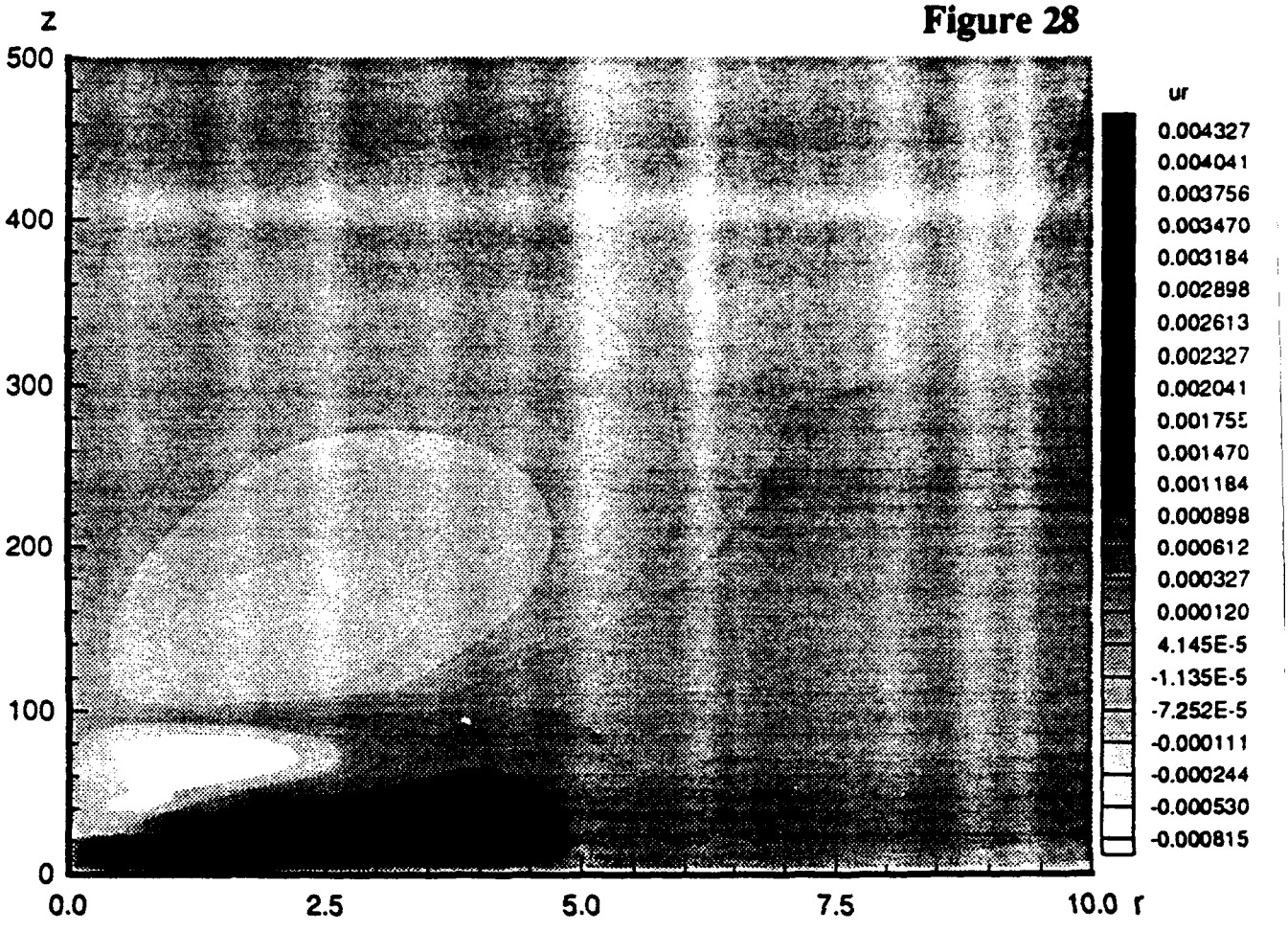

Ur DISTRIBUTION.

Figure 29

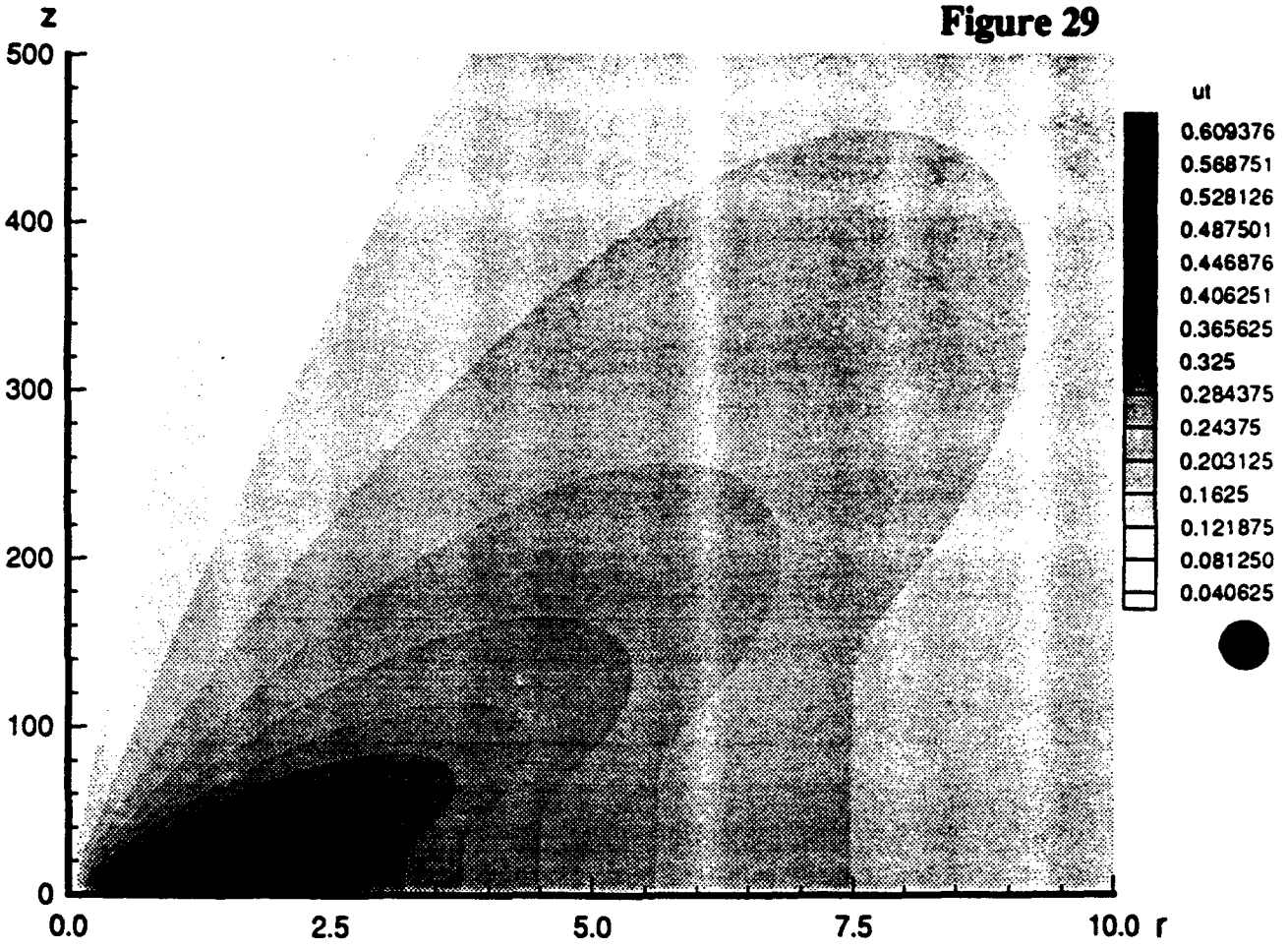

U_θ DISTRIBUTION.

Figure 30

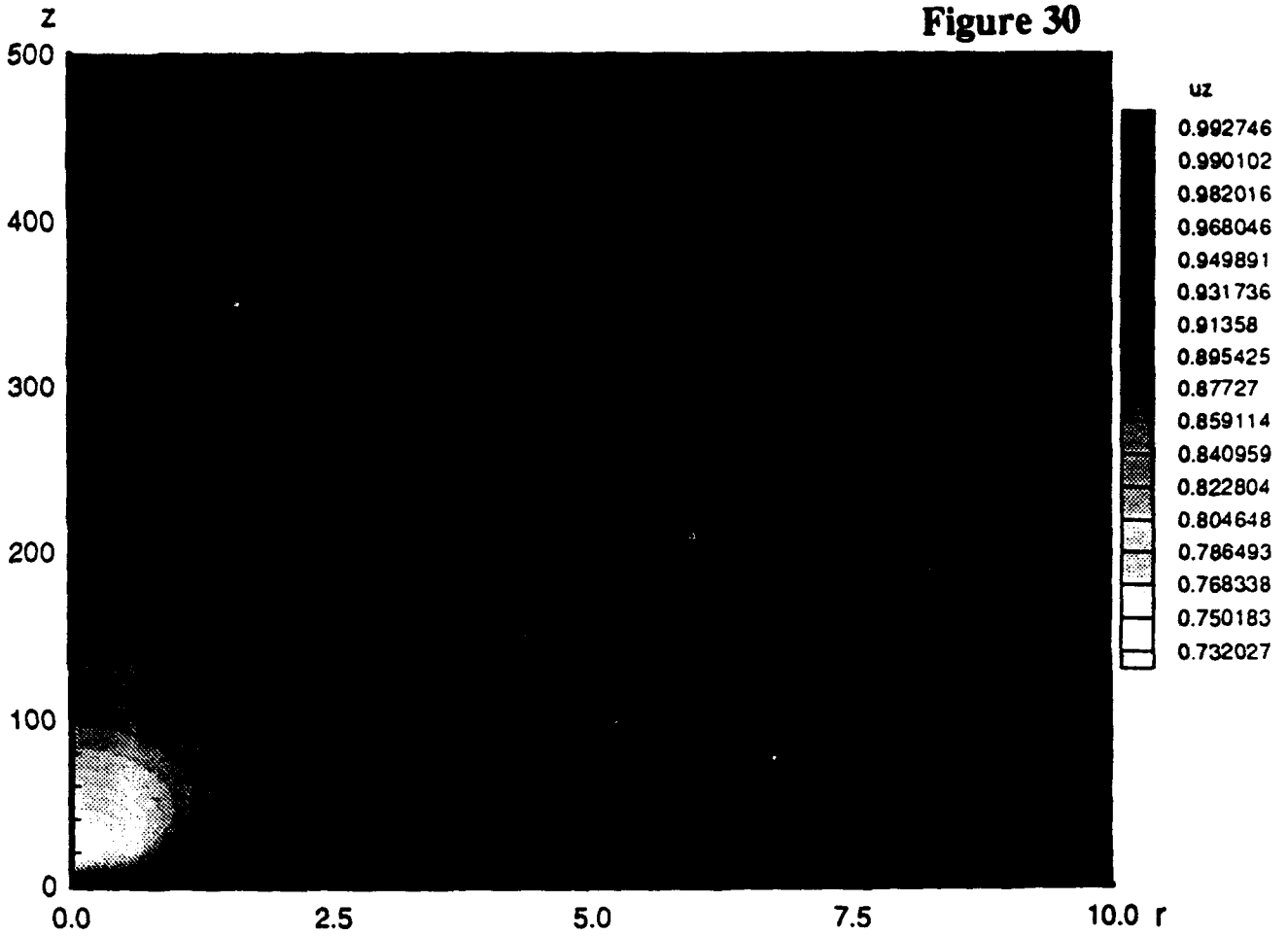

Uz DISTRIBUTION.

Figure 31

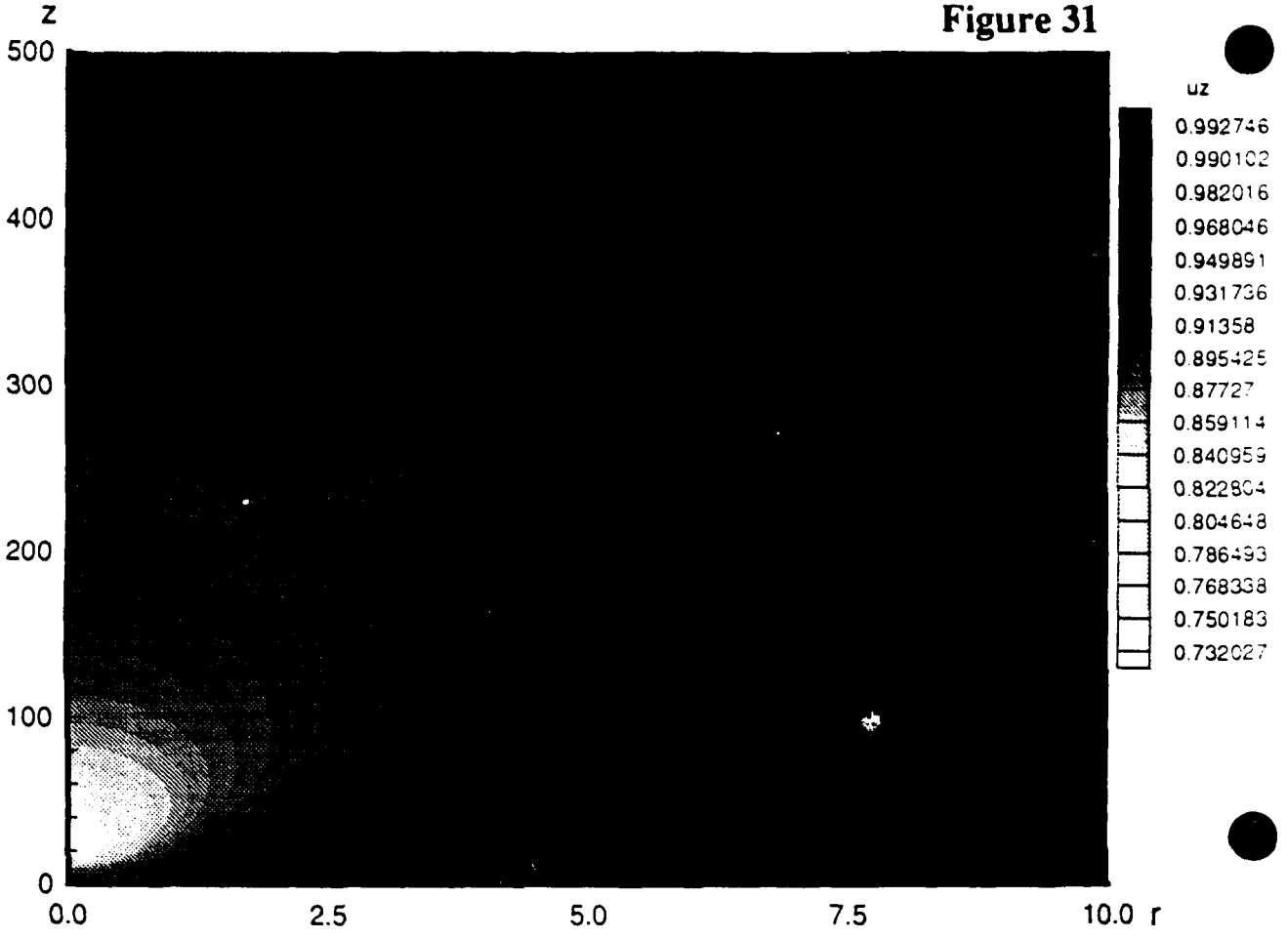

Uz DISTRIBUTION.

Figure 32

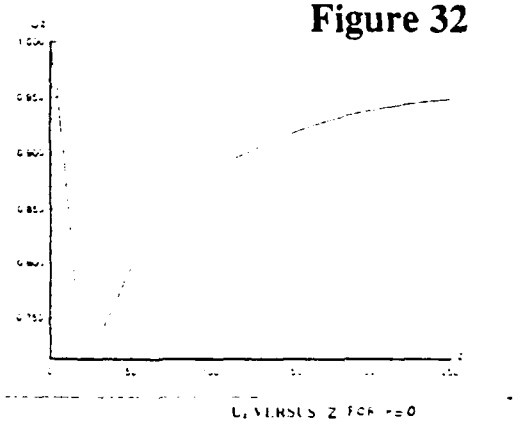

Figure 33

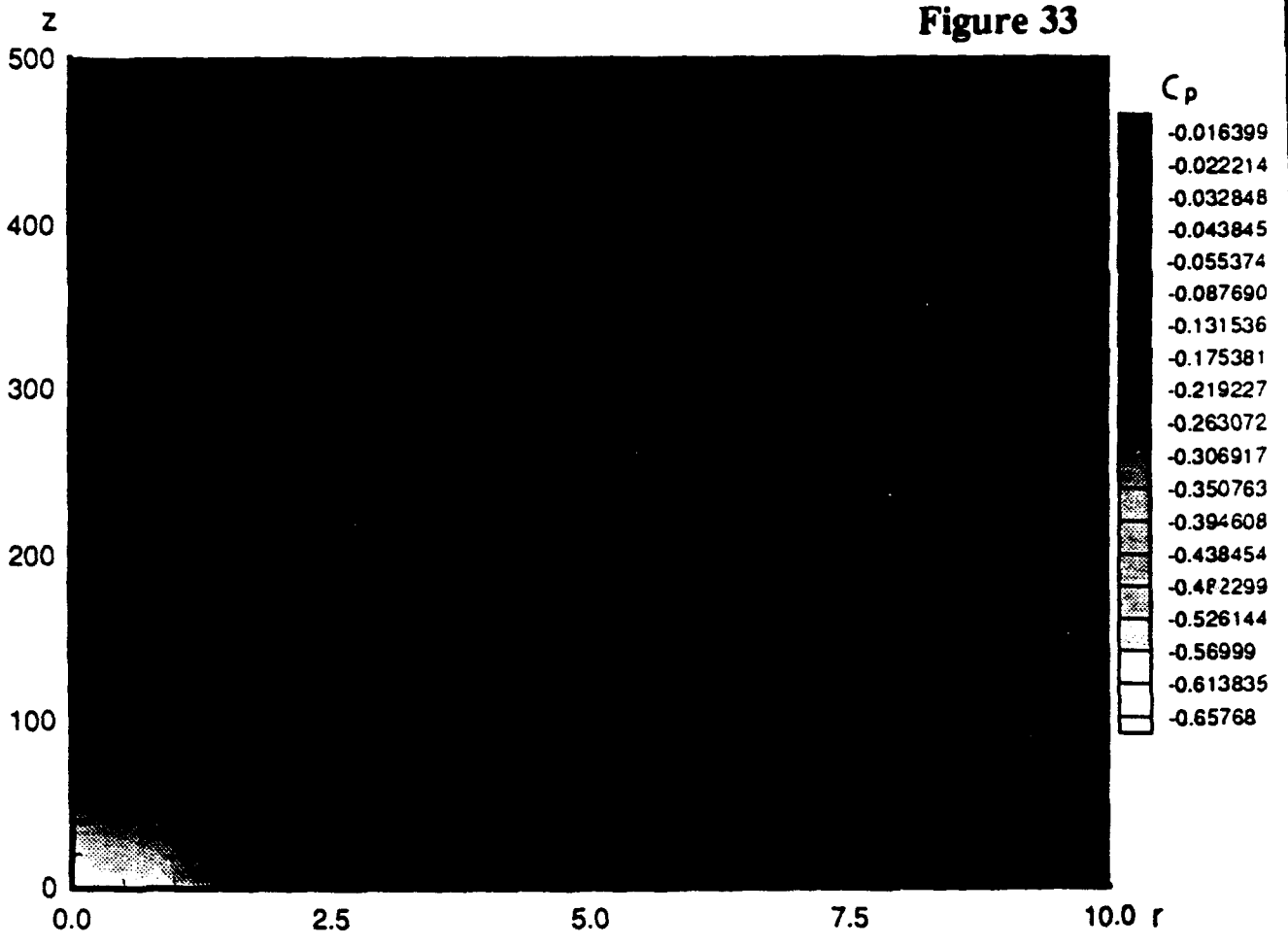

PRESSURE DISTRIBUTION.

Figure 34

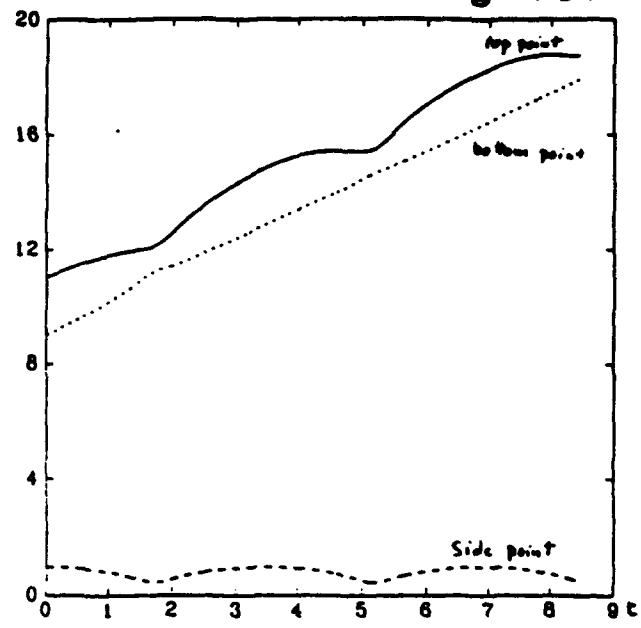

EVOLUTION OF THE CHARACTERISTIC POINTS VERSUS TIME.

Figure 35

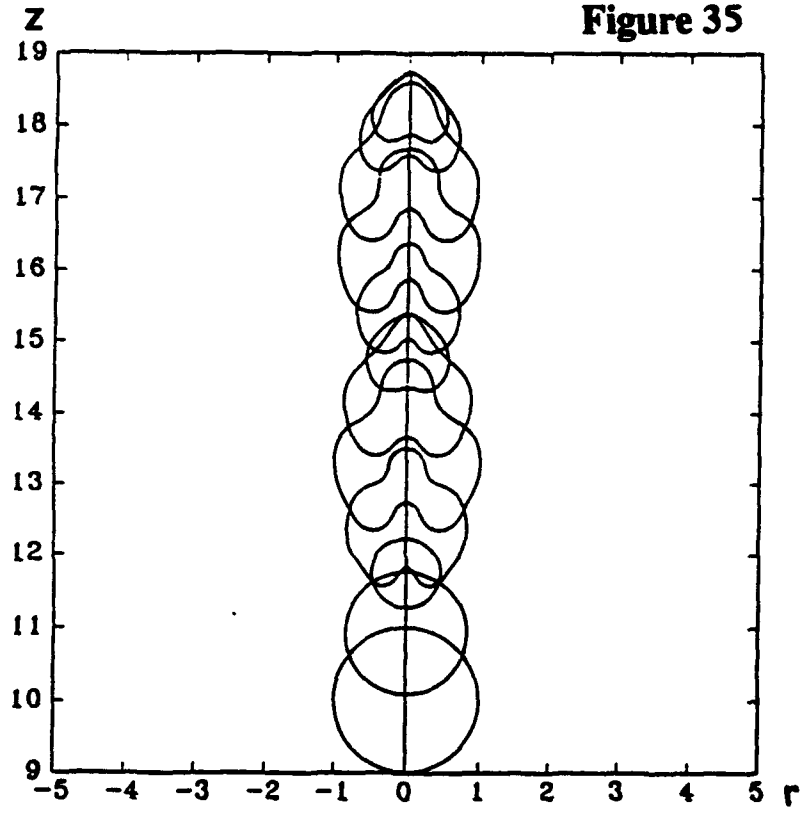

BUBBLE DEFORMATION

Figure 36

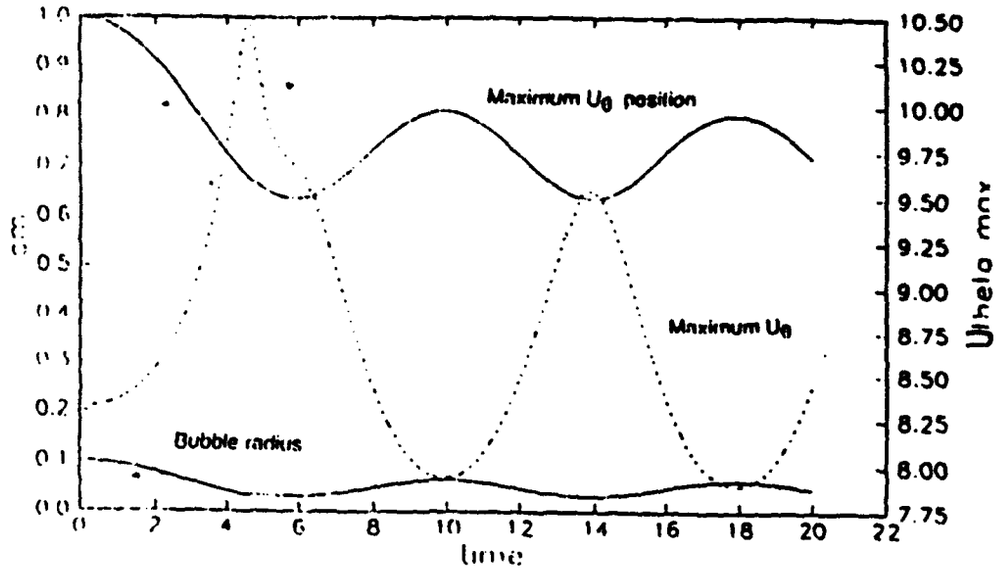

Figure 37

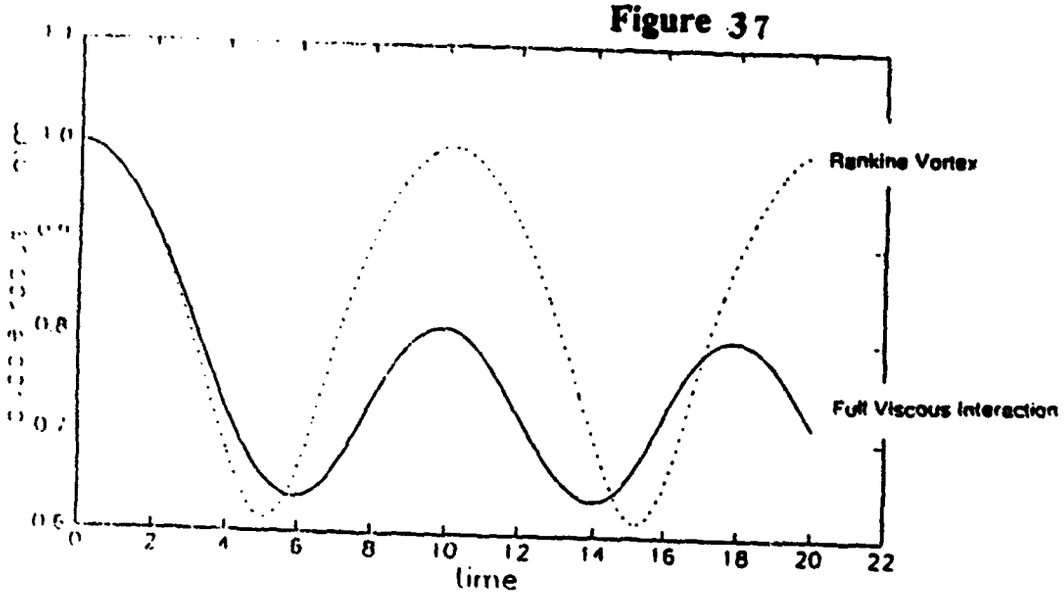

Figure 1. Interaction between a bubble and a vortex flow during bubble oscillations.
a) Bubble radius, maximum U_θ, and maximum U_θ position versus time.
b) Bubble radius versus time with and without viscous interaction.

Pgo/Paxis	0.2	0.2	2.3
Gama (m/s	0.1	0.05	0.6
Ac/a(o)	5	5	5
Figure			
Ac (m)	1.00E-02	1.00E-02	1.00E-02
a(o) (m)	2*1e-3	2*1e-3	2*1e-3
Pinf (Pa)	1.00E+05	1.00E+05	1.00E+05
Pgo (Pa)	2.00E+04	2.00E+04	2.00E+04

conditions for figures (38) to (41)

Figure 38

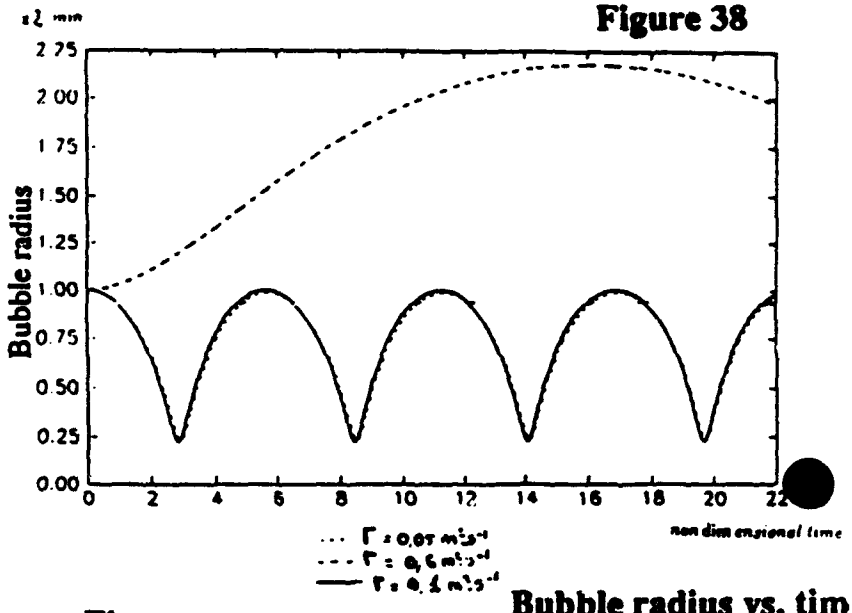

Bubble radius vs. tim

Figure 39

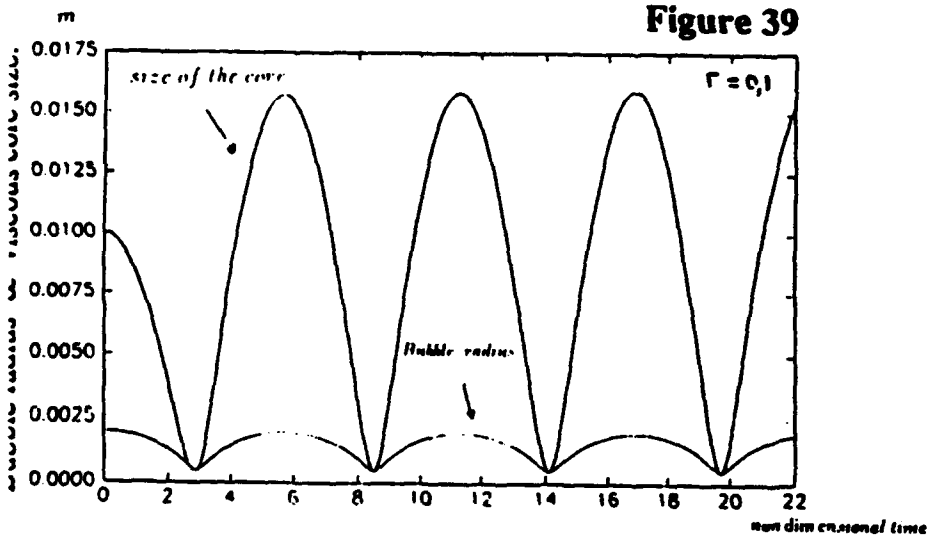

Bubble radius vs. time
& Size of the viscous core vs. time

1D viscous solver results.

Figure 40

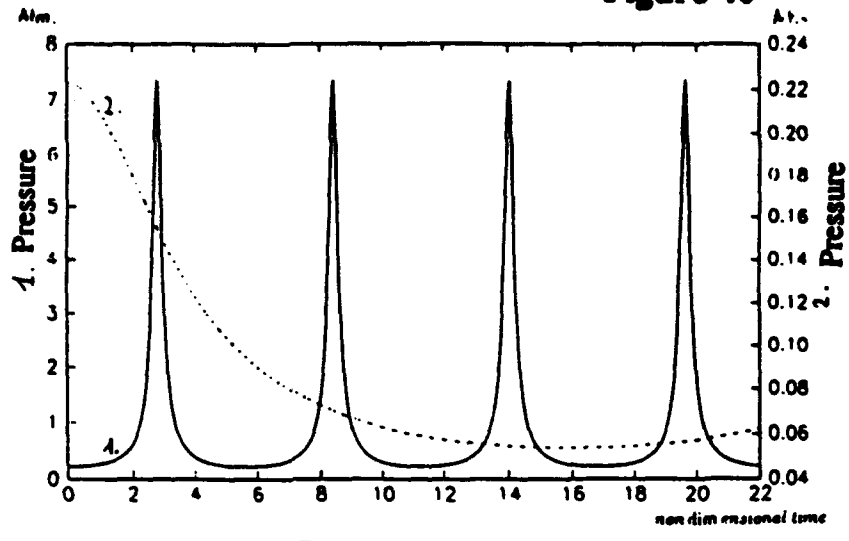

Pressure on the bubble surface vs. time

Figure 41

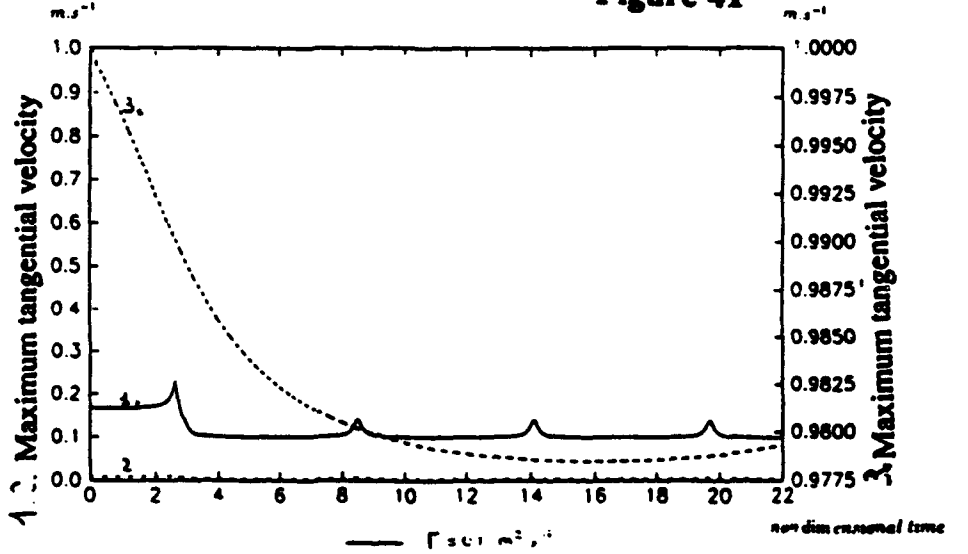

Maximum tangential velocity vs. time

1D viscous solver results

Pgo/Paxis	0.546299	0.919963
Gama (m/s	0.5	0.5
Ac/a(o)	2	1.80
Ac (m)	1.00E-02	9.00E-03
a(o) (m)	5*1e-3	5.00E-03
Pinf (Pa)	1.00E+05	1.00E+05
Pgo (Pa)	2.00E+04	2.00E+04
Paxis (Pa)	36610	21740

conditions for figures (42) to (44)

Figure 42

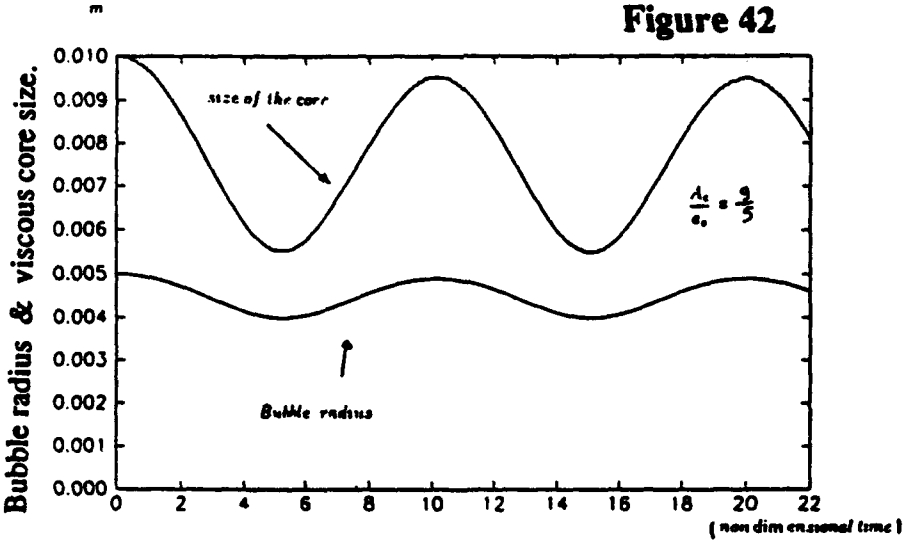

Bubble radius vs. time
& size of the viscous core vs. time

1D viscous solver results.

Figure 43

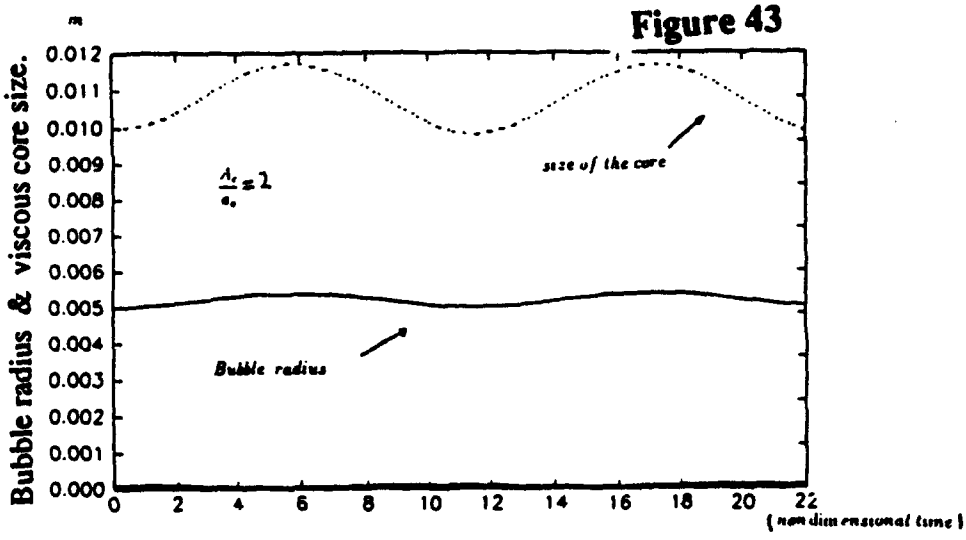

Bubble radius vs. time
& size of the viscous core vs. time

Figure 44

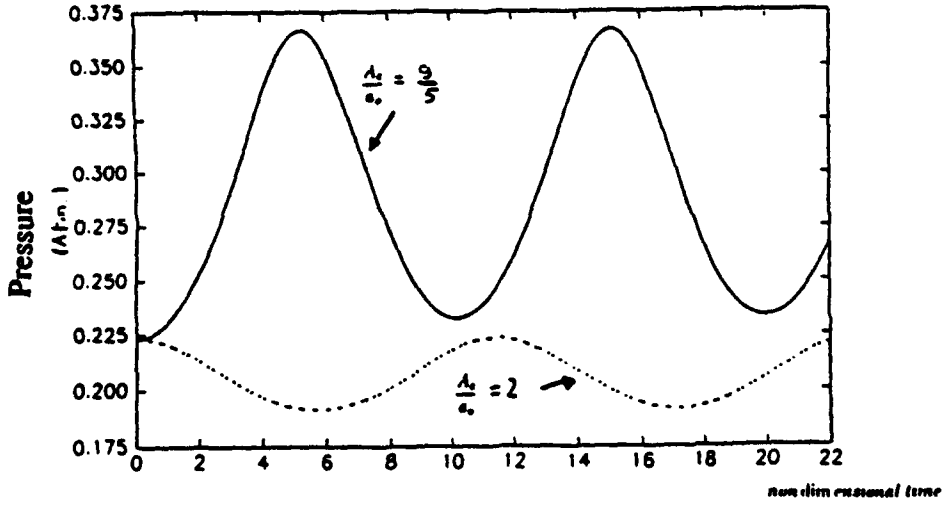

Pressure on the bubble surface vs. time

1D viscous solver results.

conditions for figures (45) to (48)

pgo/paxis	5/7*1e-3	0.40	1	3
gama	0.35	0.35	0.35	0.35
Ac/ao	1.4	1.4	1.4	1.4
Pinf (Pa)	1.00E+05	1.00E+05	1.00E+05	1.00E+05
Paxis (Pa)	7.00E+04	"		

Figure 45

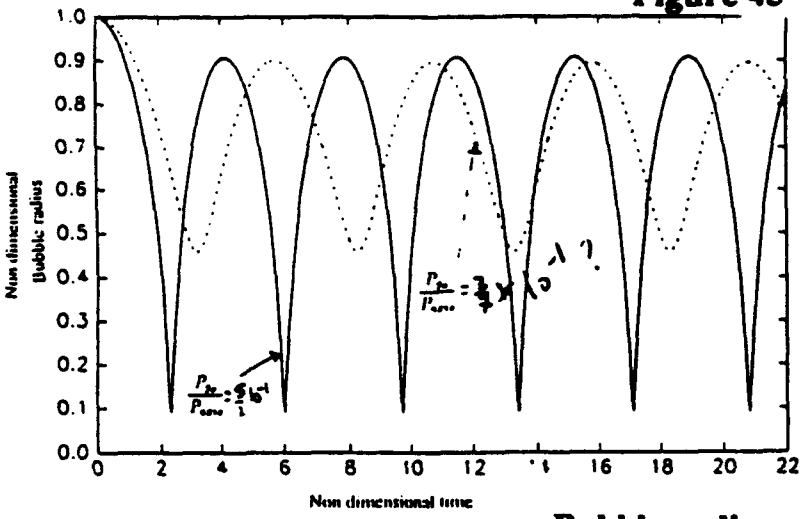

Bubble radius vs. time

Figure 46

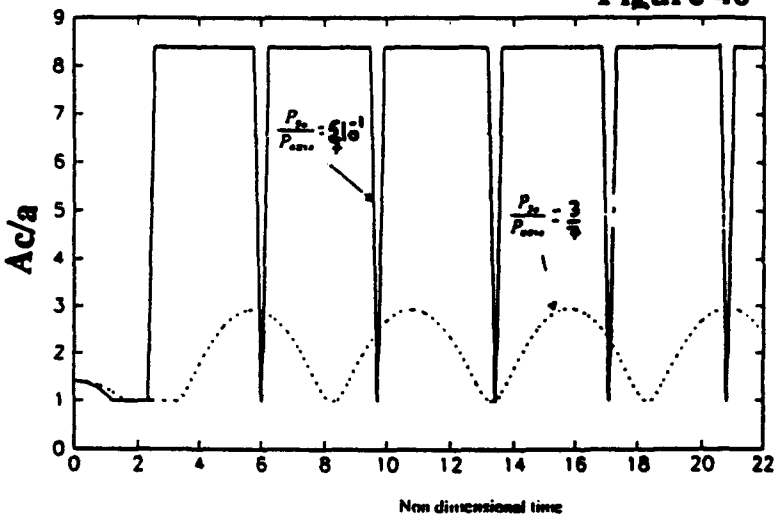

$\frac{A_c}{a_o} = 1.4$

Ratio of the viscous core radi to the bubble radius vs. time

1D viscous solver results.

Figure 47

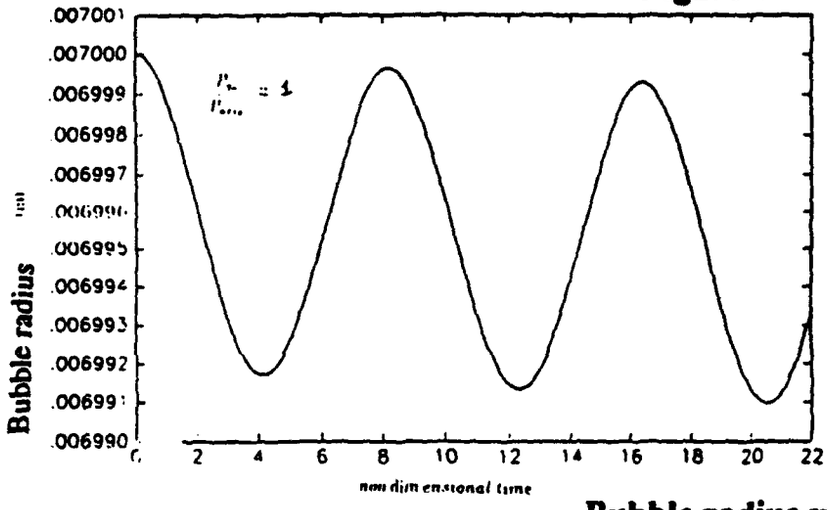

Bubble radius vs. time

Figure 48

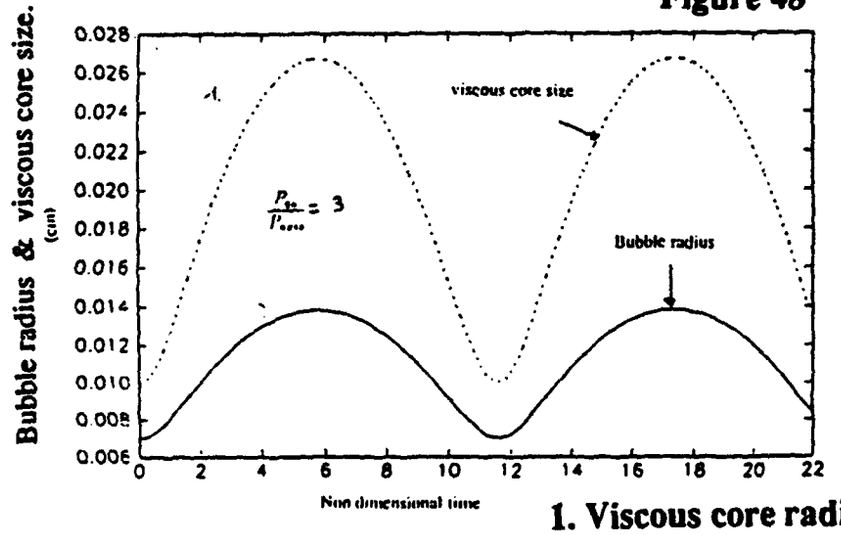

1. Viscous core radius vs. time
2. Bubble radius vs. time

1D viscous solver results.

Conditions for figures (49) to (53)

Pgo/Paxis	0.5	0.5	0.5	0.5
Gama (m/s	0.35	0.35	0.35	0.35
Ac/a(o)	1.4	2.00	5	10
Ac (m)	1.00E-02	1.00E-02	1.00E-02	1.00E-02
a(o) (m)	7*1e-3	5.00E-03	0.002	0.001
Pinf (Pa)	1.00E+05	1.00E+05	1.00E+05	1.00E+05
Pgo (Pa)	3.45E+04	3.45E+04	3.45E+04	3.45E+04
Paxis (Pa)	68938	68938	68938	68938

Figure 49

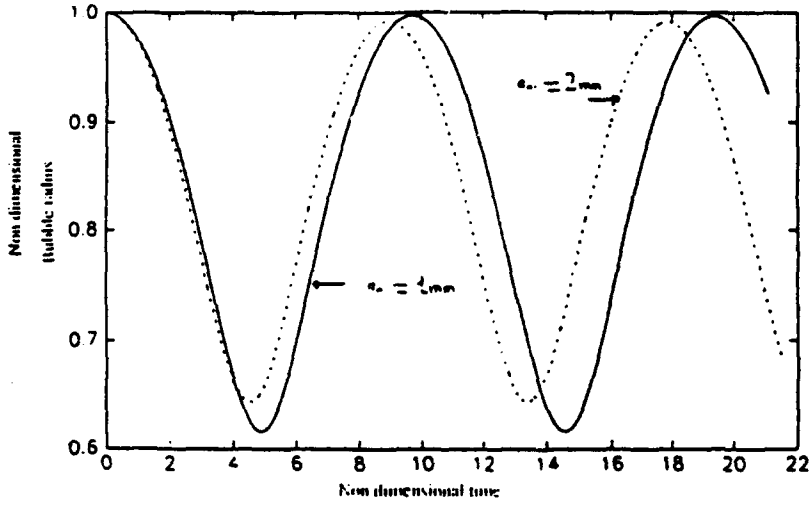

Bubble radius vs. time

Figure 50

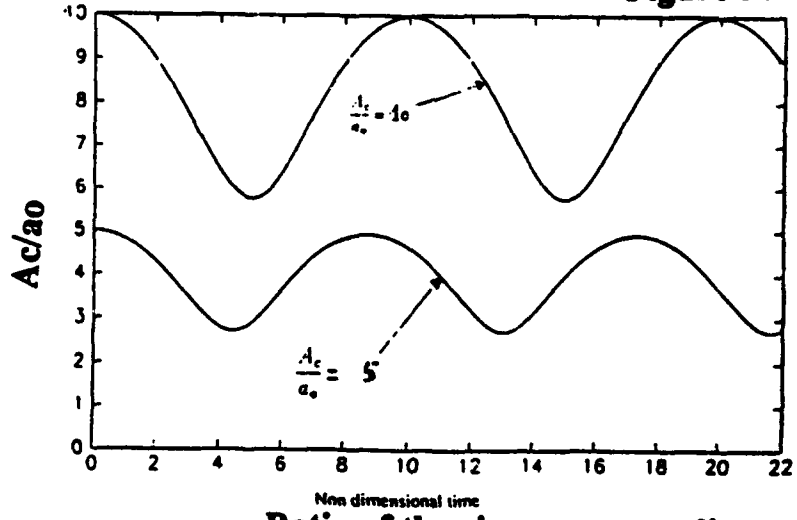

Ratio of the viscous core radius to the bubble radius vs. time

Figure 51

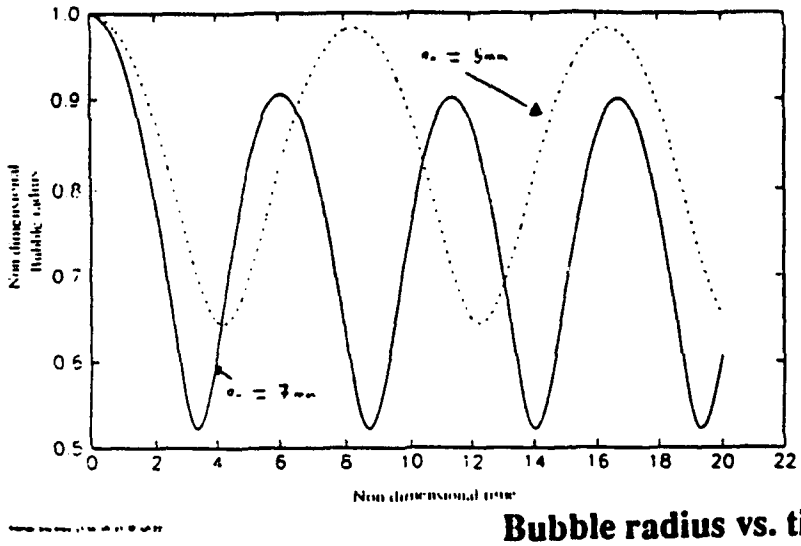

Bubble radius vs. time

Figure 52

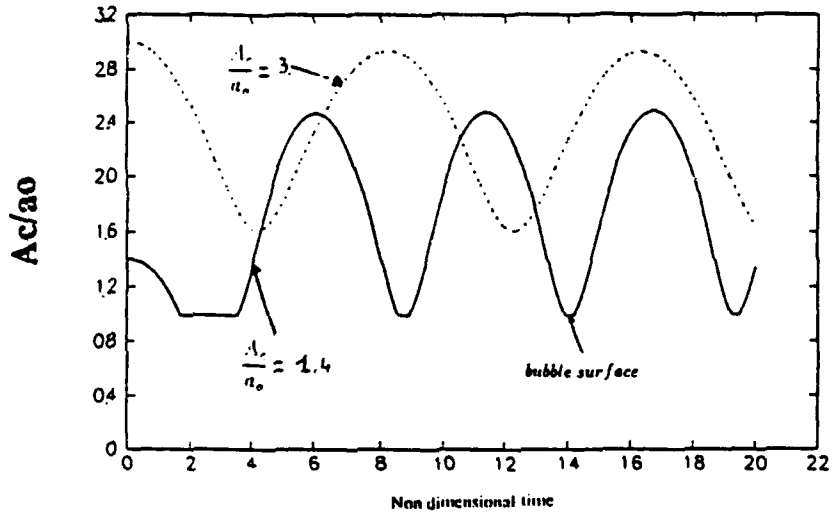

Ratio of the viscous core radius to the bubble radius vs. time

1D viscous solver result

Figure 5 3

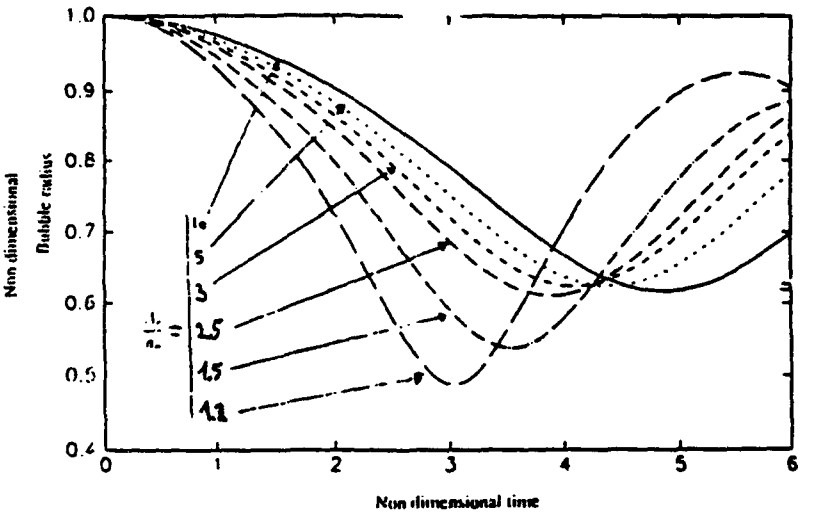

Bubble radius vs. time

1D viscous solver result

THE MOTION OF A SPHERICAL BODY BELOW A FREE SURFACE

Y. L. GUERRIER

October 1993

DYNAFLOW, INC.
7210 Pindell School Road
Fulton, MD 20759

The Motion of a Spherical Body Below A Free Surface

Y. L. GUERRIER
Student at Ecole Centrale Nantes, FRANCE

October 1993

Abstract

This study computes the deformations of the free surface of a liquid when a sphere is oscillating below the surface. The code 2DynaFS was adapted to this problem and, after determining some fundamental parameters, we proved that the surface tension effect can often be neglected. We primarily studied the importance of gravity and showed its effect on the amplitude of the resulting waves. The sphere frequency also seems to determine the amplitude. A brief experimental study was conducted which verified the conditions we had choosen and confirmed some of the numerical computations. A video recording of the observations is available.

Contents

1. Introduction

Waves are often studied in hydrodynamic circles because they carry energy. This energy can be due to the wind: the study of swell and waves breaking on shore helps to determine a way to avoid shore erosion. The study in this report is motivated by wave-resistance: when a submerged body moves below a Free Surface, it generates waves which extract energy from the body motion. We will here only study the deformations of the free surface when a sphere is oscillating below this free surface.

We conducted experiments in the laboratory DYNAFLOW in order to validate some of the computed results. Observations are available on a NTSC video tape.

1.1. Nomenclature

FS: Free Surface
Φ: velocity potential
Ψ: mathematical function
∇: gradient operator
x: Horizontal position
y: Vertical position
R: radius of the sphere
A_{mp}: amplitude of the sphere motion
ω: frequency of the sphere motion ($\frac{rad}{s}$)
T: period ($= \frac{2\pi}{\omega}$)
∇^2: Laplacian operator
$\mathcal{F}r$: Froude number
$\frac{\partial}{\partial t}$: partial derivative
Amplitude: computed amplitude of node A
s: curvilinear abscissa
ht: time step
t: absolute time
ρ: density of the fluid
P_l: pressure in the fluid
P_a: atmospheric pressure
V_n: normal speed
V_t: tangential speed
g: gravity acceleration
$(O, \overrightarrow{x}, \overrightarrow{y})$: reference frame
σ: surface tension
C_{urv}: curvature of the FS
δ_p: delta-function =0 except at p: =1
$\mathcal{W}eb$: Weber number
$\frac{d}{dt}$: total derivative
Average pos: time averaged ordinate of the node A
N_{HP}: number of half periods
d_{epth0}: initial depth of sphere
$\overrightarrow{\eta}$: vertical deformation of FS
$\overrightarrow{n}$: normal vector
V_{sph}: velocity of the sphere
Ω: domain of the study
S : boundary of Ω
$c(p)$: solid angle at p
p: point where the influence of every panel is computed
q: moving point on a panel
FT: final time
$\gamma(p)$: discrete function of p
L_{ay}: fluid layer on the sphere
$\overline{var}$: non-dimensionalized var
n_{FS}: number of panels on FS
Frequency: frequency of the FS waves

All figures are located in Appendix A.

2. Hydrodynamic problem

2.1. Equations

The conservation of the mass in the liquid of density ρ leads to the continuity equation for a flow with velocity $\overrightarrow{V}$:

$$\frac{\partial \rho}{\partial t} + div(\rho \overrightarrow{V}) = 0$$

We assume that the fluid is inviscid, incompressible and irrotational. Then it satisfies the following equations:

$$div(\overrightarrow{V}) = 0\,,$$
$$\overrightarrow{rot}(\overrightarrow{V}) = \overrightarrow{0}\,,$$

Thanks to these conditions, the flow is a *potential flow*:

$$\overrightarrow{V} = \overrightarrow{grad}(\Phi)\,,$$

where Φ is the velocity potential. We can then write the Laplace equation :

$$\nabla^2 \Phi = 0 \text{ inside the fluid domain } \Omega. \tag{2.1}$$

The motion of the sphere is forced and the location of its surface isprescribed by the relation :

$$\begin{aligned} x(\theta) &= R \cdot \cos(\theta) \qquad \theta \in \left[-\tfrac{\pi}{2}; +\tfrac{\pi}{2}\right] \\ y(x,t) &= R \cdot \sin(\arccos(\tfrac{x}{R})) + A_{mp} \cdot \sin(\omega.t) \end{aligned} \tag{2.2}$$

The velocity potential Φ also has to satisfy the Bernoulli equation :

$$\frac{\partial \Phi}{\partial t} - \frac{1}{\rho} \cdot P_l - \frac{1}{2} \cdot (V_n^2 + V_t^2) + g \cdot y = \text{Constant} \tag{2.3}$$

2.2. Boundary and initial conditions

The pressure balance on the free surface can be written:

$$P_l - P_e = -\sigma \cdot C_{surv} \tag{2.4}$$

On the Free Surface, the normal potential variation determines the motion of the FS :

$$\frac{\partial \Phi}{\partial n} = \frac{\partial \eta}{\partial t} \vec{y} . \vec{n} \quad \text{where} \quad \eta = y - Depth_0 \tag{2.5}$$

On the sphere, the potential gradient normal to the sphere surface is set equal to the normal velocity of the sphere surface :

$$\vec{\nabla} \Phi . \vec{n} = \vec{V}_{sph} . \vec{n} \tag{2.6}$$

The initial conditions are the following:
FREE SURFACE :

$$\begin{array}{l} \Phi = 0 \\ \frac{\partial \Phi}{\partial n} = 0 \end{array} \qquad at\ t = 0$$

SPHERE :

$$\begin{array}{l} y = \sqrt{1 - x^2} - A_{mp} \\ \frac{\partial y}{\partial t} = 0 \quad \left(\frac{\partial \Phi}{\partial n} = 0 \right) \end{array} \qquad at\ t = 0$$

This last condition determines the functional form for the speed of the sphere: sine instead of cosine, in order to avoid any discontinuity in the sphere speed.

The radiation condition consists in forcing both the abscissa and ordinate of the node Inf (Fig.3.5.B) not to change. We also impose a minimum *layer of liquid* on the sphere in order to allow the abscissa of the node A not to change. The value of this layer is choosen equal to 5% of the sphere radius.

3. Mathematical resolution

3.1. Laplace equation

We use the Green's identity:

$\iiint_\Omega div(\nabla\Phi)\cdot d\Omega = \iint_S \frac{\partial\Phi}{\partial n}\cdot dS$

to modify the Laplace equation by introducing a regular function Ψ that is C^∞ in our domain Ω (except at a finite number of points):

$0 = \iiint_\Omega \nabla^2\Phi\cdot\Psi\cdot d\Omega = -\iiint_\Omega \nabla\Phi\cdot\nabla\Psi\cdot d\Omega + \iint_S \frac{\partial\Phi}{\partial n}\cdot\Psi\cdot dS$

We can apply the Green's identity on the first term on the right hand side:

$\iiint_\Omega \nabla\Phi\cdot\nabla\Psi\cdot d\Omega = -\iiint_\Omega \Phi\cdot\nabla^2\Psi\cdot d\Omega + \iint_S \Phi\cdot\frac{\partial\Psi}{\partial n}\cdot dS$

And then obtain :

$$\iint_S \frac{\partial\Phi}{\partial n}\cdot\Psi\cdot dS - \iint_S \Phi\cdot\frac{\partial\Psi}{\partial n}\cdot dS + \iiint_\Omega \Phi\cdot\nabla^2\Psi\cdot d\Omega = 0 \qquad (3.1)$$

A convenient function Ψ is :

$\Psi(p,q) = \frac{1}{|p-q|}$ *where* $|p-q| = \sqrt{(x_p-x_q)^2+(y_p-y_q)^2}$

Where p is the point where the influence of every panel is computed, q is a moving point on the panels.

The Laplacian of Ψ is then quite simple : $\nabla_q^2\Psi(p,q) = -\gamma(p)\cdot\delta_p$

δ_p is the delta function: $\delta_p = 1$ at point p, $\delta_p = 0$ anywhere else.

$\gamma(p)$ depends on p $:= 4\pi$ *if* $p \in \Omega$

$= 2\pi$ *if* $p \in S$ (*regular point*)

$= c(p) =$ *solid angle if* $p \in S$ (*angular point*)

And the expression of the third term in equation (3.1) is :

$$\iiint_\Omega \Phi\cdot\nabla^2\Psi\cdot d\Omega = -\gamma(p)\cdot\Phi(p)$$

The final equation is :

$$\iint_S \frac{\partial\Phi}{\partial n}\cdot\Psi\cdot dS - \iint_S \Phi\cdot\frac{\partial\Psi}{\partial n}\cdot dS - \gamma(p)\cdot\Phi(p) = 0 \qquad (3.2)$$

At this step, all the equations are true for both the axisymmetric and the 3D problems. We now consider the axisymmetric problem. We can observe that we have reduced the dimension from 3 to 2. The next step consists in discretizing the boundaries of the free surface and the sphere into panels whose size is discussed in 4.1.1.

The power of the Boundary Element method consists in its ability to solve these integrals once we know either Φ or $\frac{\partial \Phi}{\partial n}$ on the boundaries (there can be a mixing of the two of them). For more complete explanations, the reader may refer to A.A. BECKER 'The Boundary Element Method in Engineering: a complete course'.

We grid the boundaries and then fill the matrix of influence of every panel on each node. The matrix equation system obtained is :

$$[X] \cdot \left[\frac{\partial \Phi}{\partial n}\right] + [Y] \cdot [\Phi] + [Z] = 0$$

As we know Φ for some boundaries and $\frac{\partial \Phi}{\partial n}$ for the others, we can arrange this system to represent it in this way :

$$[A] \cdot \underbrace{\begin{bmatrix} \partial\Phi_1/\partial n \\ \vdots \\ \partial\Phi_i/\partial n \\ \Phi_{i+1} \\ \vdots \\ \Phi_n \end{bmatrix}}_{unknown} = \underbrace{\begin{bmatrix} B_1 \cdot \Phi_1 + C_1 \\ \vdots \\ B_i \cdot \Phi_i + C_i \\ B_{i+1} \cdot \partial\Phi_{i+1}/\partial n + C_{i+1} \\ \vdots \\ B_n \cdot \partial\Phi_n/\partial n + C_n \end{bmatrix}}_{known}$$

The matrix A is fully populated with non-zero coefficients. This would have made too long and imprecise any iterative solution method. The Gaussian elimination has been chosen because of its robustness and absence of iteration.

We then obtain :

$$\begin{bmatrix} \partial\Phi_1/\partial n_1 \\ \vdots \\ \partial\Phi_i/\partial n_i \\ \Phi_{i+1} \\ \vdots \\ \Phi_n \end{bmatrix} = [A]^{-1} \cdot \begin{bmatrix} B_1 \cdot \Phi_1 + C_1 \\ \vdots \\ B_i \cdot \Phi_i + C_i \\ B_{i+1} \cdot \partial\Phi_{i+1}/\partial n_{i+1} + C_{i+1} \\ \vdots \\ B_n \cdot \partial\Phi_n/\partial n_n + C_n \end{bmatrix}$$

At this step, both Φ and $\frac{\partial\Phi}{\partial n}$ are determined at each node and interpolated on each panel. We can now implement these results in the equations.

3.2. Non-dimensionalization

The original code, 2DynaFS, had all its subroutines made to solve non dimensional equations (and therefore needed non-dimensional variables). As we will show below, two characteristic numbers appear in the non-dimensionalization of the Bernoulli equation.

The characteristical scales are :

R = radius of the sphere (L)

$T = \frac{2\pi}{\omega}$ period of sphere motion (T)

ρ = density of the fluid ($M.L^{-3}$)

The other parameters are non dimensionalized according to their units :

$\Phi\ (L^2 \cdot T^{-1})$ $\Psi\ (L^{-1})$ $\nabla\ (L^{-1})$

(3.2) becomes :

$$\iint_S \frac{\partial \Phi}{\partial n} \cdot \Psi \cdot dS - \iint_S \Phi \cdot \frac{\partial \Psi}{\partial n} \cdot dS - \gamma(p) \cdot \Phi(p) = 0$$

$$\iint_S \frac{R^2}{R} \frac{\partial \overline{\Phi}}{\partial \overline{n}} \cdot \frac{1}{R} \overline{\Psi} \cdot R^2 d\overline{S} - \iint_S \frac{R^2}{T} \overline{\Phi} \cdot \frac{1}{R} \frac{\partial \overline{\Psi}}{\partial \overline{n}} \cdot R^2 d\overline{S} - \gamma(p) \cdot \frac{R^2}{T} \overline{\Phi}(p) = 0$$

$$\iint_{\overline{S}} \frac{\partial \overline{\Phi}}{\partial \overline{n}} \cdot \overline{\Psi} \cdot d\overline{S} - \iint_{\overline{S}} \overline{\Phi} \cdot \frac{\partial \overline{\Psi}}{\partial \overline{n}} \cdot d\overline{S} - \gamma(p) \cdot \overline{\Phi}(p) = 0 \qquad (3.3)$$

(2.2) is immediately expressed :

$$\begin{aligned} \overline{x}(\theta) &= -\cos(\theta) \qquad \theta \in [-\pi; +\pi] \\ \overline{y}(x,t) &= \sqrt{1-\overline{x}^2} + \left(\frac{A_{mp}}{R}\right) \cdot \sin(\omega \cdot t) \end{aligned} \qquad (3.4)$$

(2.5) becomes :

$$\begin{aligned} \frac{R}{T} \cdot \frac{\partial \overline{\eta}}{\partial \overline{t}} &= \frac{R^2}{R} \cdot \frac{\partial \overline{\Phi}}{\partial \overline{y}} \\ \frac{\partial \overline{\eta}}{\partial \overline{t}} = \frac{\partial \overline{\Phi}}{\partial \overline{y}} \quad \overline{y} &= \frac{Depth_0}{R} + \overline{\eta}\ (\textit{on the free surface}) \end{aligned} \qquad (3.5)$$

(2.6) becomes :

$$\begin{aligned} \left(\frac{1}{R}\frac{R^2}{T} \cdot R\right) \overrightarrow{\nabla} \overline{\Phi} \cdot \overrightarrow{n} &= \left(\frac{R}{T} \cdot R\right) \overrightarrow{V}_{sph} \cdot \overrightarrow{n} \\ \overrightarrow{\nabla} \overline{\Phi} \cdot \overrightarrow{n} &= \overrightarrow{V}_{sph} \cdot \overrightarrow{n} \quad \textit{on the sphere surface} \end{aligned} \qquad (3.6)$$

3.3. Bernoulli equation

Far from the axis of the sphere motion, Φ is constant, the velocity is 0, $Z = depth_0$, the pressure is P_a. (2.3) can be written :

$$\frac{\partial \Phi}{\partial t} - \frac{P_l}{\rho} - \frac{1}{2} \cdot (V_n^2 + V_t^2) + g \cdot Z = 0 - \frac{P_a}{\rho} - 0 + g \cdot depth_0$$
$$\frac{\partial \Phi}{\partial t} = \frac{(P_l - P_a)}{\rho} + \frac{1}{2} \cdot (V_n^2 + V_t^2) - g \cdot (Y - depth_0)$$

If we insert (2.4) :

$$P_l - P_a = -\sigma \cdot C_{urv}$$
$$\eta = Y - depth_0$$

We finally obtain :

$$\frac{\partial \Phi}{\partial t} = \frac{1}{2} \cdot (V_n^2 + V_t^2) - g \cdot \eta - \frac{\sigma \cdot C_{urv}}{\rho}$$

Units of additional parameters : $\sigma\ (M.T^{-2})$ $C_{urv}\ (L^{-1})$ $P\ (M.L^{-1}.T^{-2})$

$$\frac{\partial \overline{\Phi}}{\partial t}\frac{R^2}{T^2} = \frac{1}{2}\frac{R^2}{T^2} \cdot (\overline{V_n^2} + \overline{V_t^2}) - g \cdot R \cdot \overline{\eta} - \frac{\sigma}{\rho} \cdot \frac{1}{R}\overline{C_{urv}}$$
$$\frac{\partial \overline{\Phi}}{\partial t} = \frac{1}{2} \cdot \overline{(V_n^2 + V_t^2)} - \left(g\frac{T^2}{R}\right) \cdot \overline{\eta} - \left(\frac{\sigma}{\rho}\frac{T^2}{R^3}\right) \cdot \overline{C_{urv}}$$

$$\frac{\partial \overline{\Phi}}{\partial \overline{t}} = \frac{1}{2} \cdot (\overline{V}_n^2 + \overline{V}_t^2) - \mathrm{Fr} \cdot \overline{\eta} - \frac{1}{\mathcal{W}eb} \cdot \overline{C_{urv}} \qquad (3.7)$$

$$\mathcal{F}r = \left(g\frac{T^2}{R}\right) \qquad \mathcal{W}eb = \left(\frac{\rho}{\sigma}\frac{R^3}{T^2}\right)$$

Here $\mathcal{F}$r is the $\mathcal{F}$roude number and $\mathcal{W}$eb is the $\mathcal{W}$eber number.

3.4. Implementation

With $\frac{\partial\Phi}{\partial n}$ on each panel,a subroutine computes the velocities of the nodes:

$$RT_i = \frac{\Phi_{i+1}-\Phi_i}{\text{distance(node i, node i+1)}} \qquad Vn_{i+1} = \frac{\partial\Phi}{\partial n}_i + \left(\frac{\partial\Phi}{\partial n}_{i+1} - \frac{\partial\Phi}{\partial n}_i\right)\cdot ds$$

$$RR_i = \left(\frac{\partial\Phi}{\partial n}\cdot\vec{n}.\vec{y} - RT\cdot\vec{n}.\vec{x}\right)_i \qquad Vt_{i+1} = RT_i + (RT_{i+1} - RT_i)\cdot ds$$

$$RZ_i = \left(\frac{\partial\Phi}{\partial n}\cdot\vec{n}.\vec{x} + RT\cdot\vec{n}.\vec{y}\right)_i \qquad Vr_{i+1} = RR_i + (RR_{i+1} - RR_i)\cdot ds$$

$$Vz_{i+1} = RZ_i + (RZ_{i+1} - RZ_i)\cdot ds$$

The indices i refers to the spatial gridding. All these results will now only have the extension *new*.

The code determines the time step: $ht = D\Phi_{\max}\cdot\frac{1}{1+\frac{1}{2}V_m^2}$. Here $D\Phi_{\max}$ is an input parameter, equal to 10^{-2} for all the runs ; V_m is the highest velocity computed at the nodes. This is made to keep the velocities in a limited range to avoid both unnecessary long runs and error in the time stepping. The displacements of the nodes are as followed:

$$x_{new} = x_{prev} + \frac{1}{2}\cdot(Vr_{new} + Vr_{prev})\cdot ht$$
$$y_{new} = y_{prev} + \frac{1}{2}\cdot(Vz_{new} + Vz_{prev})\cdot ht$$

and we can determine the positions of the panels. A subroutine gets the curvature of the free surface.

The code can then compute $\frac{\partial\Phi}{\partial t}$ thanks to the non-dimensional Bernoulli equation :

$$\frac{\partial\overline{\Phi}}{\partial\overline{t}} = \frac{1}{2}\cdot(\overline{V}_n^2 + \overline{V}_t^2) - \mathcal{F}r\cdot\overline{\eta} - \frac{1}{We b}\cdot\overline{C_{urv}}$$

With the previous values of Φ, we can then obtain the new value of the potential Φ:

$$\overline{\Phi}_{new} = \overline{\Phi}_{prev} + \frac{1}{2}\cdot\left(\frac{\partial\overline{\Phi}}{\partial\overline{t}}_{new} + \frac{\partial\overline{\Phi}}{\partial\overline{t}}_{prev}\right)\cdot ht$$

The code averages the variations of the velocities and the potential normal derivatives. This is made to minimize error accumulation.

The code realizes a regridding if necessary, implements the absolute time with the time step and then use the new values of Φ and $\frac{\partial\Phi}{\partial n}$ to redo the same work. The code ends when the time exceeds an imposed limit : FT.

3.5. Gridding

The Boundary Element Method consists in computing integrals of the influence of panels on each node. The gridding is important to obtain valid results.

In this code, the distribution of the nodes on the sphere is uniform (fig. 3.5.B). The length of the panels is constant and equal to $0.1416 * R$. This length was choosen because of the curvature of a sphere: 10 panels on half a perimeter make the gridding of the sphere precise enough.

The free surface is regularly gridded from the node we assume to be at infinity to the axis (fig. 3.5.A) but the distance between the nodes may change in time. The code calculates, at each time step, the position of each node. It then interpolates the positions of the points between the nodes. The code can then regrid the free surface in order to concentrate the panels in the fast moving zones. This option is important when the amplitude of the free surface becomes large.

The node we assume to have the highest displacement is the node above the top of the sphere. This node, number $nseg + 1$ is called *node A*.

3.6. Computational power

The codes were ran on three computers:

Computer:		*Capacity:*
MIPS RISComputer	RS 2030	12 million instructions per second
MIPS RISComputer	RC 3240	20 million instructions per second
Silicon Graphics	IRIS Indigo	85 million instructions per second

3.7. Data analysis

The code generates two data files: POLES which contains the ordinate of nodes A, B and C (Fig. 3.5.B) every 10 time steps; and 2DCONTC which contains the coordinates of every nodes - sphere and free surface - every 100 time steps.

We only focus on the node A because we estimate that the history of its ordinate has the largest variations. The second reason consists in that the abscissa of only two points cannot vary: node A and node Inf. As the node Inf is supposed not to move, we follow the *node A*.

We wrote a small fortran code, spectral.f (Appendix B), to analyze the POLES data. A subroutine calculates the *Fourier transformation* of the ordinate of node A. As the time step may vary, this transformation read the current time step in POLES. The evolution of node B (the top of the sphere Fig. 3.5.B) is also analyzed as a reference. A subroutine determines the maxima of the transform and arranges them in decreasing order.

The frequency that has the *largest weight* will be refered as the *first frequency*, the frequency that has the *second largest weight* will be refered as the *second frequency*.

Another subroutine computes the time average of the ordinate of node A, the result is *Average pos*. The code then determines the amplitude of all the half periods of A and then divides their sum by the number of amplitudes computed; the result is *Amplitude*.

$$Average\ pos\ = \frac{1}{\overline{FT}} \sum_{t=0}^{\overline{t}=\overline{FT}} \left\{ \overline{Y}_A(\overline{t}) \cdot \overline{ht}(\overline{t}) \right\}$$
$$Amplitude = \frac{1}{N_{HP}} \sum_{i=1}^{i=N_{HP}} \overline{A}_i$$

These computations are explained on the figure 3.7.A in Appendix A.

The second file 2DCONTC is used to obtain graphic representation of the evolution of the free surface. We wrote a fortran code, smart.f (Appendix B), to represent the evolution of the free surface in time, using a convenient format:

$abscissa = abscissa - \frac{\sqrt{2}}{2} \cdot Time$

$ordinate = ordinate - \frac{\sqrt{2}}{2} \cdot Time$

These figures are shown in 3.7.B in the Appendix A.

4. Results and Interpretations

4.1. Reference run

4.1.1. Panel-Width

The first part of the runs consisted in determining the range of validity of the code. We first focused on the size of the panels on the Free Surface. This was made in order to have the widest panels but without any larger than $\frac{1}{8}$ of the wave length of the generated waves when the amplitude was above $\frac{1}{8}$ of the wave length of these waves. The average size that we determined is $\frac{1}{2}$ *of the Sphere radius* :R.

On the sphere, the size of the panels is : $\frac{\pi}{10} \cdot R \simeq 0.3142 * R$

Figures 3.5.B

4.1.2. Free Surface Width

We then determined the width of the Free Surface (fig. 3.5.A). We wanted to have the smallest free surface without any change in the results (the indicator was the behavior of node A). It appeared that this FS-width is in some way related to the frequency of the sphere movement : FS-Width$_{\text{min}} = 20\ R$ for $\omega > 4\ \frac{rad}{s}$. When $\omega = 2\ \frac{rad}{s}$ and FS-Width= 40 R, the history of the node we are following does not match the history of the same node when FS-Width= $20R$ for more than 5 periods. These both conditions are valid for our runs.

The number of panels is related to the FS-Width: as the panel size is $\frac{1}{2}R$, the number of panels on the free surface is $n_{FS} = 2 \cdot \overline{FS - Width}$. As the computation time is related to n^3, where n is the number of panels, we definitely needed to have the smallest value for n. We decided to keep the sphere pulsation $\omega > 7.5$ in order to be allowed to have $n = 10 + 20 \cdot 2 = 50$ *panels.*

4.1.3. Initial depth of the sphere

In the series I.1 (1 to 6), the initial depth is the only parameter that changes. The goal was to obtain the largest deformation but still stay in a parameter range in which the calculations are stable. The code is not made to deal with the sphere contacting the air. With an initial depth below $1.5R$, the code failed to compute 20 periods because a liquid separation appeared (drop).

The average position of the node A (Fig. 4.1.3.A) is equal to the initial depth as long as the initial depth is larger than 2.5 R. At smaller initial depths, the average position stays above the initial depth as if there were a natural layer of water on the sphere. We can easily check that this layer is not the imposed layer because its value is between $\frac{1}{5}R$ and $\frac{1}{2}R$ as the imposed layer was $\frac{1}{20}R$.

The amplitude increases as the initial depth decreases, keeping the variation of the sum of Average position and Amplitude small compared to the magnitude of this sum.

We can now notice that when the initial depth is 2.25 R, neither the amplitude nor the average position seem to follow the general trend. We might be in a particular case where the conditions imposed excite a resonant frequency of the system.

A run was made with an initial depth $= 10 \cdot R$. This was to check the validity of the code without the FS / SPhere interactions. We can observe that the amplitude is almost null and the spectral distribution is then quite flat.

In all these runs, the main frequency is always 1*sphere frequency (Fig. 4.1.3.B). Its weight in the spectrum is always the highest one (Fig. 4.1.3.C) and above 40%. This means that with these conditions, the response of the FS is periodic with the same period as the excitation.

The second frequency, 1.15*sphere-freq in most of the cases, can be interpreted as a modulation of the main signal by one of its harmonic responses whose frequency is $\frac{1}{7}$ of the main frequency:

$$y = \left(Amp + B \cdot \cos(\tfrac{\omega \cdot t}{7})\right) \cdot \cos(\omega . t)$$

$$y = Amp \cdot \cos(\omega \cdot t) + B \cdot \cos(\tfrac{\omega \cdot t}{7}) \cdot \cos(\omega \cdot t)$$

$$y = Amp \cdot \cos(\omega \cdot t) + B \cdot \left(\cos(\tfrac{\omega \cdot t}{7} + \omega \cdot t) + \cos(\tfrac{\omega \cdot t}{7} - \omega \cdot t)\right)$$

$$y = Amp \cdot \cos(\omega \cdot t) + B . \cos(\tfrac{8}{7} \cdot \omega \cdot t) + B \cdot \cos(\tfrac{6}{7} \cdot \omega \cdot t)$$

$\frac{8}{7} \simeq 1.15 \qquad (\frac{6}{7} \simeq .85)$

4.1.4. Sphere frequency

The series I.2 (8 to 13) have ω as varying parameter. The $\mathcal{F}$roude and $\mathcal{W}$eber numbers are both varying with ω :

$$\mathcal{F}r = g \cdot \frac{T^2}{R} = g \cdot \frac{4\pi^2}{R \cdot \omega^2}$$
$$\mathcal{W}eb = \frac{\rho}{\sigma} \cdot \frac{R^3 \cdot \omega^2}{4\pi^2}$$

As ω increases, $\mathcal{F}$r decreases and $\mathcal{W}$eb increases. We can see that in the Bernoulli equation (3.7) : $\frac{\partial \overline{\Phi}}{\partial t} = \frac{1}{2} \cdot (\overline{V_n^2} + \overline{V_S^2}) - \mathcal{F}r \cdot \overline{\eta} - \frac{1}{\mathcal{W}eb} \cdot \overline{C_{surv}}$

gravity ($\mathcal{F}$r) and surface tension ($\mathcal{W}$eb) yield their importance to the inertial effects.

As ω increases, the average position increases and the amplitude decreases. On figures 4.1.4 we can see that the sum of Average Pos and Amplitude varies smoothly with ω.

We must be aware that in the meantime, the characteristics of the excitation have changed. We will only be able to further this study when the importance of the $\mathcal{F}$roude and $\mathcal{W}$eber numbers will be better known.

4.1.5. Amplitude

The amplitude of the sphere displacement were kept equal to R . This was kept constant in order to only focus on the effect of the $\mathcal{F}$roude and $\mathcal{W}$eber numbers. We are here mainly interested in large amplitudes. The reader may refer to A.Ergin Journal of Ship Research Vol.36 1992 for experiments with small amplitudes.

4.2. Importance of the surface tension

The effect of the surface tension is expressed in the Bernoulli equation through the inverse of the *W*eber number. In our runs we decreasesd the *W*eber number from 1394 to $\frac{1}{5}$ while maintaining the values of the other parameters (gravity and inertia).

The figures 4.2 A, B and C show us that the ***surface tension has no real effect*** on the FS deformation either for the amplitude or for the frequencies or their distibution.

$$\Delta Average\ Pos_{max} = 0.7\%$$
$$\Delta Amplitude_{max} = 0.8\%$$
$$\Delta Frequency\ 1 = 0 \quad \Delta Frequency\ 2 = 0$$
$$\Delta Weight\ 1 = 4\% \quad \Delta Weight\ 2 = 13\%$$

The average amplitude remains constant as the *W*eber number decreases; its value smoothly increases as *W*eber number is less than 1 (coefficient greater than 1).This case is reached when the surface tension is greater than 100. This value of the coefficient could be reached when the radius of the sphere is very small (but the *F*roude number would then be very large).

The high variation of the Weight of the second frequency indicates the beginning of the zone where the Surface Tension effect should no more be neglected.

4.3. Importance of the gravity

The effect of the gravity is expressed in the Bernoulli equation through the $\mathcal{F}$roude number. We noticed in the previous paragraph that the surface tension had no effect on the deformations of the FS, so the Bernoulli equation can be written :

$$\frac{\partial \overline{\Phi}}{\partial t} = \frac{1}{2} \cdot (\overline{V}_n^2 + \overline{V}_S^2) \underbrace{- \mathcal{F}r \cdot \overline{\eta}}_{gravity} \tag{4.1}$$

As there is no coefficient for the inertia effect, we can only increase or decrease the importance of the gravity. In many studies, the cases considered have either a $\mathcal{F}r \gg 1$ or $\mathcal{F}r \ll 1$ in order to either consider the gravity as the main effect or neglect it to easily linearize the Bernoulli equation.

As we have no intention to linearize this equation, it appeared interesting to study the particular case of $\mathcal{F}r \simeq 1$. The results can be observed in the series II.1, figures 4.3. A, B and C.

In these figures, ?!? show the aborted runs (less than 20 periods) caused by the apparition of drops; in these particular cases the results are altered by too limited data analysed.

The average position (Fig. 4.3.A) of the node A has no large variations (maximum 5%) except in the case $\mathcal{F}r \approx \frac{1}{10}$ but this case could be interpreted as the beginning of the category $\mathcal{F}r \ll 1$.

The amplitude seems to increase with the $\mathcal{F}$roude number. We can expect a physical limit to this amplitude because of the energy limitation.

Except in the runs #55 and #51b that failed to compute the 20 periods, the sphere frequency always appears in the wave frequencies (Fig. 4.3.B) with the first or second highest weight. The value of the harmonic frequency increases from $\frac{1}{10}$ to 1 as $\mathcal{F}r$ increases from $\frac{1}{10}$ to 50. Then the value of this harmonic frequency, after a short stay at $\simeq 1.15$, seems to drop to $\frac{1}{10}$ and then re-increase but at a slower rate than in the previous zone.

The fast decay of the weights (Fig. 4.3.C) of both the first and second frquencies reduces the meaning of the values of these frequencies. But we can also understand this decay as a flater spectrum of the wave frequencies as the $\mathcal{F}$roude number increases. When the sum of the weights of the two first frequencies becomes smaller than 40%, this diffusion of the frequencies is too important to consider any regular oscillations.

4.4. Experiments

The experimental setup is descibed in figure 1. The phenomena were recorded on a video tape from 3 points of view, always in the vertical mid-plane of theside of the tank. The first view is in the plane of the free surface. The second one is looking down at the free surface at an angle $\approx 30°$ to the horizontal. The third one is looking up at the free suface at an angle $\approx 15°$.

The experiments were made with a ping-pong ball $R = \frac{1}{2}\ inch$. The tank was square of width equal to $2 * 3\ feet$ and then $free\ surface\ width = 2 * 12 * 3R = 72R$. The frequency of the sphere was in the range $2.3Hz$ *to* $8Hz$. As the free surface is larger than $60R$, the results obtained for the small sphere frequencies are valid.

The initial depths (non dimensional) studied are 1.8, 1.6, 1.4. 1.2. In the last experiment, the sphere gets in contact with the air.

The experiments show that as the sphere frequency increases, the amplitude of the waves decreases. This verifies the global trend of the results obtained in the series I.2.

We also noticed, and this may be a consequence of the amplitude decay, that the perturbed zone around the sphere decreases as the sphere frequency increases. This phenomena is consistent with the numerical calculations in the series I.3 and supports the values selected for the free surface width and the sphere frequency range for the calculations.

5. Conclusions

The study shows that, when s sphere is oscillating below the free surface at low frequencies, the surface tension can be neglected. The average amplitude of the free surface waves increases with the gravity and a resonance mode may exist. The average amplitude is also related to the inverse of the the sphere frequency and the experimental observations validated this important phenomena (relation to the free surface width and then to the computational time).

The experiments we conducted support the choices we made for the reference parameters and the experimental observations are consistent with the trends of average amplitude and average position predicted by the numerical calculations.

6. Appendix A

Figure 3.5.A : Physical definition of the free surface
Figure 3.5.B : Gridding definition
Figure 1 : Experimental setup
Figure 3.7. : Definition of the data analysis
Figure 4.1.2 : Comparison 40/80 panels run #3 & #3b
Figure 4.1.2 : Comparison 40/120 panels run #8 & #8b
Figure I : Datas sheet series I
Figure 4.1.3.A, Abis, Ater : Deformation versus initial depth
Figure 4.1.3.B : Waves frequencies versus initial depth
Figure 4.1.3.C : Weights repartition versus inital depth
Figure 4.1.4.A, Abis : Deformation versus sphere frequency
Figure 4.1.4.B, Bbis : Waves frequencies versus sphere frequency
Figure 4.1.4.C : Weights repartition versus sphere frequency
Figure II : Datas sheet series II
Figure 4.2.A, Abis : Deformation versus Weber number
Figure 4.2.B : Wave frequencies versus Weber number
Figure 4.2.C : Weights repartition versus Weber number
Figure 4.3.A,Abis : Deformation versus Froude number
Figure 4.3.B, Bbis : Waves frequencies versus Froude number
Figure 4.3.C, Cbis : Weights repartition versus Froude number
Figure 3.7.B : semi 3D visualization : run#3 : reference
Figure 3.7.B : semi 3D visualization : run#54 : reflecting waves
Figure 3.7.B : semi 3D visualization : run#54 : standing waves
Figure 3.7.B : semi 3D visualization : run#3 : reference

7. Appendix B

Fortran code spectral.f : data analysis (Fourier transformation)
Fortran code smart.f : semi 3D visualization

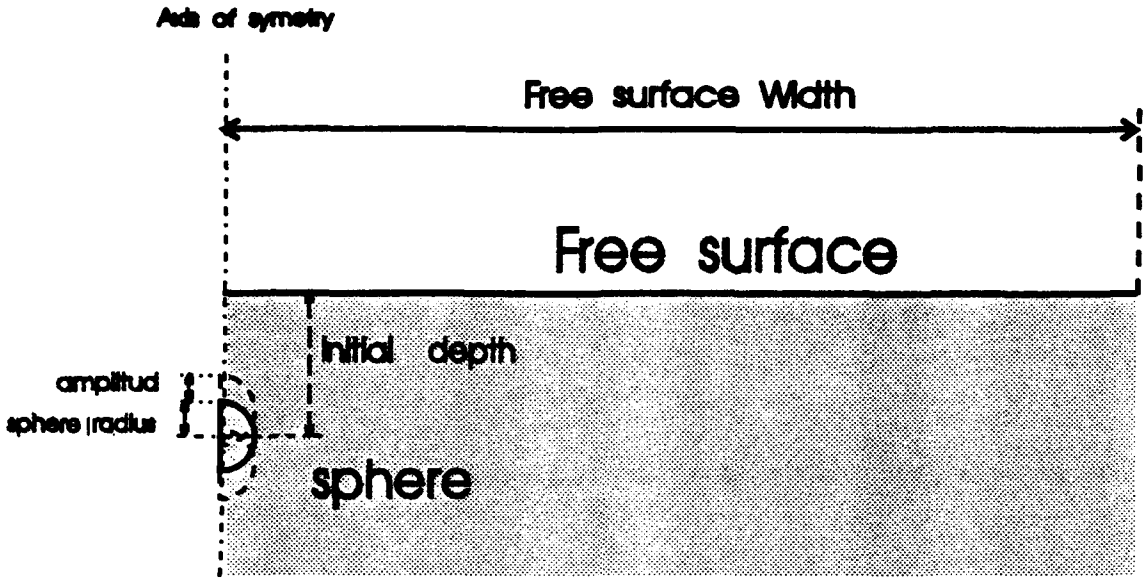

Fig. 3.5.A

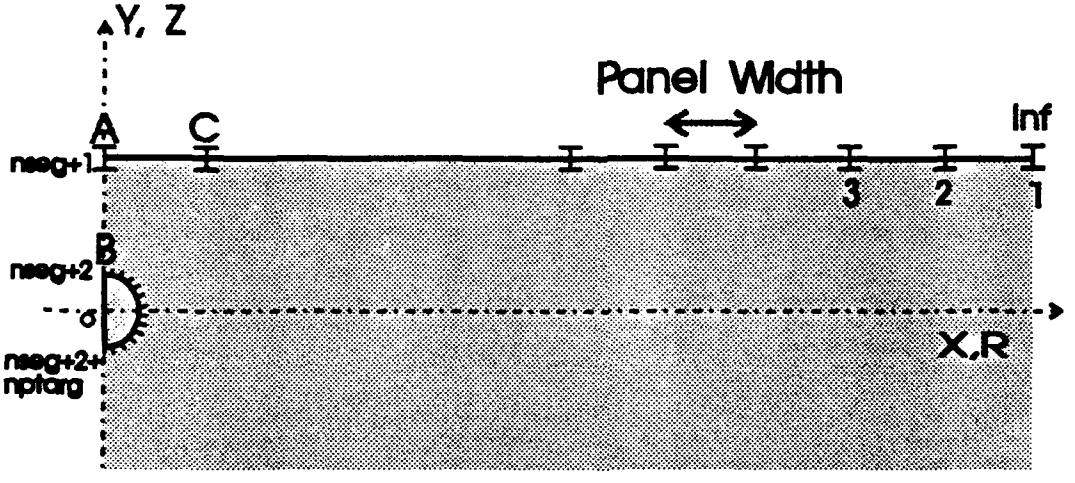

Fig. 3.5.B

Experimental Setup

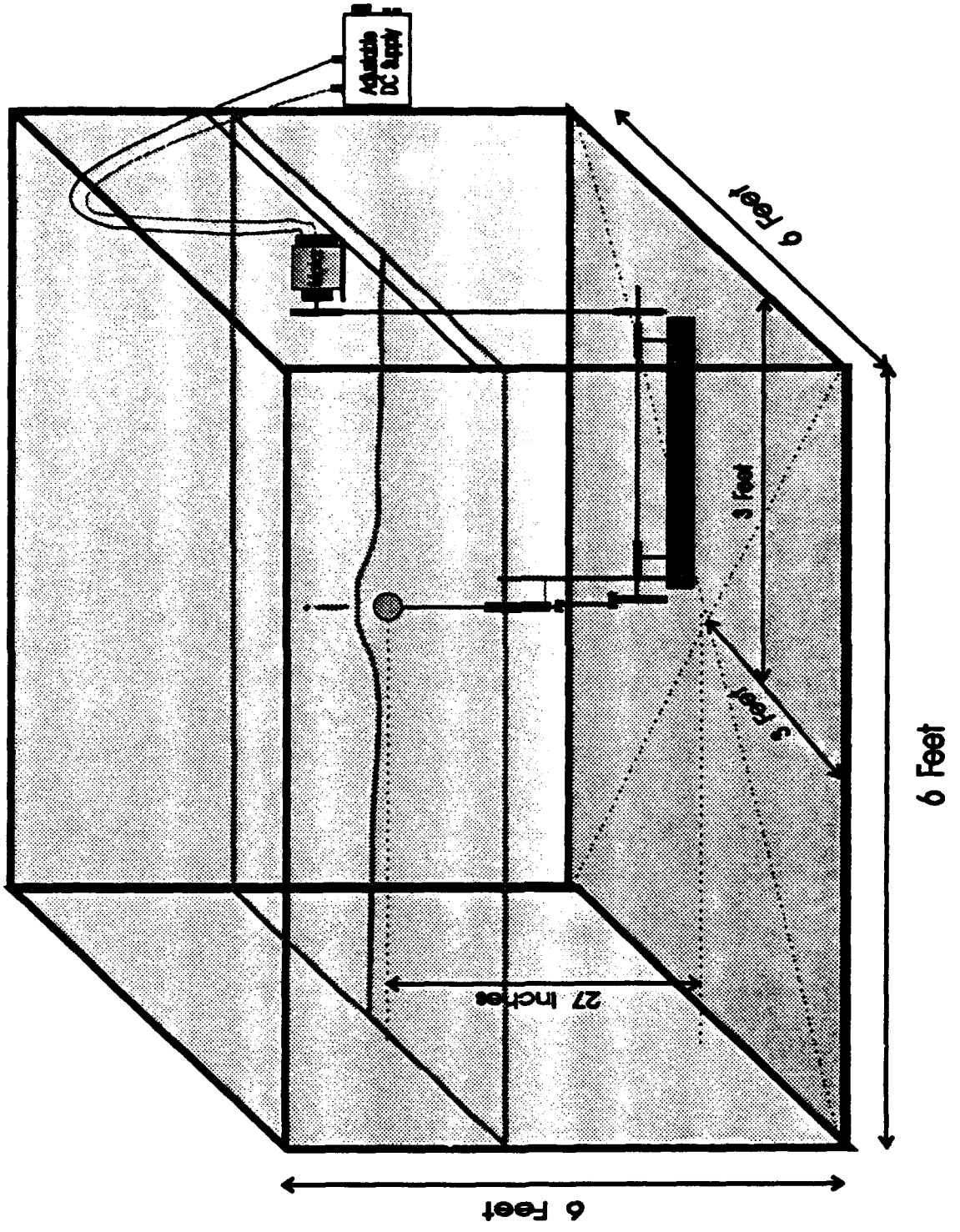

Fig. 1

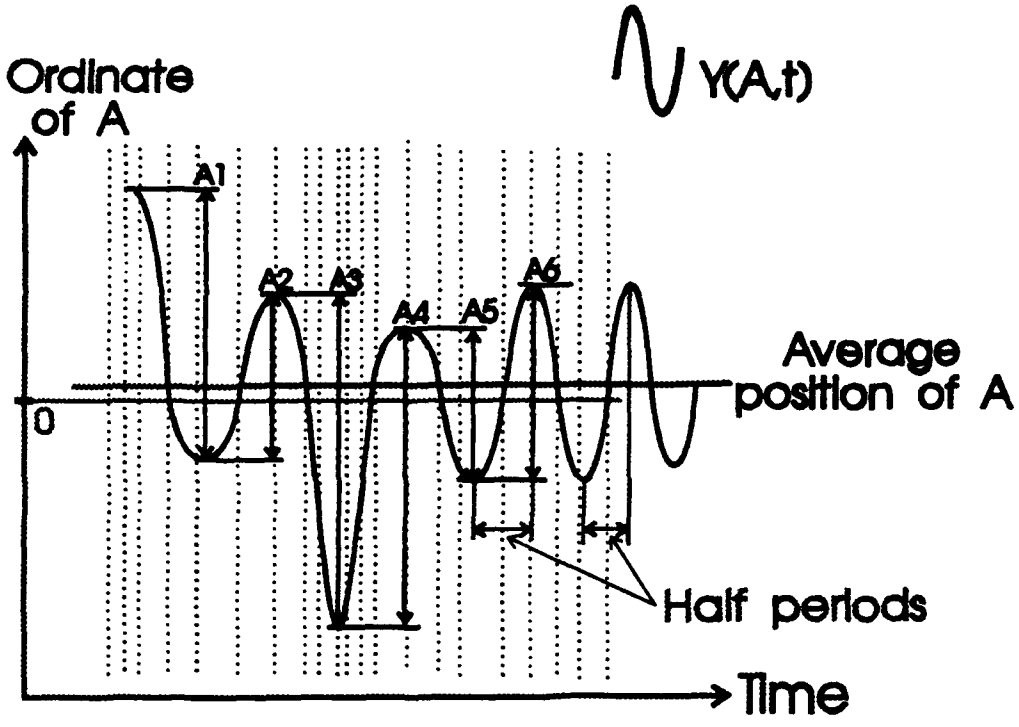

Fig. 3.7

The doted lines symbolise the time stepping: large time step when the speed of the nodes is small; small time step when the speed of the nodes is large.

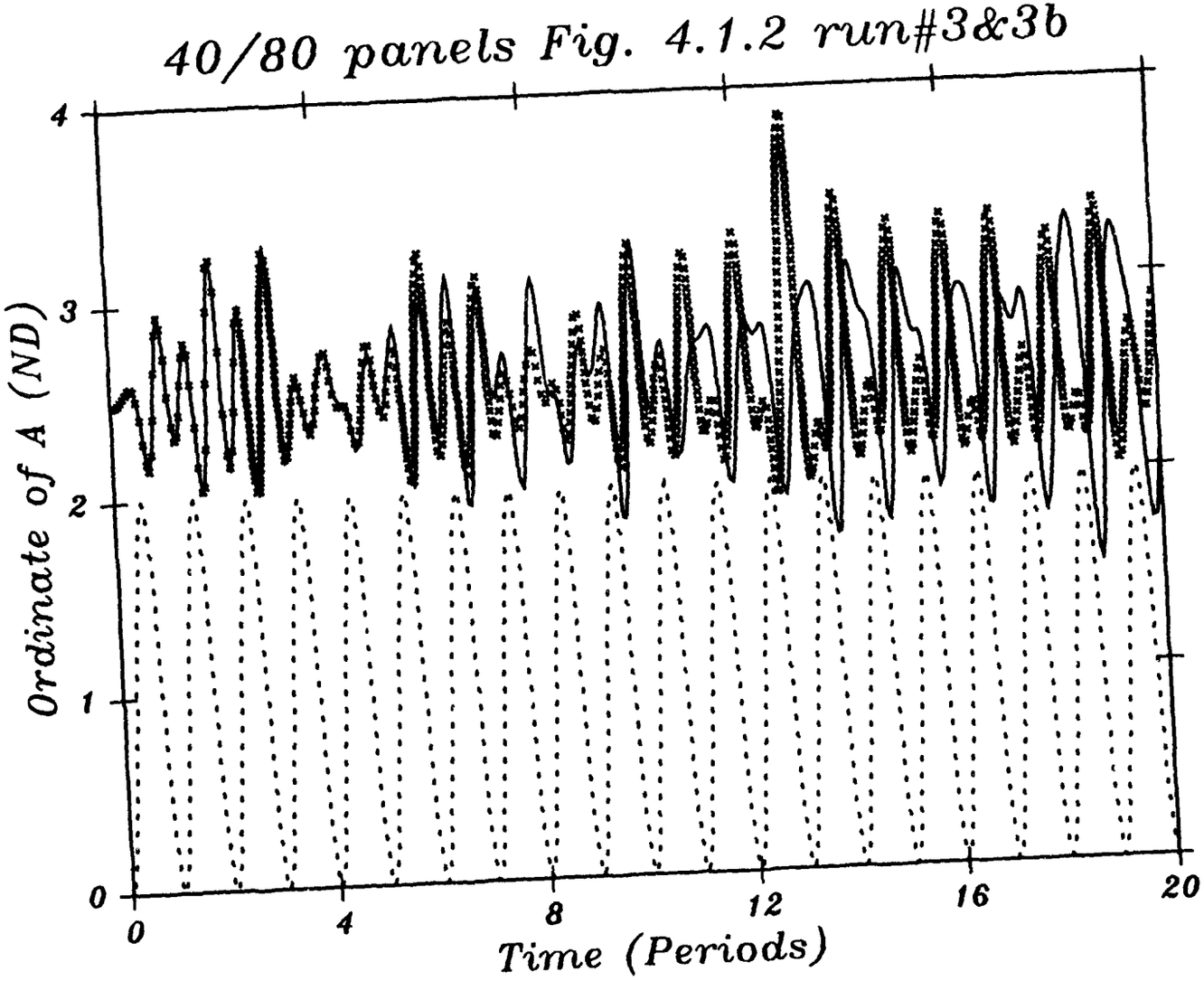

yenn: psy polva3 -a0 -y2 polva3b -a0 -y2,1 479 -aTime (Periods) -bOrdinate of A (ND) -c40/80 panels Fig. 4.1.2 run#3&3b

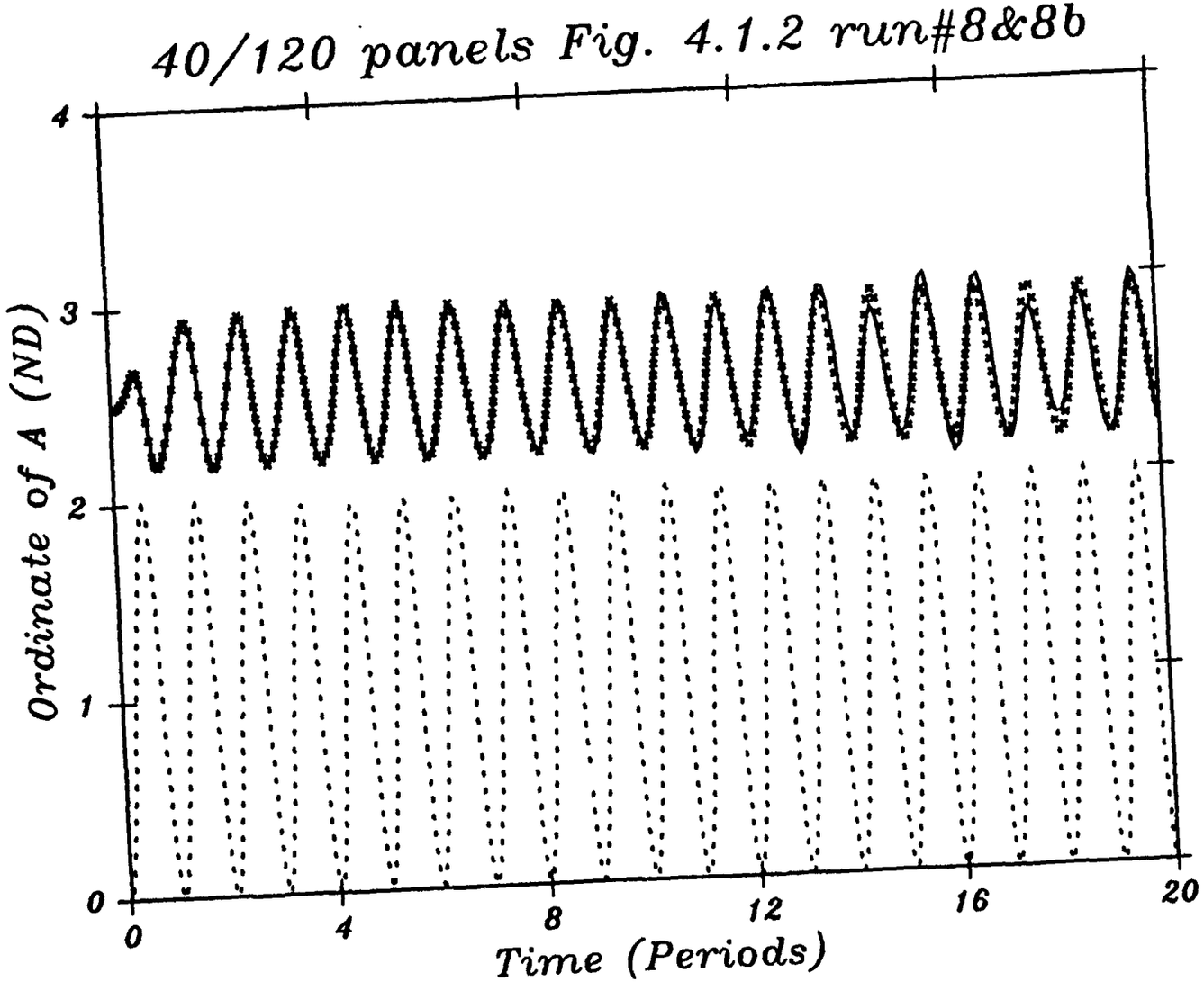
40/120 panels Fig. 4.1.2 run#8&8b
Ordinate of A (ND)
Time (Periods)
0
1
2
3
4
0
4
8
12
16
20

# exp	R	A/R	H/R	Wid/R	Pulse	FROUDE	WEBER	?	NB	Average pos	Amplitude	SP freq	freq 1	Wgth 1	freq 2	Wgth 2
	(m)	-	-	-	(1/s)	-	-			R	R	Hz	sphere freq	%	sphere freq	%
98	1	1	10	20	2	96.82066	1391.7769	OK		10	0.0188	0.31831	1	26	0.7	25
1	1	1	4	20	2	96.82066	1391.7769	OK		4.017402	0.433712	0.31831	1	49	1.15	19
2	1	1	3	20	2	96.82066	1391.7769	OK		3.0247	0.62669	0.31831	1	49	1.15	13
3	1	1	2.5	20	2	96.82066	1391.7769	OK	REF	2.5444	0.72249	0.31831	1	50	1.15	15
3b	1	1	2.25	20	2	96.82066	1391.7769	OK	1.3 / 15	2.5563	1.6486	0.31831	1	22	1.45	20
4	1	1	2	20	2	96.82066	1391.7769	OK		2.19	1.2539	0.31831	1	39	1.15	13
4b	1	1	1.75	20	2	96.82066	1391.7769	Blow-up	sev att.	1.9871	1.7919	0.31831	1	100	0	0
5	1	1	1.5	20	2	96.82066	1391.7769	OK		2.0147	3.1078	0.31831	1	34	0.58	15
6	1	1	1	20	2	96.82066	1391.7769	Blow-up	sev att.	-	-	0.31831	-	-	-	-
3	1	1	2.5	20	2	96.82066	1391.7769	OK	REF	2.5444	0.72249	0.31831	1	50	1.15	15
8	1	1	2.5	20	4	24.20516	5567.1074	OK		2.5632	0.72064	0.63662	1	73	0.7	9
9	1	1	2.5	20	8	6.051291	22268.43	OK		2.6529	0.59915	1.273241	0.5	43	1	23
95	1	1	2.5	20	12	2.689463	50103.967	OK		2.5774	0.24387	1.909861	1	81	0.35	7
10	1	1	2.5	20	16	1.512823	89073.719	OK		2.6168	0.22745	2.546481	1	70	0.25	11
105	1	1	2.5	20	20	0.968207	139177.69	OK		2.6591	0.20996	3.183102	1	64	0.2	15
11	1	1	2.5	20	32	0.378206	356294.87	OK		2.7864	0.17179	5.092962	1	43	0.15	36
12	1	1	2.5	20	64	0.094551	1425179.5	OK		3.1215	0.12071	10.18592	0.1	65	1	22
13	1	1	2.5	20	128	0.023638	5700718	OK	100 T	3.5225	0.08876	20.37185	0.02	61	0.08	15
3b	1	1	2.5	40	2	96.82066	1391.7769	OK	DISM 3/4	2.5569	0.66122	0.31831	1	47	1.2	13
8b	1	1	2.5	60	4	24.20516	5567.1074	OK	MATCH	2.5617	0.71716	0.63662	1	93	-	-
9b	1	1	2.5	60	8	6.051291	22268.43	OK	MATCH	2.6537	0.60282	1.273241	0.5	44	1	23
11b	1	1	2.5	60	32	0.378206	356294.87	OK	MATCH	2.7866	0.17322	5.092962	1	43	0.15	36

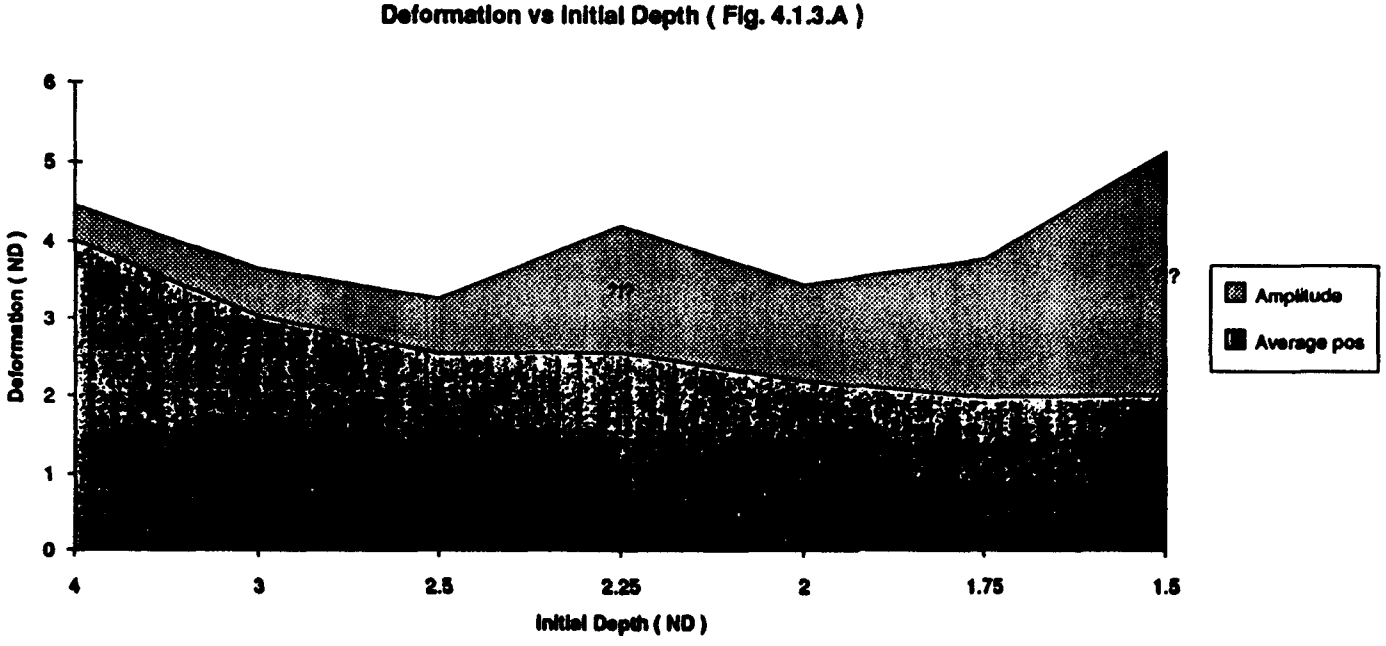
Deformation vs Initial Depth (Fig. 4.1.3.A)
Deformation (ND)
0
1
2
3
4
5
6
4
3
2.5
2.25
2
1.75
1.5
Initial Depth (ND)
Amplitude
Average pos

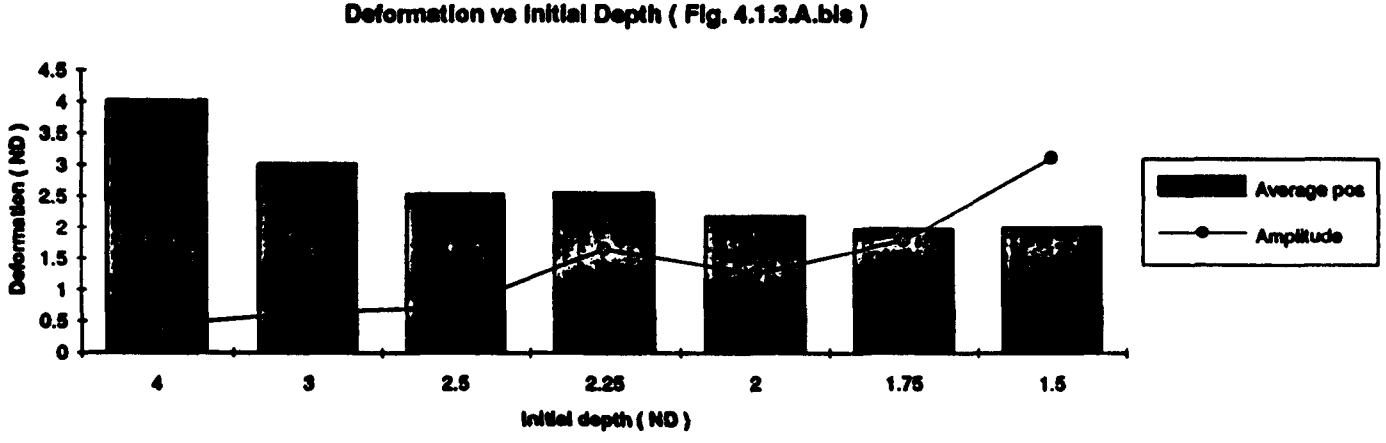
Deformation vs Initial Depth (Fig. 4.1.3.A.bis)
Deformation (ND)
0
0.5
1
1.5
2
2.5
3
3.5
4
4.5
4
3
2.5
2.25
2
1.75
1.5
Initial depth (ND)
Average pos
Amplitude

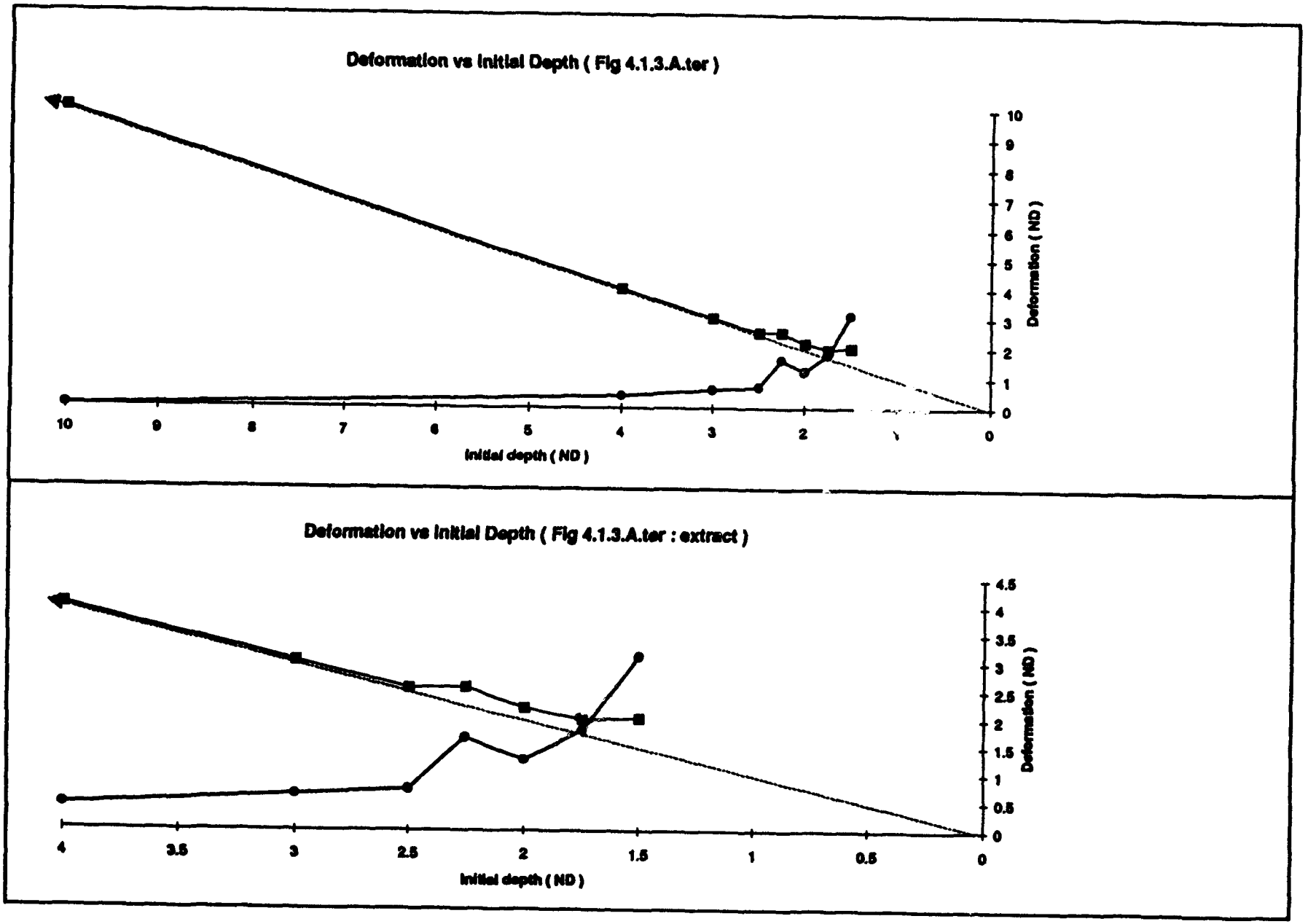
Deformation vs Initial Depth (Fig 4.1.3.A.ter)
10
9
8
7
6
5
4
3
2
1
0
Deformation (ND)
10
9
8
7
6
5
4
3
2
0
Initial depth (ND)
Deformation vs Initial Depth (Fig 4.1.3.A.ter : extract)
4.5
4
3.5
3
2.5
2
1.5
1
0.5
0
Deformation (ND)
4
3.5
3
2.5
2
1.5
1
0.5
0
Initial depth (ND)

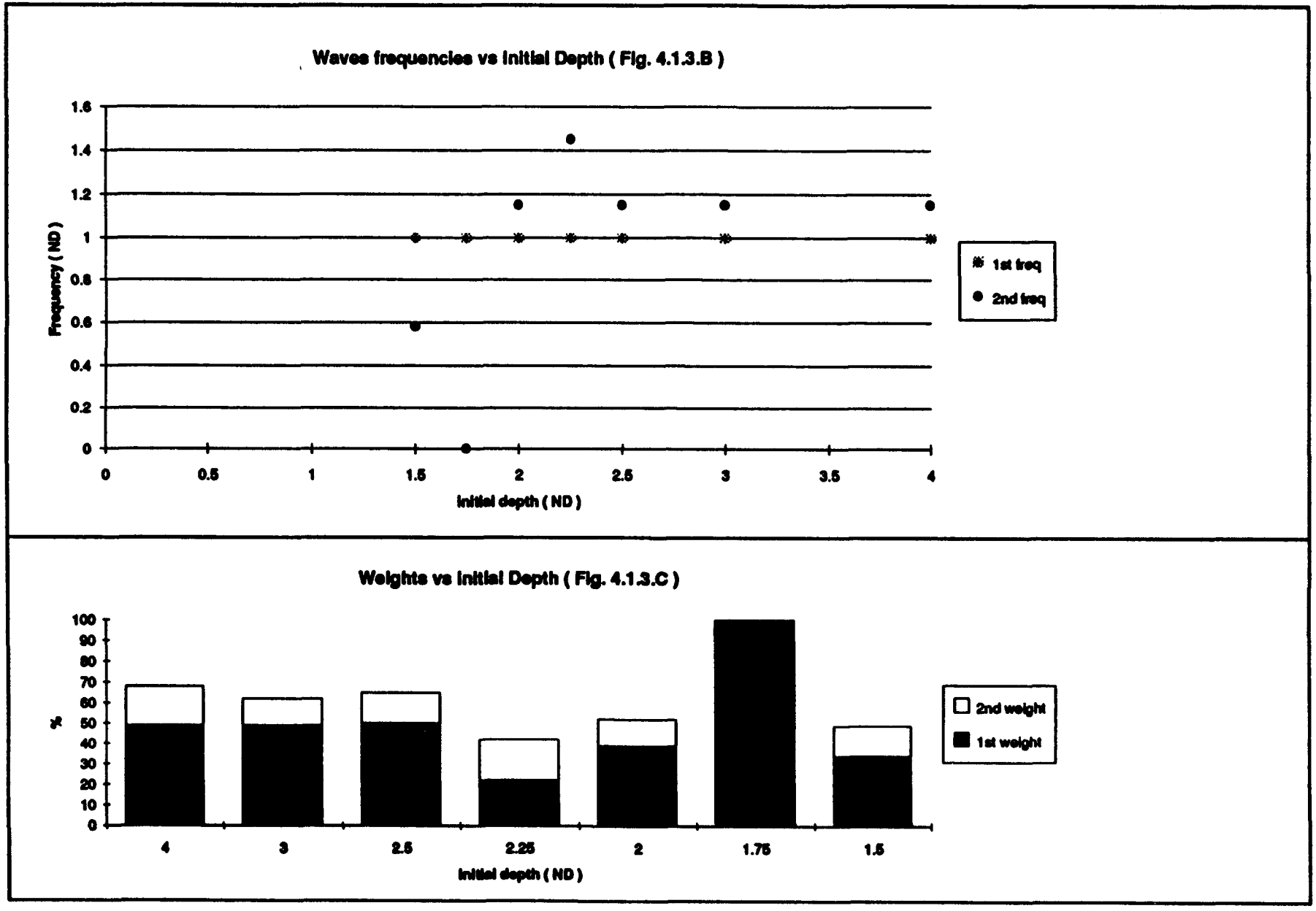
Waves frequencies vs Initial Depth (Fig. 4.1.3.B)
Frequency (ND)
1.6
1.4
1.2
1
0.8
0.6
0.4
0.2
0
0
0.5
1
1.5
2
2.5
3
3.5
4
Initial depth (ND)
1st freq
2nd freq
Weights vs Initial Depth (Fig. 4.1.3.C)
%
100
90
80
70
60
50
40
30
20
10
0
4
3
2.5
2.25
2
1.75
1.5
Initial depth (ND)
2nd weight
1st weight

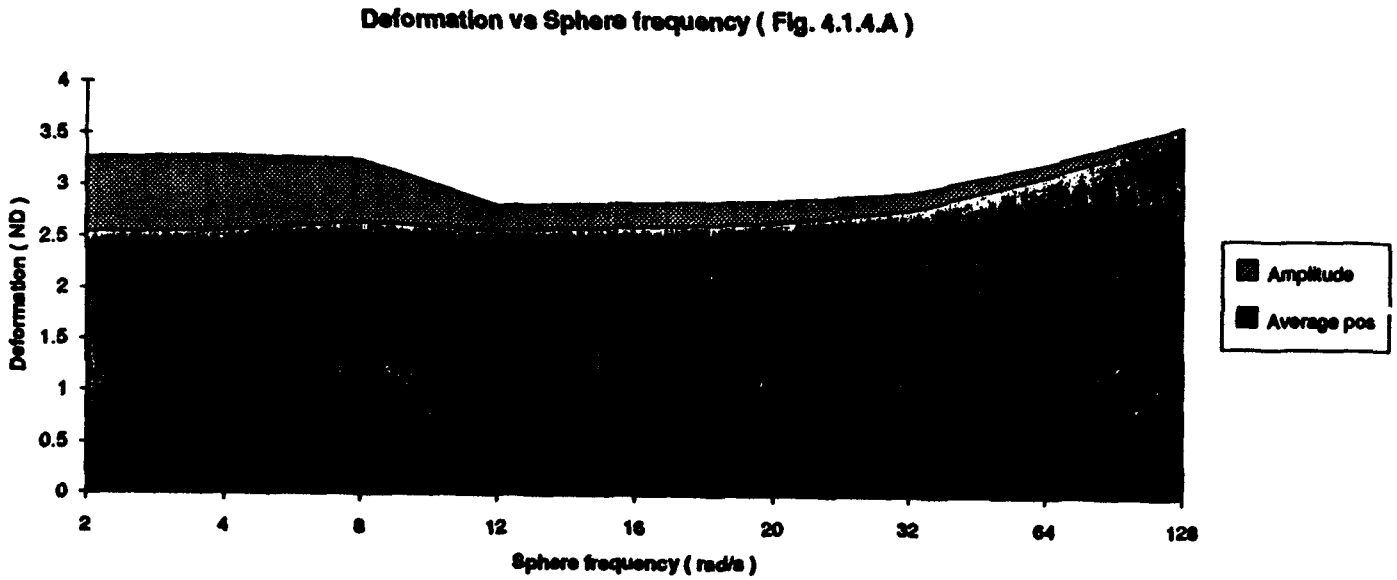
Deformation vs Sphere frequency (Fig. 4.1.4.A)
Deformation (ND)
4
3.5
3
2.5
2
1.5
1
0.5
0
2
4
8
12
16
20
32
64
128
Sphere frequency (rad/s)
Amplitude
Average pos

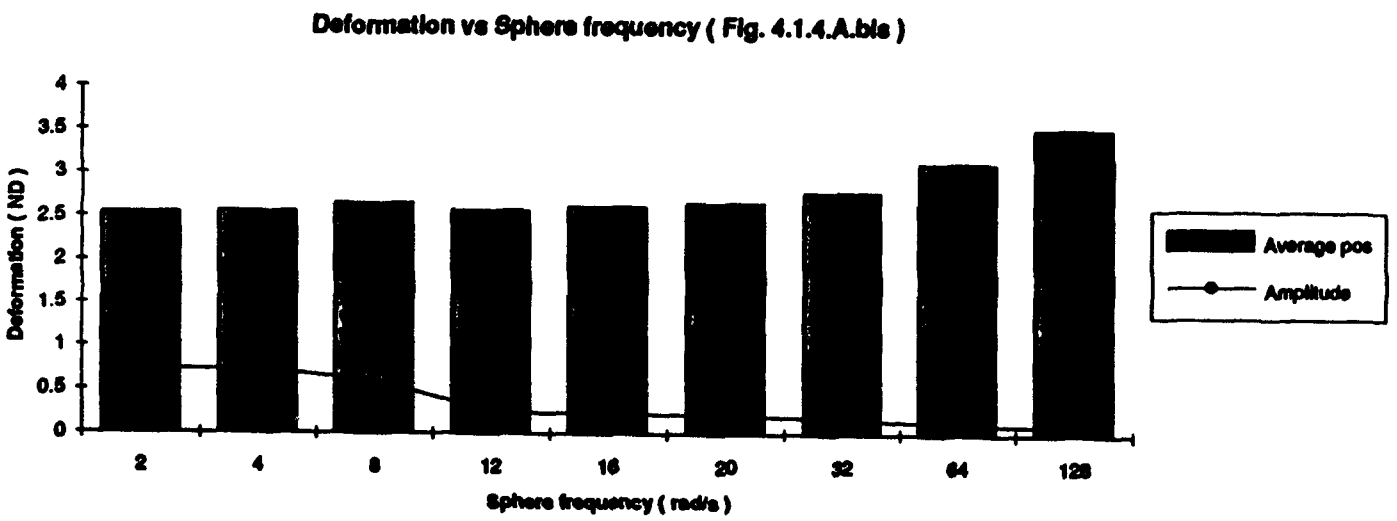
Deformation vs Sphere frequency (Fig. 4.1.4.A.bis)
Deformation (ND)
4
3.5
3
2.5
2
1.5
1
0.5
0
2
4
8
12
16
20
32
64
128
Sphere frequency (rad/s)
Average pos
Amplitude

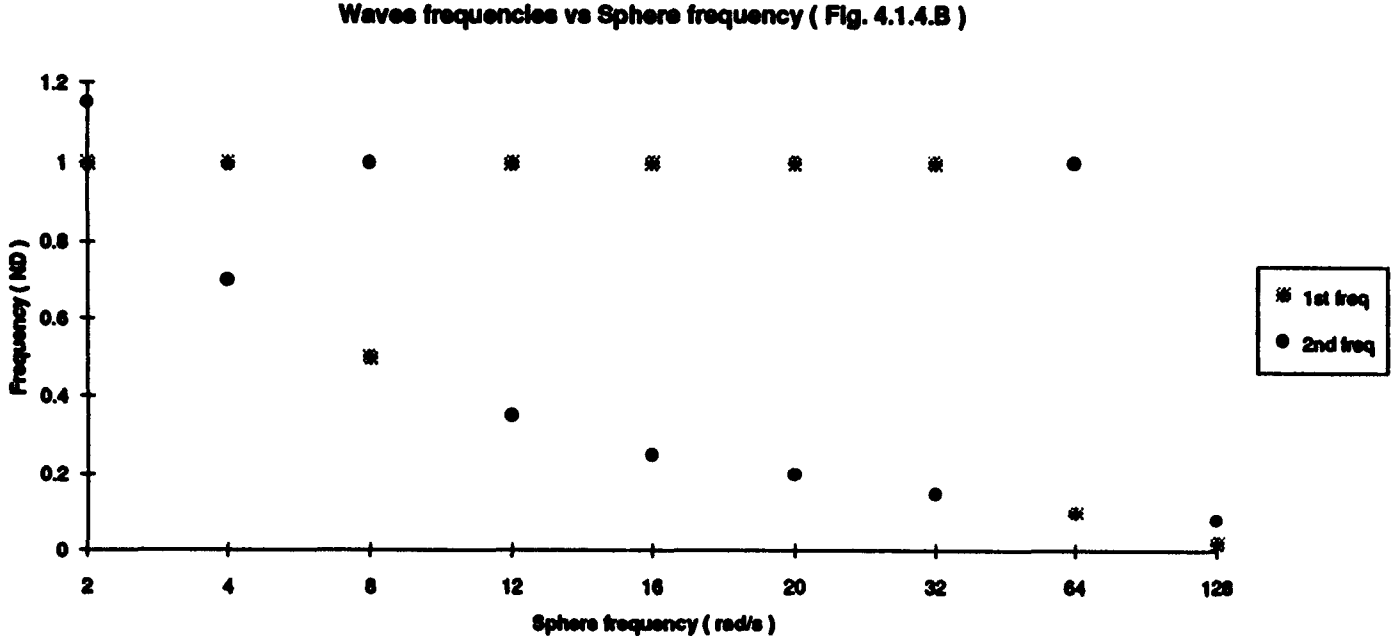
Waves frequencies vs Sphere frequency (Fig. 4.1.4.B)
Frequency (ND)
1.2
1
0.8
0.6
0.4
0.2
0
2
4
8
12
16
20
32
64
128
Sphere frequency (rad/s)
1st freq
2nd freq

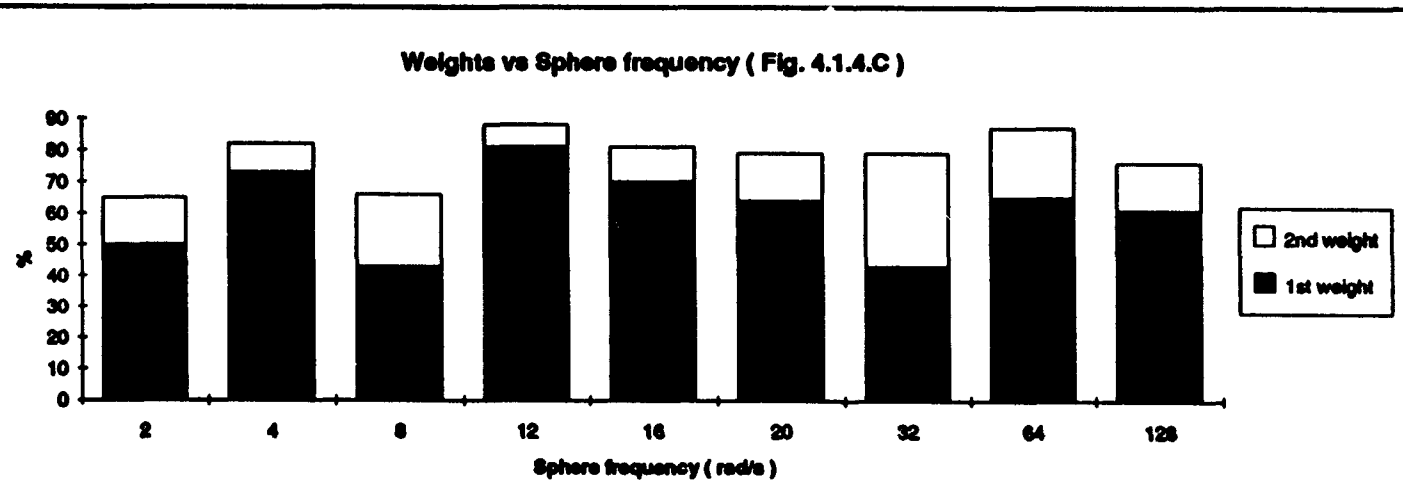
Weights vs Sphere frequency (Fig. 4.1.4.C)
%
90
80
70
60
50
40
30
20
10
0
2
4
8
12
16
20
32
64
128
Sphere frequency (rad/s)
2nd weight
1st weight

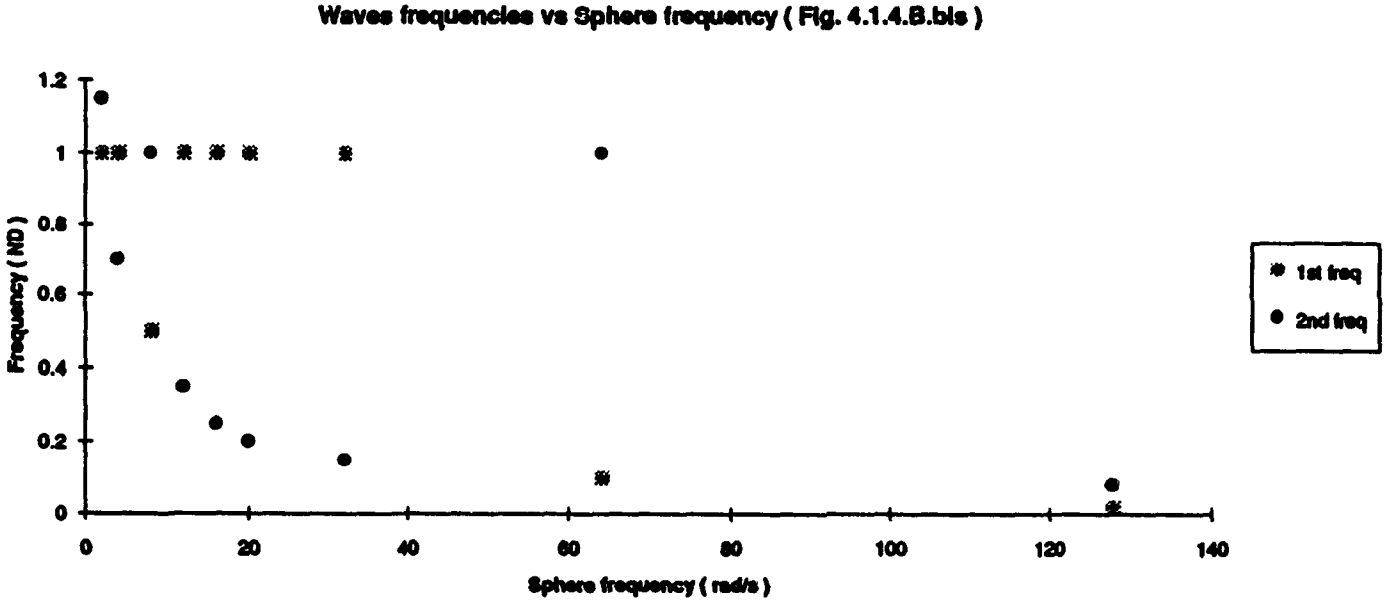
Waves frequencies vs Sphere frequency (Fig. 4.1.4.B.bis)
Frequency (ND)
1.2
1
0.8
0.6
0.4
0.2
0
0
20
40
60
80
100
120
140
Sphere frequency (rad/s)
1st freq
2nd freq

# exp	R	Gravity	Width	Freq	FROUDE	WEBER	?	NB	Average pos	Amplitude	Sp freq	freq 1	Weigth 1	freq 2	Weigth 2
	(m)	(m/s.s)	R	(rad/s)	-	-			R	R	Hz	sphere freq	%	sphere freq	%
45	0.4	0.06	20	7.091	0.094748	1391.78	OK		3.1179	0.1212	1.1285	0.1	65	1	22
46	0.4	0.5	20	7.906	0.789565	1391.78	OK		2.6818	0.2039	1.2582	1	58	0.2	22
47	0.4	1	20	7.906	1.57913	1391.78	OK		2.6132	0.2279	1.2582	1	70	0.3	10
48	0.4	4	20	7.906	6.316522	1391.78	OK		2.6777	0.67255	1.2582	0.5	43	1	18
49	0.4	9.81	20	7.906	15.49127	1391.78	OK		2.5333	0.3993	1.2582	1	71	0.45	8
50	0.4	15	20	7.906	23.68696	1391.78	OK		2.5599	0.6856	1.2582	1	72	0.7	9
51B	0.4	30	20	7.906	47.37391	1391.78	blow-up	14 T	2.9334	1.4266	1.2582	0.072	49	0.86	45
51	0.4	45	20	7.906	71.06087	1391.78	OK		2.5736	0.94792	1.2582	1	54	1.25	8
52	0.4	61	20	7.906	96.32696	1391.78	OK		2.542	0.7067	1.2582	1	50	1.15	18
53	0.4	93	20	7.906	146.8591	1391.78	OK		2.6415	1.09987	1.2582	0.1	18	1	14
54	0.4	125	20	7.906	197.3913	1391.78	blow-up	14 T	2.6992	1.14152	1.2582	0.143	26	1	25
55	0.4	157	20	7.906	247.9235	1391.78	blow-up	16 T	2.7736	1.62606	1.2582	0.059	19	0.18	16
56	0.4	190	20	7.906	300.0348	1391.78	OK		2.5627	0.78701	1.2582	1	15	0.5	11
57	0.4	222	20	7.906	350.567	1391.78	OK		2.5668	0.82365	1.2582	0.2	21	1	16
60	1	9.81	20	16	1.512823	Infinity	OK	Sig=0	2.6168	0.22745	2.5465	1	70	1.25	11
61	0.56	63	20	7.906	71.06087	1393.95	OK		2.5736	0.94831	1.2582	1	54	1.25	8
62	0.56	63	20	7.906	71.06087	878.38	OK		2.5736	0.94842	1.2582	1	54	1.25	8
63	0.56	63	20	7.906	71.06087	458.285	OK		2.5736	0.94831	1.2582	1	54	1.25	8
64	0.56	63	20	7.906	71.06087	248.238	OK		2.5736	0.9484	1.2582	1	54	1.25	8
65	0.56	63	20	7.906	71.06087	114.571	OK		2.5736	0.9485	1.2582	1	54	1.25	8
66	0.56	63	20	7.906	71.06087	38.1904	OK		2.58735	0.9474	1.2582	1	54	1.25	8
67	0.56	63	20	7.906	71.06087	11.4571	OK		2.5733	0.9456	1.2582	1	54	1.25	8
68	0.56	63	20	7.906	71.06087	3.81904	OK		2.5729	0.9485	1.2582	1	55	1.25	8
69	0.56	63	20	7.906	71.06087	2.67333	OK		2.5723	0.9481	1.2582	1	55	1.25	8
70	0.56	63	20	7.906	71.06087	0.3819	OK		2.5646	0.9489	1.2582	1	56	1.25	8
71	0.56	63	20	7.906	71.06087	0.19095	OK		2.5542	0.9563	1.2582	1	52	1.25	7

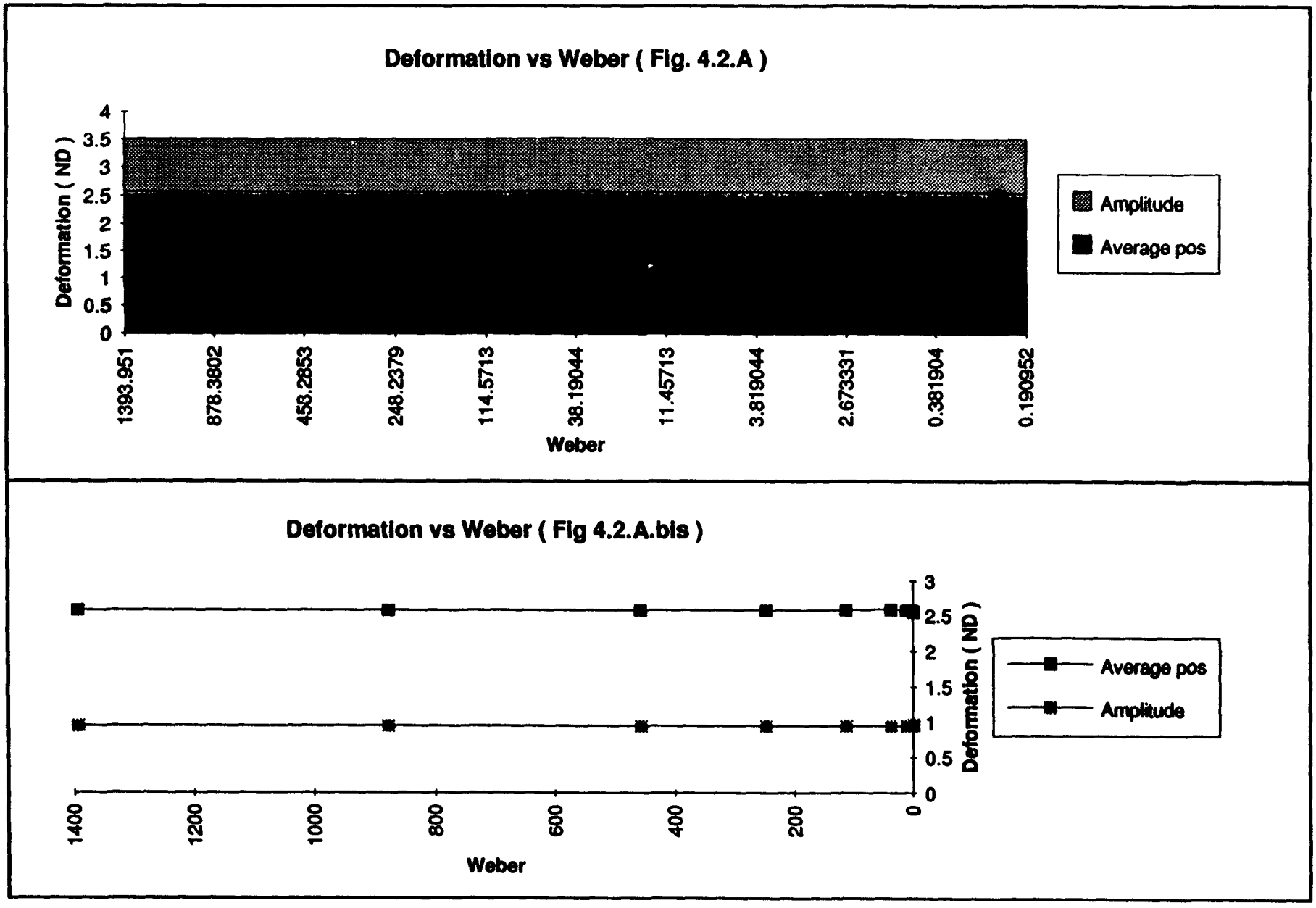
Deformation vs Weber (Fig. 4.2.A)
Deformation (ND)
4
3.5
3
2.5
2
1.5
1
0.5
0
1393.951
878.3802
458.2853
248.2379
114.5713
38.19044
11.45713
3.819044
2.673331
0.381904
0.190952
Weber
Amplitude
Average pos
Deformation vs Weber (Fig 4.2.A.bis)
3
2.5
2
1.5
1
0.5
0
Deformation (ND)
1400
1200
1000
800
600
400
200
0
Weber
Average pos
Amplitude

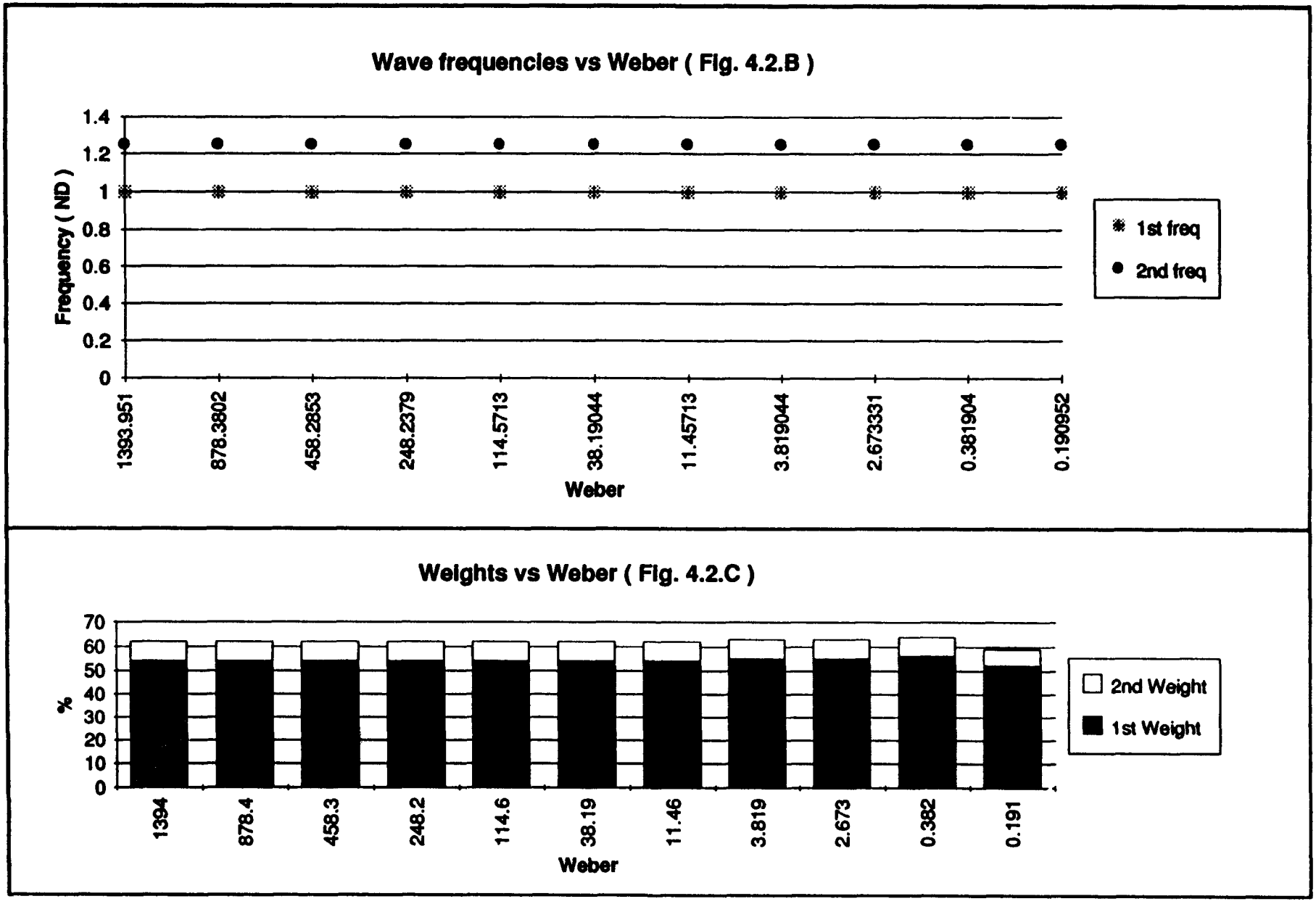
Wave frequencies vs Weber (Fig. 4.2.B)
Frequency (ND)
1.4
1.2
1
0.8
0.6
0.4
0.2
0
1393.951
878.3802
458.2853
248.2379
114.5713
38.19044
11.45713
3.819044
2.673331
0.381904
0.190952
Weber
1st freq
2nd freq
Weights vs Weber (Fig. 4.2.C)
%
70
60
50
40
30
20
10
0
1394
878.4
458.3
248.2
114.6
38.19
11.46
3.819
2.673
0.382
0.191
Weber
2nd Weight
1st Weight

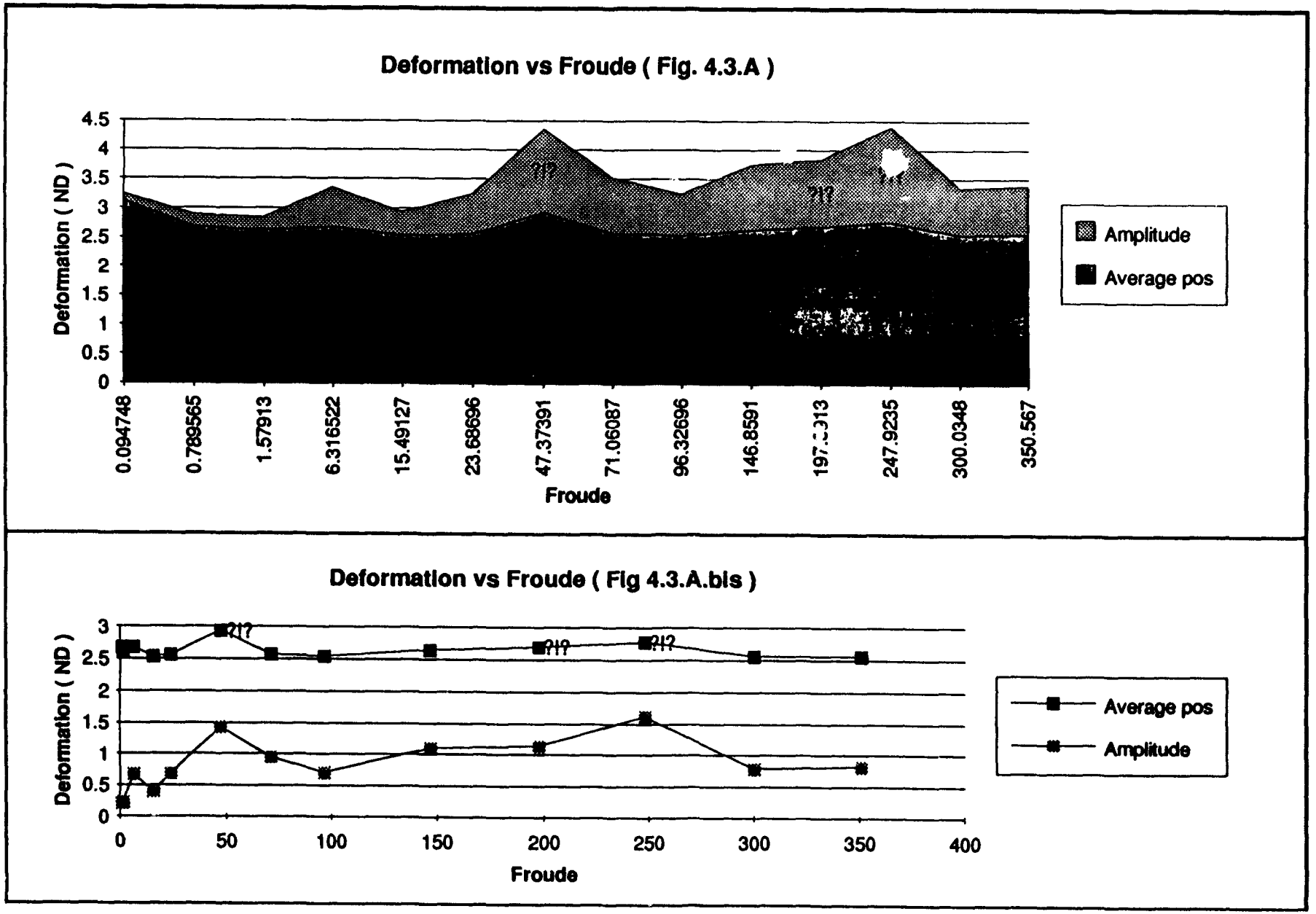
Deformation vs Froude (Fig. 4.3.A)
Deformation (ND)
4.5
4
3.5
3
2.5
2
1.5
1
0.5
0
0.094748
0.789565
1.57913
6.316522
15.49127
23.68696
47.37391
71.06087
96.32696
146.8591
247.9235
300.0348
350.567
Froude
Amplitude
Average pos
Deformation vs Froude (Fig 4.3.A.bis)
Deformation (ND)
3
2.5
2
1.5
1
0.5
0
0
50
100
150
200
250
300
350
400
Froude
Average pos
Amplitude

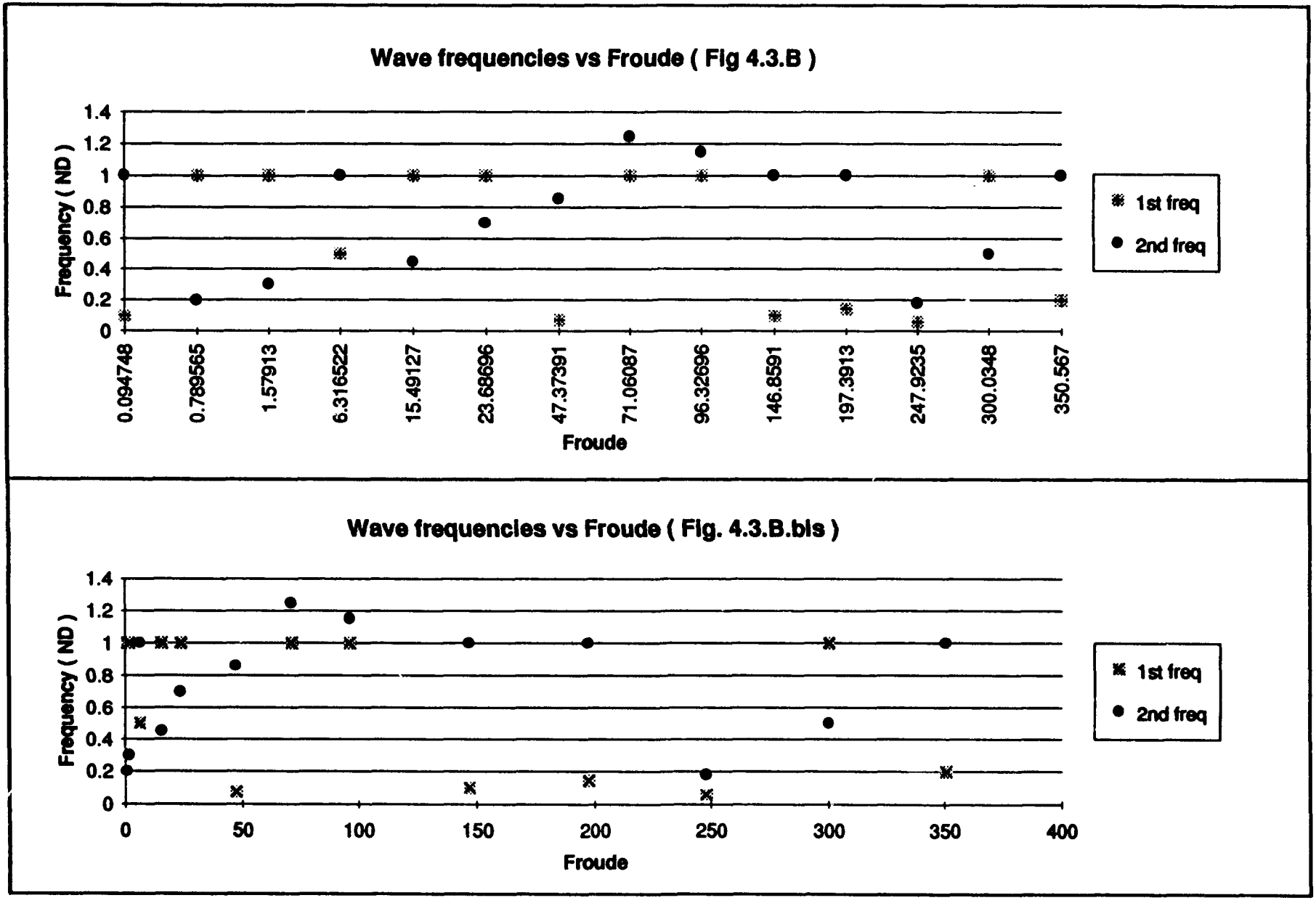
Wave frequencies vs Froude (Fig 4.3.B)
Frequency (ND)
1.4
1.2
1
0.8
0.6
0.4
0.2
0
0.094748
0.789565
1.57913
6.316522
15.49127
23.68696
47.37391
71.06087
96.32696
146.8591
197.3913
247.9235
300.0348
350.567
Froude
1st freq
2nd freq
Wave frequencies vs Froude (Fig. 4.3.B.bis)
Frequency (ND)
1.4
1.2
1
0.8
0.6
0.4
0.2
0
0
50
100
150
200
250
300
350
400
Froude
1st freq
2nd freq

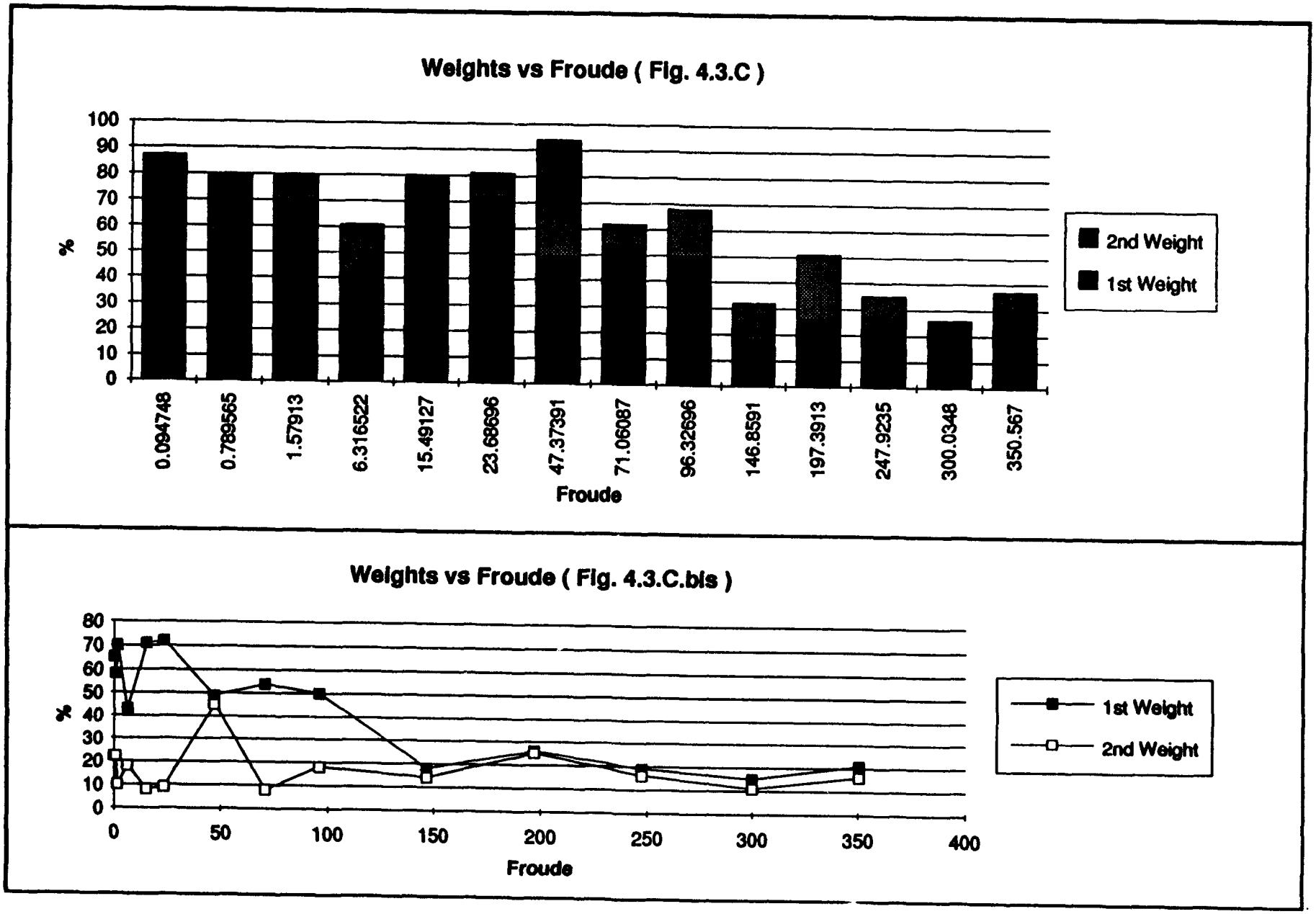
Weights vs Froude (Fig. 4.3.C)
%
100
90
80
70
60
50
40
30
20
10
0
0.094748
0.789565
1.57913
6.316522
15.49127
23.68696
47.37391
71.06087
96.32696
146.8591
197.3913
247.9235
300.0348
350.567
Froude
2nd Weight
1st Weight
Weights vs Froude (Fig. 4.3.C.bis)
%
80
70
60
50
40
30
20
10
0
0
50
100
150
200
250
300
350
400
Froude
1st Weight
2nd Weight

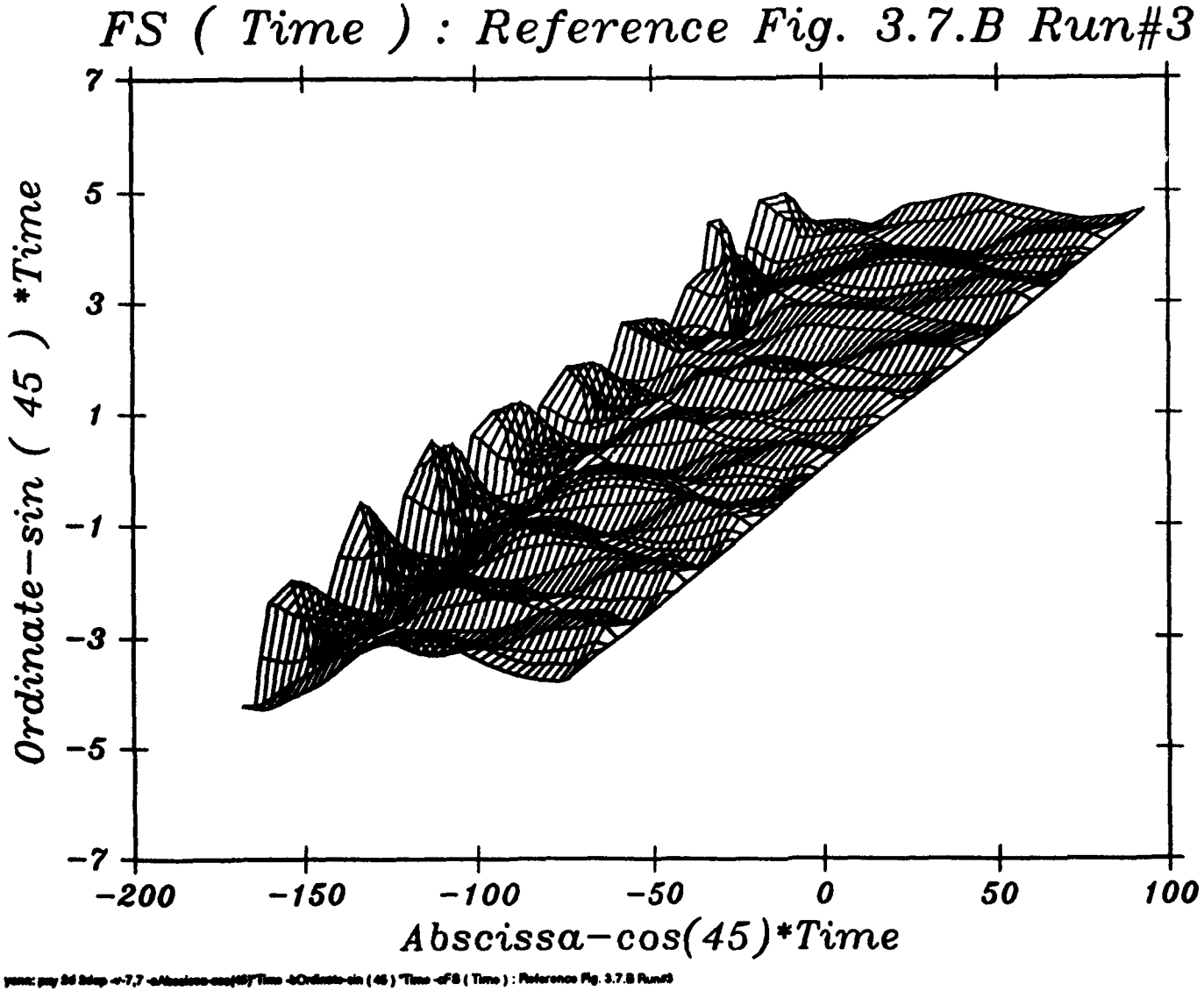
FS (Time) : Reference Fig. 3.7.B Run#3
7
5
3
1
-1
-3
-5
-7
-200
-150
-100
-50
0
50
100
Ordinate-sin (45) *Time
Abscissa-cos(45)*Time

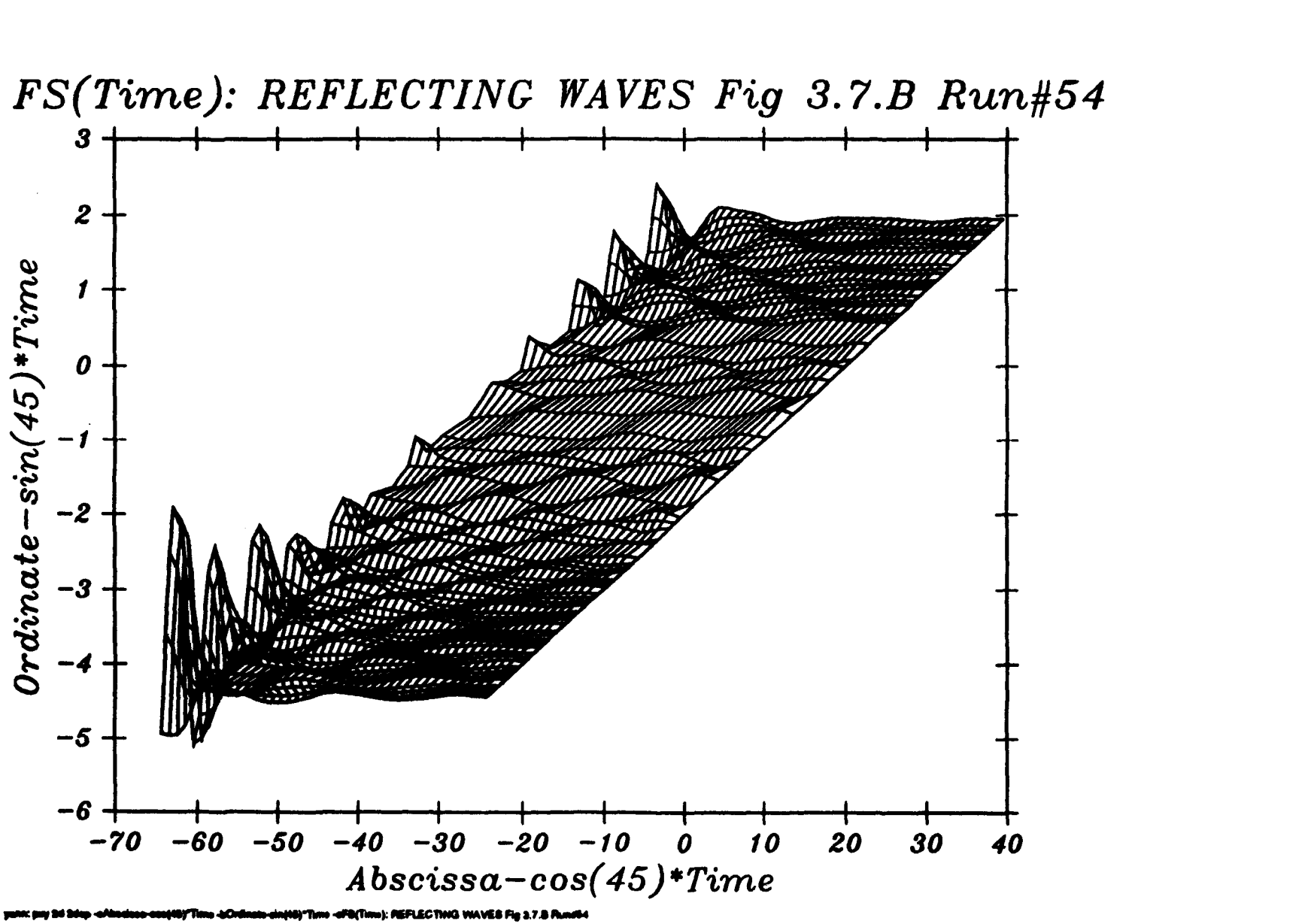
FS(Time): REFLECTING WAVES Fig 3.7.B Run#54
Ordinate-sin(45)*Time
3
2
1
0
-1
-2
-3
-4
-5
-6
-70
-60
-50
-40
-30
-20
-10
0
10
20
30
40
Abscissa-cos(45)*Time

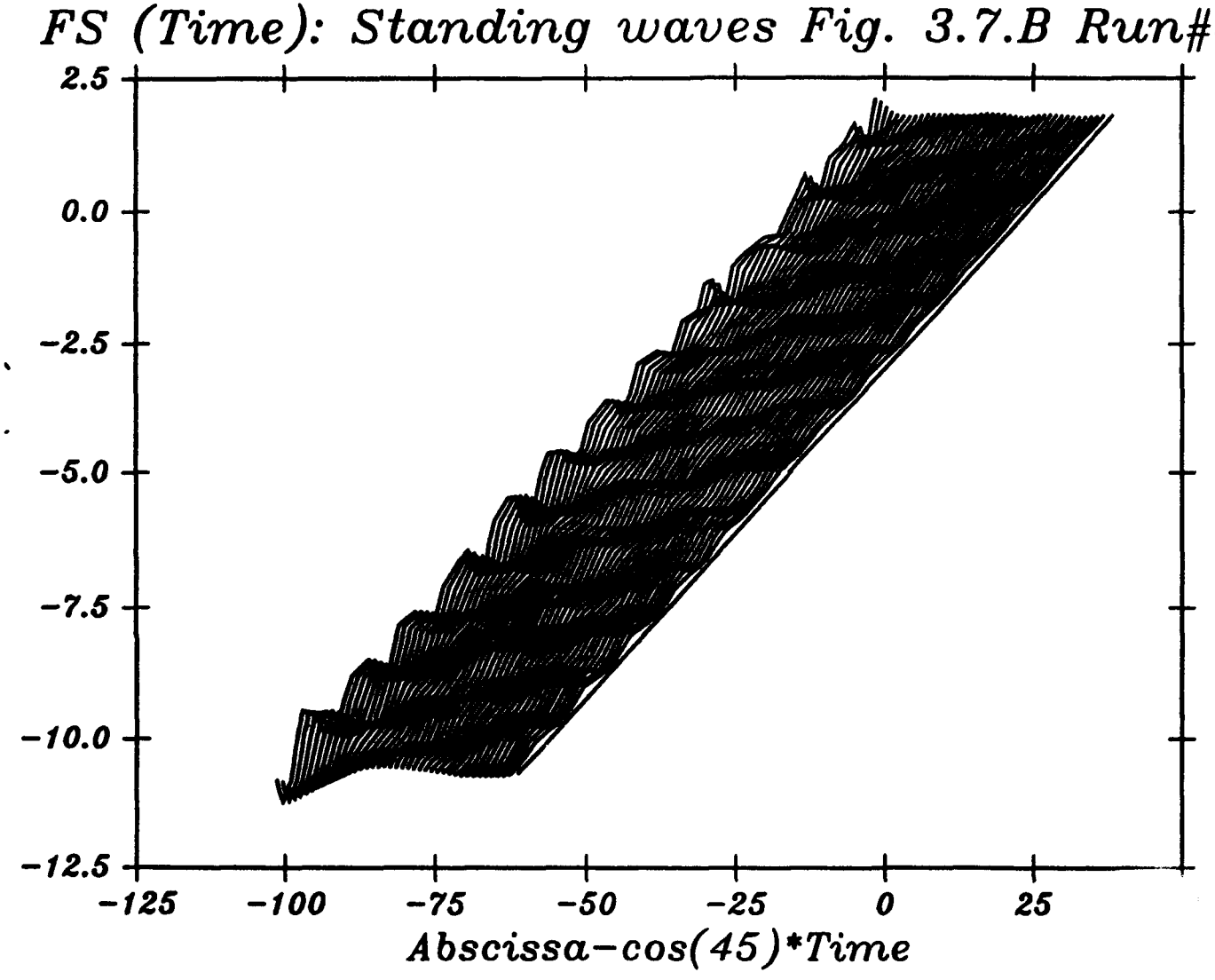
FS (Time): Standing waves Fig. 3.7.B Run#54
2.5
0.0
-2.5
-5.0
-7.5
-10.0
-12.5
-125
-100
-75
-50
-25
0
25
Abscissa-cos(45)*Time

```
 1 *
 2 *program for a spectral analysis of the output of FSURFS
 3 *YG 9/93
 4 *
 5 program spectral
 6 implicit none
 7 real z,freq,ampli,ave,freq0
 8 real freqs(100),freqf(100),props(100),propf(100)
 9 real*8 tsonx(16384)
10 real*8 sonx(16384),a(10000),b(10000)
11 real*8 sonx2(16384),a2(10000),b2(10000)
12 integer i,k,l,kf,ks
13 integer jnax,ilen,col,ref
14 character*20,filin,filout
15
16
17 write(*,*)' Enter the name of the files'
18 write(*,*)' Input :'
19 read (5,'(A)')filin
20 write(*,*)' Output :'
21 read (5,'(A)')filout
22 *write(*,*)' Enter the number of records'
23 *read (5,*)jnax
24 *write(*,*)' Enter max freqency'
25 *read (5,*)ilen
26
27
28 open (unit=1,file=filin,status='old')
29 jnax=-1
30 100continue
31     read(1,*,end=1000),z
32     jnax=jnax+1
33 goto 100
34 1000continue
35 write(*,*)jnax,' Records'
36 close(1)
37
38 open (unit=1,file=filin,status='old')
39 do i=1,jnax
40     read(1,*)tsonx(i),sonx(i),sonx2(i)
41 enddo
42 close(1)
43
44 ref=tsonx(jnax)+1
45 ilen=1.5*ref
46 print*,ilen
47
48
49 call ftrfm(jnax,tsonx,sonx,a,b,ilen)
50 call ftrfm(jnax,tsonx,sonx2,a2,b2,ilen)
51
52
53 open (unit=2,file=filout,status='unknown')
54 do i=2,ilen+1
55   write(2,*)real(i-1),100.*sqrt(a(i)**2+b(i)**2),
56      $           100.*sqrt(a2(i)**2+b2(i)**2),real(i-1)/real(ref)
57           write(2,*)real(i-1),0,0,real(i-1)/real(ref)
58           write(2,*)
59 enddo
60 close(2)
61
62
63 call frequency(filout,ilen,1,1.,ks,props,freqs)
64 call reorder (props,freqs,ks)
65
66 call frequency(filout,ilen,2,freqs(1),kf,propf,freqf)
67 call reorder (propf,freqf,kf)
68
69 ave=0
70 do i=1,jnax-1
71     ave=ave+sonx2(i)*(tsonx(i+1)-tsonx(i))
72 enddo
```

```
 73 ave=ave/(tsonx(jnax)-tsonx(1))
 74
 75 call getampli(filin,jnax,k,ampli)
 76
 77 write(*,*)' File :',filin
 78 write(*,*)
 79 write(*,*)kf,'  frequencies for the FS'
 80 do i=1,kf
 81     if (propf(i).gt.propf(1)/20.) then
 82 write(*,*)freqf(i),'  weight =  ',propf(i)*100.
 83     endif
 84 enddo
 85 write(*,*)
 86 write(*,*)ks,'  frequencies for the sphere'
 87 do i=1,ks
 88             write(*,*)freqs(i)/ref,'  weight =  ',props(i)*100.
 89 enddo
 90 write(*,*)
 91 write(*,*)' Average position at y :',ave
 92 write(*,*)' Amplitud is there     :',ampli
 93 write(*,*)
 94 write(*,*)' There were about ',k,' pseudo-periods'
 95 write(*,*)
 96 write(*,*)' Et voila ptit gars'
 97 end
 98
 99
100 C  ****************************************************************
101 C     SUBROUTINE TO CALCULATE COEFFICIENTS USING FOURIER TRANSFORM
102 C        COEFFICIENTS FIT EQUATION OF THE FORM:
103 CS(t)=Ao/2 + AnCOS(nwt) + BnSIN(nwt)
104 C  ****************************************************************
105 SUBROUTINE FTRFM(JNAX,TSONX,SONX,A,B,ILEN)
106 IMPLICIT REAL*8(A-G,O-Z)
107 DIMENSION A(10000),B(10000),TSONX(16384),SONX(16384)
108 DIMENSION DELT(16384),HTSONX(16384)
109 DATA PI/3.14159/
110 T=TSONX(JNAX)
111 WMAIN =2.*PI/T
112 DO 210 J=1,JNAX-1
113 210DELT(J)=TSONX(J+1)-TSONX(J)
114 DO 211 K=1,JNAX
115 211HTSONX(K)=TSONX(K)
116 TA=2./T
117          DO 75 NN=1,ILEN+1
118     N=NN-1
119     W=FLOAT(N)*WMAIN
120     ASUM=0.
121     BSUM=0.
122     FCLAST=SONX(1)
123     FSLAST=0.
124     DO 50 J=1,JNAX-1
125 L=J+1
126    HANGL=W*HTSONX(L)
127 FCNEXT=SONX(L)*COS(HANGL)
128 FSNEXT=SONX(L)*SIN(HANGL)
129 FCOS=(FCLAST+FCNEXT)/2.
130 FSIN=(FSLAST+FSNEXT)/2.
131 FCLAST=FCNEXT
132 FSLAST=FSNEXT
133 ASUM=ASUM+(FCOS*DELT(J))
134 BSUM=BSUM+(FSIN*DELT(J))
135  50        CONTINUE
136     A(NN)=TA*ASUM
137     B(NN)=TA*BSUM
138  75  CONTINUE
139  200RETURN
140 END
141
142 ************************************************************************
143 *subroutine to determine the main frequencies of a signal
144 ************************************************************************
```

```
145 subroutine frequency(filout,ilen,col,fre,ks,props,freqs)
146 implicit none
147 real props(100),freqs(100),spaa(2),ii,aa(2),mini,fre,tot,alf
148 integer ilen,i,ks,es,col
149 character*20,filout
150
151 open(unit=2,file=filout,status='unknown')
152 ks=0
153 es=1
154 tot=0.
155 read(2,*)ii,spaa(1),spaa(2)
156         read(2,*)alf
157 do i=2,ilen
158     read(2,*)ii,aa(1),aa(2)
159             read(2,*)alf
160     if (aa(col).lt.spaa(col)) then
161 if (es.eq.1) then
162     es=-1
163     ks=ks+1
164     freqs(ks)=(ii-1)/fre
165     props(ks)=spaa(col)
166     tot=tot+spaa(col)
167 endif
168     else
169 if (es.eq.-1) then
170     es=1
171     mini=spaa(col)
172 endif
173     endif
174     spaa(col)=aa(col)
175 enddo
176 do i=1,ks
177     props(i)=props(i)/tot
178 enddo
179 close(2)
180 return
181 end
182
183 ************************************************************************
184 *subroutine to compute the amplitud of the signal ( average )
185 ************************************************************************
186 subroutine getampli(filin,jnax,k,ampli)
187 implicit none
188 real ori,son2,son2p,amp(1000),ampli,a
189 integer k,ev,i,jnax
190 character*20,filin
191
192 k=0
193 ev=1
194
195 open(unit=1,file=filin,status='unknown')
196 read(1,*)a,a,son2p
197 ori=son2p
198 do i=2,jnax
199     read(1,*)a,a,son2
200     if (son2.gt.son2p) then
201 if (ev.eq.-1) then
202     ev=1
203     k=k+1
204     amp(k)=ori-son2p
205     ori=son2p
206 endif
207     else
208 if (ev.eq.1) then
209     ev=-1
210     k=k+1
211     amp(k)=son2-ori
212     ori=son2p
213 endif
214     endif
215     son2p=son2
216 enddo
```

```
217 close(1)
218
219 ampli=0.
220 do i=1,k
221     ampli=ampli+amp(i)/k
222 enddo
223 return
224 end
225
226 ************************************************************************
227 *subroutine to reorder a vectors in a decreasing order and make
228 *the same change in a another vector
229 ************************************************************************
230 subroutine reorder (propf,freqs,kf)
231 implicit none
232 real propf(1:1),freqs(1:1),p,f
233 integer kf,i,j
234
235 do i=2,kf
236     p=propf(i)
237     f=freqs(i)
238     do j=i-1,1,-1
239 if (propf(j).ge.p) goto 10
240 propf(j+1)=propf(j)
241 freqs(j+1)=freqs(j)
242     enddo
243     j=0
244 10    propf(j+1)=p
245     freqs(j+1)=f
246 enddo
247 return
248 end
249
250 *
251 *
252 *well, now it's done ! Shall I have a fag ?
253 *
254 *
255
```

```
 1 *
 2 *The front-cover of '3rd days of hydrodynamic'
 3 *give me an idea I gonna try to adapt to my case
 4 *YG 10/93
 5
 6 program smart
 7 implicit none
 8 real a,b(5000,140),c(5000,140),var,cor,alf
 9 integer i,j,numb,first,nod,maxi
10 character*20,filin,filout,filopti
11
12 write(*,*)' Enter the name of the files'
13 write(*,*)' Input :'
14 read (5,'(A)')filin
15 write(*,*)' Enter the number of nodes'
16 read(5,*)nod
17 write(*,*)' Output : 2d type'
18 read (5,'(A)')filout
19 write(*,*)' Output : optical type'
20 read (5,'(A)')filopti
21
22 maxi=0
23 open (unit=1,file=filin,status='old')
24 100continue
25     read(1,*,end=1000)alf
26     maxi=maxi+1
27 goto 100
28 1000continue
29 close(1)
30 maxi=maxi/nod
31
32 write(*,*)' Enter the number of sequences'
33 write(*,*)' Maximum = ',maxi
34 read (5,*)numb
35 write(*,*)' Enter the number of the first sequence'
36 read(5,*)first
37 write(*,*)' Enter the x correction ( indice )'
38 read(5,*)cor
39
40 open (unit=1,file=filin,status='old')
41 open (unit=2,file=filout,status='unknown')
42 do i=1,first-1
43     do j=1,nod
44 read(1,*)alf
45     enddo
46 enddo
47 do j=1,numb-first
48     read(1,*)a,b(j,1),c(j,1)
49     var=(a-alf)
50     b(j,1)=b(j,1)-var*cor
51     c(j,1)=c(j,1)-var
52     write(2,*)b(j,1),c(j,1)
53     do i=2,nod-11
54 read (1,*)a,b(j,i),c(j,i)
55 b(j,i)=b(j,i)-var*cor
56 c(j,i)=c(j,i)-var
57 write(2,*)b(j,i),c(j,i)
58     enddo
59     write(2,*)
60     do i=1,11
61 read(1,*)a
62     enddo
63 enddo
64 close(1)
65 close(2)
66
67 open (unit=3,file=filopti,status='unknown')
68 do i=1,nod-11
69     do j=1,numb-first
70 write(3,*)b(j,i),c(j,i)
71     enddo
72     write(3,*)
```

```
 73 enddo
 74 close(3)
 75
 76 write(*,*)' Et voila ptit gars'
 77 end
```

STUDY OF JET INSTABILITY FORMATION ON FREE SURFACES

A. VAN DER BEKEN
RAMANI DURAISWAMI
G.L. CHAHINE

July 1993

DYNAFLOW, INC.
7210 Pindell School Road
Fulton, MD 20759

Contents

Introduction

The study of free surfaces can be interesting in many respects. Any surface separating a liquid from a gaz could be called a free surface, though for a finite volume of gaz in a liquid, the term bubble is certainly more accurate. The typical example of free surface is the surface of the ocean.

When a free surface presents a deformation in one special direction, the stream of liquid created is called a jet. Jets have been used since earliest times and their behavior has been studied by scientists since the 16th century at least. Recently, studies on jets have shown new possible applications, especially since it has been discovered that they were involved in cavitation phenomena.

Simple steady jets have be studied analytically. One of the oldest hydraulic problems has been the determination of the discharge rate and contraction coefficient of an orifice.

With the advent of new computational tools, further research in the understanding of jets has become possible.

In this report, we present the continuation of a numerical study of a selected example of axisymetric free surface which leads to the formation of a high speed jet on the axis. The problem concerns the modelisation of the motion of an air/water free surface created by suddenly lifting an initially empty cylinder in a tank filled with water.

The method used to solve Laplace equation is the Boundary Element Method, for which a fortran code (2DynaFS) had already been tested by DYNAFLOW, INC.

Different hypothesis were made about the general boundary shape to be modelled and about the initial conditions to be imposed at the free surface. First, we shall report results obtained ignoring the part of the free surface located outside the cylinder, with a fixed cylinder in an infinite medium and when the liquid initially forming a flat free surface at the cylinder bottom is suddenly allowed to enter the cylinder. In fact, the modelisation of these much simpler cases turned out to be necessary to test the reliability of our code. Then we shall present our conclusions on a more physical modelisation, taking into account the presence of the tank below the cylinder and the whole free surface. Neverthless, we will keep for a future study the case of a moving cylinder.

Computational schemes were introduced to speed up the code or to produce a better modelisation of the physical problem. They are also reported in the following sections.

1 Problem formulation

1.1 Description of the physical phenomenon studied

The problem consists in modeling the free surface created by lifting a cylinder initially empty, opened at its bottom, and immerged in a tank of water. The problem is assumed to be axisymetric. We distinguish two free surfaces, the first one being limited by the interior surface of the cylinder, the second being limited by both the outward surface of the cylinder and the sides of the tank.

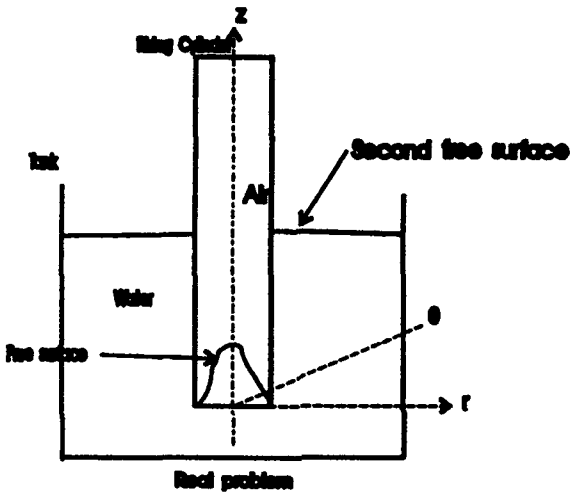

1.2 Results from previous studies

The following phenomena had been both studied numerically and observed experimentally.

1.2.1 Report from previous numerical study

The rise of liquid in the cylinder has been reported in DYNAFLOW's Bertin report [7] as sequenced into five different phases:

- A first phase where two water fronts converge simultaneously toward the axis of the cylinder from all around the cylinder
- Then, a possibility of capture of an air-bubble as the water fronts reach the axis in a violent impact
- Creation of an ultra-thin jet on the axis of the cylinder
- The rest of the free surface follows the ultra-thin jet while the jet itself can rise up to several times the initial depth of water in the tank
- The water touchs the cylinder sides. Oscillations start in the cylinder.

1.2.2 Report from previous experimental studies

Experiments have been carried out at DYNAFLOW using different depths of water and different ways to rise the cylinder. Experimental observations were made possible by using a high speed camera. They showed that the region of high velocity is localised in the vicinity of the bottom of the cylinder and inside the cylinder while the second free surface apparently did not move (the shape remains flat), velocities involved in that area being quantitatively small, except for the fluid displaced by the motion of the cylinder.

1.3 Behaviour of the fluid

1.3.1 Hypothesis

Reynolds numbers in the studied phenomenon are supposed to be large enough so that viscosity effects can be neglected in the equations of the fluid. The fluid is considered irrotationnal. The study will be restricted to cases where flow velocities remain small compared to the speed of sound in water. As a result, compressibility effects are also neglected.

The two previous assumptions lead us to consider a potential flow which follows Laplace's equation in the whole domain Ω considered :

$$\nabla^2\Phi = 0 \text{ where } \Phi \text{ is the potential for velocity } \vec{U} = \vec{\nabla}\Phi$$

and where $\Phi = \Phi(r, z)$ since the problem is axisymetric

1.3.2 Equation of motion

The equation of motion is :

$$\rho\frac{d\vec{U}}{dt} = -\vec{\nabla}(p + \rho g z)$$

The assumptions made above make it possible to re-write the equation of motion as Bernoulli's equation :

$$\frac{\partial\Phi}{\partial t} + \frac{u^2}{2} + \frac{P}{\rho} + gz = \text{Constant} \qquad (1)$$

1.3.3 Surface tension

Surface tension has to be taken into account, especially in the vicinity of the axis of the cylinder where the formation of the jet leads to high curvatures. To the contrary, surface tension effects are negligeable away from the axis and on the second free surface.

Given the atmospheric pressure $P_{atmos.}$, the pressure inside the liquid at the free surface is :

$$P_{fluid} = P_{atmos.} + \sigma \mathcal{C} \tag{2}$$

where $\mathcal{C}$ is the local curvature of the free surface.

1.3.4 Boundary conditions

Since the phenomenon we want to study first is localised near the cylinder, and since it appears to be of less interest to know the velocity field in the vicinity of the sides of the tank, we decided to consider the dimensions of the tank as infinite. Therefore, the domain Ω considered for the fluid is limited by the cylinder itself and the free surface initially at the bottom, the second free surface outside of the cylinder, and a *wall* representing the bottom of the tank. At infinity, we assume that $\Phi \underset{r\to\infty}{\to} 0$ and at least that $r.\Phi \underset{r\to\infty}{}$ *is limited.*

We shall then keep in mind for the future the hypothesis :

$$\Phi \underset{r\to\infty}{\to} 0 \text{ at least like } \frac{A}{r} \text{ where } A \text{ is a constant.} \tag{3}$$

2 Numerical resolution

2.1 The Boundary Element Method

The method used to determine the time evolution of the free surface is the Boundary Element Method. This method uses Green's identity to solve Laplace's equation. We shall sum up the main ideas of the method for an axisymetric potential problem in the following lines. For futher details, the reader may refer to [5] and [4].

Let us take $\Phi(x,y,z)$ regular enough and let us suppose $\nabla^2\Phi = 0$. Let us take Ψ, another function of space supposed to be C^∞ in the considered domain Ω limited by the surface $S(\Omega)$.

Green's formula gives us a first equation

$$\int_\Omega \nabla^2\Phi.\Psi.d\Omega = -\int_\Omega \nabla\Phi.\nabla\Psi.d\Omega + \int_S \frac{\partial\Phi}{\partial n}.\Psi.dS = 0$$

A second integration using the same identity gives

$$\int_S \frac{\partial\Phi}{\partial n}.\Psi.dS - \int_S \Phi.\frac{\partial\Psi}{\partial n}.dS + \int_\Omega \Phi.\nabla^2\Psi.d\Omega = 0$$

This equation remains true in the case where Φ and Ψ are less regular, as long as the above integrals exists. As a consequence, if $p(x_p,y_p,z_p)$ and $q(x,y,z)$ are points inside Ω or on the Boundary S, we may take for Ψ the expression

$$\Psi(q) = \frac{1}{|(x-x_p)^2+(y-y_p)^2+(z-z_p)^2|^{\frac{1}{2}}} = \frac{1}{|p-q|}$$

Several cases are now to be distinguished:

-p is inside Ω :

We know that $\nabla^2_q(\frac{1}{|p-q|}) = -4\pi\delta_p$ which means

$$\int_\Omega \nabla^2_q(\frac{1}{|p-q|}).\Phi(q).d\Omega_q = -\int_\Omega 4\pi\delta_p.\Phi(q).d\Omega_q = -4\pi\Phi(p).$$

-p is a regular point on the boundary S :

we have $\nabla^2_q(\frac{1}{|p-q|}) = -2\pi\delta_p$ then

$$\int_\Omega \nabla^2_q(\frac{1}{|p-q|}).\Phi(q).d\Omega_q = -2\pi\Phi(p)$$

-p is an angular point on the boundary S :

we have $\nabla^2_q(\frac{1}{|p-q|}) = -c(p).\delta_p$ where $c(p)$ is the solid angle from which p sees Ω, and

$$\int_\Omega \nabla^2_q(\frac{1}{|p-q|}).\Phi(q).d\Omega_q = -c(p).\Phi(p)$$

If we only consider regular surfaces in our following study, which seems an understandable hypothesis for a physical surface defined by the motion of a fluid, we therefore come to the following identity :

$$c(p).\Phi(p) + \int_S \Phi(q).\frac{\partial}{\partial n}\frac{1}{|p-q|}.dS_q = \int_S \frac{\partial \Phi}{\partial n}(q).\frac{1}{|p-q|}.dS_q \qquad (4)$$

$c(p) = 4\pi$ if p belongs to Ω and $c(p) = 2\pi$ if p belongs to the boundary S

The advantage of this integral representation is that it effectively reduces the dimension of the problem by one. If the field point p is selected to be inside the fluid domain Ω, knowing Φ and $\frac{\partial \Phi}{\partial n}$ on the boundary S appears to be enough to determine Φ everywhere else. If the field point p is selected on the boundary S, (4) gives a relation between Φ and $\frac{\partial \Phi}{\partial n}$ on the boundary S. After discretisation of this boundary (4) gives in fact a system of equations relating Φ and $\frac{\partial \Phi}{\partial n}$ at the nodes of the selected discretisation.

The Boundary Element Method in the case of a potential problem consists in solving this system of equations. Major benefit is due to this formulation, especially since it does not necessitate an heavy discretisation of the whole 3D-domain Ω.

In axisymetric problems, the integrals in (4) can be re-written in the following expression where Γ stands for the trace of the boundary S in a meridional plane:

$$c(p).\Phi(p) + \int_\Gamma \Phi(q).r_q dr_q.\int_0^{2\pi} \frac{\partial}{\partial n}\frac{1}{|p-q|}.d\theta_q = \int_\Gamma \frac{\partial \Phi}{\partial n}(q).r_q dr_q.\int_0^{2\pi} \frac{1}{|p-q|}.d\theta_q = 0 \qquad (5)$$

since $\Phi(q)$ and $\frac{\partial \Phi}{\partial n}(q)$ do not depend on the $\theta-$coordinate of point q.

Let us set

$$p = (r_0, 0, z_0)$$
$$q = (r, \theta, z)$$

$$k^2(\epsilon) = \frac{4r(\epsilon)r_0}{(r(\epsilon)+r_0)^2 + (z(\epsilon)-z_o)^2}$$

Where $\begin{Bmatrix} r(\epsilon) \\ z(\epsilon) \end{Bmatrix}$ is a given parametrisation for Γ. As reported in [6], it is possible to use the complete integral of the first kind K(k) and the complete integral of the second kind E(k) to rewrite (5) since we have for any surface S :

$$\int_S \frac{1}{|p-q|}dS = \int_0^1 d\epsilon.\frac{4r(\epsilon)\left[(\frac{dz}{d\epsilon})^2 + (\frac{dr}{d\epsilon})^2\right]K(k)}{[(r(\epsilon)+r_0)^2 + (z(\epsilon)-z_0)^2]^{\frac{1}{2}}}$$

and

$$\int_S \frac{\partial}{\partial n}(\frac{1}{|p-q|}).dS = -4\int_0^1 \frac{d\epsilon.r(\epsilon)}{[(r(\epsilon)+r_0)^2+(z(\epsilon)-z_0)^2]^{\frac{1}{2}}}$$
$$\left\{\left[\frac{dz}{d\epsilon}(r(\epsilon)+r_0) - \frac{dr}{d\epsilon}(z(\epsilon)-z_0) - \frac{2}{k^2(\epsilon)}\frac{dz}{d\epsilon}r_0\right]\frac{E(k)}{1-k^2(\epsilon)} + \frac{2}{k^2(\epsilon)}\frac{dz}{d\epsilon}r_0 K(k)\right\}$$

Expressions of E(k) and K(k) were not necessary to reprogram since we used a previous axisymetric code in which the corresponding subroutine had already been made and tested by DYNAFLOW. They are available in [8].

After discretisation of the only Γ section, it is possible to perform the integration of the above expressions so that (5) becomes of the form

$$\sum_j \widetilde{Bij}.\Phi_j + 2\pi\Phi_i = \sum_j \widetilde{Aij}(\frac{\partial\Phi}{\partial n})_j$$

which can again be rewritten as

$$\sum_j Bij.\Phi_j = \sum_j Aij.(\frac{\partial\Phi}{\partial n})_j \tag{6}$$

by including the 2π term in the matrix Bij. The expressions of the elements of A_{ij} and B_{ij} are obtained after integration over a panel, here performed using a Gaussian quadrature.

2.2 Application to our problem

2.2.1 Case of the cylinder in an infinite medium

The previous **2DynaFS** code developped by DYNAFLOW would consider close surfaces such as bubbles in an infinite domain of fluid. In this case, the Γ figure which needs to be discretised is just a cross-section of the bubble, the contribution of the surface at infinity being zero according to our hypothesis (3). For a bubble, the Boundary Element Method assume that we know Φ on the surface of the bubble at each step, so that we can compute $\frac{\partial\Phi}{\partial n}$ by solving system (6).

For the problem of the cylinder, our first studies considered also a closed surface in an infinite domain of water to modelise the rise of the water in the cylinder. That solution turned out to be the easiest way to re-use the already existing **2DynaFS** code with few modifications. A part of that surface is representing the free surface itself, another part is representing the sides and a fictitious top for the cylinder as shown below in figure 1. The introduction of that fictitious top has been necessary to close the surface S.

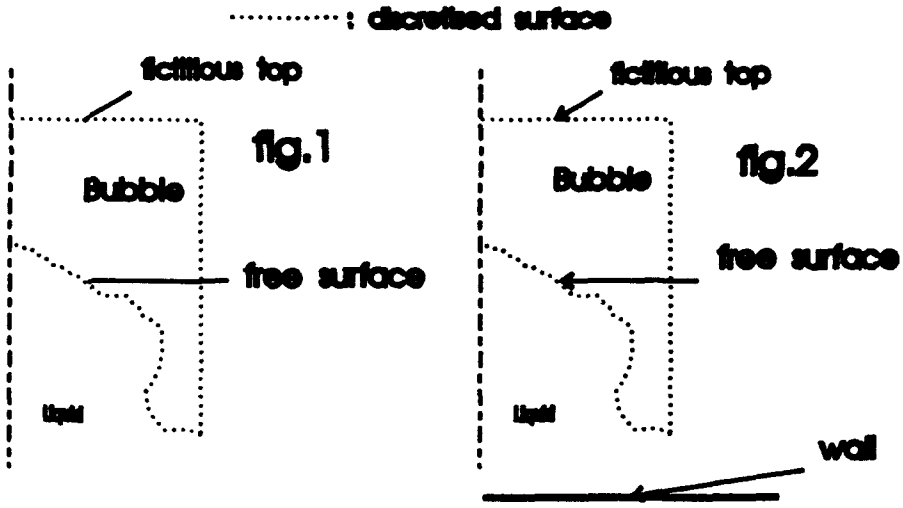

The above figure 1 suppose that the bottom of the tank is far enough from the cylinder so that it can be neglected.

On the sides and on the top of the cylinder, the fluid being inviscid, we have

$$(\frac{\partial \Phi}{\partial n})_{cyl} = 0 \tag{7}$$

As a consequence, system (6) has been re-written in order to have on one side the known quantities $\begin{pmatrix} \Phi \text{ on free surface} \\ \frac{\partial \Phi}{\partial n} = 0 \text{ on cylinder} \end{pmatrix}$ and on the other side the unknown variables $\begin{pmatrix} \frac{\partial \Phi}{\partial n} \text{ on free surface} \\ \Phi \text{ on cylinder} \end{pmatrix}$.

Consequently, if system (6) is equivalent to

$$\begin{bmatrix} B1_{ij} & B3_{ij} \\ B2_{ij} & B4_{ij} \end{bmatrix} \begin{bmatrix} \Phi_j|_{fs} \\ \Phi_j|_{cyl} \end{bmatrix} = \begin{bmatrix} A1_{ij} & A3_{ij} \\ A2_{ij} & A4_{ij} \end{bmatrix} \begin{bmatrix} \frac{\partial \Phi}{\partial n}\big|_{fs} \\ \frac{\partial \Phi}{\partial n}\big|_{cyl} = 0 \end{bmatrix} \tag{8}$$

we may replace it by

$$\begin{bmatrix} A1_{ij} & -B3_{ij} \\ A2_{ij} & -B4_{ij} \end{bmatrix} \begin{bmatrix} \frac{\partial \Phi}{\partial n}\big|_{fs} \\ \Phi_j|_{cyl} \end{bmatrix} = \begin{bmatrix} B1_{ij} & 0 \\ B2_{ij} & 0 \end{bmatrix} \begin{bmatrix} \Phi_j|_{fs} \\ 0 \end{bmatrix} \tag{9}$$

The above system is solved using a L-U decomposition.

2.2.2 Case of a cylinder near a bottom wall

In the case where we want to consider a small distance between the cylinder and the bottom of the tank, we decide to keep from the tank only the bottom part which appears as *an infinite wall*, as said before. The correspondant figure is the above figure 2.

The problem is to find a potential Φ with given values on the free surface such as before, which still satisfies Laplace's equation in the domain above the wall and satisfies the extra boundary condition:

$$(\frac{\partial \Phi}{\partial n})_{wall} = 0$$

We use here the well-known method of the image. By considering an identical twin system located symmetrically to the wall, with the same boundary conditions (same Φ on the image free surface and $(\frac{\partial \Phi}{\partial n}) = 0$ on the sides of the image cylinder), we create another problem whose solution is identical to the solution of our problem. If we use 1 as the indice for the upper (real) system and 2 for the lower (image) system, previous equation (4) remains unchanged as long as we note:

$$S = S_1 + S_2$$
$$\Omega = \Omega_1 + \Omega_2$$

We then have

$$p \in \Omega,\ c(p).\Phi(p) + \int_{s_1} \Phi(q).\frac{\partial}{\partial n}(\frac{1}{|p-q|}).ds_{q1} - \int_{s_1} \frac{1}{|p-q|}.\frac{\partial}{\partial n}(\Phi(q)).ds_{q1}$$

$$+ \int_{s_2} \Phi(q).\frac{\partial}{\partial n}(\frac{1}{|p-q|}).ds_{q2} - \int_{s_2} \frac{1}{|p-q|}.\frac{\partial}{\partial n}(\Phi(q)).ds_{q2} = 0 \qquad (10)$$

System (8) has to be replaced by:

$$\begin{bmatrix} B1_{ij} & B5_{ij} & B1_{2ij} & B5_{2ij} \\ B2_{ij} & B6_{ij} & B2_{2ij} & B6_{2ij} \\ B3ij & B7ij & B3_{2ij} & B7_{2ij} \\ B4ij & B8ij & B4_{2ij} & B8_{2iij} \end{bmatrix} \begin{bmatrix} \Phi j|_{fs_1} \\ \Phi j|_{cyl_1} \\ \Phi j|_{cyl_2} \\ \Phi j|_{fs_2} \end{bmatrix} =$$
$$\begin{bmatrix} A1_{ij} & A5_{ij} & A1_{2ij} & A5_{2ij} \\ A2_{ij} & A6_{ij} & A2_{2ij} & A6_{2ij} \\ A3ij & A7ij & A3_{2ij} & A7_{2ij} \\ A4ij & A8ij & A4_{2ij} & A8_{2ij} \end{bmatrix} \begin{bmatrix} \frac{\partial \Phi}{\partial n}|_{fs_1} \\ \frac{\partial \Phi}{\partial n}|_{cyl_1} = 0 \\ \frac{\partial \Phi}{\partial n}|_{cyl_2} = 0 \\ \frac{\partial \Phi}{\partial n}|_{fs_2} \end{bmatrix} \qquad (11)$$

And (9) becomes

$$\underbrace{\begin{bmatrix} A1_{ij} & -B5_{ij} & -B1_{2ij} & A5_{2ij} \\ A2_{ij} & -B6_{ij} & -B2_{2ij} & A6_{2ij} \\ A3_{ij} & -B7_{ij} & -B3_{2ij} & A7_{2ij} \\ A4_{ij} & -B8_{ij} & -B4_{2ij} & A8_{2ij} \end{bmatrix}}_{(M)} \begin{bmatrix} \frac{\partial \Phi}{\partial n}|_{fs_1} \\ \Phi_j|_{cyl_1} \\ \Phi j\ |_{cyl_2} \\ \frac{\partial \Phi}{\partial n}|_{fs_2} \end{bmatrix} = \begin{bmatrix} B1_{ij} & 0 & 0 & B5_{2ij} \\ B2_{ij} & 0 & 0 & B6_{2ij} \\ B3ij & 0 & 0 & B7_{2ij} \\ B4ij & 0 & 0 & B8_{2ij} \end{bmatrix} \begin{bmatrix} \Phi_j|_{fs_1} \\ 0 \\ 0 \\ \Phi j|_{fs_2} \end{bmatrix}$$

Like previously, our system could be solved using a L-U decomposition of matrix (M). Nevertheless, our problem has in addition the following symmetries:

$$\left.\frac{\partial\Phi}{\partial n}\right|_{fs_1} = \left.\frac{\partial\Phi}{\partial n}\right|_{fs_2}$$
$$\Phi_j|_{cyl_1} = \Phi j|_{cyl_2}$$

The system may then be reduced before being solved in a system of the same size as (9), by adding columns $(m-j)$ of matrix (M) to columns j (where m is the size of matrix M) and by keeping only the first resulting quarter of the matrix so as to obtain:

$$\begin{bmatrix} C1_{ij} & C3_{ij} \\ C2_{ij} & C4_{ij} \end{bmatrix} \begin{bmatrix} \left.\frac{\partial\Phi}{\partial n}\right|_{fs_1} \\ \Phi_j|_{fs_2} \end{bmatrix} = \begin{bmatrix} B1_{ij} & 0 & 0 & B5_{2ij} \\ B2_{ij} & 0 & 0 & B6_{2ij} \end{bmatrix} \begin{bmatrix} \Phi_j|_{fs_1} \\ 0 \\ 0 \\ \Phi j|_{fs_2} \end{bmatrix}$$

What remains to be solved takes therefore about the same time as in the previous case without the wall. In practice, it turned out that cases with a wall ran much slower than without. It must not be forgotten that the above reduction supposes known expression (11) and that consequently the integration has to be performed on all the panels (image included).

Nevertheless, two remarks can be made:

- firstly, by symmetry, the influence of the panel(i) of the object system on the panel(j) of the image system is identical to the influence of the panel(i) of the image system on the panel(j) of the object system. Therefore, we do not need to complete $(2N)^2$ integrations but only $2N^2$.

- secondly, another way to say the same thing would be to notice than since the potential Φ and its normal derivative $\frac{\partial\Phi}{\partial n}$ are identical on the image and on the object, (10) can be re-written as:

$$p \in \Omega,\ c(p).\Phi(p) + \int_{s_1} \Phi(q).\frac{\partial}{\partial n}\left(\frac{1}{|p-q|}+\frac{1}{|p-\tilde{q}|}\right).ds_{q1} - \int_{s_1}\left(\frac{1}{|p-q|}+\frac{1}{|p-\tilde{q}|}\right).\frac{\partial}{\partial n}(\Phi(q)).ds_{q1} = 0$$

where $\tilde{q}$ stands for the the image of q. The above expression halves too the integration work (N^2 bigger integrations and equivallent to $2N^2$ are needed) and gives directly a reduced system between Φ and $\frac{\partial\Phi}{\partial n}$. It enables a discretisation on a cross-section Γ only (and not its image) which reduces the memory space used.

These remarks have unfortunately not yet been exploited in the code.

2.2.3 Case of a second free surface outside the cylinder

We have also developped a code to take into account the second free surface, outside the cylinder. The presence of the wall is treated the same way as before and will not be re-explained here.

The corresponding figure is figure 3.

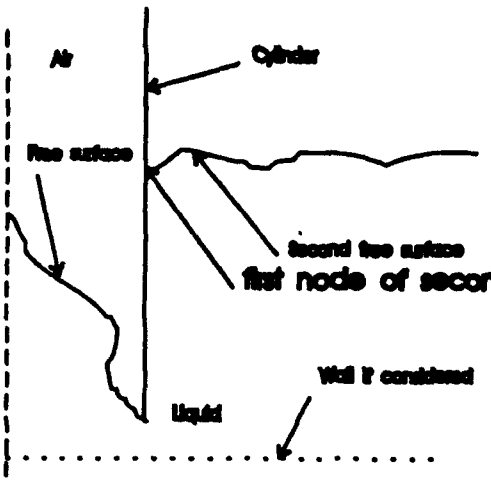

Fig 3.

If we call fs_I and fs_{II} the two free surfaces considered, and their possible images fs_{I2} and fs_{II2}, system (9) is, in the case there is no wall, replaced by

$$\begin{bmatrix} A1_{ij} & -P4_{ij} & A7_{ij} \\ A2_{ij} & -B5_{ij} & A8_{ij} \\ A3_{ij} & -B6_{ij} & A9_{ij} \end{bmatrix} \begin{bmatrix} \frac{\partial\Phi}{\partial n}\Big|_{fsI} \\ \Phi|_{cyl} \\ \frac{\partial\Phi}{\partial n}\Big|_{fsII} \end{bmatrix} = \begin{bmatrix} B1_{ij} & 0 & B7_{ij} \\ B2_{ij} & 0 & B8_{ij} \\ B3_{ij} & 0 & B9_{ij} \end{bmatrix} \begin{bmatrix} \Phi|_{fsI} \\ 0 \\ \Phi|_{fsII} \end{bmatrix}$$

and by a similar expression four times bigger if there is a wall (but it can be reduced after the integration had been made on all the panels, image included, as said previously, and by the same method). The system is then solved as before to get the normal velocity on the two free surfaces and the potential on the rigid boundary.

2.3 Time stepping

The previous sections have shown how Laplace's equation was solved at a given time. To determine the evolution of the shape of the free surface(s), it is necessary to introduce a time discretisation and to give a speed for each node of the discretisation. Given the solution to the Laplace's problem at a time t, time stepping operations consist in defining new positions for the nodes and new boundary conditions at a later time in order to prepare the next resolution of Lapace's problem.

2.3.1 For the cylinder

For the cylinder, time stepping operations are very simple. The boundary conditions used to solved Laplace's equation are always the same. As said before in (7), these conditions require that the normal velocity be zero near the cylinder.

In the case of a fixed cylinder, the nodes remain unchanged during the whole evolution if the second free surface is not taken into account. Otherwise, nodes are equally redistributed at each time step according to the new position given to the first node of the second free surface. The node located at the bottom of the cylinder does not move.

In case of a moving cylinder, we could define the movement of the nodes according to a supposedly given displacement of the cylinder, and following here again a regular distribution as it has been done in previous Bertin's study [7].

2.3.2 For the nodes on the free surface

The method used is the same for both free surfaces described in the previous section. At each time step, after system (6) or an equivallent system is solved for time t, we know $\frac{\partial \Phi}{\partial n}(t)$ on each panel of discretisation. In addition, we can differentiate the potential and compute $\frac{\partial \Phi}{\partial s}(t)$ if we first calculate the length of each panel. We therefore come to know the two components of the velocity $V_x(t)$ and $V_y(t)$ on each panel, and on each node by interpolation. Consequently, we can set a new position for each node using the Adams-Bashforth method of second order:

$$\begin{aligned} X(t+dt_{new}) &= X(t) + (dt_{new} + \tfrac{dt_{new}^2}{2dt_{old}}) * V_x(t) - \tfrac{dt_{new}^2}{2dt_{old}} * V_x(t-dt_{old}) \\ Y(t+dt_{new}) &= Y(t) + (dt_{new} + \tfrac{dt_{new}^2}{2dt_{old}}) * V_y(t) - \tfrac{dt_{new}^2}{2dt_{old}} * V_y(t-dt_{old}) \end{aligned} \tag{12}$$

To use the above expression, it is necessary to explain how to define dt_{new} and dt_{old}. We could have set once for all dt to a very small numerical value and use $dt_{new} = dt_{old} = dt$ in (12). Nevertheless, the velocity field present in the fluid changes with time, especially in a problem where a high speed jet is created. A constant dt for time stepping would either mean very large computation time by choosing a small dt, acceptable for any range of speed encountered, or give wrong results if the selected dt is too large. Consequently, an adaptative time discretisation was used, by calculating at each time step the maximun velocity V_m reached on the nodes and by adapting dt relatively to that velocity. At each step, dt_{old} is given the former value of dt_{new} and dt_{new} is re-set according to the following expression:

$$dt_{new} = \frac{dphi_{\max}}{1 + V_m^2}$$

where $dphi_{\max}$ is a selected parameter to measure the quality of time discretisation.

For the free surface(s), the boundary condition needed to solve Laplace's equation at time $t + dt_{new}$ is the potential $\Phi(t + dt_{new})$. Bernoulli's equation (1) can then be used:

$$\frac{\partial \Phi}{\partial t} + \frac{U^2}{2} + \frac{P}{\rho} + gz = Constant$$

and transformed using expression (2) for the pressure at the free surface:

$$\frac{\partial \Phi}{\partial t} + \frac{U^2}{2} + \sigma \mathcal{C} + gz = gH$$

if we suppose that the fluid is motionless at infinity where $z = H$ and $\frac{\partial \Phi}{\partial t} = 0$.

We also have:

$$\frac{d\Phi}{dt}(t) = \frac{\partial \Phi}{\partial t}(t) + \overrightarrow{U(t)}.\left(\overrightarrow{\nabla}\Phi\right)(t) = \frac{\partial \Phi}{\partial t}(t) + U^2(t)$$

Consequently, we obtain the following expression:

$$\frac{d\Phi}{dt}(t) = \frac{U^2}{2}(t) + [g(H-z)](t) - \sigma \mathcal{C}(t) \tag{13}$$

This can be used to define the new value of Φ using again the Adams-Bashforth method:

$$\Phi(t + dt_{new}) = \Phi(t) + (dt_{new} + \frac{dt_{new}^2}{2dt_{old}}) * \frac{d\Phi}{dt}(t) - \frac{dt_{new}^2}{2dt_{old}} * \frac{d\Phi}{dt}(t - dt_{old}) \tag{14}$$

2.4 Summary and flowchart

Let us summarize now the previous statements:

- We suppose that we know Φ on the free surface at the beginning time t_0 (In practice, we took zero for the initial potential on the free surface). We also know the shape of the free surface and that the normal condition (7) is satisfied on the cylinder.
- We compute using Green's Identity the value of $\frac{\partial \Phi}{\partial n}(t_0)$ at the same time t_0.
- We deduce the velocity on the boundary S.
- We define dt_{new} relatively to the maximum velocity found on the free surface(s).
- We can set the new values of $X(t_0 + dt_{new})$ and $Y(t_0 + dt_{new})$ at each node using the Adams-Bashforth method.
- We use (13) and (14) to define $\Phi(t_0 + dt_{new})$ at each node.
- We are ready to start another iteration at time $t_0 + dt_{new}$.

A more detailed flowchart of the last version of the code used is given in figures [2.4.0] and followings [2.4.1] to [2.4.9]. [2.4.0] takes into account other computational tools that will be seen in the following sections.

2.5 General assumptions made in the study

2.5.1 Assumptions

The thickness of the cylinder has been neglected.

The problem of the shape to be given initially to the free surface remains unsolved. Therefore, in most cases, it was considered an initially flat free surface inside the cylinder. The initial conditions corresponding to such a hypothesis were unfortunately unknown too. Consequently, as said before, we took $\Phi = 0$ on the initial free surface for the first time step which corresponds to assuming that all the fluid is motionless when we start.

2.5.2 Notations

We haved used the following physical parameters in our study :

H:depth of water
R: radius of the cylinder
$\Phi(r, z)$: velocity potential
l: height of the cylinder
d: distance between the cylinder and the *wall*
σ: surface tension parameter
ρ: density of water
g: gravity

2.5.3 Non-dimentionalisation

We use H as the parameter to non-dimentionalise distances so that :

$$\widetilde{H} = \frac{H}{H} = 1,\ \tilde{R} = \frac{R}{H},\ \tilde{l} = \frac{l}{H},\ \tilde{d} = \frac{d}{H}$$

We set to 1 the value of gravity which is equivalent to non-dimentionalise times by $\sqrt{\frac{H}{g}}$.

$$\tilde{T} = \frac{T}{\sqrt{\frac{H}{g}}},\ \tilde{\Phi} = \frac{\Phi}{H.\sqrt{g.H}},\ \tilde{U} = \frac{U}{\sqrt{g.H}},\ \frac{\tilde{\sigma}}{\rho} = \frac{(\frac{\sigma}{\rho})}{g.H^2}$$

Pressures do not need to be non-dimentionalised since they do not appear in equation (13).

3 Test of the reliability of the code

3.1 Necessity of the 'Regridder'

When the shape of the free surface changes, the geometrical repartition of the nodes changes too and may become uneven after a certain number of iterations. The purpose of a 'Regridder' is to prevent such an uneven distribution by a regular re-distribution of the position of the nodes after a certain number of time steps. First, it appears to be necessary to define a curvilinear abscissa s on the cross-section Γ. Then the length of the free surface is divided equally into the number of panels to assign a new curvilinear abscissa for each node. Finally, for each node, the value of $X, Y, \Phi, \frac{d\Phi}{dt}, V_x, V_y$ is re-set using a cubic interpolation of the corresponding function of s.

It is possible not to divide equally the length of the free surface in order to emphasize the accuracy and precision of the discretisation in a certain region of the free surface. In the case of the present problem, the axis of symmetry is very important since it is the location of the jet and the region of the highest velocities. So, it was decided to emphasize that region by subdividing the total free surface length according to the following distribution:

$$s(i) = s(Nb_{nodes}).(\frac{i-1}{Nb_{nodes}-1})^{\alpha} \tag{15}$$

where i is an indice for the nodes, starting at the axis, Nb_{nodes} the number of nodes on the free surface, and α a real parameter.

Results showed that this 'regridding' subroutine do not modify too much computation times. Consequently, it was used at each time step. To prevent a loss of information on the regions away from the axis of symmetry, the concentration procedure corresponding to (15) has been used only every other step (staggered regridding). Otherwise, we kept a linear re-distribution ($\alpha = 1$).

The differences introduced by the 'Regridder' appeared to be significant as is shown in figures [3.1.1],[3.1.2],[3.1.3].[3.1.3] shows that without 'Regridder', the computation is stopped very soon because the nodes are not equally distributed. We can see the formation of two numerical instabilities, near the sides of the cylinder. These instabilities are removed thanks to the 'Regridder' on figures [3.1.1],[3.1.2].[3.1.1] is a case of 'staggered regridding' and proves to be a better way of 'regridding' than [3.1.2], a case of linear regridding.

Different values of α were tried after we decided to use a 'staggered regridding'.

First we took $\alpha = 2$ like on [3.1.1] and then α was reduced to 1.1, because it turned out that the nodes were too concentrated on axis with $\alpha = 2$, especially after a great number of time steps as it is shown on figure [3.1.4].

Finally, we choose not to use any linear re-distribution but a two stage 'Regridding', using alternatively $\alpha = 0.9$ and $\alpha = 1.1$ and a good space discretisation.

In fact, it would have been very interesting if we could have replaced a good discretisation by a concentration of panels on the axis. But as said before, it had not been possible to do so because of problems at the end of computation as seen on [3.1.4].

Other different ways of regridding were also tested, such as a three stage 'Regridder', concentrating the panels on axis, then on the other extremity, and finally without concentrating any region (linear distribution). They did not give a better smoothing of the shape than the previous one, with the same number of panels.

3.2 Convergence Study on the number of panels and on time discretisation (without averaging)

After having selected a good regridding option, the first studies carried out on the code were directed to demonstrate that we had a convergence of the results on the number of panels and on time discretisation. We did not take into account the presence of the wall nor did we average here. Similar results obtained using an average procedure will be presented in the next section.

3.2.1 Effect of the discretisation on the free surface

Results are shown on figures [3.2.1.1] and [3.2.1.2]. As one can see, the position of the first node in time converges to a limit position when the number of panels increases from 14 to 40. The same observation can be made for the velocity of the first node.

3.2.2 Effect of the discretisation on the cylinder

Results are shown on figures [3.2.2.1], [3.2.2.2] and [3.2.2.3]. Here again, the consistency of the code turned out to be very satisfying and one can observe that both figures corresponding to the first node position and the first node velocity converges when the number of panels is increased from 6 to 20.

3.2.3 Effect of time discretisation

One free surface Figures [3.2.3.1] and [3.2.3.2] show respectively the position of the first node and the position of a point located at absciss 0.2 m for different values of time discretisation, by using a height l=4m for the cylinder. We notice that the convergence is quite good for the beginning of computation (before 0.3 second). We also present on the same figures (doted line) the case where the height of the cylinder is increased to 6 meters.

After 0.3 second, the convergence is not satisfying at all. Especially, the fact that the two drawings corresponding to dphi=0.008 are so different proves that the height of the cylinder is very important. In fact, what we observe at this time

is mostly the influence of the top of the cylinder, obviously less important when the height of the cylinder is 6 meters. That is why it is observed that the jet rises more slowly for a height of 4 meters than for 6 meters. Not satisfied with these results, two possibilities were offered to us. Either we would increase the height of the cylinder to 6 meters and re-do the same study, or we would test the convergence on time discretisation taking into account the two free surfaces to remove the problems created by the top of the cylinder. We decided to focus on that second possibility.

Two free surface The study was carried out with the same parameters as previously. Results are shown on figures [3.2.3.3] and [3.2.3.4]. This time, the convergence is better, even if computation was not made last as long as before. Hardly any differences can be seen between the different cases of time discretisation tested before 0.6 second for the position of the first node.

3.2.4 Interpretation-Conclusion

The tests made above were very important. They proved the reliability of the code and gave an idea of the level of discretisation to be used for real studies.

A last remark must be made about the above convergence study on discretisation (time and panels). We have shown that a quite satisfying convergence was observed for the position of the top node, for its velocity and for the position of a node at absciss =0.2m. That does not really prove that the whole shape converges so fast. An illustration is given with figures [3.2.4.1] and [3.2.4.2], which present a case made taking into account two free surfaces, and using a good space discretisation. Even if we had previously observed that the position of the first node was unchanged for dphi=0.008 and dphi=0.005, the corresponding shapes are different. Since the drops observed on [3.2.4.1] are removed with a better time discretisation on [3.2.4.2], they are probably not real, as we first thought they were. Figures [3.2.4.3] and [3.2.4.4] prove that time discretisation must also be adapted to the physical problem, and to the order magnitude of the velocities encountered. They represent the shape of the free surface at the beginning of the computation, with a unsually large depth of water (2m). The higher velocities involved make the computation stop in [3.2.4.3] (dphi=0.008), while it goes on for [3.2.4.4] (dphi=0.004)

3.3 Effects of averaging

Some numerical instabilities or perturbations can appear during the evolution of the free surface, and grow uncontrolled by the code, while in reality perturbations are smoothed and controlled by fluid viscosity. As a result, some very high speed non-physical velocities (100 m/s for instance) were sometimes encountered during computation. This is due to our modelisation which supposes the fluid to be

ideal. To prevent the formation of these instabilities, the option of averaging was made possible. An average parameter N_{avg} was used with different values, and corresponds to the following expression:

$$q_{corrected}(i) = \frac{N_{avg}.q(i) + q(i+1) + q(i-1)}{N_{avg} + 2},$$

where $q(i)$ is any quantity depending on the node indice.

First, we applied the averaging to the coordinates and to the velocity potential, but it turned out that the code was not consistant in this case and that this method was not necessary for computation. We went on with averaging only on the velocity potential.. Effect are shown on figures [3.3.1] to [3.3.4]. On these figures, the attention is laid on the fact that each drawing corresponds to the shape of the free surface at a time, without any similarity of time between figures. They are just shown to give an idea of the general evolution of the shape in each case. Figures [3.3.5] and [3.3.6] show the position in time of the first node and the position of a node at absciss=0.2 m.

It is clear that even a large number of N_{avg} (like 100 for instance) might be dangerous and smooth the shape too much. Another important remark is that average effects depend strongly on time discretisation as it is proved by figures [3.3.7] to [3.3.11]. These represent a comparison of the shape of the free surface when the parameter for time discretisation varies from 0.03 (bad) to 0.002 (good). A good time discretisation means a lot of time steps and a lot of averaging (and therefore loss of information) per unit of time. That is why it has been observed that a better time discretisation gave worse results than a coarse one when using averaging. The parameter for average is the same in the five figures [3.3.7] to [3.3.11] : $N_{avg} = 100$. As one can see, the jet is killed by using a good time discretisation and undirectly averaging so much that the shape is flatened on the axis (figures [3.3.11] and [3.3.12]).

Nevertheless, as different as figures [3.3.1] to [3.3.1] and [3.3.7] to [3.3.11] may look, it has been observed that they were very similar except for the region were the jet is localised. If we consider, for instance, the vertical position of a point located at half the radius of the cylinder from the axis, for different parameters $N_{avg} = 30, 100, 300$, and ∞ (no average), keeping constant the time discretisation, the corresponding figures are very similar as shown in figure [3.3.6]. The same observation can be made by keeping the same average parameter ($N_{avg} = 100$) and by changing time discretisation (figure [3.3.13]).

3.4 Effects of surface tension

Surface tension was introduced in this study since it was not present in the previous code used by DYNAFLOW in [7] and Bernoulli equation was replaced by the expression (13) as seen before . The curvature C is computed by calculating for each node the coordinates of the center of the circle going through this node and its

two neighbour nodes. As a general rule, tested cases turned out not to depend on whether surface tension was taken into account or not for the physical value of the σ parameter for an air-water surface (see figure [3.4]). But, it is to be noticed that this is probably normal since our results never showed especially high curvatures, except may be on the axis.

3.5 Introduction of a numerical viscosity

To stabilize the computation when numerical instabilities would occur, especially on the axis, in the area of the jet, an artificial numerical viscosity scheme was implemented. The purpose of this research was to take into account as many terms as possible from the Navier-Stokes equations by changing the time stepping expression (13). We report here the main ideas.

The Navier-Stokes equation of motion is:

$$\frac{d\vec{U}}{dt} = -\frac{1}{\rho}\vec{\nabla}(p+\rho gz) + \vec{\nabla}(\lambda div\,\vec{U}) + 2div(\mu\underline{\underline{d}})$$

with $\underline{\underline{d}} = \frac{1}{2}(\vec{\nabla}\vec{U} + (\vec{\nabla}\vec{U})^t)$.

We still neglect the fluid compressibility effects ($div\,\vec{U} = 0$) and we keep $rot\,\vec{U} = 0$. That means that we keep the assumption of a velocity potential in presence of viscous effects. As a consequence, ρ is still supposed constant and:

$$\frac{d\vec{U}}{dt} = \frac{\partial\vec{U}}{\partial t} + rot\,\vec{U}\wedge\vec{U} + \vec{\nabla}(\frac{U^2}{2}) = \frac{\partial\vec{U}}{\partial t} + \vec{\nabla}(\frac{U^2}{2}) = -\vec{\nabla}(\frac{P}{\rho}+gz) + 2div(\mu\underline{\underline{d}})$$

Therefore, expression (13) has to be replaced by:

$$\frac{d\Phi}{dt} = \frac{U^2}{2} - gz - \sigma\mathcal{C} + 2\frac{\mu}{\rho}(\underline{\underline{d}}.\underline{n}).\underline{n}$$

where $\underline{n}$ is the normal vector as shown in the scheme below:

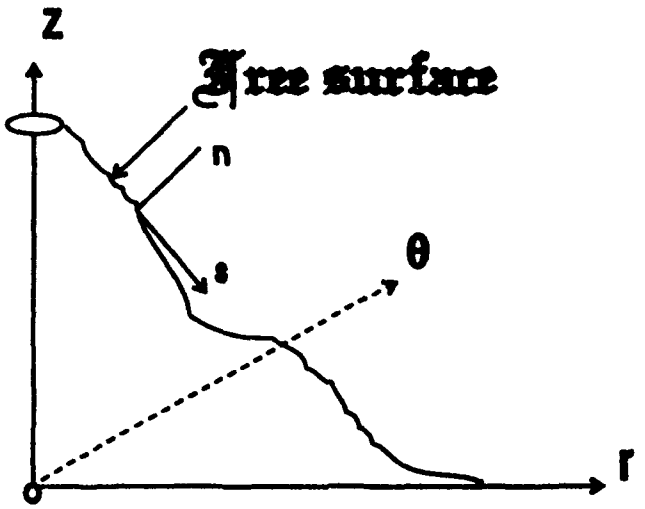

we should therefore find an evaluation of $(\underline{\underline{d}}.\underline{n}).\underline{n}$. In the code, we compute the vector $\underline{n}$ normal to the boundary which can be expressed in the cylindrical coordinates system $(\overrightarrow{e_r}, \overrightarrow{e_z})$ as:

$$\begin{array}{l} \underline{n} = \alpha\overrightarrow{e_r} + \beta\overrightarrow{e_z} \\ \underline{s} = \beta\overrightarrow{e_r} - \alpha\overrightarrow{e_z} \end{array} \quad \text{with } \alpha^2 + \beta^2 = 1$$

where α and β are known. We also have:

$$\underline{\underline{d}} = \begin{bmatrix} \frac{\partial u_r}{\partial r} & 0 & \frac{1}{2}(\frac{\partial u_r}{\partial z} + \frac{\partial u_z}{\partial r}) \\ 0 & \frac{u_r}{r} & 0 \\ \frac{1}{2}(\frac{\partial u_r}{\partial z} + \frac{\partial u_z}{\partial r}) & 0 & \frac{\partial u_z}{\partial z} \end{bmatrix}$$

so

$$(\underline{\underline{d}}.\underline{n}).\underline{n} = \alpha^2\frac{\partial u_r}{\partial r} + 2\alpha\beta(\frac{\partial u_r}{\partial z} + \frac{\partial u_z}{\partial r}) + \beta^2\frac{\partial u_z}{\partial z}$$

Let us compute $\frac{\partial^2\Phi}{\partial s^2}$:

$$\frac{\partial\Phi}{\partial s} = \frac{\partial\Phi}{\partial r}(+\beta) - \frac{\partial\Phi}{\partial z}(-\alpha)$$

$$\frac{\partial^2\Phi}{\partial s^2} = \frac{\partial^2\Phi}{\partial r^2}\beta^2 + \frac{\partial^2\Phi}{\partial z^2}\alpha^2 - 2\alpha\beta\frac{\partial^2\Phi}{\partial r\partial z} + \frac{\partial\Phi}{\partial r}(\frac{\partial\beta}{\partial s}) - \frac{\partial\Phi}{\partial z}(\frac{\partial\alpha}{\partial s})$$

Consequently, we get

$$(\underline{\underline{d}}.\underline{n}).\underline{n} = -\frac{\partial^2\Phi}{\partial s^2} + \frac{\partial^2\Phi}{\partial r^2} + \frac{\partial^2\Phi}{\partial z^2} + \frac{\partial\Phi}{\partial r}(\frac{\partial\beta}{\partial s}) - \frac{\partial\Phi}{\partial z}(\frac{\partial\alpha}{\partial s})$$

$$(\underline{\underline{d}}.\underline{n}).\underline{n} = -\frac{\partial^2\Phi}{\partial s^2} - \frac{1}{r}\frac{\partial\Phi}{\partial r} + V_r(\frac{\partial\beta}{\partial s}) - V_z(\frac{\partial\alpha}{\partial s})$$

Finally, since $\underline{s} = \beta \overrightarrow{e_r} - \alpha \overrightarrow{e_z} = \frac{dr}{ds} \overrightarrow{e_r} + \frac{dz}{ds} \overrightarrow{e_z}$, we have:

$$\frac{d\Phi}{dt} = \frac{U^2}{2} - gz - \sigma C + 2\frac{\mu}{\rho}(-\frac{\partial^2 \Phi}{\partial s^2} + V_z \left.\frac{d^2 z}{ds^2}\right|_{fs} + V_r(-\frac{1}{r} + \left.\frac{d^2 r}{ds^2}\right|_{fs}))$$

The above expression does not depend on the orientation chosen for the normal vector, and remains correct for all types of geometry. It was used in the code instead of (13) after the second derivatives $\frac{d^2 r}{ds^2}$ and $\frac{d^2 z}{ds^2}$ have been computed. The quantity $\frac{\mu}{\rho}$ has been non-dimentionalized as:

$$\frac{\widetilde{\mu}}{\rho} = \frac{\frac{\mu}{\rho}}{H.\sqrt{gH}}$$

The results were not actually satisfactory and the expected smoothing effects were not obtained for a physical value of the viscosity parameter μ. Results are shown on figure [3.5]. As one can see, no difference has been observed with and without using an artificial viscosity as long as we kept $\mu = 10^{-3} kg.m^{-1}.s^{-1}$ which correspond to the real value. For larger values of μ, a difference has been observed, but not in the right direction. On the opposite, the jet appeared more prononced and with a faster velocity field for $\mu = 10^{-2} kg.m^{-1}.s^{-1}$ than for $\mu = 10^{-3} kg.m^{-1}.s^{-1}$.

We were unfortunately unable to understand the reason of such results, except that such an artificial implementation of viscosity may not be compatible with a potential modelisation.

3.6 Adaptative space discretisation

In order to reduce computation times while improving accuracy, the idea of an adaptative space discretisation was introduced. It turned out to be easy to add to the code since the distribution of panels was already changed regularly with the 'Regridder' subroutine. As the length of the free surface changes, we adapt the number of panels proportionaly in order to gain time at the beginning of computation when that length is small. It was necessary to define a maximun number of nodes accepted, to keep the discretisation inside an acceptable range of values. The results were not very encouraging since they were in most cases the same as those obtained with an intermediate constant space discretisation nearly equivalent to the worse one in the sellected range.

3.7 Conclusions

Best results were obtained using:

- a staggered regridding using both $\alpha = 1.1$ and $\alpha = 0.9$ with the previous notations.

- no averaging. If averaging is necessary (for instance to go on the computation after the jet as become very thin), an average parameter of 500 is acceptable.

- no adaptative space discretisation, but as good a discretisation as possible (up to 100 panels was possible for the entire discretisation).

- results were independent of whether surface tension and numerical viscosity were considered or not.

The following observations can be helpful for the future studies:

- The code is very sensible to time discretisation. Dphi=0.02 is usually too coarse. Changing for a better time discretisation is often the solution to remove numerical instabilities which stop the computation.

- The space discretisation must be adapted to the physical problem. If the important region is the jet, concentrating the panels on the jet is a necessity.

- In our problem, the bottom of the cylinder was more important than the top. Concentrating at the bottom has improved the quality of the results.

- Space and time discretisation must be adapted together. We have observed, for instance, instabilities for 50 panels on FS with dphi=0.02, and no problem for 24 panels with dphi=0.02. This is because dphi=0.02 is too coarse, and some nodes would touch each other with 50 panels and not 24.

- Averaging should be used if necessary only, relatively to time discretisation.

- In case the liquid has a deformation in one special direction, scaling problems must be looked at seriously.

4 Results

4.1 Analytical approach

It is possible to get an idea of the velocity fields involved in our problem by trying to find an analytical solution of a much simpler problem. Keeping to the case where the bottom of the tank is far away from the cylinder so that it can be neglected, and also supposing the cylinder to be rigidly fixed, a solution can be easily found if we assume that the whole free surface rises with the same speed so as to remain flat all the time.

If Z(t) is the vertical position of the free surface, and $v(t)$ its vertical speed (supposed uniform), the potential is at each time:

$$\Phi(x,y,z,t) = v(t).z$$

Bernoulli's equation gives us the equation of motion of the free surface very easily and we have:

$$\frac{d^2Z}{dt^2}.Z + \frac{1}{2}.(\frac{dZ}{dt})^2 + gZ = g.H$$

Non-dimentionalised as before, it becomes:

$$\frac{d^2x}{dt^2}x + \frac{1}{2}(\frac{dx}{dt})^2 = 1 - x \tag{16}$$

We must notice that no solution satisfies both (as it is in reality):

$$\begin{array}{c} \frac{dx}{dt}(t=0) = 0 \\ x(t=0) = 0 \end{array} \tag{17}$$

We set $k(x) = (\frac{dx}{dt})^2$ so that (16) becomes:

$$\frac{dk}{dx} + \frac{k}{x} = \frac{2(1-x)}{x}$$

for which a solution is:

$$k = \frac{C}{x} + 2 - x$$
$$\textit{where } C \textit{ is a constant.}$$

If we assume that instead of (17) , we can take:

$$\begin{array}{c} \frac{dx}{dt}(t=0) = 0 \\ x(t=0) = \delta \end{array}$$

where $\delta = o(1)$, the solution is given by:

$$\frac{dx}{dt} = \begin{array}{c} + \\ - \end{array} \sqrt{(2-x) + \frac{\delta(\delta-2)}{x}}$$

Results of such a modelisation are given on figures [4.1.1],[4.1.2].

We notice that the speed of such a free surface increases fast at the beginning to reach 3.7 meters per second approximatively after 1 second in our example (depth=1m). The movement of the free surface is characterised by oscillations, as one could have obviously imagined, the frequency being around 2 seconds for a depth of 1 meter. Since this model ignores viscosity, oscillations do not decay but remain of constant amplitude while in reality, oscillations would cease after a few seconds.

We will compare the order of magnitude of our numerical results with these ones.

4.2 Numerical results

A complete convergence study on panels has not been made with the last version of the code though no difference has been noticed among all the results that were obtained with it using at least 40 panels on the first free surface (for R=0.4 m), 8 panels per meter at least on the sides of the cylinder, and 10 per meter at least on the second free surface. The radius of the cylinder was set to R=0.4 m. When the depth of water is not precised in the following results, it is meant 1 meter of water above the bottom of the cylinder. In all the cases presented below, the staggered regridding selected in 3.1 was used. When the radial distance of any node would become smaller than a very small value, averaging would start automatically in the code with a parameter $N_{avg} = 500$.

In all the cases, it was necessary to prevent the nodes to touch the sides of the cylinder to enable the computation to continue. Is was also found, especially without averaging, that the high velocity field encountered in the jet area was slowing down the computation because of our adaptative time discretisation. As soon as highly non-physical speeds were found, computation was stopped.

A particular phenomenon observed was the creation of a drop on the top of the jet as it can be seen on figures [4.2.2.2] to [4.2.2.7], [4.2.2.8] to [4.2.2.12],[4.2.2.13] to [4.2.2.16],[4.2.2.17] to [4.2.2.19] and [4.2.3.1] to [4.2.3.5]. A second drop due to the constriction of the jet at its basis (figures [4.2.2.12],[4.2.2.19],[4.2.3.5]) may also appear. These drops have also been reported in the experiments. We tried once to carry on the computation after removing the top drop, but this did not prevent the code from slowing down because of the high speeds in the jet area. Nevertheless, this showed the creation of another drop at the same place as if to replace the one that had been removed.

4.2.1 Influence of the second free surface

It was found that the motion of the second free surface is very limited for $H = 1m$ and no wall under the cylinder. Consequently, another case was considered by using a larger cylinder radius and a lower height of the water to force the water

rising in the cylinder to come from near the second free surface. We took $R = 1m$ and $H = 0.5m$ and we only considered the case without wall. It appeared that the shape of the first free surface was nearly the same as without the second free surface even in this case. Results are given on figure [4.2.1.1],[4.2.1.2],[4.2.1.3] where we can also see that the introduction of the second free surface has not changed too much the speed of the first node or its position in time by far.

We focus on the position of the second free surface at different times on figure [4.2.1.4], [4.2.1.4'] and [4.2.1.4"]. Since the depth of water used in that example is one meter, the initial shape of the second free surface is a horizontal flat line at Z=1 meter. Near the cylinder, the water seems to fall at first while it is rising in the cylinder (fig [4.2.1.4]). Then a small wave can be observed rising near the cylinder between 0.54 second and 0.71 second as the average level of water starts to decrease in the cylinder (fig [4.2.1.4']). It looks as if that wave starts to propagate away from the cylinder, as it is suggested by figure [4.2.1.4"] corresponding to time=0.739 second to 0.871 second.

Figures [4.2.1.5] and [4.2.1.6] show the velocity field at time 0.48 second. It appears that the water comes more from the sides and from under the cylinder than from the region of the second free surface. It is to notice that velocities are far more important near the bottom of the cylinder, as one would have expected.

4.2.2 Influence of the wall

Results without the wall were compared with satisfaction to the theoretical model described above. Figure [4.2.2.1] shows the speed of the free surface in the two cases. For the previously studied modelisation, the doted line shows the quantity $\frac{dZ}{dt}$ while the continous line corresponds to the speed of a point located at half the radius from the axis, which can be considered as a kind of average speed of the free surface. Though the two problems are completely different, we were surprised to observed that the two figures are very similar. We can also notice that after 0.6 second in the case studied, the average speed on the free surface is negative, which means that the level of water has reached its top position and is starting to decay and oscillate. Instabilities observed later are due to the very thin jet on axis and to contacts between some nodes of the discretisation.

The results of the study made on the distance of the wall are shown on figures [4.2.2.2] to [4.2.2.19]. Distances to the wall vary in the range [0.1 meter-1 meter]. These figures are shown seperately to see the position of the free surface vary in time for different distances to the wall.

A first observation shows that the computation lasts longer when there is no wall and then when the wall is far, because the proximity of the wall creates higher velocities which slow down and stop the code as said before. For instance, at 0.514 sec, the jet has already reached a height of 5.9 meters (probably non-physical) if the wall is at 0.1 meter, while it has only reached 3.2 meters if the wall is at 0.3 meter and 3.4 meters if the wall is at 1 meter.

We notice that the wall does not always create higher velocity fields. The jet is higher without a wall than for a 0.3 or 1 meter away wall for times 0.514 and 0.625 sec. Nevertheless, we fortunately remarked that when the distance to the wall increases, the shapes converge to the one corresponding to the absence of wall. This observation is probably more obvious on figure [4.2.2.20] were we compare the speed of the first node on the jet for different values of the distance to the wall. It is interesting to notice that without a wall or with a far distant wall, that speed increases immediately, while it takes nearly 0.1 second when the wall is 0.1 meter far. This correspond to the time for the water fronts to converge toward the axis since there is no water to rise under the cylinder in that case.

Velocity fields are shown for two distances of the wall (0.1m and 0.3m) on figures [4.2.2.21],[4.2.2.22] at time 0.25 s.

4.2.3 Influence of the depth of water

A few runs have been made with different depths of water. We have already reported (figures [3.2.4.3] and [3.2.4.4]) that with a higher depth (2 meters here), a greater velocity field was observed, as expected, and that it causes some computional problems since we had to improve by a factor of two the parameter for time discretisation to go on. Results for the shapes are reported in figures [4.2.3.1] to [4.2.3.5] and must be compared with [4.2.2.17] to [4.2.2.19]. The general shape is the same as for the 1-meter depth of water except that times are reduced. Before 0.3 second the jet is already very high and the previously reported drop already created. Figures [4.2.3.6] and [4.2.3.7] show well how much speed varies with the depth of water, while all the other parameters are unchanged (distance to the wall = 0.1m).

Conclusion

This study has helped understand better the behaviour of free surfaces and jets in a particular case.

Many computational tools were tested and introduced to take into account physical realities which we had first intended to neglect, such as a numerical viscosity. Other improvements have to be completed.

The code used for this study may be suitable with few modifications to modelise other phenomena where free surfaces are involved. Even if our attention has been mainly focused on the problem of the cylinder, the study could be extended to air-water free surfaces in general. For instance, the code used could be easily transformed with benefit to describe what finally happens when an air bubble rises in a liquid, collapses and touch the air-water surface.

We give a few examples with figures [5.1] and following.

References

[1] G.Birkhoff, E. Zarantonello.

"Jet, Wakes and Cavities", Applied Mathematics, Volume two.

Academic Press Inc. Publisher, New York, 1957.

[2] Georges L. Chahine.

"Dynamics of the interaction of non-spherical cavities", Chapter 4 in Fluid Vortices,

Edition Sheldon Green, Auwer Academic Publishing, to appear 1994.

[3] J.S. Darrozes et G.L. Chahine.

"Les recherche sur le phenomene de cavitation effectuees a l'Ecole Nationale Superieure Des Techniques Avancees".

Extrait de Sciences et techniques de l'armement, Memorial de l'artillerie francaise, Paris, imprimerie nationale, 1983.

[4] G.L. Chahine.

"Etude locale du phenomene de cavitation. Analyse des facteurs regissant la dynamique des interfaces."

These de Doctorat d' Etat, Universite Pierre et Marie Curie, Paris VI, France, Juin 1979.

[5] A.A Becker.

"The Boundary Element Method in Engineering", A complete course.

Department of Mechanical Engineering, University of Nottingham, U.K, pp125-131, 1992

[6] Bachok Bin Taib.

"Boundary Integral Method Applied to cavitation bubble Dynamic."

Ph-D Thesis from the University of Wollongong, 1985

[7] G.L. Chahine and R. Duraiswani.

Modelisation de la formation d'un jet a l'entree d'un cylindre.

DYNAFLOW,INC. Report 92002-1-Bertin, fevrier 1992.

[8] Hasting, C. Jr.,"Approximation for digital computers."

Princeton University Press, Princeton, N.J,1955.

MAIN FLOWCHART

FIG. 2.4.0

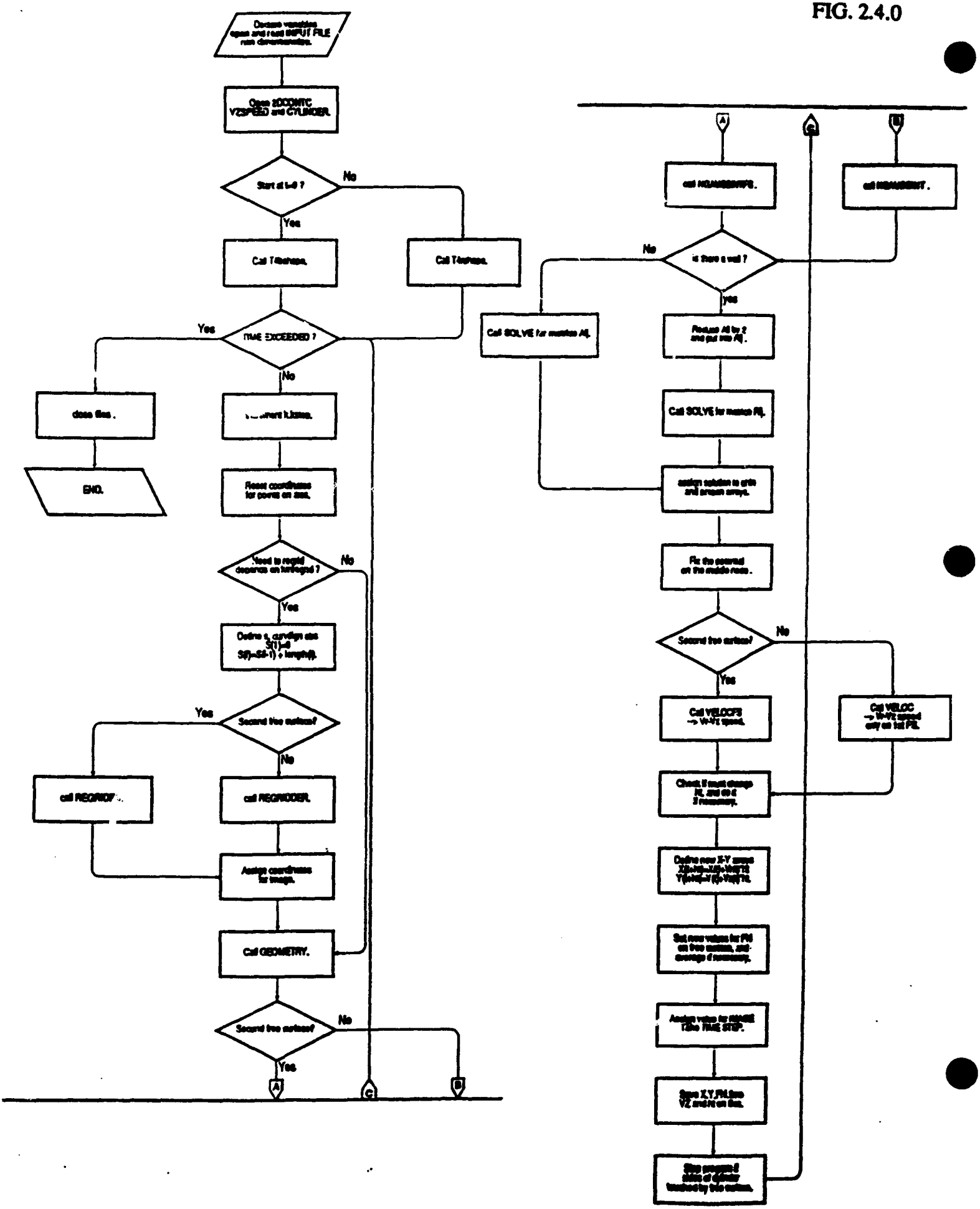

SUBROUTINE NGAUSSINT

FIG. 2.4.1

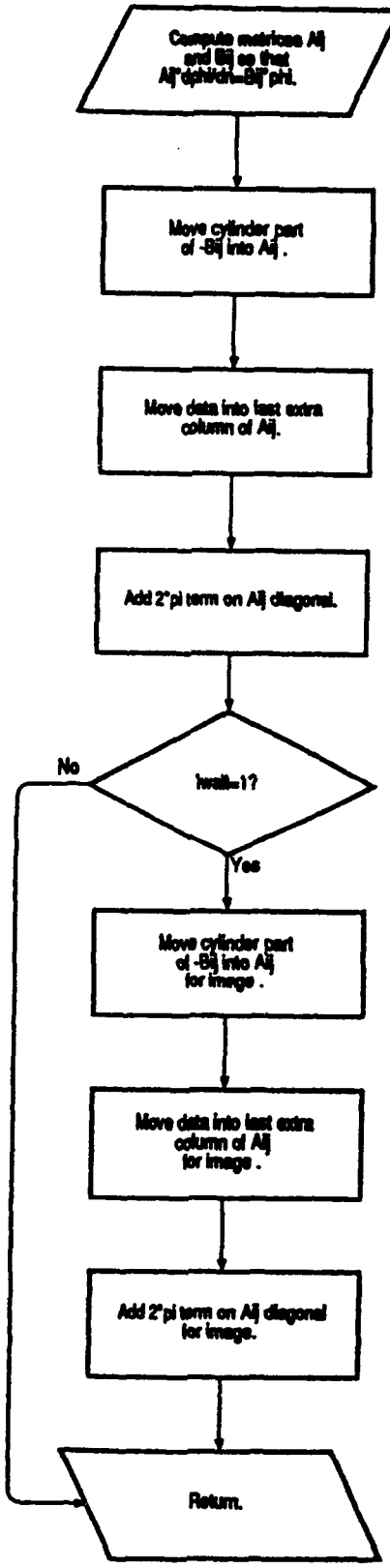

SUBROUTINE REGRIDFS

FIG. 2.4.2

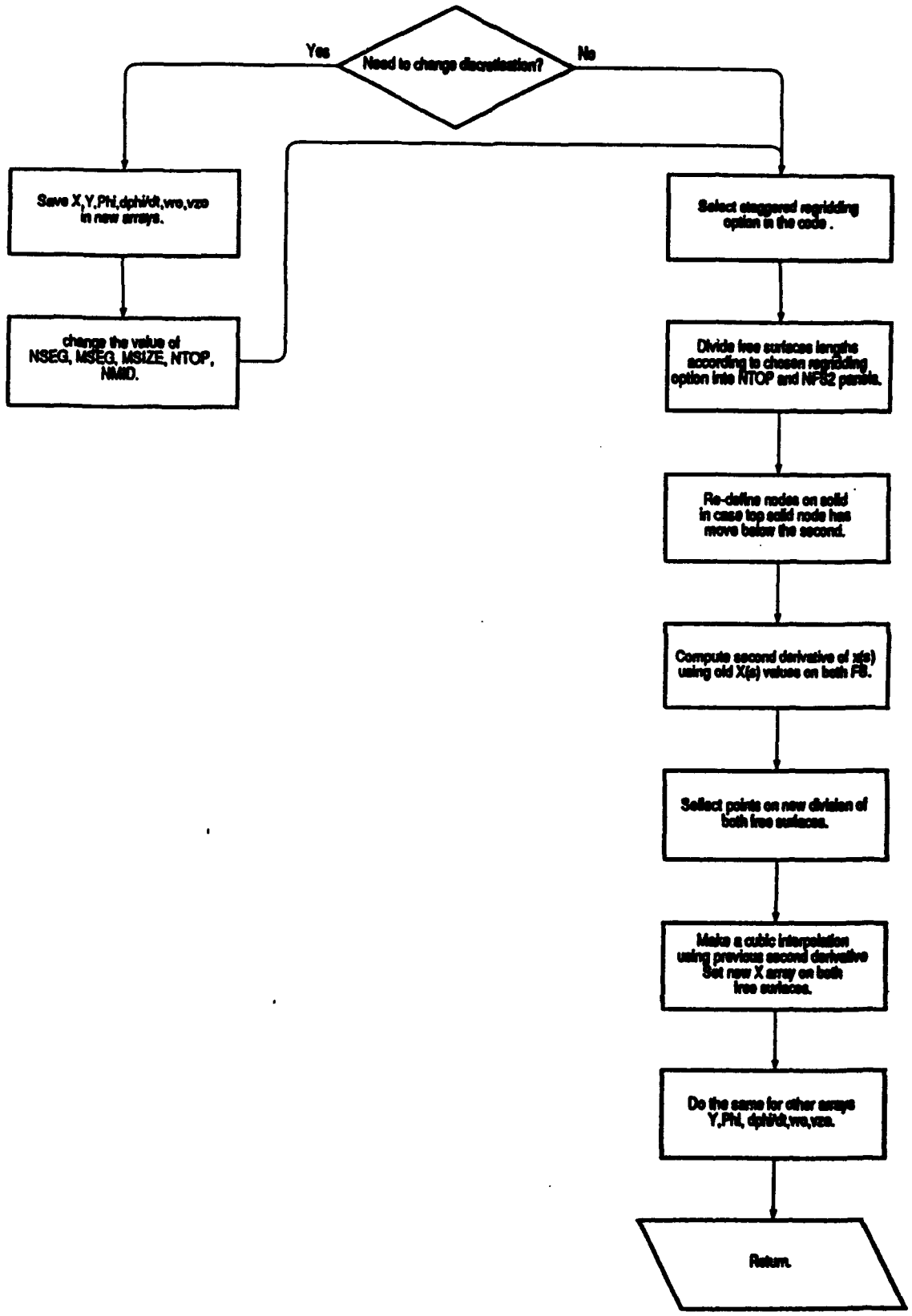

SUBROUTINE REGRIDDER

FIG. 2.4.3

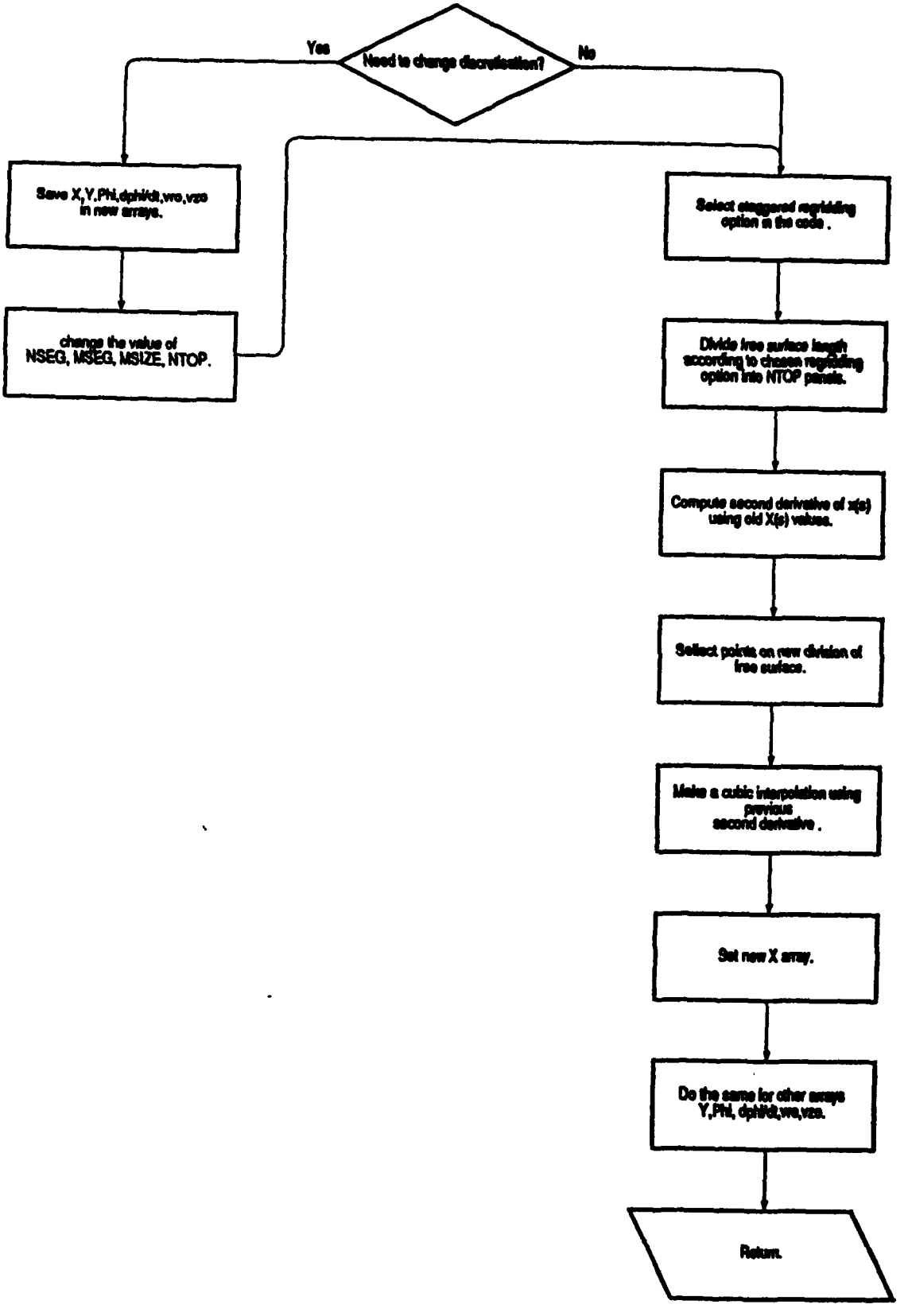

SUBROUTINE VELOCFS

FIG. 2.4.4

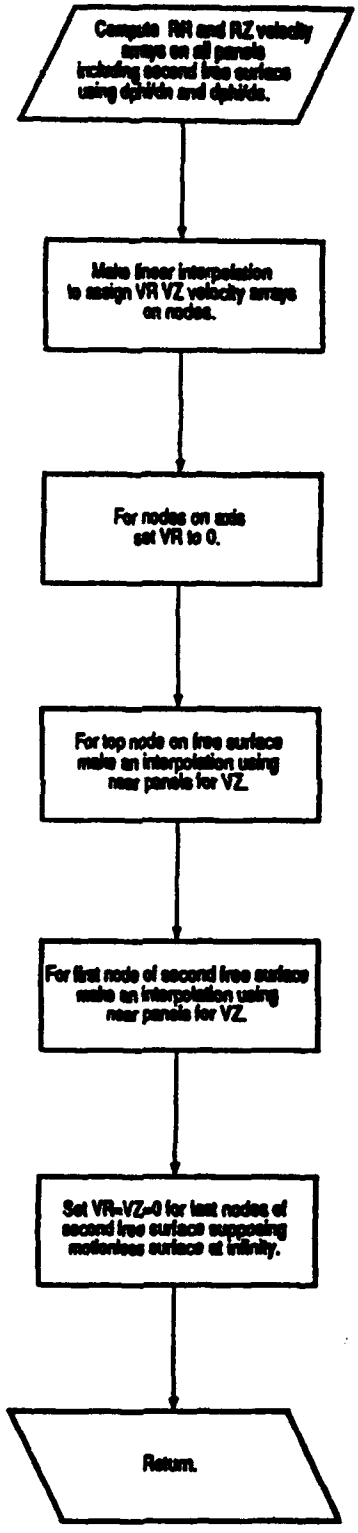

SUBROUTINE VELOC

FIG. 2.4.5

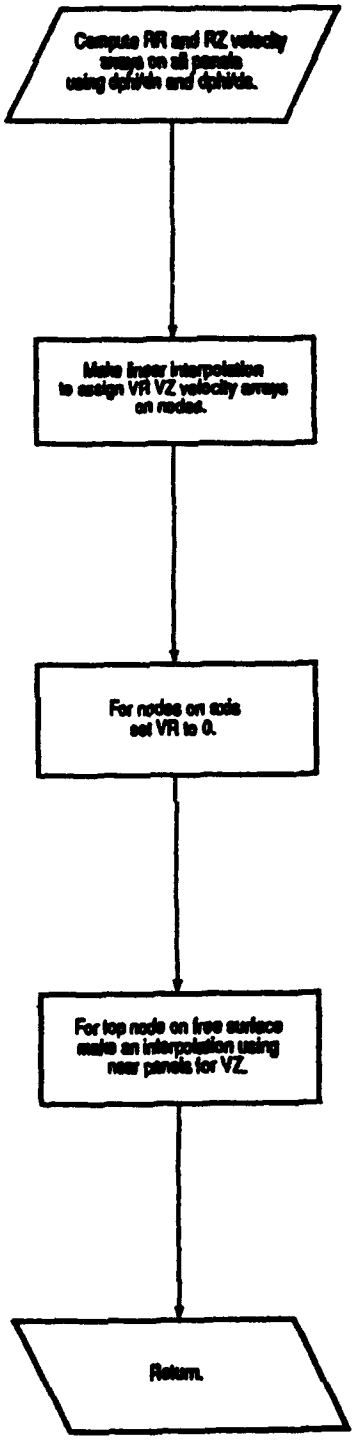

SUBROUTINE SOLVE

FIG. 2.4.6

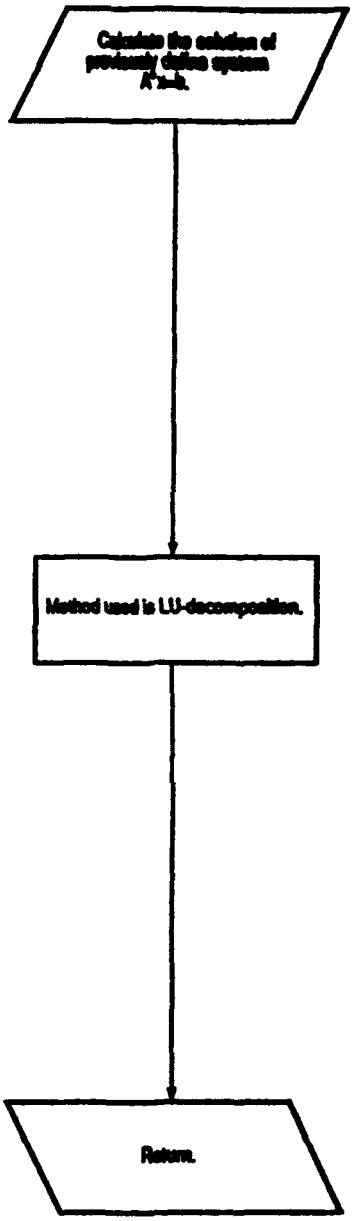

SUBROUTINE GEOMETRY

FIG. 2.4.7

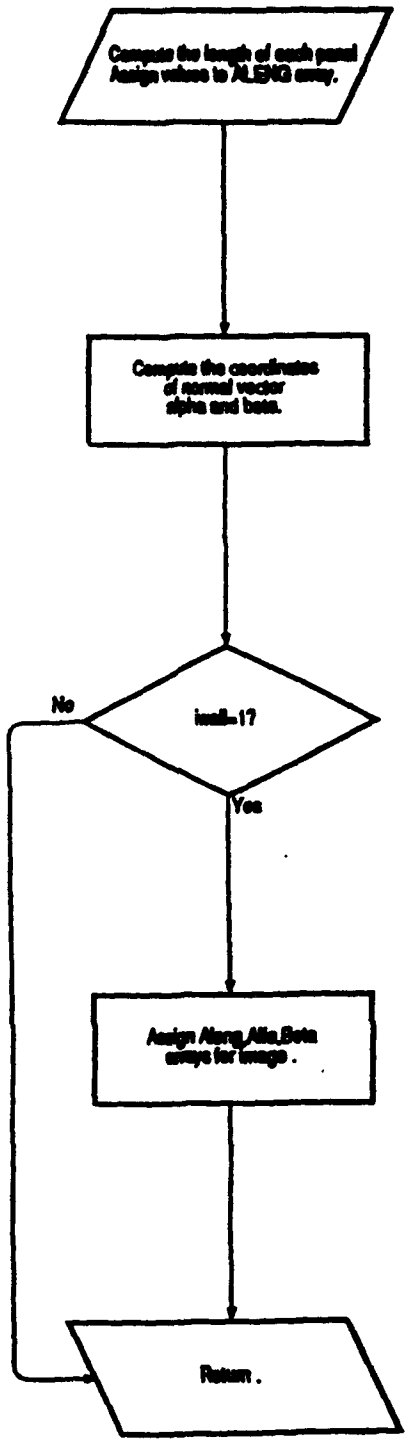

SUBROUTINE T4BSHAPE

FIG. 2.4.8

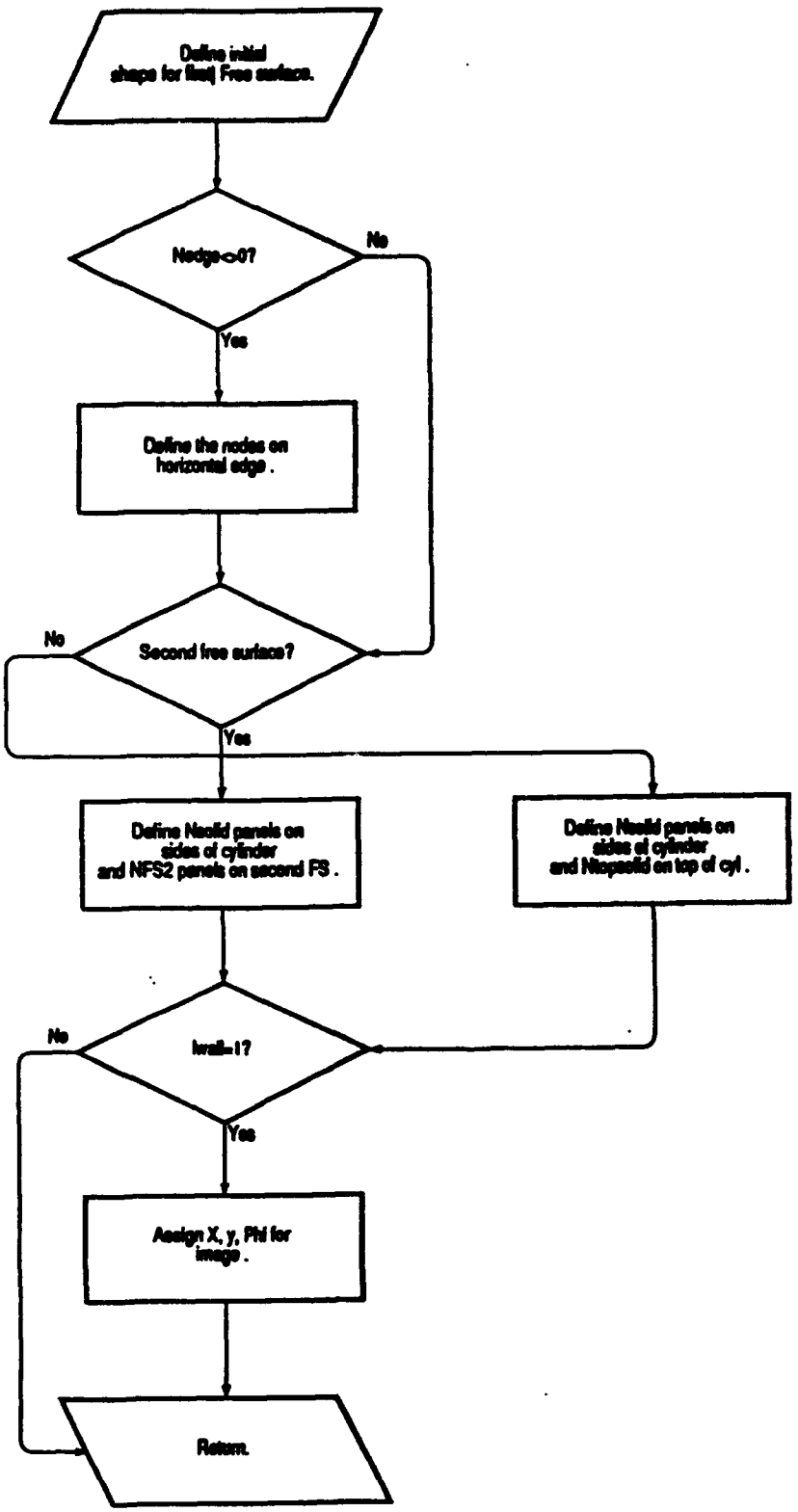

SUBROUTINE T4RSHAPE

FIG. 2.4.9

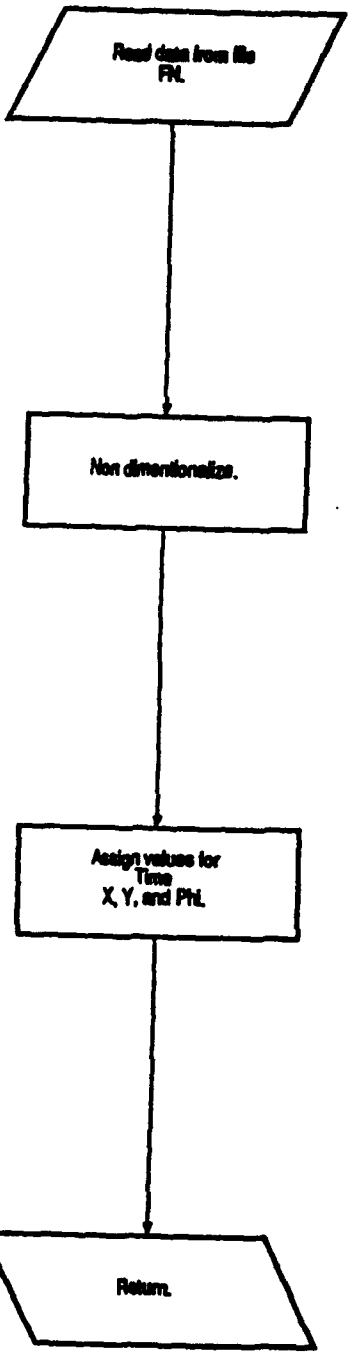

Effect of the 'Regridder'

Staggered regridding
Linear regridding
No regridding

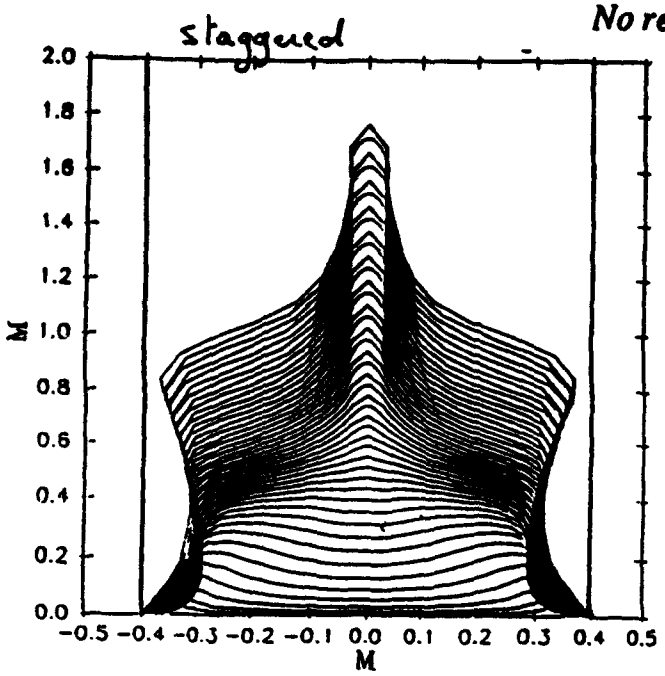

Fig. 3.1.1

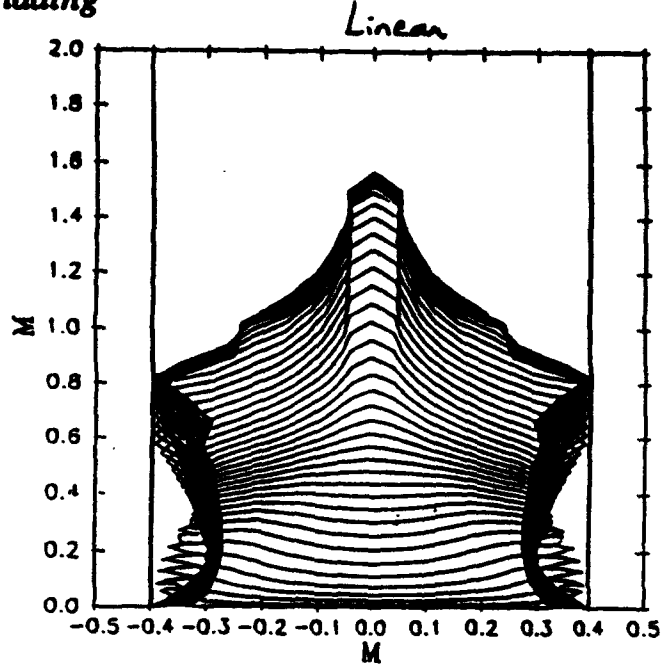

Fig. 3.1.2

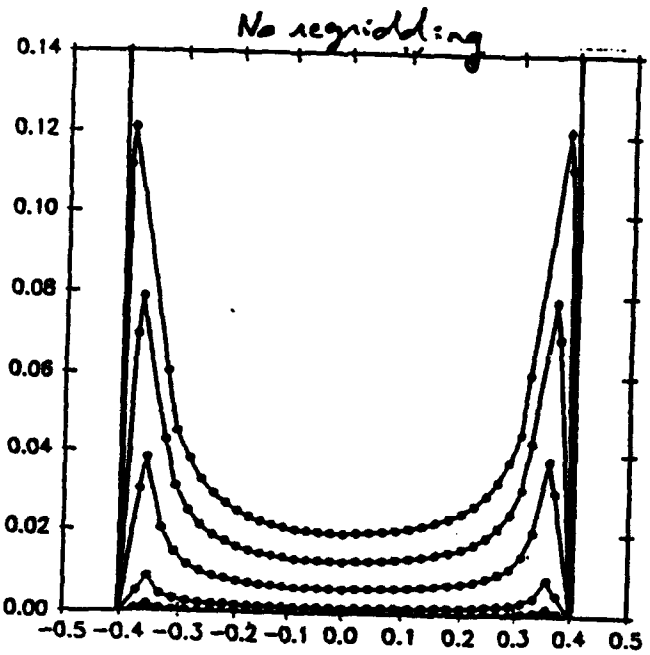

Fig. 3.1.3

Free surface(s):	1
wall:	no
radius:	R=0.4m
depth:	H=1m
average:	Navg=100
regrid:	staggered (1-2) Linear(1) no regridding
viscosity:	no
surface tension:	no
dphi:	0.02
panels:	30 on FS1 12 on cylinder

Uneven repartition of nodes after many steps

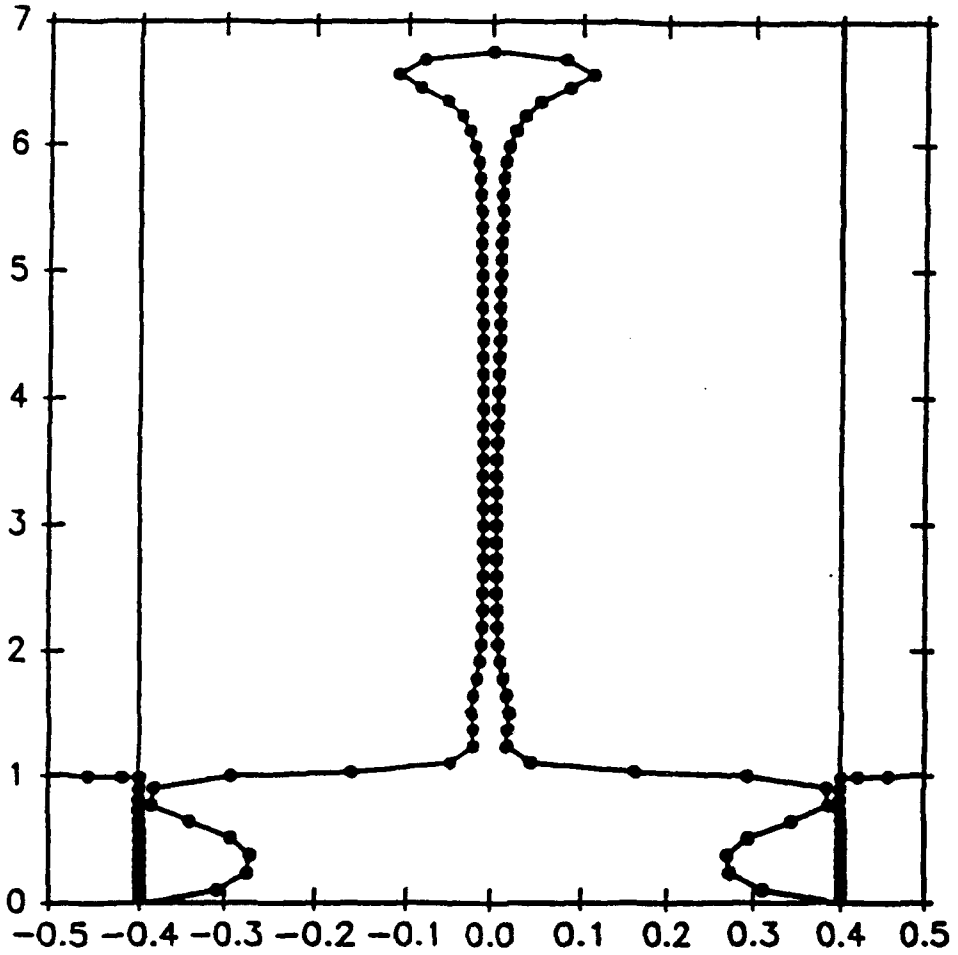

FIG. 3.1.4

Free surface(s):	2
wall:	no
radius:	R=0.4m
depth:	H=1m
average:	no
regrid:	staggered (1-2)
viscosity:	yes
surface tension:	yes
dphi:	0.008
panels:	54 on FS1
	14 on cylinder
	26 on FS2

effect of the discretisation on the Free surface:

Position of the first node

velocity of the first node

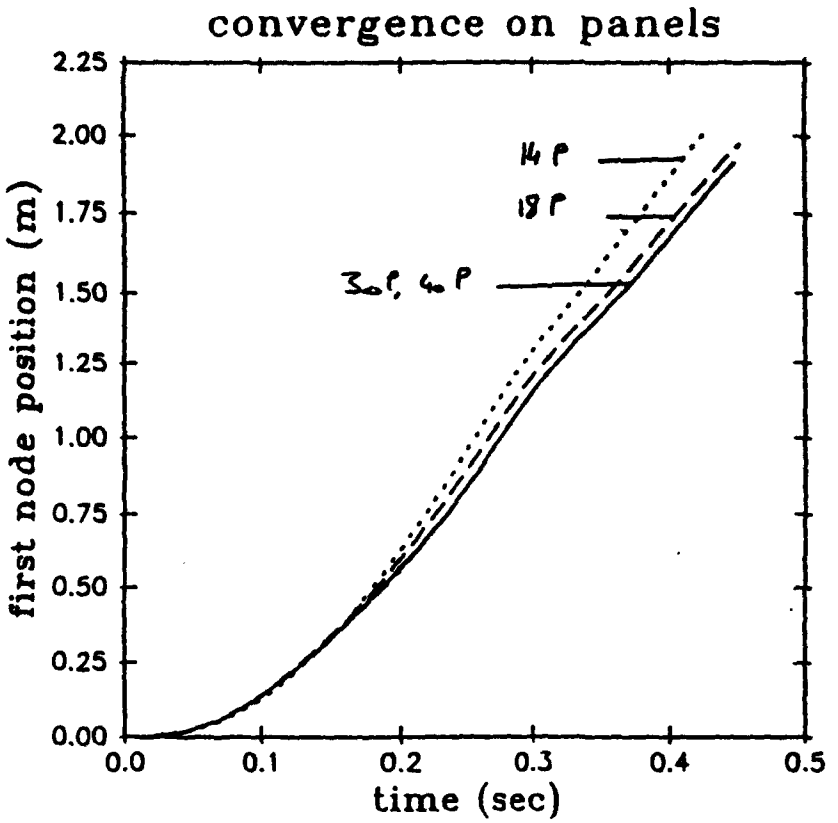

Fig. 3.2.1.1

Free surface(s):	1
wall:	no
radius:	R=0.4m
depth:	H=1m
average:	no
regrid:	staggered (0.9-1.1)
viscosity:	no
surface tension:	no
dphi:	0.008
panels:	14,18,30 and 40 on FS, 12 on cylinder

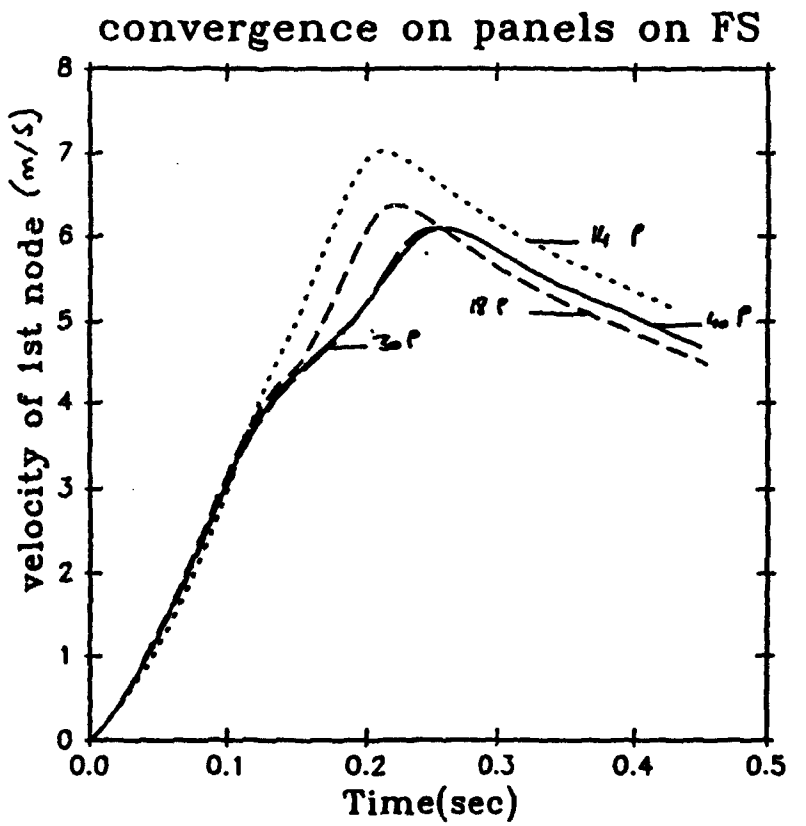

Fig. 3.2.1.2

Effect of the discretisation on the cylinder

Position of the first node

Velocity of the first node

Velocity of the first node (Zoom at the end)

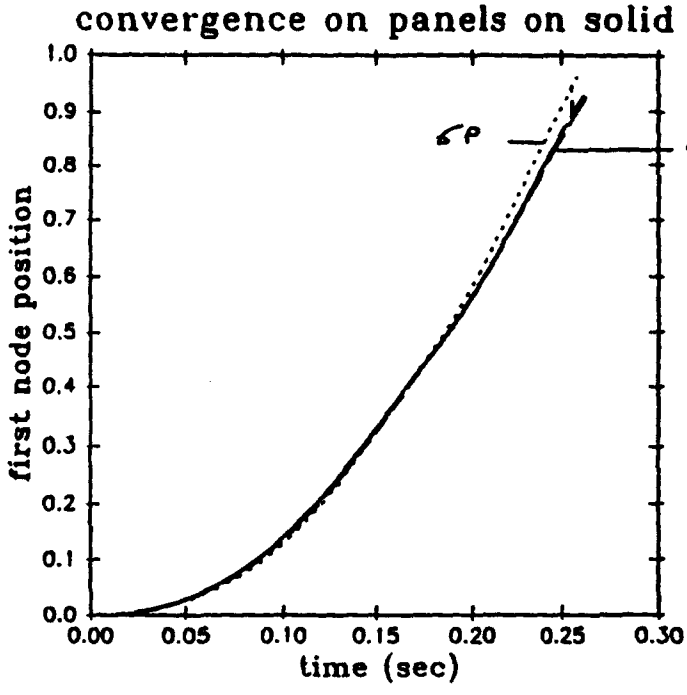

Free surface(s):	1
wall:	no
radius:	R=0.4m
depth:	H=1m
average:	no
regrid:	staggered (0.9-1.1)
viscosity:	no
surface tension:	no
dphi:	0.008
panels:	30 on FS1
	6,9,12,15 and 20 on cylinder

Fig. 3.2.2.1

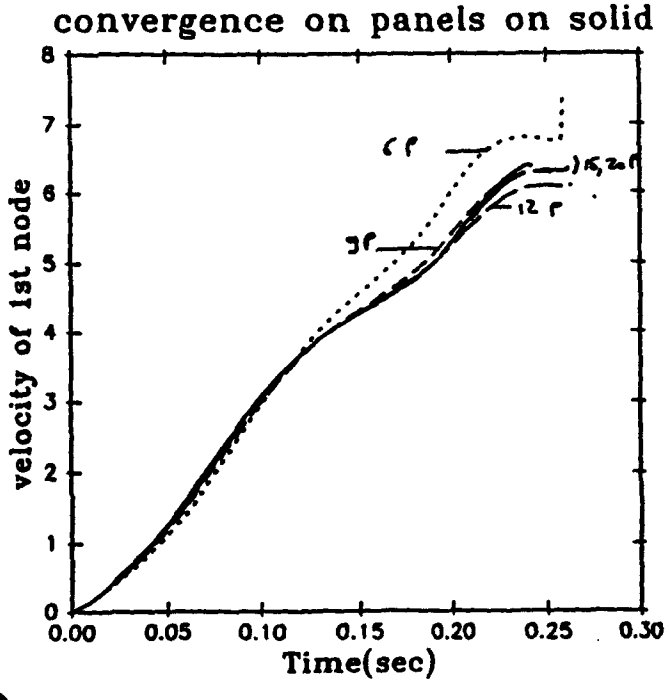

Fig. 3.2.2.2

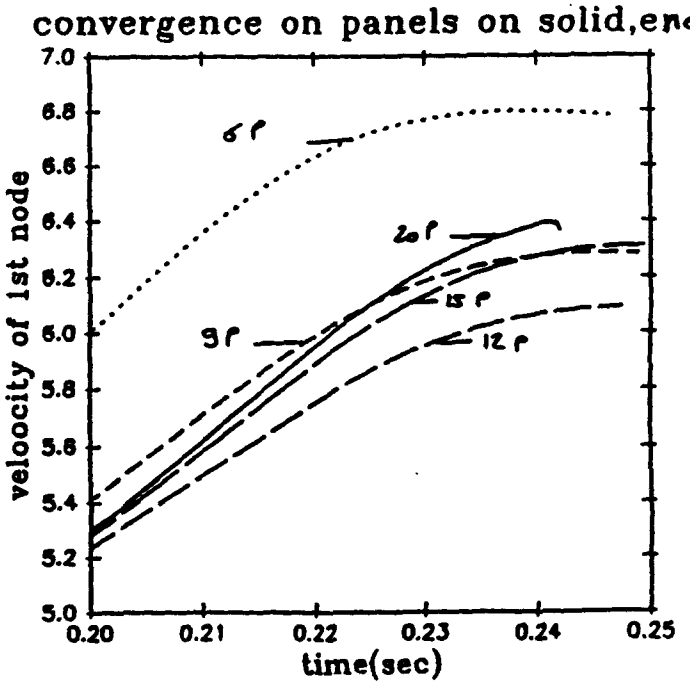

Fig. 3.2.2.3

Effect of time discretisation without average, one free surface

Vertical position of the first node

Vertical position at absciss = 0.2 m

dphi=0.02,0.01,0.008 (4m) and 0.008 (6m)

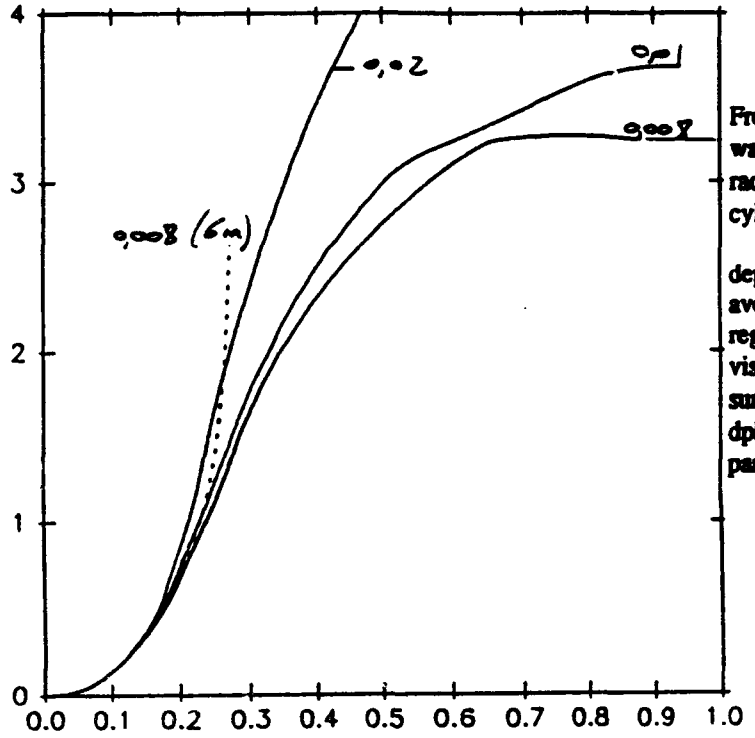

Free surface(s):	1
wall:	no
radius:	R=0.4m
cylinder height:	l=4m (0.02, 0.01, 0.008 l=6m (0.008)
depth:	H=1m
average:	no
regrid:	staggered (1-2)
viscosity:	no
surface tension:	no
dphi:	0.02 , 0.01, 0.008
panels:	30 on FS1 18 on cylinder

Fig. 3.2.3.1

dphi=0.02,0.01,0.008 (4m) and 0.008 (6m)

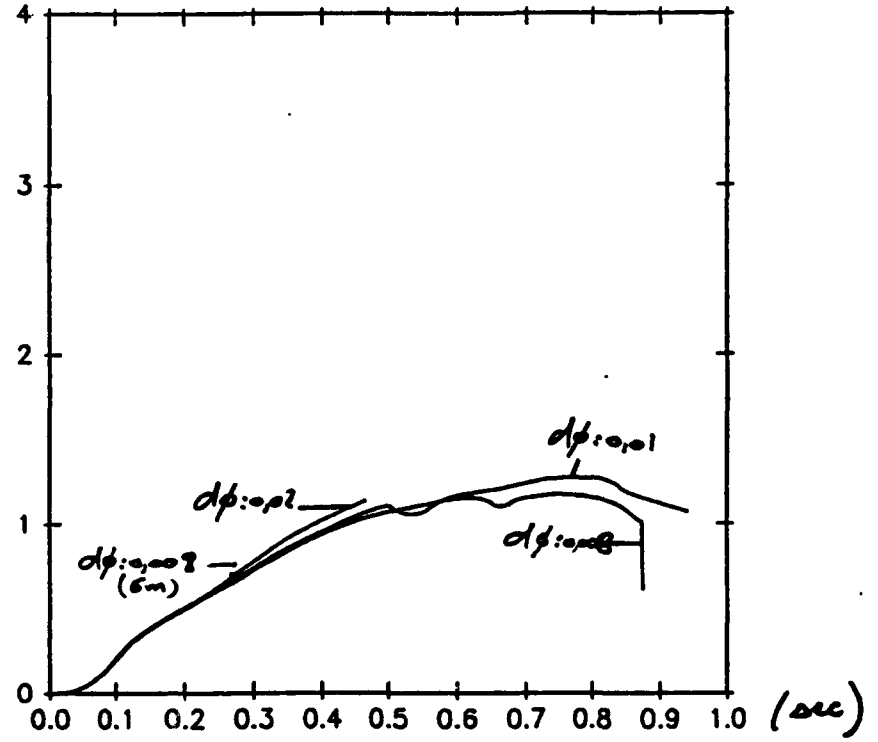

Fig. 3.2.3.2

Effect of time discretisation without average, two free surfaces

Vertical position of the first node

Vertical position at abciss = 0.2 m

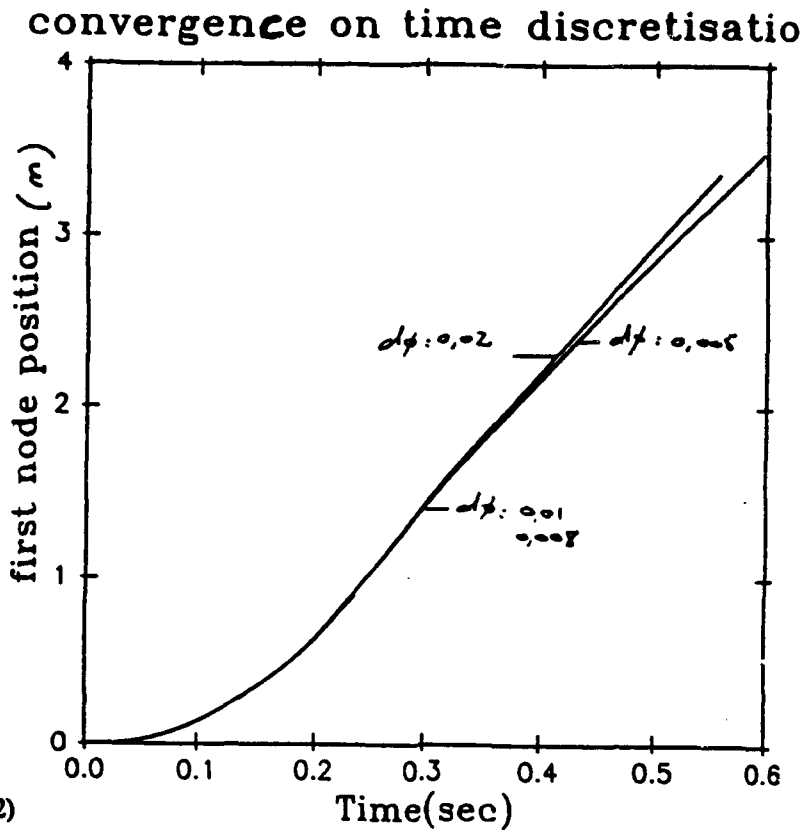

Fig. 3.2.3.3

Free surface(s):	2
wall:	no
radius:	R=0.4m
cylinder height:	l=anything
depth:	H=1m
average:	no
regrid:	staggered (1-2)
viscosity:	no
surface tension:	no
dphi:	0.02 , 0.01, 0.005, 0.008
panels:	30 on FS1 10 on cylinder 20 on FS2

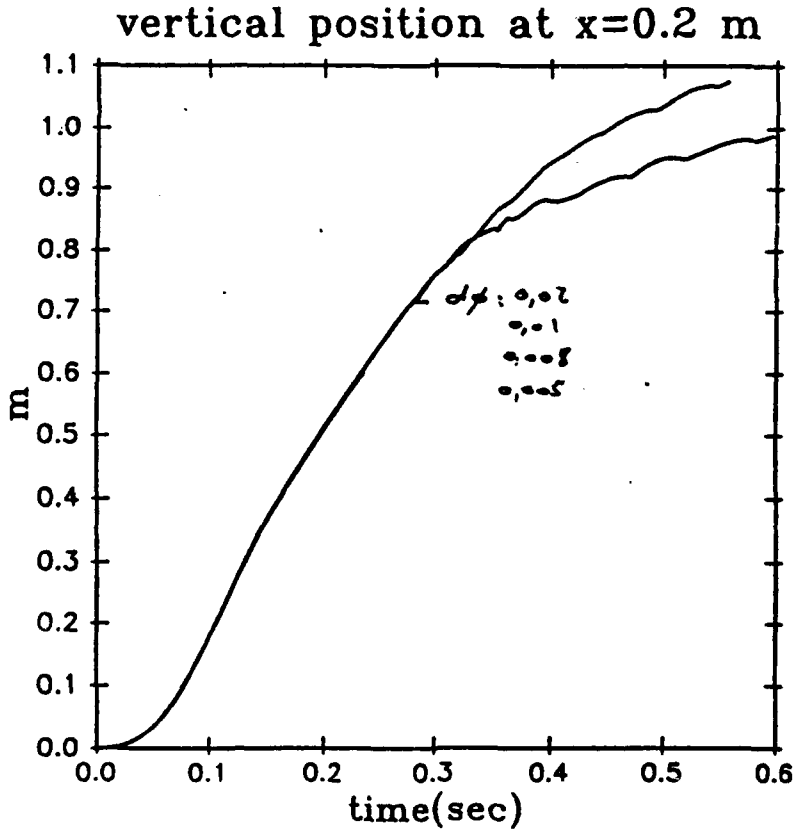

Fig. 3.2.3.4

Bad time discretisation

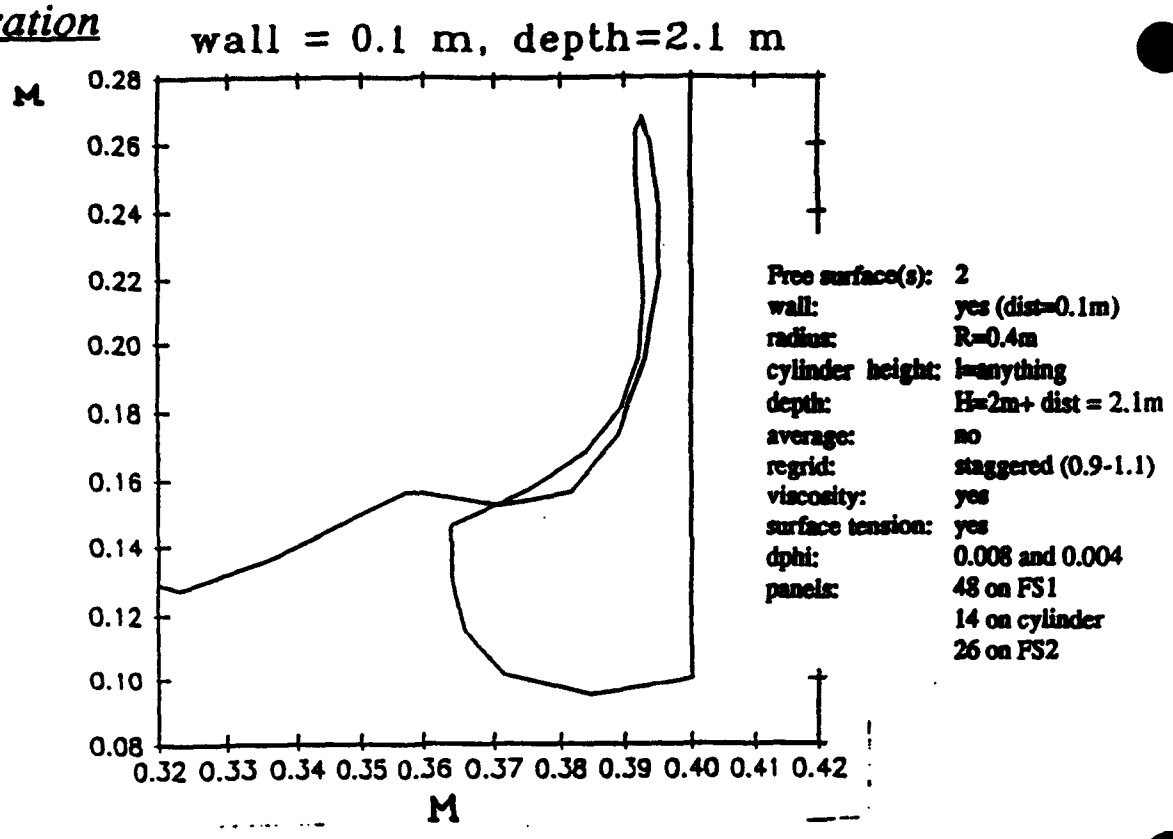

Fig. 3.2.4.3

Good time discretisation

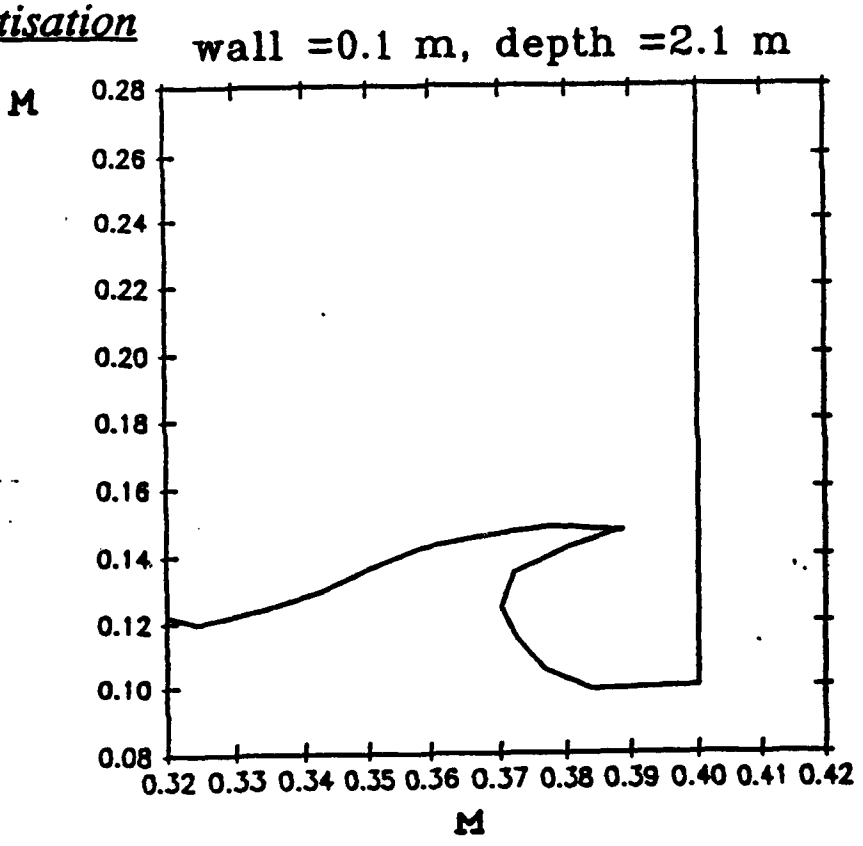

Fig. 3.2.4.4

Effect of time discretisation on the creation of drops

figure for dphi=0.008 (drops created)

figure for dphi=0.005 (no drops)

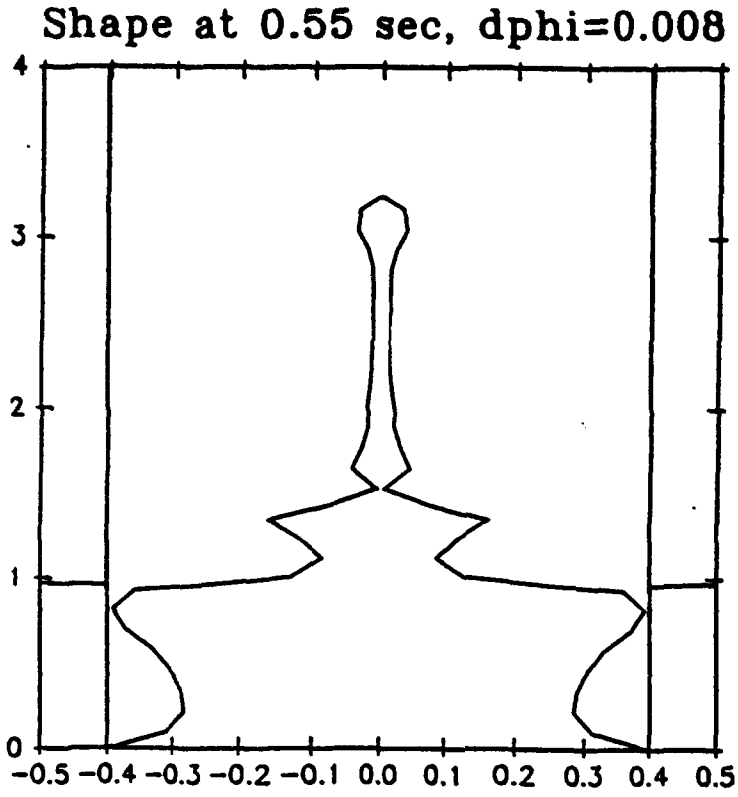

Fig. 3.2.4.1

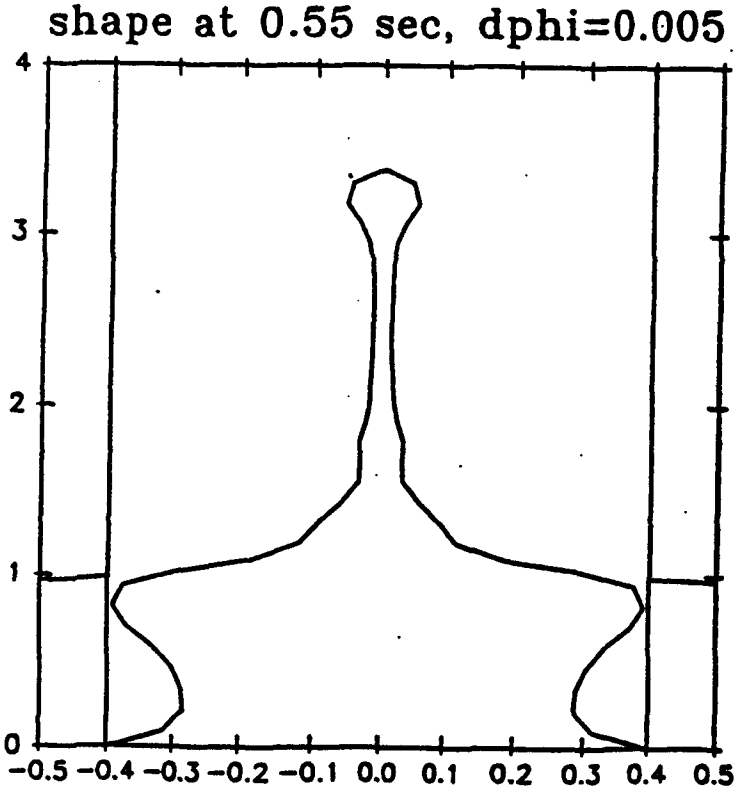

Fig. 3.2.4.2

Free surface(s):	2
wall:	no
radius:	R=0.4m
cylinder height:	h=anything
depth:	H=1m
sweage:	no
regrid:	staggered (0.9-1.1)
viscosity:	yes
surface tension:	yes
dphi:	0.008 and 0.005
panels:	48 on FS1 14 on cylinder 26 on FS2

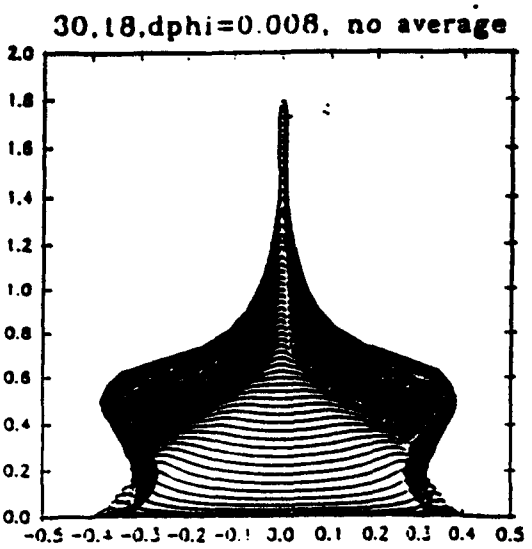

Fig. 3.3.1

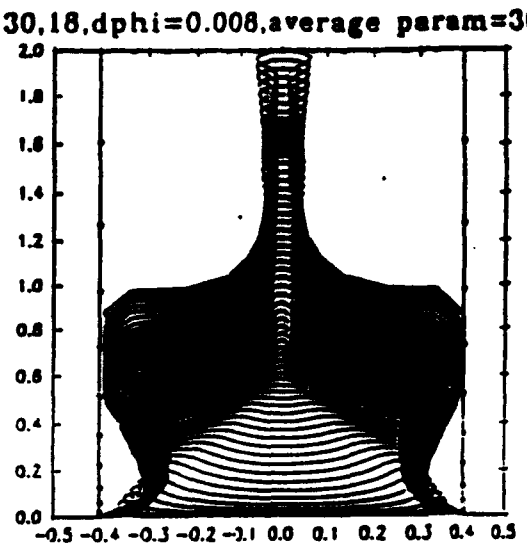

Fig. 3.3.2

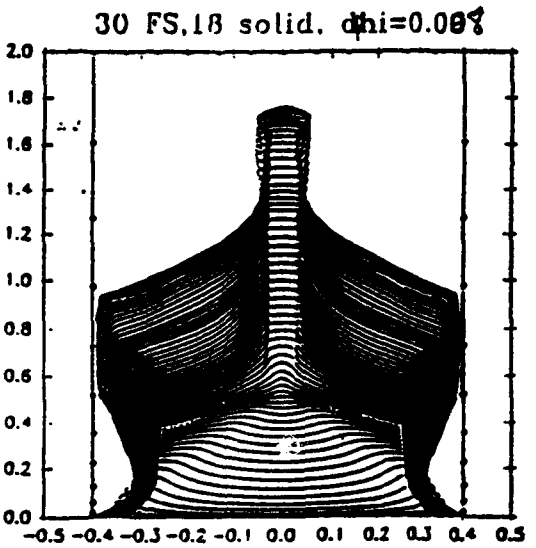

Fig. 3.3.3

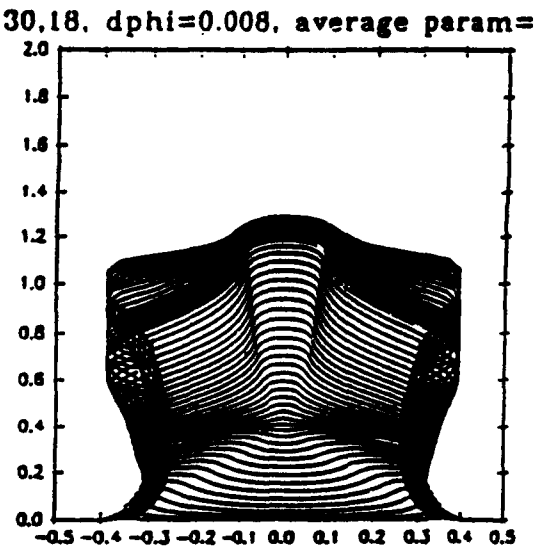

Fig. 3.3.4

Free surface(s): 1
wall: no
radius: R=0.4m
depth: H=1m
average: Navg=30 to infinite
regrid: staggered (1-2)
viscosity: no
surface tension: no
dphi: 0.008
panels: 30 on FS1
18 on cylinder

Effect of the Average parameter
30 panels on FS, 18 Panels on cylinder

Effect of the average parameter

Vertical position of the first node

Vertical position at absciss =0.2 m

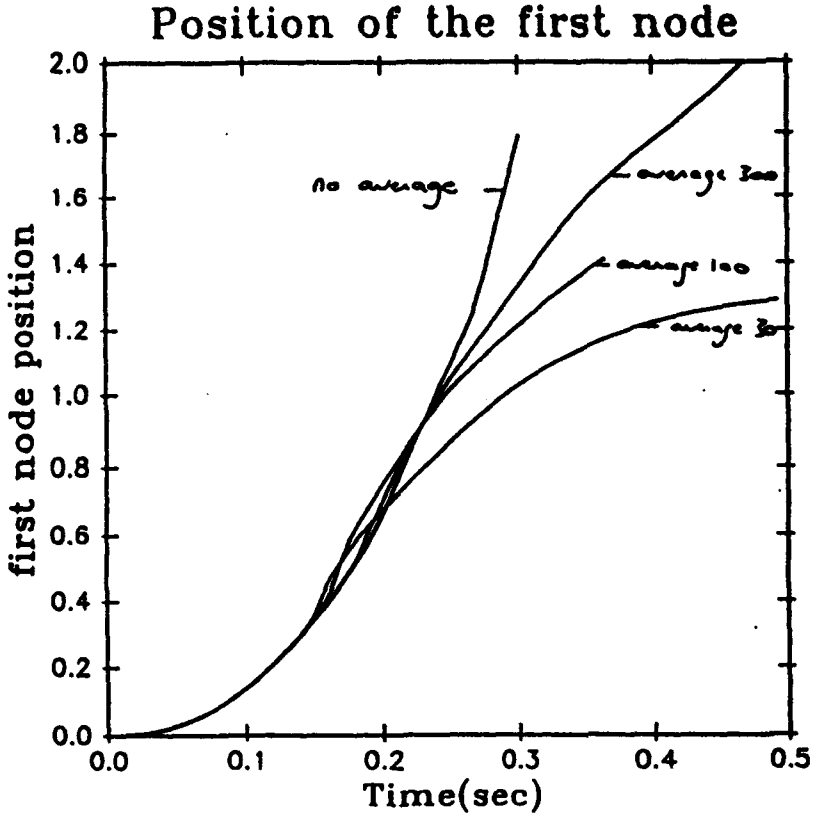

Fig. 3.3.5

Free surface(s):	1
wall:	no
radius:	R=0.4m
cylinder height:	l=2m
depth:	H=1m
average:	Navg=30 to infinite
regrid:	staggered (1-2)
viscosity:	no
surface tension:	no
dphi:	0.008
panels:	30 on FS1 18 on cylinder

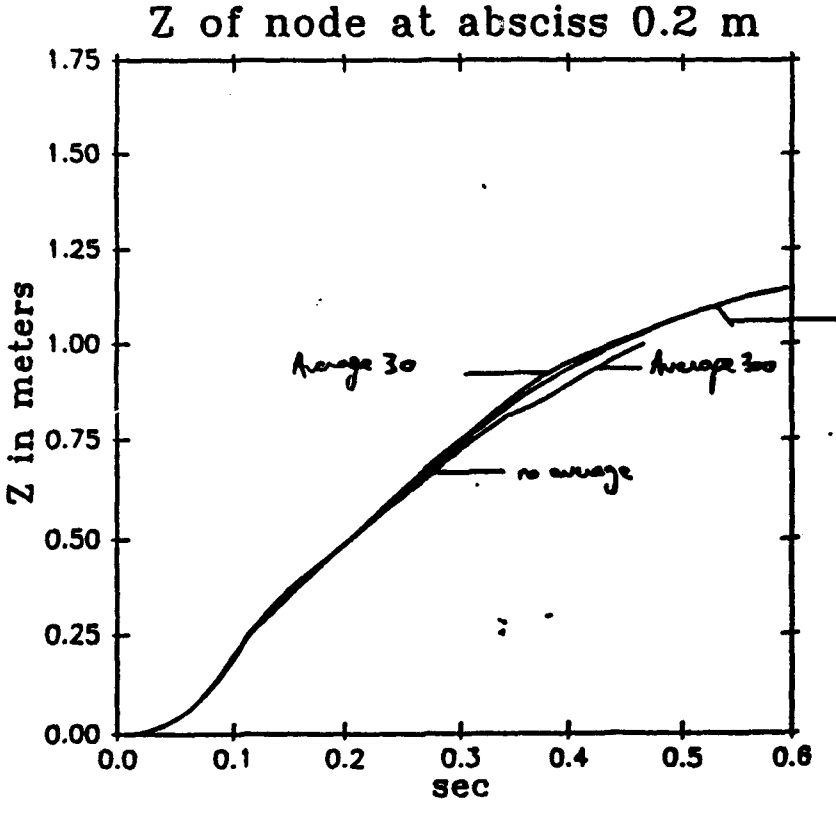

Fig. 3.3.6

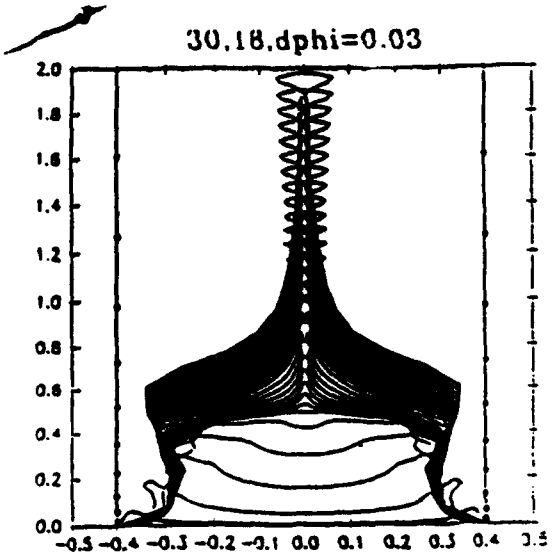

Fig. 3.3.7

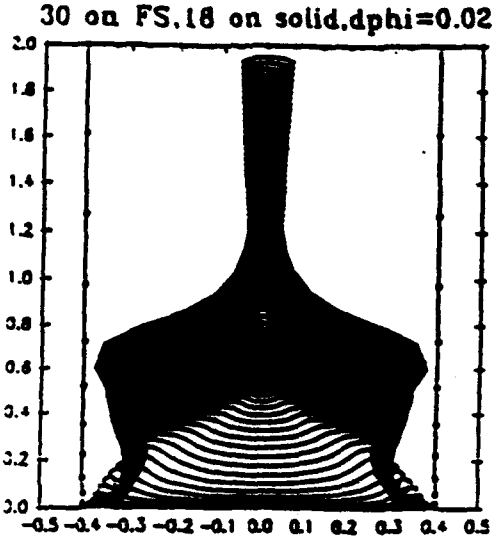

Fig. 3.3.8

Free surface(s):	1
wall:	no
radius:	R=0.4m
depth:	H=1m
average:	Navg=100
regrid:	staggered (1-2)
viscosity:	no
surface tension:	no
dphi:	0.03 to 0.002
panels:	30 on FS1
	18 on cylinder

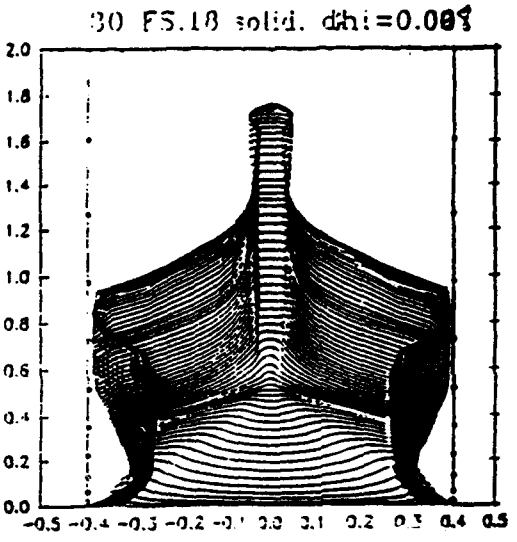

Fig. 3.3.9

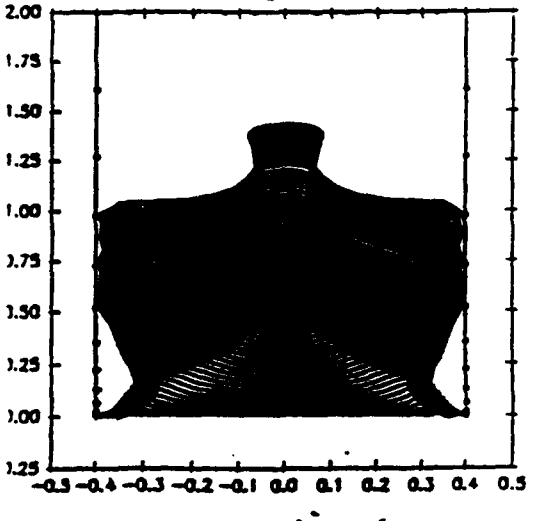

Fig. 3.3.10

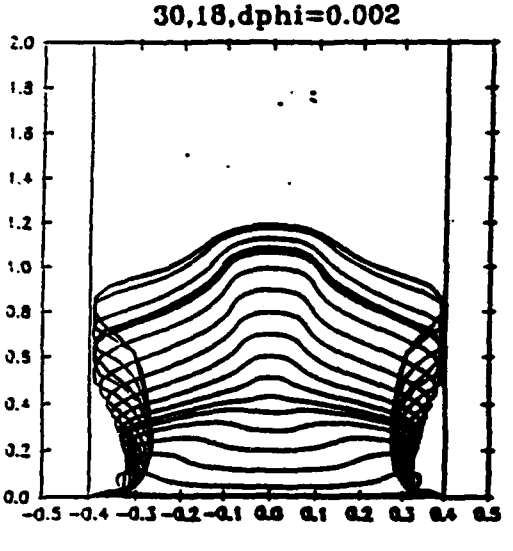

3.3.11

Effect of time discretisation using a constant average parameter

(shapes)

Effect of time discretisation using a constant average parameter (vertical positions)

Vertical position of the first node

Vertical position at absciss =0.2 m

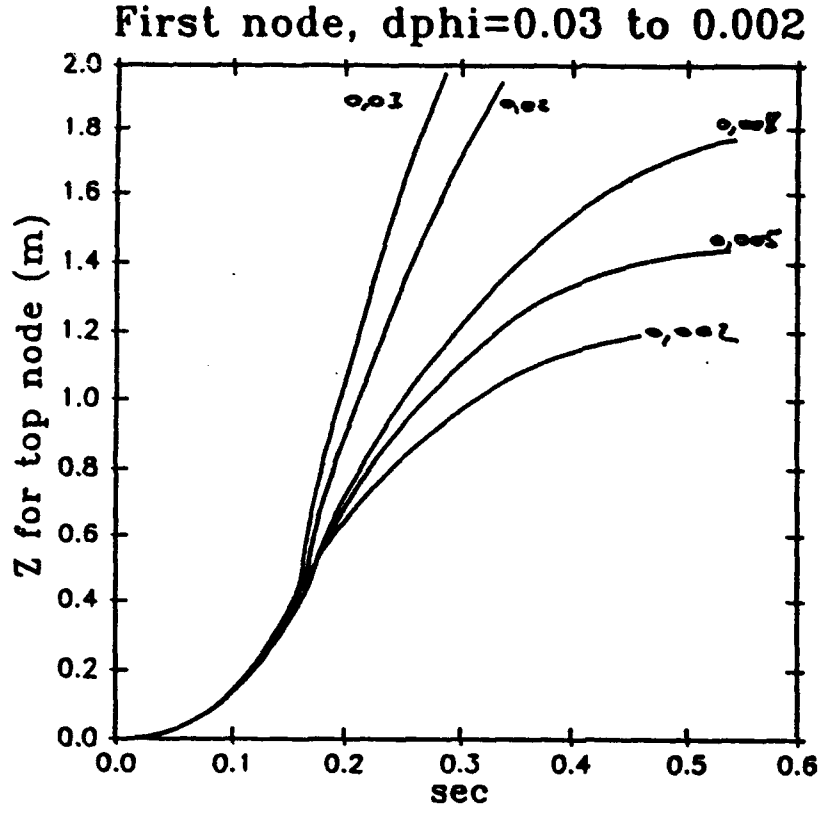

Fig. 3.3.12

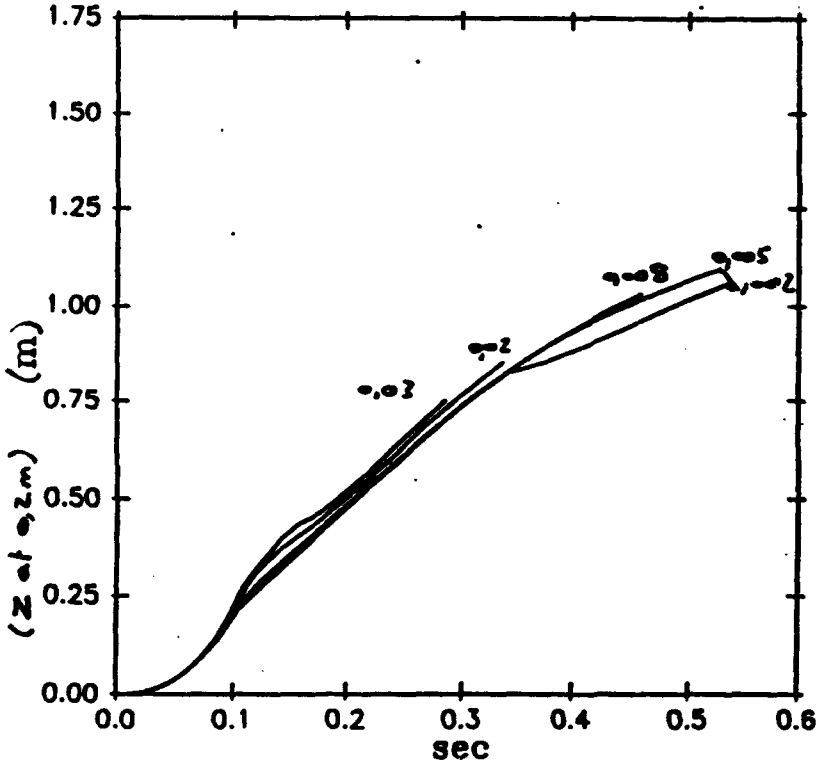

Free surface(s):	1
wall:	no
radius:	R=0.4m
cylinder height:	h=2m
depth:	H=1m
average:	no
regrid:	staggered (1-2)
viscosity:	no
surface tension:	no
dphi:	0.03 to 0.002
panels:	30 on FS1
	18 on cylinder

Fig. 3.3.13

Effect of surface tension

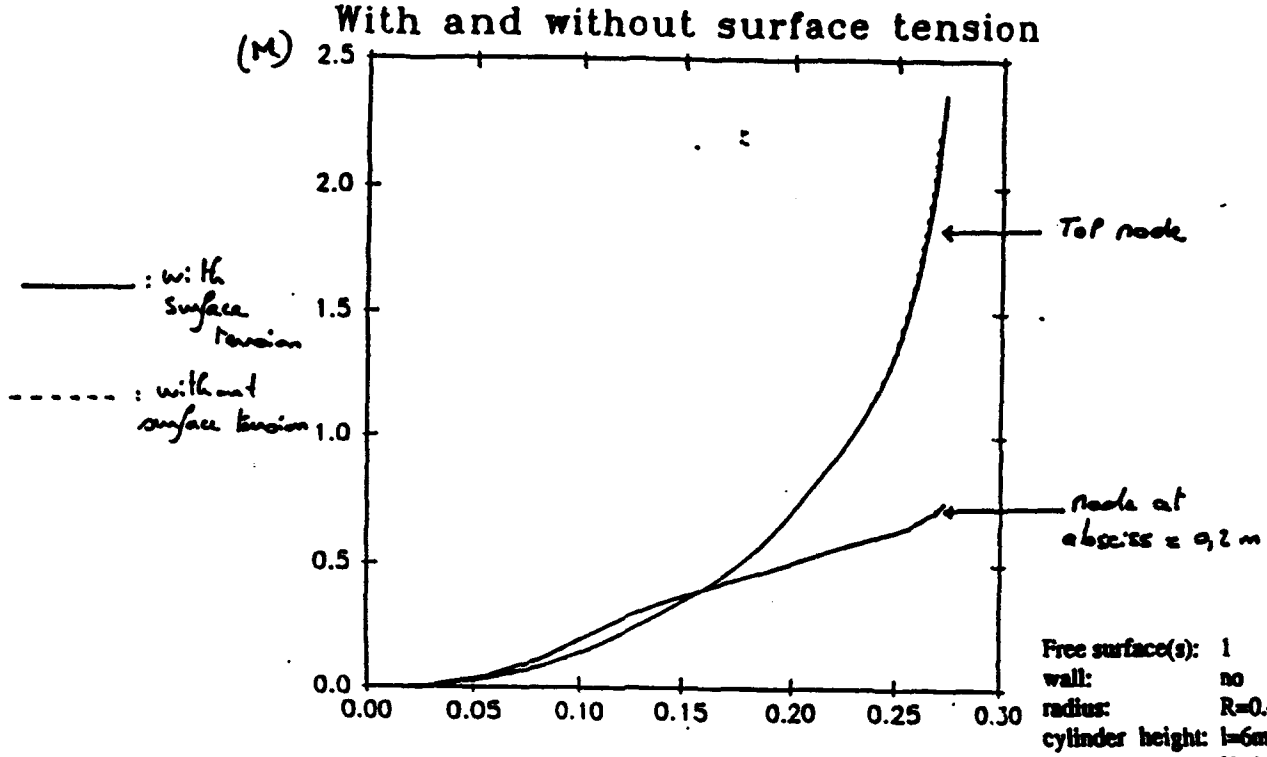

FIG. 3.4

Effect of a numerical viscosity

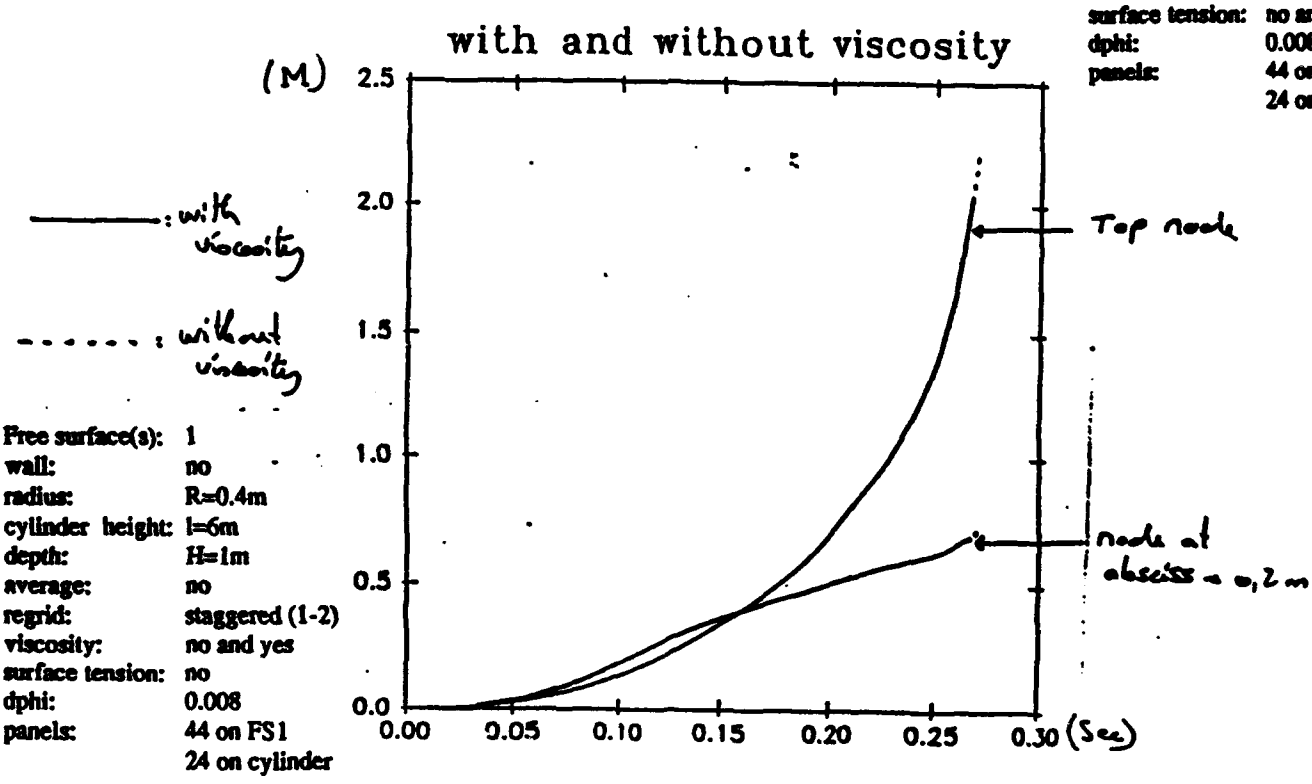

FIG. 3.5

Results of the theoretical model

Doted line: velocity (m/s)

Line: height of water in the cylinder (m)

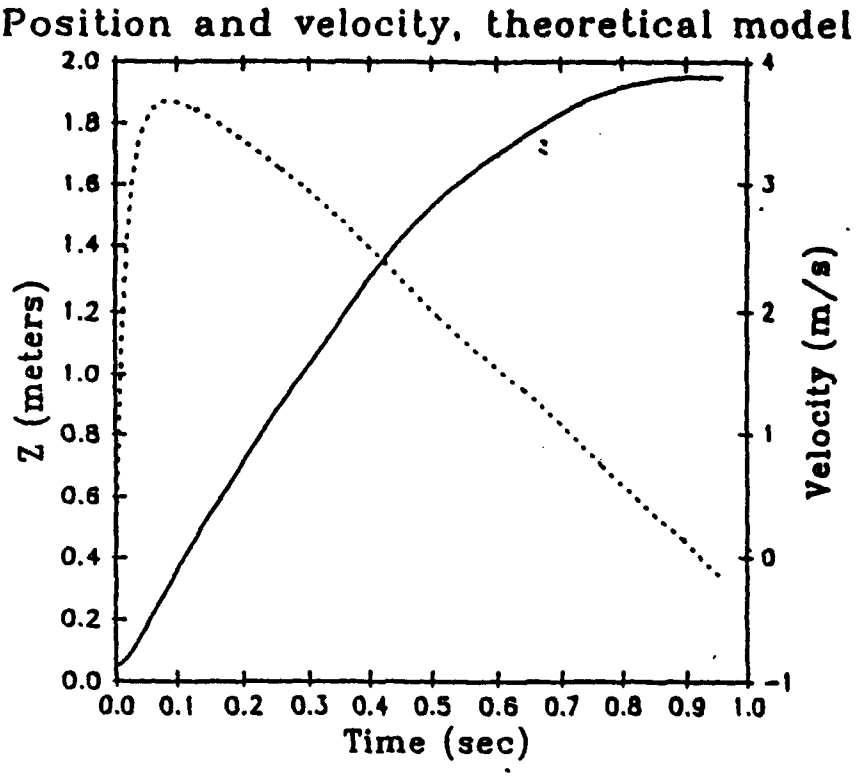

FIG. 4.1.1

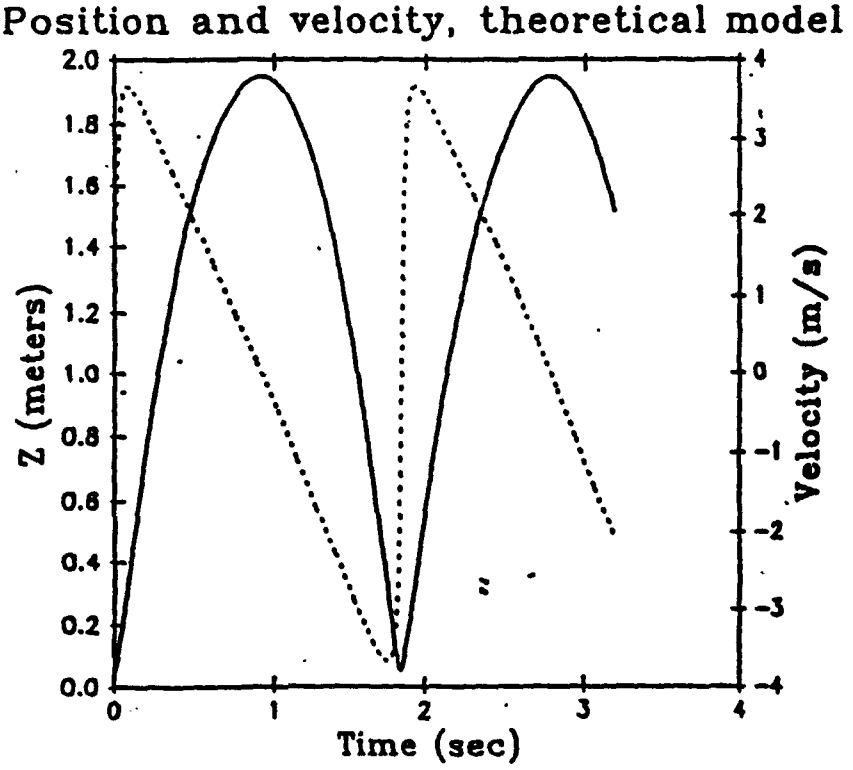

FIG. 4.1.2

Effect of the second free surface

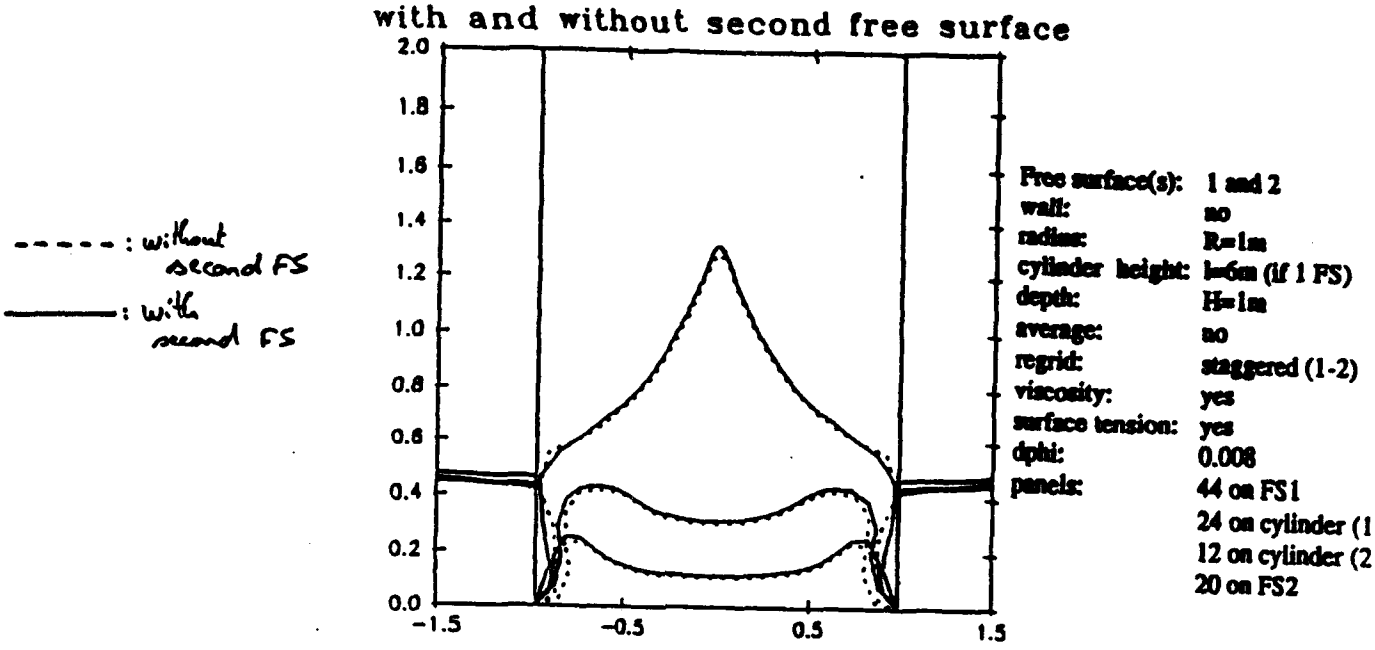

FIG. 4.2.1.1

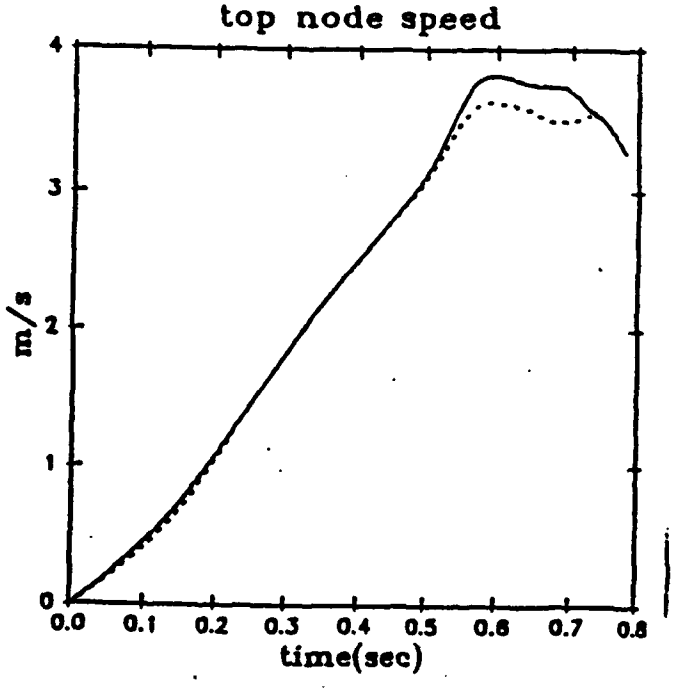

FIG. 4.2.1.2

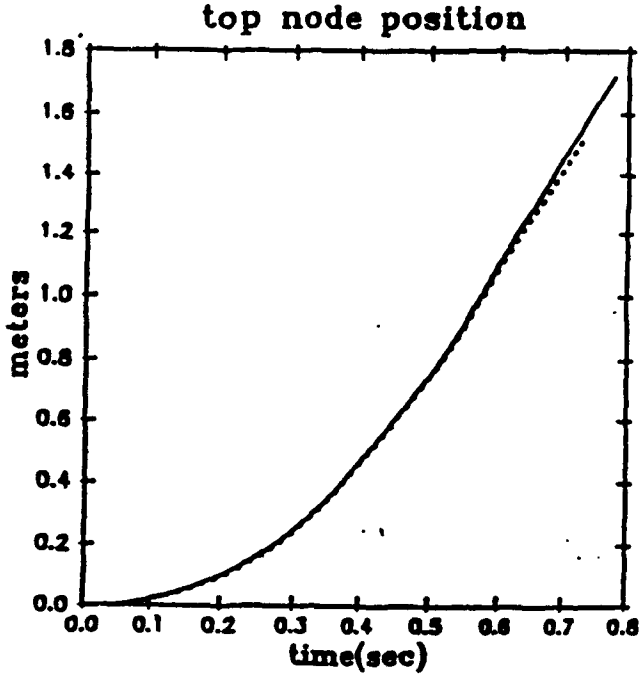

FIG. 4.2.1.3

Effect of the second free surface
Zoom on second free surface

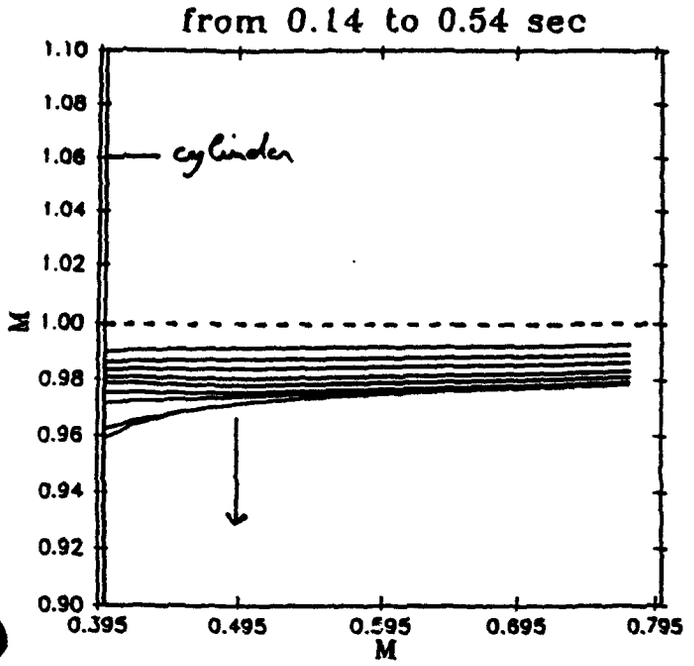

Fig. 4.2.1.4

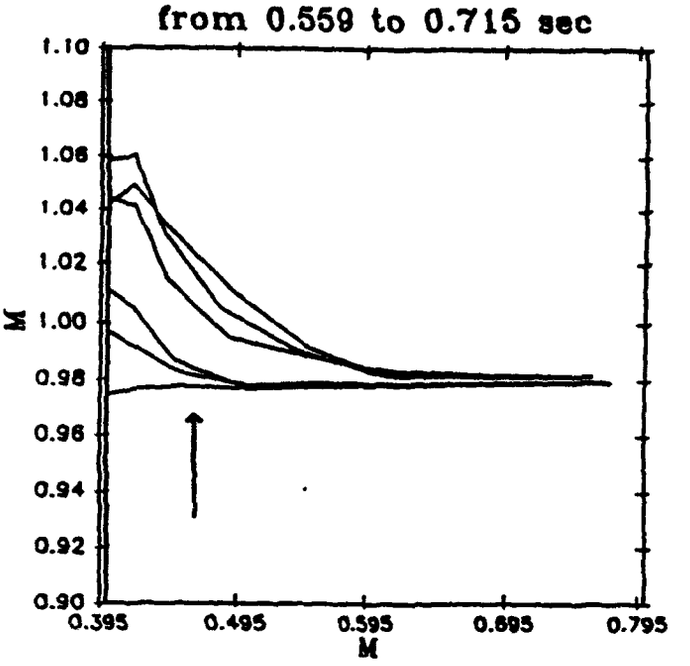

Fig. 4.2.1.4'

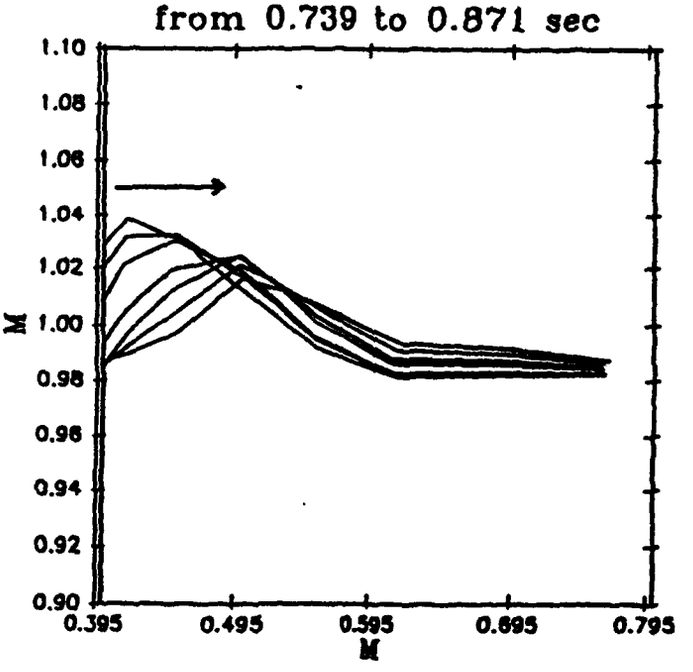

Fig.4.2.1.4"

Free surface(s):	2
wall:	no
radius:	R=0.4m
cylinder height:	h=anything
depth:	H=1m
average:	no
regrid:	staggered (0.9-1.1)
viscosity:	yes
surface tension:	yes
dphi:	0.008
panels:	48 on FS1
	12 on cylinder (2 FS
	26 on FS2

Velocity field at time 0.48 second

Interferences with the cylinder

Bottom of the cylinder

4.2.1.5

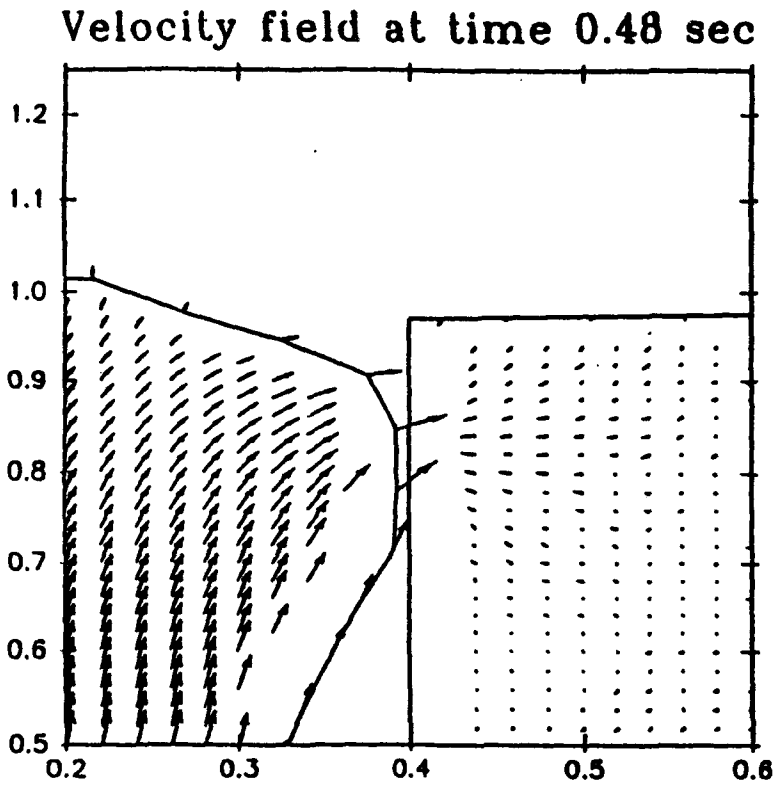

Free surface(s):	2
wall:	no
radius:	R=0.4m
cylinder height:	h=anything
depth:	H=1m
average:	no
regrid:	staggered (0.9-1.
viscosity:	yes
surface tension:	yes
dphi:	0.008
panels:	48 on FS1
	12 on cylinder (2
	26 on FS2

4.2.1.6

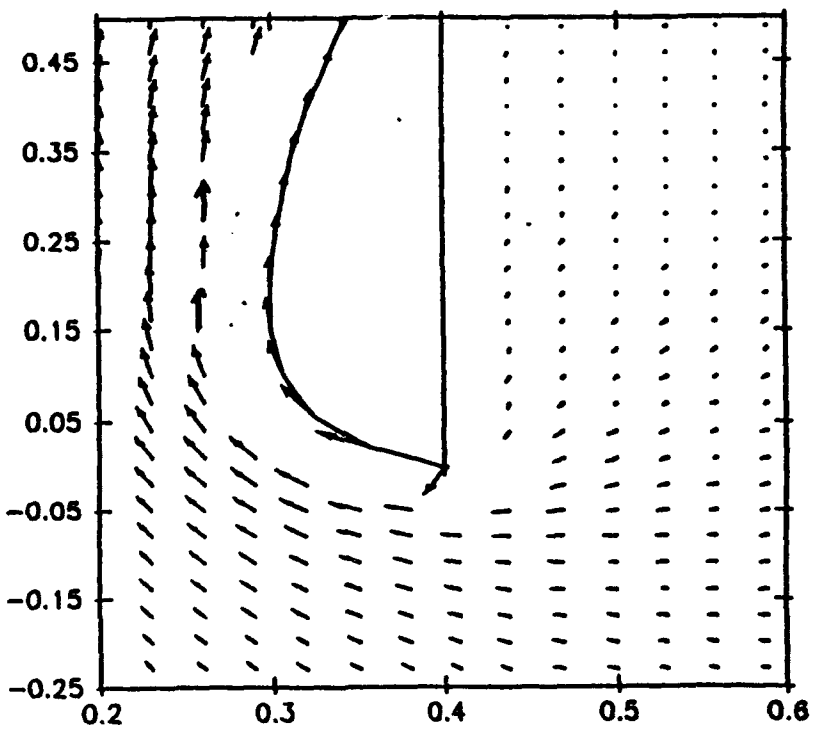

Comparison Modelisation-Code

Doted line: modelisation

Line: position at abscissa=0.2m in the code

FIG. 4.2.2.1

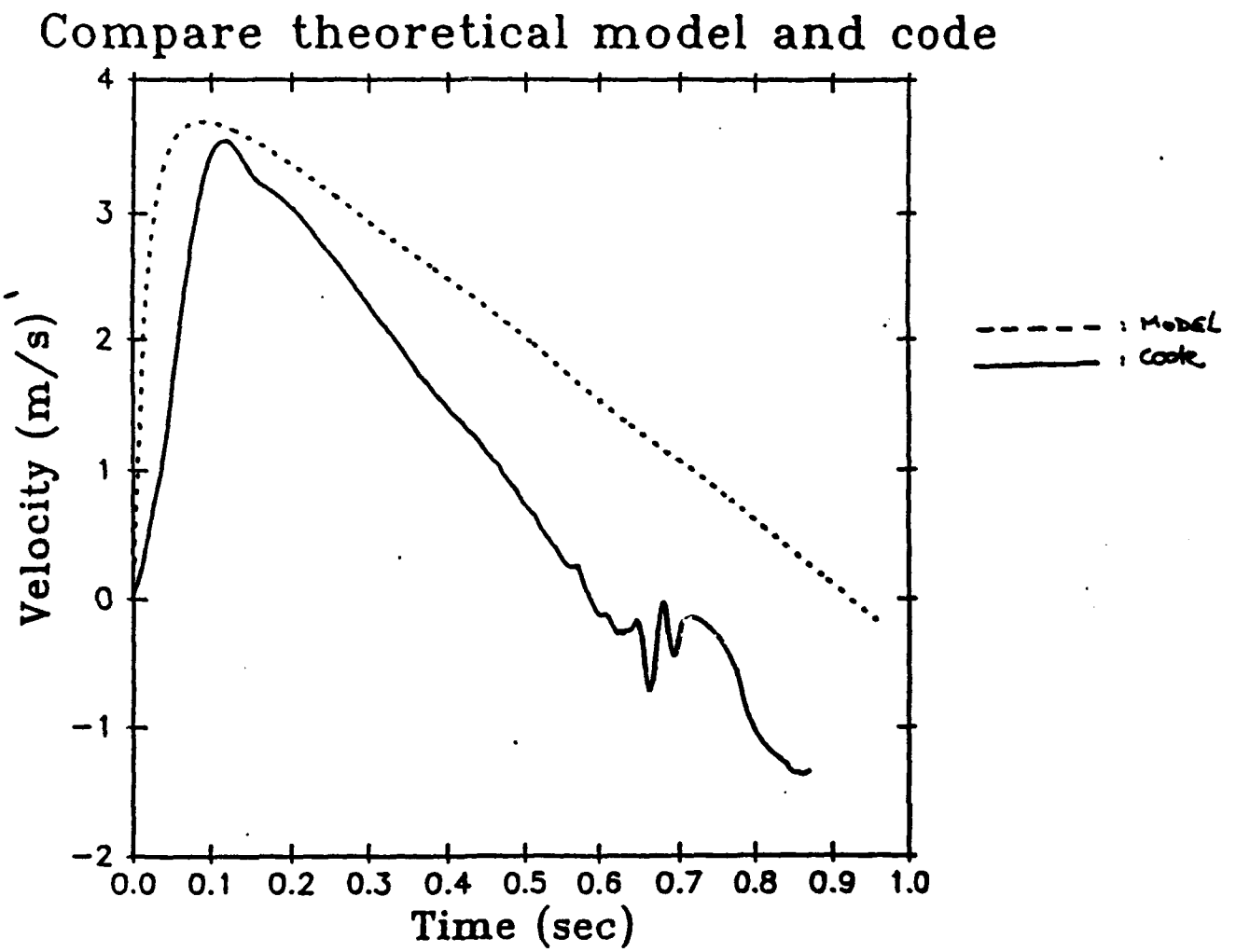

Free surface(s):	2
wall:	no
radius:	R=0.4m
cylinder height:	h=anything
depth:	H=1m
average:	no
regrid:	staggered (0.9-1.1)
viscosity:	yes
surface tension:	yes
dphi:	0.008
panels:	48 on FS1 12 on cylinder (2 FS) 26 on FS2

No wall, same conditions as 4.2.2.1

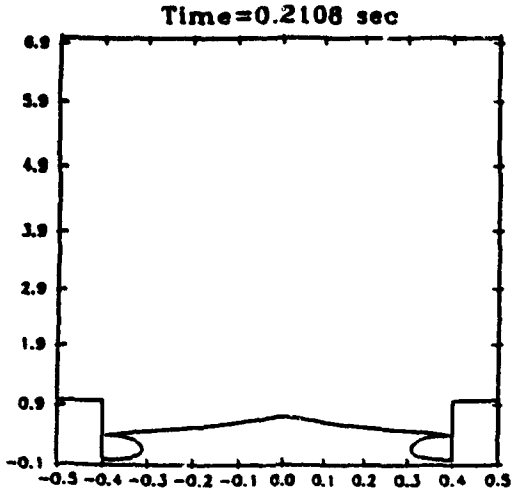

FIG. 4.2.2.2

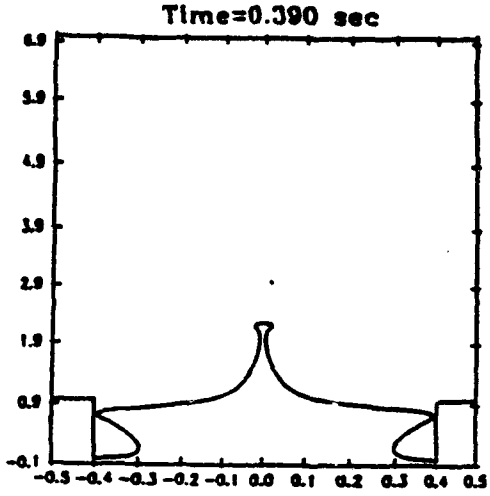

FIG. 4.2.2.3

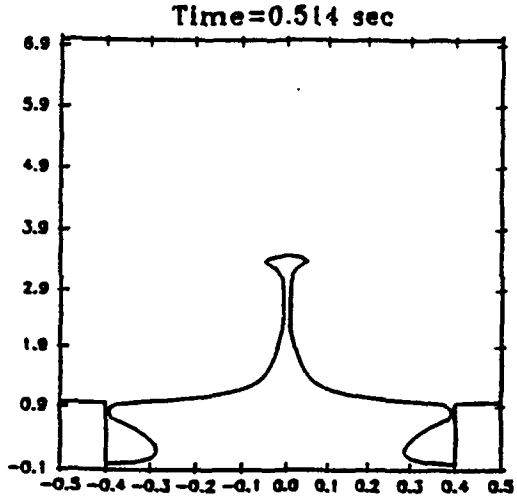

FIG. 4.2.2.4

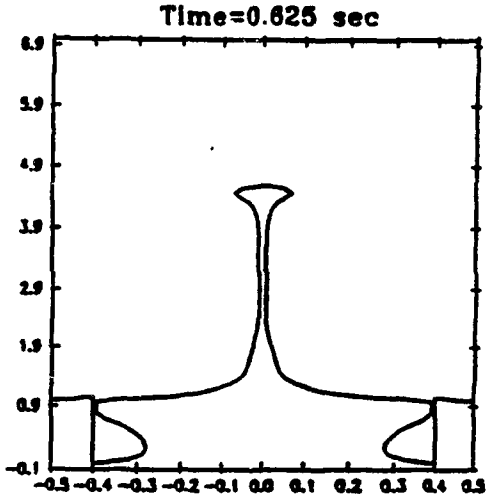

FIG. 4.2.2.5

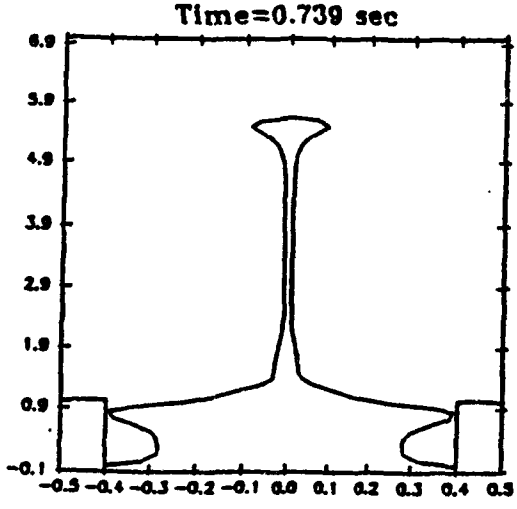

FIG. 4.2.2.6

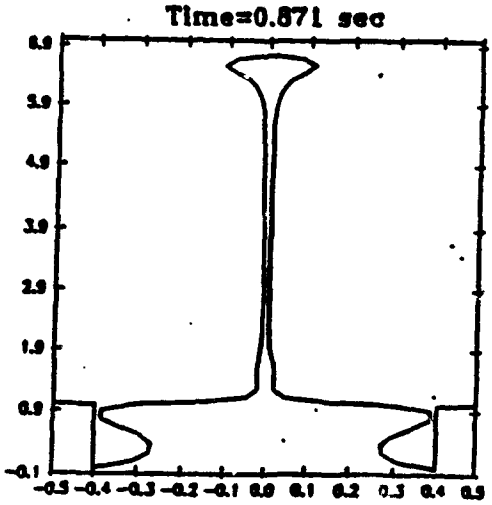

FIG. 4.2.2.7

Wall (dist = 1m), depth = 2m

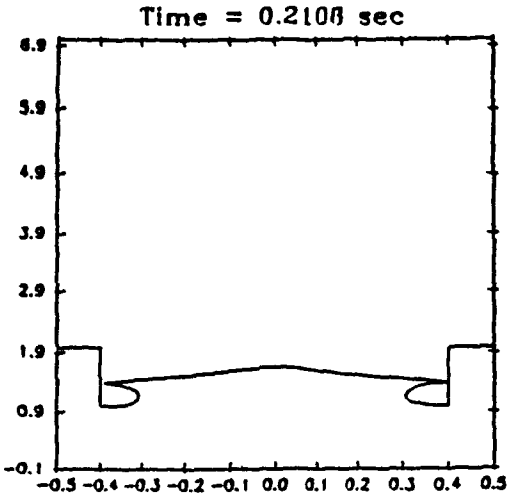

FIG 4.2.2.8

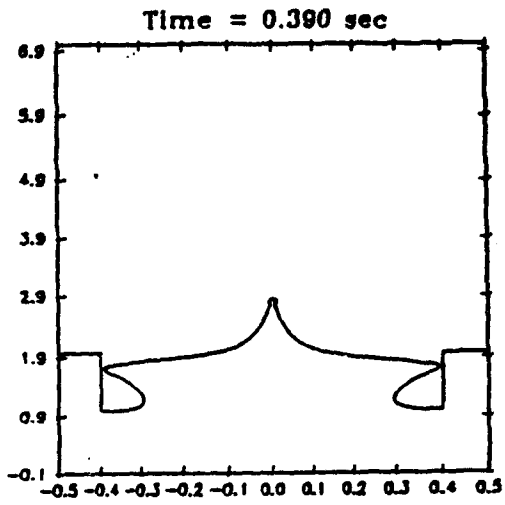

FIG. 4.2.2.9

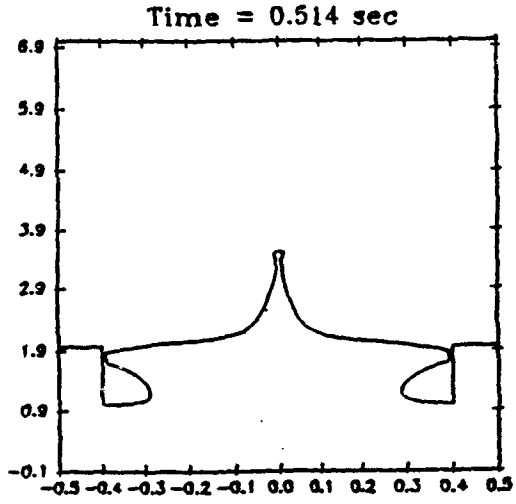

FIG. 4.2.2.10

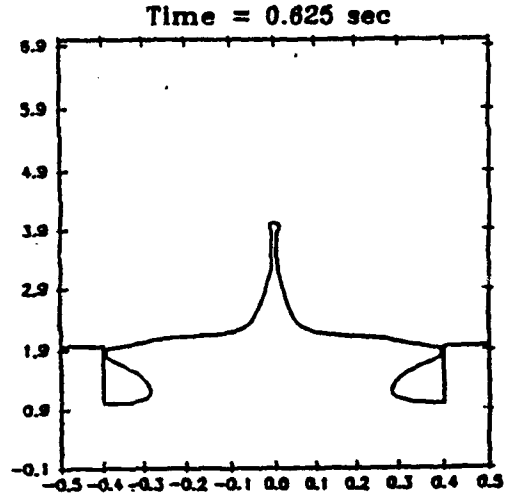

FIG. 4.2.2.11

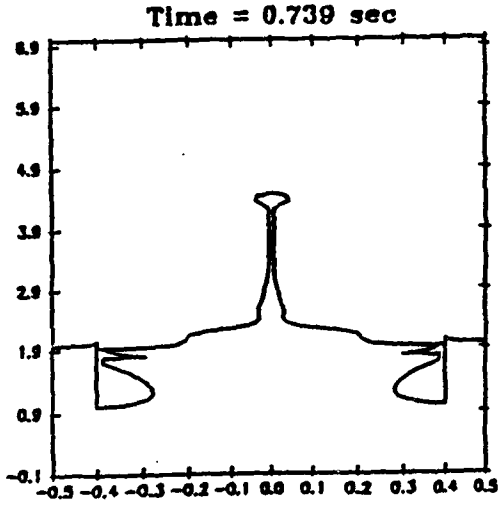

FIG. 4.2.2.12

Free surface(s):	2
wall:	yes (dist=1m)
radius:	R=0.4m
cylinder height:	l=anything
depth:	H=2m (1m ABOVE cyl.)
average:	no
regrid:	staggered (0.9-1.1)
viscosity:	yes
surface tension:	yes
dphi:	0.008
panels:	48 on FS1
	12 on cylinder
	26 on FS2

Free surface(s):	2
wall:	yes (dist=0.3m)
radius:	R=0.4m
cylinder height:	l=anything
depth:	H=1.3m (1m ABOVE cyl)
average:	no
regrid:	staggered (0.9-1.1)
viscosity:	yes
surface tension:	yes
dphi:	0.008
panels:	48 on FS1
	12 on cylinder
	26 on FS2

Wall (dist = 0.3m), depth = 1.3m

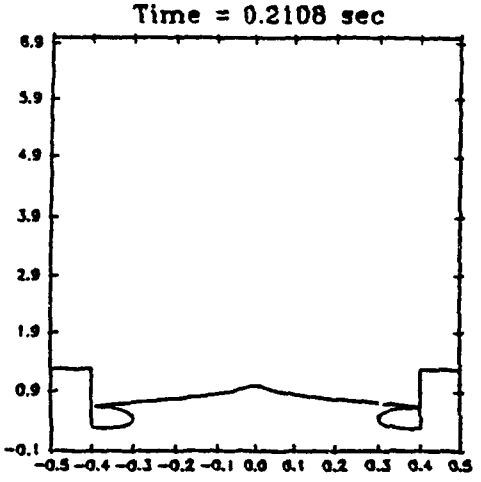

FIG. 4.2.2.13

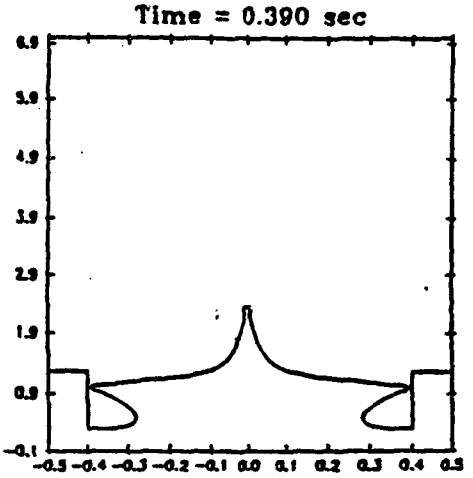

FIG. 4.2.2.14

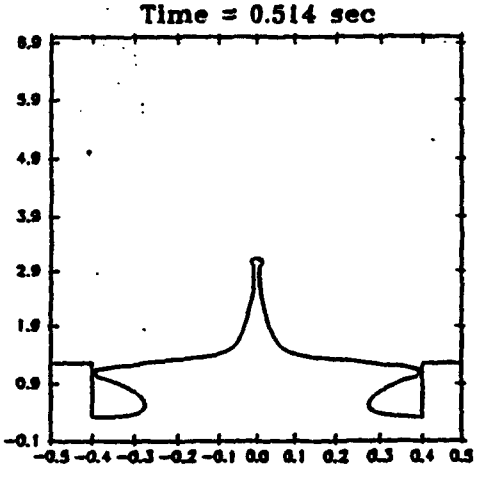

FIG. 4.2.2.15

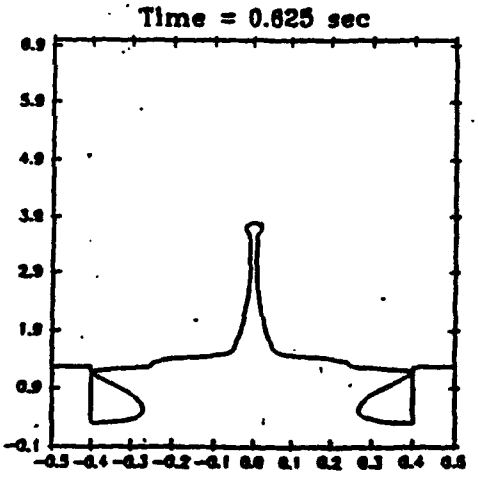

FIG. 4.2.2.16

Wall (dist = 0.1m), depth = 1.1m

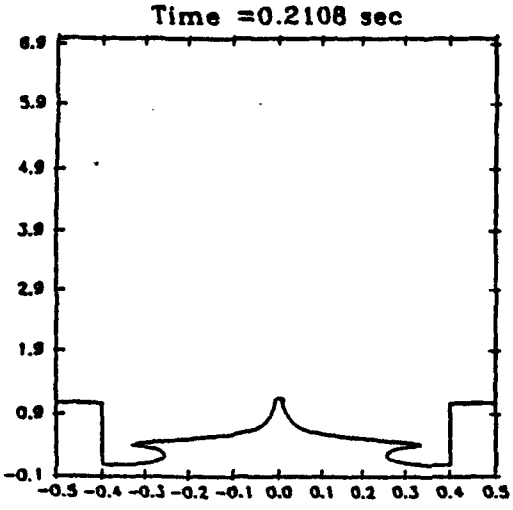

FIG. 4.2.2.17

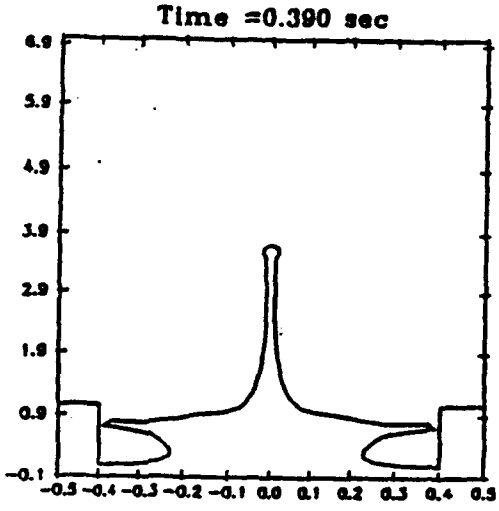

FIG. 4.2.2.18

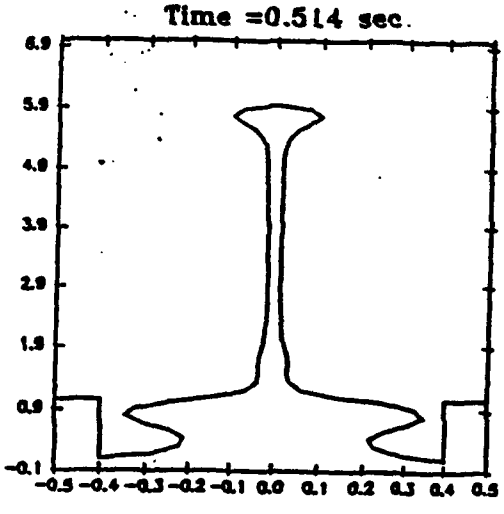

FIG. 4.2.2.19

Free surface(s):	2
wall:	yes (dist=0.1m)
radius:	R=0.4m
cylinder height:	l=anything
depth:	H=1.1m (1m ABOVE c.
average:	no
regrid:	staggered (0.9-1.1)
viscosity:	yes
surface tension:	yes
dphi:	0.008
panels:	48 on FS1 12 on cylinder 26 on FS2

Effect of the distance of the wall

FIG. 4.2.2.20

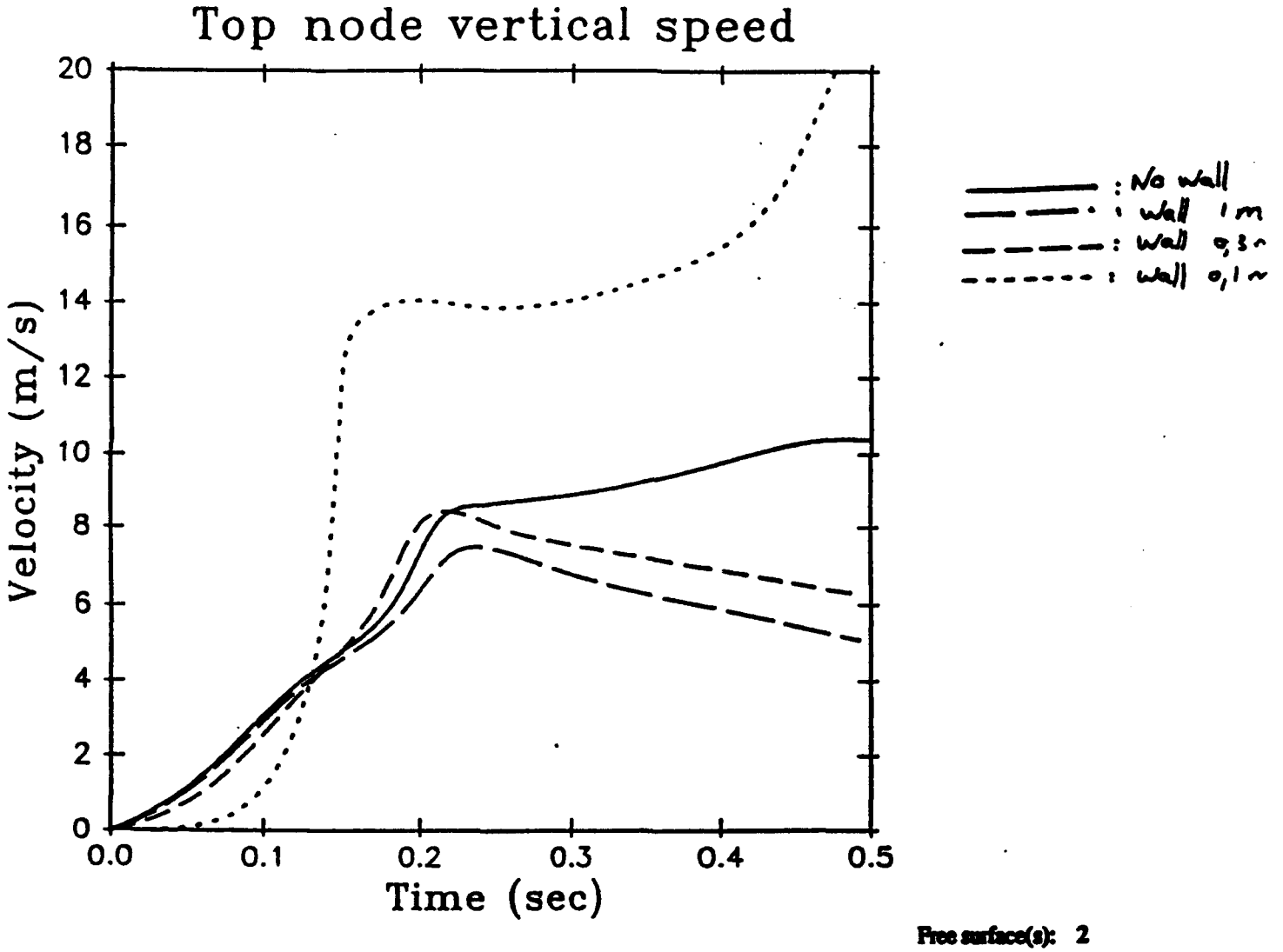

Free surface(s):	2
wall:	yes (dist=0.1m to 1m
radius:	R=0.4m
cylinder height:	h=anything
depth:	H=1m + dist.
average:	no
regrid:	staggered (0.9-1.1)
viscosity:	yes
surface tension:	yes
dphi:	0.008
panels:	48 on FS1 12 on cylinder 26 on FS2

Velocity field at time 0.25 sec.

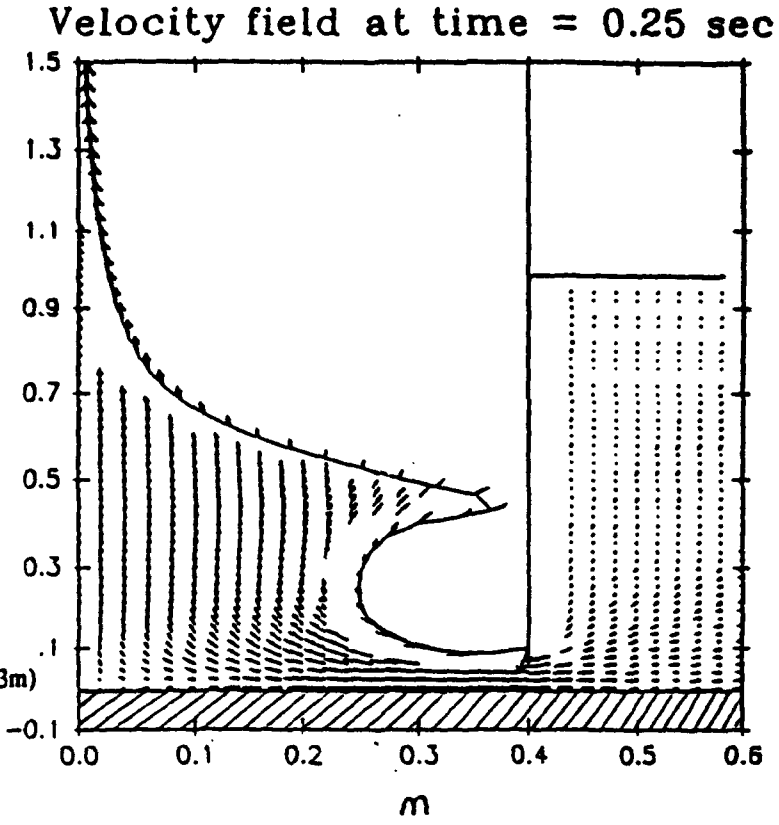

FIG. 4.2.2.21

Free surface(s):	2
wall:	yes (dist=0.1m and 0.3m)
radius:	R=0.4m
cylinder height:	l=anything
depth:	H=1m + dist.
average:	no
regrid:	staggered (0.9-1.1)
viscosity:	yes
surface tension:	yes
dphi:	0.008
panels:	48 on FS1
	12 on cylinder
	26 on FS2

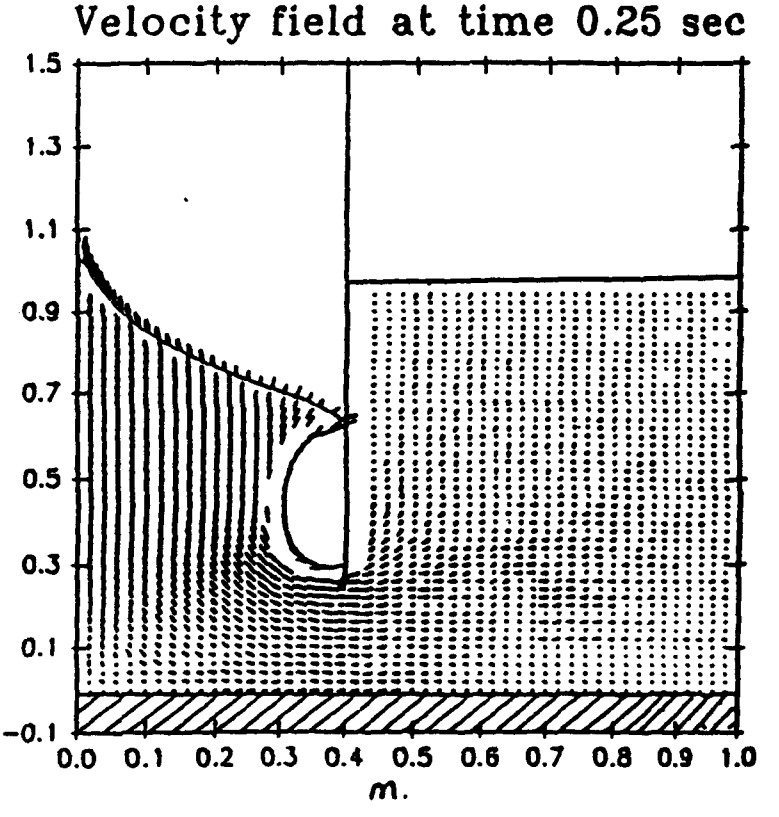

FIG. 4.2.2.22

Wall (dist = 0.1m), depth = 2.1m

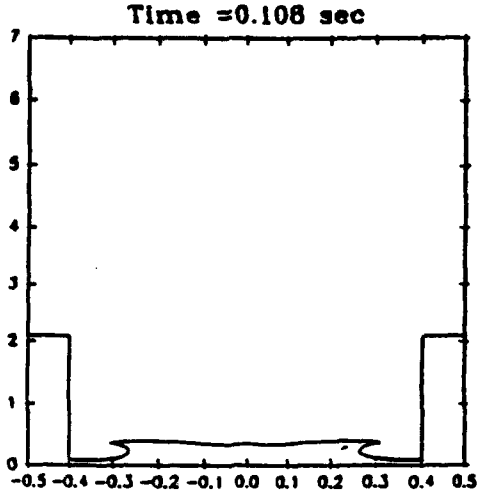

FIG. 4.2.3.1

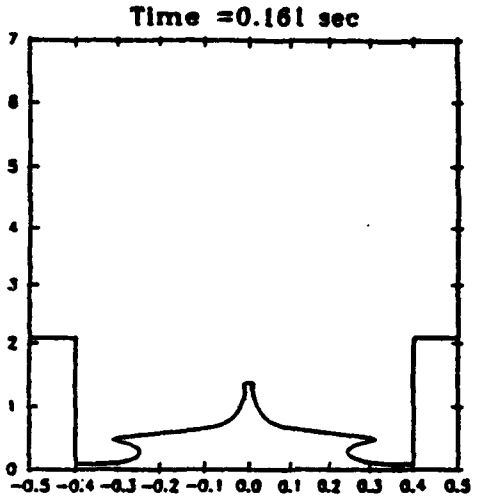

FIG. 4.2.3.2

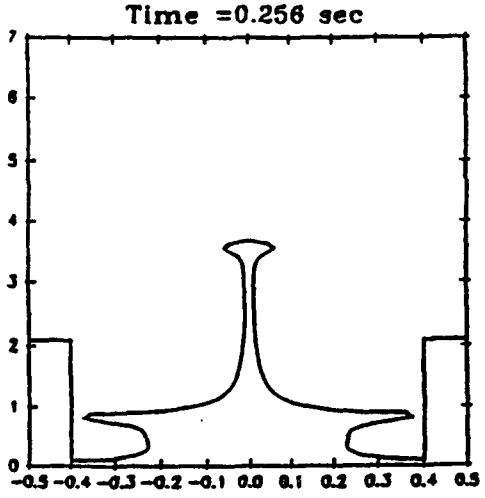

FIG. 4.2.3.3

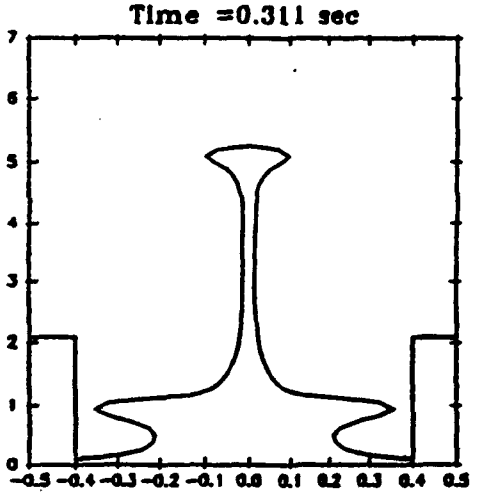

FIG. 4.2.3.4

Free surface(s):	2
wall:	yes (dist=0.1m)
radius:	R=0.4m
cylinder height:	l=anything
depth:	H=1m + dist.=2.1m
average:	no
regrid:	staggered (0.9-1.1)
viscosity:	yes
surface tension:	yes
dphi:	0.008
panels:	48 on FS1
	12 on cylinder
	26 on FS2

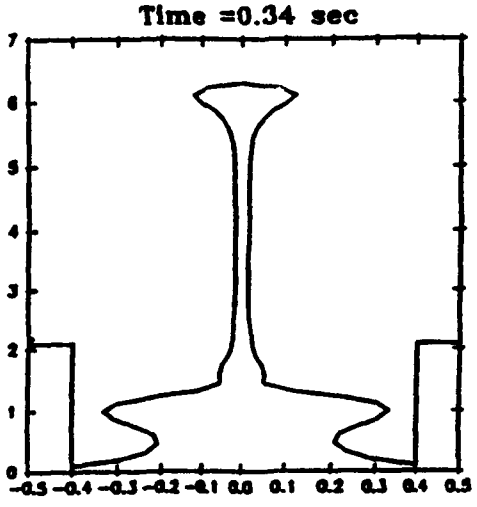

FIG. 4.2.3.5

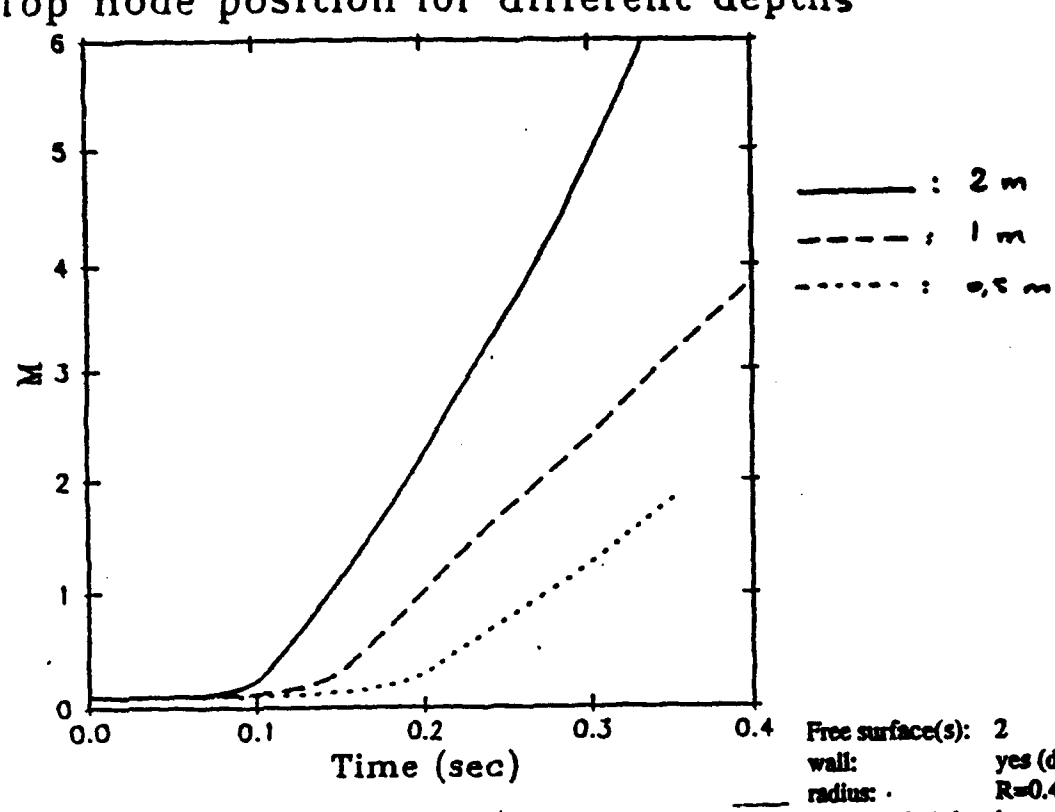

FIG. 4.2.3.6

Free surface(s):	2
wall:	yes (dist=0.1m)
radius:	R=0.4m
cylinder height:	l=anything
depth:	H=(0.5,1,2) + dist.
average:	no
regrid:	staggered (0.9-1.1)
viscosity:	yes
surface tension:	yes
dphi:	0.008
panels:	48 on FS1 12 on cylinder 26 on FS2

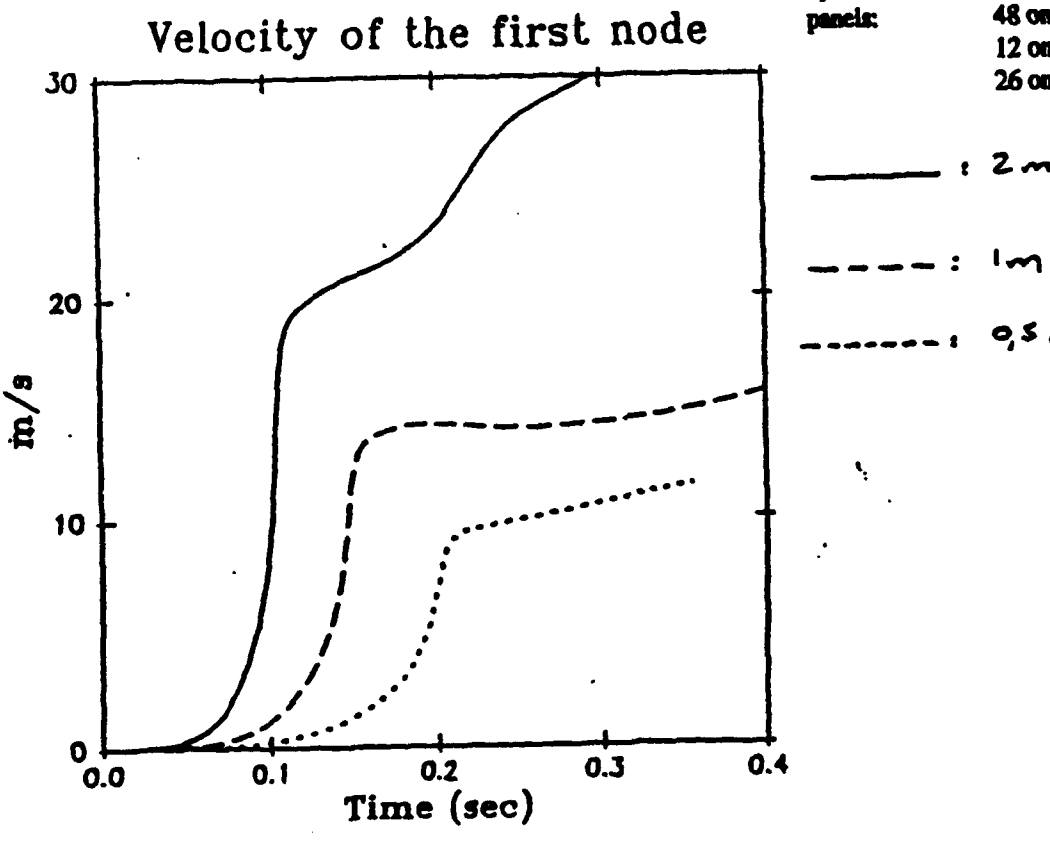

FIG. 4.2.3.7

Simulation of a falling wall of water

general shape

Zoom (creation of a bubble)

wall of water suddenly free to fall

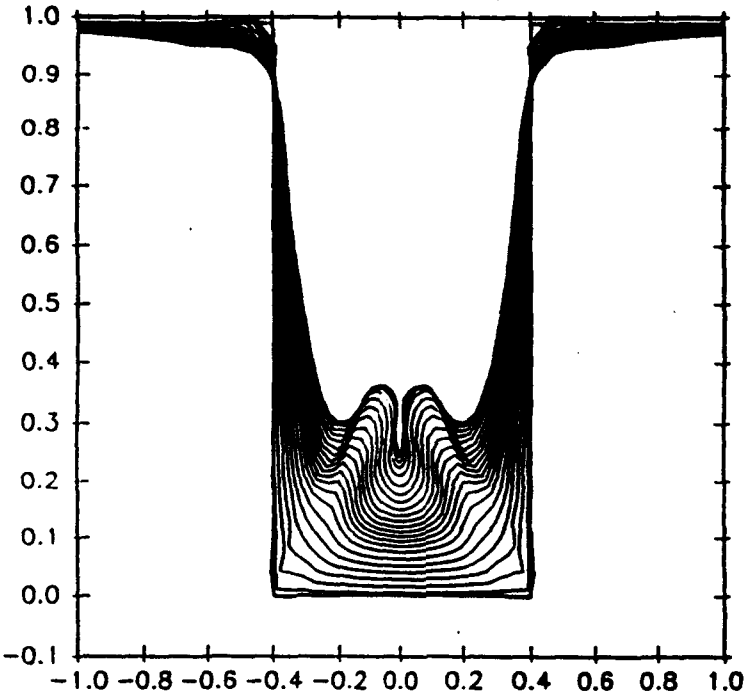

Fig. 5.1

wall of water suddenly free, Zoom

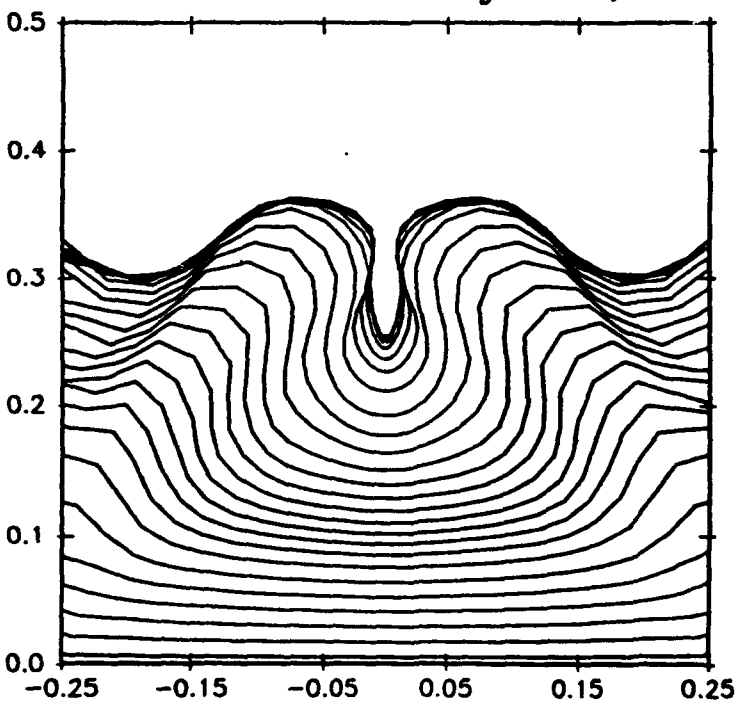

Fig. 5.2

Free surface(s):	**2**
wall:	**no**
dist from axis:	**0.4m**
Radius:	**2m**
length FS2:	**1m**
initial height of wall of water:	**0.99m**
depth:	**H=1m**
average:	**no**
regrid:	**staggered (0.9-1.**
viscosity:	**yes**
surface tension:	**yes**
dpid:	**0.008**
panels:	**40 on FS1** **2 on cylinder (ve:** **10 on FS2**

Bubble touching the surface

bubble touching the surface,t=0 to 0.015 sec

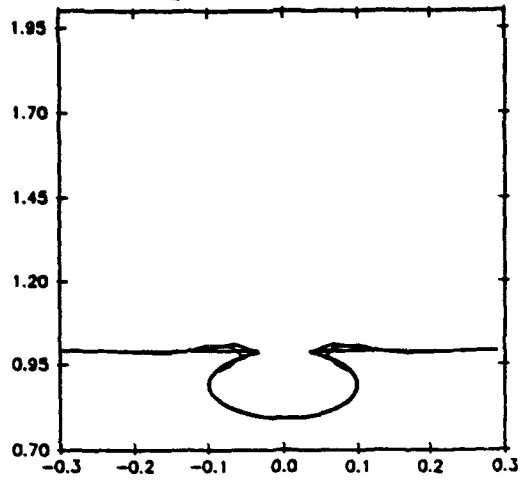

bubble touching the surface,t=0.054 to 0.082 sec

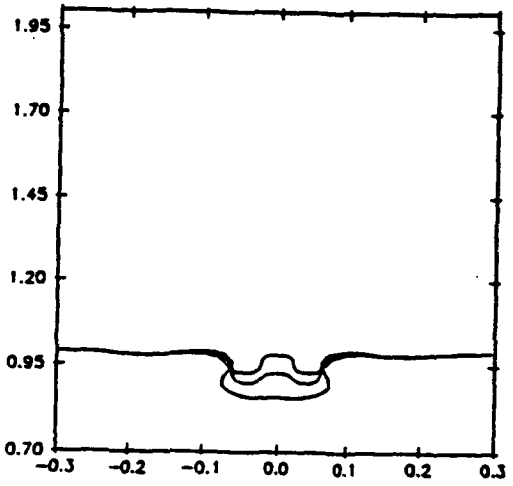

bubble touching the surface,t=0.082 to 0.097 sec

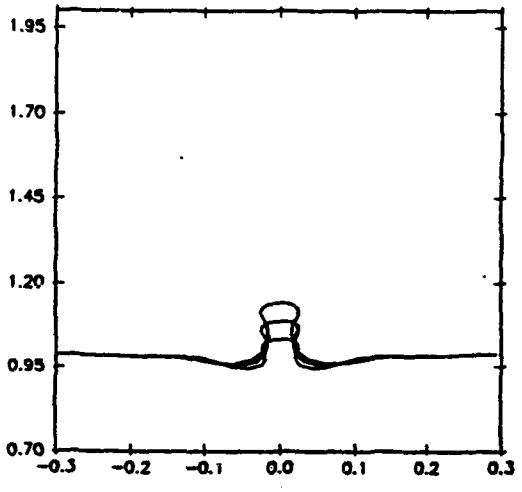

bubble touching the surface,t=0.1 to 0.1406 sec

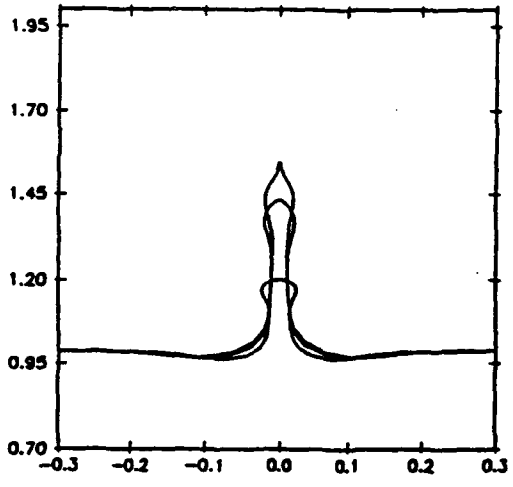

bubble touching the surface,t=0.146 to 0.153 sec

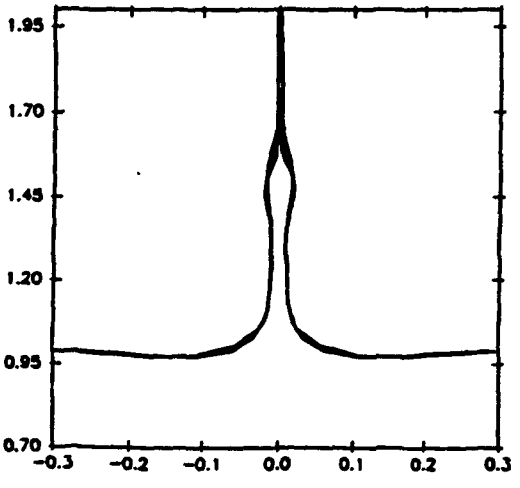

Free surface(s):	2
wall:	no
radius of bubble:	0.1 m
bubble opened:	2*20 degrees
radius:	R=4m
length FS2:	1 m
regrid:	staggered (1-1.3)
viscosity:	yes
surface tension:	yes
dphi:	0.004
panels:	74 on FS1
	2 on cylinder
	10 on FS2

Non-dimentionalisation of figures 4.2.3.6 and 4.2.3.7

Position with time and Z non-dimentionalised

Position with Z only non-dimentionalised

Velocity with time and speed non-dimentionalised

Velocity with Velocity only non-dimentionalised

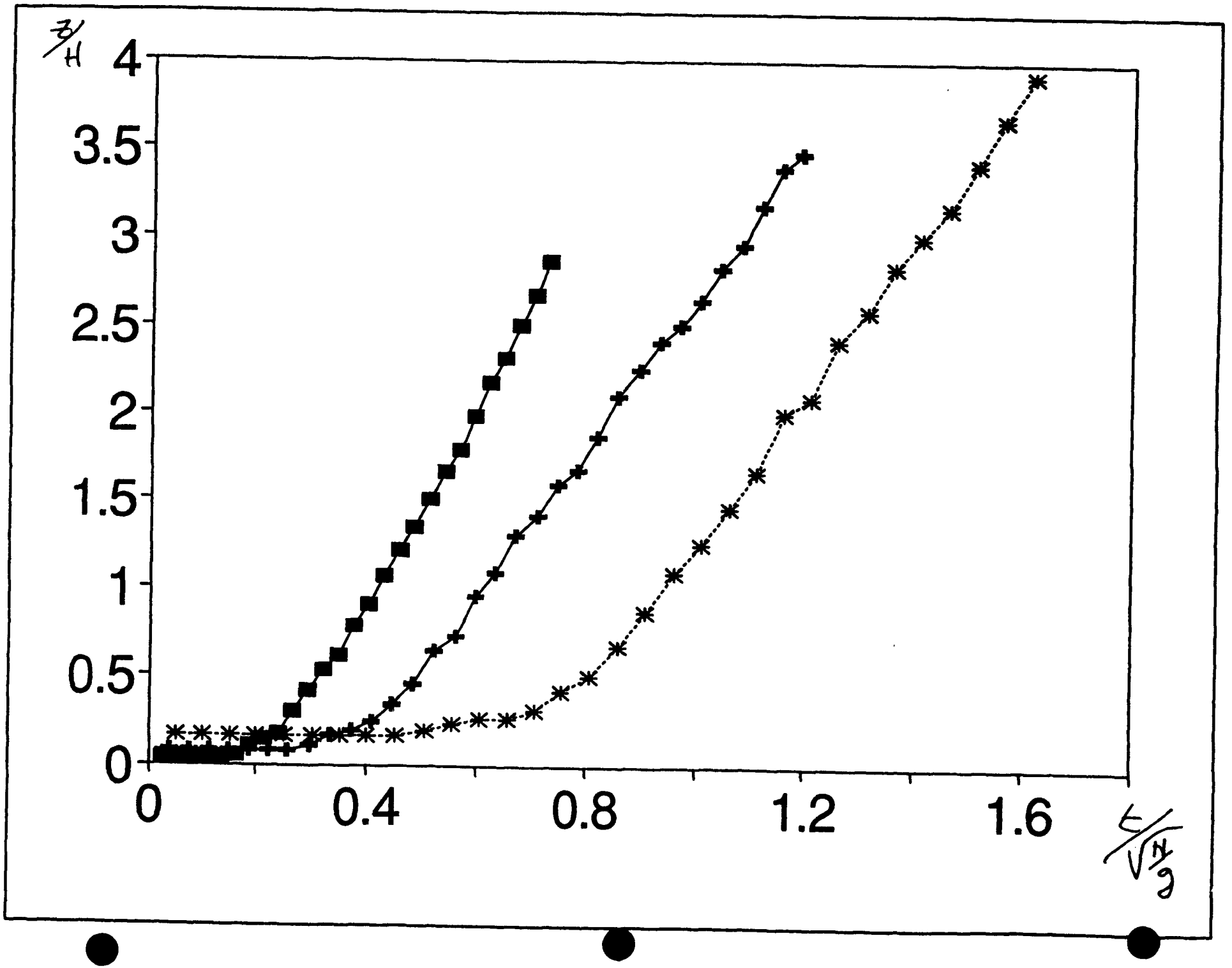
z/H
4
3.5
3
2.5
2
1.5
1
0.5
0
0
0.4
0.8
1.2
1.6
t/√(H/g)

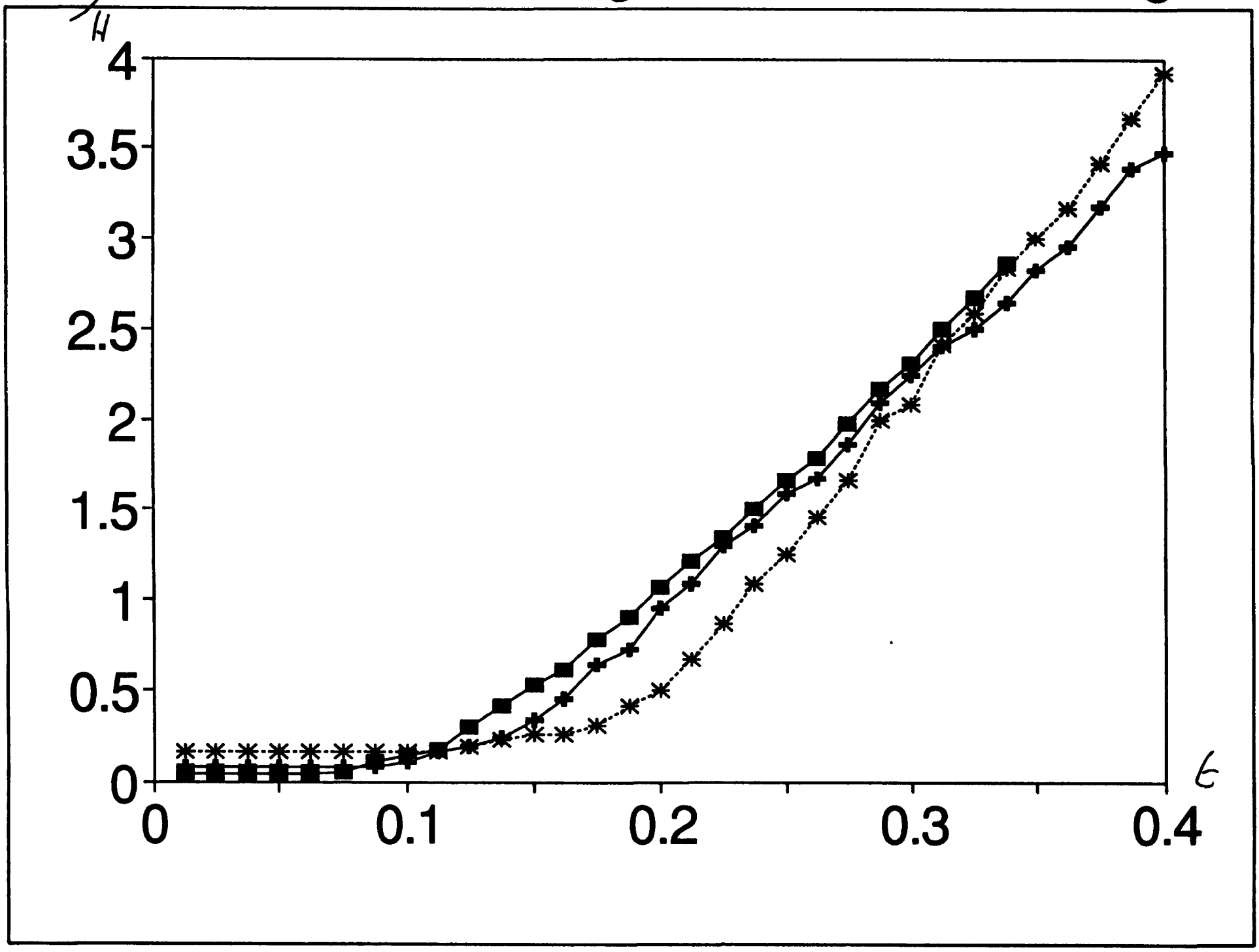
H
4
3.5
3
2.5
2
1.5
1
0.5
0
0
0.1
0.2
0.3
0.4
ε

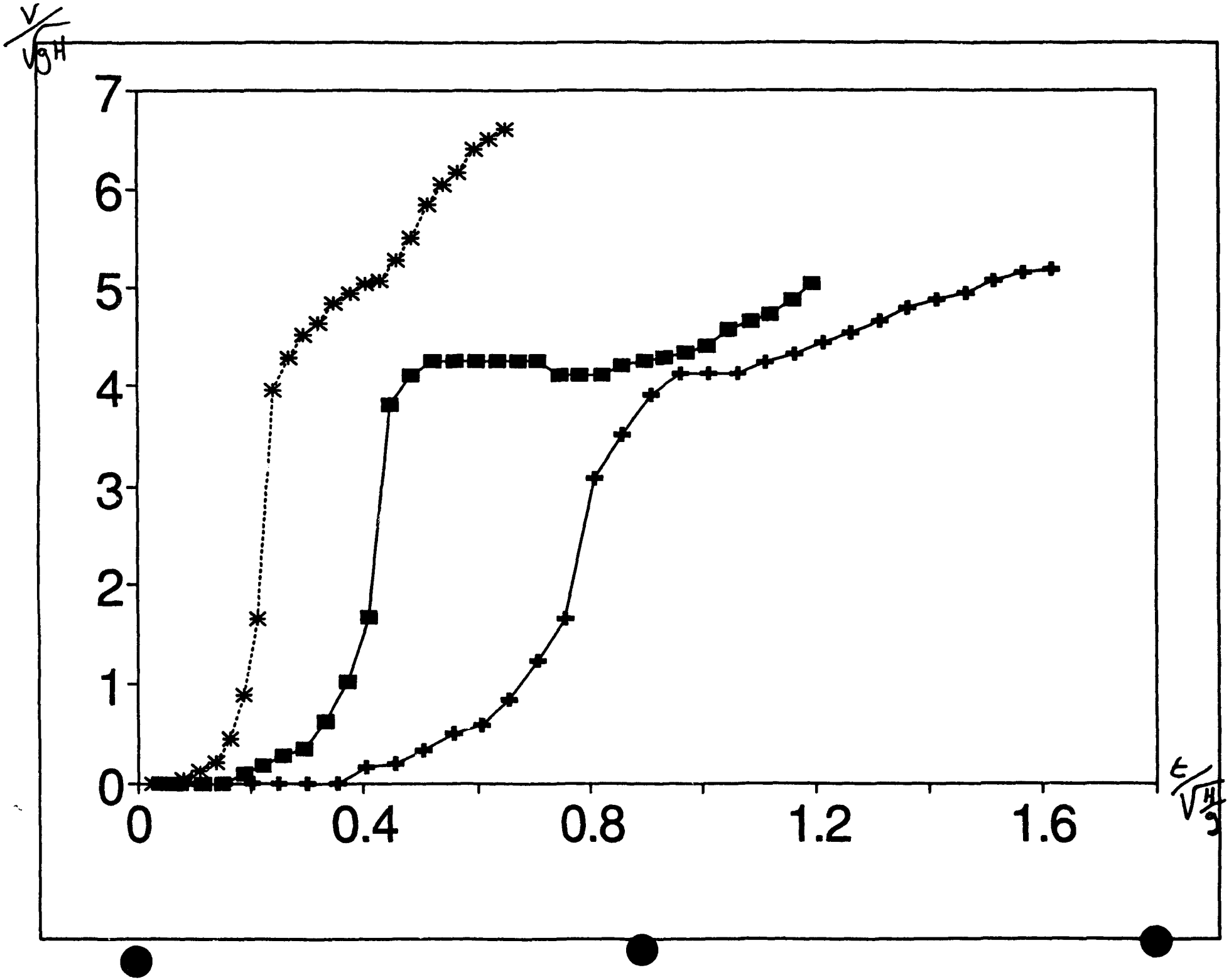
V/√(VgH)
7
6
5
4
3
2
1
0
0
0.4
0.8
1.2
1.6
ε/√(H/g)

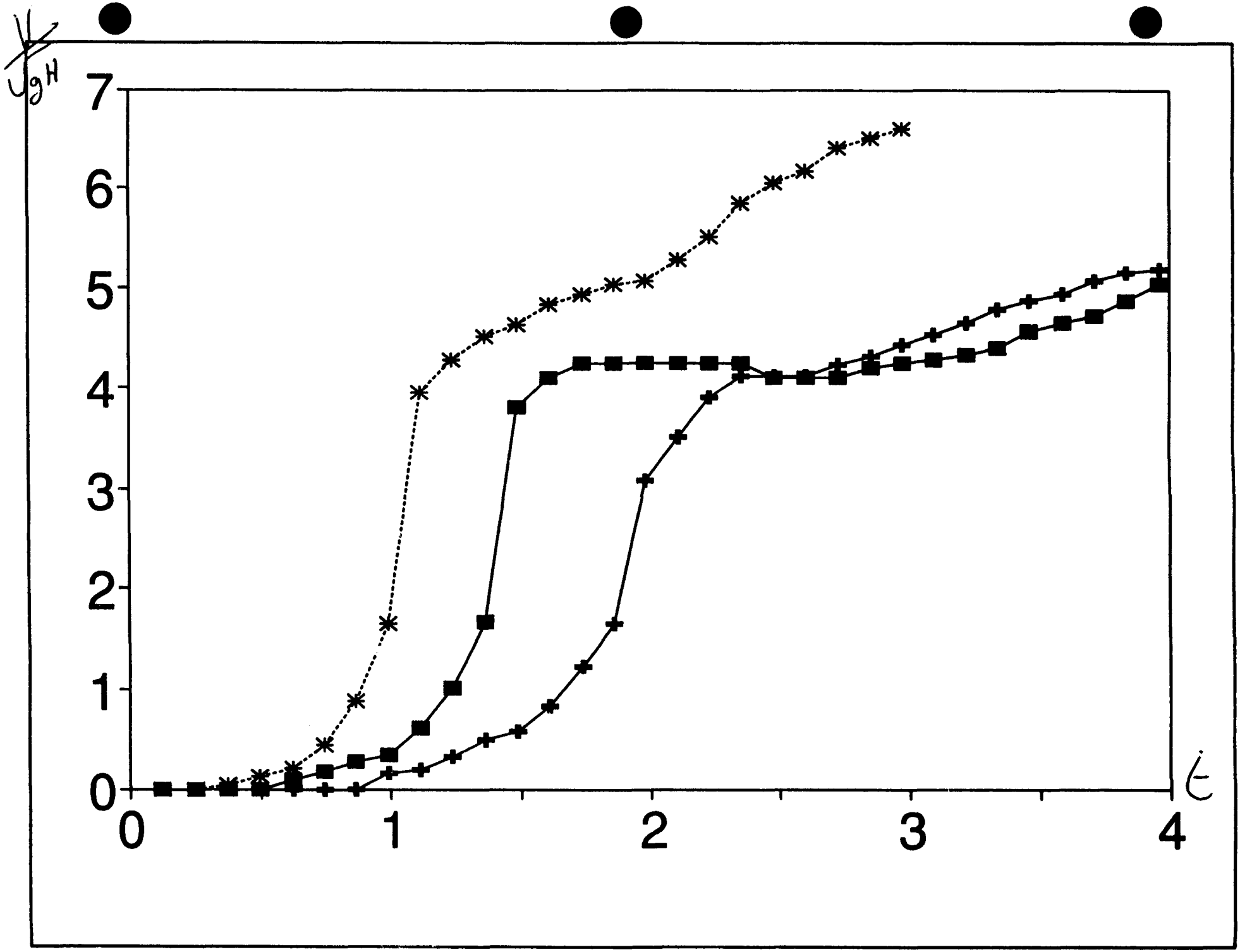
ψ_{gH}
7
6
5
4
3
2
1
0
0
1
2
3
4
ϵ

DYNAFLOW, Inc.

Report 6.002_12

ASYMPTOTIC STUDY OF BUBBLE DYNAMICS IN THE PROXIMITY OF A BODY IN POTENTIAL FLOW

by
Jean-Bernard Ville
and
Georges L. Chahine

July, 1992

Résumé

Depuis les premiers travaux de Rayleigh et Besant, beaucoup de documents ont étés consacés à l'étude d'écoulements contenant des cavités gazeuses. Avec l'apparition d'outils informatiques puissants et de méthodes à éléments finis rapides, l'attention a été portée à développer des codes de calcul tri–dimmensionnels. L'approche par développements asymptotiques raccordés permet une étude plus qualitative des résultats car elle permet de dégager directement les paramètres importants du problème.

Le but de ce travail est l'étude de l'effondrement de bulles de cavitation au voisinnage d'une paroi solide dans un écoulement potentiel, par la méthode des développements asymptotiques raccordés. Le type de problème considéré se limite à l'étude de bulles de dimensions petites relativement aux dimensions de l'écoulement. Nous adoptons donc le paramètre ϵ, rapport du rayon initial de la bulle à la dimension caractéristique de l'écoulement. A chaque étape, le problème se décompose en deux parties:

– un problème intérieur, c'est-à -dire, à l'échelle de la bulle, où la paroi solide représentée par l'ogive est considérée comme étant à l'infini.
– un problème extérieur, c'est-à -dire à l'échelle de l'écoulement, où la bulle est considérée comme perturbation de l'écoulement initial.

A chaque étape, ces deux problèmes sont reliés l'un à l'autre par une condition de raccordement: dans une zone d'espace d'échelle intermédiaire entre les deux problèmes, ils doivent aboutir à la même solution.

Les déformations d'une bulle de cavitation, et en particulier l'observation d'un jet réentrant (origine du bruit de cavitation) peuvent rouver deux origines: l'origine physique due directement à l'instabilité de la bulle dans l'écoulement eu égard aux conditions de pression et de vitesse de celui-ci; et l'origine mathématique, due au fait que le déplacement du repère et

l'intensité du jet observé dans ce repère ne sont pas indépendants. Il est cependant nécessaire d'adopter un référentiel mobile pour les calculs, car les calculs présentés deviennent faux dès que l'origine du repère sort de la bulle. Ils deviennent donc très rapidement faux si l'origine du repère ne se déplace pas avec la bulle.

Les calculs de déformations présentés jusqu'à la section 4 sont effectués dans un repère se déplaçant de la même façon qu'un point matériel dans l'écoulement potentiel initial. Appliqués au cas particulier que nous avons adopté pour les études numériques, celui d'un corps de Rankine, c'est-à -dire un potentiel pour l'écoulement initial égal à la superposition d'une source et d'un écoulement uniforme, ils permettent l'observation (figures 2 et 3) d'un jet réentrant orienté vers la paroi solide et opposé au déplacement de la bulle.

La section 5 présente les calculs effectués dans un repère dont l'origine est prise à chaque instant égale au centre de gravité de la bulle. Ce choix élimine toutes les déformations non-sphériques de la bulle; c'est pourquoi les comparaisons montrées par les figures 4 permettent de constater l'absence de jet dans ce repère. Ce type de calcul n'a été effectué que jusqu'à l'ordre ε. Ils peuvent être sans difficultés poursuivis pour les ordres supérieurs, afin d'allonger la durée de validité des calculs. A l'ordre ε^2, en particulier, ceci permettrait d'observer des déformations plus importantes.

La section 6 étudie le probème de la représentation de lignes de courant. Son but est de démontrer que la meilleure méthode de représentation reste la méthode d'Euler et non la recherche d'une pseudo fonction de courant.

La dernière partie de ce travail (section 7) présente les calculs du développement de la forme de la bulle à l'ordre ε^2. Ceux-ci sont effectués dans un référentiel dont l'origine se déplace à la vitesse du point matériel équivalent dans l'écoulement initial. Ces calculs restent à vérifier. Leur application au cas particulier que nous avons choisi montrent de fortes déformations des bulles de cavitation.

La complexité formelle, due à la méthode des développements asymptotiques elle-même, entraîne rapidement des erreurs numériques. Il paraît donc indispensable d'en comparer les résultats avec ceux fournis par un calcul fondé sur la méthode des éléments finis.
Outre ces remarques d'ordre numérique, plusieurs points restent ouverts. Ainsi, négliger les efforts de tension superficielle n'est pas nécessairement un

choix pertinent. De même, les choix de repères mobiles effectués représentent deux types de choix extrêmes : dans un cas, tous les déplacements sont comptabilisés comme déformations, dans l'autre, aucun jet réentrant ne peut être observé. Il est possible d'introduire dans le modèle un paramétre permettant de choisir la mobilité du repère de façon à se situer entre ces deux cas extrêmes. Un tel mode de calcul conduirait vraisemblablement à un choix optimal de ce paramètre, et donc à une représentation optimale du phénomène d'effondrement. Enfin, une introduction de la viscosité dans le modèle permettrait une extension de son champs d'application.

Asymptotic study of bubble dynamics in the proximity of a body in potential flow

Jean-Bernard Ville and Georges L. Chahine
DYNAFLOW, Inc.
7210 Pindell School Road,
Fulton, MD 20759
Tel: (301)-604-3688, Fax: (301)-604-3689

Abstract

The behaviour of a bubble in a flow field near a body is studied using a matched asymptotic expansion, the small parameter (r_0/l_0) being the ratio of the initial bubble radius to the initial bubble standoff distance to the wall. Assuming the bubble to be small compared with the flow field length scale, a Taylor expansion of the pressure and velocity of the flow field can be done. The nature of the interaction between the bubble and the flow becomes more complex as the expansion increases. The theory is applied to the problem of a bubble collapsing near a semi-infinite bluff body in a uniform flow field. Results obtained at order ε and order ε^0 show the formation of a curved jet moving opposite to the bubble trajectory and towards the wall and an imparted rotation of the bubble. Analytical results from at ε^2 are given, and have been computed. In order to lengthen the validity lap of the calculations, a translation velocity of the center of the frame has been introduced at order ε. Results have still to be compared with a 3D boundary element method.

Introduction

The understanding of bubble and cavity dynamics has preoccupied reserchers and engineers over the past several decades. Since the early work of Rayleigh and Besant, numerous papers and books have been devoted to the study of cavity flows. With the advent of new mathematical and computational tools, increasing attention has been given to develop three-dimensional nonlinear numerical codes. Approximate theoretical approaches are very useful, since they give results at a much lower cost but they may be somewhat less precise than fully 3D methods. Bovis studied the collapse of a bubble near a wall using the simplifying assumption of neglecting the pressure and velocity gradient across the bubble. In this study we shall present results from a numerical and analytical study of the growth and collapse of a bubble in a general potential flow in the vicinity of a solid object. The selected analytical approach consists of using the method of matched asymptotic expansions. The small parameter of the expansion (ε), is chosen to be the ratio of the initial bubble radius to its distance to the wall. At every order the problem is decomposed into two pieces: an 'inner' problem where the characteristic length is the bubble radius and an 'outer' problem characterised by the bubble standoff distance from the wall. The effect of the wall appears only as a limit condition at infinity for the inner problem, and for the outer problem the bubble appears as a perturbation at the origin. A new fictitious flow is introduced by substracting the the initial flow (no bubble) from the real flow (presence of the bubble and the object). Studying this flow has the advantage of having staightforward boundary conditions at infinity. The calculations are done in a frame moving with the bubble so as to follow the bubble behaviour over a longer period of time otherwise the results become wrong as soon as the origin of the frame is outside the bubble. The bubble is assumed to be filled with liquid vapour and non-condensable gas which follows the polytropic law $PV^k = constant$. A dimensional analysis will leads us to make assumptions on the initial flow, for example the initial radius of the bubble has to be small compared with the length scale of the flow. The theory developed here can be applied to any potential flow which has at least one plane of symmetry (easier calculations) and will be applied to the problem of a bubble collapsing near a semi-infinite bluff body in a uniform flow field. In the example presented, the potential used is that of a source in a uniform flow field so that the complete problem has a plane of symmetry.

1 Problem formulation

We first set the system of equations of our problem in a moving frame which we take such as its origin is inside the collapsing bubble. Its characteristics regarding to a fixed frame are given by its velocity $\vec{V}_e$ and its rotation $\vec{\omega}$. We will note :

$\vec{V}_0$ the velocity due to the initial potential flow without the bubble

ϕ the additionnal potential due to the presence and dynamics of the bubble, in the moving frame

$r = R(\theta, \psi, t)$ the bubble shape equation in the moving frame.

Let us note O the frame center, $\vec{n}$ the normal to the bluff-body wall or to the bubble wall, $p(r,t)$ the pressure due to the initial flow ,$p_O(O,t)$ the pressure due to the initial flow at point O, and M a field point. Therefore, the equations of the problem are :

$$\nabla^2\phi = 0 \tag{1}$$

$$\lim_{M\to\infty} \phi = 0 \tag{2}$$

$$\{\nabla\phi.\vec{n}\}_{bodywall} = 0 \tag{3}$$

$$\{\nabla\phi.\vec{n}\}_{r=R} = \frac{\partial R}{\partial t} + \{[(\vec{V}_e - \vec{V}_0(O,t)) + \vec{\omega}\times O\vec{M}].\vec{n}\}_{r=R} \tag{4}$$

$$\{\frac{\partial\phi}{\partial t} + \frac{1}{2}(\nabla\phi)^2 + (\vec{V}_0(\vec{r},t) - \vec{V}_e - \vec{\omega}\times O\vec{M}).\nabla\phi + \frac{1}{2}(V_0^2(\vec{r},t) - V_0^2(O,t)) + \frac{p}{\rho}\}_{r=R} = \frac{p_0(t)}{\rho} \tag{5}$$

Taking into account the fact that the pressure inside the bubble is supposed to be spatially uniform and that the gaz inside the bubble follows a polytropic law ($PV^k = constant$), we may transform the last equation of our initial system in:

$$\rho\{\frac{\partial\phi}{\partial t} + \frac{1}{2}(\nabla\phi)^2 + (\vec{V}_0(\vec{r},t) - \vec{V}_e - \vec{\omega}\times O\vec{M}).\nabla\phi + \frac{1}{2}(V_0^2(\vec{r},t) - V_0^2(O,t)) + \frac{p}{\rho}\}_{r=R} =$$

$$(p_0(t) - p_{init}) + (p_{init} - p_v)(1 - \frac{\mathcal{V}^{-k}}{\mathcal{V}_0^{-k}}) + \frac{2\gamma}{r_0}(r_0 C - \frac{\mathcal{V}^{-k}}{\mathcal{V}_0^{-k}}) \tag{6}$$

where:
- p_v = initial partial vapour pressure in the bubble
- p_{init} = initial total pressure inside the bubble
- r_0 = initial bubble radius
- $\mathcal{V}_0$ = initial bubble volume
- $\mathcal{V}$ = bubble volume
- C = bubble surface curvature
- γ = surface tension coefficient

2 Non–dimmensionnalization of the problem

In so far as we limit our study to problems such as the bubble dimensions are small compared to the characteristic initial flow field dimension, we will use the matched asymptotic expansion method to calculate the complete flow field evolution, including the bubble collapse. This will lead us to set a small parameter that we will denote ε to separate the scales of the inner and the outer problem.

2.1 Notations

Two problems have to be solved simultaneously:

– An inner problem, that is to say, the problem of the bubble behaviour in the potential flow, whose scale is given by the characteristic size of the bubble (r_0), and whose variables will be denoted $\tilde{X}$:

$$\begin{aligned}
r &= r_0\tilde{r} \\
p &= (\Delta p)\tilde{p} \\
t &= T_0\tilde{t} \\
\phi &= \frac{r_0^2}{T_0}\tilde{\phi} \\
\vec{V}_0 &= v_0\tilde{\vec{V}}_0 \\
\nabla V_0 &= M(\tilde{\nabla}V_0) \\
\nabla\nabla V_0 &= N(\tilde{\nabla}\tilde{\nabla}V_0) \\
\omega &= \Omega\tilde{\omega}
\end{aligned}$$

– An outer problem, that is to say, the modification of the initial flow due to the presence of the bubble, whose scale is defined by the characteristic size of the flow : the radius of the semi–infinite bluff–body (l_0); and whose variables will be noted $\bar{X}$.

Therefore, the small parameter we use to expand these two problems is the ratio between the two scales :

$$\varepsilon = \frac{r_0}{l_0}$$

and we will use the following asymptotic expansions for the problem unknowns :

$$\begin{aligned}
\tilde{\phi}(\tilde{r},\theta,\psi,\tilde{t}) &= \tilde{\phi}_0(\tilde{r},\tilde{t}) + \varepsilon\tilde{\phi}_I(\tilde{r},\theta,\psi,\tilde{t}) + \varepsilon^2\tilde{\phi}_{II}(\tilde{r},\theta,\psi,\tilde{t}) + o(\varepsilon^2) \\
\bar{\phi}(\bar{r},\theta,\psi,\bar{t}) &= \bar{\phi}_0(\bar{r},\bar{t}) + \varepsilon\bar{\phi}_I(\bar{r},\theta,\psi,\bar{t}) + \varepsilon^2\bar{\phi}_{II}(\bar{r},\theta,\psi,\bar{t}) + o(^2) \\
\tilde{R}(\theta,\psi,\tilde{t}) &= \tilde{R}_0(\tilde{t}) + \varepsilon\tilde{R}_I(\theta,\psi,\tilde{t}) + \varepsilon^2\tilde{R}_{II}(\theta,\psi,\tilde{t}) + o(\varepsilon^2)
\end{aligned}$$

To match both problems, we write that they give the same solution in an intermediate–range zone:
for $r_0 \ll r \ll l_0$ we must have : $\phi_{inner}(\vec{r}) = \phi_{outer}(\vec{r})$.

2.2 Expansions calculations

We develop the following expressions using Taylor series :

2.2.1 Initial velocity field

We will first use a moving frame which origin moves at the equivalent material point in the initial flow velocity, and which x axis is always parallel to this velocity : $\vec{V}_e = \vec{V}_0(O,t)$ and, $\vec{V}_0(O,t) = v_0 v_x(t)\vec{e}_x$ in the moving frame. Therefore, we can write a Taylor series expansion as follows:

$$\begin{aligned}
\vec{V}_0(\vec{r},t) - \vec{V}_e &= M\tilde{r}_0\tilde{\nabla}V_0(O) + \tfrac{1}{2}r_0^2 N\tilde{\vec{r}}.\tilde{\nabla}\tilde{\nabla}V_0(O).\tilde{\vec{r}} + ... \\
(V_0(\vec{r},t) - \vec{V}_e).\nabla\phi &= \frac{r_0^2}{T_0^2}\tilde{\nabla}\phi.(MT_0\tilde{\vec{r}}.\tilde{\nabla}\vec{V}_0(O) + \tfrac{1}{2}NT_0 r_0\tilde{\vec{r}}.\tilde{\nabla}\tilde{\nabla}\vec{V}_0(O).\tilde{\vec{r}} + ...) \\
\tfrac{1}{2}(V_0^2(\vec{r},t) - V_e^2) &= \frac{r_0^2}{T_0^2}(MT_0^2\frac{m}{r_0}\tilde{\vec{r}}.\tilde{\nabla}\vec{V}_0(O) + \tfrac{1}{2}T_0^2 v_0 N\tilde{\vec{r}}.\tilde{\nabla}\tilde{\nabla}V_0(O).\tilde{\vec{r}}.\vec{V}_0(O) \\
&\quad + \tfrac{1}{2}(MT_0\tilde{\vec{r}}.\tilde{\nabla}V_0(O))^2 + ...)
\end{aligned}$$

We suppose the problem to be symmetrical about the (Oxz) plane in the moving frame. Thus, recalling that $\nabla.\vec{V}_0 = 0$ and $\nabla \times \vec{V}_0 = 0$, we must write :

$$\tilde{\nabla}V_0(O) = \begin{bmatrix} \alpha_1 & 0 & \alpha_2 \\ 0 & 0 & 0 \\ \alpha_2 & 0 & -\alpha_1 \end{bmatrix}$$

Calculating $\tilde{\nabla}V_0.\tilde{\vec{r}}$ and $\tilde{\vec{r}}.\tilde{\nabla}\tilde{\nabla}V_0.\tilde{\vec{r}}$ in the moving frame polar coordinates we obtain :

$$\begin{aligned}
\tilde{\nabla}V_0.\tilde{\vec{r}} &= r\begin{bmatrix} 2\alpha_2 \sin\theta\cos\theta\cos\psi + \alpha_1(\sin^2\theta\cos^2\psi - \cos^2\theta) \\ \alpha_1 \sin\theta\cos\theta(\cos^2\psi + 1) + \alpha_2\cos\psi\cos 2\theta \\ -\alpha_1\sin\theta\cos\psi\sin\psi - \alpha_2\sin\psi\cos\theta \end{bmatrix}_{e_r,e_\theta,e_\psi} \\
&= r\begin{bmatrix} G_r(\theta,\psi) \\ G_\theta(\theta,\psi) \\ G_\psi(\theta,\psi) \end{bmatrix}_{e_r,e_\theta,e_\psi}
\end{aligned}$$

and:

$$\vec{r}.\vec{\nabla}\vec{\nabla}V_0.\vec{r} = r^2 \left[\begin{array}{c} H_r \\ H_\theta \\ H_\psi \end{array} \right]_{e_r,e_\theta,e_\psi}$$

with:

$$H_r = (\frac{\partial \alpha_2}{\partial z} + 2\frac{\partial \alpha_1}{\partial x})(cos^2\theta\ sin\theta\ cos\psi) + (\frac{\partial \alpha_2}{\partial x} + 2\frac{\partial \alpha_1}{\partial z})(\cos\theta\ \sin^2\theta\ cos^2\psi)$$

2.2.2 Moving frame rotation

Since the problem has a plane of symmetry, we shall take $\vec{\omega} = \omega(t)\vec{e}_Y$.

$$\vec{\omega} \times O\vec{M} = \omega r(\vec{e}_Y \times \vec{e}_r) \tag{7}$$

$$= \omega r \left[\begin{array}{c} 0 \\ cos\psi \\ -sin\psi\ sin\theta \end{array} \right]_{e_r,e_\theta,e_\psi} \tag{8}$$

$$(\vec{\omega} \times O\vec{M}) \cdot \vec{n} = \frac{r_0}{T_0}\left(-\omega T_0 cos\psi \frac{\partial R}{\partial \theta} + \omega T_0 \frac{sin\psi\ cos\theta}{sin\theta}\frac{\partial R}{\partial \psi}\right) \tag{9}$$

$$(\vec{\omega} \times O\vec{M}) \cdot \nabla\phi = \frac{r_0^2}{T_0^2}\left(\omega T_0 cos\psi \frac{\partial \phi}{\partial \theta} - \omega T_0 \frac{sin\psi\ cos\theta}{sin\theta}\frac{\partial \phi}{\partial \psi}\right) \tag{10}$$

Let Ω be the characteristic rotation speed of the frame. We shall assume that ΩT_0 is of order ϵ.

$$\omega = \Omega\tilde{\omega}$$

$$\omega T_0 = \epsilon\tilde{\omega}$$

2.2.3 Geometrical data expansions

VOLUME :

The expansion of the volume is necessary to know the pressure terms :

$$\begin{aligned}
\tilde{V} &= \frac{3}{4\pi}\int\int\int r^2 \sin\theta \, dr \, d\theta \, d\psi \\
&= \frac{1}{4\pi}\int_0^{2\pi} d\psi \int_0^{\pi} \sin\theta \, (\tilde{R}_0^3 + 3\epsilon \tilde{R}_0^2 \tilde{R}_I + 3\epsilon^2(\tilde{R}_0 \tilde{R}_I^2 + \tilde{R}_0^2 \tilde{R}_{II}))\, d\theta \\
&= \tilde{R}_0^3 + 3\epsilon \tilde{R}_0^2 R_{I00} \\
&\quad +3\epsilon^2(\tilde{R}_0^2 R_{II00} + \tilde{R}_0(R_{I00}^2 + \frac{1}{3}R_{I10}^2 + \frac{2}{3}R_{I11}^2 + \frac{6}{5}R_{I21}^2 + \frac{1}{3}R_{If}^2))
\end{aligned}$$

at order ϵ^2.

CURVATURE :

In the same way, we can work out the expansion of the curvature, to develop the surface tension terms: if $B(\theta,\psi) = \tilde{r} - \tilde{R}_0 - \epsilon \tilde{R}_I(\theta,\psi) - \epsilon^2 \tilde{R}_{II}(\theta,\psi)$,

$$\begin{aligned}
\tilde{C} &= \nabla.\left(\frac{\nabla B}{|\nabla B|}\right) \\
\tilde{C} &= \frac{1}{\tilde{R}_0} + \epsilon(-\frac{\tilde{R}_I}{\tilde{R}_0^2} - \frac{cos\,\theta}{2\tilde{R}_0^2 sin\,\theta}\frac{\partial \tilde{R}_I}{\partial\theta} - \frac{1}{2\tilde{R}_0^2}\frac{\partial^2 \tilde{R}_I}{\partial\theta^2} - \frac{1}{2(\tilde{R}_0 sin\,\theta)^2}\frac{\partial^2 \tilde{R}_I}{\partial\psi^2}) \\
&\quad +\epsilon^2(\frac{cos\,\theta}{\tilde{R}_0^2 sin\,\theta}\frac{\tilde{R}_I}{\tilde{R}_0}\frac{\partial \tilde{R}_I}{\partial\theta} - \frac{cos\,\theta}{2\tilde{R}_0^2 sin\,\theta}\frac{\partial \tilde{R}_{II}}{\partial\theta} + \frac{\tilde{R}_I}{\tilde{R}_0^3}\frac{\partial^2 \tilde{R}_I}{\partial\theta^2} - \frac{\tilde{R}_I}{2\tilde{R}_0^2}\frac{\partial^2 \tilde{R}_{II}}{\partial\theta^2} \\
&\quad +\frac{\tilde{R}_I}{2\tilde{R}_0^3 sin\,\theta^2}\frac{\partial^2 \tilde{R}_I}{\partial\psi^2} - \frac{1}{2(\tilde{R}_0 sin\,\theta)^2}\frac{\partial^2 \tilde{R}_{II}}{\partial\psi^2} + \frac{1}{2\tilde{R}_0^3 sin^2\,\theta}\frac{\partial^2 \tilde{R}_I}{\partial\psi^2})
\end{aligned}$$

NORMAL :

Using the same function B as before, we have:

$$\vec{n} = \frac{\nabla B}{|\nabla B|}$$

since the scalar product with other terms will lead to higher order terms, we just need to know the expansion of the normal till order ϵ :

$$\vec{n} = \vec{e}_r - \epsilon(\frac{1}{\tilde{R}_0}\frac{\partial \tilde{R}_I}{\partial\theta}\vec{e}_\theta + \frac{1}{\tilde{R}_0 sin\,\theta}\frac{\partial \tilde{R}_I}{\partial\psi}\vec{e}_\psi)$$

2.3 Consistency of the different scales

By application of least degeneracy principle to equations (4) and (6) , we get the relative values for the different variables we need : we must have :

$$\begin{aligned} \frac{\Delta p T_0^2}{\rho r_0^2} &= 1 \\ M T_0 &= \epsilon \\ N r_0 T_0 &= \epsilon^2 \\ \Omega T_0 &= \epsilon \end{aligned}$$

To complete the non-dimmensionnalization of the inner problem, let us define:

$$\begin{aligned} \mu &= v_0 \frac{T_0}{r_0} \\ \mathcal{P} &= \frac{p_{init} - p_v}{\Delta p} \\ \frac{1}{W} &= \frac{2\gamma}{r_0 \Delta p} \end{aligned} \tag{11}$$

3 Problem formulation till order ϵ

3.1 Outer problem

Till order ϵ^2, we can approximate the shape of the bluff-body as seen by the bubble by a flat plane : we shall take $\{\vec{n}\}_{bodywall} = \vec{e}_z$. The outer problem obeys the following system :

$$\nabla^2 \bar{\phi} = 0 \tag{12}$$

$$\lim_{r \to \infty} \bar{\phi} = 0 \tag{13}$$

$$\{\nabla \bar{\phi} . \vec{e}_z\}_{bodywall} = 0 \tag{14}$$

3.2 Inner problem

We neglect the surface tension strength, in order to simplify the future developments on spherical harmonics. The expansion of equations (4) and (6) give us the system of equation for the inner problem till order ϵ :

$$\nabla^2\tilde{\phi} = 0 \tag{15}$$

$$\{\nabla\tilde{\phi}.\vec{n}\}_{\tilde{r}=\tilde{R}} = \frac{\partial\tilde{R}}{\partial\tilde{t}} - \epsilon\{(\tilde{\vec{r}}.\tilde{\nabla}V_0(O) + \tilde{\vec{\omega}}\times\tilde{\vec{r}}).\vec{n}\}_{\tilde{r}=\tilde{R}} \tag{16}$$

$$\{\frac{\partial\tilde{\phi}}{\partial\tilde{t}} + \frac{1}{2}(\tilde{\nabla}\tilde{\phi})^2 + \epsilon.\nabla\tilde{\phi}(\tilde{\vec{r}}.\tilde{\nabla}V_0(O) + \tilde{\vec{\omega}}\times\tilde{\vec{r}}) + \epsilon\mu\tilde{\vec{V}}_0.(\tilde{\vec{r}}.\tilde{\nabla}V_0)\}_{\tilde{r}=\tilde{R}} = \Delta\tilde{p}(\tilde{t}) + 3\epsilon kP\frac{\tilde{R}_{I00}}{\tilde{R}_0} \tag{17}$$

4 Resolution

4.1 Order ϵ^0

4.1.1 Outer problem at order ϵ^0

System of equation (12) to (14) for the order zero becomes:

$$\nabla^2\bar{\phi}_0 = 0 \tag{18}$$

$$\lim_{r\to\infty}\bar{\phi}_0 = 0 \tag{19}$$

$$\{\nabla\bar{\phi}_0\cdot\vec{n}\}_{r=\frac{1}{\cos\theta}} = 0 \tag{20}$$

The general solution to this problem is a combination of spherical harmonics, such as :

$$\sum(\phi'_{jm}\bar{r}^j + \frac{\phi''_{jm}}{\bar{r}^{j+1}})Y_{jm}$$

where Y_{jm} are spherical harmonics depending on the values of the angular positions (see equation (42), section 4.2.2). To satisfy equation (19), we have to leave out all the terms in r^n. To respect the condition given by equation (20) we have to introduce an image bubble, symmetrical about the solid-body wall. If we write r' the distance between M and the center of this new bubble, and take into account the preceding remark, we can develop the outer potential at order 0 as :

$$\tilde{\phi}_0 = \sum_{n=0}^{\infty} B_n(\tilde{t})\, P_n(\cos\theta)\,(\frac{1}{\tilde{r}^{n+1}} + \frac{1}{\tilde{r'}^{n+1}}) \tag{21}$$

P_n are the Legendre polynomia of degree n.

4.1.2 Inner problem at order ϵ^0

System of equation (15) to (17) for the order zero becomes:

$$\nabla^2 \tilde{\phi}_0 = 0 \tag{22}$$

$$\{\frac{\partial \tilde{\phi}_0}{\partial \tilde{r}}\}_{\tilde{r}=\tilde{R}_0} = \dot{\tilde{R}}_0 \tag{23}$$

$$\{\frac{\partial \tilde{\phi}_0}{\partial \tilde{t}} + \frac{1}{2}(\frac{\partial \tilde{\phi}_0}{\partial \tilde{r}})^2\}_{\tilde{r}=\tilde{R}_0} = \Delta\tilde{p}(\tilde{t}) + \mathcal{P}(1 - \frac{V^{-k}}{V_0^{-k}}) + \frac{1}{\mathcal{W}}(\tilde{C} - \frac{V^{-k}}{V_0^{-k}}) \tag{24}$$

From (23) we get the solution

$$\tilde{\phi}_0 = \frac{q}{\tilde{r}} \text{ with } q = -\tilde{R}_0{}^2 \dot{\tilde{R}}_0 \tag{25}$$

where $\tilde{R}_0(\tilde{t})$ is determined by the Rayleigh-Plesset equation:

$$\tilde{R}_0\ddot{\tilde{R}}_0 + \frac{3}{2}\dot{\tilde{R}}_0^2 = -\Delta\tilde{p}(\tilde{t}) + \mathcal{P}(\tilde{R}_0{}^{-3K} - 1) + \frac{1}{\mathcal{W}}(\tilde{R}_0{}^{-3K} - \frac{1}{\tilde{R}_0}) \tag{26}$$

the initial conditions are $\tilde{R}_0 = 1$ and $\dot{\tilde{R}}_0 = 0$

4.1.3 Matching condition at order zero

If we replace the potentials by their expansions, the matching condition is:

$$\frac{r_0^2}{T_0}\left(\tilde{\phi}_0(\frac{r}{r_0}) + \epsilon\tilde{\phi}_I(\frac{r}{r_0}) + \epsilon^2\tilde{\phi}_{II}(\frac{r}{r_0}) + O(\epsilon^3)\right) = \phi_{ext}\left(\tilde{\phi}_0(\frac{r}{l_0}) + \epsilon\tilde{\phi}_I(\frac{r}{l_0}) + \epsilon^2\tilde{\phi}_{II}(\frac{r}{l_0}) + O(\epsilon^3)\right) \tag{27}$$

The solution to $\tilde{\phi}_0$ is $\tilde{\phi}_0 = \sum_{n=0}^{\infty} B_n(\tilde{t}) P_n(\cos\theta)(\frac{1}{\tilde{r}^{n+1}} + \frac{1}{\tilde{r'}^{n+1}})$

$\tilde{\phi}_0$ is $\tilde{\phi}_0 = \frac{q}{\tilde{r}} + C$ $\quad$ C is a constant to be determined

$$\epsilon\frac{r_0^2}{T_0}\left(\frac{q}{r}+C+\epsilon\tilde{\phi}_I(\frac{r}{r_0})\right)=\phi_{ext}\left(\sum_{n=0}^{\infty}B_n(\tilde{t})\,P_n(\cos\theta)\,\frac{1}{r^{n+1}}(1+(\frac{r}{2l_0})^{n+1})+\frac{\epsilon}{l_0}\tilde{\phi}_I(\frac{r}{l_0})+\cdots\right) \quad (28)$$

At leading order we have:

$$C = 0 \quad (29)$$

$$\phi_{ext} = \epsilon\frac{r_0^2}{T_0} \quad (30)$$

$$B_n(\tilde{t}) = \delta_{n,0}\,q(\tilde{t}) \quad (31)$$

To obtain the limit condition on $\tilde{\phi}_I$, we must continue the expansion.

$$\tilde{\phi}_I(\frac{r}{r_0})+\epsilon\tilde{\phi}_{II}(\frac{r}{r_0})+O(\epsilon^2)=\frac{q}{2}+\frac{q}{4}\frac{r}{l_0}\cos\theta+\epsilon\tilde{\phi}_I(\frac{r}{r_0})+O(\left(\frac{r}{r_0}\right)^2) \quad (32)$$

$\frac{r}{l_0}$ is of order $O(\epsilon)$ so equating terms at leading order give us:

$$\lim_{\tilde{r}\to\infty}\tilde{\phi}_I=\frac{q}{2} \quad (33)$$

4.2 Order ϵ

4.2.1 Inner problem at order ϵ

Remembering that $\tilde{R}_0$ and $\tilde{\phi}_0$ only depend on time, at order ϵ the problem becomes:

$$\Delta\tilde{\phi}_I=0 \quad (34)$$

$$\lim_{\tilde{r}\to\infty}\tilde{\phi}_I=\frac{q}{2} \quad (35)$$

$$\{\frac{\partial\tilde{\phi}_I}{\partial\tilde{r}}+\tilde{R}_I\frac{\partial^2\tilde{\phi}_0}{\partial\tilde{r}^2}\}_{\tilde{r}=\tilde{R}_0}=\frac{\partial\tilde{R}_I}{\partial\tilde{r}}-G_r\tilde{R}_0 \quad (36)$$

$$\{\frac{\partial\tilde{\phi}_I}{\partial\tilde{t}}+\tilde{R}_I\frac{\partial^2\tilde{\phi}_0}{\partial\tilde{t}\partial\tilde{r}}+\frac{\partial\tilde{\phi}_I}{\partial\tilde{r}}\frac{\partial\tilde{\phi}_0}{\partial\tilde{r}}+\tilde{R}_I\frac{\partial\tilde{\phi}_0}{\partial\tilde{r}}\frac{\partial^2\tilde{\phi}_0}{\partial\tilde{r}^2}+\tilde{R}_0G_r\frac{\partial\tilde{\phi}_0}{\partial\tilde{r}}+\mu v_z(t)\tilde{R}_0\,F(\theta,\psi)\}_{\tilde{r}=\tilde{R}_0}=$$

$$3K\mathcal{P}\tilde{R}_I\tilde{R}_0^{-3K-1} \quad (37)$$

where $G_r = 2\alpha_2\cos\theta\sin\theta\cos\psi+\alpha_1(\sin^2\theta\cos^2\psi-\cos^2\theta)$ (38)

$F = \alpha_1\sin\theta\cos\psi+\alpha_2\cos\theta$ (39)

4.2.2 Resolution of the order ϵ

Let us take:

$$\tilde{\phi}_I = \sum_{j=0}^{\infty} \sum_{m=-j}^{j} (A_{Ijm}\tilde{r}^j + \frac{B_{Ijm}}{\tilde{r}^{j+1}})Y_{jm} \tag{40}$$

$$\tilde{R}_I = \sum_{j=0}^{\infty} \sum_{m=-j}^{j} R_{Ijm}Y_{jm} \tag{41}$$

Y_{jm} are the spherical harmonics:

$$Y_{jm} = \begin{cases} P_j^m(\cos\theta)\cos m\psi & \text{for } m \geq 0 \\ P_j^{|m|}(\cos\theta)\sin |m|\psi & \text{for } m < 0 \end{cases} \tag{42}$$

The limit condition at infinity on $\tilde{\phi}_I$ leads us to take:

$$A_{Ijm} = \delta_{j,0}\frac{q}{2} \tag{43}$$

Since the problem is symmetrical about the (Oxz) plane, there will not be any terms in $\sin\psi$, we do not have to consider $m < 0$. Knowing that

$$\cos\theta \sin\theta \cos\psi = \frac{1}{3}Y_{21} \tag{44}$$

$$\sin^2\theta \cos^2\psi - \cos^2\theta = -Y_{20} + \frac{Y_{22}}{6} = Y_f \tag{45}$$

Equation (36) and (37) become:

$$-\frac{j+1}{\tilde{R}_0^{j+2}}B_{Ijm}Y_{jm} + \frac{2q}{\tilde{R}_0^3}R_{Ijm}Y_{jm} = \dot{R}_{Ijm}Y_{jm} - \frac{2}{3}\tilde{R}_0\alpha_2 Y_{21} + \alpha_1\tilde{R}_0(Y_{20} - \frac{Y_{22}}{6}) \tag{46}$$

$$\frac{\dot{q}}{2} + \frac{\dot{B}_{Ijm}}{\tilde{R}_0^{j+1}}Y_{jm} - \frac{\dot{q}}{\tilde{R}_0^2}R_{Ijm}Y_{jm} + q\frac{j+1}{\tilde{R}_0^{j+4}}B_{Ijm}Y_{jm} - 2\frac{q^2}{\tilde{R}_0^5}R_{Ijm}Y_{jm} - \frac{2}{3\tilde{R}_0}q\alpha_2 Y_{21} -$$

$$\frac{q}{\tilde{R}_0}\alpha_1(-Y_{20} + \frac{Y_{22}}{6}) + \mu\tilde{R}_0 v_x(\alpha_1 Y_{11} + \alpha_2 Y_{10}) = \dot{R}_{I00}Y_{00}3K\mathcal{P}\tilde{R}_0^{-3K-1} \tag{47}$$

For $j > 2$ we have a homogeneous linear differential system where the initial conditions are zero. The solution is therefore $R_{Ijm} = B_{Ijm} = 0\ \forall j > 2$

4.2.3 Resolution for $m = j = 0$

We have to solve the following differential system:

$$-\frac{B_{I00}}{\tilde{R}_0^2} + 2q\frac{\tilde{R}_{I00}}{\tilde{R}_0^3} = \dot{\tilde{R}}_{I00} \tag{48}$$

$$\frac{\dot{q}}{2} + \frac{\dot{B}_{I00}}{\tilde{R}_0} + \frac{q}{\tilde{R}_0^4}B_{I00} - (\frac{2q^2}{\tilde{R}_0^5} + \frac{\dot{q}}{\tilde{R}_0^2})\tilde{R}_{I00} = \tilde{R}_{I00}\{3K\mathcal{P}\tilde{R}_0^{-3K-1} + \frac{1}{\mathcal{W}}(3K\tilde{R}_0^{-3K-1} - \frac{1}{\tilde{R}_0^2})\} \tag{49}$$

$\tilde{R}_{I00}$ is the solution of the linear differential equation:

$$\tilde{R}_0\ddot{\tilde{R}}_{I00} + 3\dot{\tilde{R}}_0\dot{\tilde{R}}_{I00} + \ddot{\tilde{R}}_0\tilde{R}_{I00} = -\tilde{R}_0\dot{\tilde{R}}_0^2 - \frac{1}{2}\tilde{R}_0^2\ddot{\tilde{R}}_0 - \tilde{R}_{I00}\{3K\mathcal{P}\tilde{R}_0^{-3K-1} + \frac{1}{\mathcal{W}}(3K\tilde{R}_0^{-3K-1} - \frac{1}{\tilde{R}_0^2})\} \tag{50}$$

and B_{I00} is computed using:

$$B_{I00} = -(\tilde{R}_0^2\dot{\tilde{R}}_{I00} + 2\tilde{R}_0\dot{\tilde{R}}_0\tilde{R}_{I00}) \tag{51}$$

4.2.4 Resolution for $j = 1$

We have the same differential system to solve for $\tilde{R}_{I10}$ and $\tilde{R}_{I11}$. We just have to replace α_1 and $\tilde{R}_{I10}$ by α_2 and $\tilde{R}_{I11}$ in the system giving $\tilde{R}_{I10}$ to obtain the system leadding to $\tilde{R}_{I11}$.

Resolution for $m = 0$ We have to solve the following differential system:

$$-2\frac{B_{I10}}{\tilde{R}_0^3} + 2q\frac{\tilde{R}_{I10}}{\tilde{R}_0^3} = \dot{\tilde{R}}_{I10} \tag{52}$$

$$\frac{\dot{B}_{I10}}{\tilde{R}_0^2} + 2\frac{q}{\tilde{R}_0^5}B_{I10} - (\frac{2q^2}{\tilde{R}_0^5} + \frac{\dot{q}}{\tilde{R}_0^2})\tilde{R}_{I10} + \mu\tilde{R}_0 v_x\alpha_1 = 0 \tag{53}$$

$\tilde{R}_{I10}$ is the solution of the linear differential equation:

$$\tilde{R}_0\ddot{\tilde{R}}_{I10} + 3\dot{\tilde{R}}_0\dot{\tilde{R}}_{I10} = 2\mu\tilde{R}_0\alpha_1 v_x \tag{54}$$

$$\dot{\tilde{R}}_{I10} = \frac{1}{\tilde{R}_0^3}\int_0^t 2\mu\tilde{R}_0^3 v_x\alpha_1 dt \tag{55}$$

and B_{I10} is computed using:

$$B_{I10} = -\frac{1}{2}\tilde{R}_0^3\dot{\tilde{R}}_{I10} - \tilde{R}_0^2\dot{\tilde{R}}_0\tilde{R}_{I10} \tag{56}$$

Resolution for $m = 1$ $\tilde{R}_{I11}$ and B_{I11} are computed using:

$$\dot{\tilde{R}}_{I11} = \frac{1}{\tilde{R}_0^3}\int_0^t 2\mu\tilde{R}_0^3 v_z \alpha_2 dt \tag{57}$$

$$B_{I11} = -\frac{1}{2}\tilde{R}_0^3\dot{\tilde{R}}_{I11} - \tilde{R}_0^2\dot{\tilde{R}}_0\tilde{R}_{I11} \tag{58}$$

4.2.5 Resolution for $j = 2$

We have the same differential system to solve for $\tilde{R}_{I21}$ and $\tilde{R}_{If}$. As before, to get the system giving $\tilde{R}_{If}$ from the system giving $\tilde{R}_{I21}$, we just have to replace α_1 by $\frac{2}{3}\alpha_2$.

Resolution for $m = 1$ We have to solve the following differential system:

$$-3\frac{B_{I21}}{\tilde{R}_0^4} + 2q\frac{\tilde{R}_{I00}}{\tilde{R}_0^3} = \ddot{\tilde{R}}_{I21} - \frac{2}{3}\tilde{R}_0\alpha_2 \tag{59}$$

$$\frac{\dot{B}_{I21}}{\tilde{R}_0^3} + 3\frac{q}{\tilde{R}_0^6}B_{I21} - (\frac{2q^2}{\tilde{R}_0^5} + \frac{\dot{q}}{\tilde{R}_0^2})\tilde{R}_{I21} - \frac{2q}{3\tilde{R}_0}\alpha_2 = 0 \tag{60}$$

$\tilde{R}_{I21}$ is the solution of the linear differential equation:

$$\tilde{R}_0\dddot{\tilde{R}}_{I21} + 3\dot{\tilde{R}}_0\ddot{\tilde{R}}_{I21} - \ddot{\tilde{R}}_0\dot{\tilde{R}}_{I21} = \frac{10}{3}\dot{\tilde{R}}_0\tilde{R}_0\alpha_2 + \frac{2}{3}\tilde{R}_0^2\dot{\alpha}_2 \tag{61}$$

and B_{I21} is computed using:

$$B_{I21} = -\frac{\tilde{R}_0^4}{3}\ddot{\tilde{R}}_{I21} - \frac{2}{3}\tilde{R}_0^3\dot{\tilde{R}}_0\dot{\tilde{R}}_{I21} + \frac{2}{9}\tilde{R}_0^5\alpha_2 \tag{62}$$

Resolution of the coefficient in front of Y_f $\tilde{R}_{If}$ is the solution of the linear differential equation:

$$\tilde{R}_0\dddot{\tilde{R}}_{If} + 3\dot{\tilde{R}}_0\ddot{\tilde{R}}_{If} - \ddot{\tilde{R}}_0\dot{\tilde{R}}_{If} = 5\dot{\tilde{R}}_0\tilde{R}_0\alpha_1 + \tilde{R}_0^2\dot{\alpha}_1 \tag{63}$$

and B_{If} is computed using:

$$B_{If} = -\frac{\tilde{R}_0^4}{3}\ddot{\tilde{R}}_{If} - \frac{2}{3}\tilde{R}_0^3\dot{\tilde{R}}_0\dot{\tilde{R}}_{If} + \frac{1}{3}\tilde{R}_0^5\alpha_1 \tag{64}$$

The potential and radius at order ϵ are:

$$\tilde{\phi}_I = \frac{q}{2} + \frac{B_{I00}}{\tilde{r}} + \frac{1}{\tilde{r}^2}(B_{I10}\cos\theta + B_{I11}\sin\theta\cos\psi) +$$

$$\frac{1}{\tilde{r}^3}(3B_{I21}\sin\theta\cos\theta\cos\psi + B_{If}(\sin^2\theta\cos^2\psi - \cos^2\theta)) \tag{65}$$

$$\tilde{R}_I = \tilde{R}_{I00} + \tilde{R}_{I10}\cos\theta + \tilde{R}_{I11}\sin\theta\cos\psi + 3\tilde{R}_{I21}\sin\theta\cos\theta\cos\psi + \tilde{R}_{If}(\sin^2\theta\cos^2\psi - \cos^2\theta) \quad (66)$$

5 Recentring the moving frame

5.1 Problem formulation

In this section, we fix the origin of the moving frame in which we caculate the bubble shape to the center of gravity of the bubble. To do so, we introduce a translation velocity $\vec{V}_t$ in the primary set of equations: writing $\vec{V}_e = \vec{V}_0(O,t) + \vec{V}_t$, the system to solve is :

$$\Delta\phi = 0 \quad (67)$$

$$\lim_{\infty}\phi = 0 \quad (68)$$

$$\{\nabla\phi.\vec{n}\}_{bodywall} = 0 \quad (69)$$

$$\{\nabla\phi.\vec{n}\}_{r=R} = \frac{\partial R}{\partial t} + \{[\vec{V}_0(O,t) + \vec{V}_t - \vec{V}_0(r,t) + \vec{\omega}\times O\vec{M}].\vec{n}\}_{r=R} \quad (70)$$

$$\{\frac{\partial\phi}{\partial t} + \frac{1}{2}(\nabla\phi)^2 + (\vec{V}_0(r,t) - \vec{V}_0(O,t) - \vec{V}_t - \vec{\omega}\times O\vec{M}).\nabla\phi + \frac{1}{2}(V_0^2(r,t) - V_0^2(O,t)) + \frac{p}{\rho}\}_{r=R} = \frac{p_0(O,t)}{\rho} \quad (71)$$

If we expand this translation velocity by developing it : $\vec{V}_t = \vec{V}_O + \epsilon\vec{V}_I + \epsilon^2\vec{V}_{II} + \ldots$, the system at order 0 just contains $\tilde{\phi}_0$ and $\tilde{R}_0$ which have only spherical deformations. At order 0, the origin of the frame, moving with the equivalent material point in the flow field is fixed to the center of the bubble. Thus, we shall take $\vec{V}_O = 0$ and only consider $\vec{V}_t$ for order ϵ and further.

Let us choose a scale for $\vec{V}_I$ in order to non-dimmensionnalize the set of equations. If we take $V_I = \tilde{V}_I.\frac{r_0}{T_0}$, the system at order ϵ becomes :

$$\vec{V}_t = \epsilon\frac{r_0}{T_0}.\vec{\tilde{V}}_I \quad (72)$$

$$\{\frac{\partial\tilde{R}_I}{\partial\tilde{r}} + \tilde{R}_I\frac{\partial^2\tilde{\phi}_0}{\partial\tilde{r}^2}\}_{\tilde{r}_0=\tilde{R}_0} = \frac{\partial\tilde{R}_I}{\partial\tilde{t}} - G_r\tilde{R}_0 + (\vec{\tilde{V}}_I.\vec{e}_x)\sin\theta\cos\psi + (\vec{\tilde{V}}_I.\vec{e}_y)\sin\theta\sin\psi + (\vec{\tilde{V}}_I.\vec{e}_z)\cos\theta \quad (73)$$

$$\frac{\partial \tilde{\phi}_I}{\partial \tilde{t}} + \tilde{R}_I \frac{\partial^2 \tilde{\phi}_0}{\partial \tilde{t} \partial \tilde{r}} + \frac{\partial \tilde{\phi}_I}{\partial \tilde{r}} \frac{\partial \tilde{\phi}_0}{\partial \tilde{r}} + \tilde{R}_I \frac{\partial \tilde{\phi}_0}{\partial \tilde{r}} \frac{\partial^2 \tilde{\phi}_0}{\partial \tilde{r}^2} + \tilde{R}_0 G_r \frac{\partial \tilde{\phi}_0}{\partial \tilde{r}} + \mu v_z(t) \tilde{R}_0 F$$

$$-\frac{\partial \tilde{\phi}_0}{\partial \tilde{r}}((\tilde{\vec{V}}_I.\vec{e}_x)\sin\theta\cos\psi + (\tilde{\vec{V}}_I.\vec{e}_y)\sin\theta\sin\psi + \tilde{\vec{V}}_I.\vec{e}_z)\cos\theta) = 3kP\tilde{R}_I\tilde{R}_0^{-3k-1} \quad (74)$$

if we neglect the surface tension.
Let us write the condition for the origin of the frame to be at the center of the bubble.

5.2 Conditions on the value of $\tilde{R}_I$

If O is the center of the bubble, then

$$\int\int\int_{bubble} \tilde{\vec{r}} d\Omega = 0 \quad (75)$$

with : $\tilde{\vec{r}} = (\tilde{R}_0(t) + \epsilon \tilde{R}_I(\theta, \psi, t) + \epsilon^2 \tilde{R}_{II})\vec{e}_r$
Expressing this condition :

$$\int\int\int_{bubble} \tilde{\vec{r}} d\Omega = \int\int_{bubble} \frac{1}{4}(\tilde{R}_0 + \epsilon \tilde{R}_I)^4 \sin\theta \, \vec{e}_r d\theta d\psi \quad (76)$$

At order ϵ, $\frac{1}{4}(\tilde{R}_0 + \epsilon \tilde{R}_I)^4 = \frac{1}{4}\tilde{R}_0^4 + \epsilon \tilde{R}_0^3 \tilde{R}_I + O(\epsilon^2)$
Thus, the condition has to be written, at order ϵ :

$$\int\int_{bubble} \tilde{R}_0^3 \tilde{R}_I \sin\theta \, \vec{e}_r d\theta d\psi = 0 \quad (77)$$

Recalling that

$$\tilde{R}_I = \tilde{R}_{I00} + \tilde{R}_{I10}\cos\theta + \tilde{R}_{I11}\sin\theta\cos\psi + 3\tilde{R}_{I21}\sin\theta\cos\theta\cos\psi + \tilde{R}_{If}(\sin^2\theta\cos^2\psi - \cos^2\theta) \quad (78)$$

$$\vec{e}_r(\theta, \psi) = \cos\theta \, \vec{e}_z + \sin\theta\cos\psi \, \vec{e}_x + \sin\theta\sin\psi \, \vec{e}_y \quad (79)$$

we obtain the condition, at order ϵ (taking into account the symmetries of the problem):

$$\tilde{R}_{I11} = \tilde{R}_{I10} = 0 \quad (80)$$

5.3 Calculation of the translation velocity

Let us note $\tilde{V}_{Ix} = \tilde{\vec{V}}_I.\vec{e}_x, \tilde{V}_{Iy} = \tilde{\vec{V}}_I.\vec{e}_y, \tilde{V}_{Iz} = \tilde{\vec{V}}_I.\vec{e}_z$.
If we re-write the projection of the system on the spherical harmonics, we have now the new linear system :

$$-\frac{j+1}{\tilde{R}_0^{j+2}} B_{Ijm} Y_{Ijm} + \frac{2q}{\tilde{R}_0^3} \tilde{R}_{Ijm} Y_{jm} = \dot{\tilde{R}}_{Ijm} Y_{jm} - \frac{2}{3} \tilde{R}_0 \alpha_2 Y_{21} + \alpha_1 \tilde{R}_0 (Y_{20} - \frac{Y_{22}}{6}) + \tag{81}$$

$$\tilde{V}_{Ix} Y_{11} + \tilde{V}_{Iz} Y_{10} + \tilde{V}_{Iy} \sin\theta \sin\psi$$

$$\frac{\dot{q}}{2} Y_{00} + \frac{\dot{B}_{Ijm}}{\tilde{R}_0^{j+1}} Y_{jm} - \frac{\dot{q}}{\tilde{R}_0^2} \tilde{R}_{Ijm} Y_{jm} + (j+1) \frac{q}{\tilde{R}_0^{j+4}} B_{Ijm} Y_{jm} - 2\frac{q^2}{\tilde{R}_0^5} \tilde{R}_{Ijm} - \frac{2}{3\tilde{R}_0} q \alpha_2 Y_{21} - \tag{82}$$

$$\frac{q}{\tilde{R}_0} \alpha_1 (-Y_{20} + \frac{Y_{22}}{6}) + \mu \tilde{R}_0 v_x(t) (\alpha_1 Y_{11} + \alpha_2 Y_{10}) + \frac{q}{\tilde{R}_0^2} (\tilde{V}_{Ix} Y_{11} + \tilde{V}_{Iz} Y_{10} + \tilde{V}_{Iy} \sin\theta \sin\psi) =$$

$$3\dot{\tilde{R}}_{I00} Y_{00} k P \tilde{R}_0^{-3k-1}$$

As no term of the development contains spherical harmonics in $\sin\psi$, we may immediately deduce : $V_{Iy} = 0$.
We re-obtain the same system for $j = 0, m = 0; j = 2, m = 0, 1, 2$. For $j = 1$, the system is different, because of the condition $\tilde{R}_{I10} = \tilde{R}_{I11} = 0$. For $j = 1$, the two linear systems are transformed into:

m=0

$$\frac{\dot{B}_{I10}}{\tilde{R}_0^2} + 2\frac{q}{\tilde{R}_0^5} B_{I10} + \mu \tilde{R}_0 \alpha_1 v_x + \frac{q}{\tilde{R}_0^2} \tilde{V}_{Iz} = 0 \tag{83}$$

$$-\frac{2}{\tilde{R}_0^3} B_{I10} = \tilde{V}_{Iz} \tag{84}$$

which gives:

$$\tilde{V}_{Iz} = \frac{2\mu}{\tilde{R}_0^3} \int_0^{\tilde{t}} \tilde{R}_0^3 \alpha_1 v_x d\tilde{t}$$

m=1

$$\frac{\dot{B}_{I11}}{\tilde{R}_0^2} + 2\frac{q}{\tilde{R}_0^5} B_{I11} + \mu \tilde{R}_0 \alpha_2 v_x + \frac{q}{\tilde{R}_0^2} \tilde{V}_{Ix} = 0 \tag{85}$$

$$-\frac{2}{\bar{R}_0^3} B_{I11} = \bar{V}_{Iz} \tag{86}$$

which gives:

$$\bar{V}_{Iz} = \frac{2\mu}{\bar{R}_0^3} \int_0^{\bar{t}} \bar{R}_0^3 \alpha_2 v_z d\bar{t}$$

6 Streamlines

The purpose of this section is to show that the most convenient way to draw streamlines in 3-D problems is to use Euler's method. We will apply it, afterwards, to the flow we are studying (including the bubble).

6.1 2-D problem

In two dimensions, the most convenient way to draw streamlines is to introduce a stream-function defined by the system :

$$\begin{aligned} \frac{\partial \phi}{\partial x} &= -\frac{\partial \psi}{\partial y} \\ \frac{\partial \phi}{\partial y} &= \frac{\partial \psi}{\partial x} \end{aligned} \tag{87}$$

Along a line such as $\psi(x,y) = constant$, we have :

$$f(x,y) = \psi(x,y) - constant = 0$$

which gives :

$$\nabla f = \left[\begin{array}{l} \frac{\partial f}{\partial x} = -\frac{\partial \phi}{\partial y} \\ \frac{\partial f}{\partial y} = \frac{\partial \phi}{\partial x} \end{array} \right.$$

That is to say, the normal to the line at each point is normal to the velocity of the point in the flow field. In other terms, tangentes to points on lines such as $\psi(x,y) = constant$ are equal to velocities. Thus, these lines are streamlines.
Let us remark that such a definition is made mathematically consistent by the fact that $\nabla^2 \phi = 0$. (To define a stream-function, we shall have :

$$\frac{\partial^2\psi}{\partial x\partial y} = \frac{\partial^2\psi}{\partial y\partial x}$$

This condition, in terms of ϕ is equivalent to $\nabla^2\phi = 0$)

6.2 3-D problem

In three dimensions, let us show that the previously described kind of approach is not applicable :
If the problem has no special symmetry (plane of symmetry, axis of symmetry), it is not possible to exhibit a stream-function : let us suppose an equation such as $\psi(x, y, z) = 0$, this equation gives a surface and no line (except in the unlikely case of degeneracy).
Thus, it is not consistent to try to describe a streamline by such an equation in most general cases.
Let us assume the flow field to have a plane of symmetry. Let $z = 0$ be this plane. In this plane, we have :

$$\frac{\partial\phi}{\partial z} = 0$$

A stream-line beginning with a starting point belonging to the plane must belong to the plane. Thus, in the plane (Oxy), we may describe this curve as :

$$f(x, y) = 0$$

All the stream-lines belonging to the plane of symmetry may be described by $\psi(x, y) = \textit{constant}$, where the *constant* depends on the starting point.
The condition on this 2-D stream-function to fit the problem is that its gradient is perpendicular to the velocity :

$$\frac{\partial\psi}{\partial x} = -k(x, y).\frac{\partial\phi}{\partial y} \tag{88}$$

$$\frac{\partial\psi}{\partial y} = k(x, y).\frac{\partial\phi}{\partial x} \tag{89}$$

Trying to solve the problem in the same terms as a 2-D problem leads to:

$$\frac{\partial\psi}{\partial x} = -\frac{\partial\phi}{\partial y} \tag{90}$$

$$\frac{\partial\psi}{\partial y} = \frac{\partial\phi}{\partial x} \tag{91}$$

and the consistency condition :

$$\frac{\partial^2\psi}{\partial x\partial y} = \frac{\partial^2\psi}{\partial y\partial x}$$

leads to :

$$\frac{\partial^2\phi}{\partial x^2} + \frac{\partial^2\phi}{\partial y^2} = 0$$

which is not valid in most cases, since

$$\frac{\partial^2\phi}{\partial x^2} + \frac{\partial^2\phi}{\partial y^2} + \frac{\partial^2\phi}{\partial z^2} = 0$$

Thus,we must introduce a coefficient $k(x,y)$ in the system (90)-(91), which gives the system (88)-(89).

To have the superposition property, we shall impose that $\nabla^2\psi = 0$. (This is obviously respected in the 2-D calculations). Let us figure out this condition:

$$\begin{aligned}\frac{\partial^2\psi}{\partial x^2} &= k(x,y).(-\frac{\partial^2\phi}{\partial x\partial y}) - \frac{\partial\phi}{\partial y}.\frac{\partial k}{\partial x} \\ \frac{\partial^2\psi}{\partial y^2} &= k(x,y).(\frac{\partial^2\phi}{\partial x\partial y}) + \frac{\partial\phi}{\partial x}.\frac{\partial k}{\partial y}\end{aligned} \tag{92}$$

As we have imposed $\nabla^2\psi = 0$, this gives :

$$-\frac{\partial\phi}{\partial y}.\frac{\partial k}{\partial x} + \frac{\partial\phi}{\partial x}.\frac{\partial k}{\partial y} = 0$$

which is: $\left[\begin{array}{ll}\alpha.\frac{\partial\phi}{\partial x} &= \frac{\partial k}{\partial x} \\ \alpha.\frac{\partial\phi}{\partial y} &= \frac{\partial k}{\partial x}\end{array}\right.$ *where* α is a proportionnality coefficient, not depending on position.
The mathematical consistency condition may then be expressed as :

$$\begin{aligned}\frac{\partial^2\psi}{\partial x\partial y} &= -k(x,y).\frac{\partial^2\phi}{\partial y^2} - \alpha(\frac{\partial\phi}{\partial y})^2 \\ \frac{\partial^2\psi}{\partial x\partial y} &= k(x,y).\frac{\partial^2\phi}{\partial x^2} + \alpha(\frac{\partial\phi}{\partial x})^2\end{aligned} \tag{93}$$

which leads to :

$$k(x,y).\left(\frac{\partial^2\phi}{\partial x^2} + \frac{\partial^2\phi}{\partial y^2}\right) = -\alpha\left((\frac{\partial\phi}{\partial x})^2 + (\frac{\partial\phi}{\partial y})^2\right)$$

We know that $\nabla^2\phi = 0$, therefore, we must have:

$$k(x,y).\frac{\partial^2\phi}{\partial x^2} = \alpha\left((\frac{\partial\phi}{\partial x})^2 + (\frac{\partial\phi}{\partial y})^2\right)$$

From :

$$\begin{aligned} \frac{\partial k}{\partial x} &= \alpha \frac{\partial \phi}{\partial x} \\ \frac{\partial k}{\partial y} &= \alpha \frac{\partial \phi}{\partial y} \end{aligned} \tag{94}$$

we get: $k = \alpha\phi + \beta$; then :

$$(\alpha\phi + \beta)\frac{\partial^2 \phi}{\partial z^2} = \alpha \left((\frac{\partial \phi}{\partial x})^2 + (\frac{\partial \phi}{\partial y})^2 \right)$$

which leads to :

$$[-\phi . \frac{\partial^2 \phi}{\partial z^2} + (\frac{\partial \phi}{\partial x})^2 + (\frac{\partial \phi}{\partial y})^2] \frac{1}{\frac{\partial^2 \phi}{\partial z^2}} = constant$$

This condition is not always respected for any kind of potential one can take (respective of the plane symmetry condition).

If we just try to solve the problem for each case separately, the approach is exactly the same, but, the single condition to remain is the mathematical consistency one :

$$k(x,y) . \frac{\partial^2 \phi}{\partial z^2} = \frac{\partial \phi}{\partial y} . \frac{\partial k}{\partial y} + \frac{\partial \phi}{\partial x} . \frac{\partial k}{\partial x}$$

Therefore, to find out the streamline we are looking for, we have to compute the following system:

$$\begin{aligned} k(x,y)(\frac{\partial^2 \phi}{\partial z^2})_{z=0} &= \frac{\partial \phi}{\partial y}\frac{\partial k}{\partial y} + \frac{\partial \phi}{\partial x}\frac{\partial k}{\partial x} \\ \frac{\partial \psi}{\partial x} &= -k(x,y) . \frac{\partial \phi}{\partial y} \\ \frac{\partial \psi}{\partial y} &= k(x,y) . \frac{\partial \phi}{\partial x} \end{aligned}$$

and, afterwards, to solve the equation : $\psi(x,y) = constant$
This system is more complicated to solve numerically than the implementation of Euler's method, that is to say, at a given instant, to start from a chosen point in the field and to find out the next point of the streamline by expressing the fact that the streamline from one point to the next is equal to the velocity given by the flow field on this little step of space.

6.3 Results

The pictures show streamlines calculated by Euler's method, at order ϵ in both cases of a growing bubble and a collapsing bubble.

7 Inner problem at order ϵ^2

7.1 Terms of order ϵ^2

We need the terms of order ϵ^2 for the following expressions :

$$
\begin{aligned}
\frac{\partial \tilde{\phi}}{\partial \tilde{r}} &: \frac{\partial \tilde{\phi}_{II}}{\partial \tilde{r}} + \tilde{R}_I \frac{\partial^2 \tilde{\phi}_I}{\partial \tilde{r}^2} + \tilde{R}_{II} \frac{\partial^2 \tilde{\phi}_0}{\partial \tilde{r}^2} + \frac{1}{2} \tilde{R}_I^2 \frac{\partial^3 \tilde{\phi}_0}{\partial \tilde{r}^3} \\
-\frac{1}{\tilde{R}^2} \frac{\partial \tilde{\phi}}{\partial \theta} \frac{\partial \tilde{R}}{\partial \theta} &: -\frac{1}{\tilde{R}_0^2} \frac{\partial \tilde{\phi}_I}{\partial \theta} \frac{\partial \tilde{R}_I}{\partial \theta} \\
-\frac{1}{\tilde{R}^2 sin^2\theta} \frac{\partial \tilde{\phi}}{\partial \psi} \frac{\partial \tilde{R}}{\partial \psi} &: -\frac{1}{\tilde{R}_0^2 sin^2\theta} \frac{\partial \tilde{\phi}_I}{\partial \psi} \frac{\partial \tilde{R}_I}{\partial \psi} \\
(\vec{V}_e - \vec{V}_O) \cdot \vec{n} &: -\frac{1}{2} \tilde{R}_0^2 H_r - G_r \tilde{R}_I - G_\theta \frac{\partial \tilde{R}_I}{\partial \theta} - \frac{G_\psi}{sin\,\theta} \frac{\partial \tilde{R}_I}{\partial \psi} \\
&\quad -\frac{1}{\tilde{R}_0} \frac{\partial \tilde{R}_I}{\partial \theta} \tilde{\vec{V}}_I . \vec{e}_\theta - \frac{1}{\tilde{R}_0 sin\,\theta} \tilde{\vec{V}}_I . \vec{e}_\psi + \tilde{\vec{V}}_{II} . \vec{e}_r \\
-(\vec{\omega} \times O\vec{M}) \cdot \vec{n} &: \tilde{\omega} (cos\,\psi \frac{\partial \tilde{R}_I}{\partial \theta} - \frac{sin\,\psi\, cos\,\theta}{sin\,\theta} \frac{\partial \tilde{R}_I}{\partial \psi}) \\
\frac{\partial \tilde{\phi}}{\partial \tilde{t}} &: \frac{\partial \tilde{\phi}_{II}}{\partial \tilde{t}} + \tilde{R}_I \frac{\partial^2 \tilde{\phi}_I}{\partial \tilde{t} \partial \tilde{r}} + \tilde{R}_{II} \frac{\partial^2 \tilde{\phi}_0}{\partial \tilde{t} \partial \tilde{r}} + \frac{1}{2} \tilde{R}_I^2 \frac{\partial^3 \tilde{\phi}_0}{\partial \tilde{t} \partial \tilde{r}^2} \\
\frac{1}{2} \left(\frac{\partial \tilde{\phi}}{\partial \tilde{r}} \right)^2 &: \frac{\partial \tilde{\phi}_0}{\partial \tilde{r}} \left(\frac{\partial \tilde{\phi}_{II}}{\partial \tilde{r}} + \tilde{R}_I \frac{\partial^2 \tilde{\phi}_I}{\partial \tilde{r}^2} + \tilde{R}_{II} \frac{\partial^2 \tilde{\phi}_0}{\partial \tilde{r}^2} + \frac{1}{2} \tilde{R}_I^2 \frac{\partial^3 \tilde{\phi}_0}{\partial \tilde{r}^3} \right) + \\
&\quad \frac{1}{2} (\frac{\partial \tilde{\phi}_I}{\partial \tilde{r}})^2 + \frac{1}{2} \tilde{R}_I^2 (\frac{\partial^2 \tilde{\phi}_0}{\partial \tilde{r}^2})^2 + \tilde{R}_I \frac{\partial \tilde{\phi}_I}{\partial \tilde{r}} \cdot \frac{\partial^2 \tilde{\phi}_0}{\partial \tilde{r}^2} \\
\frac{1}{2\tilde{R}^2} \left(\frac{\partial \tilde{\phi}}{\partial \theta} \right)^2 &: \frac{1}{2\tilde{R}_0^2} \left(\frac{\partial \tilde{\phi}_I}{\partial \theta} \right)^2
\end{aligned}
$$

$$\frac{1}{2\tilde{R}^2 sin^2\theta}\left(\frac{\partial\tilde{\phi}}{\partial\psi}\right)^2 \;:\; \frac{1}{2\tilde{R}_0^2 sin^2\theta}\left(\frac{\partial\tilde{\phi}_I}{\partial\psi}\right)^2$$

$$(\vec{V}_O - \vec{V}_e)\cdot\nabla\tilde{\phi} \;:\; \frac{1}{2}\tilde{R}_0^2 H_r\frac{\partial\tilde{\phi}_0}{\partial\tilde{r}} + G_r\left(\tilde{R}_I\frac{\partial\tilde{\phi}_0}{\partial\tilde{r}} + \tilde{R}_0\frac{\partial\tilde{\phi}_I}{\partial\tilde{r}}\right) + G_\theta\frac{\partial\tilde{\phi}_I}{\partial\theta} + G_\psi\frac{\partial\tilde{\phi}_I}{\partial\psi}$$
$$-\tilde{\vec{V}}_I.\vec{e}_r\frac{\partial\tilde{\phi}_I}{\partial\tilde{r}} - \tilde{\vec{V}}_{II}.\vec{e}_r\frac{\partial\tilde{\phi}_0}{\partial\tilde{r}}$$

$$\frac{1}{2}\left(V_O^2 - V_O^2(O,t)\right) \;:\; \mu v_x(t)\tilde{R}_I(\alpha_2 cos\theta + \alpha_1 sin\theta\, cos\psi) + \tilde{R}_0^2(G_r^2 + G_\theta^2 + \psi^2)$$
$$+\frac{1}{2}\mu v_x(t)\tilde{R}_0^2(\gamma_1 cos^2\theta + \gamma_3 sin\theta\, cos\theta\, cos\psi)$$

$$\vec{\omega}\times\vec{OM}\cdot\nabla\tilde{\phi} \;:\; \tilde{\omega}(cos\psi\frac{\partial\tilde{\phi}_I}{\partial\theta} - \frac{sin\psi\, cos\theta}{sin\theta}\frac{\partial\tilde{\phi}_I}{\partial\psi})$$

7.2 Problem formulation

As before, the problem is described by the following system :

$$\nabla^2\phi_2 = 0 \tag{95}$$

$$\frac{\partial\tilde{\phi}_{II}}{\partial\tilde{r}} + A.\tilde{R}_{II} - \frac{\partial\tilde{R}_{II}}{\partial\tilde{t}} = B \tag{96}$$

$$\frac{\partial\tilde{\phi}_{II}}{\partial\tilde{t}} + C.\tilde{R}_{II} + D.\frac{\partial\tilde{\phi}_{II}}{\partial\tilde{r}} = E \tag{97}$$

where the ϵ^2 order unknowns are $\tilde{\phi}_{II}$ and $\tilde{R}_{II}$. A, B, C, D and E are functions depending on time and on position for C, E, D ; given directly by the asymptotic expansions of the primary system.
If we work out the values of these coefficients, we obtain :

$$A = \frac{\partial^2\tilde{\phi}_0}{\partial\tilde{r}^2}$$

$$B = -\tilde{R}_I\frac{\partial^2\tilde{\phi}_I}{\partial\tilde{r}^2} - \frac{\tilde{R}_I^2}{2}\frac{\partial^3\tilde{\phi}_0}{\partial\tilde{r}^3} + \frac{1}{\tilde{R}_0^2}\frac{\partial\tilde{\phi}_I}{\partial\theta}\frac{\partial\tilde{R}_I}{\partial\theta} + \frac{1}{\tilde{R}_0^2 sin^2\theta}\frac{\partial\tilde{\phi}_I}{\partial\psi}\frac{\partial\tilde{R}_I}{\partial\psi} - \frac{\tilde{R}_0^2}{2}H_r - G_r\tilde{R}_I$$
$$+G_\theta\frac{\partial\tilde{R}_I}{\partial\theta} + \frac{G_\psi}{sin\theta}\frac{\partial\tilde{R}_I}{\partial\psi} - \tilde{\omega}(cos\psi\frac{\partial\tilde{R}_I}{\partial\theta} - sin\psi\frac{cos\theta}{sin\theta}\frac{\partial\tilde{R}_I}{\partial\psi})$$
$$-\frac{1}{\tilde{R}_0}\frac{\partial\tilde{R}_I}{\partial\theta}\tilde{\vec{V}}_I.\vec{e}_\theta - \frac{1}{\tilde{R}_0 sin\theta}\frac{\partial\tilde{R}_I}{\partial\psi}\tilde{\vec{V}}_I.\vec{e}_\psi + \tilde{\vec{V}}_{II}.\vec{e}_r$$

$$C = \frac{\partial^2\tilde{\phi}_0}{\partial\tilde{t}\partial\tilde{r}} + \frac{\partial\tilde{\phi}_0}{\partial\tilde{r}}\frac{\partial^2\tilde{\phi}_0}{\partial\tilde{r}^2}$$

$$D = \frac{\partial\tilde{\phi}_0}{\partial\tilde{r}}$$

$$
\begin{aligned}
E \;=\; & -\tilde{R}_I\frac{\partial^2\tilde{\phi}_I}{\partial\tilde{t}\partial\tilde{r}} - \frac{\tilde{R}_I^2}{2}\frac{\partial^3\tilde{\phi}_0}{\partial\tilde{t}\partial\tilde{r}^2} - \tilde{R}_I\frac{\partial\tilde{\phi}_0}{\partial\tilde{r}}\frac{\partial^2\tilde{\phi}_I}{\partial\tilde{r}^2} - \frac{\tilde{R}_I^2}{2}\frac{\partial\tilde{\phi}_0}{\partial\tilde{r}}\frac{\partial^3\tilde{\phi}_0}{\partial\tilde{r}^3} - \frac{1}{2}(\frac{\partial\tilde{\phi}_I}{\partial\tilde{r}})^2 - \frac{\tilde{R}_0^2}{2}H_r\frac{\partial\tilde{\phi}_0}{\partial\tilde{r}} \\
& -\frac{\tilde{R}_I^2}{2}(\frac{\partial^2\tilde{\phi}_0}{\partial\tilde{r}^2})^2 - \tilde{R}_I\frac{\partial\tilde{\phi}_I}{\partial\tilde{r}}\frac{\partial^2\tilde{\phi}_0}{\partial\tilde{r}^2} - \frac{1}{2\tilde{R}_0^2}((\frac{\partial\tilde{\phi}_I}{\partial\theta})^2 - \frac{1}{sin^2\theta}(\frac{\partial\tilde{\phi}_I}{\partial\psi})^2) \\
& -G_r(\tilde{R}_I\frac{\partial\tilde{\phi}_0}{\partial\tilde{r}} + \tilde{R}_0\frac{\partial\tilde{\phi}_I}{\partial\tilde{r}}) - G_\theta\frac{\partial\tilde{\phi}_I}{\partial\theta} - \frac{G_\psi}{sin\,\theta}\frac{\partial\tilde{\phi}_I}{\partial\psi} \\
& -\mu v_x(t)\tilde{R}_I(\alpha_2 cos\,\theta + \alpha_1\, sin\,\theta\, cos\,\psi) - \tilde{R}_0^2(G_r^2 + G_\theta^2 + G_\psi^2) \\
& -\frac{\mu}{2}v_x(t)\tilde{R}_0^2(\gamma_1 cos^2\theta + \gamma_3\, sin\,\theta\, cos\,\theta\, cos\,\psi) \\
& +\tilde{\omega}(cos\,\psi\frac{\partial\tilde{\phi}_I}{\partial\theta} - sin\,\psi\,\frac{cos\,\theta}{sin\,\theta}\frac{\partial\tilde{\phi}_I}{\partial\psi}) + 3kP(\tilde{R}_0^{-3k-1}\tilde{R}_{II00} + ...) \\
& +\vec{\tilde{V}}_I.\vec{e}_r\frac{\partial\tilde{\phi}_I}{\partial\tilde{r}} + \vec{\tilde{V}}_{II}.\vec{e}_r\frac{\partial\tilde{\phi}_0}{\partial\tilde{r}}
\end{aligned}
$$

7.3 Inner problem expansion on spherical harmonics

The matching condition of the inner and the outer problems enables us to limitate the development of $\tilde{\phi}_{II}$ on spherical harmonics. The outer problem's solution at order ϵ is like:

$$\tilde{\phi}_I = K(\frac{1}{\tilde{r}} + \frac{1}{\tilde{r}'}) + L(\vec{\tilde{r}}) \qquad K \text{ is a constant to be determined}$$

In equation (32), we can replace $\tilde{\phi}_I$ by its value:

$$\tilde{\phi}_I = \frac{q}{2} + \frac{B_{I00}}{\tilde{r}} + ...$$

Thus:

$$B_{I00} + \frac{r}{l_0}\tilde{\phi}_{II}(\frac{r}{r_0}) + O(\epsilon\frac{r}{r_0}) = K(1 + \frac{1}{2}\frac{r}{l_0}) + \frac{q}{4}\frac{r^2}{r_0 l_0}cos\,\theta + L\frac{r}{l_0}$$

We can take $\frac{r^2}{l_0 r_0} = \tilde{r}\tilde{r} \ll 1$, term which shall appear with $\tilde{\phi}_{II}$. Finally $K = B_{I00}$.

$$\tilde{\phi}_{II}(\frac{r}{r_0}) + O(\epsilon) = \frac{B_{I00}}{2} + L + \frac{q}{4}\frac{r}{r_0}cos\,\theta + O(\frac{r^2}{r_0 l_0})$$

$$\Rightarrow \lim_{\tilde{r}\to\infty}(\tilde{\phi}_{II}(\tilde{r}) - \frac{B_{I00}}{2} - L - \frac{q}{4}\tilde{r}\,cos\,\theta) = 0$$

Therefore, we shall use the following development on spherical harmonics :

$$\tilde{\phi}_{II}(\vec{\tilde{r}},\tilde{t}) = \frac{B_{I00}(\tilde{t})}{2} + L + \frac{q(\tilde{t})}{4}\tilde{r}\,cos\,\theta + \sum B_{IIjm}(\tilde{t})\frac{Y_{jm}}{\tilde{r}^{j+1}} \qquad (98)$$

In the same way, we are going to develop $\tilde{R}_{II}$ as:

$$\tilde{R}_{II} = \sum \tilde{R}_{IIjm}(\tilde{t})Y_{jm} \qquad (99)$$

7.4 Resolution of the problem

Using developments (98) and (99) found in section before, we now can work out system (96) and (97) in terms of the independent spherical harmonics Y_{jm} :

$$\frac{q}{4}Y_{10} - \sum \frac{(j+1)}{\tilde{r}^{j+2}} B_{IIjm} Y_{jm} + A \sum R_{IIjm} Y_{jm} - \sum \dot{R}_{jm} Y_{jm} = \sum B_{jm} Y_{jm} \qquad (100)$$

$$\frac{\dot{B}_{I00}}{2} + \frac{\dot{q}}{4}\tilde{r}\cos\theta + \sum \frac{1}{\tilde{r}^{j+1}} \dot{B}_{IIjm} Y_{jm} + C \sum R_{IIjm} Y_{jm} \qquad (101)$$

$$-D\left(\frac{q}{4}Y_{10} - \sum \frac{(j+1)}{\tilde{r}^{j+2}} B_{IIjm} Y_{jm}\right) = \sum E_{jm} Y_{jm}$$

We have developed the previous equations respective of the fact that :

$$A = A_{00}(\tilde{t})Y_{00}; C = C_{00}(\tilde{r},\tilde{t})Y_{00}; D = D_{00}(\tilde{r},\tilde{t})Y_{00}$$

from (100), we get an expression for $\dot{B}_{IIjm}$:

$$\dot{B}_{IIjm} = -\frac{\tilde{R}_0^{j+2}}{j+1}\left(\dot{B}_{jm} + \ddot{\tilde{R}}_{IIjm} - \dot{A}\tilde{R}_{IIjm} - A\dot{\tilde{R}}_{IIjm}\right) - \frac{j+2}{j+1}\dot{\tilde{R}}_0\tilde{R}_0^{j+1}\left(B_{jm} + \dot{\tilde{R}}_{IIjm} - A\tilde{R}_{IIjm}\right) \qquad (102)$$

Then, we can replace $\dot{B}_{IIjm}$ by its value in equation (101) to obtain a second-order in time differential equation on coefficients $\tilde{R}_{IIjm}$:

$$\ddot{\tilde{R}}_{IIjm}(-\frac{\tilde{R}_0}{j+1}) + \dot{\tilde{R}}_{IIjm}(A\frac{\tilde{R}_0}{j+1} - \frac{j+2}{j+1}\dot{\tilde{R}}_0 - D) \qquad (103)$$

$$+\tilde{R}_{IIjm}(\dot{A}\frac{\tilde{R}_0}{j+1} + \frac{j+2}{j+1}A\dot{\tilde{R}}_0 + C + AD) = E_{jm} + DB_{jm} + \frac{j+2}{j+1}\dot{\tilde{R}}_0 B_{jm} + \frac{\tilde{R}_0}{j+1}\dot{B}_{jm}$$

for $(j,m) = (0,0)$ and $(j,m) = (1,0)$, the second member of the previous equation has to be completed by the following additional terms:

$$(j,m) = (1,0) \;:\; -\frac{3}{8}q\dot{\tilde{R}}_0 - \frac{3}{8}\dot{q}\tilde{R}_0$$

$$(j,m) = (0,0) \;:\; -\frac{\dot{B}_{I00}}{2} + (3kP)\tilde{R}_0^{-3k-2}\left(1 - \frac{3k(k+1)}{2}\right)\left(\tilde{R}_{I00}^2 + \frac{1}{3}\tilde{R}_{I10}^2 + \frac{2}{3}\tilde{R}_{I11}^2 + \frac{6}{5}\tilde{R}_{I21}^2 + \frac{1}{3}\tilde{R}_{If}^2\right)$$

The calculation of the differential equation coefficients gives :

$$A = -2\frac{\dot{\tilde{R}}_0}{\tilde{R}_0}$$

$$\frac{dA}{d\tilde{t}} = 2\frac{\dot{\tilde{R}}_0^2}{\tilde{R}_0^3} - 2\frac{\ddot{\tilde{R}}_0}{\tilde{R}_0}$$
$$C = \ddot{\tilde{R}}_0$$
$$D = \dot{\tilde{R}}_0$$

We now can sum-up these results by the following differential equation:

$$C_0(j)\ddot{\tilde{R}}_{IIjm} + C_1(j)\dot{\tilde{R}}_{IIjm} + C_2(j)\tilde{R}_{IIjm} = E_{jm} + C_3(j)B_{jm} + C_4(j)\dot{B}_{jm} \qquad (104)$$

at which we add the following terms, in both cases $(j,m) = (0,0)$ and $(j,m) = (1,0)$:

$$(j,m) = (0,0) \ : \ -\frac{\dot{B}_{I00}}{2} + (3kP)\tilde{R}_0^{-3k-2}\left(1 - \frac{3k(k+1)}{2}\right)\left(\tilde{R}_{I00}^2 + \frac{1}{3}\tilde{R}_{I10}^2 + \frac{2}{3}\tilde{R}_{I11}^2 + \frac{6}{5}\tilde{R}_{I21}^2 + \frac{1}{3}\tilde{R}_{If}^2\right)$$
$$(j,m) = (1,0) \ : \ \frac{9}{8}\tilde{R}_0^2\dot{\tilde{R}}_0^2 + \frac{3}{8}\tilde{R}_0^3\ddot{\tilde{R}}_0$$

The coefficients $C_i(j)$ are given by the following array :

j	C_0	C_1	C_2	C_3	C_4
0	$-\tilde{R}_0$	$-5\dot{\tilde{R}}_0$	$-\ddot{\tilde{R}}_0 - 4\frac{\dot{\tilde{R}}_0^2}{\tilde{R}_0} - 3kP\tilde{R}_0^{-3k-1}$	$3\dot{\tilde{R}}_0$	$\tilde{R}_0$
1	$-\frac{\tilde{R}_0}{2}$	$-\frac{7}{2}\dot{\tilde{R}}_0$	$-4\frac{\dot{\tilde{R}}_0^2}{\tilde{R}_0}$	$\frac{5}{2}\dot{\tilde{R}}_0$	$\frac{1}{2}\tilde{R}_0$
2	$-\frac{\tilde{R}_0}{3}$	$-\frac{11}{4}\dot{\tilde{R}}_0$	$\frac{1}{3}\ddot{\tilde{R}}_0 - 4\frac{\dot{\tilde{R}}_0^2}{\tilde{R}_0}$	$\frac{7}{3}\dot{\tilde{R}}_0$	$\frac{1}{3}\tilde{R}_0$
3	$-\frac{\tilde{R}_0}{4}$	$-\frac{11}{4}\dot{\tilde{R}}_0$	$\frac{1}{2}\ddot{\tilde{R}}_0 - 4\frac{\dot{\tilde{R}}_0^2}{\tilde{R}_0}$	$\frac{9}{4}\dot{\tilde{R}}_0$	$\frac{1}{4}\tilde{R}_0$
4	$-\frac{\tilde{R}_0}{5}$	$-\frac{13}{5}\dot{\tilde{R}}_0$	$\frac{3}{5}\ddot{\tilde{R}}_0 - 4\frac{\dot{\tilde{R}}_0^2}{\tilde{R}_0}$	$\frac{11}{5}\dot{\tilde{R}}_0$	$\frac{1}{5}\tilde{R}_0$

Terms of order 1, $\tilde{R}_I$ and $\tilde{\phi}_I$ are componed of harmonics up to order 2. Their product will lead us to harmonics up to order 4; that is to say, we are going to develop 15 independent differential linear equations from Y_{00} up to Y_{44}.
Let us write E'_{jm} the sum $E_{jm} + C_3(j).B_{jm}$.
Results for calculations of terms B_{jm} and E'_{jm} for the 15 spherical harmonics are given in the following pages :

Resolution for j=0

$$B_{00} = -\frac{\tilde{R}_{I00}}{\tilde{R}_0^3}(2B_{I00} + 3\tilde{R}_0\dot{\tilde{R}}_0\tilde{R}_{I00}) - \frac{\tilde{R}_{I10}}{\tilde{R}_0^4}(\frac{4}{3}B_{I10} + \dot{\tilde{R}}_0\tilde{R}_0^2\tilde{R}_{I10}) - \frac{\tilde{R}_{I11}}{\tilde{R}_0^4}(\frac{7}{6}B_{I11} + \tilde{R}_0^2\dot{\tilde{R}}_0\tilde{R}_{I11})$$

$$-\frac{\tilde{R}_{I21}}{\tilde{R}_0^5}(\frac{18}{5}B_{I21} + \frac{1}{5}\dot{\tilde{R}}_0\tilde{R}_0^3\tilde{R}_{I21}) - \frac{\tilde{R}_{If}}{\tilde{R}_0^5}(\frac{29}{5}B_{If} + \frac{4}{5}\dot{\tilde{R}}_0\tilde{R}_0^3\tilde{R}_{If}) + \frac{4}{35}\alpha_2\tilde{R}_{I21} - \frac{4}{15}\alpha_1\tilde{R}_{If}$$

$$E'_{00} = \frac{\tilde{R}_{I00}}{\tilde{R}_0^3}(4\tilde{R}_0\dot{\tilde{R}}_0^2 + 2\dot{\tilde{R}}_0B_{I00} + \ddot{\tilde{R}}_0\tilde{R}_0^2\tilde{R}_{I00} + \tilde{R}_0\dot{B}_{I00})$$

$$+\frac{\tilde{R}_{I10}}{\tilde{R}_0^4}(\frac{4}{3}\dot{\tilde{R}}_0^2\tilde{R}_0^2\tilde{R}_{I10} - \frac{22}{3}\dot{\tilde{R}}_0B_{I10} + \ddot{\tilde{R}}_0\tilde{R}_0^3\tilde{R}_{I10} + \frac{2}{3}\tilde{R}_0\dot{B}_{I10} - \frac{\mu}{3}\alpha_2v_x\tilde{R}_0^4)$$

$$+\frac{\tilde{R}_{I11}}{\tilde{R}_0^4}(\frac{4}{3}\dot{\tilde{R}}_0^2\tilde{R}_0^2\tilde{R}_{I11} + \ddot{\tilde{R}}_0\tilde{R}_0^3\tilde{R}_{I11} - \frac{41}{6}\dot{\tilde{R}}_0B_{I11} + \frac{2}{3}\tilde{R}_0\dot{B}_{I11} - \frac{\mu}{3}v_x\alpha_1\tilde{R}_0^4)$$

$$+\frac{\tilde{R}_{I21}}{\tilde{R}_0^5}(-\frac{18}{5}\dot{\tilde{R}}_0^2\tilde{R}_0^3\tilde{R}_{I21} + \ddot{\tilde{R}}_0\tilde{R}_0^4\tilde{R}_{I21} - \frac{108}{5}B_{I21}\dot{\tilde{R}}_0 - \frac{72}{35}\alpha_2\dot{\tilde{R}}_0\tilde{R}_0^5 + \frac{9}{5}\tilde{R}_0\dot{B}_{I21})$$

$$+\frac{\tilde{R}_{If}}{\tilde{R}_0^5}(-\frac{56}{15}\dot{\tilde{R}}_0^2\tilde{R}_0^3\tilde{R}_{If} + \ddot{\tilde{R}}_0\tilde{R}_0^4\tilde{R}_{If} - \frac{111}{5}\dot{\tilde{R}}_0B_{If} - \frac{16}{15}\alpha_1\dot{\tilde{R}}_0\tilde{R}_0^5 + \frac{4}{5}\tilde{R}_0\dot{B}_{If})$$

$$-\frac{B_{I00}^2}{2\tilde{R}_0^4} - \frac{B_{I10}^2}{\tilde{R}_0^6} - \frac{7}{12\tilde{R}_0^6}B_{I11}^2 + \frac{B_{I21}}{\tilde{R}_0^3}(-\frac{3}{8}\frac{B_{I21}}{\tilde{R}_0^5} + \frac{13}{70}\alpha_2)$$

$$+\frac{B_{If}}{\tilde{R}_0^3}(-\frac{11}{6}\frac{B_{If}}{\tilde{R}_0^5} + \frac{4}{5}\alpha_1) - \tilde{R}_0^2(\frac{7}{12}\alpha_1^2 + \frac{2}{3}\alpha_2^2)$$

$$+(3kP)\tilde{R}_0^{-3k-2}(1 - \frac{3k(k+1)}{2})(\tilde{R}_{I00}^2 + \frac{1}{3}\tilde{R}_{I10}^2 + \frac{2}{3}\tilde{R}_{I11}^2 + \frac{6}{5}\tilde{R}_{I21}^2 + \frac{1}{3}\tilde{R}_{If}^2)$$

Resolution for j=1, m=0

$$B_{10} = -\frac{\tilde{R}_{I00}}{\tilde{R}_0^4}(6B_{I10} + 6\tilde{R}_0^2\dot{\tilde{R}}_0\tilde{R}_{I10}) - \frac{\tilde{R}_{I10}}{\tilde{R}_0^5}(2B_{I00} - \frac{12}{5}\dot{\tilde{R}}_0\tilde{R}_0^3\tilde{R}_{If} - \frac{18}{5}B_{If})$$

$$-\frac{\tilde{R}_{I11}}{\tilde{R}_0^5}(\frac{27}{5}B_{I21} + \frac{18}{5}\tilde{R}_0^3\dot{\tilde{R}}_0\tilde{R}_{If}) - \frac{3}{10}\frac{\tilde{R}_{I21}}{\tilde{R}_0^4}B_{I11}$$

$$+\frac{6}{5}\frac{\tilde{R}_{If}}{\tilde{R}_0^4}B_{I10} - \frac{1}{5}\alpha_1\tilde{R}_{I10} - \frac{3}{10}\alpha_2\tilde{R}_{I11} + \frac{1}{10}\alpha_2\tilde{R}_{I21} - \omega\tilde{R}_{I11} - \frac{\tilde{R}_0^2}{10}(\gamma_2 + 2\gamma_3)$$

$$E'_{10} = \frac{\tilde{R}_{I00}}{\tilde{R}_0^4}(2\tilde{R}_0\dot{B}_{I10} - 20\dot{\tilde{R}}_0B_{I10} - 20\dot{\tilde{R}}_0^2\tilde{R}_0^2\tilde{R}_{I10} + 2\tilde{R}_0^3\ddot{\tilde{R}}_0\tilde{R}_{I10} - \mu v_z\alpha_2\tilde{R}_0^4)$$

$$+\frac{\tilde{R}_{I10}}{\tilde{R}_0^5}(\tilde{R}_0^3\dot{B}_{I00} - 9\tilde{R}_0^2\dot{\tilde{R}}_0B_{I00} + \frac{98}{5}\tilde{R}_0^3\dot{\tilde{R}}_0^2\tilde{R}_{If} - \frac{4}{5}\ddot{\tilde{R}}_0\tilde{R}_0^4\tilde{R}_{If} + \frac{81}{5}\dot{\tilde{R}}_0B_{If} - \frac{6}{5}\tilde{R}_0\dot{B}_{If} - \frac{1}{10}\alpha_1\dot{\tilde{R}}_0\tilde{R}_0^5) +$$

$$\frac{\tilde{R}_{I11}}{\tilde{R}_0^5}(\frac{12}{5}\tilde{R}_0\dot{B}_{I21} - \frac{51}{2}\dot{\tilde{R}}_0B_{I21} + \frac{6}{5}\tilde{R}_0^4\tilde{R}_{If}\ddot{\tilde{R}}_0 - 15\dot{\tilde{R}}_0^2\tilde{R}_0^3\tilde{R}_{If} - \frac{23}{20}\dot{\tilde{R}}_0\tilde{R}_0^5\alpha_2 - \frac{5}{2}\dot{\tilde{R}}_0\tilde{R}_0^5\omega)$$

$$+\frac{\tilde{R}_{I21}}{\tilde{R}_0^4}(-\frac{27}{4}\dot{\tilde{R}}_0B_{I11} + \frac{6}{5}\tilde{R}_0\dot{B}_{I11} - \frac{3}{5}\mu v_z\alpha_1\tilde{R}_0^4 + \frac{5}{4}\alpha_2\dot{\tilde{R}}_0\tilde{R}_0^4)$$

$$+\frac{\tilde{R}_{If}}{\tilde{R}_0^4}(\frac{4}{5}\tilde{R}_0\dot{B}_{I10} - \dot{\tilde{R}}_0B_{I10} + \frac{2}{5}\mu\alpha_2v_z\tilde{R}_0^4 + \frac{5}{4}\alpha_2\dot{\tilde{R}}_0\tilde{R}_0^4)$$

$$-\frac{7}{20}\dot{\tilde{R}}_0^2\tilde{R}_0^2(\gamma_2 + 2\gamma_3) + \frac{B_{I10}}{5\tilde{R}_0^2}(18\frac{B_{If}}{\tilde{R}_0^5} - 10\frac{B_{I00}}{\tilde{R}_0^3} + 3\alpha_1) + \frac{B_{I11}}{5\tilde{R}_0^2}(-12\frac{B_{I21}}{\tilde{R}_0^5} + \alpha_2 + 5\omega)$$

Resolution for j=1, m=1

$$B_{11} = -\frac{\tilde{R}_{I00}}{\tilde{R}_0^4}(6B_{I11} + 6\dot{\tilde{R}}_0\tilde{R}_0^2\tilde{R}_{I11}) - \frac{\tilde{R}_{I10}}{\tilde{R}_0^5}(\frac{27}{5}B_{I21} + \frac{18}{5}\dot{\tilde{R}}_0\tilde{R}_0^3\tilde{R}_{I21})$$

$$-\frac{\tilde{R}_{I11}}{\tilde{R}_0^5}(2\tilde{R}_0^2B_{I00} + \frac{12}{5}\dot{\tilde{R}}_0\tilde{R}_0^3\tilde{R}_{If} + \frac{18}{5}B_{If})$$

$$-\frac{9}{5\tilde{R}_0^4}\tilde{R}_{I21}B_{I10} - \frac{6}{5\tilde{R}_0^4}B_{I11}\tilde{R}_{If} + \frac{1}{5}\alpha_2\tilde{R}_{I10} - \frac{1}{5}\alpha_1\tilde{R}_{I11} + \frac{902}{875}\alpha_2\tilde{R}_{If} - \frac{\tilde{R}_0^2}{10}(\gamma_1 + 2\gamma_4)$$

$$+\omega(\tilde{R}_{I10} + \frac{1237}{40}\tilde{R}_{If})$$

$$E'_{11} = \frac{\tilde{R}_{I00}}{\tilde{R}_0^4}(2\tilde{R}_0\dot{B}_{I11} - 19\dot{\tilde{R}}_0^2\tilde{R}_0^2\tilde{R}_{I11} + 2\ddot{\tilde{R}}_0\tilde{R}_0^3\tilde{R}_{I11} - 19\dot{\tilde{R}}_0B_{I11} - \alpha_1\mu v_z\tilde{R}_0^4)$$

$$+\frac{\tilde{R}_{I10}}{\tilde{R}_0^5}(\frac{9}{5}\dot{B}_{I21}\tilde{R}_0 - \frac{189}{10}\dot{\tilde{R}}_0B_{I21} - \frac{57}{50}\dot{\tilde{R}}_0^2\tilde{R}_0^3\tilde{R}_{I21} + \frac{6}{5}\ddot{\tilde{R}}_0\tilde{R}_0^4\tilde{R}_{I21} - \frac{1}{10}\alpha_2\dot{\tilde{R}}_0\tilde{R}_0^5)$$

$$+\frac{\tilde{R}_{I11}}{\tilde{R}_0^5}(\tilde{R}_0^3\dot{B}_{I00} + \frac{6}{5}\tilde{R}_0\dot{B}_{If} - \frac{38}{5}\tilde{R}_0^3\dot{\tilde{R}}_0^2\tilde{R}_{If} + \frac{4}{5}\ddot{\tilde{R}}_0\tilde{R}_0^4\tilde{R}_{If} - 7\dot{\tilde{R}}_0\tilde{R}_0^2B_{I00} - \frac{63}{5}B_{If}\dot{\tilde{R}}_0 - \frac{7}{10}\alpha_1\dot{\tilde{R}}_0\tilde{R}_0^5)$$

$$+\frac{\tilde{R}_{I21}}{\tilde{R}_0^4}(\frac{6}{5}\tilde{R}_0\dot{B}_{I10} - \frac{87}{10}\dot{\tilde{R}}_0B_{I10} - \frac{3}{2}\mu\alpha_2v_z\tilde{R}_0^4)$$

$$+\frac{\tilde{R}_{If}}{\tilde{R}_0^4}(\frac{4}{5}\tilde{R}_0\dot{B}_{I11} - \frac{29}{5}\dot{\tilde{R}}_0B_{I11} - \frac{2}{5}\mu v_z\alpha_1\tilde{R}_0^4 + \frac{1353}{875}\alpha_2v_z\tilde{R}_0^4)$$

$$-\frac{13}{5\tilde{R}_0^7}B_{If}B_{I11} - \frac{27}{5\tilde{R}_0^7}B_{I10}B_{I21} - \frac{2}{\tilde{R}_0^5}B_{I00}B_{I11} - \frac{3}{5}\alpha_1\frac{B_{I11}}{\tilde{R}_0^3}$$

$$+\frac{4}{5}\alpha_1\frac{B_{I10}}{\tilde{R}_0^3} - \frac{3}{5\tilde{R}_0^2}\alpha_2B_{I10} - \frac{902}{875}\alpha_2\frac{B_{If}}{\tilde{R}_0^3} - \frac{1}{4}\dot{\tilde{R}}_0\tilde{R}_0^2(\gamma_1 + 2\gamma_4)$$

$$-\omega\frac{B_{I10}}{\tilde{R}_0^3} - \frac{1237}{400}\frac{B_{If}}{\tilde{R}_0^3} + \frac{3}{2}\dot{\tilde{R}}_0\omega(\tilde{R}_{I10} + \frac{1237}{400}\tilde{R}_{If})$$

Resolution for j=2, m=0

$$B_{20} = \frac{\tilde{R}_{I00}}{\tilde{R}_0^5}(12B_{If} + 6\dot{\tilde{R}}_0\tilde{R}_0^3\tilde{R}_{If})$$

$$-\frac{\tilde{R}_{I10}}{\tilde{R}_0^4}(2\dot{\tilde{R}}_0\tilde{R}_0^2\tilde{R}_{I10} + \frac{14}{5}B_{I10}) + \frac{\tilde{R}_{I11}}{\tilde{R}_0^5}(\dot{\tilde{R}}_0\tilde{R}_0^3\tilde{R}_{I11} + \frac{13}{6}\tilde{R}_0B_{I11})$$

$$-\frac{\tilde{R}_{I21}}{\tilde{R}_0^5}(\frac{1}{7}\dot{\tilde{R}}_0\tilde{R}_0^3\tilde{R}_{I21} + \frac{27}{7}B_{I21}) - \frac{\tilde{R}_{If}}{\tilde{R}_0^5}(\frac{50}{21}B_{If} + \frac{4}{7}\dot{\tilde{R}}_0\tilde{R}_0^3\tilde{R}_{If})$$

$$+\frac{2}{\tilde{R}_0^3}B_{I00}\tilde{R}_{If} - \frac{16}{21}\alpha_1\tilde{R}_{If} + \frac{1}{7}\alpha_2\tilde{R}_{I21} + \alpha_1\tilde{R}_{I00} - 3\omega\tilde{R}_{I21}$$

$$E'_{20} = \frac{\tilde{R}_{I00}}{\tilde{R}_0^5}(-\frac{3}{5}\tilde{R}_0\dot{B}_{If} + 24\dot{\tilde{R}}_0^2\tilde{R}_0^3\tilde{R}_{If} - 2\ddot{\tilde{R}}_0\tilde{R}_0^4\tilde{R}_{If} + \frac{206}{5}\dot{\tilde{R}}_0B_{If} + \frac{10}{3}\alpha_1\dot{\tilde{R}}_0\tilde{R}_0^5)$$

$$+\frac{\tilde{R}_{I10}}{\tilde{R}_0^4}(\frac{4}{3}\tilde{R}_0\dot{B}_{I10} - 8\dot{\tilde{R}}_0^2\tilde{R}_0^2\tilde{R}_{I10} + \frac{2}{3}\ddot{\tilde{R}}_0\tilde{R}_0^3\tilde{R}_{I10} - \frac{158}{9}\dot{\tilde{R}}_0B_{I10} - \frac{2}{3}\alpha_2v_z\mu\tilde{R}_0^4)$$

$$+\frac{\tilde{R}_{I11}}{\tilde{R}_0^4}(-\frac{2}{3}\tilde{R}_0\dot{B}_{I11} + 4\dot{\tilde{R}}_0^2\tilde{R}_0^2\tilde{R}_{I11} - \frac{1}{3}\ddot{\tilde{R}}_0\tilde{R}_0^3\tilde{R}_{I11} + \frac{133}{8}\dot{\tilde{R}}_0B_{I11} + \frac{1}{3}\alpha_1v_z\mu\tilde{R}_0^4)$$

$$+\frac{\tilde{R}_{I21}}{\tilde{R}_0^5}(\frac{9}{7}\tilde{R}_0\dot{B}_{I21} - \frac{52}{21}\dot{\tilde{R}}_0^2\tilde{R}_0^2\tilde{R}_{I21} + \frac{3}{7}\ddot{\tilde{R}}_0\tilde{R}_0^3\tilde{R}_{I21} - \frac{117}{7}\dot{\tilde{R}}_0B_{I21} - \frac{1}{21}\alpha_2v_z\mu\tilde{R}_0^5 - 7\omega\tilde{R}_0^5)$$

$$+\frac{\tilde{R}_{If}}{\tilde{R}_0^5}(\frac{4}{7}\tilde{R}_0\dot{B}_{If} - \dot{B}_{I00}\tilde{R}_0^3 - \frac{36}{21}\tilde{R}_{If}\dot{\tilde{R}}_0^2\tilde{R}_0^3 + \frac{4}{21}\ddot{\tilde{R}}_0\tilde{R}_0^4 - \frac{566}{63}\dot{\tilde{R}}_0B_{If} + \frac{26}{3}B_{I00}\dot{\tilde{R}}_0\tilde{R}_0^2 - \frac{124}{63}\alpha_1\dot{\tilde{R}}_0\tilde{R}_0^5)$$

$$-\frac{1}{\tilde{R}_0^6}{B_{I10}}^2 + \frac{7}{12\tilde{R}_0^6}{B_{I11}}^2 + \frac{3}{7\tilde{R}_0^6}{B_{I21}}^2 - \frac{38}{21\tilde{R}_0^6}{B_{If}}^2 + \frac{3}{\tilde{R}_0^4}B_{I00}B_{If} + \frac{3}{7}\alpha_2\frac{B_{I21}}{\tilde{R}_0^3}$$

$$+\frac{15}{14}\alpha_1\frac{B_{If}}{\tilde{R}_0^3} - \frac{\mu}{3}v_z\gamma_1 - \frac{1}{6}\tilde{R}_0^2({\alpha_1}^2 + 2{\alpha_2}^2) + 3\omega\frac{B_{I21}}{\tilde{R}_0^3}$$

Resolution for j=2, m=1

$$B_{21} = -\frac{\tilde{R}_{I00}}{\tilde{R}_0^5}(12B_{I21} + 6\dot{\tilde{R}}_0\tilde{R}_0^3\tilde{R}_{I21}) - \frac{\tilde{R}_{I10}}{\tilde{R}_0^4}(\frac{7}{3}B_{I11} + \frac{2}{3}\dot{\tilde{R}}_0\tilde{R}_0^3\tilde{R}_{I11}) - \frac{7}{30\tilde{R}_0^4}\tilde{R}_{I11}B_{I10}$$
$$-\frac{2}{\tilde{R}_0^3}B_{I00}\tilde{R}_{I21} - \frac{2}{3}\alpha_2\tilde{R}_{I00} + \frac{17}{20}\alpha_1\tilde{R}_{I21} + \frac{1}{6}\tilde{R}_{If}(\alpha_2 - \omega)$$

$$E'_{21} = \frac{\tilde{R}_{I00}}{\tilde{R}_0^5}(3\tilde{R}_0\dot{B}_{I21} - 24\dot{\tilde{R}}_0^2\tilde{R}_0^3\tilde{R}_{I21} + 2\ddot{\tilde{R}}_0\tilde{R}_0^4\tilde{R}_{I21} - \frac{476}{15}\dot{\tilde{R}}_0B_{I21} - \frac{55}{18}\alpha_2\dot{\tilde{R}}_0\tilde{R}_0^5)$$
$$+\frac{\tilde{R}_{I10}}{\tilde{R}_0^4}(\frac{2}{3}\tilde{R}_0\dot{B}_{I11} - 8\dot{\tilde{R}}_0^2\tilde{R}_0^3\tilde{R}_{I11} + \frac{2}{3}\ddot{\tilde{R}}_0\tilde{R}_0^3\tilde{R}_{I11} - \frac{79}{9}\dot{\tilde{R}}_0B_{I11} - \frac{1}{3}\alpha_1v_z\mu\tilde{R}_0^4)$$
$$+\frac{\tilde{R}_{I11}}{\tilde{R}_0^4}(\frac{2}{3}\tilde{R}_0\dot{B}_{I11} - \frac{79}{9}\dot{\tilde{R}}_0B_{I10} - \frac{1}{3}\alpha_2v_z\mu\tilde{R}_0^4)$$
$$+\frac{\tilde{R}_{I21}}{\tilde{R}_0^3}(\tilde{R}_0\dot{B}_{I00} - \frac{26}{3}\dot{\tilde{R}}_0B_{I00} + \frac{119}{60}\alpha_1\dot{\tilde{R}}_0\tilde{R}_0^3) + \frac{7}{18}\tilde{R}_{If}\dot{\tilde{R}}_0(\alpha_2 - \omega)$$
$$+\frac{2}{3}\alpha_2B_{I00} - \frac{1}{\tilde{R}_0^6}B_{I10}B_{I11} + \frac{1}{\tilde{R}_0^6}B_{If}B_{I21} - \frac{3}{4\tilde{R}_0^4}B_{I00}B_{I21}$$
$$-\frac{\mu}{6}v_z\tilde{R}_0^2\gamma_3 + \frac{1}{6}\omega\frac{B_{If}}{\tilde{R}_0^3} - \frac{17}{20}\alpha_1\frac{B_{I21}}{\tilde{R}_0^3} - \frac{1}{6}\alpha_2\frac{B_{If}}{\tilde{R}_0^3}$$

Resolution for j=2, m=2

$$B_{22} = -\frac{\tilde{R}_{I00}}{\tilde{R}_0^5}(2B_{If} + \dot{\tilde{R}}_0\tilde{R}_0^3\tilde{R}_{If})$$

$$-\frac{\tilde{R}_{I11}}{\tilde{R}_0^5}(\frac{1}{2}\dot{\tilde{R}}_0\tilde{R}_0^3\tilde{R}_{I11} + \frac{7}{6}\tilde{R}_0 B_{I11}) - \frac{\tilde{R}_{I21}}{\tilde{R}_0^5}(\frac{9}{14}\dot{\tilde{R}}_0\tilde{R}_0^3\tilde{R}_{I21} + \frac{5939}{3080}B_{I21})$$

$$-\frac{\tilde{R}_{If}}{\tilde{R}_0^5}(\frac{2}{7}\dot{\tilde{R}}_0\tilde{R}_0^3\tilde{R}_{If} + \frac{6}{7}B_{If} + \frac{1}{3}\tilde{R}_0^2 B_{I00}) + \frac{1}{2}\tilde{R}_{I21}(\omega + \frac{1}{7}\alpha_2) - \frac{2}{21}\alpha_1\tilde{R}_{If} - \frac{1}{6}\alpha_1\tilde{R}_{I00}$$

$$E'_{22} = \frac{\tilde{R}_{I00}}{\tilde{R}_0^5}(\frac{1}{2}\tilde{R}_0\dot{B}_{If} + \frac{2}{3}\dot{\tilde{R}}_0^2\tilde{R}_0^3\tilde{R}_{If} + \frac{1}{3}\ddot{\tilde{R}}_0\tilde{R}_0^4\tilde{R}_{If} - \frac{23}{3}\dot{\tilde{R}}_0 B_{If} - \frac{5}{9}\alpha_1\dot{\tilde{R}}_0\tilde{R}_0^5)$$

$$+\frac{\tilde{R}_{I11}}{\tilde{R}_0^4}(\frac{1}{3}\tilde{R}_0\dot{B}_{I11} - 2\dot{\tilde{R}}_0^2\tilde{R}_0^3\tilde{R}_{I11} + \frac{1}{6}\ddot{\tilde{R}}_0\tilde{R}_0^4\tilde{R}_{I11} - \frac{79}{18}\dot{\tilde{R}}_0 B_{I11} - \frac{1}{6}\alpha_1 v_s\mu\tilde{R}_0^4)$$

$$+\frac{\tilde{R}_{I21}}{\tilde{R}_0^4}(\frac{9}{14}\tilde{R}_0\dot{B}_{I21} - \frac{18}{7}\dot{\tilde{R}}_0^2\tilde{R}_0^3\tilde{R}_{I21} + \frac{3}{14}\ddot{\tilde{R}}_0\tilde{R}_0^4\tilde{R}_{I21} - \frac{77213}{9240}\dot{\tilde{R}}_0 B_{I21} + \frac{1}{42}\alpha_2\dot{\tilde{R}}_0\tilde{R}_0^4 + \frac{7}{6}\omega\dot{\tilde{R}}_0\tilde{R}_0^4)$$

$$+\frac{\tilde{R}_{If}}{\tilde{R}_0^5}(\frac{1}{6}\tilde{R}_0^3\dot{B}_{I00} + \frac{2}{7}\tilde{R}_0\dot{B}_{If} - \frac{37}{63}\dot{\tilde{R}}_0^2\tilde{R}_0^3\tilde{R}_{If}$$

$$+\frac{2}{21}\ddot{\tilde{R}}_0\tilde{R}_0^4\tilde{R}_{I21} - \frac{13}{9}\dot{\tilde{R}}_0\tilde{R}_0^2 B_{I00} - \frac{26}{7}\dot{\tilde{R}}_0 B_{If} - \frac{61}{126}\alpha_1\dot{\tilde{R}}_0\tilde{R}_0^5)$$

$$-\frac{1}{2\tilde{R}_0^3}B_{I21}\omega - \frac{11}{24\tilde{R}_0^6}{B_{I11}}^2 - \frac{10231}{6160\tilde{R}_0^8}{B_{I21}}^2 - \frac{2}{7\tilde{R}_0^8}{B_{If}}^2 - \frac{1}{6\tilde{R}_0^4}B_{I00}B_{If}$$

$$-\frac{5}{56\tilde{R}_0^3}\alpha_2 B_{I21} + \frac{2}{7}\alpha_1\frac{B_{If}}{\tilde{R}_0^3} + \frac{1}{6}\alpha_1\frac{B_{I00}}{\tilde{R}_0} - \frac{1}{6}{\alpha_1}^2\tilde{R}_0^2 - \frac{1157}{55440}{\alpha_2}^2\tilde{R}_0^2$$

Resolution for j=3, m=0

$$B_{30} = \frac{\tilde{R}_{I10}}{\tilde{R}_0^5}(\frac{42}{5}B_{If} + \frac{18}{5}\dot{\tilde{R}}_0\tilde{R}_0^3\tilde{R}_{If})$$

$$+\frac{\tilde{R}_{I11}}{\tilde{R}_0^5}(\frac{42}{5}B_{I21} + \frac{18}{5}\dot{\tilde{R}}_0\tilde{R}_0^3\tilde{R}_{I21}) - \frac{13}{5\tilde{R}_0^4}\tilde{R}_{I21}B_{I11} + \frac{24}{5\tilde{R}_0^4}\tilde{R}_{If}B_{I10}$$

$$+\frac{6}{5}\alpha_1\tilde{R}_{I10} + \frac{51}{50}\alpha_1\tilde{R}_{If} + \frac{\tilde{R}_0^2}{10}(\gamma_2 + 2\gamma_3)$$

$$E'_{30} = \frac{\tilde{R}_{I10}}{\tilde{R}_0^5}(-\frac{9}{5}\tilde{R}_0\dot{B}_{If} + \frac{141}{10}\dot{\tilde{R}}_0^2\tilde{R}_0^3\tilde{R}_{If} - \frac{6}{5}\ddot{\tilde{R}}_0\tilde{R}_0^4\tilde{R}_{If} + \frac{171}{5}\dot{\tilde{R}}_0B_{If} + \frac{33}{10}\alpha_1\dot{\tilde{R}}_0\tilde{R}_0^5)$$

$$+\frac{\tilde{R}_{I11}}{\tilde{R}_0^5}(-\frac{9}{5}\tilde{R}_0\dot{B}_{I21} + \frac{141}{10}\dot{\tilde{R}}_0^2\tilde{R}_0^3\tilde{R}_{I21} - \frac{6}{5}\ddot{\tilde{R}}_0\tilde{R}_0^4\tilde{R}_{I21} + \frac{171}{5}\dot{\tilde{R}}_0B_{I21} + \frac{11}{5}\alpha_2\dot{\tilde{R}}_0\tilde{R}_0^5)$$

$$+\frac{\tilde{R}_{I21}}{\tilde{R}_0^4}(\frac{6}{5}\tilde{R}_0\dot{B}_{I11} - \frac{237}{20}\dot{\tilde{R}}_0^2\tilde{R}_0^3\tilde{R}_{I11} + \frac{3}{5}\alpha_1\mu v_z\tilde{R}_0^4)$$

$$+\frac{\tilde{R}_{If}}{\tilde{R}_0^4}(-\frac{6}{5}\tilde{R}_0\dot{B}_{I10} + \frac{94}{5}\dot{\tilde{R}}_0B_{I10} + \frac{459}{200}\alpha_1\dot{\tilde{R}}_0\tilde{R}_0^5 + \frac{3}{5}\mu v_z\alpha_2\tilde{R}_0^4)$$

$$+\frac{13}{40}\dot{\tilde{R}}_0\tilde{R}_0^2(\gamma_2 + 2\gamma_3) + \frac{12}{5\tilde{R}_0^7}B_{I10}B_{If} + \frac{12}{5\tilde{R}_0^7}B_{I11}B_{I21}$$

$$-\frac{6}{5}\alpha_2\frac{B_{I11}}{\tilde{R}_0^2} - \frac{9}{5}\alpha_1\frac{B_{I10}}{\tilde{R}_0^2} - \frac{51}{50}\alpha_1\frac{B_{If}}{\tilde{R}_0^3}$$

Resolution for j=3, m=1

$$B_{31} = -\frac{\tilde{R}_{I10}}{\tilde{R}_0^5}(\frac{28}{5}B_{I21} + \frac{12}{5}\dot{\tilde{R}}_0\tilde{R}_0^3\tilde{R}_{I21})$$

$$-\frac{\tilde{R}_{I11}}{\tilde{R}_0^5}(\frac{23}{15}B_{If} + \dot{\tilde{R}}_0\tilde{R}_0^3\tilde{R}_{If}) - \frac{16}{5\tilde{R}_0^4}\tilde{R}_{I21}B_{I10} - \frac{8}{15\tilde{R}_0^4}\tilde{R}_{If}B_{I11} - \frac{\tilde{R}_0^2}{15}(\gamma_1 + 2\gamma_4)$$

$$-\frac{451}{250}\tilde{R}_{If}(\frac{1}{8}\alpha_2 + \omega) - \frac{32}{45}\alpha_2\tilde{R}_{I10} + \frac{1}{15}\alpha_1\tilde{R}_{I11}$$

$$E'_{31} = \frac{\tilde{R}_{I10}}{\tilde{R}_0^5}(\frac{6}{5}\tilde{R}_0\dot{B}_{I21} - \frac{47}{5}\dot{\tilde{R}}_0^2\tilde{R}_0^3\tilde{R}_{I21} + \frac{4}{5}\ddot{\tilde{R}}_0\tilde{R}_0^4\tilde{R}_{I21} - \frac{99}{5}\dot{\tilde{R}}_0B_{I21} - \frac{71}{5}\alpha_2\dot{\tilde{R}}_0\tilde{R}_0^5)$$

$$+\frac{\tilde{R}_{I11}}{\tilde{R}_0^5}(\frac{1}{2}\tilde{R}_0\dot{B}_{If} - \frac{47}{12}\dot{\tilde{R}}_0^2\tilde{R}_0^3\tilde{R}_{If} + \frac{1}{3}\ddot{\tilde{R}}_0\tilde{R}_0^4\tilde{R}_{If} - \frac{129}{20}\dot{\tilde{R}}_0B_{If} - \frac{1}{60}\alpha_1\dot{\tilde{R}}_0\tilde{R}_0^5)$$

$$+\frac{\tilde{R}_{I21}}{\tilde{R}_0^4}(\frac{4}{5}\tilde{R}_0\dot{B}_{I10} - \frac{56}{5}\dot{\tilde{R}}_0B_{I10} - \frac{2}{5}\alpha_2\mu v_z\tilde{R}_0^4)$$

$$+\frac{\tilde{R}_{If}}{\tilde{R}_0^4}(\frac{1}{3}\tilde{R}_0\dot{B}_{I11} - \frac{43}{15}\dot{\tilde{R}}_0B_{I11} + \frac{4059}{1000}\dot{\tilde{R}}_0\tilde{R}_0^5(\frac{1}{8}\alpha_2 + \omega))$$

$$-\frac{1}{12}\dot{\tilde{R}}_0\tilde{R}_0^2(\gamma_1 + 2\gamma_4) - \frac{8}{5\tilde{R}_0^7}B_{I10}B_{I21} - \frac{22}{15\tilde{R}_0^7}B_{I11}B_{If} + \frac{451}{250}\omega\frac{B_{If}}{\tilde{R}_0^3}$$

$$-\frac{7}{30}\alpha_1\frac{B_{I11}}{\tilde{R}_0^2} + \frac{4}{15}\alpha_2\frac{B_{I10}}{\tilde{R}_0^2} + \frac{451}{2000}\alpha_2\frac{B_{If}}{\tilde{R}_0^3}$$

Resolution for j=3, m=2

$$B_{32} = -\frac{1}{15\tilde{R}_0^5}\tilde{R}_{I10}(7B_{If} + 3\dot{\tilde{R}}_0\tilde{R}_0^3\tilde{R}_{If}) - \frac{\tilde{R}_{I11}}{\tilde{R}_0^5}(\frac{15}{8}B_{I21} + \frac{3}{5}\dot{\tilde{R}}_0\tilde{R}_0^3\tilde{R}_{I21})$$

$$-\frac{41}{40\tilde{R}_0^4}\tilde{R}_{I21}B_{I11} - \frac{4}{15\tilde{R}_0^4}\tilde{R}_{If}B_{I10} - \frac{\tilde{R}_0^2}{60}(\gamma_1 + 2\gamma_3) - \frac{5}{24}\alpha_2\tilde{R}_{I11} - \frac{1}{15}\alpha_1\tilde{R}_{I10} - \frac{29}{900}\alpha_1\tilde{R}_{If}$$

$$E'_{32} = \frac{\tilde{R}_{I10}}{\tilde{R}_0^5}(\frac{1}{10}\tilde{R}_0\dot{B}_{If} - \frac{57}{60}\dot{\tilde{R}}_0^2\tilde{R}_0^3\tilde{R}_{If} + \frac{1}{15}\ddot{\tilde{R}}_0\tilde{R}_0^4\tilde{R}_{If} - \frac{33}{20}\dot{\tilde{R}}_0B_{If} - \frac{3}{20}\alpha_1\dot{\tilde{R}}_0\tilde{R}_0^5)$$

$$+\frac{\tilde{R}_{I11}}{\tilde{R}_0^5}(\frac{3}{20}\tilde{R}_0\dot{B}_{I21} - \frac{47}{20}\dot{\tilde{R}}_0^2\tilde{R}_0^3\tilde{R}_{I21} + \frac{1}{5}\ddot{\tilde{R}}_0\tilde{R}_0^4\tilde{R}_{I21} - \frac{813}{60}\dot{\tilde{R}}_0B_{I21} - \frac{771}{1440}\alpha_2\dot{\tilde{R}}_0\tilde{R}_0^5)$$

$$+\frac{\tilde{R}_{I21}}{\tilde{R}_0^4}(\frac{1}{5}\tilde{R}_0\dot{B}_{I11} - \frac{529}{160}\dot{\tilde{R}}_0B_{I11} - \frac{1}{10}\alpha_1\mu v_z\tilde{R}_0^4)$$

$$+\frac{\tilde{R}_{If}}{\tilde{R}_0^4}(\frac{1}{15}\tilde{R}_0\dot{B}_{I10} - \frac{14}{15}\dot{\tilde{R}}_0B_{I10} - \frac{261}{3600}\alpha_1\dot{\tilde{R}}_0\tilde{R}_0^4 - \frac{1}{30}\mu v_z\alpha_2\tilde{R}_0^4)$$

$$-\frac{2}{15}B_{I10}\frac{B_{If}}{\tilde{R}_0^7} - \frac{9}{8}B_{I11}\frac{B_{I21}}{\tilde{R}_0^7} - \frac{13}{240}\tilde{R}_0^2\dot{\tilde{R}}_0(\gamma_2 + 2\gamma_3)$$

$$+\frac{1}{30}\alpha_1\frac{B_{I10}}{\tilde{R}_0^2} + \frac{29}{900}\alpha_1\frac{B_{If}}{\tilde{R}_0^3} + \frac{17}{120}\alpha_2\frac{B_{I11}}{\tilde{R}_0^2}$$

Resolution for j=3, m=3

$$B_{33} = -\frac{1}{30\tilde{R}_0^5}\tilde{R}_{I11}(7B_{If} + 3\dot{\tilde{R}}_0\tilde{R}_0^3\tilde{R}_{If}) - \frac{2}{15\tilde{R}_0^4}\tilde{R}_{If}B_{I11} - \frac{1}{30}\alpha_1\tilde{R}_{I11}$$

$$+\frac{1}{20}\tilde{R}_{If}(\frac{1}{4}\alpha_2 + \frac{3}{35}\omega)$$

$$E'_{33} = \frac{\tilde{R}_{I11}}{\tilde{R}_0^5}(\frac{1}{20}\dot{\tilde{R}}_0\dot{B}_{If} - \frac{47}{120}\dot{\tilde{R}}_0^2\tilde{R}_0^3\tilde{R}_{If} + \frac{1}{30}\ddot{\tilde{R}}_0\tilde{R}_0^4\tilde{R}_{If} - 31\alpha_1\dot{\tilde{R}}_0\tilde{R}_0^5)$$

$$+\frac{\tilde{R}_{If}}{\tilde{R}_0^4}(\frac{1}{30}\tilde{R}_0\dot{B}_{I11} - \frac{7}{15}\dot{\tilde{R}}_0B_{I11} - \frac{1}{60}\mu\alpha_1 v_z\tilde{R}_0^4 + \frac{9}{80}\dot{\tilde{R}}_0\tilde{R}_0^4(\frac{1}{4}\alpha_2 + \frac{3}{35}\omega))$$

$$-\frac{13}{90\tilde{R}_0^7}B_{I11}B_{If} + \frac{1}{60}\alpha_1\frac{B_{I11}}{\tilde{R}_0^2} - \frac{3}{700}\omega\frac{B_{If}}{\tilde{R}_0^3} - \frac{1}{80}\alpha_2\frac{B_{If}}{\tilde{R}_0^3}$$

Resolution for j=4, m=0

$$B_{40} = \frac{36}{35}\frac{\tilde{R}_{I21}}{\tilde{R}_0^5}(16B_{I21} + 3\dot{\tilde{R}}_0\tilde{R}_0^3\tilde{R}_{I21}) - \frac{19}{35}\frac{\tilde{R}_{If}}{\tilde{R}_0^5}(16B_{If} + 3\dot{\tilde{R}}_0\tilde{R}_0^3\tilde{R}_{If})$$

$$-\frac{19}{35}\alpha_1\tilde{R}_{If} + \frac{72}{35}\alpha_2\tilde{R}_{I21}$$

$$E'_{40} = \frac{\tilde{R}_{I21}}{\tilde{R}_0^5}(\frac{6336}{175}\dot{\tilde{R}}_0B_{I21} - \frac{108}{35}\tilde{R}_0\dot{B}_{I21} + \frac{2088}{175}\dot{\tilde{R}}_0^2\tilde{R}_0^3\tilde{R}_{I21} - \frac{36}{35}\ddot{\tilde{R}}_0\tilde{R}_0^4\tilde{R}_{I21} + \frac{912}{175}\alpha_2\dot{\tilde{R}}_0\tilde{R}_0^5)$$

$$+\frac{\tilde{R}_{If}}{\tilde{R}_0^5}(-\frac{9}{10}\tilde{R}_0\dot{B}_{If} - \frac{3344}{175}\dot{\tilde{R}}_0B_{If} - \frac{1102}{175}\dot{\tilde{R}}_0^2\tilde{R}_0^3\tilde{R}_{If} + \frac{57}{35}\ddot{\tilde{R}}_0\tilde{R}_0^4\tilde{R}_{If} - \frac{684}{175}\alpha_1\dot{\tilde{R}}_0\tilde{R}_0^5)$$

$$+\frac{90}{35\tilde{R}_0^8}B_{I21}{}^2 - \frac{19}{10\tilde{R}_0^8}B_{If}{}^2 - \frac{24}{7\tilde{R}_0^3}\alpha_2B_{I21} + \frac{57}{35\tilde{R}_0^3}\alpha_1B_{If}$$

Resolution for j=4, m=1

$$B_{41} = \frac{3}{5\tilde{R}_0^5}\tilde{R}_{I21}(8B_{If} + 3\dot{\tilde{R}}_0\tilde{R}_0^3\tilde{R}_{If}) + \frac{24}{5\tilde{R}_0^5}\tilde{R}_{If}B_{I21} + \frac{1}{5}\alpha_2\tilde{R}_{If} + \frac{9}{10}\alpha_1\tilde{R}_{I21}$$

$$E'_{41} = \frac{\tilde{R}_{I21}}{\tilde{R}_0^5}(-\frac{9}{10}\dot{\tilde{R}}_0\dot{B}_{If} + \frac{174}{25}\dot{\tilde{R}}_0^2\tilde{R}_0^3\tilde{R}_{If} - \frac{3}{5}\ddot{\tilde{R}}_0\tilde{R}_0^4\tilde{R}_{If} + \frac{291}{25}\dot{\tilde{R}}_0B_{If} + \frac{114}{50}\alpha_1\dot{\tilde{R}}_0\tilde{R}_0^5)$$

$$+\frac{\tilde{R}_{If}}{\tilde{R}_0^5}(-\frac{9}{10}\dot{B}_{I21} + \frac{399}{25}\dot{\tilde{R}}_0^2\tilde{R}_0^3\tilde{R}_{I21} + \frac{16}{25}\alpha_2\dot{\tilde{R}}_0\tilde{R}_0^5) + \frac{3}{2\tilde{R}_0^8}B_{If}B_{I21} - \frac{3}{2\tilde{R}_0^3}\alpha_1B_{I21} - \frac{3}{5\tilde{R}_0^8}\alpha_2B_{If}$$

Resolution for j=4, m=2

$$B_{42} = -\frac{1}{40\tilde{R}_0^4}\tilde{R}_{I11}B_{I11} - \frac{\tilde{R}_{I21}}{\tilde{R}_0^5}(\frac{841}{616}B_{I21} + \frac{9}{35}\dot{\tilde{R}}_0\tilde{R}_0^3\tilde{R}_{I21})$$

$$+\frac{\tilde{R}_{If}}{\tilde{R}_0^5}(\frac{16}{35}B_{If} + \frac{3}{35}\dot{\tilde{R}}_0\tilde{R}_0^3\tilde{R}_{If}) + \frac{1}{35}\alpha_1\tilde{R}_{If} + \tilde{R}_{I21}(\frac{3}{40}\omega - \frac{317}{1848}\alpha_2)$$

$$E'_{42} = -\frac{11}{200\tilde{R}_0^4}\dot{\tilde{R}}_0\tilde{R}_{I11}B_{I11} + \frac{\tilde{R}_{I21}}{\tilde{R}_0^5}$$

$$(\frac{9}{35}\tilde{R}_0\dot{B}_{I21} - \frac{1986}{1935}\dot{\tilde{R}}_0^2\tilde{R}_0^3\tilde{R}_{I21} + \frac{3}{35}\ddot{\tilde{R}}_0\tilde{R}_0^4\tilde{R}_{I21} - \frac{8939}{1960}B_{I21}\dot{\tilde{R}}_0 - \frac{2113}{9240}\alpha_2\dot{\tilde{R}}_0\tilde{R}_0^5 + \frac{33}{200}\omega\dot{\tilde{R}}_0\tilde{R}_0^5)$$

$$+\frac{\tilde{R}_{If}}{\tilde{R}_0^5}(-\frac{3}{35}\tilde{R}_0\dot{B}_{If} + \frac{1986}{5985}\dot{\tilde{R}}_0^2\tilde{R}_0^3\tilde{R}_{If} - \frac{1}{35}\ddot{\tilde{R}}_0\tilde{R}_0^4\tilde{R}_{If} + \frac{266}{105}\dot{\tilde{R}}_0B_{If} + \frac{16}{105}\alpha_1\dot{\tilde{R}}_0\tilde{R}_0^5)$$

$$-\frac{541}{1232}\frac{{B_{I21}}^2}{\tilde{R}_0^8} + \frac{{B_{If}}^2}{14\tilde{R}_0^8} + \frac{2}{7}\alpha_2 - \frac{1}{80\tilde{R}_0^8}{B_{I11}}^2 + \frac{2}{7}\alpha_2\frac{B_{I21}}{\tilde{R}_0^3} - \frac{3}{4\tilde{R}_0^3}\omega B_{I21} - \frac{3}{35\tilde{R}_0^3}\alpha_1B_{If}$$

Resolution for j=4, m=3

$$B_{43} = -\frac{\tilde{R}_{I21}}{\tilde{R}_0^5}\left(\frac{3919}{21875}B_{If} + \frac{3}{70}\dot{\tilde{R}}_0\tilde{R}_0^3\tilde{R}_{If}\right)$$

$$-\frac{3919}{21875\tilde{R}_0^5}B_{I21}\tilde{R}_{If} - \frac{4713}{87500}\alpha_1\tilde{R}_{I21} - \tilde{R}_{If}\left(\frac{521}{43750}\alpha_2 - \frac{67}{9375}\omega\right)$$

$$E'_{43} = \frac{\tilde{R}_{I21}}{\tilde{R}_0^5}\left(\frac{3}{140}\tilde{R}_0\dot{B}_{If} - \frac{114343}{218750}\dot{\tilde{R}}_0B_{If} - \frac{29}{75}\dot{\tilde{R}}_0^2\tilde{R}_0^3\tilde{R}_{If} + \frac{1}{70}\ddot{\tilde{R}}_0\tilde{R}_0^4\tilde{R}_{If} - \frac{54983}{437500}\alpha_1\dot{\tilde{R}}_0\tilde{R}_0^5\right)$$

$$+\frac{\tilde{R}_{If}}{\tilde{R}_0^5}\left(\frac{3}{140}\tilde{R}_0\dot{B}_{I21} - \frac{114343}{218750}\dot{\tilde{R}}_0B_{I21} - \frac{20318}{656250}\alpha_2\dot{\tilde{R}}_0\tilde{R}_0^5 + \frac{77}{46875}\omega\dot{\tilde{R}}_0\tilde{R}_0^5\right)$$

$$+\frac{2579}{87500\tilde{R}_0^8}B_{If}B_{I21} + \frac{5963}{87500\tilde{R}_0^3}\alpha_1B_{I21} + \frac{2813}{131250\tilde{R}_0^3}\alpha_2B_{If} - \frac{67}{9375\tilde{R}_0^3}B_{If}\omega$$

Resolution for j=4, m=4

$$B_{44} = -\frac{\tilde{R}_{If}}{\tilde{R}_0^5}\left(\frac{79}{1120}B_{If} + \frac{1}{280}\dot{\tilde{R}}_0\tilde{R}_0^3\tilde{R}_{If}\right) - \frac{197}{6720}\alpha_1\tilde{R}_{If}$$

$$E'_{44} = \frac{\tilde{R}_{If}}{\tilde{R}_0^5}\left(\frac{1}{20}\tilde{R}_0\dot{B}_{If} - \frac{29}{100}\dot{\tilde{R}}_0^2\tilde{R}_0^3\tilde{R}_{If} + \frac{1}{840}\ddot{\tilde{R}}_0\tilde{R}_0^4 - \frac{989}{5600}\dot{\tilde{R}}_0B_{If} - \frac{2207}{33600}\dot{\tilde{R}}_0\tilde{R}_0^5\alpha_1\right)$$

$$-\frac{3}{560\tilde{R}_0^8}B_{If}^2 - \frac{7}{240\tilde{R}_0^3}\alpha_1B_{If}$$

We give the values of the 15 harmonics used as a reminder for numerical computation:

$$
\begin{aligned}
Y_{10} &= \cos\theta \\
Y_{11} &= \sin\theta\cos\psi \\
\\
Y_{20} &= \frac{3}{2}\cos^2\theta - \frac{1}{2} \\
Y_{21} &= 3\sin\theta\cos\theta\cos\psi \\
Y_{22} &= 3\sin^2\theta\cos 2\psi \\
Y_f &= \sin^2\theta\cos^2\psi - \cos^2\theta \\
\\
Y_{30} &= \frac{5}{2}\cos^3\theta - \frac{3}{2}\cos\theta \\
Y_{31} &= \frac{3}{2}\sin\theta(5\cos^2\theta - 1)\cos\psi \\
Y_{32} &= 15\sin^2\theta\cos\theta\cos 2\psi \\
Y_{33} &= 15\sin^3\theta\cos 3\psi \\
\\
Y_{40} &= \frac{1}{8}(35\cos^4\theta - 30\cos^2\theta + 3) \\
Y_{41} &= \frac{1}{2}(35\cos^3\theta - 15\cos\theta)\sin\theta\cos\psi \\
Y_{42} &= \frac{1}{2}(105\cos^2\theta - 15)\sin^2\theta\cos 2\psi \\
Y_{43} &= 105\cos\theta\sin^3\theta\cos 3\psi \\
Y_{44} &= 105\sin^4\theta\cos 4\psi
\end{aligned}
$$

To calculate $\tilde{R}_I$ and $\tilde{\phi}_I$, we use the expressions found previously :

$$
\begin{aligned}
\tilde{R}_I &= \tilde{R}_{I00} + \tilde{R}_{I10}Y_{10} + \tilde{R}_{I11}Y_{11} + \tilde{R}_{I21}Y_{21} + \tilde{R}_{If}Y_f \\
\tilde{\phi}_I &= \frac{q}{2} + \frac{B_{I00}}{\tilde{r}} + \frac{1}{\tilde{r}^2}(B_{I10}Y_{I10} + B_{I11}Y_{I11}) + \frac{1}{\tilde{r}^3}(B_{I21}Y_{21} + B_{If}Y_{If})
\end{aligned}
$$

Potential at order 1 and q (intensity of the equivalent source for the bubble at order 0) are computed using the expressions found previously:

$$
\begin{aligned}
q &= -\tilde{R}_0^2\dot{\tilde{R}}_0 \\
B_{I00} &= -(\tilde{R}_0^2\dot{\tilde{R}}_{I00} + 2\tilde{R}_0\dot{\tilde{R}}_0R_{I00}) \\
B_{I10} &= -\frac{\tilde{R}_0^3}{2}\dot{\tilde{R}}_{I10} - \tilde{R}_0^2\dot{\tilde{R}}_0\tilde{R}_{I10}
\end{aligned}
$$

$$B_{I11} = -\frac{\tilde{R}_0^3}{2}\dot{\tilde{R}}_{I11} - \tilde{R}_0^2\dot{\tilde{R}}_0\tilde{R}_{I11}$$

$$B_{I21} = -\frac{\tilde{R}_0^4}{3}\dot{\tilde{R}}_{I21} - \frac{2}{3}\tilde{R}_0^3\dot{\tilde{R}}_0\tilde{R}_{I21} + \frac{2}{9}\tilde{R}_0^5\alpha_2$$

$$B_{If} = -\frac{\tilde{R}_0^4}{3}\dot{\tilde{R}}_{If} - \frac{2}{3}\tilde{R}_0^3\dot{\tilde{R}}_0\tilde{R}_{If} + \frac{1}{3}\tilde{R}_0^5\alpha_2$$

$\tilde{\omega}$ which didn't appear in the previous equations is calculated as follows:

$$\vec{\omega} = \frac{1}{|V_0|^2}(\vec{V}_0 \times \frac{d\vec{V}_0}{dt}) \tag{105}$$

where V_0 is the velocity of the origin of the frame. The normalisation of ω is given by the scale Ω such as : $\Omega T_0 = e$. In the particular case where the origin of the frame is following a material point in the initial flow field, the expression of ω is easy to find : if we denote $W_r\vec{e_r} + \vec{V_\infty}$ the velocity of this point,

$$\frac{d\vec{V}_0}{dt} = \frac{dW_r}{dr}(\vec{V}_0.\vec{e_r}) + \frac{W_r}{r}(\vec{V}_0 - \frac{dr}{dt}\vec{e_r}) \tag{106}$$

which gives:

$$\omega = -\sin\theta\frac{V_\infty}{|V_0|^2}(W_r + V_\infty\cos\theta)(\frac{W_r}{r} - \frac{dW_r}{dr}) \tag{107}$$

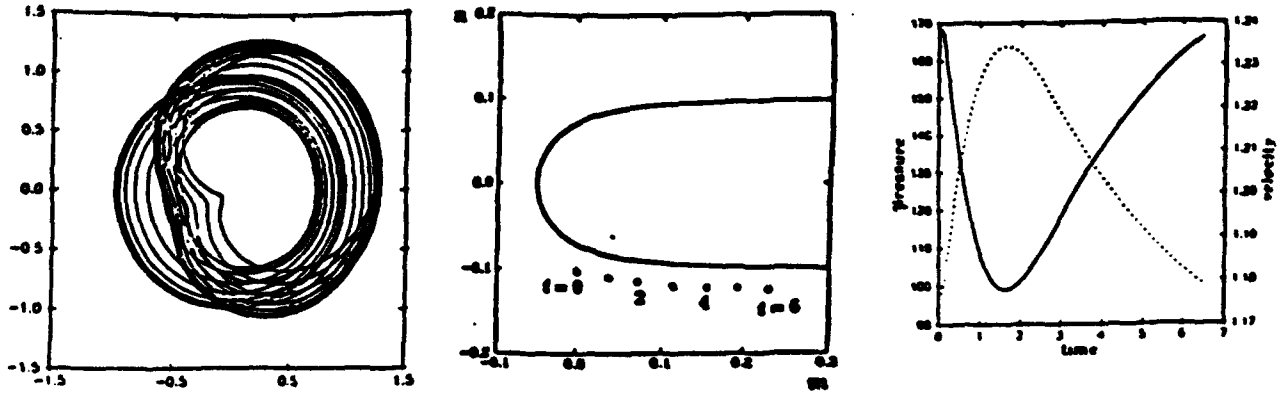

a b c

Figure 1a-c: Fig. 1b and Fig. 1c show the geometry and flow field of the problem considered. The trajectory of the bubble center along the headform (of radius 10 cm) is indicated in Fig. 1b. The pressure (in Pa - y axis) and the velocity (in ms^{-1} - right y axis) of the basic flow along this streamline, are plotted against the non-dimensional time. The free stream velocity is 1.15 ms^{-1}. Fig. 1a shows the computed bubble contours for $\epsilon = 0.3$, and time between $0.1T_0$ to $2T_0$. Bubble translation, rotation and re-entrant jet formation are clearly seen.

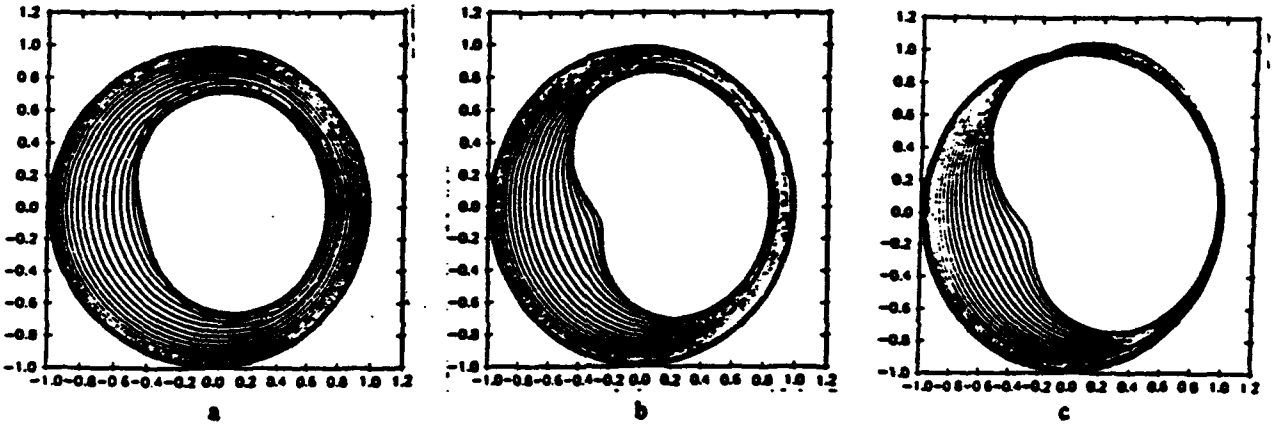

a b c

Figure 2a-c: Bubble contours at various times for $\epsilon = 0.15, 0.3$ and 0.6. Here the initial bubble radius was kept constant at 1 cm, while the initial standoff from the head form was varied to change ϵ. Increasing interaction is seen with decreasing standoff.

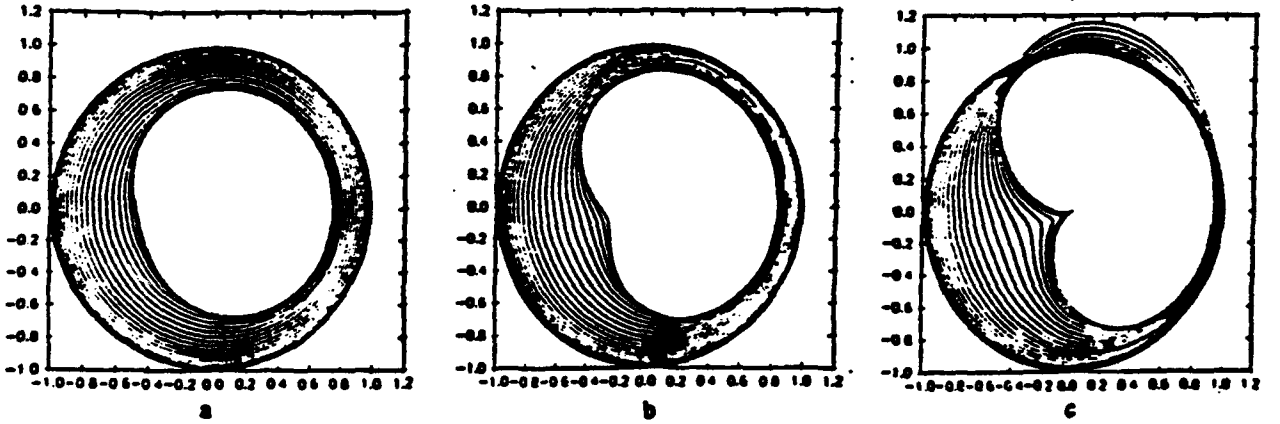

a b c

Figure 3a-c: Bubble contours at various times for $\epsilon = 0.15, 0.3$ and 0.6. Here the initial standoff distance l_0 was kept constant at 3.333 cm, while the initial radius was varied to change ϵ. Increasing interaction is seen with increasing initial bubble size.

8 Conclusion

Application of the theory previously described has been made in the case of a Rankine body, described by the initial flow potential :

$$\phi_0 = V_\infty x + \frac{Q}{r}$$

The broadth of the body at infinity is : $R = 2\sqrt{\frac{Q}{\pi V_\infty}}$
and the stagnation point occurs for: $x = -\frac{R}{4}$

Figures 1,2 and 3 describe the conditions of calculations, and show results for a frame moving with the equivalent point on the streamline at order ϵ (section 4).

Figures 4 show the comparison at order ϵ between results obtained in a frame moving with the equivalent point on the streamline and a frame fixed at the center of the bubble (section 5).

Figures 5 are results for streamlines at order 1 for the inner problem: they encounter of the streamlines obtained in the potential $\phi_0 + \phi_{ext}\bar{\phi}_0$, in both cases of a growing bubble and a collapsing bubble (section 6).

Figures 6 are results for bubble shapes at order ϵ^2. They enable the comparison with results of order ϵ. The frame center is moving as the equivalent material point in the initial potential flow. The re-entering jet is rotating increasingly towards the body wall as ϵ grows. (x axis is directed towards the trajectory, y axis is directed opposite to the body wall). Taking a frame center moving as the bubble mass center would allow results closer to the end of the collapse.

9 Improvments

In order to describe the evolution of the bubble collapse longer, a translation velocity of the frame should be introduced. The description of the reentering jet has two causes: the bubble collapse is the physical one, the movement of the frame is the second one. Using the fact that the frame is moving with the equivalent point on the streamline or that the frame is fixed to the center of the bubble are two different assumptions, and, therefore, the results obtained are different. The most interesting description would probably be to use a frame moving with a velocity belonging to the two extreme cases we have selected. This has to be completed.
The introduction of the surface tension at orders ϵ^1 and ϵ^2 would also be an improvment.
Finally, results should be compared with those of the three dimensional boundary element method (3DYNAFS).

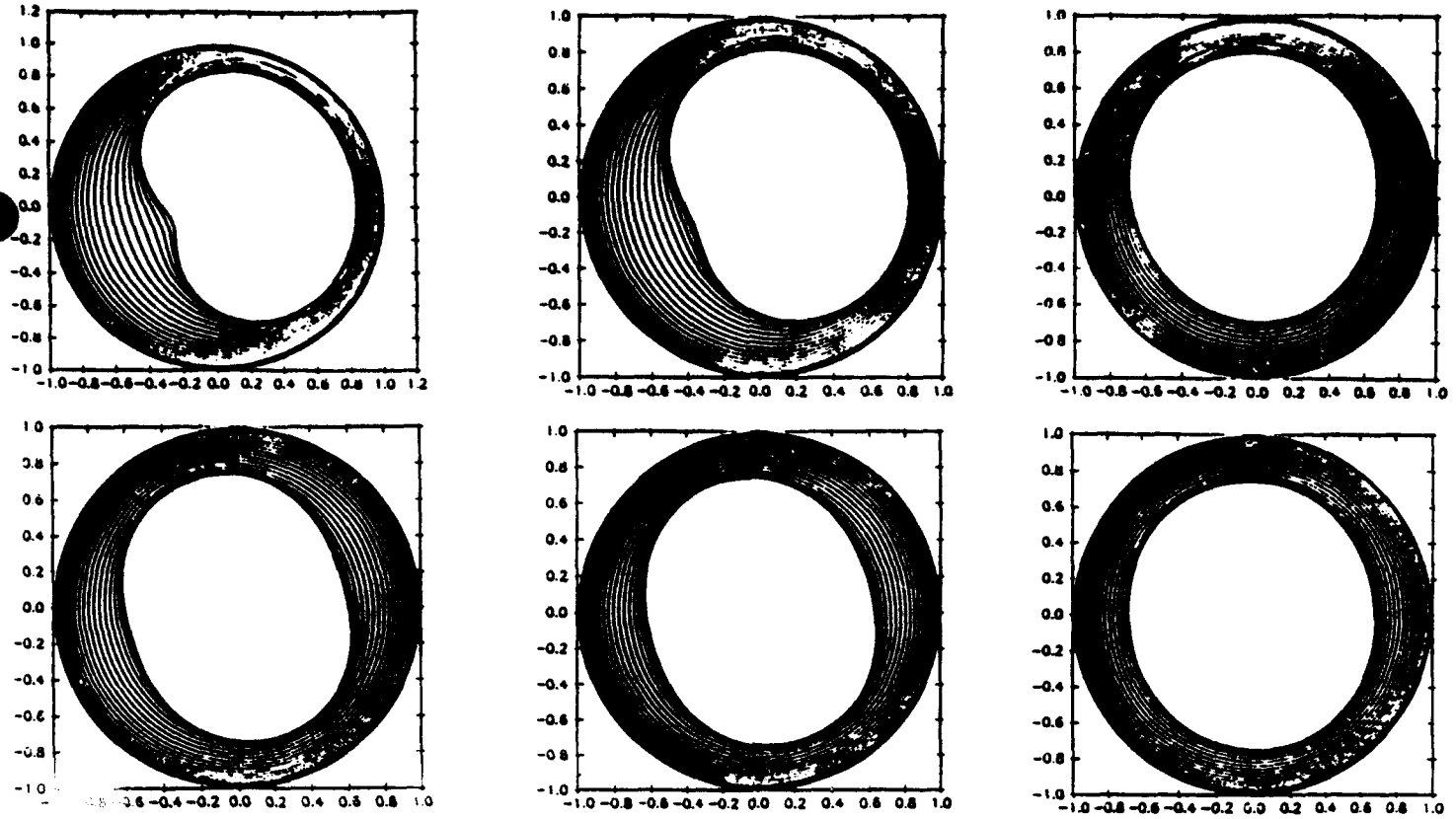

Figures 4 : Bubble contours at various times and for various values of angle ψ. Figures above are for $\varepsilon = 0.3$ and figures below are for $\varepsilon = 0.6$. From the left to the right, we have : $\psi = 0, \pi/4, \pi/2$. Top ones correspond to a frame fitted to the equivalent material point on the stream-line, bottom ones correspond to a frame such as the origin is kept at bubble center. The standoff distance to the Rankine body wall is kept constant equal to 3.33 cm.

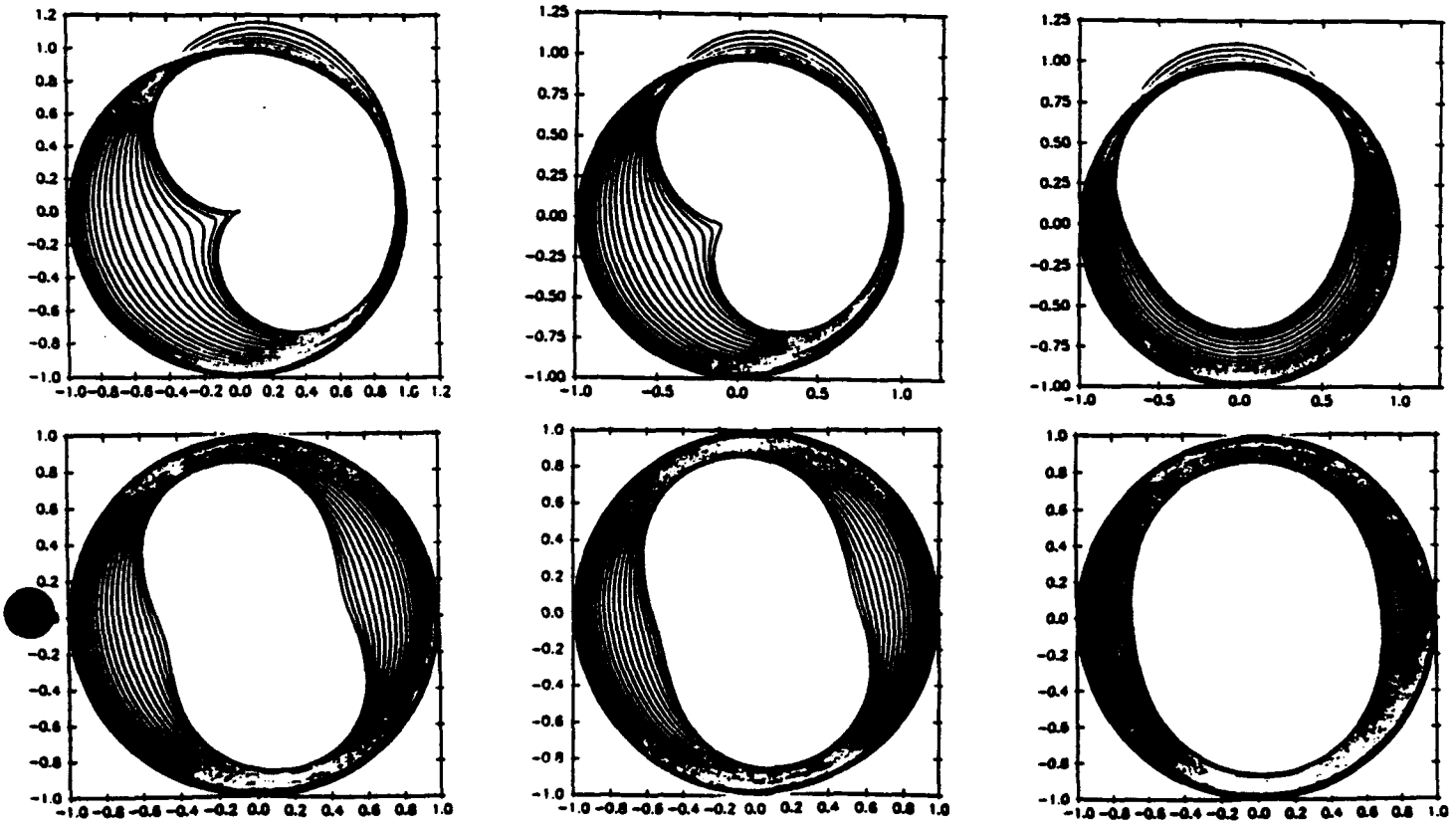

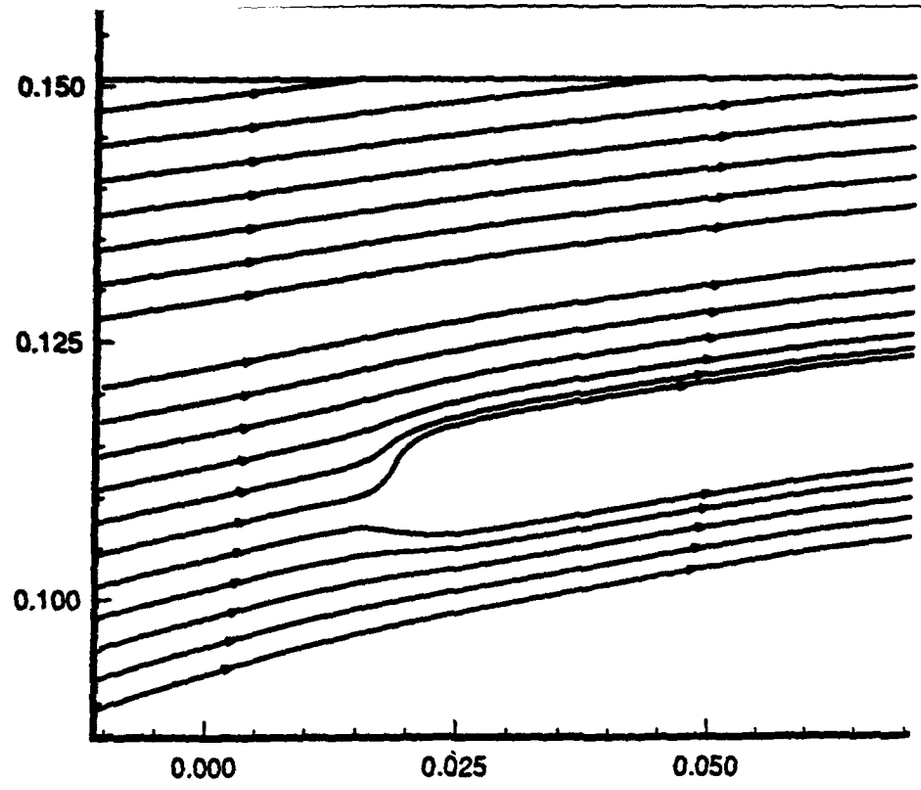

Figures 5 : Flow field stream-lines modified by the presence of the bu ble, in the plane (Oxz).
Figure above corresponds to a growing bubble, figure below to a collapsi one ($\epsilon = 0.3$, same case than figure 4 during the expansion and the collap ing).
Both have been computed using Euler's method.

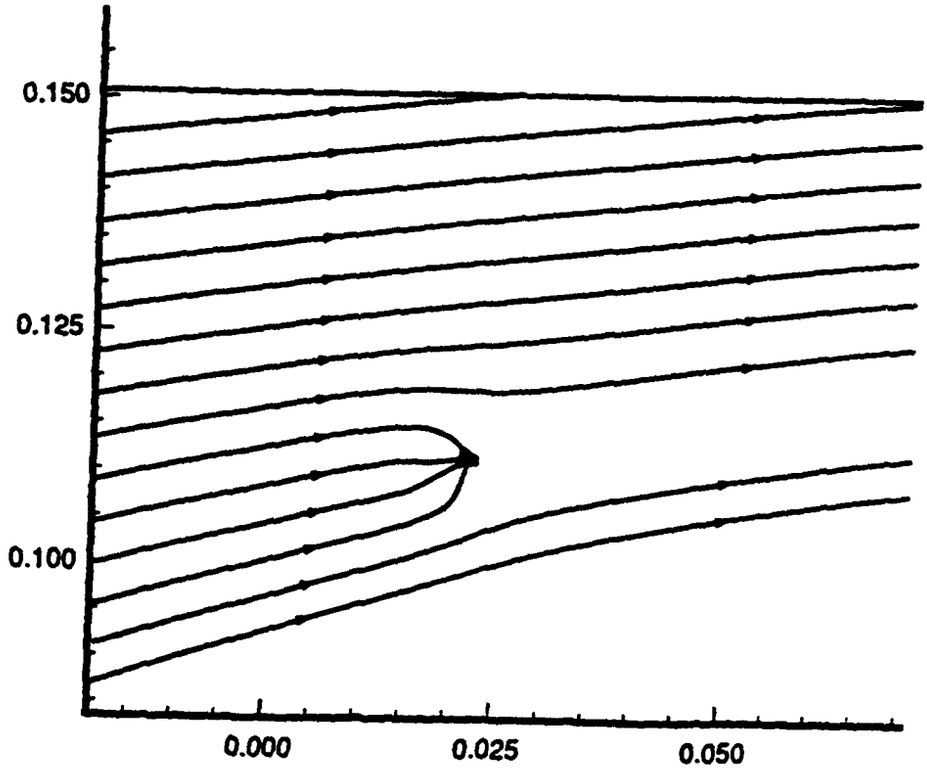

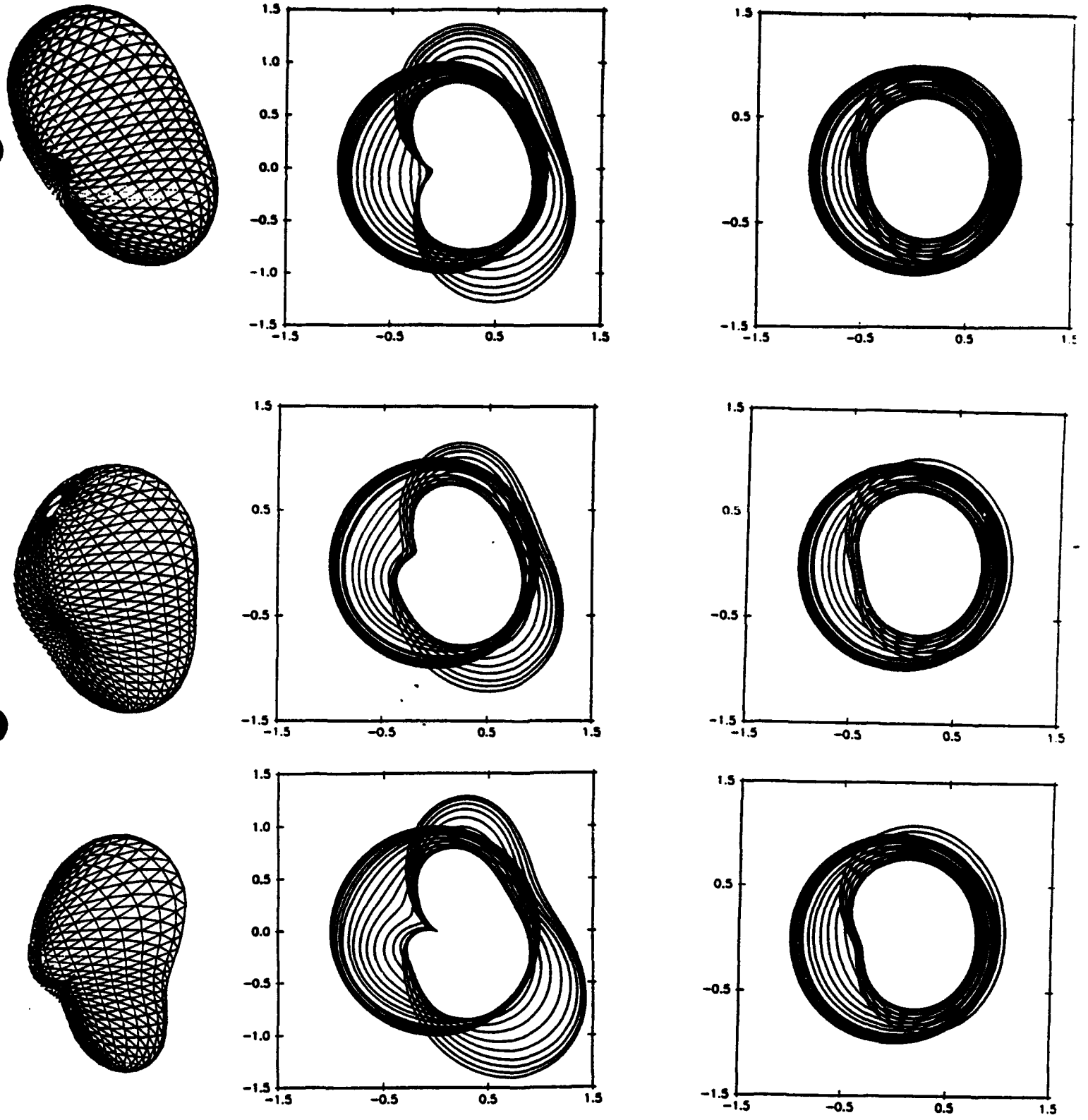

Figures 6: From top to bottom, bubble contours for $\epsilon = 0.3; 0.4$ and 0.5. 3D ones and left cross-cuts are contours of order ϵ^2. Right cross-cuts are contours of order ϵ. The standoff distance to the body wall has been kept constant equal to 3.33cm. Bubbles radius have been aimed to fit the different values of ϵ.
The jet is much stronger and rotates more at order ϵ^2; also remark that the opposite face of the bubble flattens.

DYNAFLOW, Inc.

Report 6.002_11

ASYMPTOTIC STUDY OF BUBBLE CLOUD DYNAMICS IN A SLIGHTLY COMPRESSIBLE FLUID

by
Laurent Mauduit
and
Georges L. Chahine

July, 1992

Introduction

Every liquid which is not completely pure contains many microscopic bubbles. In an oscillating pressure field these bubbles can grow explosively and collapse developing high pressures: this phenomenon is called cavitation.

Useful or harmful cavitation can arise in numerous applications, anti-submarine warefare is surely the most famous one. In fact, naval research programs include a great part on cavitation. Localization and identification of submarine can be facilitated by cavitation, also erosion of propeller blade is caused by cavitation. The power of underwater explosion can be increased thanks to progress in control of the generated bubble collapse. Cavitation is used for medical purposes like eye surgery. Industry needs cavitation to emulsify a system of two immiscible liquids such as oil and water. It is used in ultrasonic cleaning systems. Recently it has been reported that a Japanese company plans to market ultrasonic washing machines and dishwashers. The cavitation which appears sometimes in nuclear reactors becomes very harmful for the cooling system.

Although cavitation mostly occurs in a cluster of microbubbles, most of the models are developed using a single bubble dynamics. However most of the time the interaction with the collapse of surrounding bubbles cannot be neglected. Thus in this report we will try to modelise the dynamic of a bubble cloud. Indeed the past studies proposed by G. Chahine [3] gave us a model neglecting the compressibility of the fluid. The object of this work is to introduce the influence of compressibility in the equations and to compute the change using Chahine's software.

The first part of this report shows the influence of the compressibility of the fluid at order 0 using Keller-Herring equation [] and Chahine's numerical code [3] . In the second part we try to develop a model of bubble cloud taking into account the weaknesses of previous studies: the medium is compressible not only because of the fluid itself but also because of the presence of gas. We will try to combine the approaches of Prosperetti and Lezzi [5] and that of D'Agostino and Brennen [6].

1 Cloud behaviour in a slightly compressible flow

1.1 Asymptotic theory for bubble flow interactions

Consider a cloud of N bubbles of radius r_b^i, $i = 1, \ldots, N$ immersed in a liquid. The bubbles are initially assumed to be at rest and at equilibrium with the surrounding fluid. The characteristic radius of the bubbles is r_{b0} . We denote the initial distance between bubbles i and j as l_0^{ij}, which we take to be of the order of the characteristic distance l_0 .

The asymptotic method that we have developed is centered on the following approach. The problem is addressed by a decomposition of both time and space domains into multiple scales. For instance, the dynamics of any bubble is obtained by considering an inner problem of scales r_{b_0} and T_i (a characteristic inner problem time scale), and a outer problem of scale l_o and T_o. An asymptotic analysis of the problem can be developed when these various scales are of different orders of magnitude. For the bubble interactions the expansion may be realised when the scale of the inner problem and the outer problem are really different. We introduce in this case a small parameter that will be responsible for the perturbation. Let's call ϵ this perturbation parameter: $\epsilon = \frac{r_{b_0}}{l_0}$. We assume in the following $\epsilon \ll 1$.

In sections 2.2 and 2.3 the outer problem is associated with the macroscopic behaviour of the cloud. A bubble then appears as a superposition of singularities of various orders, whereas the inner problem provides the microscopic details of the behaviour of the flow in the vicinity of an individual bubble center B_i. The boundary conditions at infinity for the inner problem are therefore obtained at each order of approximation by the asymptotic behaviour of the outer solution in the vicinity of B_i. Thus if one knows the behaviour of all bubbles except B_i, the motion, deformation and pressure field due to this cavity can be determined by solving easier linearized forms of the equations. At the lowest order, $\epsilon = 0$, each bubble (of index i) behaves spherically. The combination of all these first approximations of each inner problem provides a description of the whole first order flow field (i.e. a distribution of sources or sinks representing all bubble oscillations). The behaviour of this outer flow field in the vicinity of each bubble sets the

boundary conditions at infinity at the following order of approximation, ϵ, for the corresponding inner problem. The same process is then repeated for the successive orders.

1.2 Incompressible fluid

The study of the cloud in an incompressible fluid, using the preceding method, has been done by G. Chahine, K. Kalumuck and T. Perdue [3] .

For this work we will use the numerical codes they have created where they neglect not only the viscosity and the compressibility but also the heat and mass transfer. The great contribution of these reseachers was to discover that until order $O(\epsilon^3)$ the problem of the cloud was similar to a problem of two bubbles: the bubble i and an equivalent bubble G_i (*figure 1*). This constatation simplifies a lot the problem without affecting the precision of the calculation.

figure 1: Multibubble Interaction Equivalence Concept

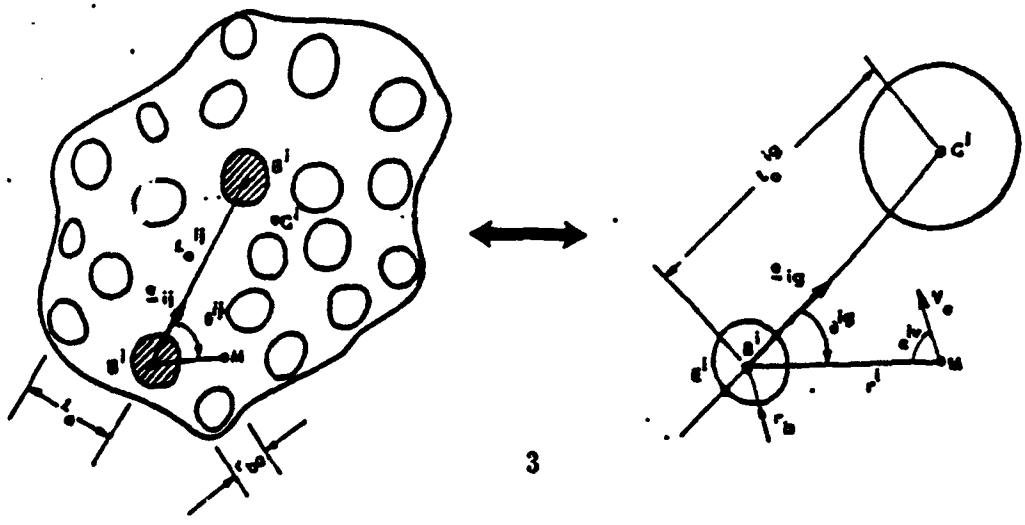

During this study we showed using the work of Takahira and Akamatsu [7] that at higher orders the above approximation was not justified. We will not explain all the resolution of Chahine's work, but we just give the most important equations to understand the goal of the work. Thanks to the concept of equivalent bubble the equations are easier, at least for the lowest orders. Neglecting the compressibility Chahine considers two different problems: the inner and the outer problem. In the next section we will come back on this assumption.

The equivalent bubble is centered at G_i. The growth rate and position of this equivalent bubble are determined by the distribution and the growth rate of the other cavities. In general, this fictituous bubble equivalent to the "rest-of-the-cloud", and the corresponding "cloud center" and "equivalent bubble intensity" are different for each bubble. If θ_{ig} is the angle between the centers' direction B_iG_i and the direction of a field point B_iM, the equation of the surface of the axisymmetric bubble B_i can be written in the form:

$$\begin{aligned} R(\theta_{ig},\phi,t) &= a_0^i(t) + \epsilon a_1^i(t) + \epsilon^2\left[a_2^i(t) + f_2^i(t).cos\theta_{ig}\right] \\ &\quad + \epsilon^3\left[a_3^i(t) + f_3^i(t).cos\theta_{ig} + g_3^i(t)\mathcal{P}_2(cos\theta_{ig})\right] + o(\epsilon^3) \end{aligned}$$

where $\mathcal{P}_2$ is the Legendre polynomial of order 2, and argument $cos\theta_{ig}$. The components, a_n^i, f_n^i and g_n^i, satisfy linear second order differential equations which can be written in symbolic form as follows:

$$D_2\left(y_n^i\right) = \sum\left(\frac{l_o}{l_0^{ij}}\right)^m F_j^i\left(y_0^i,\ldots,y_{n-1}^i\right) P_m(cos\theta_{ig}).$$

Here $D_2(y_n^i)$ represents a differential operator of the second order in time acting on the radius component y_n^i (one of a_n^i, f_n^i , g_n^i) of the bubble i; m is an integer indicating the order of the spherical harmonic.

The behaviour of B_i can be computed by integration of the obtained system of differential equations using a multi-Runge-Kutta procedure. the behaviour of the whole cloud is thus obtained. Earlier studies have shown that collective bubble behaviour can have a dramatic effect on both bubble growth and implosion. Specifically, bubble growth is inhibited by bubble interactions, while bubble collapse is enhanced. This cumulative effects come from the fact that the interaction reduces any driving pressure drop as a result of the other bubble growth, while it increases the collapse driving pressure as a result of the other bubble collapse. Due to the cumulative effects of the collapse of all the bubbles in the cloud, each bubble ends its collapse under the influence of a pressure which is orders of magnitude higher than that for an isolated bubble.

1.3 Slightly compressible fluid.

We will not go into the details of obtention of the equations which we will do in the next section. We will say that the component $a_0^i(t)$ of the bubble i ($r = R(\theta_{ig}, \phi, t) = a_0^i(t) + \varepsilon a_1^i(t) + \dots$) verifies the Rayleigh-Plesset equation (Equation 1).

$$\rho\left[a\ddot{a} + \frac{3}{2}\dot{a}^2\right] = p_B - p_\infty \tag{1}$$

where p_B is the pressure at the bubble wall:

$$p_B = p_v + p_{g0}\left(\frac{V_0}{V}\right)^\gamma - C\sigma, \tag{2}$$

where p_{g0} and V_0 are the initial gas pressure and volume respectively, σ is the surface tension, C the local curvature of the bubble, V the instantaneous value of the bubble i volume, and γ the polytropic constant, with $\gamma = 1$ for isothermal behaviour and $\gamma = 1.4$ for adiabatic conditions. Here p_{g0} and V_0 are known quantities at $t = 0$.

In fact introducing the compressibility of the fluid at order 0 modifies the equation of the radius of the bubble. The classical Rayleigh-Plesset equation becomes of the Keller-Herring form (Equation 3).

This equation can be written as

$$\rho\left[\left(1 - \frac{\dot{a}}{c}\right)a\ddot{a} + \frac{3}{2}\left(1 - \frac{\dot{a}}{3c}\right)\dot{a}^2\right] = \left(1 + \frac{\dot{a}}{c} + \frac{a}{c}\frac{d}{dt}\right)(p_B - p_\infty) \tag{3}$$

where c is the sound speed.

To nondimensionalize this equation we need to introduce a new perturbation parameter M which is a Mach number:

$$M = \frac{r_{b_0}/T_i}{c_{ref}} \tag{4}$$

where c_{ref} is the sound speed in the fluid at rest.

Let's call

$U = (V_0/V)^\gamma$

$\mathcal{P} = (p_{0_\infty} - p_v)/\Delta P$

$\mathcal{W} = (r_{b_0}\Delta P)/2\sigma$: Weber number

$\Delta P = \max |p_\infty(t) - p_{0_\infty}|$

$a = a(t)$ radius of the bubble at time t
p_{0_∞} initial pressure at infinity
a_0 initial radius of the bubble

Equation (3) becomes:

$$\left(1 - M\dot{\bar{a}}\right)\bar{a}\ddot{\bar{a}} + \frac{3}{2}\left(1 - M\dot{\bar{a}}\right)\dot{\bar{a}}^2 =$$

$$\left(1 + M\dot{\bar{a}}\right)\left[\mathcal{P}\left(U - 1 - 3\gamma U\dot{\bar{a}}\right) + 2\mathcal{W}^{-1}\left(\frac{U}{\bar{a}_0} - \frac{1}{\bar{a}} - \frac{3\gamma M U\dot{\bar{a}}}{\bar{a}_0} + M\frac{\dot{\bar{a}}}{\bar{a}}\right)\right.$$

$$\left. -\bar{p}_\infty(\bar{t} + M\bar{a}) + \bar{p}_{0_\infty}\right] \qquad (5)$$

Taking $M = 0$ in (5), we find the classical equation of Rayleigh-Plesset (1).

This equation verified at order ϵ^0 by the component of the radius a_0 of each bubble shows that the compressibility at order M is only a correction of the Rayleigh evolution of each bubble. As we know that the behaviour of each bubble has a cumulative effect on the collapse of all bubbles, we may predict that the compressibility can have a strong effect on the cloud. To verify this assumption and to know how strong is the effect of the compressibility on the cloud, we have investigated the effects of this equation on Chahine's code. In most figures shown below the bubbles are in the same plane OYZ. This simplification could seem useless if we know how Chahine's code proceeds: each bubble is computed using the equivalent bubble concept. One could have used more general cases. Our choice was motivated by

two reasons. The first one is because it is easier to understand the changes of the cloud seeing the all bubbles together. The most accurate representation is to cut the cloud by a plane including all the shapes. Then one has only to compute the translations and the rotations of all the bubbles. The second reason is that we could compare the results of this code with those obtained with a completly different method which accounts for large bubble deformations. Indeed Dynaflow Inc. is working on a 3D code (3DynaFS). Most of the studied cases were in a plane.

1.4 Figures :

Figure 2 shows $R(\theta_{ig} = 0, t)$ versus time for one bubble in a 6-bubble cloud. The bubbles are at equilibrium at $t = 0$ when they are subjected to a sudden pressure drop. The bubbles have an initial radius of 0.01 cm and are arranged at equal distances from the origin along the three coordinate axes:

$$r_{b_0} = 10^{-4}\ m$$
$$\varepsilon = 0.07$$
$$\sigma = 7.28 \times 10^{-2}\ \text{N / m}$$
$$\mathcal{P} = \frac{p_{0_\infty} - p_v}{\Delta P} = 2$$
$$\mathcal{W} = \frac{r_{b_0} \Delta P}{2\sigma} = 680$$
$$\Delta P = \max | p_\infty(t) - p_{0_\infty} | = 10^6\ Pa$$

The solid line indicates the incompressible solution. Also plotted is the corresponding curve for $M = 0.01$ (small dashes), $M = 0.03$ (small dash-dot), and $M = \epsilon = 0.07$ (dash dot). Even if for $M = \epsilon$ our approximation is not completly justified this figure gives a good idea of the effect of the compressibility. Not only the compressibility reduces the magnitude of the radius variation but also it changes slightly the frequence of the oscillations. This is fundamental from an acoustician point of view.

Figure 2

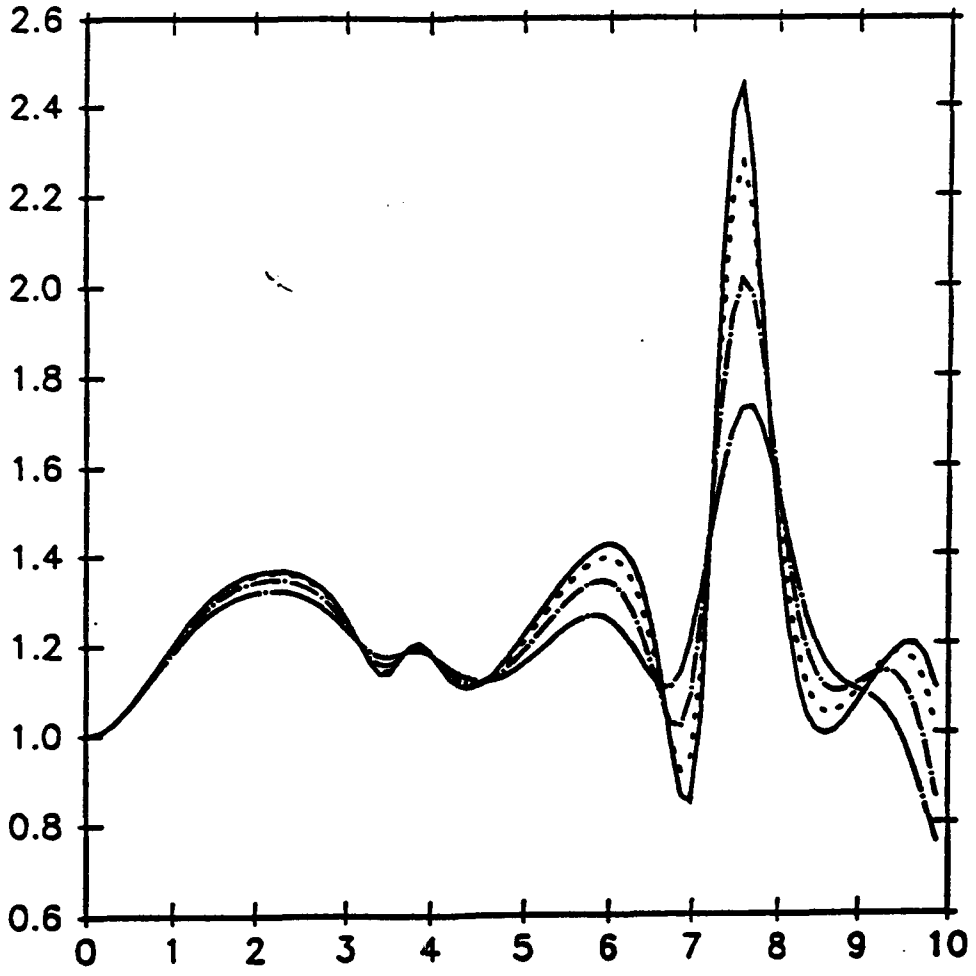

Figures 3, 4, 5, 6 shows a 6-bubble cloud evolution in a liquid more or less compressible. The bubbles are at equilibrium at $t = 0$ when they are subjected to a sudden pressure drop. The bubbles have an initial radius of 10^{-3} m and are arranged in the plane OYZ symetricaly with respect of the two coordinate axes: *figure 3* shows $R(\theta_{ij} = 0, t)$ versus time, the solid line indicates the incompressible solution which breaks down at $t = 3.2$. Also plotted is the corresponding curve for $M = 0.08$ (small dashes), and $M = \epsilon = 0.2$ (dash dot). *Figure 4* shows growth and collapse of the bubble cloud in an incompressible fluid. *Figure 5* shows growth and collapse of the bubble cloud in a slightly compressible fluid: $M = 0.08$. *Figure 6* shows growth and collapse of the bubble cloud in a compressible fluid: $M = \epsilon = 0.2$

.

$$r_{b_0} = 10^{-3}\ m$$
$$\epsilon = 0.2$$
$$\sigma = 7.28 \times 10^{-2}\ \text{N / m}$$
$$\mathcal{P} = \frac{P_{\infty_0} - P_v}{\Delta P} = 2$$
$$\mathcal{W} = \frac{r_{b_0} \Delta P}{2\sigma} = 680$$

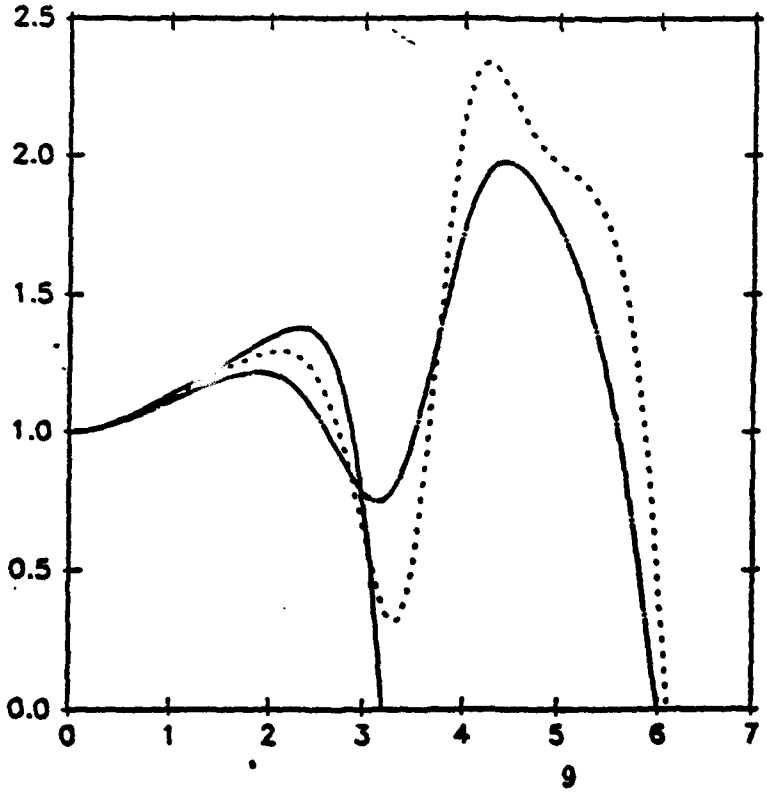

Figure 3

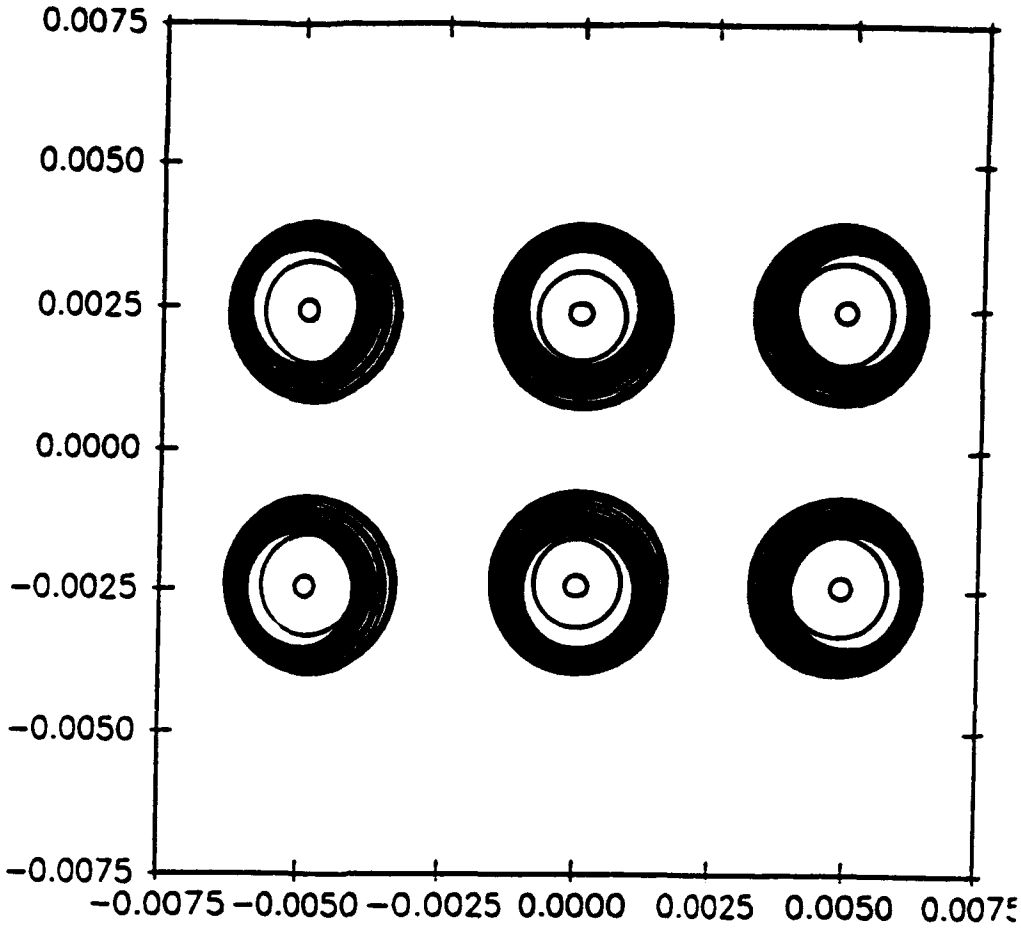

Figure 4: $M = 0$

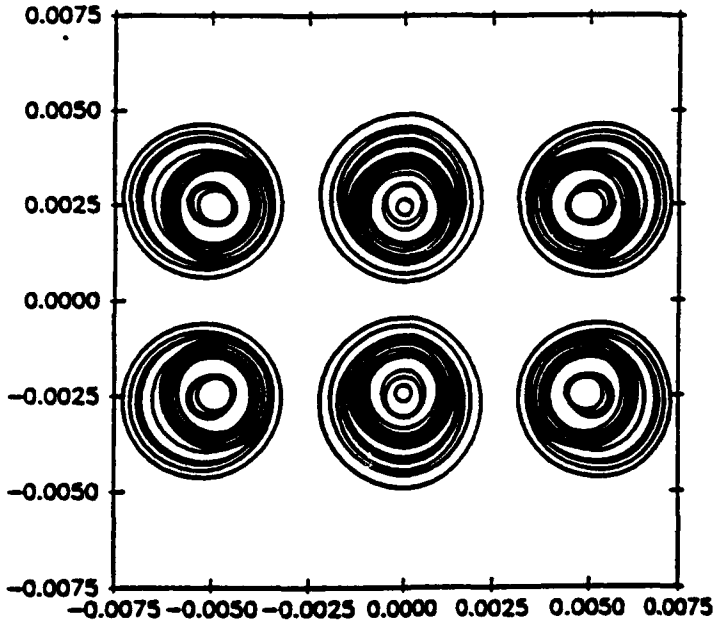

Figure 5: $M = 0.08$

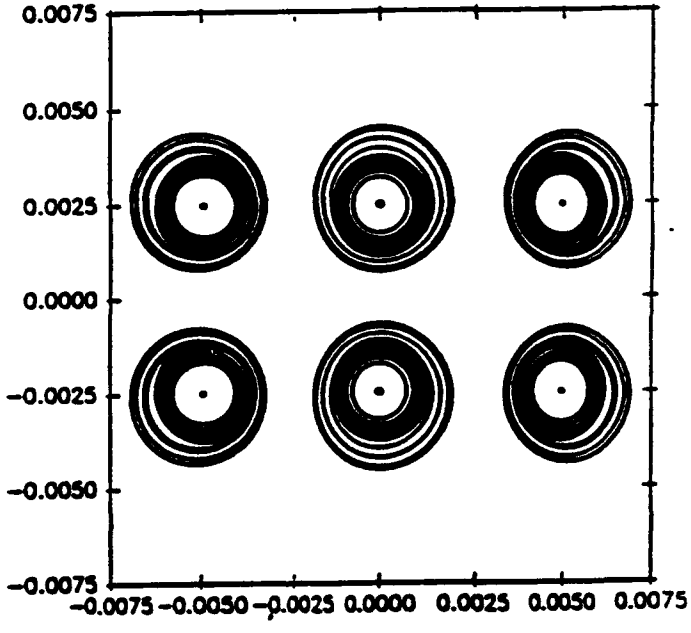

Figure 6: $M = \epsilon = 0.2$

The *figures 7, 8, 9, 10* shows a 4-bubble cloud evolution in a liquid compressible or not. The bubbles are at equilibrium at $t = 0$ when they are subjected to a sudden pressure drop. The initial radius of the big bubble is 5×10^{-3} m and 10^{-3} m for the small one. They are arranged in the plane OYZ symetricaly with respect to the two coordinate axes:

Figure 7 shows $R(\theta_{ig} = 0, t)$ versus time of the big bubble. *Figure 8* shows $R(\theta_{ig} = 0, t)$ versus time of the small bubble. The solid line indicates the incompressible solution. Also plotted is the corresponding curve for $M = 0.2$ (small dashes). *Figure 9* shows the cloud in a compressible fluid $M = 0.2$. *Figure 10* shows the cloud in a incompressible fluid. On this figures we observe clearly the formation of the jet. The collapse in the compressible fluid is slightly delayed.

$$r_{b_0} = 5 \times 10^{-3}\ m$$
$$\varepsilon = 0.25$$
$$\sigma = 7.28 \times 10^{-2}\ \text{N / m}$$
$$\mathcal{P} = \frac{P_{\infty_0} - P_v}{\Delta P} = 0.5$$
$$W = \frac{r_{b_0} \Delta P}{2\sigma} = 680$$

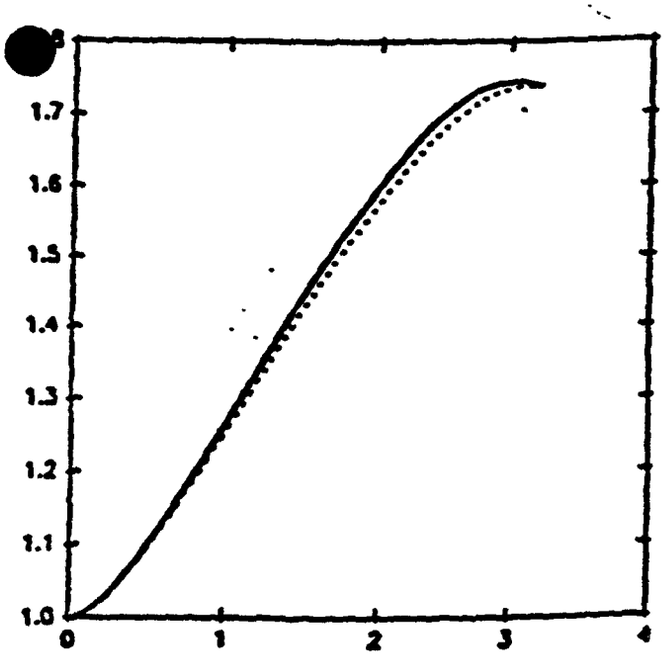

Figure 7

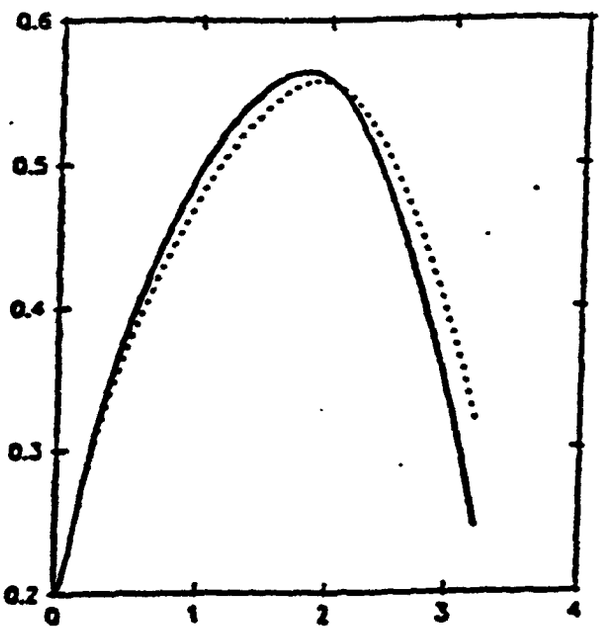

Figure 8

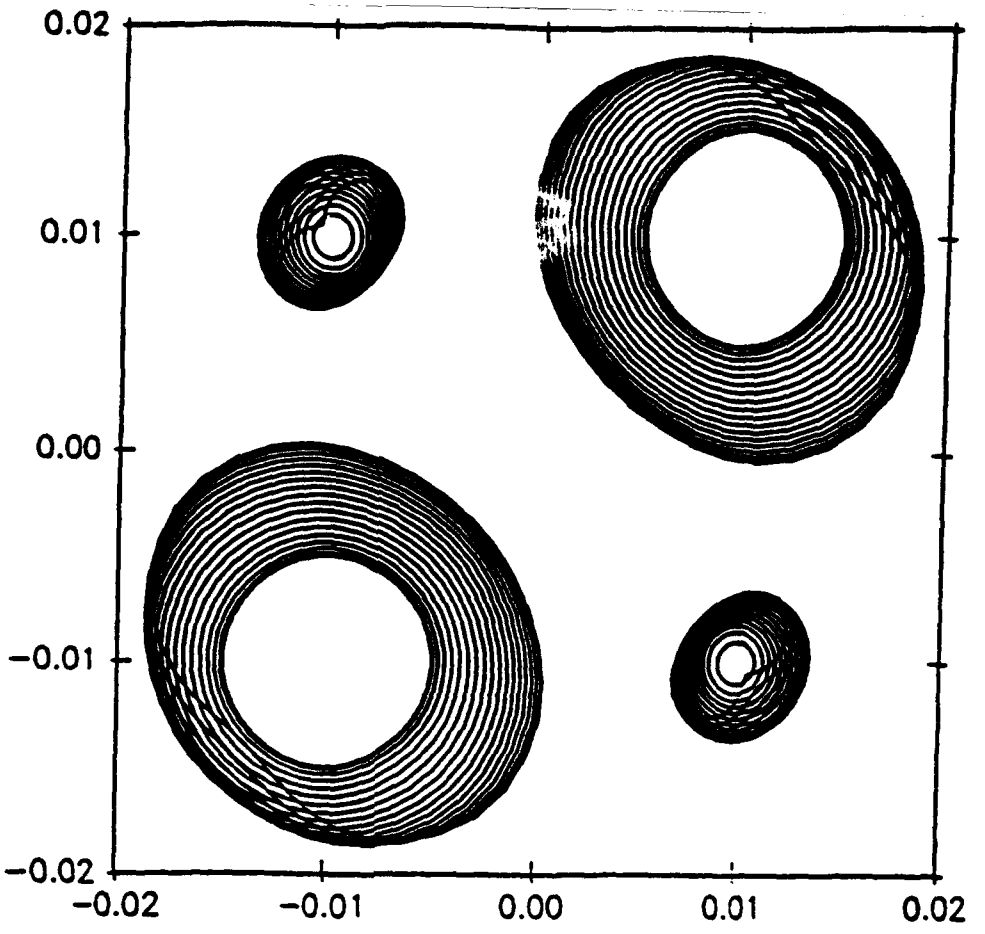

Figure 9

Figure 10

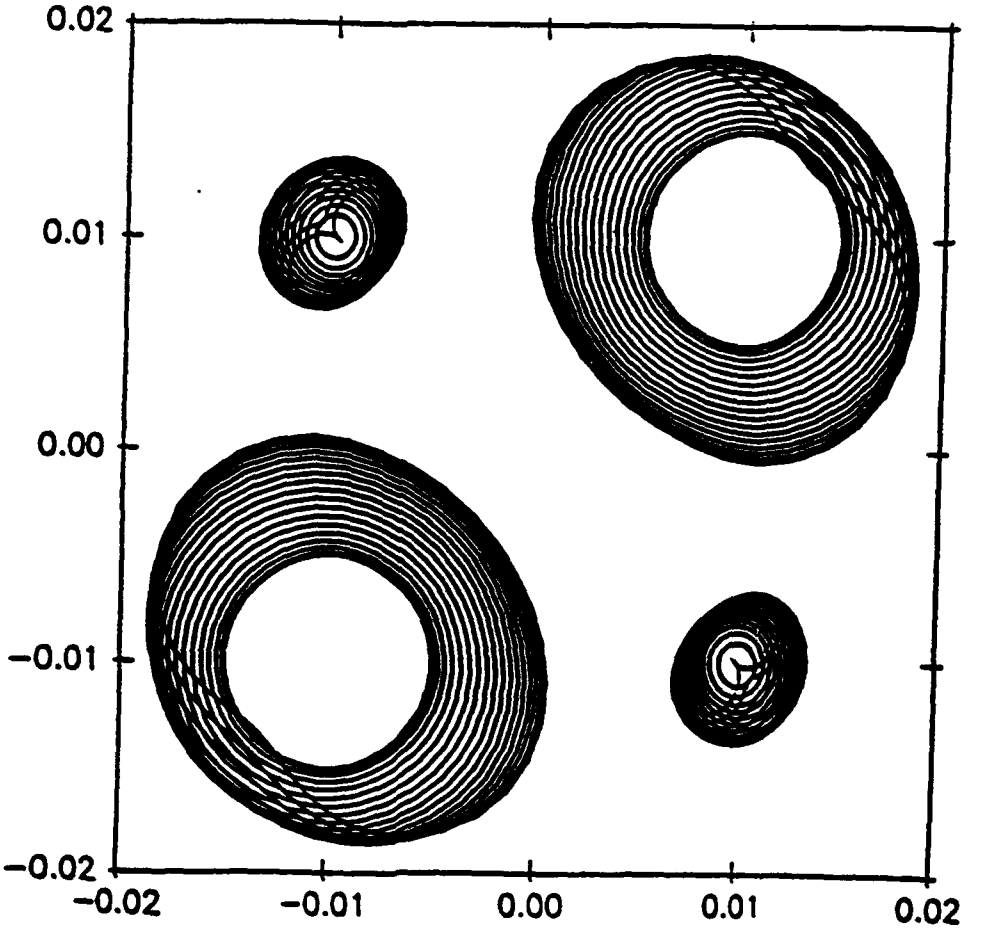

These following figures show a 12-bubble cloud in an incompressible fluid. All bubbles have not the same initial size. Initial radius of big bubbles is 5×10^{-3} m, initial radius of medium bubbles is 2.5×10^{-3} m, initial radius of small bubbles is 10^{-3} m. The reason for taking different sizes of bubble is that the code is limited by the collapse of bubbles. With same size bubble cloud the collapse of bubbles which are inside the cloud appears too early. Then the collapse of the cloud is not interesting. Thus we have chosen a bubble cloud with two big bubbles inside and four small bubbles at extremities. The bubbles are at equilibrium at $t = 0$ when they are subjected to a sudden pressure drop.

$$r_{b_0} = 5 \times 10^{-3}\ m$$
$$\epsilon = 0.25$$
$$\sigma = 7.28 \times 10^{-2}\ \text{N / m}$$
$$\mathcal{P} = \frac{p_{l_{\infty}} - p_v}{\Delta P} = 5 \times 10^{-3}$$
$$W = \frac{r_{b_0} \Delta P}{2\sigma} = 680$$

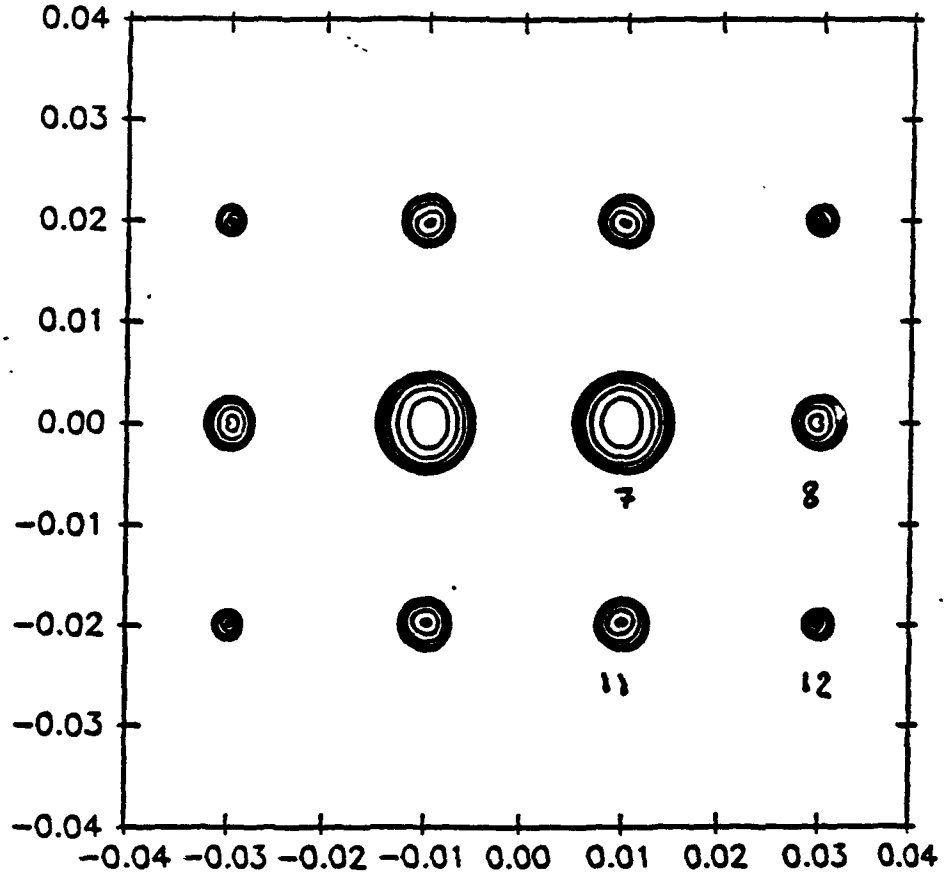

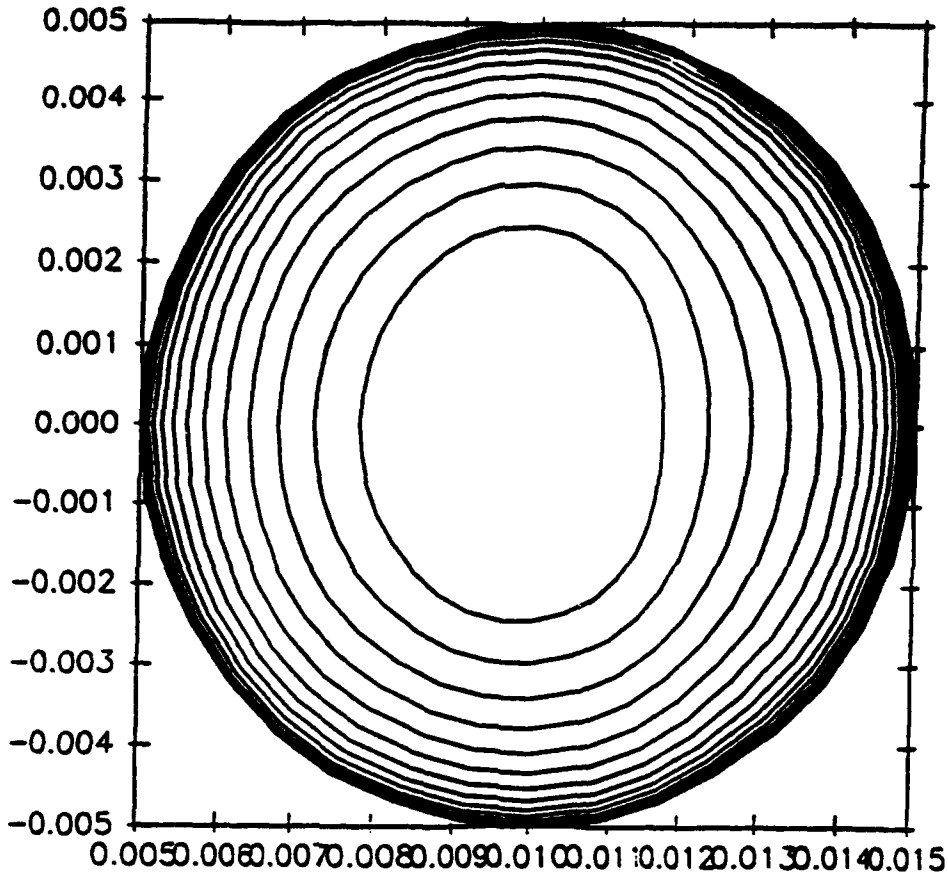

Bubble 7

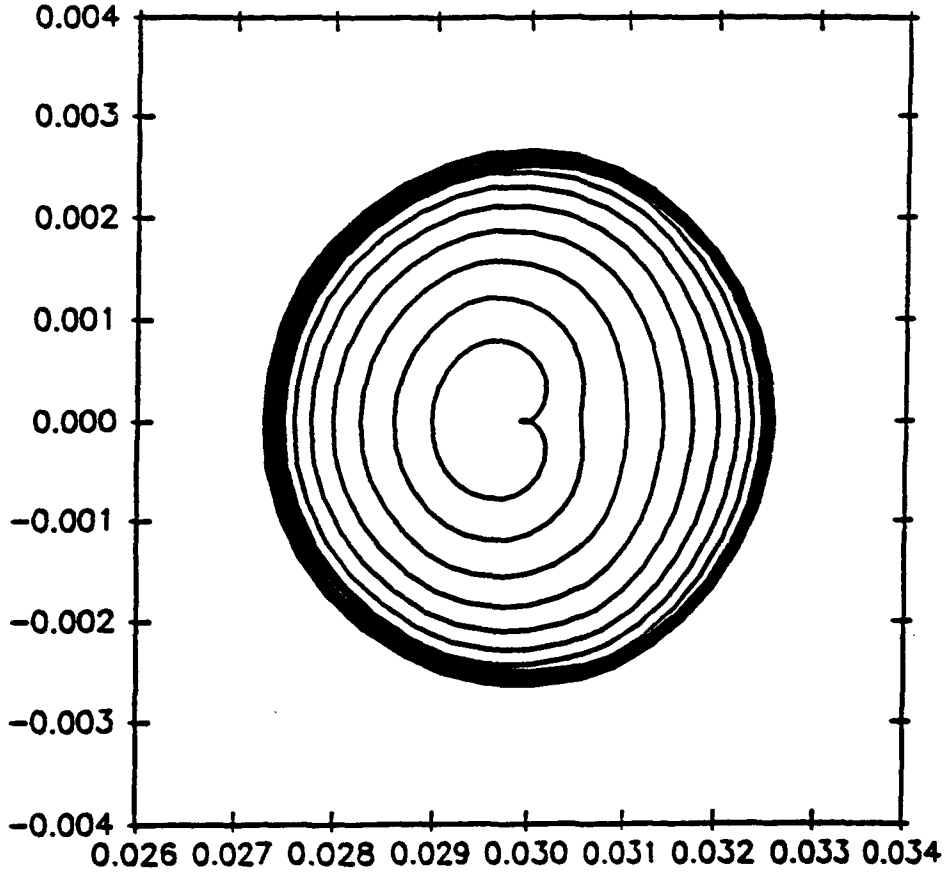

Bubble 8

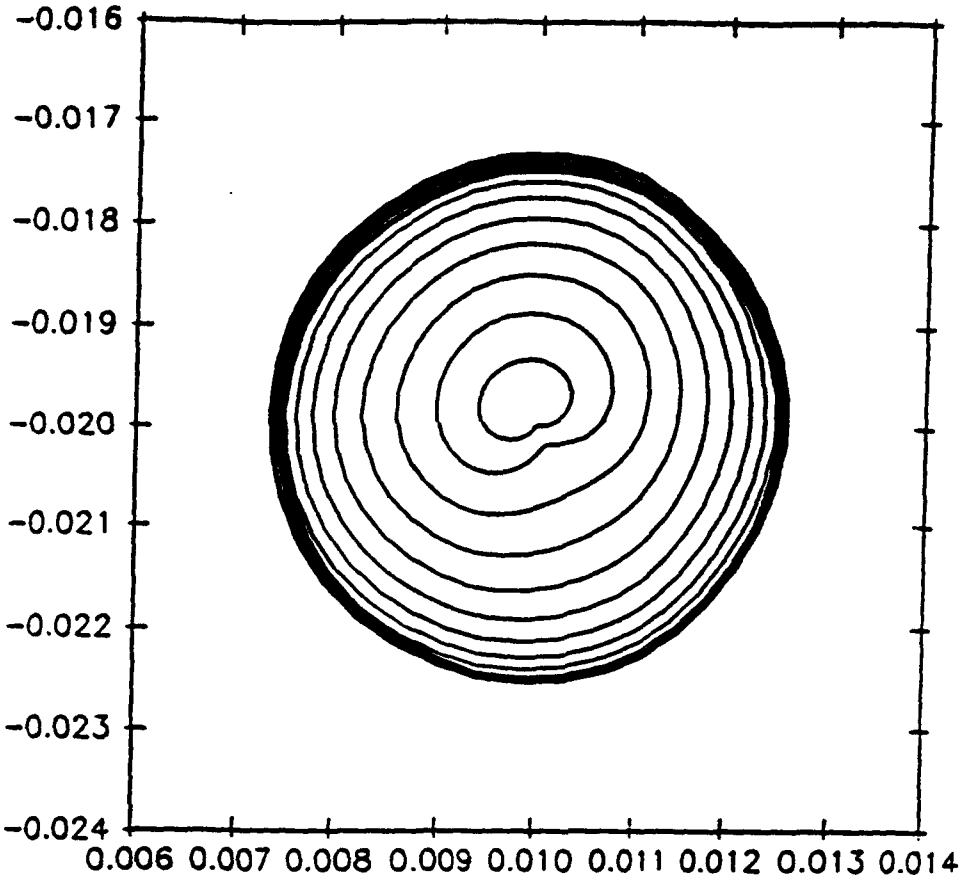

Bubble 11

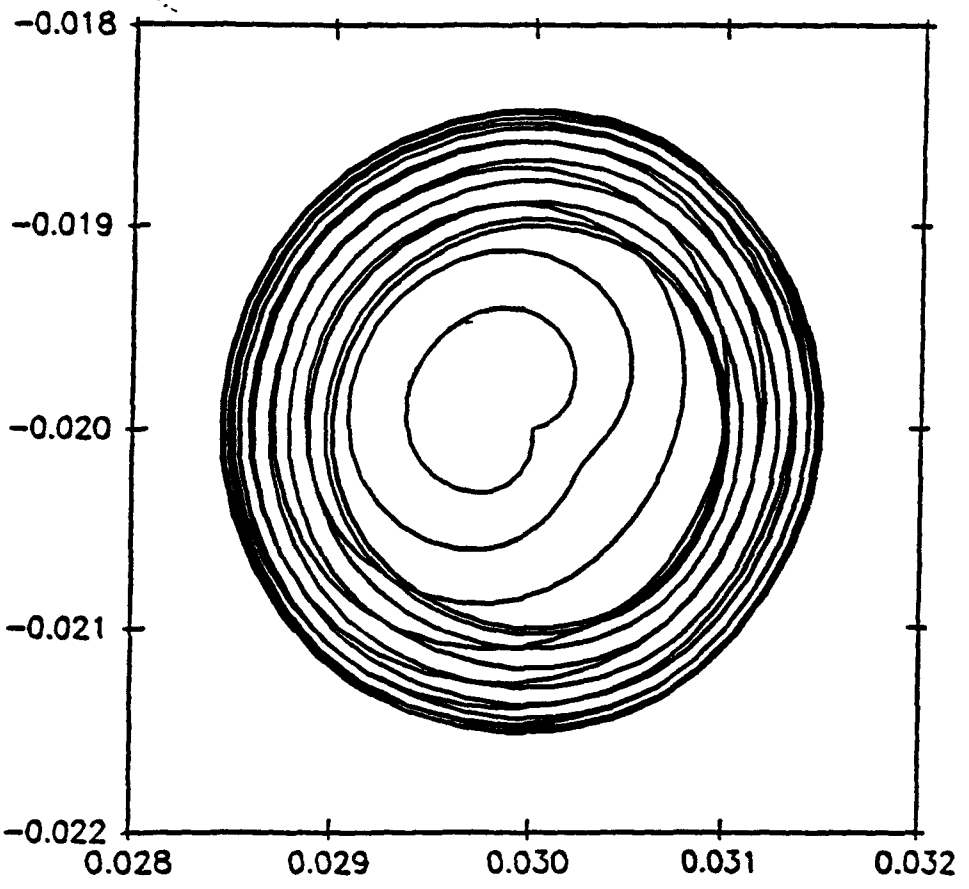

Bubble 12

These figures represent the same cloud with the same initial conditions but in a compressible fluid $M = \epsilon = 0.25$.

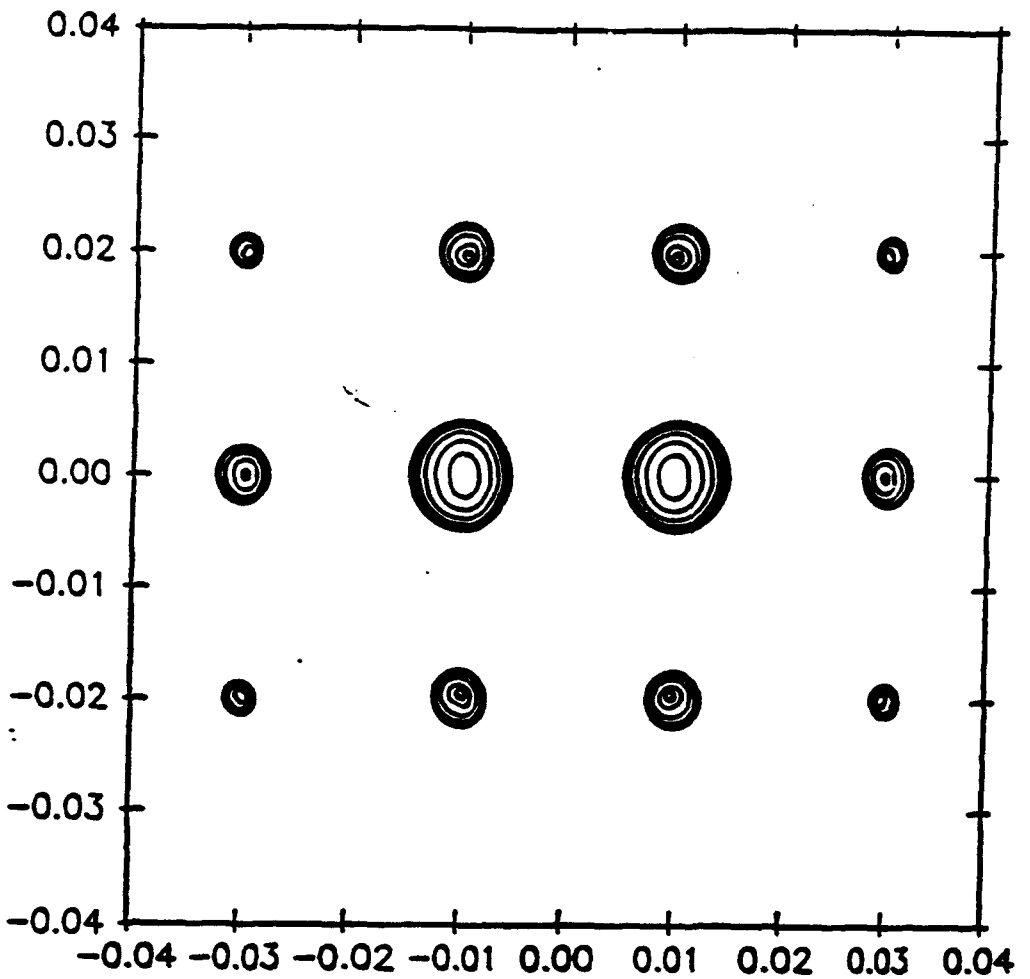

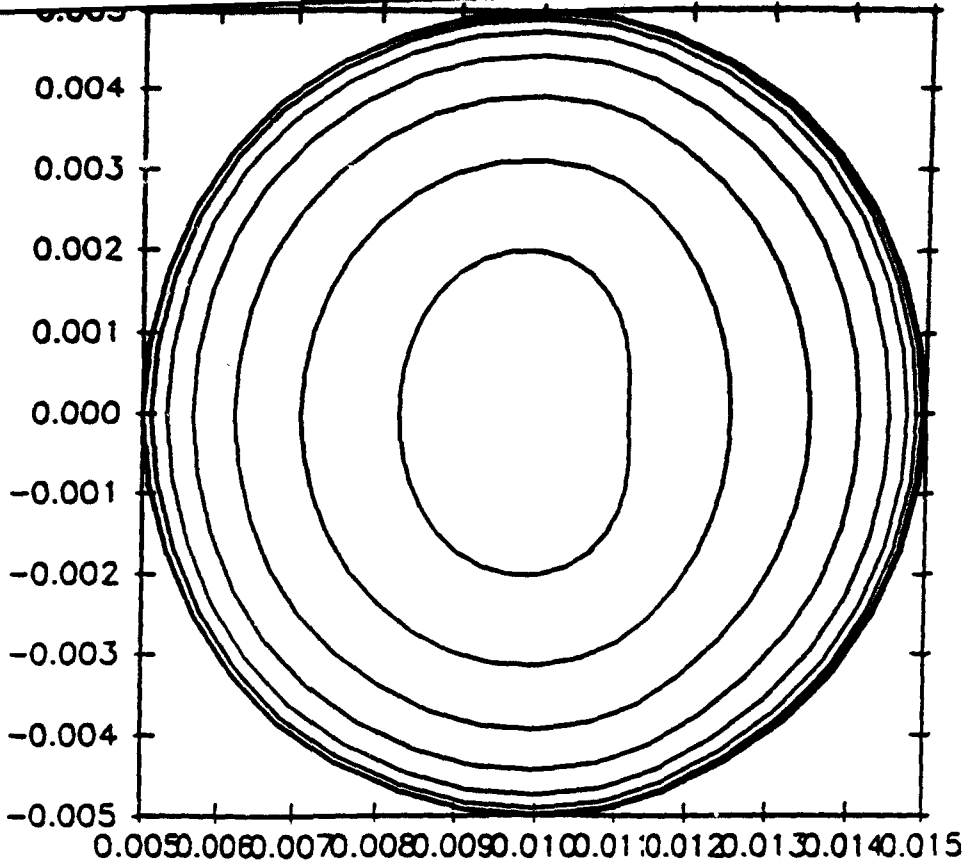

Bubble 7

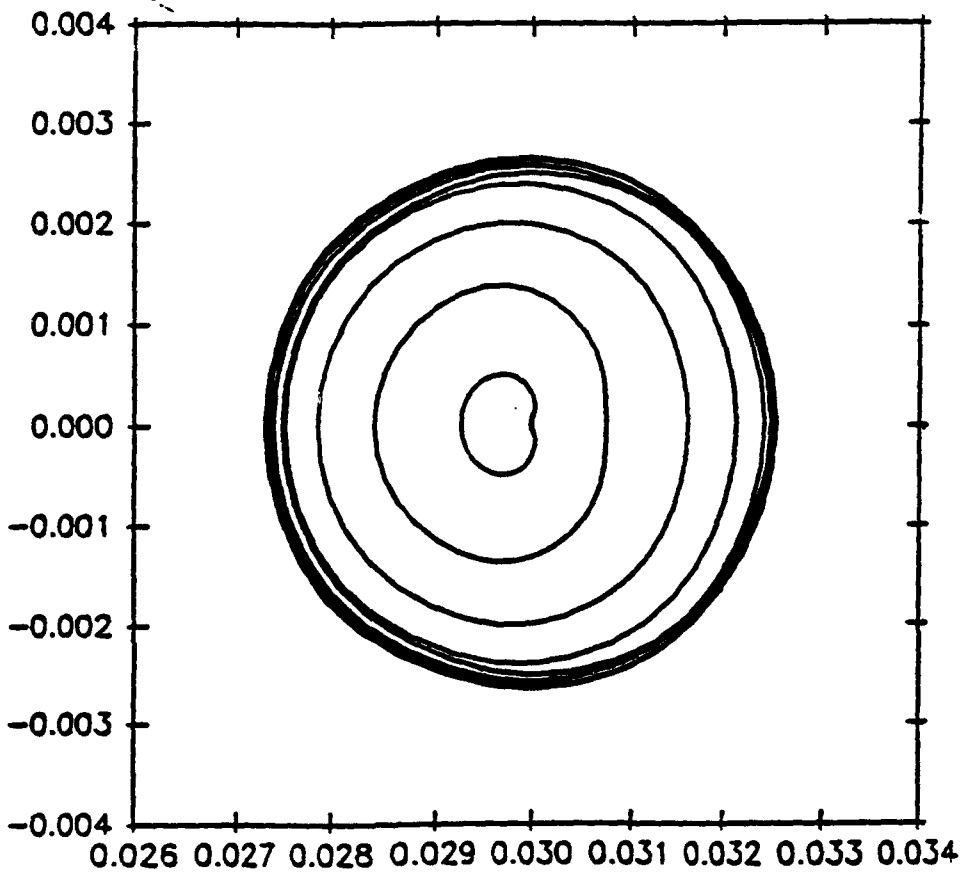

Bubble 8

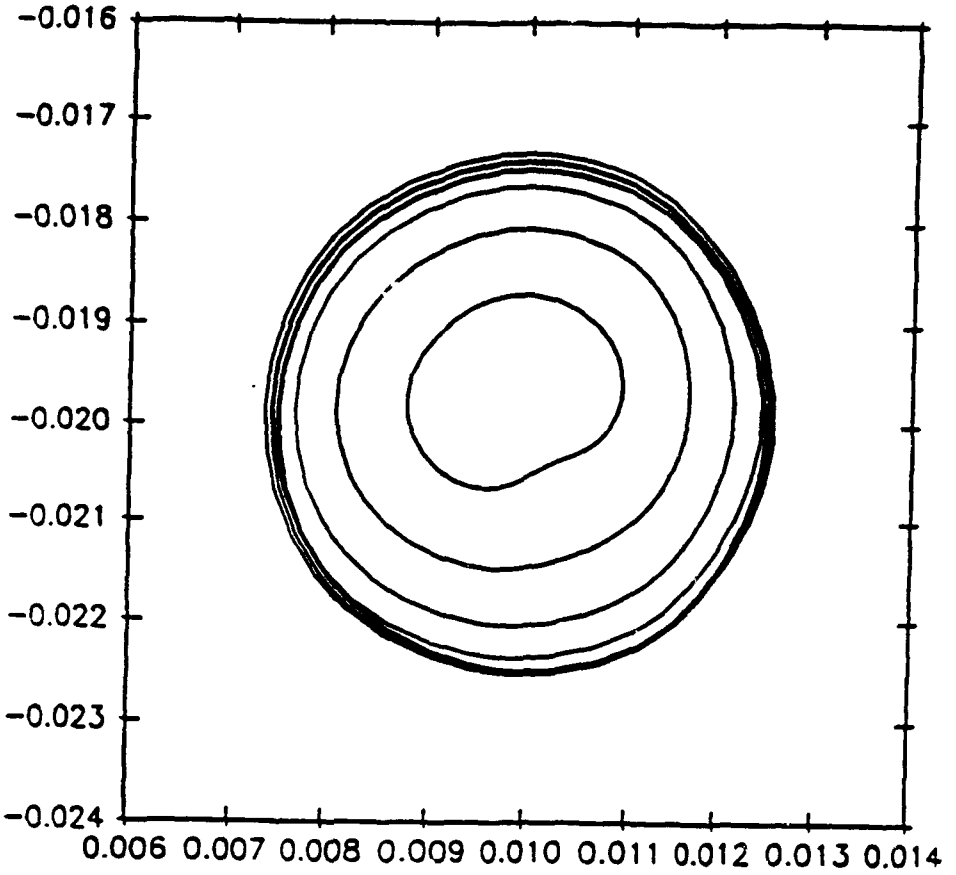

Bubble 11

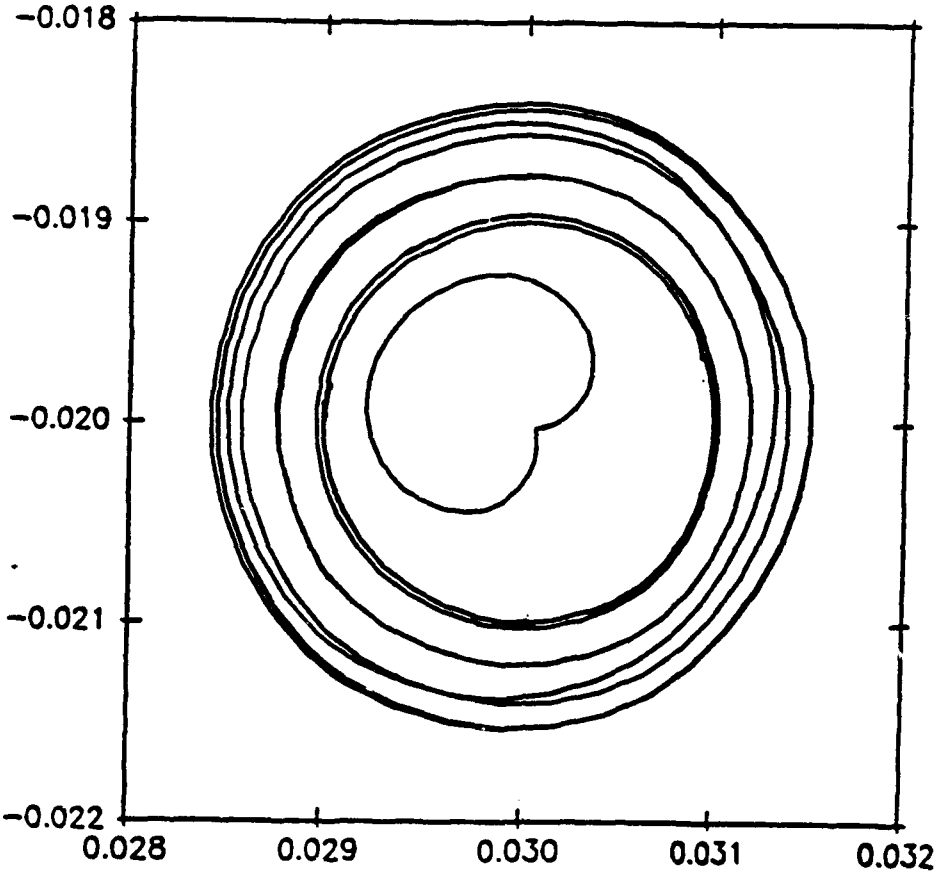

Bubble 12

2 Dynamic of the cloud

2.1 Problem statement

The reader should have certainly noticed the different approximations made in the previous problem. In this section we try to take into account most effects of the compressibility. The resolution of the "inner" and the "outer" problems will be very similar to Chahine's study, the difference is that we include the compressibility of the fluid. However, a very important change occurs when compressibility is included. The pressure imposed at infinity in the "inner" and "outer" problems now depends on the local volumic mass i.e. at the scale of the cloud on the void fraction. Therefore at the bubble scale or at the cloud scale the fluid has to be considered differently. In fact we need to consider two different global scale: the microscale problem and the macroscale one. In the first one the fluid is seen as a compressible fluid with bubbles inside it, in the second one the liquid is a two-phase medium and the compressibility comes mainly from the presence of the gas phase and not from the compressibility of the fluid itself.

Characteristic scales:

$$microscale \begin{cases} \text{inner: } r_{b_0}, T_i \\ \text{outer: } l_o, T_o \end{cases}$$

$$macroscale \begin{cases} \text{cloud: } l_c, T_c \\ \text{far away: } l_f, T_f \end{cases}$$

microscale

inner: r_{b_0}, T_i

outer: l_o, T_o

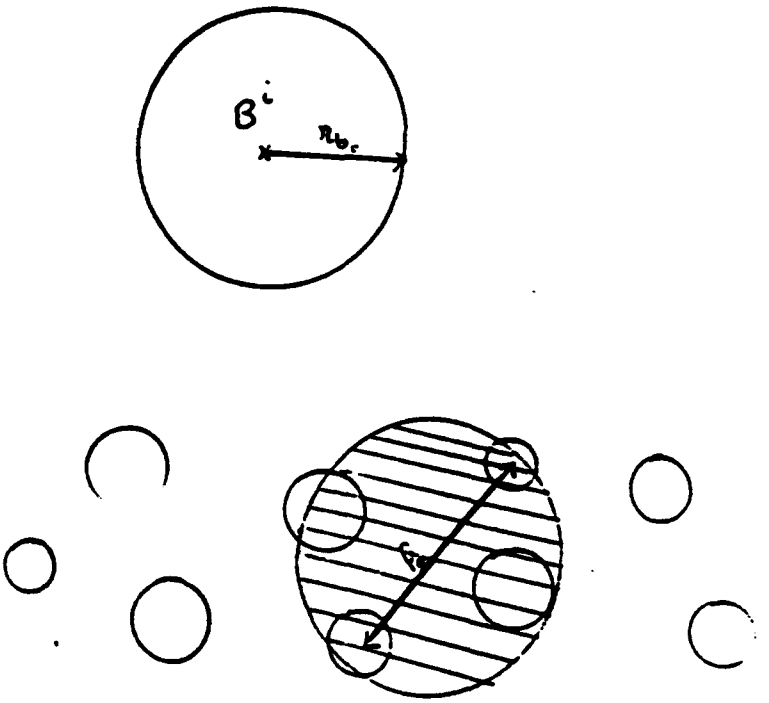

macroscale

cloud: l_c, T_c

far away: l_f, T_f

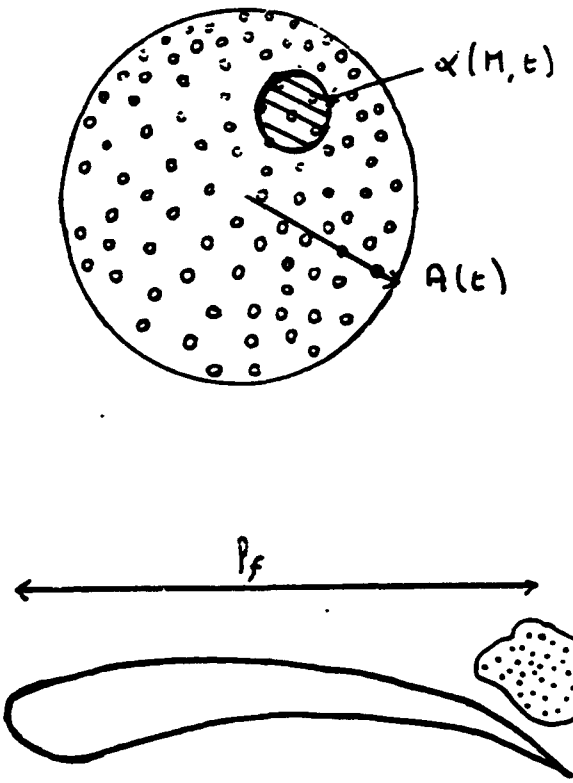

2.2 Microscale problem

The microscale problem is a zoom on the bubble cloud and it can be decomposed into an "inner" and an "outer" problems. Thus there is not a single "inner" problem but as many "inner" problems as there are bubbles. To each "inner" problem corresponds an "outer" problem.

At the length scale of the microscale problem each bubble being far away for other bubbles, sees a compressible liquid. Explicit expressions for the sound speed, c, and the enthalpy, h, will be needed. To this end we make use of an equation of state of the modified Tait form for water:

$$\frac{p+B}{p_{ref}+B} = \left(\frac{\rho}{\rho_{ref}}\right)^n \tag{6}$$

Here the reference is chosen in the undisturbed liquid (subscript ref). The values $B = 3049.13$ bars, $n = 7.15$ give an excellent fit to the experimental pressure-density relation for water up to 10^5 bars (Fujikawa and Akamatsu 1980). With (6) we find the following relation:

$$\frac{dp}{d\rho} = c^2 = \frac{n(p+B)}{\rho} \quad . \tag{7}$$

$c_{ref}^2 = n(p_{ref}+B)/\rho_{ref}$ is the square of the undisturbed speed of sound in the liquid.

2.2.1 "Inner" problem

Mathematical formulation:

Let's call $p^i(M,t)$ the pressure at a point M in the liquid at time t in the "inner" problem. Let's call $p^i_\infty(t)$ the pressure at time t at infinity at the scale of the "inner" problem. Let's call $p^o(M,t)$ the pressure at a point M in the liquid at time t in the "outer" problem. Let's call $p^o_\infty(t)$ the pressure at infinity at the scale of the "outer" problem. The value of $p^i_\infty(t)$ is given by the boundary condition of the "outer" problem:

$$p^i_\infty = \lim_{r \to \infty} p^i(M,t) = \lim_{r \to B^i} p^o(M,t) \tag{8}$$

Let's take the nondimensionalized pressure parameter ΔP_i:

$$\Delta P_i = \max | p^i(M,t) - p^i_\infty(t) |$$

We denote $\tilde{p} = \frac{p(M,t)-p_{ref}}{\Delta P_i}$; $\tilde{p}_\infty = \frac{p_\infty(t)-p_{ref}}{\Delta P_i}$.

Let's call $\eta_i^2 = \frac{\Delta P_i}{\rho_{ref} c^2_{ref}}$ and assume that $\eta_i \ll 1$.

We have:

$$\frac{1}{\rho} = \frac{1}{\rho_{ref}} \left(\frac{p^i + B}{p_{ref} + B} \right)^{-\frac{1}{n}} = \frac{1}{\rho_{ref}} \left(1 + \frac{p^i - p_{ref}}{p_{ref} + B} \right)^{-\frac{1}{n}}$$

$$= \frac{1}{\rho_{ref}} \left(1 + \frac{n}{\rho_{ref} c^2_{ref}} \left(p^i - p_{ref} \right) \right)^{-\frac{1}{n}} = \frac{1}{\rho_{ref}} \left(1 + n\, \tilde{p}\, \eta_i^2 \right)^{-\frac{1}{n}}$$

We can do the following expansion for $\eta_i \ll 1$ up to order $O(\eta_i^4)$:

$$\frac{1}{\rho} = \frac{1}{\rho_{ref}} \left(1 - \tilde{p}\eta_i^2 + \frac{n+1}{2} \tilde{p}^2 \eta_i^4 + o(\eta_i^4) \right) \tag{9}$$

Thanks to this expansion we can express h^i up to order $O(\eta_i^4)$.

$$h^i = \int_{p_\infty}^{p} \frac{dp}{\rho} = \int_{\tilde{p}_\infty}^{\tilde{p}} \frac{\Delta P_i}{\rho} d\tilde{p}$$

$$h^i = \eta_i^2 c^2_{ref} \left(\tilde{p} - \tilde{p}_\infty - \frac{1}{2} \left(\tilde{p}^2 - \tilde{p}^2_\infty \right) \eta_i^2 + \frac{n+1}{6} \tilde{p}^3 \eta_i^4 + o(\eta_i^4) \right) \tag{10}$$

Using the same kind of expansion we get $\frac{1}{c^{i2}}$:

$$c^{i2} = \frac{dp}{d\rho} = \frac{n(p+B)}{\rho} = \frac{1}{\rho} \left(n(p - p_{ref}) + n(p_{ref} + B) \right)$$

$$c^{i2} = \frac{\rho_{ref} c_{ref}^2}{\rho} \left(1 + n\,\tilde{p}\,\eta_i^2\right) = c_{ref}^2 \left(1 + n\,\tilde{p}\,\eta_i^2\right)^{1-1/n} \tag{11}$$

$$\begin{aligned} \frac{1}{c^{i2}} &= \frac{1}{c_{ref}^2} \Big(1 + (1-n)\tilde{p}\eta_i^2 \\ &\quad + \frac{1}{2}(1-n)(1-2n)\tilde{p}^2\eta_i^4 + o(\eta_i^4)\Big) \end{aligned} \tag{12}$$

First, we will consider the expansion until order $o(\eta_i^3)$, equation (11) and (12) become:

$$\frac{1}{c^{i2}} = \frac{1}{c_{ref}^2} \left(1 + (1-n)\tilde{p}\eta_i^2 + o(\eta_i^3)\right) \tag{13}$$

$$h^i = \eta_i^2 c_{ref}^2 \left(\tilde{p} - \tilde{p}_\infty - \frac{1}{2}\left(\tilde{p}^2 - \tilde{p}_\infty^2\right)\eta_i^2 + o(\eta_i^3)\right) \tag{14}$$

Motion equations

The bubble behaviour and the motion of the liquid in the neighborhood of each bubble is governed by the equation of continuity

$$\frac{\partial \rho}{\partial t} + \nabla\left(\rho u^i\right) = 0\,, \tag{15}$$

and the momentum equation

$$\rho\left(\frac{\partial u^i}{\partial t} + u^i\,\nabla\,u^i\right) + \nabla\,p^i = 0. \tag{16}$$

Furthermore with the assumption that the motion is irrotational, we may introduce a velocity potential ϕ such that: $u^i = \nabla\,\phi$. With this definiton equation (15) may be rewritten as

$$\frac{1}{c^{i2}}\left(\frac{\partial h^i}{\partial t} + \nabla\,\phi\nabla\,h^i\right) + \nabla^2\,\phi = 0. \tag{17}$$

while equation (16) may be integrated once to give

$$\frac{\partial \phi}{\partial t} + \frac{1}{2} | \nabla \phi |^2 + h^i = 0. \tag{18}$$

To complete this mathematical formulation we need the kinematic boundary condition at each bubble wall $r = R^i(t)$

$$\text{for each bubble } i: \quad (\nabla \phi^i . n^i)_{r=R^i(t)} = \frac{\partial R^i(t)}{\partial t} e_{r^i} . n^i \tag{19}$$

where n^i represents the normal at the bubble i surface , $r = R^i(t)$ is the equation of its surface, e_{r^i} is the radial vector in a frame linked to the center of the bubble .

The pressure in the liquid at each bubble B_i surface:

$$p^i_{B_i} = p^i_v + p^i_{g0} \left(\frac{V^i_0}{V^i} \right)^\gamma - C^i \sigma, \tag{20}$$

where p^i_{g0} and V^i_0 are the initial gas pressure and volume respectively, σ is the surface tension, C^i the local curvature of the bubble, V^i the instantaneous value of the bubble i volume, and γ the polytropic constant, with $\gamma = 1$ for isothermal behaviour and $\gamma = 1.4$ for adiabatic conditions. Here p^i_{g0} and V^i_0 are known quantities at $t = 0$. The curvature $C^i$and the normal n^i to the surface B^i are given by:

$$C^i = \nabla n^i \quad ; \quad n^i = \frac{\nabla B^i}{| \nabla B^i |}. \tag{21}$$

Nondimensionalisations

In the inner problem the parameters we will use for the nondimensionalisation are :

r	=	$r_{b_0} \tilde{r}$	r_{b_0} : the initial characteristic bubble radius
$\max \| p^i(M,t) - p^i_\infty \|$	=	ΔP_i	ΔP_i : pressure change scale
t	=	$T_i \tilde{t}$	T_i : the characteristic collapse time
ϕ	=	$\phi_i . \tilde{\phi}$	ϕ_i : inner velocity potential scale
η_i^2	=	$\frac{\Delta P_i}{\rho_{ref} c^2_{ref}}$	
M	=	$\frac{r_{b_0} / T_i}{c_{ref}}$	M : Mach number

We will use: $\tilde{p}^2 - \tilde{p}_{\infty}^2 = (\tilde{p} - \tilde{p}_{\infty})(\tilde{p} + \tilde{p}_{\infty})$

Previous equations (17), (18), (19) become:

$$\frac{\phi_i}{r_{b_0}^2} \nabla^2 \tilde{\phi} +$$

$$\eta_i^2 \left(\frac{1}{T_i} \frac{\partial}{\partial \tilde{t}} (\tilde{p} - \tilde{p}_{\infty}) + \frac{\phi_i}{r_{b_0}^2} \left(\nabla \tilde{\phi} \,.\, \nabla \right) (\tilde{p} - \tilde{p}_{\infty}) \right) + O\left(\eta_i^4\right) = 0 \qquad (22)$$

$$\frac{\phi_i}{T_i} \frac{\partial \tilde{\phi}}{\partial \tilde{t}} + \frac{1}{2} \frac{\phi_i^2}{r_{b_0}^2} \mid \nabla \tilde{\phi} \mid^2 +$$

$$\eta_i^2 c_{ref}^2 (\tilde{p} - \tilde{p}_{\infty}) \left[1 - \frac{1}{2} \eta_i^2 (\tilde{p} + \tilde{p}_{\infty}) + O\left(\eta_i^4\right) \right] = 0 \qquad (23)$$

$$\frac{\phi_i}{r_{b_0}} \left(\nabla \tilde{\phi}^i . \, n^i \right)_{\tilde{r} = \tilde{R}^i(t)} = \frac{r_{b_0}}{T_i} \frac{\partial \tilde{R}^i(t)}{\partial \tilde{t}} e_{r^i} . \, n^i \quad \text{for each bubble } i. \qquad (24)$$

The least degeneracy of equation (24) gives the order of ϕ_i :

$$\phi_i = \frac{r_{b_0}^2}{T_i} \qquad (25)$$

The least degeneracy of equation (23) gives the order of T_i : $\frac{T_i^2}{r_{b_0}^2} \eta_i^2 c_{ref}^2 = 1$:

$$T_i = r_{b_0} \sqrt{\frac{\rho_{ref}}{\Delta P_i}} \qquad (26)$$

which gives the value of η_i :

$$\eta_i^2 = \frac{\Delta P_i}{\rho_{ref} c_{ref}^2} = \left(\frac{r_{b_0}}{T_i} \frac{1}{c_{ref}} \right)^2 = M^2 \qquad (27)$$

it means that η_i is exactly the previous Mach number M. Thus the assumption we made about η_i is justified for a slightly compressible fluid.

The inner problem equations are:

$$\nabla^2 \tilde{\phi} + M^2 \left(\left(\frac{\partial}{\partial \tilde{t}} + \left(\nabla \tilde{\phi} \,.\, \nabla \right) \right) (\tilde{p} - \tilde{p}_\infty) \right) + O\left(M^4\right) = 0 \qquad (28)$$

$$\frac{\partial \tilde{\phi}}{\partial \tilde{t}} + \frac{1}{2} \mid \nabla \tilde{\phi} \mid^2 + (\tilde{p} - \tilde{p}_\infty) \left[1 - \frac{1}{2} M^2 (\tilde{p} + \tilde{p}_\infty) \right] + O\left(M^4\right) = 0 \qquad (29)$$

$$\left(\nabla \tilde{\phi}^i . \, n^i \right)_{\tilde{r} = \tilde{R}^i(t)} = \frac{\partial \tilde{R}^i(t)}{\partial \tilde{t}} e_{r^i} . \, n^i \quad \text{for each bubble } i. \qquad (30)$$

$$\tilde{p} = \frac{1}{\Delta P_i} \left(p_v^i - p_{ref} + p_{g0}^i \left(\frac{V_0^i}{V^i} \right)^\gamma - C^i \sigma \right), \quad \text{at each bubble wall} \qquad (31)$$

2.2.2 Outer problem

Mathematical formulation:

Let's call $p^o(M,t)$ the pressure at a point M at time t in the outer problem. Let's call $p^o_\infty(t)$ the pressure at time t at infinity at the scale of the outer problem. Let's call $p^c(M,t)$ the pressure at a point M at time t in the cloud problem. The value of $p^o_\infty(t)$ is given by the boundary condition of the cloud problem:

$$p^o_\infty = \lim_{r \to \infty} p^o(M,t) = \lim_{r \to B^i} p^c(M,t) \qquad (32)$$

Let's call the scale pressure parameter ΔP_o. We have

$$\tilde{p} = \frac{p(M,t) - p_{ref}}{\Delta P_o} \quad ; \quad \tilde{p}_\infty = \frac{p_\infty(t) - p_{ref}}{\Delta P_o}. \tag{33}$$

Let's call $\eta_o^2 = \frac{\Delta P_o}{\rho_{ref} c_{ref}^2}$ we assume that $\eta_o \ll 1$.

We have like in the previous section:

$$\frac{1}{\rho} = \frac{1}{\rho_{ref}} \left(\frac{p+B}{p_{ref}+B} \right)^{-\frac{1}{n}} = \frac{1}{\rho_{ref}} \left(1 + n\tilde{p}\eta_o^2 \right)^{-\frac{1}{n}}$$

We can make the same expansion for $\eta_o \ll 1$ up to order $O(\eta_o^4)$ and we get h^o and c^o

$$\frac{1}{\rho} = \frac{1}{\rho_{ref}} \left(1 - \tilde{p}\eta_o^2 + \frac{n+1}{2}\tilde{p}^2\eta_o^4 + o(\eta_o^4) \right) \tag{34}$$

Thanks to this expansion we can expand h^o up to order $O(\eta_o^4)$,

$$h^o = \int_{p_\infty}^{p} \frac{dp}{\rho} = \int_{\tilde{p}_\infty}^{\tilde{p}} \frac{\Delta P_o}{\rho} d\tilde{p}$$

$$h^o = \eta_o^2 c_{ref}^2 \left(\tilde{p} - \tilde{p}_\infty - \frac{1}{2}\left(\tilde{p}^2 - \tilde{p}_\infty^2 \right) \eta_o^2 + \frac{n+1}{6}\tilde{p}^3\eta_o^4 + o(\eta_o^4) \right) \tag{35}$$

and c^o up to order $o(\eta_o^4)$.

$$\begin{aligned} \frac{1}{c^{o^2}} &= \frac{1}{c_{ref}^2} \Big(1 + (1-n)\,\tilde{p}\,\eta_o^2 \\ &\quad + \frac{1}{2}(1-n)(1-2n)\,\tilde{p}^2\,\eta_o^4 + o(\eta_o^4) \Big) \end{aligned} \tag{36}$$

First, we will consider the expansion until order $O(\eta_o^3)$:

$$\frac{1}{c^{o2}} = \frac{1}{c_{ref}^2}\left(1+(1-n)\ \bar{p}\ \eta_o^2+o(\eta_o^3)\right) \tag{37}$$

$$h^o = \eta_o^2 c_{ref}^2\left(\bar{p}-\bar{p}_\infty-\frac{1}{2}\left(\bar{p}^2-\bar{p}_\infty^2\right)\eta_o^2+o(\eta_o^3)\right) \tag{38}$$

Motion equations

With the assumption that the motion is irrotational, we find again the same motion equations:

$$\frac{1}{c^{o2}}\left(\frac{\partial h^o}{\partial t}+\nabla\ \phi\nabla\ h^o\right)+\nabla^2\ \phi=0. \tag{39}$$

$$\frac{\partial\phi}{\partial t}+\frac{1}{2}\mid\nabla\ \phi\mid^2+h^o=0. \tag{40}$$

In this case the kinematic boundary conditions derived from the fact that there are singularity points located at the center of each of the bubbles. These singularities are sources to the first order of approximation.

Nondimensionalisations

In the outer problem the parameters we will use for the nondimensionalisation are :

R	$=$	$l_o\bar{R}$	l_o : the characteristic distance between two bubbles
$p(M,t)-p_{ref}$	$=$	$\Delta P_o\bar{p}$	ΔP_o : pressure change scale
t	$=$	$T_o\ \bar{t}$	T_o : the characteristic collapse time
ϕ	$=$	$\phi_o\ .\ \bar{\phi}$	ϕ_o : outer velocity potential scale
η_o^2	$=$	$\frac{\Delta P_o}{\rho_{ref}c_{ref}^2}$	
M	$=$	$\frac{r_{bo}/T_i}{c_{ref}}$	

Previous equations (38) and (39) become:

$$\frac{\phi_o}{l_o^2}\nabla^2\,\bar{\phi} + \eta_o^2\left\{\left(\frac{1}{T_o}\frac{\partial}{\partial\bar{t}} + \frac{\phi_o}{l_o^2}(\nabla\,\bar{\phi}\,.\,\nabla)\right)(\bar{p}-\bar{p}_\infty)\right.$$
$$-\eta_o^2\left[\frac{1}{2}\left(\frac{1}{T_o}\frac{\partial}{\partial\bar{t}} + \frac{\phi_o}{l_o^2}(\nabla\,\bar{\phi}\,.\,\nabla)\right)(\bar{p}^2-\bar{p}_\infty^2)\right.$$
$$\left.\left.-(1-n)\bar{p}\left(\frac{1}{T_o}\frac{\partial}{\partial\bar{t}} + \frac{\phi_o}{l_o^2}(\nabla\,\bar{\phi}\,.\,\nabla)\right)(\bar{p}-\bar{p}_\infty)\right] + O\left(\eta_o^4\right)\right\} = 0 \qquad (41)$$

$$\frac{\phi_o}{T_o}\frac{\partial\bar{\phi}}{\partial\bar{t}} + \frac{1}{2}\frac{\phi_o^2}{l_o^2}\mid\nabla\,\bar{\phi}\mid^2 +$$
$$\eta_o^2 c_{ref}^2(\bar{p}-\bar{p}_\infty)\left(1-\frac{1}{2}\eta_o^2(\bar{p}+\bar{p}_\infty)\right) + O\left(\eta_o^4\right) = 0 \qquad (42)$$

i.e.

$$\nabla^2\,\bar{\phi} + \left\{\frac{\eta_o^2 l_o^2}{T_o\phi_o}\frac{\partial}{\partial\bar{t}} + \eta_o^2(\nabla\,\bar{\phi}\,.\,\nabla)\right\}(\bar{p}-\bar{p}_\infty)$$
$$-\eta_o^2\left[\frac{1}{2}\left\{\frac{\eta_o^2 l_o^2}{T_o\phi_o}\frac{\partial}{\partial\bar{t}} + \eta_o^2(\nabla\,\bar{\phi}\,.\,\nabla)\right\}(\bar{p}^2-\bar{p}_\infty^2)\right.$$
$$\left.-(1-n)\bar{p}\left\{\frac{\eta_o^2 l_o^2}{T_o\phi_o}\frac{\partial}{\partial\bar{t}} + \eta_o^2(\nabla\,\bar{\phi}\,.\,\nabla)\right\}(\bar{p}-\bar{p}_\infty)\right] + O\left(\eta_o^4\right) = 0 \qquad (43)$$

$$\frac{\partial\bar{\phi}}{\partial\bar{t}} + \frac{1}{2}\frac{\phi_o T_o}{l_o^2}\mid\nabla\,\bar{\phi}\mid^2 +$$
$$\frac{T_o\eta_o^2 c_{ref}^2}{\phi_o}(\bar{p}-\bar{p}_\infty)\left(1-\frac{1}{2}\eta_o^2(\bar{p}+\bar{p}_\infty)\right) + O\left(\eta_o^4\right) = 0 \qquad (44)$$

the matching condition is :

$$\lim_{\bar{r}\to 0}\phi_o\,\bar{\phi} = \lim_{\bar{r}\to\infty}\phi_i\,\bar{\phi} \qquad (45)$$

$$\lim_{\tilde{r}\to 0} \Delta P_o\ \tilde{p} = \lim_{\tilde{r}\to\infty} \Delta P_i\ \tilde{p} \tag{46}$$

The least degeneracy of equation (44) using the kinematic boundary conditions gives the order of ϕ_o :

$$\phi_o = \epsilon\, \frac{r_{l_0}^2}{T_i} = \epsilon \phi_i \tag{47}$$

The least degeneracy of equation (42) and (43) give the following order:

$$\frac{\eta_o^2 l_o^2}{\phi_o T_o} = \eta_o^2 \frac{T_i}{T_o \epsilon^3} = 1 \tag{48}$$

and

$$\frac{T_o \eta_o^2 c_{ref}^2}{\phi_o} = \frac{\eta_o}{M}^2 \frac{T_o}{T_i \epsilon} \tag{49}$$

thus

$$\eta_o = \epsilon\sqrt{M} \tag{50}$$

$$T_o = \frac{M T_i}{\epsilon} = \frac{l_o}{c_{ref}} \tag{51}$$

The previous equations (42) and (43) become:

$$\begin{aligned} &\nabla^2 \bar{\phi} + \left\{\frac{\partial}{\partial \bar{t}} + M\epsilon^2 (\nabla \bar{\phi} \,.\, \nabla)\right\}(\bar{p} - \bar{p}_\infty) \\ &-M\epsilon^2 \left[\frac{1}{2}\left\{\frac{\partial}{\partial \bar{t}} + M\epsilon^2 (\nabla \bar{\phi} \,.\, \nabla)\right\}(\bar{p}^2 - \bar{p}_\infty^2)\right. \\ &\left.-(1-n)\bar{p}\left\{\frac{\partial}{\partial \bar{t}} + M\epsilon^2 (\nabla \bar{\phi} \,.\, \nabla)\right\}(\bar{p} - \bar{p}_\infty)\right] + O(\epsilon^4) = 0 \end{aligned} \tag{52}$$

$$\begin{aligned} &\frac{\partial \bar{\phi}}{\partial \bar{t}} + \frac{1}{2} M\epsilon^2 \mid \nabla \bar{\phi} \mid^2 \\ &+ (\bar{p} - \bar{p}_\infty)\left(1 - \frac{1}{2} M\epsilon^2 (\bar{p} + \bar{p}_\infty)\right) + O(\epsilon^4) = 0 \end{aligned} \tag{53}$$

i.e.:

$$\nabla^2 \bar{\phi} + \frac{\partial(\bar{p} - \bar{p}_\infty)}{\partial \bar{t}}$$
$$+M\epsilon^2 \left[(\nabla \bar{\phi} \cdot \nabla)(\bar{p} - \bar{p}_\infty) - \frac{1}{2}\frac{\partial(\bar{p}^2 - \bar{p}_\infty^2)}{\partial \bar{t}} + (1-n)\bar{p}\frac{\partial(\bar{p} - \bar{p}_\infty)}{\partial \bar{t}} \right]$$
$$+O(\epsilon^4) = 0 \quad (54)$$

$$\frac{\partial \bar{\phi}}{\partial \bar{t}} + \frac{1}{2}M\epsilon^2 \mid \nabla \bar{\phi} \mid^2$$
$$+ (\bar{p} - \bar{p}_\infty)\left(1 - \frac{1}{2}M\epsilon^2(\bar{p} + \bar{p}_\infty)\right) + O(\epsilon^4) = 0 \quad (55)$$

But the equation (50) shows that the speed at this scale is of order c_{ref} it doesn't agree with the previous assumption. The perturbations don't include shock wave. Thus we need to use the second order of degeneracy.

$$\frac{T_o \phi_o}{l_o^2} = \frac{\epsilon^3 T_o}{T_i} \quad (56)$$

$$\frac{T_o \eta_o^2 c_{ref}^2}{\phi_o} = \frac{\eta_o}{M}^2 \frac{T_o}{T_i \epsilon} \quad (57)$$

thus

$$\eta_o = \epsilon^2 M = \frac{l_o/T_o}{c_{ref}} \quad (58)$$

$$T_o = \frac{lo}{\epsilon^2 c_{ref}} \quad (59)$$

The outer problem equations are:

$$\nabla^2 \bar{\phi} + \epsilon^4 M^2 \left\{ \frac{\partial}{\partial \bar{t}} + (\nabla \bar{\phi} \cdot \nabla) \right\} (\bar{p} - \bar{p}_\infty) + O(\epsilon^4) = 0 \quad (60)$$

$$\frac{\partial \bar{\phi}}{\partial \bar{t}} + \frac{1}{2} \mid \nabla \bar{\phi} \mid^2 + (\bar{p} - \bar{p}_\infty)\left(1 - \frac{1}{2}\epsilon^4 M^2 (\bar{p} + \bar{p}_\infty)\right) + O(\epsilon^4) = 0 \quad (61)$$

i.e.:

$$\nabla^2 \bar{\phi} \ + O(\epsilon^4) = 0 \tag{62}$$

$$\frac{\partial \bar{\phi}}{\partial \bar{t}} + \frac{1}{2} \mid \nabla \bar{\phi} \mid^2 + (\bar{p} - \bar{p}_\infty) \ + O(\epsilon^4) = 0 \tag{63}$$

2.3 Macroscale problem

In the macroscale problem we consider the medium as a continuous mixture of liquid and gas. This is the classical point of view of two-phase flow studies. The compressibility of the liquid can be neglected with respect to the compressibility due to the presence of the bubbles.

2.3.1 Cloud problem

Mathematical formulation:

The medium is composed by a liquid and a gas, the void fraction is $\alpha(M,t)$. The liquid and the gas are assumed inviscid and incompressible, with a respective density ρ_f and ρ_g. We assume that no bubbles are created or disappear. The volumic mass of the medium is:

$$\rho = \rho_f (1 - \alpha(M,t)) + \rho_g \, \alpha(M,t) \tag{64}$$

The void fraction $\alpha(M,t)$ is taken in the small volume element $dV = \frac{4}{3}\pi l_o^3$ which contains $n(M)$ bubbles at the point M, l_o being the scale of the outer problem in the microscale. The order of $\alpha(M,t)$ is:

$$\alpha(M,t) = n\epsilon^3\alpha^*(M,t) \quad (\alpha(M,t) \ll 1 \text{ for } \epsilon \ll 1). \tag{65}$$

where n is the average value of $n(M)$ in the cloud. $\alpha^*(M,t)$ is of order unity.

Thanks to the work of Van Wijngaarden [4], we know how the sound speed is modified in a two-phase medium. Under the further assumption that gas and fluid move at the same velocity, the mass of gas in a unit mass of the mixture is constant,

$$\frac{\rho_g\alpha(M,t)}{\rho_f(1-\alpha(M,t))} = constant. \tag{66}$$

In a homogeneous mixture, as envisaged here, the pressure p in the mixture equals the pressure p_g in the gas, which is at constant temperature T proportional to ρ_g^γ (isentropic case),

$$\frac{p^{\frac{1}{\gamma}}\alpha(M,t)}{\rho_f(1-\alpha(M,t))} = constant. \tag{67}$$

For the sound velocity c, we have from equation (63),

$$\frac{1}{c^2} = (1-\alpha(M,t))\frac{d\rho_f}{dp} + \alpha(M,t)\frac{d\rho_g}{dp} + (\rho_g - \rho_f)\frac{d\alpha(M,t)}{dp} \tag{68}$$

i.e.

$$\frac{1}{c^2} = \frac{(1-\alpha(M,t))}{c_f^2} + \frac{\alpha(M,t)}{c_g^2} + (\rho_g - \rho_f)\frac{d\alpha(M,t)}{dp} \tag{69}$$

Let's note $\alpha(M,t)$ by α. Differentiation of equation (65) gives:

$$d\alpha = \alpha(1-\alpha)\left(\frac{d\rho_f}{\rho_f} - \frac{d\rho_g}{\rho_g}\right) . \tag{70}$$

Differentiation of equation (66) gives:

$$d\alpha = \alpha(1-\alpha)\left(\frac{d\rho_f}{\rho_f} - \frac{dp}{\gamma p}\right) \tag{71}$$

Using (69) and (70)

$$\frac{1}{c^2} = \frac{(1-\alpha)^2}{c_f^2} + \frac{\alpha^2}{c_g^2} + \frac{\rho_f \alpha(1-\alpha)}{\gamma p} + \frac{\rho_g}{\rho_f}\frac{\alpha(1-\alpha)}{c_g^2} \tag{72}$$

We have assumed that $p\rho_g^{-\gamma} = constant$ i.e.:

$$\frac{d\rho_g}{dp} = \frac{1}{c_j^2} = \frac{\rho_g}{\gamma p} \tag{73}$$

thus we can write :

$$\frac{1}{c^2} = \frac{(1-\alpha)^2}{c_f^2} + \frac{\alpha^2}{c_g^2} + \frac{\rho_f}{\rho_g}\frac{\alpha(1-\alpha)}{c_g^2} + \frac{\rho_g}{\rho_f}\frac{\alpha(1-\alpha)}{c_g^2} \tag{74}$$

Using equation (73) the speed of sound in a bubbly fluid is lower than the speed of sound in a pure gas. We know that $\alpha \sim n\epsilon^3$, for water $c_f^2 \sim 25c_g^2$, and $\rho_f \sim 1000\rho_g$. With the assumption that $\alpha \gg (\rho_g c_g^2 \,/\, \rho_f c_f^2)$ i.e. $n\epsilon^3 \gg 1/25000$, the speed can be approximate in an isentropic case by :

$$c^2 = \frac{dp}{d\rho} = \frac{\gamma p}{\rho_f (1-\alpha(M,t))\alpha(M,t)} \tag{75}$$

According to equation (66) we have :

$$p = \mathcal{P}_o \frac{(1-\alpha)^\gamma}{\alpha^\gamma} \tag{76}$$

$\mathcal{P}_o$ is given by the initial conditions.

$$\mathcal{P}_o = p_\infty \left(\frac{\alpha_o}{1-\alpha_o}\right)^\gamma \tag{77}$$

where p_∞ is the pressure in the fluid at rest at $t = 0$ and α_o is the void fraction in the bubble cloud at $t = 0$. Then

$$c^2 = \frac{\gamma \mathcal{P}_o}{\rho_f}\frac{(1-\alpha)^{\gamma-1}}{\alpha^{1+\gamma}} \tag{78}$$

Moreover

$$\rho = \rho_f(1-\alpha) + \rho_g\alpha = \rho_f\left(1 - n\epsilon^3\alpha^*\right) + \rho_g n\epsilon^3\alpha^* \,. \tag{79}$$

With the previous assumption we may approximate ρ with:

$$\rho \sim \rho_f\left(1 - n\epsilon^3\alpha^*\right) \tag{80}$$

Motion equations

Let's call $p^c(M,t)$ the pressure at the point M at time t in the cloud problem. Let's call $p^c_\infty(t)$ the pressure at time t at infinity at the scale of the cloud problem. Let's call $p^f(M,t)$ the pressure at the point M at time t in the far away problem. The value of $p^c_\infty(t)$ is given by the boundary condition of the cloud problem:

$$p^c_\infty = \lim_{r\to\infty} p^c(M,t) = \lim_{r\to C} p^f(M,t) \tag{81}$$

where C is the fictituous center of the bubble cloud. In our problem where the fluid is at rest the pressure p^c_∞ is a known of the problem, this is the pressure imposed on the bubble cloud. We find using (76) and (77) that

$$\nabla\, p^c = -\rho_f c^2 \nabla\, \alpha \tag{82}$$

. The medium behaviour is governed by the equation of continuity

$$\frac{\partial \rho}{\partial t} + \nabla(\rho u) = 0\,, \tag{83}$$

where u is the speed of the medium, and momentum

$$\rho\left(\frac{\partial u}{\partial t} + u\,\nabla\, u\right) + \nabla\, p^c = 0. \tag{84}$$

These equations give

$$\nabla\, u - \frac{1}{1-\alpha}\left(\frac{\partial \alpha}{\partial t} + u.\nabla\, \alpha\right) = 0 \tag{85}$$

$$\frac{\partial u}{\partial t} + u.\nabla\, u - \frac{c^2}{1-\alpha}\nabla\, \alpha = 0. \tag{86}$$

We may consider the cloud like a bubble with its own oscillations, the boundary conditon is also

$$(u.n)_{r=A(t)} = \frac{\partial A(t)}{\partial t} e_r.\, n \tag{87}$$

where n represents the normal at the cloud surface , $r = A(t)$ is the equation of its surface, e_r is the radial vector in a frame linked to the center of the cloud .

Nondimensionalisations

In the cloud problem the parameters we will use for the nondimensionalisation are :

$r = l_c r^*$ $\quad l_c$: the characteristic distance of the bubble cloud
$t = T_c\, t^*$ $\quad T_c$: the characteristic time of the bubble cloud
$u = U_c.\, u^*$
$\alpha = n\varepsilon^3\, \alpha^*$

We will use the following expansion for $1/25000 \ll n\varepsilon^3 \ll 1$:

$$\frac{1}{1-\alpha} = \left(1 - n\varepsilon^3\, \alpha^*\right)^{-1} = 1 + n\varepsilon^3\, \alpha^* + O(\varepsilon^4) \tag{88}$$

Expansion of c^2:

$$\begin{aligned} c^2 &= \frac{\gamma \mathcal{P}_o}{\rho_f} \frac{(1-\alpha)^{\gamma-1}}{\alpha^{1+\gamma}} \\ &= \frac{\gamma p_\infty}{\rho_f n\varepsilon^3} \frac{\alpha_o^{*\gamma}}{\alpha^{*\gamma}} \left[1 + n\varepsilon^3((1-\gamma)\alpha^* + \gamma\alpha_o^*) + O(\varepsilon^4)\right] \\ &= \frac{\gamma p_\infty}{\rho_f n\varepsilon^3} c^{*2} \end{aligned} \tag{89}$$

where c^* is of order unity. Previous equations (84) and (85) become:

$$\nabla u^* - \frac{1}{1 - n\varepsilon^3\, \alpha^*} \left(\frac{n\varepsilon^3}{U_c} \frac{l_c}{T_c} \frac{\partial \alpha^*}{\partial t^*} + n\varepsilon^3 u^*.\nabla\, \alpha^* \right) = 0 \tag{90}$$

$$\frac{\partial u^*}{\partial t^*} + \frac{U_c T_c}{l_c} u^* . \nabla u^* - \frac{T_c}{U_c l_c} \frac{\gamma p_\infty}{\rho_f} \frac{1}{1 - n\varepsilon^3 \alpha^*} c^{*2} \nabla \alpha^* = 0. \tag{91}$$

The least degeneracy of equation (89) gives the characteristic speed U_c:

$$U_c = n\varepsilon^3 \frac{l_c}{T_c} , \tag{92}$$

and the least degeneracy of equation (90) gives the characteristic time T_c:

$$T_c = l_c \sqrt{\frac{n\varepsilon^3 \rho_f}{\gamma p_\infty}} . \tag{93}$$

Thus equation (89) and (90) give:

$$\nabla u^* - \left(1 + n\varepsilon^3 \alpha^* + O(\varepsilon^4)\right) \left(\frac{\partial \alpha^*}{\partial t^*} + n\varepsilon^3 u^* . \nabla \alpha^*\right) = 0 \tag{94}$$

$$\frac{\partial u^*}{\partial t^*} + n\varepsilon^3 u^* . \nabla u^* - \left(1 + n\varepsilon^3 \alpha^* + O(\varepsilon^4)\right) c^{*2} \nabla \alpha^* = 0. \tag{95}$$

i.e. up to order $o(\varepsilon)$:

$$\nabla u^* - \frac{\partial \alpha^*}{\partial t^*} + o(\varepsilon) = 0 \tag{96}$$

$$\frac{\partial u^*}{\partial t^*} - c^{*2} \nabla \alpha^* + o(\varepsilon) = 0. \tag{97}$$

If c^* was constant, we would find the classic wave equation:

$$\nabla^2 u^* - \frac{\partial^2 u^*}{\partial t^{*2}} = 0 \tag{98}$$

or

$$\nabla^2 \alpha^* - \frac{\partial^2 \alpha^*}{\partial t^{*2}} = 0 \tag{99}$$

2.3.2 Far away problem:

This problem is easier, the cloud is only a small disruption at the center of the frame. We just need to write the equations of the outer problem of an incompressible fluid with a single bubble.

$$\nabla^2 \phi = 0 \tag{100}$$

and the boundary condition:

$$\lim_{r \to \infty} \nabla \phi = 0 \tag{101}$$

$p^f_\infty(t)$ is given by the user.

Conclusion:

The first part of this report has showed how strong could be the influence on a bubble cloud of a slightly compressible fluid. The second part has lightened all the assumptions made in the first one, and raised the equations we need to solve numerically for the problem which takes into account all the effects of the compressibility.

At $t = 0$, we know the pressure every where in the fluid. We may solve step by step, the inner, the outer, then the cloud and at least the far away problem. We get the behaviour of the cloud at time dt i.e. the value of $\alpha(M, dt)$ every where in the cloud and the pressure at this time. We need to go back step by step to the inner problem and we obtain the motion of each bubble. This recurrence is easy to compute using the concept of equivalent bubble.

In fact the main application of this modelisation is to know precisely the growth and the collapse of the bubbles in the cloud near a certain profile.

References

[1] Georges L. Chahine.
Etude locale du phénomène de cavitation. Analyse des facteurs régissants la dynamique des interfaces.
Thèse de doctorat d'état, *Université Pierre et Marie Curie -Paris VI-, France*, Juin 1979.

[2] Alain Bovis.
Etude Asymptotique du phénomène de cavitation: Cavités non sphériques.
Thèse de doctorat d'état, *Université Pierre et Marie Curie -Paris VI-, France*, Juin 1980.

[3] Georges L. Chahine, Kenneth M. Kalumuck, Thomas O. Perdue.
Cloud Cavitation and Collective Bubble Dynamics, March 1986.
David Taylor Naval Ship Research and Development Center, USA, under contract N00014-83-C-0244.

[4] L. Van Winjngarden.
One dimensional flow of liquids containing small gas bubbles, 1972.
Twente Institute of Technology, The Netherlands.

[5] A. Lezzi and A. Prosperretti.
Bubble dynamics in a compressible liquid, 1985.
Universitá degli Studi, Italy.

[6] Luca d'Agostino and Christopher E. Brennen.
Linearized dynamics of spherical bubble clouds, 1988.
California Institute of Technology, USA.

[7] Hiroyuki Takahira and Teruaki Akamatsu.
A theoretical study on the dynamics of a cluster of bubbles, 1988.
Kyoto University, Japan.

J. Fluid Mech. (1993), *vol.* 257, *pp.* 147–181

The final stage of the collapse of a cavitation bubble near a rigid wall

By SHEGUANG ZHANG[1], JAMES H. DUNCAN[1] AND GEORGES L. CHAHINE[2]

[1] Department of Mechanical Engineering, The University of Maryland, College Park, MD 20742, USA

[2] DYNAFLOW, Inc., 7210 Pindell School Road, Fulton, MD 20759, USA

(Received 17 November 1992 and in revised form 13 May 1993)

During the collapse of an initially spherical cavitation bubble near a rigid wall, a re-entrant jet forms from the side of the bubble farthest from the wall. This re-entrant jet impacts and penetrates the bubble surface closest to the wall during the final stage of the collapse. In the present paper, this phenomenon is modelled with potential flow theory, and a numerical approach based on conventional and hypersingular boundary integral equations is presented. The method allows for the continuous simulation of the bubble motion from growth to collapse and the impact and penetration of the re-entrant jet. The numerical investigations show that during penetration the bubble surface is transformed to a ring bubble that is smoothly attached to a vortex sheet. The velocity of the tip of the re-entrant jet is always directed toward the wall during penetration with a speed less than its speed before impact. A high-pressure region is created around the penetration interface. Theoretical analysis and numerical results show that the liquid–liquid impact causes a loss in the kinetic energy of the flow field. Variations in the initial distance from the bubble centre to the wall are found to cause large changes in the details of the flow field. No existing experimental data are available to make a direct comparison with the numerical predictions. However, the results obtained in this study agree qualitatively with experimental observations.

1. Introduction

Cavitation is an important engineering phenomenon that commonly occurs in fluid machinery, piping systems, liquid jets and a variety of boundary-layer flows. The major harmful effects of cavitation are erosion, noise and decrease in fluid-machinery efficiency (Hammitt 1980; Arndt 1981). In an effort to understand the fundamental physics of cavitation phenomena, a number of researchers have investigated the growth and collapse of individual bubbles near rigid boundaries. Experiments have been performed by Benjamin & Ellis (1966); Gibson (1968); Lauterborn & Bolle (1975); Chahine (1979, 1982); Gibson & Blake (1982); Tomita & Shima (1986); and Vogel, Lauterborn & Timm (1989). Using spark-generated or laser-generated cavitation bubbles and high-speed photographs it was found that, once generated, the bubble grows to a maximum size, and then starts to collapse, inducing a radial flow directed toward the bubble centroid. As the collapse proceeds, the surface of the bubble farthest from the wall moves much faster than the surface closer to the wall. This asymmetric motion creates a wall-directed re-entrant jet as the volume of the bubble decreases. Eventually, a liquid–liquid impact occurs between the front of the re-entrant jet and the

opposite side of the bubble. During this impact process, the jet penetrates the slower-moving fluid close to the wall.

Numerous theoretical and numerical studies of an individual bubble collapsing near a rigid boundary have also been made (see review articles by Prosperetti 1982; Blake & Gibson 1987). Because the available theoretical analysis is limited to asymptotic studies in which the deformation of the bubble is confined to a small perturbation range (Chahine 1982), numerical simulation has become an important tool for investigating the detailed physics of this phenomenon. Using a finite-difference approach, Plesset & Chapman (1971) conducted the first fully numerical study. Later, Mitchell & Hammitt (1973) used a modified Marker-and-Cell method to simulate similar cases. An approximate integral-equation approach was introduced by Bevir & Fielding (1974). In this work, sources and doublets were distributed along the axis of symmetry inside the bubble. Though this method requires less computational effort than the finite-difference method, it failed to simulate the formation of the re-entrant jet. Gibson & Blake (1980) and Blake & Gibson (1981) modified this method to study the bubble collapse near a rigid wall and a free surface. Based on Green's theorem and the direct boundary-integral approach, more detailed studies of cavitation bubbles near rigid boundaries have been presented by Guerri, Lucca & Prosperetti (1981); Cerone & Blake (1984); and Blake, Taib & Doherty (1986) for axisymmetric cases and by Chahine & Perdue (1988) and Chahine (1991) for three-dimensional cases. The numerical calculations of the migration of the bubble toward the rigid wall, the profiles of the bubble and the formation of the re-entrant jet were found to be in excellent agreement with experimental observations (Blake *et al.* 1986).

Once the re-entrant jet begins to penetrate the opposite side of the bubble, difficulties in experiments, theory and numerical calculations appear. Most experiments use photographs to track the bubble surface. Unfortunately, the jet impact process occurs inside a toroidal bubble and the images are consequently blurred and difficult to interpret. Theoretical analysis of the jet impact and penetration process is difficult because of the nonlinearity associated with the large motions of the bubble surface. Benjamin & Ellis (1966) postulated that upon jet impact the bubble must be transformed into a vortex ring bubble in order to conserve the Kelvin impulse of the flow. Several attempts have been made to simulate the jet impact and penetration processes numerically. Rogers *et al.* (1990) and Szymczak *et al.* (1993) have assumed an inviscid incompressible flow and used a finite-difference field approach. They demonstrated the capabilities of the method by simulating a single bubble collapse near a rigid wall including the impact of the re-entrant jet. Owing to limits in computing time and memory, the calculation was done at low resolution. It was therefore difficult to resolve the impact interface and there was a non-physical energy loss before impact. Attempts to use the direct boundary element method without modification to simulate the penetration process have failed. The failure is due to the inherent mathematical degeneracy of the conventional integral equation under this circumstance. In an effort to avoid this degeneracy problem, Best (1993) devised a two-phase procedure to carry out the calculations with the conventional boundary integral equation. The first phase includes the growth and collapse of the bubble up to the point in time when the north and the south poles of the bubble meet. Then, in the second phase, a ring bubble is assumed with a continuous velocity field everywhere in the fluid. The initial conditions for the ring bubble problem are based on the fluid motion just before impact and some *ad hoc* assumptions about the geometry of the ring bubble and the fluid velocity in the vicinity of the impact surfaces. The entire impact process occurs instantaneously in this

model. A similar two-phase method with a boundary integral approach was also reported by Lundgren & Mansour (1991) for the simulation of a vortex ring bubble.

In the present paper, the physics of cavitation bubbles is studied with a new boundary-integral technique that can compute the growth and collapse of the bubble including the impact and penetration of the re-entrant jet. This method allows for a continuous liquid–liquid impact as the two curved sides of the bubble collide, the penetration of the re-entrant jet into the fluid close to the wall and the formation of a shear layer along the impact interface. The physical and mathematical modelling of these processes is presented in §2. This modelling uses modified conventional and hypersingular boundary integral equations with non-regular boundaries to form a well-posed problem for times before and during jet impact and penetration. The details of the numerical scheme are discussed in §3. This scheme is verified and tested in §4 by computing static and dynamic problems with known solutions. The results of simulations are presented in §5. These results include velocity and pressure fields and bubble profiles. Calculations showing changes in the circulation and energy of the flow during jet impact and penetration are also computed and discussed in this section. The concluding remarks of this study are given in §6.

2. Mathematical formulation

2.1. *Physical assumptions, definitions and coordinates*

In the present paper, as well as numerous previously published studies of bubble collapse, the fluid motion is treated by potential theory. Viscous effects are neglected on the grounds that the timescale for viscous diffusion is much longer than the timesale for the collapse. Thus, the vorticity generated at the boundaries does not have sufficient time to diffuse into the flow. The extension of these studies to include the penetration phase of the motion does not alter this conclusion. In studies of bubble collapse before jet impact, the assumption of incompressibility has been made based on the idea that only a small fraction of the energy of the bubble motion is radiated away as sound. In the present case, the jet impact will cause an increase in the radiated sound; however, it will be shown that the potential flow model allows for the loss of energy due to impact. Surface tension effects are also neglected in the present calculations. Though the influence of surface tension grows as the bubble volume becomes very small, it has been shown that the inertia and pressure terms are still dominant (Hammitt 1980).

Profiles of a cavitation bubble just before the impact of the re-entrant jet and at a time later in the evolution of the bubble are shown in figures 1 (*a*) and 1 (*b*), respectively. These profiles are from the results of the present numerical model. From figure 1 (*a*), it can be seen that the radius of curvature at the north pole (N_p, defined as the point on the bubble axis that is farthest from the wall) is less than the radius of curvature at the south pole, S_p. Thus, the jet impact process begins with impact at a single point. This instant in time is defined as the initial impact. As the process continues, more and more of the two surfaces impact in a continuous manner and the bubble volume decreases. The fluid that was originally above the bubble in the figure penetrates into the fluid that is below the bubble creating the profile as shown in figure 1 (*b*). In a real flow, the interface between the fluid from above and below the bubble (called the impact or penetration interface in this paper) contains a mixture of gas, vapour and micro-bubbles, and a local shear layer is generated with the fluid in the jet moving toward the wall and the fluid outside the jet moving away from the wall. In the present potential flow approximation, the penetration interface is represented as a sheet with infinitesimal thickness. This sheet has the properties of a vortex sheet in that the

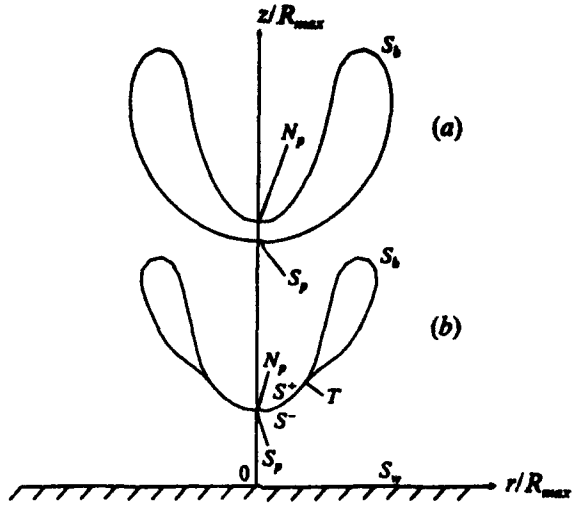

FIGURE 1. A cylindrical coordinate system and two axisymmetric bubble profiles corresponding to stages (*a*) before and (*b*) after penetration. The profiles have been separated vertically for clarity. S_b represents a regular surface, S^+ and S^- comprise a common surface which is connected to S_b at the triple point T, and S_w denotes an infinite rigid wall. N_p and S_p are respectively the north and south poles on the bubble surface.

pressure and normal velocities of the fluid are required to be continuous across the sheet while the tangential velocities are allowed to be discontinuous. The remainder of the bubble is toroidal in shape and is called a ring bubble. The circular line at which the vortex sheet attaches to the ring bubble is called the triple-point line and its intersection with the plane of the paper is denoted by the point T in figure 1 (*b*). In the experiments, the ring-bubble contains some non-condensible gas which will cause the bubble to grow again after reaching a minimum volume. In the present model, the pressure in the bubble is assumed to be constant, therefore rebound will not occur. Current efforts are being directed toward simulating the rebound process with a volume-dependent pressure inside the bubble.

A cylindrical coordinate system is used to describe the motion of the fluid and bubble surface, with r, θ and z representing the radial, circumferential and axial coordinates, respectively. The fluid motion is assumed to be axisymmetric. A rigid wall is located in the plane $z = 0$ and extends to infinity. The pressure in the fluid far from the bubble, P_∞, is maintained constant as is the pressure in the bubble, P_0. Before initial impact, the bubble surface, as shown in figure 1 (*a*), is entirely a regular surface (Kellogg 1953) and the fluid domain, D, is a simply connected region bounded by the bubble surface, S_b, the rigid wall, S_w, and an imaginary boundary at infinity, S_∞. After initial impact, S_b is transformed into an irregular surface as shown in figure 1 (*b*). This surface consists of two different regions: a common surface region which comprises the two surfaces S^+ and S^-, representing the vortex sheet, and a regular surface region S_b which includes the ring bubble. The fluid domain is still simply connected when the internal boundary is taken as the union of S_b, S^+ and S^-.

The lengthscale for the problem is taken as R_{max} (the maximum radius the bubble would have achieved in an infinite fluid), the timescale is taken as $R_{max}[\rho/(P_\infty - P_0)]^{\frac{1}{2}}$ (the collapse time of a spherical bubble in an infinite fluid of density ρ), and the

pressure scale is $P_\infty - P_0 = \Delta P$. With respect to the three scaling parameters, the non-dimensionalized coordinates, r^* and z^*, time t^* and pressures P^* can be expressed as

$$\{r^*, z^*, t^*, P^*\} = \left\{\frac{r}{R_{max}}, \frac{z}{R_{max}}, \frac{t}{R_{max}}\left(\frac{\Delta P}{\rho}\right)^{\frac{1}{2}}, \frac{P}{\Delta P}\right\}. \tag{1}$$

Other geometric, kinematic and dynamic quantities in the following mathematical formulations are non-dimensionalized in the same manner. In the remainder of this paper, all variables are dimensionless and the superscript * is dropped for convenience.

2.2. *Mathematical statement of problem*

Based on potential flow theory, the velocity u can be represented by the gradient of the velocity potential ϕ, $u = \nabla\phi$, with ϕ satisfying Laplace's equation inside the fluid domain D,

$$\nabla^2\phi(x, t) = 0, \quad x \in D, \tag{2}$$

where x is the spatial coordinate. Initially, the bubble boundary is assumed to be a spherical surface with radius R_0. Over this surface, a uniformly distributed velocity potential ϕ is prescribed using Rayleigh's (1917) spherical bubble theory:

$$\phi_0 = -R_0\left[\frac{2\Delta P}{3\rho}\left(\frac{R_{max}^3}{R_0^3} - 1\right)\right]^{\frac{1}{2}}. \tag{3}$$

The boundary conditions before the impact of the re-entrant jet are as follows. The kinematic boundary condition on S_b is

$$\frac{dx_p}{dt} = \nabla\phi, \quad x_p \in S_b, \tag{4}$$

where x_p is the position vector to a material point p. The kinematic boundary conditions on the rigid wall, S_w, and at infinity are, respectively,

$$\frac{\partial\phi}{\partial n} = 0, \tag{5}$$

and

$$|\nabla\phi| \to 0. \tag{6}$$

The dynamic boundary condition on S_b is

$$P(x_p, t) = P_0, \quad x_p \in S_b. \tag{7}$$

After initial impact, the boundary conditions (4) and (7) still apply without modification to fluid particles on S_b; however, matching conditions must be introduced on the common surface, $S^+ \cap S^-$. The component of the velocity normal to the common surface must be continuous across the surface,

$$\left.\frac{\partial\phi^+}{\partial n_p^+}\right|_{p\in S^+} = -\left.\frac{\partial\phi^-}{\partial n_p^-}\right|_{p\in S^-}, \tag{8}$$

where n_p^+ and n_p^- are outward normals (directed away from the fluid) to S^+ and S^- at p^+ and p^-, respectively. The pressure across the common surface must also be continuous,

$$P|_{p\in S^+} = P|_{p\in S^-}. \tag{9}$$

Note that the pressure varies along the common surface and is not in general equal to P_0.

In order to solve the problem, the dynamic boundary conditions on the bubble surface and the common surface, (7) and (9), must be written in terms of ϕ. On S_b, the condition on ϕ is Bernoulli's equation written in material derivative form:

$$\frac{D\phi}{Dt} = \tfrac{1}{2}|\nabla\phi|^2 + \frac{P_\infty - P_0}{\rho}, \quad p \in S_b. \tag{10}$$

To derive the equation for ϕ on the common surface, consider Bernoulli's equation written for p^+:

$$\frac{\partial\phi^+}{\partial t} + \left(\frac{\partial\phi^+}{\partial n^+}\right)^2 = \frac{1}{2}\left[\left(\frac{\partial\phi^+}{\partial n^+}\right)^2 - \left(\frac{\partial\phi^+}{\partial s^+}\right)^2\right] + \frac{P_\infty - P^+}{\rho}, \tag{11}$$

and for p^-:

$$\frac{\partial\phi^-}{\partial t} + \left(\frac{\partial\phi^-}{\partial n^-}\right)^2 = \frac{1}{2}\left[\left(\frac{\partial\phi^-}{\partial n^-}\right)^2 - \left(\frac{\partial\phi^-}{\partial s^-}\right)^2\right] + \frac{P_\infty - P^-}{\rho}. \tag{12}$$

The left-hand sides of these two equations are the time rates of change of ϕ following the component of the fluid motion in the direction normal to the common surface. After subtracting (12) from (11) and employing the matching conditions (8) and (9), the above equations become

$$\frac{D(\phi^+ - \phi^-)}{D_n t} = -\frac{1}{2}\left[\left(\frac{\partial\phi^+}{\partial s^+}\right)^2 - \left(\frac{\partial\phi^-}{\partial s^-}\right)^2\right], \tag{13}$$

where the subscript n indicates the derivative following the normal component of the flow.

2.3. *Conditions at the instant of impact*

As was pointed out in §2.1, the liquid–liquid impact occurs continuously. In the numerical model, this continuous impact will be simulated by a finite number of discrete impacts of surface panels of finite size. Each panel impact generates pressure impulses and, as is shown below, temporal discontinuities in ϕ and $\nabla\phi$ at the instant of the impact. The pressure impulse, I, is defined by

$$I = \lim_{t' \to t} \int_{t'}^{t''} P \, dt, \tag{14}$$

where P is the impact pressure and t' and t'' represent the instants just before and just after the impact, respectively. Since the interval from t' to t'' is infinitesimal, it can be shown from Bernoulli's equation that the velocity potential and pressure impulse satisfy the following relation (Batchelor 1967):

$$\phi'' - \phi' = -I/\rho, \tag{15}$$

in which ϕ' and ϕ'' are, respectively, the velocity potentials just before and immediately after the impact. This equation states that whenever an impact occurs, the velocity potential is discontinuous at that instant and has a jump which is equal to $-I/\rho$. For any two impacting material points (p^+ and p^-) on the bubble surface, the above condition can be written as

$$\phi''^+(x_{p^+}, t) = \phi'^+(x_{p^+}, t) - I^+/\rho, \tag{16}$$

$$\phi''^-(x_{p^-}, t) = \phi'^-(x_{p^-}, t) - I^-/\rho. \tag{17}$$

Subtracting (17) from (16) and noting that I^+ is equal to I^- at the impact point, a relation for the difference in ϕ across the impact surface at the instant of impact is obtained,

$$\phi''^+(x_{p^+}, t) - \phi''^-(x_{p^-}, t) = \phi'^+(x_{p^+}, t) - \phi'^-(x_{p^-}, t). \tag{18}$$

This relation states that the difference in ϕ between two impacting points remains the same during the impact. In the present model, the difference in ϕ varies along the impact interface. Best (1993) derived the same relationship, but applied it only to the impact of the north and south poles. After impact, he created a simply connected fluid domain by using a fictitious cut along which the difference in ϕ was assumed constant.

2.4. *Boundary integral equations*

The initial boundary value problem for the velocity potential ϕ as defined in the previous subsections, is solved by the boundary integral equation method. For times before initial impact, the numerical solution method, which is explained in the following section, is the one used by Blake *et al.* (1986) and others. In this method, the boundary conditions, (4) and (10), are integrated over each time step to yield the new position of S_b and the value of ϕ on this surface. To proceed on to the next time step, the values of $\partial\phi/\partial n$ on S_b must be determined. This problem is solved with a well-known boundary integral representation derived from Green's theorem:

$$\int_{S_b \cup S_\infty} \left[G(p,q) \frac{\partial \phi(q)}{\partial n_q} - \frac{\partial G(p,q)}{\partial n_q} \phi(q) \right] dS_q = \begin{cases} 2\pi\phi(p), & p \in S_b \cup S_\infty \\ 4\pi\phi(p), & p \in D, \end{cases} \tag{19}$$

where p is a field point, q is a source point varying as an integration variable on the surfaces $S_b \cup S_\infty$, dS_q is the differential area element of $S_b \cup S_\infty$, n_q is the normal to $S_b \cup S_\infty$ at q directed outward from the fluid and the kernel $G(p,q)$ is equal to $1/|p-q|$. Equation (19) is often called the conventional boundary integral equation (CBIE) in the sense that the kernels involved are weakly singular for $G(p,q)$ and Cauchy singular for $\partial G(p,q)/\partial n_q$, which are integrable without the need of any special treatment.

Unfortunately, the above approach fails when the re-entrant jet approaches the opposite surface of the bubble in the final stage of the collapse. This failure is caused by two problems with the CBIE. First, just before initial impact, an equation written for a point on the tip of the re-entrant jet will be nearly identical to that written for a corresponding point near the south pole of the bubble. Thus, for instance, if one is solving for $\partial\phi/\partial n$ with known ϕ, an ill-conditioned or nearly singular coefficient matrix will result in the boundary element calculations. Second, just after initial impact, due to the matching condition (8) the integral of $\partial\phi/\partial n$ along S^+ and S^- will cancel. Thus, additional equations are needed to calculate $\partial\phi/\partial n$ along the common surface. In the following, a new approach is presented in which the CBIE is modified to account for the common surface and a hypersingular boundary integral equation (HBIE) is introduced to form a closed equation system. With this new approach, the calculations based on the boundary integral equation method can be carried out continuously from before initial impact into the penetration process.

Making use of the properties of single- and double-layer potentials (Günter 1967; Burton & Miller 1971) as well as the matching condition (8), the CBIE (19) is modified in Appendix A for cases with a common surface to yield

$$\int_{S_b \cup S_\infty} \left[G(p,q) \frac{\partial \phi(q)}{\partial n_q} - \frac{\partial G(p,q)}{\partial n_q} \phi(q) \right] dS_q - \int_{S^+} \frac{\partial G(p,q)}{\partial n_q^+} [\phi^+(q) - \phi^-(q)]\, dS_q^+ = \begin{cases} 2\pi\phi(p), & p \in S_b \cup S_\infty \\ 2\pi[\phi^+(p) + \phi^-(p)], & p \in S^+ \end{cases} \tag{20}$$

In this modified CBIE, the equation is written with respect to $p \in S^+$ when the field point p is on the common surface $S^+ \cap S^-$. In the following section, on the numerical technique, it will be shown that during penetration the boundary conditions can be

integrated over each time step to yield the new positions of the surfaces S_b and $S^+ \cap S^-$, the values of ϕ on S_b and the values of $\phi^+ - \phi^-$ on $S^+ \cap S^-$. With these values, $\partial\phi/\partial n$ on S_b and $\phi^+ + \phi^-$ on $S^+ \cap S^-$ can be determined from (20). However, $\partial\phi/\partial n$ on the sheet is still unknown.

In order to find an analytical expression for $\partial\phi/\partial n$ on the common surface, the modified HBIE is derived in Appendix A by performing a directional derivative of the CBIE with p inside the domain D and then letting p approach the boundary along a direction normal to the boundary. The expression of the modified HBIE has the form

$$\int_{S_b \cup S_w} \left[\frac{\partial G(p,q)}{\partial n_p} \frac{\partial \phi(q)}{\partial n_q} - \frac{\partial^2 G(p,q)}{\partial n_p \partial n_q} \phi(q) \right] dS_q - \int_{S^*} \frac{\partial^2 G(p,q)}{\partial n_p \partial n_q} [\phi^+(q) - \phi^-(q)] \, dS_q^* = \begin{cases} 2\pi \partial\phi(p)/\partial n_p, & p \in S_b \cup S_w \\ 4\pi \partial\phi^+(p)/\partial n_p^*, & p \in S^* \end{cases}, \quad (21)$$

where n_p is the outward normal of the surface at p. Like (20), this modified HBIE is valid for the field point p either on the common surface or on the rest of the boundaries. From (21), $\partial\phi/\partial n$ on both $S^* \cap S^-$ and S_b can be determined as long as ϕ on the surfaces $S_b \cup S_w$ and $\phi^+ - \phi^-$ on S^* are prescribed.

2.5. *Energy considerations*

The equation governing the energy of the flow is

$$\int_{V_f(t)} \tfrac{1}{2}\rho q^2 \, dV - \int_{V_f(0)} \tfrac{1}{2}\rho q^2 \, dV + \frac{P_\infty - P_g}{\rho} (V_g(t) - V_g(0)) = 0, \quad (22)$$

where the integration limits $V_f(t)$ and $V_f(0)$ are the fluid volumes at times t and $t = 0$, respectively, and $V_g(t)$ and $V_g(0)$ are the volumes of the bubble at times t and $t = 0$, respectively (see Duncan & Zhang 1991, equation (12)). The first two terms on the left are the kinetic energies of the fluid at the two times and can be calculated from surface integrals over the bubble and the common surface (Lamb 1945):

$$\int_{V_f(t)} \tfrac{1}{2}\rho q^2 \, dV = \frac{1}{2} \int_S \phi \frac{\partial \phi}{\partial n} \, dS, \quad (23)$$

where S is the internal boundary $S_b \cup S^* \cup S^-$. The third term in (22) is the potential energy defined as the work done against the pressure at infinity due to changes in the bubble volume.

For times up to the instant before initial impact, the total energy of the system is constant. During the collapse phase before impact, the potential energy decreases and the kinetic energy increases by equal amounts. However, there is a loss of kinetic energy associated with the liquid–liquid impact and this energy is not converted to potential energy. Thus, the total energy decreases. This kinetic energy loss is given by the following equation which is derived in Appendix B:

$$\Delta E_k = \int_D \tfrac{1}{2}\rho (\nabla\phi^+)^2 - \tfrac{1}{2}\rho (\nabla\phi^-)^2 \, dV = -\frac{1}{2} \int_{S^*} I^* (\nabla(\phi^+)^* - \nabla(\phi^-)^-) \cdot n_* \, dS. \quad (24)$$

Rogers *et al.* (1990) and Szymczak *et al.* (1993) also noted an energy loss during impact and presented a similar formula. In the above equation, the value of I^* is a positive maximum at the impact interface since the gradient of I must accelerate the fluid on both sides of the interface in directions away from the interface. The difference in the normal components of the velocities inside the brackets is always positive as long as there is an impact. Thus, ΔE_k must be less than zero. It should be noted that the above

expression was derived on the assumption that the colliding surfaces stick together after impact. It is this assumption that causes the loss in energy.

As an example of a simple impact problem demonstrating the energy loss, consider two parallel liquid layers of infinite extent in planes normal to the z-axis. One layer is above the $z = 0$ plane and has a uniform velocity $v = -V\hat{k}$ and a thickness h^+ while the other layer is below the plane $z = 0$ and has a uniform velocity $v = V\hat{k}$ and a thickness h^-. Impact occurs when the 'inner' surfaces meet at $z = 0$. In this example, the divergence of equation (B 1) yields

$$\frac{\partial^2 I}{\partial z^2} = -2\rho V\delta(z), \tag{25}$$

which has the solution

$$I^+ = \frac{-2\rho Vh^-}{h^+ + h^-}(z - h^+) \tag{26}$$

in the upper layer. Evaluation of (24) in this case yields

$$\Delta E_k = 2\rho V^2 \frac{h^+h^-}{h^+ + h^-} \tag{27}$$

per unit area. Thus, for the case when $h^+ = h^- = H$, the kinetic energy change is $-\rho V^2 H$ per unit area. This change is equal to the total kinetic energy before impact and indicates that, as expected, the two layers will come to rest after impact.

3. Numerical scheme

The numerical schemes to be discussed in this section deal with two issues: the accurate solution of the integral equation system (20) and (21) at a given time instant and the time advancement of the boundary conditions (4), (10) and (13). For the first issue, it is important to note that while the introduction of the modified HBIE (21) produces a well-posed system of equations during penetration, it unfortunately makes the numerical scheme more complicated than schemes that use the CBIE alone in cases before penetration. These complications arise out of the need for regularizing the hypersingular kernel, making the solutions unique and discretizing the geometry and density functions properly. For the second issue, the kinematic boundary condition must be modified slightly to treat the node points on the vortex sheet.

3.1. *Regularization of the hypersingular integral*

As can be seen from (21), the kernel $\partial^2 G(p, q)/\partial n_p \partial n_q$ has a third-order singularity $(1/|p - q|^3)$ as p approaches q, which makes it non-integrable in the ordinary sense. Several regularization techniques to treat integrals of this kind exist (Meyer, Bell & Zinn 1978; Ingber & Rudolph 1990; Krishnasamy *et al.* 1990). In this paper, the hypersingular kernel has been transformed to a Cauchy-singular kernel. The relation between the two kernels can be expressed in the identity (Ingber & Rudolph 1990)

$$\int_S \phi(q)\frac{\partial^2 G(p, q)}{\partial n_p \partial n_q} dS_q = \int_S [n_q \times \nabla_q \phi(q)] \cdot [n_p \times \nabla_p G(p, q)]\, dS_q, \tag{28}$$

where the gradient operator with a subscript indicates that the operation is carried out with that subscript as a variable. The decomposition of this integral in a cylindrical coordinate system with axisymmetry transforms the density function $\phi(q)$ in (28) to the density function $\partial\phi(q)/\partial s_q$, where s_q is the arclength along the surface. The corresponding derivations related to this decomposition and expressions for other terms in (21) can be found in Appendix C.

3.2. *Uniqueness of solutions of the hypersingular integral equation*

Using the hypersingular integral equation (21) alone to solve the Dirichlet problem of Laplace's equation will result in non-unique solutions. (Solutions are only unique up to an additive constant.) This non-uniqueness can be easily deduced from the identity (28) in that, if $\phi(q)$ is a constant along the surface, the integral with the hypersingular kernel is identically equal to zero; thus, (21) will yield $\partial\phi/\partial n = 0$ at all points on the surface. However, this contradicts the well-known case of a Rayleigh spherical bubble in an infinite fluid where a uniformly distributed ϕ on the bubble corresponds to a non-zero $\partial\phi/\partial n$ on the surface. In the present work, this non-uniqueness is resolved by introducing a combined scheme in which the modified CBIE and HBIE are jointly used. In this combined scheme, the CBIE is responsible for recovering the constant in ϕ along the surface which would be lost if the HBIE were used alone.

3. *Time advancement algorithm*

The time advancement techniques for times before and during penetration are discussed separately in the following subsection. All of the temporal integrations are performed by the following predictor-corrector scheme. Given an ordinary differential equation $dy/dt = f(t, y)$ with an initial condition $y(t_0) = y_0$, the numerical solution for y at step $i+1$ ($i = 0, 1, \ldots$) is given by

predictor step:
$$y^{\circ}_{i+1} = y_i + (t_{i+1} - t_i) f(t_i, y_i), \tag{29}$$

corrector step:
$$y_{i+1} = y_i + \tfrac{1}{2}(t_{i+1} - t_i)\{f(t_i, y_i) + f(t_{i+1}, y^{\circ}_{i+1})\}. \tag{30}$$

For ease of presentation, only the predictor step is presented in the following.

3.3.1 *Time marching before initial impact*

Let us assume that at time t all quantities are known. To proceed on to $t + \Delta t$, the boundary conditions (4) and (10) are integrated following the fluid particle p on the surface S_b.

$$x_p(t + \Delta t) = x_p(t) + \nabla\phi(x_p, t)\,\Delta t, \tag{31}$$

$$\phi(x_p, t + \Delta t) = \phi(x_p, t) + \Delta t\left(\frac{|\nabla\phi(x_p, t)|^2}{2} + \frac{P_a - P_g}{\rho}\right). \tag{32}$$

These equations yield the new position of S_b and the values of ϕ on this surface at $t + \Delta t$. From this information, the derivative of ϕ in the direction tangent to the surface can be computed. In order to proceed to integrate (4) and (10) over the next time step the values of $\partial\phi/\partial n$ are required. These values are obtained by solving the integral equations.

3.3.2. *Time marching after initial impact*

After initial impact, material points on the toroidal bubble are treated like those before impact by integrating (4) and (10). The integration of the boundary conditions for points on the common surface is somewhat more complicated since two fluid particles, p^+ on S^+ and p^- on S^-, occupying the same location on each side of the surface at time t will in general not be together at the next time step (the tangential velocities are not equal on each side of the sheet). The relation between the velocity of a fluid particle p and the velocity of its projection in the direction normal to the surface is

$$\left(\frac{dx^{\circ}_p}{dt}\cdot n_p\right) n_p = \frac{\partial\phi}{\partial n} n_p = \frac{dx^{\circ}_p}{dt}. \tag{33}$$

where x_p^n is the position vector of the projection of x_p in the normal direction n_p. Writing this relation at p^+ and p^- on S^+ and S^- for the predictor step yields

$$x_p^n(t+\Delta t) = x_p^n(t) + \Delta t \frac{\partial \phi^+}{\partial n_p^+} n_p^+, \tag{34}$$

and

$$x_p^n(t+\Delta t) = x_p^n(t) + \Delta t \frac{\partial \phi^-}{\partial n_p^-} n_p^-, \tag{35}$$

respectively. In view of the matching conditions (8) and the fact that $n_p^+ = -n_p^-$, the above equations reduce to a single equation yielding the new position of the common surface at time $t+\Delta t$. The boundary condition (13) integrated for the predictor step is

$$\phi_n^+(t+\Delta t) - \phi_n^-(t+\Delta t) = \phi_n^+(t) - \phi_n^-(t) - \frac{\Delta t}{2}\left[\left(\frac{\partial \phi^+}{\partial s^+}\right)^2 - \left(\frac{\partial \phi^-}{\partial s^-}\right)^2\right], \tag{36}$$

where the subscript n indicates the values of ϕ at a point following the normal flow.

It should be emphasized that it is the values of ϕ on the bubble surface (S_b) and the values of $\Delta\phi\,(=\phi^+-\phi^-)$ on the impact interface ($S^+ \cap S^-$) that are advanced in time by (32) and (36). Both quantities are continuous with respect to time.

3.3.3. *Time step determination*

In the time advancement, a variable time step technique is adopted. At each step, the time increment Δt is determined by

$$\Delta t = \frac{C}{1+0.5V_{max}^2}, \tag{37}$$

where V_{max} is the maximum velocity on the bubble surface at the current time step and C is a constant that is taken as 0.04 before penetration when the CBIE is used and 0.01 during penetration when the combined scheme is employed. The determination of these values of C is explored in §4.3.

3.4. *Numerical implementation of the integral equations*

The modified CBIE (20) and HBIE (21) are solved by the boundary element method. The infinite rigid wall is simulated by an image bubble. The bubble surface is discretized by n_b panels. Given the r- and z-coordinates of n_b+1 panel nodes along the surface, the coordinates r and z along each panel can be written as functions of a cubic spline parameter, ζ, which is chosen as a variable along the chord length of each panel (Dommermuth & Yue 1987; and Press *et al.* 1989),

$$r = r(\zeta), \quad z = z(\zeta). \tag{38}$$

Thus, the arclength coordinate, s, along each panel can be calculated by

$$s(\zeta) = \int_0^\zeta ds = \int_0^\zeta \left[\left(\frac{dr}{d\zeta}\right)^2 + \left(\frac{dz}{d\zeta}\right)^2\right]^{\frac{1}{2}} d\zeta. \tag{39}$$

Other geometric quantities in the integral equations such as $G(p,q)$ and $\nabla G(p,q)$ are computed from the above equations. The most stable calculations were performed with the density functions ϕ and $\partial\phi/\partial n$ inside each panel interpolated as cubic spline and linear functions of s, respectively.

The spline fitting of the surface during penetration is complicated by the presence of the triple point where the common surface attaches to the ring bubble. In the present

work, the surface is fitted continuously from the north pole to south pole by a path covering S^+, S_b and S^- sequentially. As a result, the normal to the surface directed into the fluid changes continuously during the integration around the surface and a cusp is formed in the bubble at the triple point (see figure 1*b*). This treatment is based on the fact that at the final stage of the bubble collapse, the speed of the surface of the re-entrant jet is generally on the order of 10^1–$10^2(\Delta P/\rho)^{\frac{1}{2}}$ while the fluid near the wall is moving more slowly in the opposite direction. Thus, there exists a strong shear layer in the region close to the triple point. In experiments, this shear layer contains a layer of gas. A similar flow is generated when a liquid jet impacts on a flat water surface and air entrainment occurs along the periphery of the jet. Surface tension forces have the tendency to round the cusp, but in the present case this does not occur owing to the effects of inertia and the short timescale.

Since the problem is axisymmetric about the z-axis, the terms in the integral equations can first be integrated analytically with respect to the circumferential variable θ. The resulting terms then involve elliptical integrals of the first and second kinds as functions of the arclength s in the $\theta = 0$ plane (see Appendix C). The field points (collocation points or nodes) are taken at the edge points of the panels. As a result, the integral equations (20) and (21) can be written in discretized forms within each panel,

$$\sum_{j=m}^{n_b-m+1}\int_{L_j}\left[C_{ij}\left(\frac{\partial\phi}{\partial n}\right)^j + D_{ij}\phi^j\right]ds_j + \sum_{j=1}^{m-1}\int_{L_j} D_{ij}[(\phi^+)^j - (\phi^-)^j]\,ds_j + J_1 = \begin{cases} 2\pi\phi_i; & i = m+1,\ldots,n_b-m+1 \\ 2\pi(\phi_i^+ + \phi_i^-); & i = 1,\ldots,m, \end{cases} \tag{40}$$

$$\sum_{j=m}^{n_b-m+1}\int_{L_j}\left[E_{ij}\left(\frac{\partial\phi}{\partial n}\right)^j + F_{ij}\left(\frac{\partial\phi}{\partial s}\right)^j\right]ds_j + \sum_{j=1}^{m-1}\int_{L_j} F_{ij}\left[\left(\frac{\partial\phi}{\partial s^+}\right)^j + \left(\frac{\partial\phi}{\partial s^-}\right)^j\right]ds_j + J_2 = \begin{cases} 2\pi(\partial\phi/\partial n)_i; & i = m+1,\ldots,n_b-m+1 \\ 4\pi(\partial\phi^+/\partial n)_i; & i = 1,\ldots,m, \end{cases} \tag{41}$$

where m is the index of the triple point; i and j represent the indexes of the field point and source panel, respectively; L_j is the arclength of panel j; J_1 and J_2 are the terms corresponding to the contribution from the image bubble; C_{ij}, D_{ij}, E_{ij} and F_{ij} are functions of the elliptic integrals and can be found in Appendix C; ϕ^j, $(\partial\phi/\partial n)^j$ and $(\partial\phi/\partial s)^j$ are functions of the arclength inside the panel j; and ϕ_i and $(\partial\phi/\partial n)_i$ are values at the point i. Gauss–Legendre quadrature formulae were used to calculate the integrals in (40) and (41), in which the regular integrands were integrated with a 5-point formula while the non-regular integrands, which contain logarithmic singularities, were treated with the formulation given by Anderson (1965). The linear system of algebraic equations formed in this way were solved with the LDU Algorithm (Press *et al.* 1989).

Various combinations of (40) and (41) were applied at the nodes during different phases of the calculations. For cases without a common surface, two combinations were used. In some cases the CBIE was applied at all the nodes. In other cases, the HBIE was applied at the first n_d nodes on top of the bubble starting with the north pole and the last n_d nodes ending with the south pole while the CBIE was applied at the remaining $n_b + 1 - 2n_d$ nodes. In cases during penetration with m double nodes along the common surface, the HBIE was applied at the first $n_d + 1 - m$ nodes starting with the north pole and the CBIE was applied to the last m nodes ending with the south pole.

The adjustment of the time step during the impact of adjacent nodes was found to be critical to achieving an accurate calculation. The general technique employed here was to adjust the time step so that, given the distance and relative velocity between the nodes at the current time, the nodes would impact at the end of the time step. To implement this scheme a minimum distance ϵ was chosen. If the distance between one or more pairs of nodes on the ring bubble adjacent to the triple point was less than ϵ, the time step was adjusted so that all of these pairs collided by the end of the time step. In performing the calculations, it was found that as ϵ was decreased the calculation converged initially. However, if ϵ was too small, an overlapping of the nodes on the ring bubble near the triple point occurred at the next time step. It is thought that these problems arise because the Green's function between nearly touching nodes from opposite sides of the bubble becomes singular as the distance between the nodes tends to zero. Thus, for small enough ϵ the solutions of the boundary integral equations are probably inaccurate. After a number of test calculations, it was found that $\epsilon = 0.002$ was a typical minimum value that produced a converged calculation without overlapping of adjacent nodes. This value was used for all the calculations presented in this paper.

3.5. *Numerical instabilities*

The numerical method presented above exhibits unstable behaviour when the volume of the ring bubble approaches the initial volume of the bubble. The causes of the numerical instability are not clear. There is no theoretical analysis available to examine the numerical instability because the boundary conditions (4), (10) and (13) are coupled and the conditions (10) and (13) are nonlinear. Several researchers (Longuet-Higgins & Cokelet 1976; Dommermuth & Yue 1987; Oğuz & Prosperetti 1990) have reported similar instabilities encountered in boundary element calculations employing higher-order elements when simulating nonlinear waves and water droplets.

To cope with the instabilities, a 5-point smoothing technique (Mathematical Handbook 1977, pp. 907–908) was introduced. Given a data set $y_i (i = 0, 1, 2, \ldots, m)$, the modified data set $y'_i (i = 0, 1, 2, \ldots, m)$ is computed by the following smoothing formulations:

$$y'_i = \tfrac{1}{35}[-3(y_{i-2} + y_{i+2}) + 12(y_{i-1} + y_{i+1}) + 17y_i], \quad i = 2, \ldots, m-2, \tag{42}$$

$$y'_0 = \tfrac{1}{35}(31y_0 + 9y_1 - 3y_2 - 5y_3 + 3y_4), \tag{43}$$

$$y'_1 = \tfrac{1}{35}(9y_0 + 13y_1 + 12y_2 + 6y_3 - 5y_4), \tag{44}$$

$$y'_{m-1} = \tfrac{1}{35}(-5y_{m-4} + 6y_{m-3} + 12y_{m-2} + 13y_{m-1} + 9y_m), \tag{45}$$

$$y'_m = \tfrac{1}{35}(3y_{m-4} - 5y_{m-3} - 3y_{m-2} + 9y_{m-1} + 31y_m). \tag{46}$$

Mesh regridding is also adopted to keep equal panel sizes during the time stepping.

4. Verification of the numerical modelling

In this section, the results of several static and dynamic tests designed to verify the mathematical model and to assess the performance of the combined numerical scheme developed in §§2 and 3 are presented.

4.1. *A sheet attached to a toroid*

The first test of the numerical model is to examine the accuracy of the boundary element solver with the combined scheme on a static problem. In order for this test to have relevance to the penetration problem, it must satisfy the following conditions: the boundary geometry must include both regular and common surfaces, across the

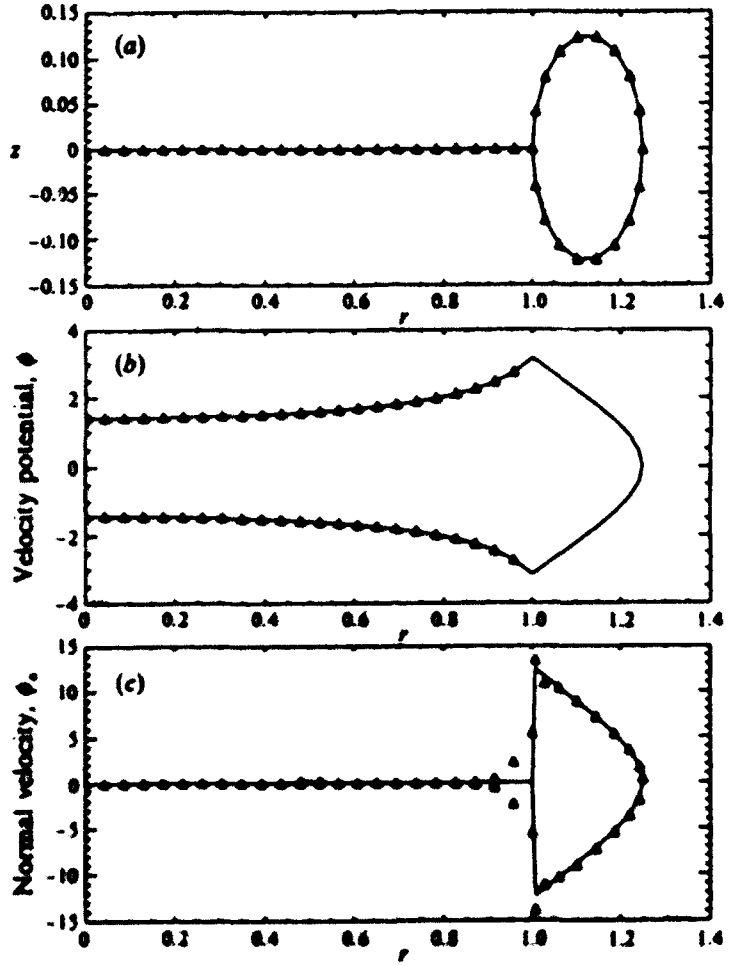

FIGURE 2. Comparisons of the results of the combined scheme with analytical solutions for a toroidal surface and a two-layer sheet. (*a*) Geometry of the sheet, toroid and mesh distributions (△, nodal point). (*b*) Calculated (△) and analytical (——) ϕ on the sheet. (*c*) Calculated (△) and analytical (——) $\partial\phi/\partial n$ on the sheet and toroid.

common surface ϕ and $\partial\phi/\partial s$ must be discontinuous while $\partial\phi/\partial n$ must be continuous, $|\nabla\phi|$ must vanish at infinity, and ϕ must be sufficiently continuous inside the domain. The boundary geometry of the chosen problem is that of a toroid about the z-axis connected to a flat circular sheet on the plane $z = 0$ as shown in figure 2(*a*). In the domain exterior to this boundary, Laplace's equation can be easily solved in toroidal coordinates (η, θ, ψ) given by the following transformations (for axisymmetric problems):

$$x = \frac{a\sinh(\eta)}{\cosh(\eta)-\cos(\theta)}, \tag{47}$$

$$z = \frac{a\sin(\theta)}{\cosh(\eta)-\cos(\theta)}. \tag{48}$$

Thus, the cross-section of the toroid is given by $\eta = \eta_0$, $-\pi \leqslant \theta \leqslant \pi$ and $\psi = 0$ in the (η, θ, ψ) system or $(x - a\coth\eta_0)^2 + z^2 = a^2/\sinh^2(\eta_0)$ and $y = 0$ in the (x, y, z) system,

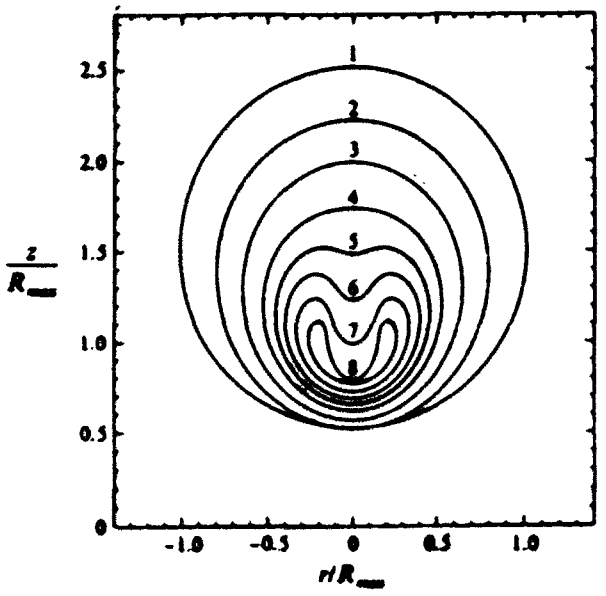

FIGURE 3. Comparison of bubble profiles between the conventional (——) and combined (·····) schemes for a transient cavitation bubble collapsing near a rigid wall with $R_0 = 0.1$ and $Z_0 = 1.5$. The numbers 1 to 8 correspond to the non-dimensional times $t = 0.983$, 1.707, 1.877, 1.972, 2.014, 2.043, 2.068, and 2.086.

while the cross-section of the sheet is given by $0 \leqslant \eta \leqslant \eta_0$, $\theta = \pm\pi$ and $\psi = 0$ or $0 \leqslant x \leqslant a\coth\eta_0 - a/\sinh\eta_0$, $y = 0$ and $z = 0$ in the two different coordinate systems, respectively. In the present test, η_0 is chosen as 2.890454 and a is 1.117637. From the infinite number of particular solutions of Laplace's equation in the (η, θ, ψ) system (Moon & Spencer 1961, pp. 369–372), one is chosen such that it satisfies the requirements of the numerical tests cited above. Thus, given ϕ on the sheet and the toroid in the form

$$\phi(\eta, \theta) = (\cosh(\eta) - \cos(\theta))^{\frac{1}{2}} \sin(\tfrac{1}{2}\theta), \tag{49}$$

the corresponding expressions for $\partial\phi/\partial n$ are, respectively,

$$\partial\phi/\partial n = 0 \quad \text{on the sheet,} \tag{50}$$

$$\partial\phi/\partial n = (\cosh(\eta) - \cos(\theta))^{\frac{1}{2}} \sinh(\eta) \sin(\tfrac{1}{2}\theta)/(2a) \quad \text{on the toroid.} \tag{51}$$

In the numerical calculations, ϕ was specified on the toroid and $\phi^+ - \phi^-$ was specified on the sheet from the analytical solution (49). The integral equations (20) and (21) were then solved with the combined scheme for $\partial\phi/\partial n$ on the entire surface and ϕ on the sheet. The comparison between the analytical and numerical calculations of ϕ on the sheet and $\partial\phi/\partial n$ on both the sheet and toroid are plotted in figures 2(*b*) and 2(*c*). The results show that the numerical calculations agree well with the analytical ones with the errors in $\partial\phi/\partial n$ and ϕ at the north pole less than 0.3% and 0.2%, respectively. The deviation of $\partial\phi/\partial n$ near the triple point between the sheet and toroid is as expected because the numerical scheme is constructed on the basis of a smooth surface generated by a cubic-spline fitting rather than a non-smooth connection at that point as in this test case. This is not considered to be a problem since, in the simulation of the penetration process, the tangent along the bubble surface is always assumed to vary continuously.

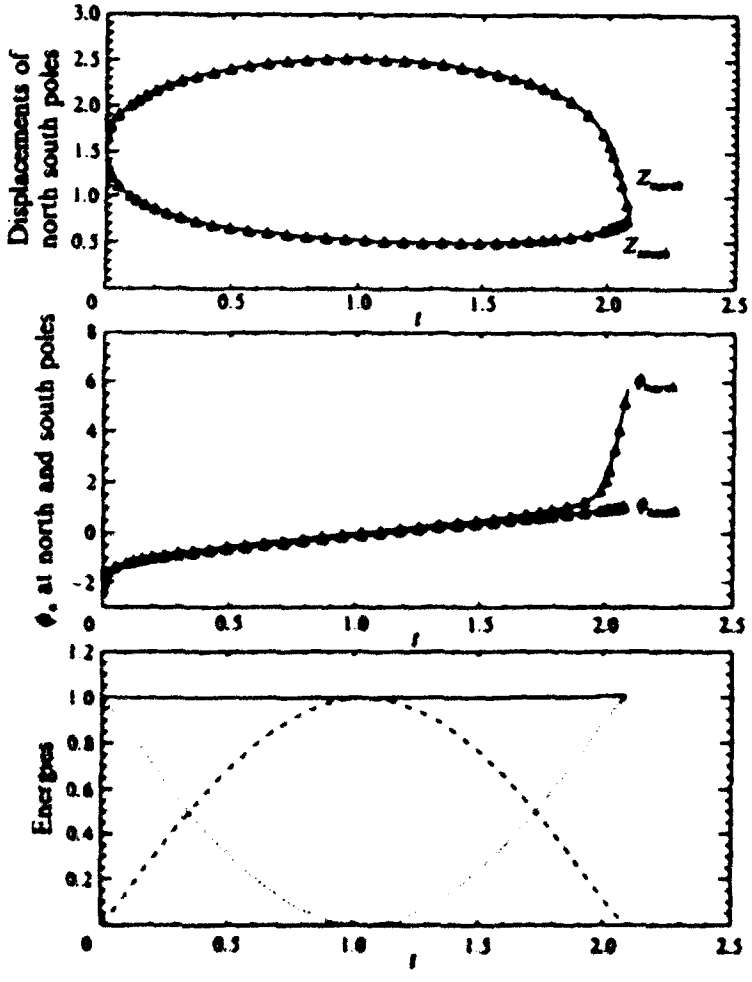

FIGURE 4. Various quantities plotted versus time for the bubble collapse depicted in figure 3. (*a*) The *z*-coordinates of the north and south poles of the bubble: ——, conventional scheme; △, combined scheme. (*b*) The velocity potentials at the north and south poles versus time: ——, conventional scheme; △, combined scheme. (*c*) The energies versus time for the combined scheme: total mechanical energy (——), kinetic energy (·····), and potential energy (——).

4.2. *A cavitation bubble collapsing near a rigid wall*

As a dynamic test, the combined scheme was used to compute the growth and collapse of a cavitation bubble adjacent to a rigid wall up to the time just before penetration begins. Because there is no analytical solution available for this non-spherical collapse case, the numerical calculations using the combined scheme are compared with those using the CBIE scheme. The results of the present CBIE scheme were compared to similar calculations in the literature and found to be in excellent agreement. Initially, the bubble is spherical and centred at $r = 0$ and $Z_0 = 1.5$ with radius $R_0 = 0.1$. The combined scheme was used with $n_b = 32$ and $n_d = 16$. Linear isoparametric elements were employed for the conventional scheme, also with $n_b = 32$. In figure 3, the bubble profiles at different time instants in the collapse phase obtained by both the combined and conventional scheme are plotted together. Both schemes give almost the same

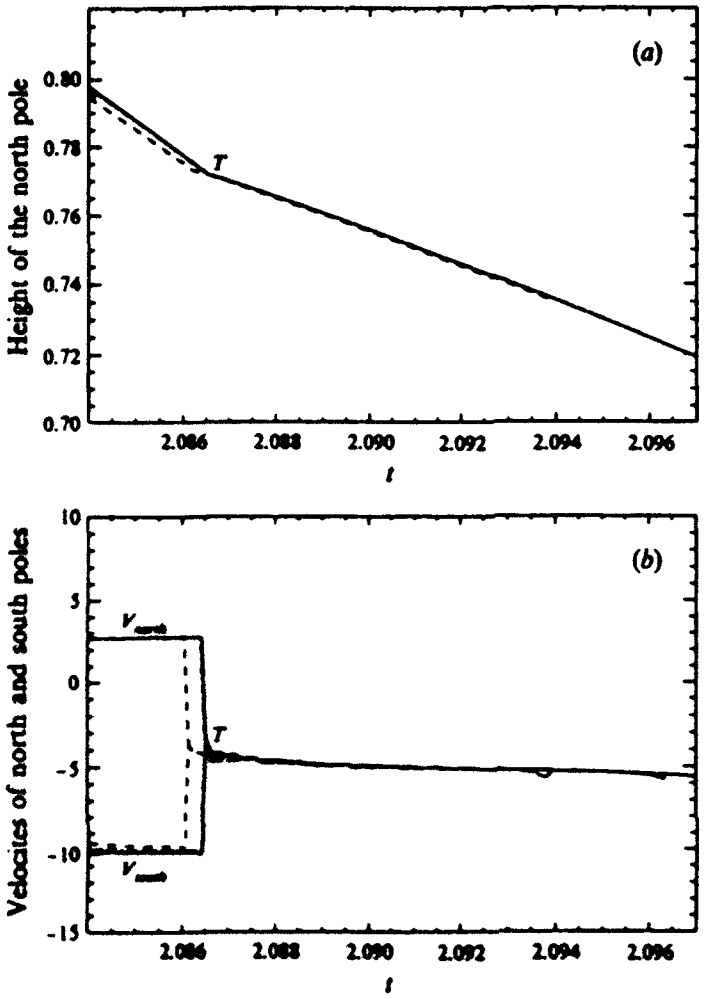

FIGURE 5. Convergence as a function of mesh size for the combined scheme before and after penetration. (*a*) The height of the north pole versus time; (*b*) the normal velocity of the north and south poles versus time. ——, $n_0 = 32$; – · – · –, $n_0 = 48$, and ——, $n_0 = 64$. *T* denotes the instant of initial impact.

bubble profiles at the same time. The heights of the north and south poles, the velocity potentials at the north and south poles and the kinetic and potential energies of the flow are plotted versus time in figures 4(*a*), 4(*b*) and 4(*c*), respectively, for both schemes. There is good agreement in all cases.

4.3. *Convergence studies*

Several computations aimed at examining the convergence of the combined scheme versus panel size and time step size during penetration simulations were also made. Figure 5(*a*) and 5(*b*) show the height and velocity of the north pole from before penetration through the penetration process for various panel numbers. As can be seen from the figure, the results converge as the number of panels increases. Figures 6(*a*) and 6(*b*) show the same quantities converging as the time step decreases. The number of panels and time step used in the present results are given in the following section.

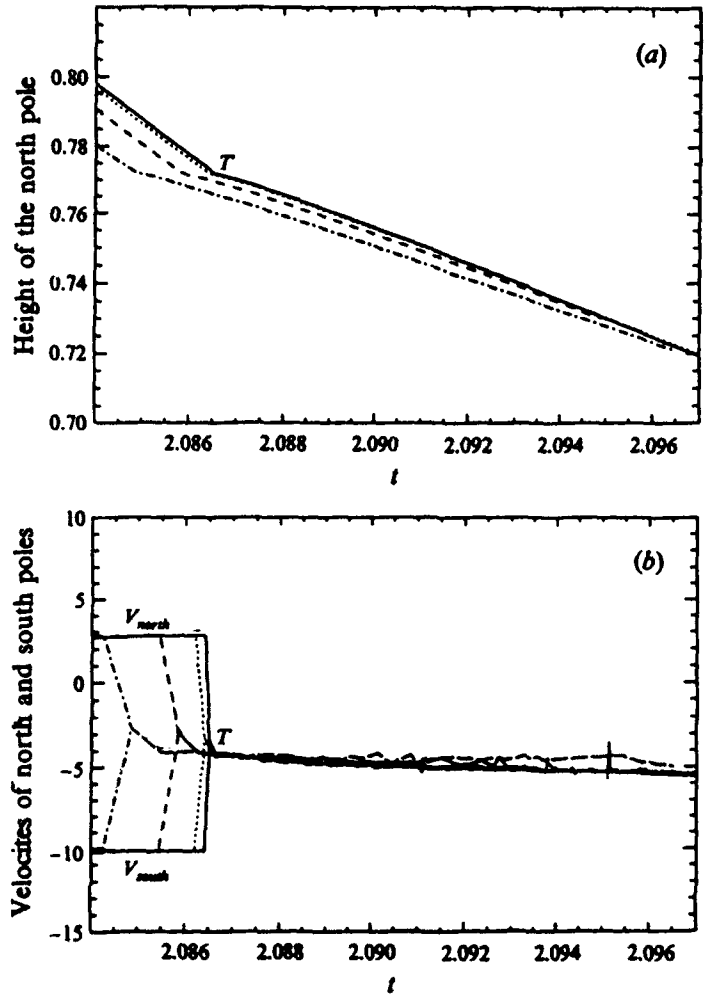

FIGURE 6. Convergence as a function of time step size for the combined scheme before and after penetration. (*a*) The height of the north pole versus time; (*b*) the normal velocity of the north and south poles versus time. -·-·-, $C = 0.06$; ——, $C = 0.04$; ·····, $C = 0.02$; ——, $C = 0.01$. The parameter C is related to the variable time step, $\Delta t = C/(1+0.5V^2_{max})$. T denotes the instant of initial impact.

The tests conducted in this section show that the combined scheme developed in §§2 and 3 is valid in both static and dynamic cases.

5. Simulation of the penetration process

The calculations presented in this section were done with $n_b = 64$ and $R_0 = 0.1$. From the initial instant up to the time when the distance between the north and south poles becomes less than 0.03, the CBIE method is used for all nodes. At this point, the scheme is switched to the combined CBIE–HBIE method with $n_d = 32$. When penetration begins, the scheme is again switched to that described in §3.4 for cases with a common surface. The parameter C for time stepping is taken as 0.04 before penetration and 0.01 during penetration. The value of ϵ is chosen as 0.002 (see §3.4).

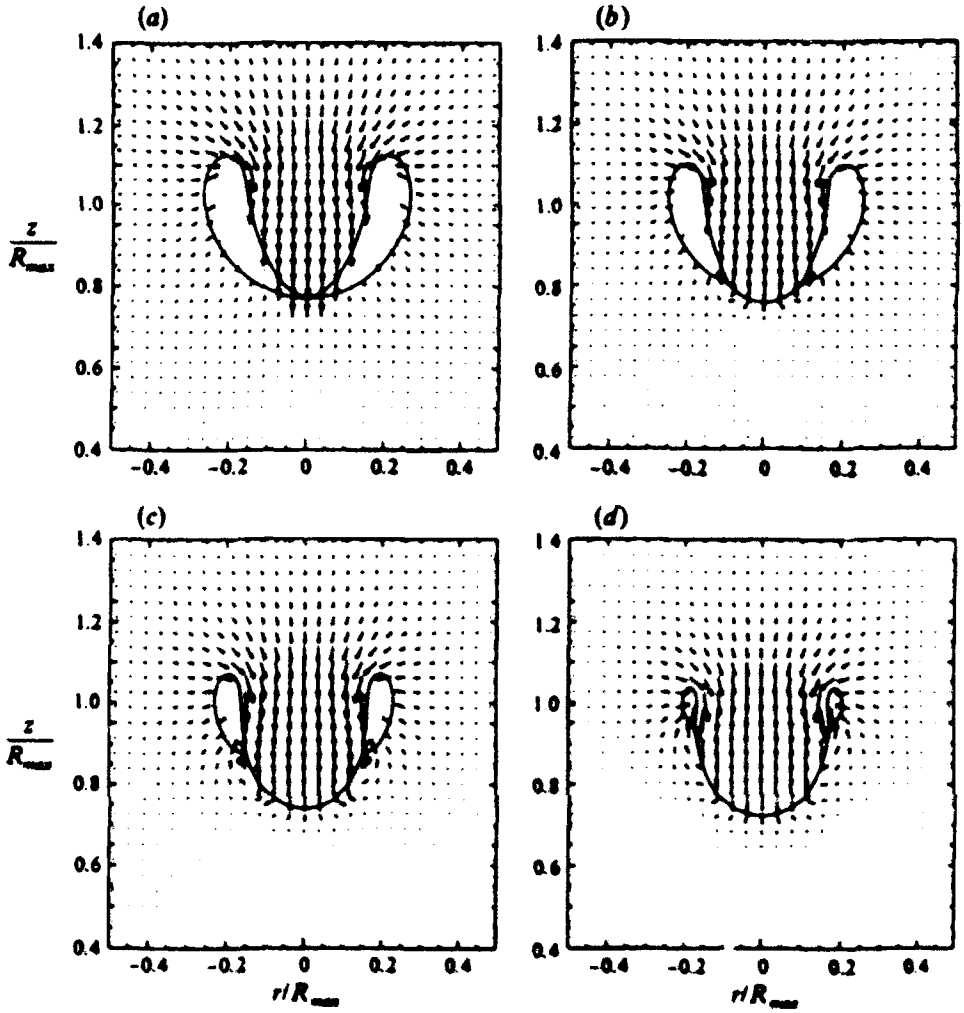

FIGURE 7. Bubble profiles and velocity fields for $Z_0 = 1.5$ and $R_0 = 0.1$: (*a*) $t = 2.08545$, (*b*) $t = 2.08861$, (*c*) $t = 2.09241$, (*d*) $t = 2.09551$. The lengths of the velocity vectors are scaled with respect to the flow speeds at the location ($r = 0$, $z = 1.1375$) in each plot. These speeds are 8.43, 7.94, 7.17 and 6.30 in (*a*), (*b*), (*c*) and (*d*), respectively.

Z_0	T_c	Z_c	V_n	V_s	V_r	Γ_∞
1.1	2.16048	0.099	−9.055	0.042	−4.254	5.400
1.25	2.13679	0.318	−8.459	1.126	−4.167	5.331
1.5	2.09013	0.777	−11.574	3.480	−4.079	4.717
1.75	2.05396	1.172	−12.013	4.550	−4.235	4.371

TABLE 1. Z_0: initial height of the bubble centroid; T_c: collapse time; Z_c: collapse height (z of north and south pole at $t = T_c$); V_n: velocity of the north pole before impact (in the $-z$ direction); V_s: velocity of the south pole before impact; V_r: velocity of the north (or south) pole just after the initial impact; Γ_∞: circulation around the ring bubble at the instant of the initial impact

In the following, results are presented for $Z_0 = 1.1$, 1.25, 1.5 and 1.75. The results for $Z_0 = 1.5$ and 1.1 are presented first and in more detail than those for the other Z_0 values. For reference throughout the discussion, table 1 gives the time (T_c), the height (Z_c), the velocities of the north and south poles of the bubble (V_n and V_s) at the instant before initial impact and the velocity of the north pole of the sheet (V_c) as well as the circulation (Γ_{sh}, defined below) at the instant after initial impact for all four values of Z_0.

5.1 *Bubble profiles and velocity fields*

The general features of the flow field just before and during penetration are illustrated in figure 7, for $Z_0 = 1.5$. Figure 7(*a*) shows the flow field one time step before penetration. The re-entrant jet has formed at the top of the bubble surface and is moving toward the rigid wall. The fluid on the lower side of the bubble has not yet sensed the jet and is still moving away from the wall. The relative normal velocity between the north and south poles at this instant is 15.05 (see table 1). The poles of the bubble meet at $z = 0.78$ and the flow field soon after penetration is shown in figure 7(*b*). As can be seen in the figure, the geometry of the bubble surface has become a ring bubble with an attached sheet. The flow pattern has suddenly changed such that the flow on the lower side of the bubble has reversed direction and is now moving toward the wall. The velocity of the re-entrant jet is still directed toward the wall but with a much smaller magnitude (4.08) than before impact (11.57). The velocity components tangent to the common surface and the ring bubble surface are directed mainly toward the axis of symmetry on the jet side of the common surface and bubble and away from the axis on the other side, this indicates that there are vortex elements along the sheet and in the bubble that circle the z-axis. The mechanism that brings about this sudden change in the flow field is the liquid-liquid impact during jet penetration.

Further development of the penetration process is shown in figure 7(*c*). The dominant changes in the bubble profile are the drastic reduction in the volume of the ring bubble and the extension of the vortex sheet due to continuing impacts of the surface panels of the ring bubble. There is also some translational motion of the bubble and the sheet in the direction of the rigid wall. In figure 7(*d*), the volume of the ring bubble has reached about 0.72 times the initial bubble volume. The calculation becomes unstable soon after this time. It is presumed that if gas were included in the bubble, the bubble would begin a second growth phase at approximately this time, depending on the amount of gas. The flow pattern in figure 7(*d*) is characterized by a large vortex sheet attached to a small ring bubble with a rotating flow concentrated in the area around the ring bubble in the vicinity of the triple point.

Bubble profiles and velocity fields for $Z_0 = 1.1$ are given in figure 8. As in the previous case, the impact of the re-entrant jet results in the formation of a ring bubble and a vortex sheet. At the instant before initial impact, the north and south poles of the bubble are much closer to the wall ($z = 0.10$) than in the previous case and the relative normal velocity between the north and south poles is 9.10 compared to 15.05 for $Z_0 = 1.5$, see table 1. The remaining bubble volume at the instant of impact (46.19 for $Z_0 = 1.1$) is much larger than in the case for $Z_0 = 1.5$. Later in the penetration process, the tip of the vortex sheet hits the rigid wall for $Z_0 = 1.1$ (figure 8*c*, *d*) while the tip of the sheet for $Z_0 = 1.5$ is still relatively far away from the wall even at the end of the first collpse. The shape of the vortex sheet also shows marked differences between the two cases. For $Z_0 = 1.5$, the vortex sheet is 'U'-shaped while for $Z_0 = 1.1$ the sheet rolls up at the sides due to the stronger influence of the wall. The calculation for $Z_0 = 1.1$ is terminated when the bubble volume is reduced to about 7.1 times its initial volume because of numerical instabilities

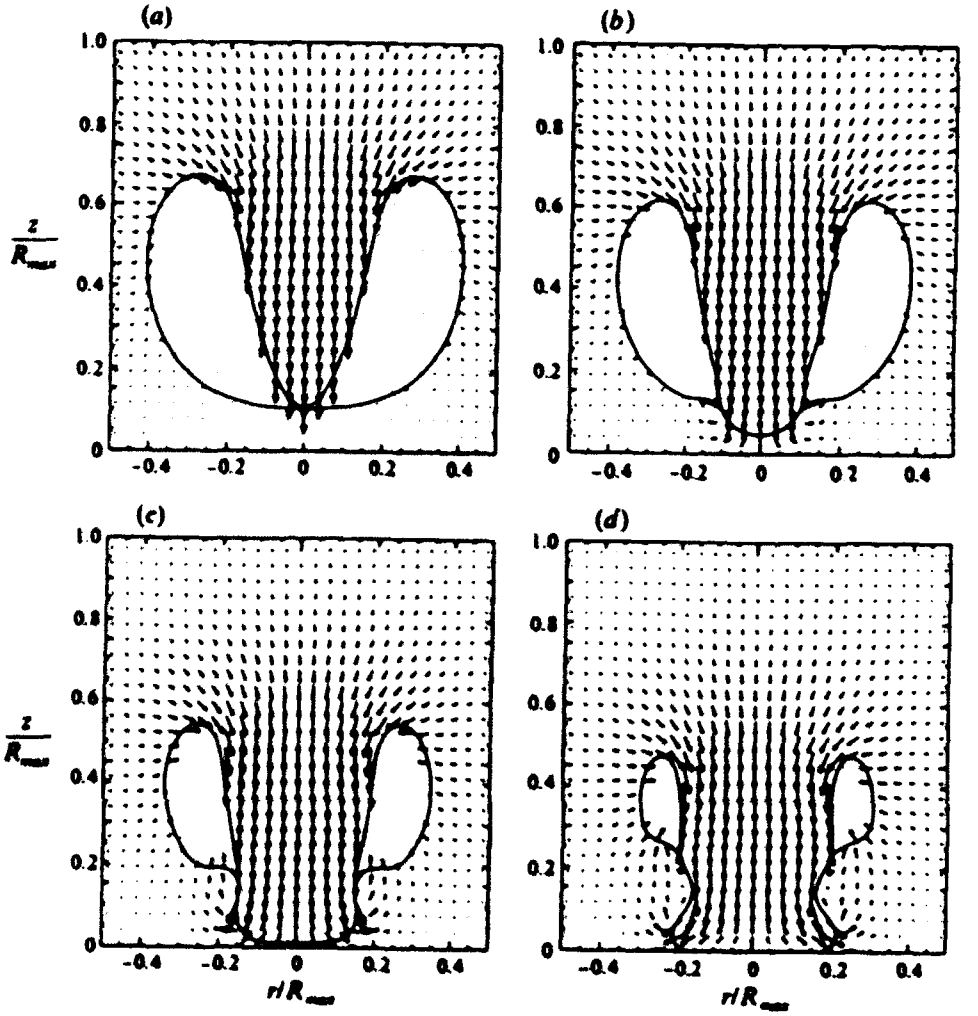

FIGURE 8. Bubble profiles and velocity fields for $Z_0 = 1.1$ and $R_0 = 0.1$: (*a*) $t = 2.15059$, (*b*) $t = 2.16400$, (*c*) $t = 2.18074$, (*d*) $t = 2.19429$. The lengths of the velocity vectors are scaled with respect to the flow speeds at the location ($r = 0$, $z = 0.7125$) in each plot. These speeds are 5.16, 4.30, 3.24 and 2.45 in (*a*), (*b*), (*c*) and (*d*), respectively.

5.2. *Pressure fields*

The pressure at any point in the fluid domain was computed from the non-dimensional Bernoulli equation,

$$\frac{P - P_\infty}{P_\infty - P_0} = -\frac{\partial \phi}{\partial t} - \frac{1}{2}\left[\left(\frac{\partial \phi}{\partial r}\right)^2 + \left(\frac{\partial \phi}{\partial z}\right)^2\right]. \tag{52}$$

The required spatial and temporal derivatives of ϕ were calculated by finite difference from local values of ϕ that are calculated from the integral equations (A 7) and (A 13) in Appendix A using values of ϕ and $\partial\phi/\partial n$ on the surface of the bubble and the vortex sheet. Note that the pressure can be computed after the calculation of the bubble motion is completed. Unfortunately, during penetration, at each time instant when new surface panels of finite size come together, ϕ goes through finite jumps as can be

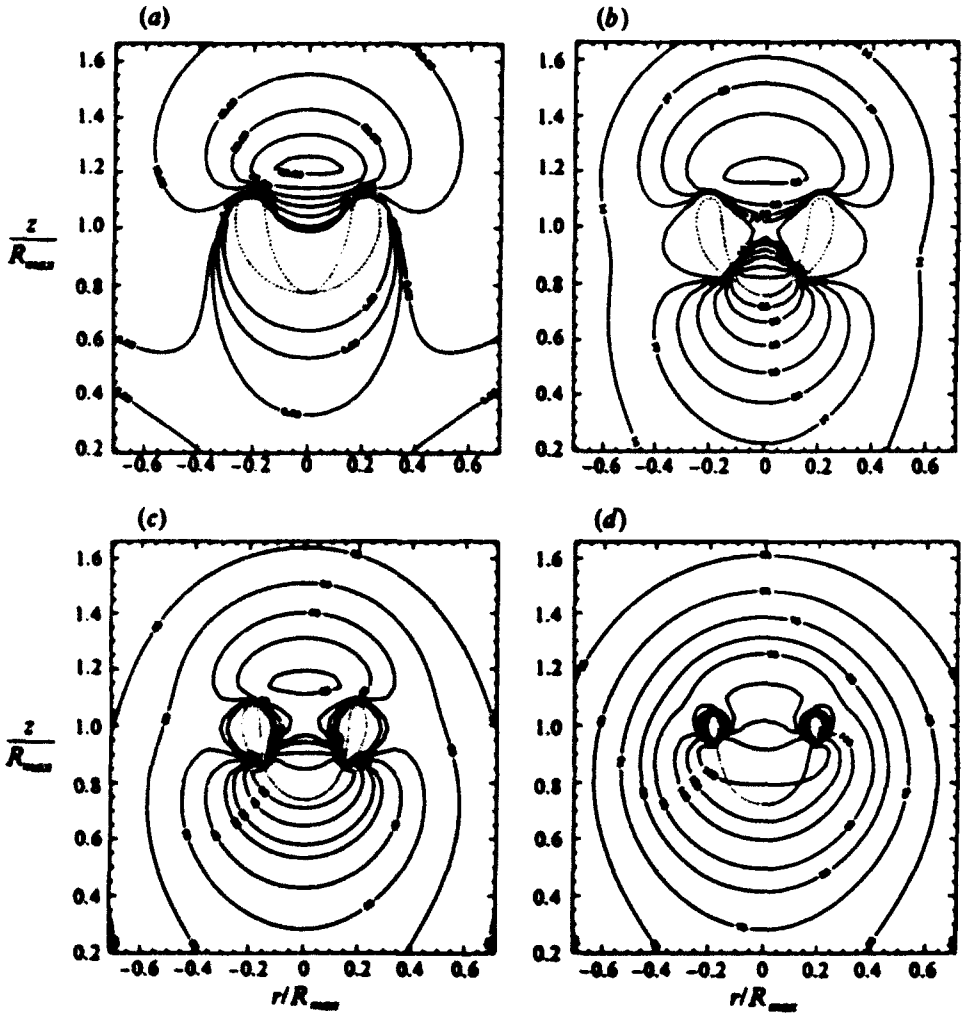

FIGURE 9. Pressure contours for $Z_0 = 1.5$ and $R_0 = 0.1$: (a) $t = 2.08545$, (b) $t = 2.08861$, (c) $t = 2.09241$ and (d) $t = 2.09551$. The bubble profiles are shown as a dotted line.

seen from (15). These jumps cause the derivative of ϕ with respect to time, and thus the pressure, to fluctuate wildly. If the panel size were infinitesimal these jumps in ϕ would also be infinitesimal and the pressure would vary rapidly but in a smooth manner. To remedy this problem, a linear least-squares fitting technique was used to smooth ϕ in a given time interval before computing $\partial\phi/\partial t$ and the pressures.

Corresponding to the flow fields in figure 7(*a–d*) for $Z_0 = 1.5$, four plots of the pressure contours are presented in figure 9(*a–d*), respectively. The pressure contours are given as solid lines while the profiles of the bubble are shown as dotted lines. The pressure field one step before penetration is given in figure 9(*a*). The highest pressure region in the field is within the contour with magnitude 29 which is located on the *z*-axis above the bubble. The pressure field just after impact, figure 9(*b*), is dramatically different than that before impact. The highest pressure region in figure 9(*b*) is at the tip of the jet where the magnitude of the enclosing contour is 80. This high-pressure buildup at the penetration interface in turn causes a large deceleration of the fluid in

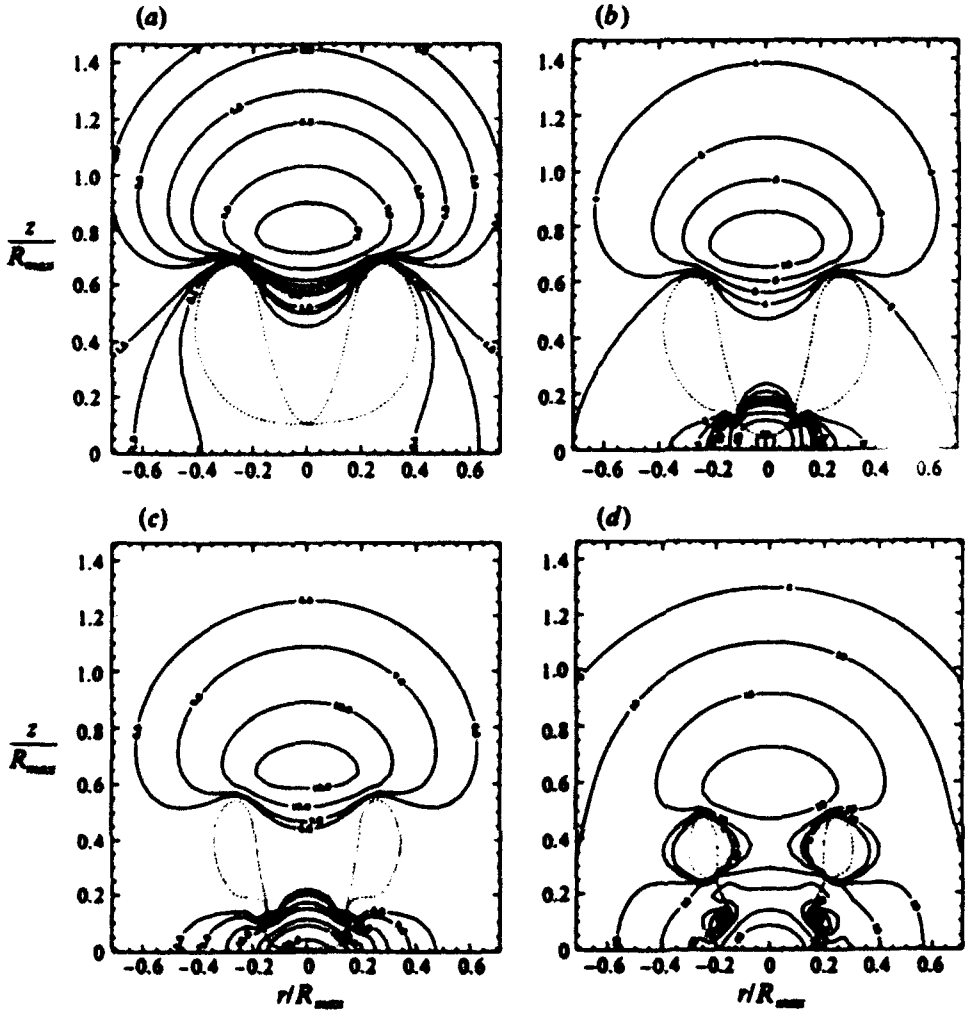

FIGURE 10. Pressure contours for $Z_0 = 1.1$ and $R_0 = 0.1$. (*a*) $t = 2.15059$ and (*b*) $t = 2.16400$, (*c*) $t = 2.18074$ and (*d*) $t = 2.19429$. The bubble profiles are shown as dotted lines.

the re-entrant jet and an acceleration toward the wall of the fluid between the sheet and the wall. From the pressure contours in figure 9(*c*, *d*), it can be seen that the pressure at the penetration interface continues to increase, reaching 165 in the final figure. The pressure contours far from the bubble are nearly circular at this time.

The pressure contours corresponding to the velocity fields in figure 8(*a*–*d*) for $Z_0 = 1.1$ are presented in figure 10(*a*–*d*), respectively. As can be seen from figure 10(*a*), at the instant just before penetration, a high-pressure region is again located on the *z*-axis above the bubble. The maximum pressure contour in this case is 9, considerably less than in the case for $Z_0 = 1.5$. Immediately following the initial impact, figure 10(*b*), large pressures are located around the impact interface. The pressure contour surrounding this region has a magnitude of 30 and intersects the wall. The further development of the pressure fields is given in figure 10(*c*, *d*) from which it can be seen that the pressure reaches more than 45 at the penetration interface and the wall. It should be noted that the high-pressure region on the wall covers a smaller area for

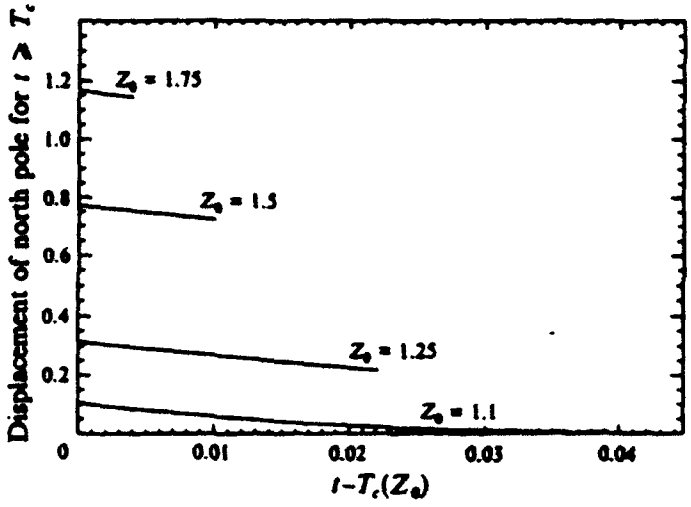

FIGURE 11. The displacements of the north pole on the common surface for various values of Z_0 as functions of time after initial impact, $t-T_c(Z_0)$.

$Z_0 = 1.1$ compared to $Z_0 = 1.5$. This concentration may be partially responsible for the well-known increase in the potential for surface damage as Z_0 is decreased. Also of interest in figure 10(*d*) are the two pairs of closed low-pressure contours. The upper pair encloses the ring bubble while the lower pair, which is located near the bend in the vortex sheet, indicates the presence of a localized vortex-ring-like structure. This structure is also visible in the velocity contours in figure 8(*d*).

5.3. *Motion of the north and south poles*

In this and the following subsections, selected quantities from four calculations with $Z_0 = 1.75$, 1.5, 1.25 and 1.1 are examined as functions of time. In order to make comparisons of various quantities after initial impact, it was decided to define a common time origin, T_c, the time when the north and south poles of the bubble meet at the instant of initial impact. From the data in table 1, it can be seen that T_c increases with decreasing Z_0. The heights of the north pole for the four cases are plotted in figure 11. After initial impact, the north pole is defined as the point where the vortex sheet intersects the z-axis. As can be seen from figure 11, the north pole continues moving toward the wall after the initial impact in all cases. The relative velocity of the north and south poles of the bubble just before initial impact can be found in table 1 along with the velocity of the vortex sheet just after initial impact. The relative velocity, $V_s - V_n$, decreases steadily from 16.56 at $Z_0 = 1.75$ to 9.10 at $Z_0 = 1.1$; however, the speed of the jet tip just after initial impact is between 4.1 and 4.25 in all four cases. The slope of the curves in figure 11 indicates the velocities of the north poles. As can be seen from the figure the velocity is relatively constant after initial impact for the larger Z_0; however, for small Z_0, the velocity decreases with time and is nearly zero at the end of the collapse for $Z_0 = 1.1$.

5.4. *Pressure at the centre of the wall*

In figures 12(*a*) and 12(*b*), the velocity potential ϕ and the pressure on the wall directly under the centre of the bubble ($(r, z) = (0, 0)$) are plotted versus time for different Z_0. Note that the plot of ϕ starts at $t = 0$ while the plot of the pressure starts fairly late in

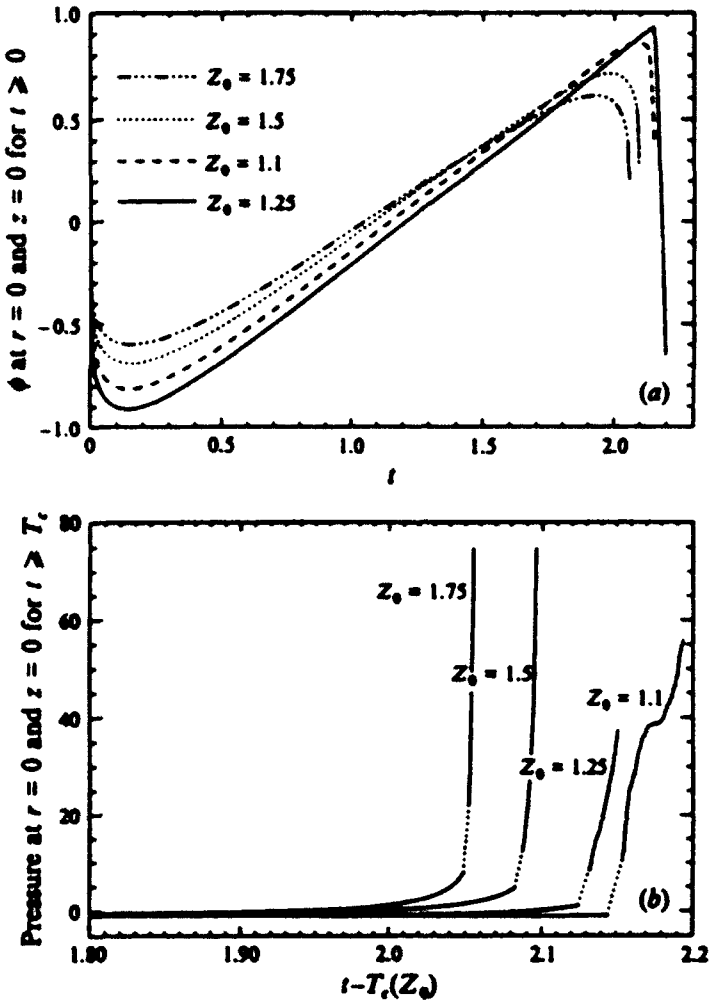

FIGURE 12. (*a*) The velocity potential and (*b*) the pressure at the centre of the rigid wall for various values of Z_0 as functions of time.

the collapse phase, $t = 1.80$. From Bernoulli's equation (52), the pressure at the centre of the wall is equal to $-\partial\phi/\partial t$ since $u = 0$ at this location. Thus, the pressures plotted in figure 12(*b*) were obtained by differentiating the curves of ϕ in figure 12(*a*). Before differentiation, the ϕ-data were smoothed with a running 40-point least-squares fit of a second-order polynomial in order to eliminate the jumps in ϕ caused by the panel impacts. Each pressure curve has a short gap near the time of the initial impact. This gap is due to the inability of the second-order polynomial to fit the ϕ-data well due to the rapid fluctuations at that point in time. All cases show sudden rises in the pressure during jet penetration. For the case of $Z_0 = 1.1$, there is a plateau in the pressure after initial impact at about the time when the vortex sheet reaches the wall.

Figure 12(*b*) provides useful information of the time history of the pressure at the centre of the wall. However, it should be pointed out that the 'maximum' values in this plot occur while the pressure is still rising at the point when the calculations terminate due to numerical instabilities. To obtain a true maximum value of the impulsive

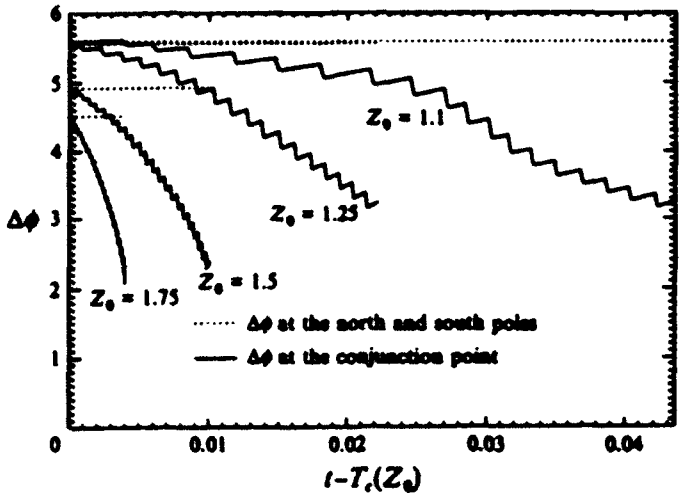

FIGURE 13. The total circulation, $\Gamma_{ss} = \phi^+_{sp} - \phi^-_{sp}$, and the circulation associated with the ring bubble, $\phi^+_T - \phi^-_T$, versus time after initial impact, $t - T_c(Z_0)$, for various values of Z_0.

pressure on the wall, a rebounding mechanism such as that provided by a non-condensible gas inside the bubble must be considered. A study of the impulsive pressure due to a gas bubble collapse and rebound is currently underway.

5.5. *Circulation*

Before penetration, the fluid domain is simply connected and the bubble boundary is a regular surface. In this case, there is no circulation along any closed path inside the fluid. However, after initial impact, if a closed path is drawn such that it pierces the vortex surface, the circulation along this path is not zero, and the fluid domain is no longer simply connected. The generation of this circulation is due to the liquid–liquid impact rather than viscous effects. If a closed path is drawn starting from the south pole and ending at the north pole of the bubble and enclosing the sheet and ring bubble, the circulation for this path, Γ_{ss}, is given by $(\phi^+ - \phi^-)$ evaluated at $r = 0$. From (13) it is easy to show that

$$\frac{d\Gamma_{ss}}{dt} = \left.\frac{D(\phi^+ - \phi^-)}{Dt}\right|_{r=0} = 0 \tag{53}$$

since $\partial\phi/\partial s = 0$ at $r = 0$. This finding was used in the two-step method of Best (1991) to choose a value of the circulation for the ring bubble. The values of Γ_{ss} are given in table 1. As can be seen from the table the circulation increases monotonically from 4.37 to 5.40 as Z_0 decreases from 1.75 to 1.1. It is also interesting to examine the division of the source of the circulation between the vortex sheet and the ring bubble. This division can be seen by comparing the total circulation, Γ_{ss}, to the circulation around the ring bubble, Γ_b, which is obtained with a path that starts at the triple point on the underside of the bubble, extends around the outer side of the bubble and ends on the top side of the bubble at the triple point. Thus, $\Gamma_b = \phi^+_T - \phi^-_T$, where the subscript T refers to the triple point. The values of the two circulations are plotted versus time in figure 13 for the four values of Z_0. The solid lines in this figure represent the circulations associated with the ring bubbles, Γ_b, while the differences between the dotted and solid lines are the circulations associated with the vortex sheets for different Z_0. As noted in the previous subsections, the step-like appearance of the plots is due

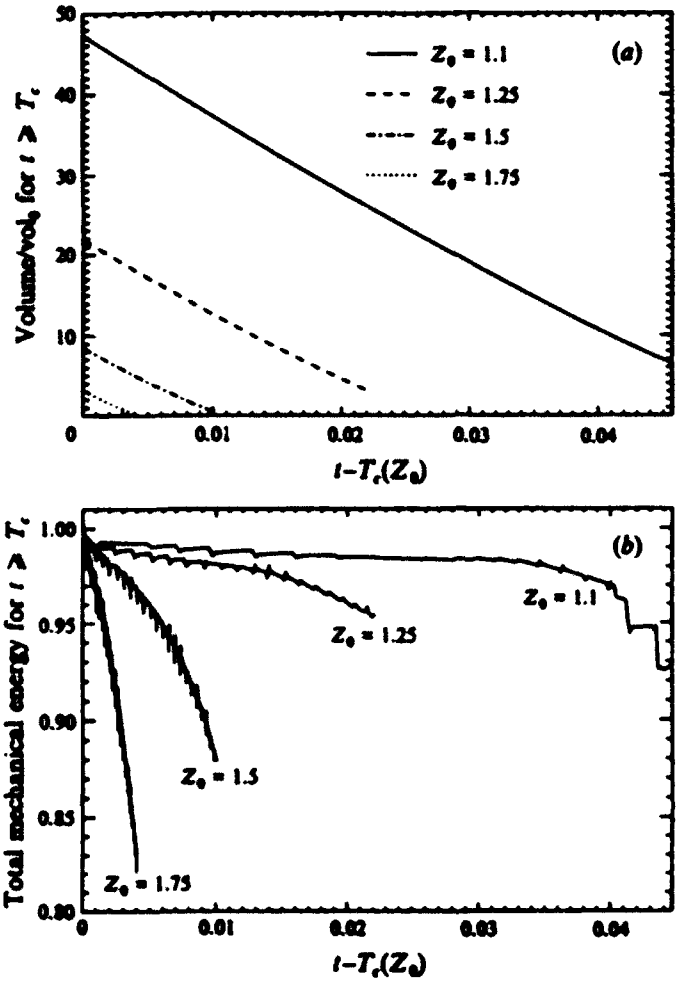

FIGURE 14. (*a*) The bubble volume, (Volume/Vol$_0$), and (*b*) the total mechanical energy for various values of Z_0 as functions of time after initial impact, $t-T_c(Z_0)$. Vol$_0$ is the initial bubble volume.

to the discrete panel impacts. This figure shows that, for all four cases, after penetration the circulation associated with the ring bubble decreases with time and, since the total circulation is constant, the circulation associated with the sheet increases with time. As Z_0 decreases, the rate of increase of circulation associated with the vortex sheet increases. At the end of the simulations the percentage of the total circulation associated with the sheet is on the order of 50% for the cases with larger Z_0.

5.6. *Energy*

The potential and kinetic energies of the flow were calculated using (22) and (23). Figure 4(*c*) is a plot of the potential, kinetic and total energy versus time from $t = 0$ up to the instant before initial impact for $Z_0 = 1.5$. As can be seen from the figure, the total energy is constant. Figures 14(*a*) and 14(*b*) give information on the energy versus time after initial impact. The potential energy is proportional to the bubble volume, which is plotted in figure 14(*a*). As can be seen from the figure, the volume at the first

instant of impact increases with decreasing Z_0. For example, the bubble volume for $Z_0 = 1.75$ has reduced to almost its initial volume at $t = T_c$ while the corresponding volume for $Z_0 = 1.1$ is about 48 times as large as its initial value. Note also from figure 14(*a*) that the bubbles with larger volume at the first instant of impact take a longer time to reach minimum volume while the rate of decrease in volume with time does not vary appreciably with Z_0. The total mechanical energy versus time after initial impact is presented in figure 14(*b*). As was noted in §2.5, the total mechanical energy of the system should decrease with time for $t > T_c$ owing to the liquid–liquid impacts of the panels. Energy loss should only occur at the time steps where an impact between two or more surface panels occurs. This behaviour is generally evident in the results of the calculation as is shown in figure 14(*b*) at early times for $Z_0 = 1.25$ and 1.1. It is believed that the changes in energy between impacts in the other calculations are caused by the extensive regridding of the surfaces necessitated by the movement of the panels from S_0 to $S^+ \cup S^-$ combined with finite panel sizes and time steps. In general, the rate of energy loss with time increases as Z_0 is increased. For $Z_0 = 1.75$, the flow loses about 18% of its total energy by the time the calculation becomes unstable. When the calculation for $Z_0 = 1.1$ becomes unstable, the energy loss has reached only 7% of its original value. In a compressible flow this energy would primarily be radiated away in the form of sound or shock waves. In the present incompressible calculations this energy is effectively radiated away at infinite speed.

6. Conclusions

The final stage of the collapse of a cavitation bubble near a rigid wall has been simulated with a boundary element method. The method allows for the simulation of the growth and collapse of the bubble including the re-entrant jet impact and penetration processes that occur toward the end of the collapse. During the impact process, the bubble is transformed into a toroidal-shaped cavity (ring bubble). This ring bubble is attached to an impact interface that separates the fluid masses that were initially on opposite sides of the bubble. The impact interface is assumed to be infinitesimally thin and the pressure and the normal velocity across the interface are assumed to be continuous. This modelling allows for the formation of a vortex sheet along the interface.

The results of the calculation show that the impact of the re-entrant jet starts at a single point on the north and south poles of the bubble. As the process continues, more and more of the surface of the bubble participates in the impact process. Before initial impact, the fluid in the re-entrant jet is moving toward the wall with high speed and the fluid on the other side of the bubble is moving away from the wall. The relative velocity of the poles of the bubble at the instant before initial impact increases with increasing Z_0 (the initial distance of the bubble centroid from the wall). During impact, a high-pressure region that is generated around the vortex sheet dramatically decelerates the fluid in the re-entrant jet and forces the fluid on the other side of the bubble to accelerate toward the wall. The impact process generates circulation in the potential flow system. The circulation along a closed path that starts at the north pole, ends at the south pole and encloses both the impact interface and the ring bubble is constant after the initial instant of impact. This circulation increases with decreasing Z_0. Just after initial impact, the source of this circulation is a bound vortex in the ring bubble. However, by the end of the calculation as much as one-half of this total circulation is associated with the vortex sheet. The liquid–liquid impact process results in a loss of energy in the potential flow system. The energy loss increases with

increasing Z_0 and its value at $Z_0 = 1.75$ is about 17% of the total flow energy. In a compressible flow this energy would primarily generate pressure waves. It is thought that in the potential flow system this energy is radiated away suddenly by the infinite sound speed. When Z_0 is small (on the order of the maximum bubble radius), the impact interface forms very close to the wall and the pressure on the wall directly under the bubble increases suddenly upon initial impact. This high-pressure region is quite small in radial extent. As Z_0 increases, the pressure rise at the wall due to impact is spread over a larger area. This may explain the enhanced potential for cavitation erosion with small Z_0 values.

The authors would like to thank Drs Ugo Piomelli and Ramani Duraiswami for a number of useful discussions during this work. Thanks are also due to Dr John Blake for his valuable comments and suggestions during his visit to DYNAFLOW, Inc. in the summer of 1992, and to Dr William Szymczak for helpful discussions concerning the energy losses during impact. S.Z. and J.H.D. acknowledge the support of the state of Maryland and DYNAFLOW, Inc. under a Maryland Industrial Partnerships contract between the University of Maryland and DYNAFLOW, Inc.

Appendix A. Derivations of the integral equations with regular and non-regular surfaces

Let D_i and D_e be defined as the interior and exterior regions, respectively, in a three-dimensional space. An interior boundary dividing D_i and D_e is denoted by S. The field point is represented by p which can be inside D_i or D_e or on S, while the source point, q, is on S only. Based on potential theory (Günter 1967; Burton & Miller 1971), the single-layer and double-layer potentials are, respectively,

$$V[\sigma(p)] = \int_S G(p,q)\,\sigma(q)\,\mathrm{d}S_q, \tag{A 1}$$

and

$$W[\sigma(p)] = \int_S \frac{\partial G(p,q)}{\partial n_q}\,\sigma(q)\,\mathrm{d}S_q, \tag{A 2}$$

where σ is the density function. Assuming that σ is sufficiently continuous on S, as the field point p approaches the boundary S from D_i or D_e, the single-layer potential and the normal derivative of the double-layer potential are continuous across the boundary,

$$V(\sigma)|_S = V(\sigma)|_{int} = V(\sigma)|_{ext}, \tag{A 3}$$

$$\left.\frac{\partial W(\sigma)}{\partial n_p}\right|_S = \left.\frac{\partial W(\sigma)}{\partial n_p}\right|_{int} = \left.\frac{\partial W(\sigma)}{\partial n_p}\right|_{ext}, \tag{A 4}$$

where in (A 3) and (A 4), S, *int* and *ext* subscripts represent the limit values of a function of p for the cases of $p \in S$, $p \to S$ from D_i and $p \to S$ from D_e, respectively, and n_p is the outward normal to S at the field point p. However, the double-layer potential and the normal derivative of the single-layer potential are discontinuous as p crosses S. These discontinuities satisfy the following relations:

$$\left.\frac{\partial V(\sigma)}{\partial n_p}\right|_S = \left.\frac{\partial V(\sigma)}{\partial n_p}\right|_{int} - 2\pi\sigma = \left.\frac{\partial V(\sigma)}{\partial n_p}\right|_{ext} + 2\pi\sigma, \tag{A 5}$$

$$W(\sigma)|_S = W(\sigma)|_{int} + 2\pi\sigma = W(\sigma)|_{ext} - 2\pi\sigma. \tag{A 6}$$

According to these fundamental relations, the modified conventional and hypersingular boundary integral equations with common points are derived as follows.

A.1. *Modified CBIE with a common surface*

In view of the fact that the surface S is composed of a regular surface S_b and a common surface $S^+ \cap S^-$ (see figure 1*b*), and on the common surface is imposed

$$\frac{\partial \phi^+(p)}{\partial n_p^+} = -\frac{\partial \phi^-(p)}{\partial n_p^-},$$

the CBIE (19) can be rewritten as, for $p \in D_t$,

$$4\pi\phi(p) = \int_{S_b}\left[G(p,q)\frac{\partial \phi(q)}{\partial n_q} - \frac{\partial G(p,q)}{\partial n_q}\phi(q)\right]dS_q - \int_{S^*}\frac{\partial G(p,q)}{\partial n_q^+}(\phi^+(q)-\phi^-(q))\,dS_q^+. \quad (A\ 7)$$

As p approaches S^+ from D_t, the discontinuity condition (A 6) requires that

$$\int_S \frac{\partial G}{\partial n_q}\phi\,dS_q\Big|_{i=i} = \int_S \frac{\partial G}{\partial n_q}\phi\,dS_q\Big|_S - 2\pi\phi. \quad (A\ 8)$$

Thus, the integral along S^+ in (A 7) becomes

$$\int_{S^*}\frac{\partial G(p,q)}{\partial n_q^+}(\phi^+(q)-\phi^-(q))\,dS_q^+\Big|_{i=i} = \int_{S^*}\frac{\partial G(p,q)}{\partial n_q^+}(\phi^+(q)-\phi^-(q))\,dS_q^+\Big|_{S^*} - 2\pi(\phi^+(p)-\phi^-(p)). \quad (A\ 9)$$

The substitution of (A 9) into (A 7) yields the modified CBIE with a common surface $S^+ \cap S^-$ for $p \in S^+$:

$$2\pi[\phi^+(p)+\phi^-(p)] = \int_{S_b}[G(p,q)\frac{\partial \phi(q)}{\partial n_q} - \frac{\partial G(p,q)}{\partial n_q}\phi(q)]\,dS_q - \int_{S^*}\frac{\partial G(p,q)}{\partial n_q^+}(\phi^+(q)-\phi^-(q))\,dS_q^+. \quad (A\ 10)$$

For $p \in S_b$, the left-hand side of (A 10) becomes $2\pi\phi(p)$ and there is no change on the right-hand side.

A.2. *Modified HBIE with a common surface*

A hypersingular integral equation with a common surface can be derived in a similar fashion. First, the directional differentiation of (A 7) with respect to n_p with $p \in D_t$ yields

$$4\pi\frac{\partial \phi(p)}{\partial n_p} = \int_{S_b}\left[\frac{\partial G(p,q)}{\partial n_p}\frac{\partial \phi(q)}{\partial n_q} - \frac{\partial^2 G(p,q)}{\partial n_p \partial n_q}\phi(q)\right]dS_q - \int_{S^*}\frac{\partial^2 G(p,q)}{\partial n_p \partial n_q^+}(\phi^+(q)-\phi^-(q))\,dS_q^+. \quad (A\ 11)$$

Then, let n_p be an outward normal to the boundary S at the inner limit of p on S and pass the limit of p from D_t along the normal n_p to the boundary S. From (A 5), only

the derivative of the single-layer potential, the first integral in (A 11), has a jump according to the relation

$$\int_S \frac{\partial G}{\partial n_p}\frac{\partial \phi}{\partial n_q}\mathrm{d}S_q\bigg|_{\text{int}} = \int_S \frac{\partial G}{\partial n_p}\frac{\partial \phi}{\partial n_q}\mathrm{d}S_q\bigg|_S + 2\pi\frac{\partial \phi}{\partial n_p}, \tag{A 12}$$

while the other two integrals along S_b and S^+ in (A 11) are continuous according to (A 4). Thus, (A 11) becomes

$$c_p\frac{\partial \phi(p)}{\partial n_p} = \int_{S_b}\left[\frac{\partial G(p,q)}{\partial n_p}\frac{\partial \phi(q)}{\partial n_q} - \frac{\partial^2 G(p,q)}{\partial n_p \partial n_q}\phi(q)\right]\mathrm{d}S_q - \int_{S^+}\frac{\partial^2 G(p,q)}{\partial n_p \partial n_q}(\phi^+(q)-\phi^-(q))\,\mathrm{d}S_q^+, \tag{A 13}$$

where c_p satisfies

$$c_p = \begin{cases} 0, & p \in D_e \\ 2\pi, & p \in S_b \\ 4\pi, & p \in D_i \cup S^+. \end{cases}$$

Appendix B. Derivation of the equation for the energy loss

The first step in the analysis that demonstrates the energy loss due to impact is to take the gradient of the pressure impulse equation (15):

$$\nabla\phi^+ = -\nabla I/\rho + \nabla\phi^-, \tag{B 1}$$

where ϕ^- and ϕ^+ are the velocity potentials of any point inside the fluid domain at the instants just before and just after the impact, respectively. Next, the difference in the kinetic energy per unit volume before and after the impact, Δe_k, is calculated by squaring (B 1) and rearranging the terms:

$$\Delta e_k = \tfrac{1}{2}\rho(\nabla\phi^+)^2 - \tfrac{1}{2}\rho(\nabla\phi^-)^2 = -\nabla I\cdot\nabla\phi^- + (\nabla I)^2/2\rho. \tag{B 2}$$

Since the boundaries of the flow move only an infinitesimal amount over the time of the impulse, the total energy loss is found by integrating e_k over the simply connected volume bounded internally by S_b, S^+ and S^- and externally by S_∞ and $S_{-\infty}$:

$$\Delta E_k = \int_D e_k\,\mathrm{d}V = \int_D -\nabla I\cdot\nabla\phi^-\,\mathrm{d}V + \int_D (\nabla I)^2/2\rho\,\mathrm{d}V. \tag{B 3}$$

The first term on the right-hand side can be manipulated using the chain rule to obtain

$$\int_D \nabla I\cdot\nabla\phi^-\,\mathrm{d}V = \int_D \nabla\cdot(I\nabla\phi^-)\,\mathrm{d}V - \int_D I\nabla^2\phi^-\,\mathrm{d}V. \tag{B 4}$$

The last term on the right in this equation is equal to zero since the flow field is incompressible before (and after) impact and D is a simply connected region. Using Gauss's theorem and the fact that $I = 0$ on S_b and S_∞, $\nabla\phi^-\cdot n_\infty = 0$ on $S_{-\infty}$ and $n_- = -n_+$ and $I^+ = I^-$ on the common surface, the first term on the right of (B 3) can be written as

$$\int_D \nabla I\cdot\nabla\phi^-\,\mathrm{d}V = \int_{S^+} I^+(\nabla(\phi^-)^+ - \nabla(\phi^-)^-)\cdot n_+\,\mathrm{d}S. \tag{B 5}$$

The second term on the right of (B 3) can be manipulated in a similar manner. First, the chain rule is used to obtain

$$\int_D (\nabla I)^2 \,\mathrm{d}V = \int_D \nabla\cdot(I\nabla I)\,\mathrm{d}V - \int_D I\nabla^2 I\,\mathrm{d}V. \tag{B 6}$$

The second term on the right of this equation is equal to zero since the Laplacian of the pressure impulse is zero in D, as can be seen by taking the divergence of (B 1). Using Gauss's theorem, and the conditions $I = 0$ on S_∞ and S_b,

$$\nabla I\cdot n_w = \rho(\nabla\phi'\cdot n_w - \nabla\phi''\cdot n_w) = 0 \text{ on } S_w$$

(see (B 1)), and $I^+ = I^-$ and $n_- = -n_+$ on the common surface, the first term on the right of (B 6) can be written

$$\int_D \nabla\cdot(I\nabla I)\,\mathrm{d}V = \int_{S^+} I^+(\nabla I^+ - \nabla I^-)\cdot n_+\,\mathrm{d}S. \tag{B 7}$$

This last integral can be further manipulated using (B 1) and the matching condition on the common surface (8) just after impact to obtain

$$\int_D \nabla\cdot(I\nabla I)\,\mathrm{d}V = \rho\int_{S^+} I^+(\nabla(\phi')^+ - \nabla(\phi')^-)\cdot n_+\,\mathrm{d}S. \tag{B 8}$$

Finally, plugging (B 5) and (B 8) into (B 3) the equation for the change in kinetic energy is obtained:

$$\Delta E_k = -\frac{1}{2}\int_{S^+} I^+(\nabla(\phi')^+ - \nabla(\phi')^-)\cdot n_+\,\mathrm{d}S. \tag{B 9}$$

Appendix C. Representation of the hypersingular integral equations in terms of elliptical integrals

Assume a cylindrical coordinate system (r, θ, z), and let the three unit vectors in the r-, θ- and z-directions be denoted by e_r, e_θ and e_z, respectively. Assume that both the source point $q(r_q, \theta_q, z_q)$ and the field point $p(r_p, \theta_p, z_p)$ are on the surface S_b and that $\theta_p = 0$. Since the problem is axisymmetric about the z-axis, the two unit vectors representing the outward normals to S_b at p and q are given by $n_p(\sin\alpha_p, 0, \cos\alpha_p)$ and $n_q(\sin\alpha_q, 0, \cos\alpha_q)$, respectively, where α_p (or α_q) is the angle between n_p (or n_q) and the positive r-direction. With the above assumptions and definitions, (28) can be written as

$$\begin{aligned}\int_S \phi(q)\frac{\partial^2 G(p,q)}{\partial n_p \partial n_q}\,\mathrm{d}S_q &= \int_S [n_q\times\nabla_q\phi(q)]\cdot[n_p\times\nabla_p G(p,q)]\,\mathrm{d}S_q \\ &= \int_S\left[\sin\alpha_p\frac{\partial(G\cos\theta_q)}{\partial r_p} - \cos\alpha_p\frac{\partial(G\cos\theta_q)}{\partial r_p}\right]\frac{\partial\phi}{\partial s_q}\,\mathrm{d}S_q.\end{aligned} \tag{C 1}$$

The above equation can also be written as

$$\int_S \phi(q)\frac{\partial^2 G(p,q)}{\partial n_p \partial n_q}\,\mathrm{d}S_q = \int_S\left[-\sin\alpha_p\frac{\partial G}{\partial r_q} + \cos\alpha_p\frac{\partial(G\cos\theta_q)}{\partial z_q}\right]\frac{\partial\phi}{\partial s_q}\,\mathrm{d}S_q \tag{C 2}$$

by using the relation $\nabla_p G(p,q) = -\nabla_q G(p,q)$. This latter equation is easier to treat than (C 1) as $r_p \to 0$.

The integral equations in §2 can be integrated analytically in the θ-direction and represented in terms of elliptical integrals. Introducing the elliptical integrals of the first kind $K(m)$ and the second kind $E(m)$ as

$$K(m) = \int_0^{\pi/2} \frac{\mathrm{d}\beta}{(1-m^2\sin\beta)^{\frac{1}{2}}}, \tag{C 3}$$

$$E(m) = \int_0^{\pi/2} (1-m^2\sin\beta)^{\frac{1}{2}}\,\mathrm{d}\beta, \tag{C 4}$$

where $m^2 = 4r_p r_q/A$ and $A = (r_p+r_q)^2+(z_p-z_q)^2$, the terms resulting from the θ-integrations in (21) are

$$I_1 = 4K(m)/A^{\frac{1}{2}}, \tag{C 5}$$

$$I_2 = [8(K(m)-E(m))/m^2 - 4K(m)]/A^{\frac{1}{2}}. \tag{C 6}$$

Substituting these relations into (19) and (21) yields

$$c_p\phi(p) = \int_L \left[C_{pq}\frac{\partial\phi(q)}{\partial n_q} + D_{pq}\phi(q)\right]\mathrm{d}L_q, \tag{C 7}$$

$$c_p\frac{\partial\phi(p)}{\partial n_p} = \int_L \left[E_{pq}\frac{\partial\phi(q)}{\partial n_q} + F_{pq}\frac{\partial\phi(q)}{\partial s_q}\right]\mathrm{d}L_q, \tag{C 8}$$

where L is an intersection curve between S_b and the plane $\theta = 0$, and

$$C_{pq} = r_q I_1, \tag{C 9}$$

$$D_{pq} = -r_q\,\partial I_1/\partial n_q, \tag{C 10}$$

$$E_{pq} = r_q\,\partial I_1/\partial n_p, \tag{C 11}$$

$$F_{pq} = -r_q(-\sin\alpha_p\,\partial I_1/\partial r_q + \cos\alpha_p\,\partial I_2/\partial z_q). \tag{C 12}$$

With the relations

$$\frac{\mathrm{d}K(m)}{\mathrm{d}m} = \frac{1}{m}\left(\frac{E(m)}{1-m^2} - K(m)\right), \tag{C 13}$$

$$\frac{\mathrm{d}E(m)}{\mathrm{d}m} = \frac{E(m)-K(m)}{m}, \tag{C 14}$$

the partial derivatives of I_1 and I_2 needed to calculate D_{pq}, E_{pq} and F_{pq} can be expressed as follows

$$\frac{\partial I_1}{\partial r_q} = \frac{4(r_p-r_q)\,E(m)}{A^{\frac{1}{2}}(1-m^2)} - \frac{2(K(m)-E(m))}{A^{\frac{1}{2}}r_q}, \tag{C 15}$$

$$\frac{\partial I_1}{\partial z_q} = \frac{4(z_p-z_q)\,E(m)}{A^{\frac{1}{2}}(1-m^2)}, \tag{C 16}$$

$$\frac{\partial I_1}{\partial r_p} = -\frac{4(r_p-r_q)\,E(m)}{A^{\frac{1}{2}}(1-m^2)} - \frac{2(K(m)-E(m))}{A^{\frac{1}{2}}r_p}, \tag{C 17}$$

$$\frac{\partial I_1}{\partial z_p} = -\frac{4(z_p-z_q)\,E(m)}{A^{\frac{1}{2}}(1-m^2)}, \tag{C 18}$$

$$\frac{\partial I_2}{\partial z_q} = -\frac{8(z_p-z_q)(K(m)-E(m))}{A^{\frac{1}{2}}m^2} + \frac{4(z_p-z_q)\,E(m)}{A^{\frac{1}{2}}(1-m^2)}. \tag{C 19}$$

REFERENCES

ANDERSON, D. C. 1965 Gaussian quadrature formulae for $-\int_0^1 \ln(x) f(x)\,dx$. *Math. Comput.* **19**, 477–481.

ARNDT, R. E. 1981 Recent advances in cavitation research. *Adv. Hydrosci.* **12**, 1–78.

BATCHELOR, G. K. 1967 *An Introduction to Fluid Dynamics*. Cambridge University Press.

BENJAMIN, T. B. & ELLIS, A. T. 1966 The collapse of cavitation bubbles and the pressures thereby produced against solid boundaries. *Phil. Trans. R. Soc. Lond.* A **260**, 221–240.

BEST, J. 1993 The formation of toroidal bubbles upon the collapse of transient cavities. *J. Fluid Mech.* **251**, 79–107.

BEVIR, M. K. & FIELDING, P. J. 1974 Numerical solution of incompressible bubble collapse with jetting. In *Moving Boundary Problems in Heat Flow and Diffusion* (ed. J. R. Ockendon & W. R. Hodgkins). Clarendon.

BLAKE, J. R. & GIBSON, D. C. 1981 Growth and collapse of a vapour cavity near a free surface. *J. Fluid Mech.* **111**, 123–140.

BLAKE, J. R. & GIBSON, D. C. 1987 Cavitation bubbles near boundaries. *Ann. Rev. Fluid Mech.* **19**, 99–123.

BLAKE, J. R., TAIB, B. B. & DOHERTY, G. 1986 Transient cavities near boundaries. Part 1. Rigid boundary. *J. Fluid Mech.* **170**, 474–497.

BURTON, A. J. & MILLER, G. F. 1971 The application of integral equation methods to the numerical solution of some exterior boundary-value problems. *Proc. R. Soc. Lond.* A **323**, 201–210.

CERONE, P. & BLAKE, J. R. 1984 A note on the instantaneous streamlines, pathlines and pressure contours for a cavitation bubble near a rigid boundary. *J. Austral. Math. Soc.* B **26**, 31–44.

CHAHINE, G. L. 1979 Etude locale du phénomène de cavitation – analyses des facteurs régissant la dynamique des interfaces. Doctorat D'Etat Es-Sciences Thesis, Université Pierre et Marie Curie.

CHAHINE, G. L. 1982 Experimental and asymptotic study of nonspherical bubble collapse. *Appl. Sci. Res.* **38**, 187–197.

CHAHINE, G. L. 1991 Dynamics of the interaction of non-spherical cavities. In *Mathematical Approaches in Hydrodynamics* (ed. T. Miloh). SIAM.

CHAHINE, G. L. & PERDUE, T. O. 1988 Simulation of the three-dimensional behavior of an unsteady large bubble near a structure. In *Drops and Bubbles, Third Intl Colloq., Monterey, CA* (ed. T. G. Wang), pp. 188–199. American Institute of Physics.

DOMMERMUTH, D. G. & YUE, D. K. P. 1987 Numerical simulations of nonlinear axisymmetric flows with a free surface. *J. Fluid Mech.* **178**, 195–219.

DUNCAN, J. H. & ZHANG, S. 1991 On the interaction of a collapsing cavity and a compliant wall. *J. Fluid Mech.* **226**, 401–423.

GIBSON, D. C. 1968 Cavitation adjacent to plane boundaries. *Proc. 3rd Austral. Conf. on Hydraulics and Fluid Mech.*, pp. 210–214. Institution of Engineers, Sydney, Australia.

GIBSON, D. C. & BLAKE, J. R. 1980 Growth and collapse of cavitation bubble near flexible boundaries. *Proc. 7th Austral. Hydraulics and Fluid Mech. Conf., Brisbane*, pp. 283–286. Institution of Engineers, Sydney, Australia.

GIBSON, D. C. & BLAKE, J. R. 1982 The growth and collapse and bubbles near deformable surfaces. *Appl. Sci. Res.* **28**, 215–224.

GUERRI, L., LUCCA, G. & PROSPERETTI, A. 1981 A numerical method for the dynamics of non-spherical cavitation bubbles. *Proc. 2nd Intl Colloq. on Drops and Bubbles, California*, pp. 175–181.

GÜNTER, N. M. 1956 *Potential Theory and Its Application to Basic Problems of Mathematical Physics*. Frederick Ungar.

HAMMITT, F. G. 1980 *Cavitation and Multiphase Flow Phenomena*. McGraw-Hill.

INGBER, M. S. & RUDOLPHI, T. J. 1990 Solution of potential problems using combinations of the regular and derivative boundary integral equations. *Appl. Math. Modeling* **14**, 536–543.

KELLOGG, O. D. 1953 *Foundations of Potential Theory*. Dover.

KRISHNASAMY, G., SCHMERR, L. W., RUDOLPHI, T. J. & RIZZO, F. J. 1990 Hypersingular boundary integral equations: some applications in acoustic and elastic wave scattering. *Trans. ASME* E: *J. Appl. Mech.* **57**, 404–414.

LAMB, H. 1945 *Hydrodynamics*. Dover.

LAUTERBORN, W. & BOLLE, H. 1975 Experimental investigations of cavitation-bubble collpase in the neighbourhood of a solid boundary. *J. Fluid Mech.* 72, 391–399.

LONGUET-HIGGINS, M. S. & COKELET, E. D. 1976 The deformation of steep surface waves in water, I. A numerical method of computation. *Proc. R. Soc. Lond.* A 350, 1–26.

LUNDGREN, T. S. & MANSOUR, N. N. 1991 Vortex ring bubbles. *J. Fluid Mech.* 224, 177–196.

MATHEMATICAL HANDBOOK EDITORIAL GROUP 1977 Mathematical Handbook. Beijing: Higher Education Publications (in Chinese).

MEYER, W. L., BELL, W. A. & ZINN, B. T. 1978 Boundary integral solutions of three dimensional acoustics radiation problems. *J. Sound Vib.* 59, 245–262.

MITCHELL, T. M. & HAMMITT, F. G. 1973 Axisymmetric cavitation bubble collapse. *Trans. ASME* I: *J. Fluids Engng* 95, 29–37.

MOON, P. & SPENCEL, D. E. 1961 *Field Theory Handbook*. Springer.

OĞUZ, H. N. & PROSPERETTI, A. 1990 Bubble entrainment by the impact of drops on liquid surfaces. *J. Fluid Mech.* 219, 143–159.

PLESSET, M. S. & CHAPMAN, R. B. 1971 Collapse of an initially spherical vapour cavity in the neighbourhood of solid boundary. *J. Fluid Mech.* 47, 283–290.

PRESS, H. W., FLANNERY, B. P., TENKOLSKY, S. A. & VETTELING, W. T. 1989 *Numerical Recipes*. Cambridge University Press.

PROSPERETTI, A. 1982 Bubble dynamics: a review and some recent results. *Appl. Sci. Res.* 38, 145–164.

RAYLEIGH, LORD 1917 On the pressure developed in a liquid during the collapse of a spherical void. *Phil. Mag.* 34, 94–98.

ROGERS, J. C. W., SZYMCZAK, W. G., BERGER, A. E. & SOLOMON, J. M. 1990 Numerical solution of hydrodynamic free boundary problems. *Intl Series Numer. Maths* 95, 241–266.

SHIMA, A., TOMITA, Y., GIBSON, D. C. & BLAKE, J. R. 1989 The growth and collapse of cavitation bubbles near composition surfaces. *J. Fluid Mech.* 203, 199–214.

SZYMCZAK, W. G., ROGERS, J. C. W., SOLOMON, J. M. & BERGER, A. E. 1993 A numerical algorithm for hydrodynamic free boundary problems. *J. Comput. Phys.* 106, 319–336.

TOMITA, Y. & SHIMA, A. 1986 Mechanisms of impulsive pressure generation and damage pit formation by bubble collapse. *J. Fluid Mech.* 169, 535–564.

VOGEL, A., LAUTERBORN, W. & TIMM, R. 1989 Optical and acoustic investigations of the dynamics of laser-produced cavitation bubbles near a solid boundary. *J. Fluid Mech.* 206, 299–338.

Proceedings *Cavitation and Multiphase Flow Forum*, ASME New York, vol. 153, 1993.

STUDY OF THE INTERACTION BETWEEN A BUBBLE AND A VORTICAL STRUCTURE

Georges L. Chahine, Eric Delepoule*, and Pierre Hauwaert**
DYNAFLOW, Inc.
7210 Pindell School
Fulton, Maryland 20759

ABSTRACT

Some aspects of the interaction between bubbles and shear flows were simulated experimentally and numerically. In the experimental set-up the shear flow was obtained using a vortex ring. A spark-generated bubble is produced where needed and interacts with the ring. The degree of interaction between the vortex shear flow and the bubble is modified and investigated. The dynamics of both the vortex ring and the bubble are observed using dye injection and high speed photography. Bubble deformation is seen to significantly increase with shear. These observations are used to check a 3D numerical method developed to study large bubble deformations. Good comparison between the model and the experimental observations can be seen.

INTRODUCTION

Practical liquid flows contain many microscopic bubbles which respond dynamically to the flow. These bubbles can grow explosively and collapse, leading to cavitation noise, erosion and decrease in performance. A better understanding of the bubble dynamics may give new solutions for delaying cavitation inception or using cavitation's destructive effects for useful purposes. In practice, unlike for most cavitation modeling studies, the bubbles grow and collapse in non-uniform flows and do not remain spherical or axisymmetric. Such flows can be due either to the presence of nearby solid walls flow or to vorticity shed from obstacles[1]. In this paper we will consider bubble behavior in such a flow both experimentally and numerically. To do this a fundamental experiment consisting of the observation of the interaction between a vortex ring and a bubble is considered. The results of the experiment are then compared with those obtained with a numerical model based on the 3D free surface dynamics numerical code 3DynaFS.

*Students on Practical Training from Ecole Navale, Brest, France.

EXPERIMENTAL STUDY.

A Plexiglas cylinder equipped with a $2.5cm$ radius piston was attached to the top cover of a Plexiglas tank of inner dimensions: $37.6cm \times 37.6cm \times 27.3cm$ filled with water. A shaft is attached to the piston and crosses the cover of the tank through a sealed hole to interact with an electro-magnet. A magnetic plate located outside the tank holds the piston/shaft assembly in its high position when the electro-magnet is powered. The pressure on both faces of the piston can be controlled by pumps. Once the electro-magnet power is turned off, the piston moves due to the difference of pressure between its two faces and pushes the water out of the cylinder, generating a vortex ring. To minimize pressure variations behind the piston an additional reservoir maintained at the same pressure is connected to the volume behind the piston. The cylinder has an sharp lip exit to enhance the roll up of the fluid vortex generated at the lip. This results in an vortex ring with a diameter slightly larger than that of the cylinder [2].

The water in the tank is degassed. A gap between the surface of the water and the tank cover is left to allow air evacuation and creation of a partial vacuum in the tank. Most of the case studies presented here were conducted with a partial vacuum ($\simeq$5000 Pascals) maintained in the tank. Two manometers are used to read the pressure in the tank and behind the piston.

The spark generated bubbles are produced using two tungsten electrodes submerged in the tank which can be manipulated from outside the tank to be placed where desired. The spark is produced by discharging during a very short time period ($\simeq 10^{-4}$s.) a high voltage (6000 volts) from a series of capacitors.

The pressure and temperature of the plasma generated by the spark are much higher than those of the surrounding water. This forces a vapor/gas bubble to grow until fluid inertia prevents further growth. The bubble then reaches its maximum radius with an internal pressure much lower than the fluid pressure. It then starts to implode and its behavior is governed by the pressure differences as for a cavitation bubble. This classical way of generating simulated cavitation bubbles allows one to choose precisely when and where the phenomenon will occur which is essential to coordinating the positions of the bubble and the ring and the starting time of the high speed camera.

Measurement equipment

The pressure at selected locations in the tank was measured using a BNC model 101A05 transducer. The pressure signal was recorded using a digital storage oscilloscope and a PC with a GPIB interface. A triggering line (Fig. 1) allows one to synchronize the departure of the piston and the triggering of the spark generator. It includes the piston magnet, the transducer power supply, a delay generator, an amplifier and a power generator. The operator turns off the magnet power supply at time T_0. As the piston starts to move down, a pressure pulse is created in the tank by the fluid impulsive motion which is detected by the transducer probe $3.3 \times 10^{-4}s$ later the time to travel the distance ($50cm$) between the piston and the probe. This delay is very small compared to the time needed for the ring to reach the electrodes ($\simeq 0.5s$). The output of the transducer is amplified to trigger the delay generator. The output signal, a very short pulse, then triggers the spark generator.

Visualization was obtained using a high speed camera, a video camera and a regular reflex camera. High speed photography was employed using a HYCAM 2 camera with a rotating prism capable of 11,000 frames per second. Before taking a film with the high speed camera, a video camera was used to check each case and to determine in first approximation the characteristics of the ring (its velocity, diameter).

The pressure signal detected by a transducer located on the axis of the vortex ring was used to determine the correct time to initiate the spark-generated bubble for a given vortex flow configuration. After the initial pressure signal following the 'impulsive' ejection of the water from the cylinder the transducer detects the pressure field of the translating vortex ring. When the ring plane is at the level of the probe the detected pressure is at its minimum. The shape of the pressure signals depends on whether or not the ring is cavitating.

EXPERIMENTAL RESULTS

A total of seventeen high speed movies were taken covering a large range of shear rates obtained by varying either the relative distance between the generated bubble and the initial vortex ring center or by varying the ring circulation. The ring diameter varied between 6 and $6.4cm$ while its velocity varied between 0.2 and $0.8m/s$ giving ring Reynolds numbers between 1.2×10^4 and 5×10^4. A reference movie was also taken with the bubble isolated in the absence of the vortex ring.

On three of the films and on many of the videos very small gas bubbles were left under the piston when the movie sequences were taken. The visualization of the motion of these bubbles allows one to observe their trajectory around the ring. The existence of a "viscous core" was apparent from the velocity profile whether or not the vortex ring was cavitating. For the cavitating cases, the "viscous core" surrounded the vaporous/gaseous core. A typical trajectory of the small bubbles is shown in Figure 2. Also shown in this figure is a sketch of a bubble and the particle trajectory line (T). Figure 2 also shows the geometric characteristics of the bubble/ring positions. D_1 is the distance between the bubble center and the viscous core center when the bubble is at its maximum volume and has the equivalent maximum radius R_m . D_2 is the horizontal distance between the bubble and the center of the viscous core. The normalized quantities $\overline{D_1} = D_1/R_m$ and $\overline{D_2} = D_2/R_m$ characterize the bubble / vortex ring interactions. It is expected and confirmed below that smaller $\overline{D_1}$ and $\overline{D_2}$ correspond to stronger interactions and larger bubble deformations.

Bubble shape deformation

Figure 3a-c drawn in the ring reference frame shows the bubble motion and deformation with time for three selected cases of increasing bubble/shear interaction. The electrodes position shown on each graph is the one at the instant of the spark generation. The vortex ring side view indicates the position of the reference frame..

As can be seen from the pictures in Figure 4a ($\overline{D_1} = 2.16$, $\overline{D_2} = 0$, $V_{ring} = 0.28m/s$) and from the contours in Figure 3a , the bubble remains practically spherical during its growth. The interaction is weak due to the relatively large distance between the bubble and the ring, and also due to the relatively

small circulation of the ring. The first collapse is too fast and no significant deformation of the bubble is seen until the rebound when a reentrant jet appears on the bottom face of the bubble followed after the rebound by an outgoing jet on the top face. It appears that during the first bubble oscillation period the bubble translation velocity is smaller than the vortex generated fluid velocity. The bubble therefore sees a flow moving upward. The jet direction (including the reentrant and the outside jet) is on a pathline of shear flow, and the bubble motion after the collapse follows a particle path line while oscillating and cutting itself in two.

In Figure 4b ($\overline{D_1} = 2.38$, $\overline{D_2} = 1.5$, $V_{ring} = 0.78m/s$) the bubble first grows spherically, then it starts to stretch into an ovoid shape: the bottom face is less curved and the top face more curved than in the spherical case. Here the distance $\overline{D_1}$ is not too different from the previous case but the circulation in the vortex ring is about three times larger. When the bubble volume decreases, the stretching due to the shearing action becomes more pronounced and two reentrant jets (or rather a constriction along the bubble periphery) appear. This constriction appears along the pathlines (T) around the bubble. The bubble then rebounds with a dumbbell shape.

In Figure 4c ($\overline{D_1} = 1.1$, $\overline{D_2} = 0.37$, $V_{ring} = 0.82m/s$) the bubble appears to be stretched more and more in the pathlines direction during its growth, with the top region more stretched than the bottom one, and the top right part growing more than the left one. When the bubble collapses, its left part continues to be sheared by the flow into a pathline direction and a beak forms at the top left part and becomes more pronounced once the volume of the bubble starts to decrease. Then, there is a constriction all around the bubble which appears first on the top face of the bubble. The bubble then cuts itself in two and rebounds as two side-by-side very distorted bubbles (or bubble clouds). The left one then touches the cavitating ring and splits again into two parts. The deformations of the bubble are more significant in this case than in the two previous cases, because the bubble is closer to the center of the ring core and sees a strong shear flow. In addition, there appears to be a "venturi effect" between the bubble and the viscous core that further increases the stretching of the left part of the bubble

Within the margin of errors of the measurements comparison of the time variation of the average radius of each bubble shows no significant effect of the presence of shear on the bubble period. However, indications of a lengthening effect of the bubble period can be seen on the characteristic distances between the bubble 'center' and the two upstream and downstream points along a particle pathline (direction (T)) . This effect however seems small in the cases presented here and should be investigated further.

Physical explanations

The observations made above can be explained by considering the velocity and pressure fields around the bubble. The motion of each point on the surface of the bubble is the result of the combination of the underlying (shear) fluid velocity and of the velocity of the bubble growth or collapse. The effect of the underlying fluid flow (whose characteristic speed is about $2m/s$) is minor during initial bubble growth and later bubble collapse phases, but becomes most important at the end of the growth and at the beginning of the collapse where bubble wall velocities reach a minimum. Indeed, right after the spark generation, the speed of each point of the bubble surface is very high (about $40m/s$). It then decreases to zero at about the maximum radius, and then increase during the bubble collapse. For a bubble in a uniform flow, the existence of the flow reflects on the bubble shape by a larger bubble growth in the downstream direction and by a flattening of the bubble shape in the upstream direction. Later on due to inertia, the downstream part that has extended further collapses faster forming a reentrant jet directed upstream in the plane of symmetry of the bubble.

When the flow is not uniform, a similar phenomenon occurs but is stronger on one side of the bubble than on the other due to the typical asymmetry of a shear flow. In addition, the possibility that the underlying shear flow becomes at some point during the bubble history stronger than the bubble wall velocity creates the possibility of an underlying flow generated jet which can be opposite to the one described above and directed downstream. In the case of the figures shown here the velocity profile seen by the bubble decreases from left to right. When the bubble starts to grow, the speed of each point is much more important than the velocity of the fluid flow: the bubble is therefore almost spherical. Then, when the speed of each point decreases, the influence of the fluid flow increases. The top part of the bubble grows more than without the presence of the basic flow and, due to the shear, the left part grows more than the right one. In addition the top part is more stretched than the bottom face because on the top, the speeds

add up while they subtract on the bottom. The opposite is true during the collapse where velocities add up on the bottom part of the bubble and subtract on the top.

As the fluid flow is moving upward, the reentrant jet is expected to appear on the top face [7, 10]. However, due to the strong shear the left part of the bubble is prevented from collapsing forcing a compensating middle of the bubble constriction all along the bubble, with a tendency to form reentrant jets on both ends of the bubble along the pathline. This constricted shape of the bubble is similar to that obtained with a bubble collapsing between two walls.

NUMERICAL MODELING

In order to model the bubble/shear flow interaction described above, DYNAFLOW's 3D Boundary Element Method (BEM) code for the description of free surface deformations, 3DynaFS was used. The BEM method uses Green's identity to solve Laplace's equation. If the velocity potential, ϕ , or its normal derivative is known on the fluid boundaries (points M), and ϕ satisfies the Laplace equation, then ϕ can be determined anywhere in the domain of the fluid (field points P) using the identity:

$$\int\int_s [-\frac{\partial \phi}{\partial n}\frac{1}{|\,\mathbf{MP}\,|} + \phi\frac{\partial}{\partial n}(\frac{1}{|\,\mathbf{MP}\,|})]ds = a\pi\phi(p), \tag{1}$$

where $a\pi = \Omega$ is the solid angle under which P sees the fluid. a = 4, if P is a point in the fluid, a = 2, if P is a point on a smooth surface, and a < 4, if P is a point at a sharp corner of the discretized surface.

If the field point P is selected to be on the boundary of the fluid domain, then a closed system of equations can be obtained and used at each time step to solve for values of $\partial\phi/\partial n$ (or ϕ) assuming that all values of ϕ (or $\partial\phi/\partial n$) are known at the preceding step. The method was described in details in previous publications [4-7]. The above equation is subjected to kinematic and dynamic boundary conditions on the bubble wall. In absence of underlying flow the liquid pressure at the bubble interface is given by the unsteady Bernoulli equation which is used to solve for $D\phi/Dt$, the total material derivative of ϕ,

$$\frac{D\phi}{Dt} = \frac{\partial\phi}{\partial t} + |\,\nabla\phi\,|^2 = \frac{P_a - P_L}{\rho} - gz + \frac{1}{2}\,|\,\nabla\phi\,|^2\,. \tag{2}$$

Using an appropriate time step, all values of ϕ on the bubble surface can be updated using ϕ at the preceding time step and $D\phi/Dt$. New coordinate positions of the nodes are then obtained using the position at the previous time step and the knowledge of the boundary velocities.

This time stepping procedure is repeated throughout the bubble oscillation period, resulting in a shape history of the bubbles. This method has been extended to the case where the bubble is embedded in an underlaying fluid flow characterized by its velocity field $\mathbf{V_0}$ and pressure field P_o . If we then define bubble flow velocity and pressure variables, $\mathbf{V_b}$ and P_b, as follows:

$$\mathbf{V_b} = \mathbf{V} - \mathbf{V_0}, \qquad P_b = P - P_0. \tag{3}$$

and assume that this bubble flow field ($\mathbf{V_b}$ and P_b) is potential, we can use the BEM to study the bubble dynamics. Within this restriction, Equation (2) is replaced by a modified Bernoulli equation

$$\nabla\left[\frac{\partial\phi_b}{\partial t} + \frac{1}{2}\,|\,\mathbf{V_b}\,|^2 + \mathbf{V_0}\cdot\mathbf{V_b} + \frac{P_b}{\rho}\right] = \mathbf{V_b}\times(\nabla\times\mathbf{V_0}). \tag{4}$$

THE VORTEX RING

In order to simulate the problem at hand in the above described experiments, the flow field of the moving vortex ring was modeled using the following classical expression for the velocity potential at the point M produced by a vortex ring (R):

$$\phi(M) = -\frac{\Gamma}{4\Pi}\iint_S \frac{\mathbf{e_t}.\mathbf{PM}}{|\mathbf{PM}|^2}ds_P,$$

where Γ is the circulation, and S is any surface limited by the ring vortex ring line (R), and $\mathbf{e_t}$ is the tangential direction along (R). This enables one to determine the velocity and pressure field outside of the "viscous core" region of the vortex ring. The velocity in the core region is modeled using a matching solution to an infinite vortex line model. Since, for a non-zero value of the viscous core the velocity obtained from the inviscid solution is not the same when the viscous core is approached from the inside of the vortex ring as from its outside, the pressure at the center line was set to be the average value between the pressure at each end of the core diameter. The two points on the edge of the viscous core were then connected to the value on the axis using two sections of parabola whose tangents are horizontal when $r = 0$. These approximations were needed to start the computation but had little influence on the results since the studied bubbles were outside of the viscous core most of the time.

NUMERICAL RESULTS

In order to test the code the conditions of Fig. 4c were reproduced, then the circulation was reduced to obtain other cases in the same physical conditions but with a smaller circulation of the vortex ring. This simulates qualitatively only the two other cases shown above. The cross-sections obtained with a plane perpendicular to the ring axis and which contain the initial bubble center are shown in figure 5a-c. The viscous core radius was assumed to be $0.6cm$, a value given by movie analysis. The ambient pressure, ring velocity and initial position of the bubble are those of Fig. 4c. A set of runs was made with the bubble discretized with 162 nodes and 320 panels. The conditions of the run were as follows: ambient pressure:$12,600Pa$, minimum bubble radius: $1mm$; Maximum bubble radius, $R_{m=}1cm$, gas compression constant $k = 1.25$, initial gas pressure, $P_{go} = 2.58 \times 10^7 Pa$, viscous core radius, $A_c = 0.6cm$, Ring radius, $A_0 = 0.031m$, ring translation speed: $0.8m/s$, bubble radial distance from ring : $0.042m$, bubble vertical distance from the ring :$0.025m$.

Figure 5c shows simulations for these same experimental conditions as in Figure 4c with $\Gamma = 0.12m^2/s.$, while Figures 5a and 5b show the same conditions but for $\Gamma = 0.25m^2/s.$ and $\Gamma = 0.10m^2/s.$ As in the experiment Figure 5c shows elongation of the left side of the bubble in the shear flow direction. The formation of a beak at the end of the bubble growth is also evident but not as pronounced as in the experiment. Later a constriction in the bubble shape along the fluid pathline is also apparent. The overall comparison between this numerical modeling and the experiment is encouraging. However, the strong shearing effect on the beak preventing the bubble top from collapsing from the left side is not as strongly reproduced in the numerical simulation. This is most probably due to the fact that the simulation neglected the *bubble* vortex ring behavior and did not include any modification of the flow due to the growth of the ring bubble near the spark-generated bubble creating the venturi effect we mentioned earlier.

At the smaller circulation the tendency of the bubble to elongate and then cut itself into two is clearly apparent as in the experiments.

CONCLUSIONS

The study presented here has enabled us to achieve two main objectives:

1. The behavior of a bubble in a particular shear flow was observed and tested
2. The capability of the program **3DynaFS** to simulate such a flow was demonstrated.

The shear flow was seen to significantly influence the bubble behavior. During the collapse and rebound the bubble shape deformation was seen to always be significantly affected. During the bubble growth the bubble behavior and shape is the more affected the larger is the degree of interaction between the bubble and the vortex; that is the closer is the bubble to the vortex core center, or the greater is the vortex circulation.

ACKNOWLEDGMENTS

We would like to acknowledge the support of the Office of Naval Research, Contract N00014-89-C-0025 and Dr. Edwin Rood's interest. We also acknowledge the French Ecole Navale for making the stay at DYNAFLOW of the last two authors possible.

REFERENCES

1. P.Kezios, and W.R. Schowalter, "Rapid Growth and Collapse of single Bubbles in Polymer Solutions Undergoing Shear," phys. Fluids 29 (10), 3172-3181, Oct 1986.
2. K. Kalumuck, and G.L. Chahine, "Cavitating Vortex Ring Formation and Dynamics.' ASME paper, Cavitation and Multiphase Flow Forum, Toronto, June 1990.
3. G.L. Chahine and T.O. Perdue, "Simulation of the Three-Dimensional Behavior of an Unsteady Large Bubble Near a Structure," in "Drops and Bubbles" edited by T.G. Wang, A.I.P. Conference Proceedings, 197, 169-187, 1989.
4. G.L. Chahine, "Nonspherical Bubble Dynamics in a Line Vortex," in Proceedings of the Cavitation and Multiphase Flow Forum, Toronto, June 1990.
5. G.L. Chahine, "Numerical Modeling of the Dynamic Behavior of Bubbles in Nonuniform Flow Fields" ASME 1990 Symposium on Numerical Methods for Multiphase Flows, Toronto, Canada, June 1990.
6. G.L. Chahine "Dynamics of the Interaction of Non-Spherical Cavities," in "Mathematical Approaches in Hydrodynamics," ed. T. Miloh, SIAM, Philadelphia, 1991.

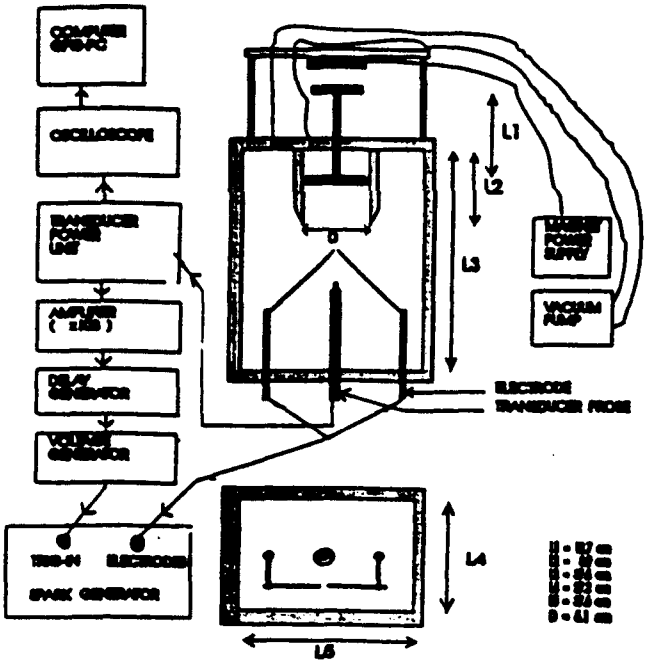

Fig 1. Sketch of experimental setup.

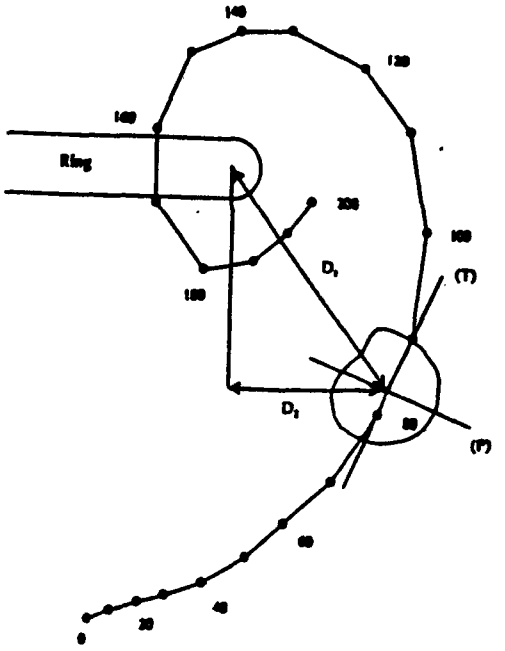

Fig 2. Particle trajectory around the ring viscous core and sketch of bubble position parameters.

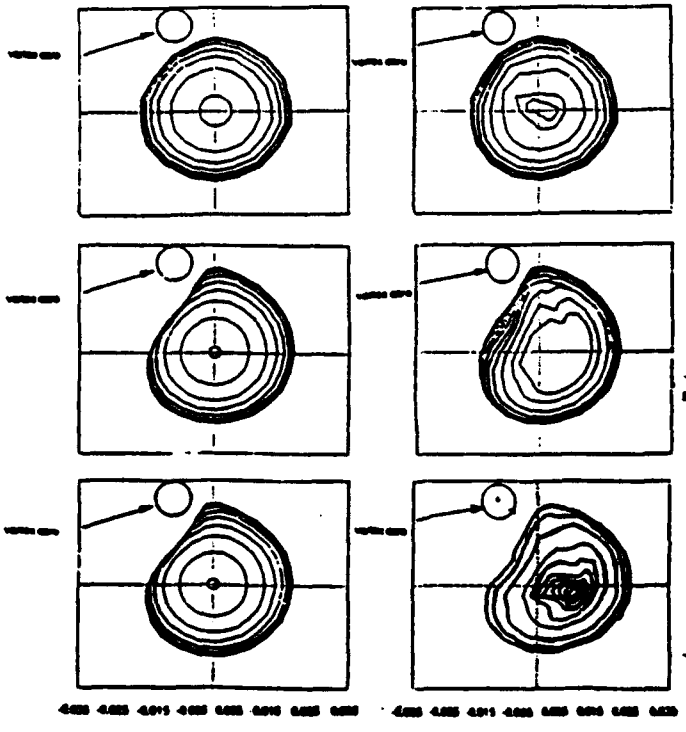

Fig 3. Bubble contours at various times from HS sequences of Fig 4. a) $\overline{D_1} = 2.16$, $\overline{D_2} = 0$, $V_{ring} = 0.28m/s$; b) $\overline{D_1} = 2.38$, $\overline{D_2} = 1.5$, $V_{ring} = 0.78m/s$; c) $\overline{D_1} = 1.1$, $\overline{D_2} = 0.37$, $V_{ring} = 0.82m/s$.

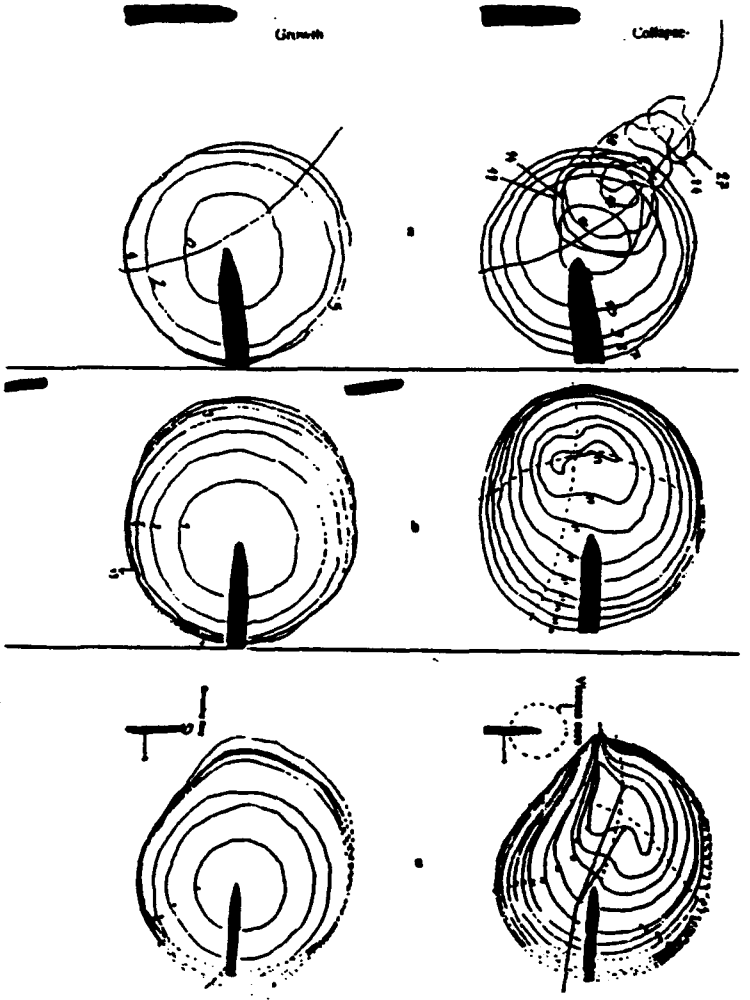

Fig 5. Numerical simulation of bubble/vortex ring interaction a) circulation: 0.025 m^2/s; b) circulation: 0.10 m^2/s; c) circulation: 0.12 m^2/s : corresponds to Fig 3c and 4c.

Fig. 4. High Speed Movie sequences of bubble/vortex ring interaction a) $\bar{D}_1 = 2.16$, $\bar{D}_2 = 0$, $V_{ring} = 0.28$m/s; b) $\bar{D}_1 = 2.38$, $\bar{D}_2 = 1.5$, $V_{ring} = 0.78$m/s; c) $\bar{D}_1 = 1.11$, $\bar{D}_2 = 0.37$, $V_{ring} = 0.82$m/s;

Proceedings, ASME *Cavitation and Multiphase Flow Forum*, Los Angeles, 1992.

Asymptotic Study of Bubble Dynamics in a Nonuniform Potential Flow

MATTHIEU REBUT* and GEORGES L. CHAHINE†
DYNAFLOW, Inc.
7210 Pindell School Road,
Fulton, MD 20759

abstract

The dynamic behavior of a bubble in a nonuniform flow is studied using a matched asymptotic expansion method, the small parameter ϵ being the ratio of the initial bubble radius, r_0, to the initial bubble distance to the body wall, l_0. The theory is applied to the problem of a bubble collapsing in the shear region near a semi-infinite bluff body advancing at a constant speed. Results obtained at orders ϵ^0 and ϵ show the imposition of a rotation on the bubble and the formation of a jet directed upstream and towards the wall. As the order of the expansions increases, more complex aspects of the interaction between the bubble and the flow are uncovered. Analytical results at order ϵ^2 are given while numerical solutions of the equations at that order are still not completed and are given up to order ϵ for the case of a bubble near a Rankine ogive body.

Introduction

The understanding of bubble and cavity dynamics has preoccupied researchers and engineers over the past several decades. However, due to the complexity of the general problem, most bubble dynamic studies have either neglected bubble deformation and based their approach on isolated spherical bubble dynamics, or considered axisymmetric deformations. With the advent of computational techniques and facilities, significant attention has been given over the last decade to the study of axisymmetric bubble dynamics, particularly in the vicinity of a solid infinite wall or a free surface (Shima et al., 1977, Guerri et al., 1981, Chahine et al., 1982, 1983 ; Blake et al., 1986, 1987, Wilkerson, 1989, Duncan, 1990). However, deviations from this simplifying axisymmetry assumption which render the problem fully three-dimensional and are expected to significantly affect the results were not considered. For instance, near a solid wall and in the presence of a pressure gradient or a nonuniform flow a relative velocity between the bubble and the flow exist leading to significant three-dimensional effects on the bubble dynamics. To address this general problem a fully three-dimensional approach is being developed (Chahine et al. 1989, 1990, 1991). However, this method is purely numerical and should be supplemented by an analytical approach, even if approximate, since this will enable, at a much lower cost, a better understanding of the influence of the parameters in the domain of validity of the method.

In this paper we will present such an analytical study of the growth and collapse of a bubble in a general potential flow in the vicinity of a solid object. This approach is based on the method of matched asymptotic expansions. The small parameter of the expansion, ϵ, is chosen to be the ratio of the initial bubble radius to its distance to the wall. This approach follows earlier work by Chahine and Bovis (1983) who studied the axisymmetric case of the collapse of a bubble near a wall, and later the studies of Chahine et al. (19) who considered the dynamical behavior of a bubble cloud.

At every order of approximation the problem is decomposed into two subproblems: an *inner* problem where the characteristic length is the characteristic bubble radius and an *outer* problem where the characteristic length is the standoff distance between the bubble and the wall. The effect of the wall appears only through the limit condition at infinity for the *inner* problem. For the *outer* problem the bubble appears as a singular perturbation at the origin. The calculations are performed in a frame of reference attached to the bubble so as to follow its behavior over a longer period of time, otherwise the mathematical expressions become non-univocal as soon as any bubble wall point crosses the origin of coordinates. The bubble is assumed to be filled with vapor of the host liquid and non-condensible gas with a polytropic compression law.

The results of the theory presented here can be applied to any potential flow which has a plane of symmetry parallel to the flow direction (non fundamental assumption only used to simplify the analytical expressions). As illustration the problem of a bubble collapsing near a semi-infinite bluff axisymmetric body in a uniform flow field is considered. In that case the *basic* potential flow used is that of a source in a uniform flow field.

Problem formulation

Let us consider a *basic* flow field (flow in absence of the bubble) that is potential, with a velocity vector $\vec{V}_0(M)$ deriving from the potential $\phi_0(M)$. Let the pressure be $p_0(M)$ and the liquid density ρ. The velocity potential satisfies the Laplace equation and the Bernoulli equation:

$$\Delta\phi_0 = 0, \tag{1}$$

$$\frac{1}{2}(\nabla\phi_0)^2 + \frac{p_0}{\rho} = constant. \tag{2}$$

The no-flow condition across the submerged body wall is

$$\{\nabla\phi_0 \cdot \vec{n}\}_{wall} = 0. \tag{3}$$

Let ϕ', $\vec{V}'$ and p' be the potential, the speed and pressure in presence of the bubble, and let $r = R'(t, \theta', \psi')$ be the bubble wall equation. We now have similar equations as (1-3) with these complete flow variables. In addition, a fourth equation describes the continuity of the normal velocities at the bubble wall.

*Ecole Polytechnique, Palaiseau, France
†Also Research Professor The Johns Hopkins University, Baltimore, MD

$$\{\nabla\phi' \cdot \vec{n}\}_{r=R'} = \{\frac{\partial R'}{\partial t}\vec{e}_r' \cdot \vec{n}\}_{r=R'} \quad (4)$$

and far away from the bubble, we have $\phi' = \phi_0$.

We will consider now the *bubble potential*, ϕ_b, difference of the potentials ϕ' and ϕ_0.

$$\phi_b = \phi' - \phi_0. \quad (5)$$

Since at infinity V_b and ϕ_b decay to zero, and the pressure is p_0, the Bernoulli equation becomes:

$$\{\frac{\partial\phi_b}{\partial t} + \frac{1}{2}(\nabla\phi_b)^2 + \frac{1}{2}V_0^2 + \nabla\phi_b \cdot V_0 + \frac{p'}{\rho}\}_{r=R'} = \{\frac{1}{2}V_0^2 + \frac{p_0}{\rho}\}_{M=\infty} \quad (6)$$

If we limit the study to the case where the *basic* flow is steady, $\partial\phi_0/\partial t = 0$, the right hand side of the equation is a constant of the basic flow field, which can be written for instance at any selected reference point, O.

Let us choose now a general frame of reference $\mathcal{R}$ with rotation relative to the fixed frame defined by $\vec{\omega}$, and whose origin O has a translation velocity $\vec{V}_e$ (see figure 1 for definitions). Since:

$$\vec{V}_M = \vec{V}_e + \vec{\omega} \times \vec{OM}. \quad (7)$$

We now have the relationships:

$$\frac{\partial\phi_b}{\partial t} = \frac{\partial\phi}{\partial t} - \vec{V}_e \cdot \nabla\phi - (\vec{\omega} \times \vec{OM}) \cdot \nabla\phi, \quad (8)$$

$$\frac{\partial R'}{\partial t}\vec{e}_r' = \frac{\partial R}{\partial t}\vec{e}_r + \vec{V}_e + \vec{\omega} \times \vec{OM}, \quad (9)$$

where ϕ is the *bubble velocity potential* in the *moving* frame $\mathcal{R}$. The system of equations of the problem then becomes:

$$\Delta\phi = 0, \quad (10)$$

$$\lim_{\infty}\phi = 0, \quad (11)$$

$$\{\nabla\phi \cdot \vec{n}\}_{wall} = 0, \quad (12)$$

$$\{\nabla\phi \cdot \vec{n}\}_{r=R} = \frac{\partial R}{\partial t} + \{(\vec{V}_e - \vec{V}_0) + \vec{\omega} \times \vec{OM}) \cdot \vec{n}\}_{r=R}, \quad (13)$$

$$\left\{\frac{\partial\phi}{\partial t} + \frac{1}{2}(\nabla\phi)^2 + (\vec{V}_0 - \vec{V}_e - \vec{\omega} \times \vec{OM}) \cdot \nabla\phi + \right.$$

$$\left. + \frac{1}{2}(V_0^2 - V_0^2(O,t)) + \frac{p}{\rho}\right\}_{r=R} = \frac{p_0(O,t)}{\rho}. \quad (14)$$

Pressure inside the bubble

We will assume that the pressure inside the bubble is spatially uniform and thus only depends on time. p_{init} being the initial pressure inside the bubble, we can write:

$$p_{init} = p_v + p_g^0, \quad (15)$$

where p_v is the vapor pressure and p_g^0 the initial noncondensible gas pressure which obeys the polytropic law $PV^k = constant$. At any time the balance of pressures on the surface of the bubble can be written:

$$p(R,t) = p_v + p_g - 2\gamma C \quad (16)$$

where C is the local curvature of the bubble surface and γ the surface tension. We finally obtain for equation(14):

$$\rho\{\frac{\partial\phi}{\partial t} + \frac{1}{2}(\nabla\phi)^2 + (\vec{V}_0 - \vec{V}_e - \vec{\omega} \times \vec{OM}) \cdot \nabla\phi + \right.$$

$$\left. + \frac{1}{2}(V_0^2 - V_0^2(O,t))\}_{r=R} = (p_0(O,t) - p_{init}) + \right.$$

$$+ (p_{init} - p_v)(1 - \frac{V^{-k}}{V_0^{-k}}) + \frac{2\gamma}{r_0}(r_0 C - \frac{V^{-k}}{V_0^{-k}}) \quad (17)$$

Matched Asymptotic Expansions

We consider the case where the ratio ϵ between the bubble radius r_0 and the distance l_0 between the center of bubble and the wall is small:

$$\epsilon = r_0/l_0 \ll 1. \quad (18)$$

Using the matched asymptotic expansions method the problem can be subdivided into two subproblems: an *inner* problem where the characteristic length is the bubble radius r_0 and the wall is considered to be at infinity, and an *outer* problem where the characteristic length is l_0 and the bubble appears only as a singular perturbation at the origin.

Outer problem

In the *outer* problem we only have Equations (10),(11) and (12) to satisfy. They can be written using non-dimensional variables $r = l_0\,\tilde{r}$ and $\phi = \phi_{ref}\,\tilde{\phi}$, as:

$$\Delta\tilde{\phi} = 0, \quad (19)$$

$$\lim_{\tilde{r}\to\infty}\tilde{\phi} = 0, \quad (20)$$

$$\{\nabla\tilde{\phi} \cdot \vec{n}\}_{object} = 0, \quad (21)$$

Inner problem

In the *inner* problem we nondimensionalize Equations (15) through (18) using the following normalizations:

R	$= r_0\,\tilde{R}$	r_0 : the initial bubble radius
p	$= \Delta p\,\tilde{p}$	Δp :characteristic pressure change in the initial flow
t	$= T_0\,\tilde{t}$	T_0 :characteristic collapse time
ϕ	$= r_0^2\tilde{\phi}/T_0$	
V_0	$= v_0\tilde{V}_0$	v_0 :characteristic initial flow velocity
∇V_0	$= M\,\tilde{\nabla}V_0$	M :characteristic initial flow velocity gradient
$P_0(O,t) - p_{init}$	$= \Delta p\,\tilde{\Delta p}(t)$	

Matching conditions

The matching conditions between the *inner* and the *outer* solutions - these being nothing but two approximations of the same velocity potential ϕ which are valid in two separate regions - is obtained by formally writing that there exists an intermediate region characterized by r^*, where both solutions are valid. For the *inner* problem, this region must be at infinity so that $r^* \gg r_0$, whereas for the *outer* problem, it must be close to the origin so $r^* \ll l_0$. This can be written as:

$$r_0 \ll r^* \ll l_0 \quad (22)$$

$$\phi_{inner}(r) = \phi_{outer}(r), \quad where, \quad r = r_0\tilde{r} = l_0\tilde{r} \quad (23)$$

$$\Leftrightarrow \frac{r_0^2}{T_0}\tilde{\phi}(\frac{r}{r_0}) = \phi_{ref}\,\tilde{\phi}(\frac{r}{l_0}) \quad (24)$$

Taylor series expansions of the basic velocity field

Since we are considering the case where the size of the inner region is small compared to the characteristic length of the basic flow, we can express the velocity field in the *inner* region as a Taylor series expansion about the selected origin O.

$$\vec{V}_0(\vec{r}) = \vec{V}_0(O) + \vec{r} \cdot \nabla\vec{V}_0(O) + \frac{1}{2}\vec{r} \cdot \nabla\nabla\vec{V}_0(O) \cdot \vec{r} + O(r_0^3) \quad (25)$$

Let v_0 be the characteristic velocity of the flow field, M the characteristic dimension of the velocity gradient and N the characteristic dimension of the velocity bigradient. We will choose an orthogonal coordinate system fixed to a streamline so that $\vec{V}_e = \vec{V}_0(O(t))$ so that the z-axis is parallel to $V_0(O)$.

$$\frac{\vec{V}_0}{v_0} = \tilde{V}_0 = v_z(t)\vec{e}_z \quad (26)$$

Note that v_0 is the characteristic velocity of the initial flow and is a constant whereas $v_z(t)$ is a function of time.

In order to compute the various terms in Equation (14) we need the following quantities.

$$\vec{V}_0(\vec{r}) - \vec{V}_c = M r_0 \vec{r}\cdot\vec{\nabla}\vec{V}_0(O) + \frac{1}{2} r_0^2 N \vec{r}\cdot\vec{\nabla}\vec{\nabla}\vec{V}_0(O)\cdot\vec{r} + \cdots \quad (27)$$

$$(\vec{V}_0(\vec{r}) - \vec{V}_c)\cdot\nabla\phi = \frac{r_0^2}{T_0^2}\nabla\tilde{\phi}\cdot(MT_0\vec{r}\cdot\vec{\nabla}\vec{V}_0(O) + \frac{1}{2}NT_0^2 r_0\vec{r}\cdot$$

$$\cdot\vec{\nabla}\vec{\nabla}\vec{V}_0(O)\cdot\vec{r} + \cdots) \quad (28)$$

$$\frac{1}{2}(\vec{V}_0^2(\vec{r}) - \vec{V}_c^2) = \frac{r_0^2}{T_0^2}(M T_0^2 \frac{u_0}{r_0}\vec{r}\cdot\vec{\nabla}V_0(O)\cdot\vec{V}_0(O) +$$

$$+\frac{1}{2}T_0^2 u_0 N\vec{r}\cdot\vec{\nabla}\vec{\nabla}\vec{V}_0(O)\cdot\vec{r}\cdot\vec{V}_0(O) + \frac{1}{2}\left(M T_0 \vec{r}\cdot\vec{\nabla}\vec{V}_0(O)\right)^2 + \cdots) \quad (29)$$

If we consider the case where the problem is symmetrical about the (Oxz) plane then

$$\vec{\nabla}\vec{V}_0(O) = \begin{bmatrix} a_1 & 0 & a_2 \\ 0 & 0 & 0 \\ a_2 & 0 & -a_1 \end{bmatrix}_{e_x,e_y,e_z} \quad (30)$$

Choosing such an arbitrary gradient is consistent with having a potential flow since we still have $\nabla\cdot\vec{V}_0 = 0$ and $\nabla\times\vec{V}_0 = 0$. Rewritten also in polar coordinates we have:

$$\vec{\nabla}\vec{V}_0(O)\begin{bmatrix} x \\ y \\ z \end{bmatrix}_{e_x,e_y,e_z} = \begin{bmatrix} a_1 x + a_2 z \\ 0 \\ -a_1 z + a_2 x \end{bmatrix}_{e_x,e_y,e_z} = r\begin{bmatrix} G_r(\theta,\psi) \\ G_\theta(\theta,\psi) \\ G_\psi(\theta,\psi) \end{bmatrix}_{e_r,e_\theta,e_\psi}$$

$$\begin{bmatrix} x \\ y \\ z \end{bmatrix}_{e_x,e_y,e_z}\cdot\nabla\vec{\nabla}\vec{V}_0(O)\begin{bmatrix} x \\ y \\ z \end{bmatrix}_{e_x,e_y,e_z} = \begin{bmatrix} \gamma_1 x^2 + 2\gamma_2 xz \\ 0 \\ \gamma_4 x^2 + 2\gamma_2 xz \end{bmatrix}_{e_x,e_y,e_z} = r^2\begin{bmatrix} H_r \\ H_\theta \\ H_\psi \end{bmatrix}_{e_r,e_\theta,e_\psi} \quad (31)$$

where:

$$\gamma_1 = \frac{\partial a_2}{\partial x},\quad \gamma_2 = \frac{\partial a_2}{\partial z},\quad \gamma_3 = \frac{\partial a_1}{\partial x},\quad \gamma_4 = \frac{\partial a_1}{\partial z}. \quad (32)$$

Since the problem has a plane of symmetry, we shall take $\vec{\omega} = \omega(t)\vec{e}_Y$,

$$\vec{\omega}\times O\vec{M} = \omega r(\vec{e}_Y\times\vec{e}_r), \quad (33)$$

and define Ω as the characteristic rotation speed of the frame

$$\omega = \Omega\tilde{\omega}. \quad (34)$$

Discussion on the relative size of the problem scales

The problem has six nondimensional parameters representing ratios between the various scales. These are presented below with their selected size relative to ϵ the main parameter of the problem. The choice of the relative size was determined first by a least degeneracy principle to conserve the maximum terms, then by a relaxation of this constraint for some parameters in order to be able to obtain solutions in some practical physical configurations.

1. The characteristic length of the *inner* problem is much smaller than that of the *outer* problem:

$$\frac{r_0}{l_0} = \epsilon \quad (35)$$

2. The characteristic velocity of the initial flow, u_0, is of same order as the characteristic collapse velocity, r_0/T_0 :

$$\frac{u_0}{v_{collapse}} = \mu = O(1) \quad (36)$$

3. The characteristic velocity gradient at the scale of the *inner* problem is far smaller than that of the *inner* problem:

$$MT_0 = \frac{M r_0}{v_{collapse}} = \mu\epsilon = O(\epsilon) \quad (37)$$

4. The characteristic velocity bigradient at the scale of the *inner* problem is far smaller than that of the *inner* problem.

$$NT_0 r_0 = \frac{N r_0^2}{v_{collapse}} = \mu\epsilon^2 = O(\epsilon^2) \quad (38)$$

5. The characteristic rotation speed at the scale of the *inner* problem is far smaller than the collapse velocity:

$$\omega T_0 = \frac{\Omega r_0}{v_{collapse}} = O(\epsilon) \quad (39)$$

6. The collapse velocity is directly related to the local pressure by:

$$\frac{\Delta p}{\rho v_{collapse}^2} = O(1) \quad (40)$$

The bubble is considered to be close to the submerged body so that at leading order, ϵ^0, in the *outer* problem, the body is considered to be a flat plane. At the next order, the curvature is taken into account. Mathematically, this means that the ratio of the bubble standoff distance to the local curvature of the body is of order ϵ. In the *inner* problem, the effect of the wall is seen first at order ϵ for the potential and at order ϵ^2 for the bubble radius. The effect of the curvature only interferes at order ϵ^2 on the potential and will only add a constant to the equations.

Resolution

We will use the following notations for the expansions:

$$\tilde{\phi} = \tilde{\phi}_0 + \epsilon\tilde{\phi}_I(\vec{r},\theta,\tilde{t}) + \epsilon^2\tilde{\phi}_{II}(\vec{r},\theta,\tilde{t}) + \cdots \quad (41)$$

$$\tilde{\phi} = \tilde{\phi}_0 + \epsilon\tilde{\phi}_I(\vec{r},\theta,\tilde{t}) + \epsilon^2\tilde{\phi}_{II}(\vec{r},\theta,\tilde{t}) + \cdots \quad (42)$$

$$\tilde{R} = \tilde{R}_0 + \epsilon\tilde{R}_I(\vec{r},\theta,\tilde{t}) + \epsilon^2\tilde{R}_{II}(\vec{r},\theta,\tilde{t}) + \cdots \quad (43)$$

Order ϵ^0

Outer problem at order ϵ^0

The system of equation (20) to (22) for the order zero becomes:

$$\Delta\tilde{\phi}_0 = 0 \quad (44)$$

$$\lim_{r\to\infty}\tilde{\phi}_0 = 0 \quad (45)$$

$$\{\nabla\tilde{\phi}_0\cdot\vec{n}\}_{r=\frac{1}{\epsilon+\delta}} = 0 \quad (46)$$

The general solution to this problem is a combination of spherical harmonics which decay at infinity and include the image of the bubble symmetric with respect to the wall at a distance r' from the field point:

$$\tilde{\phi}_0 = \sum_{n=0}^{\infty}\tilde{B}_n(\tilde{t})\,P_n(\cos\theta)\left(\frac{1}{r^{n+1}} + \frac{1}{r'^{n+1}}\right) \quad (47)$$

$P_n(x)$ are the Legendre polynomial of degree n.

Inner problem at order ϵ^0

The system of equations (10) to (14) for the order zero becomes:

$$\Delta\tilde{\phi}_0 = 0, \quad (48)$$

$$\frac{\partial\tilde{\phi}_0}{\partial r}(\tilde{R}_0) = \dot{\tilde{R}}_0, \quad (49)$$

$$\left\{\frac{\partial\tilde{\phi}_0}{\partial t} + \frac{1}{2}\left(\frac{\partial\tilde{\phi}_0}{\partial r}\right)^2\right\}_{r=R_0} = \Delta\tilde{p}(\tilde{t}) + \mathcal{P}\left(1 - \frac{V^{-\delta}}{V_0^{-\delta}}\right) + \frac{1}{W}\left(\tilde{C} - \frac{V^{-\delta}}{V_0^{-\delta}}\right) \quad (50)$$

From (48) we get the solution

$$\tilde{\phi}_0 = \frac{q}{r} \text{ with } q = -\tilde{R}_0^2\dot{\tilde{R}}_0. \quad (51)$$

where $\tilde{R}_0(\tilde{t})$ is determined by the Rayleigh-Plesset equation

$$\tilde{R}_0\ddot{\tilde{R}}_0 - \frac{3}{2}\dot{\tilde{R}}_0^2 = -\Delta\tilde{p}(\tilde{t}) + \mathcal{P}\left(\tilde{R}_0^{-3\delta} - 1\right) + \frac{1}{W}\left(\tilde{R}_0^{-3\delta} - \frac{1}{\tilde{R}_0}\right) \quad (52)$$

with the initial conditions $\tilde{R}_0 = 1$ and $\dot{\tilde{R}}_0 = 0$.

Matching condition at order zero

If we replace the potentials by their expansions, Equation (25) becomes:

$$\frac{r_0^2}{T_0}\left[\tilde{\phi}_0(\frac{r}{r_0}) + \epsilon\tilde{\phi}_1(\frac{r}{r_0}) + \epsilon^2\tilde{\phi}_{11}(\frac{r}{r_0}) + O(\epsilon^3)\right] = \phi_{ext}$$

$$\left[\tilde{\phi}_0(\frac{r}{l_0}) + \epsilon\tilde{\phi}_1(\frac{r}{l_0}) + \epsilon^2\tilde{\phi}_{11}(\frac{r}{l_0}) + O(\epsilon^3)\right] \quad (53)$$

The solutions are

$$\phi_0 = \sum_{n=0}^{\infty} B_n(\tilde{t})P_n(\cos\theta)(\frac{1}{r^{n+1}} + \frac{1}{r^{n+1}})$$

$$\tilde{\phi}_0 = \frac{q}{r} + C \qquad \textit{where } C \text{ is a constant to be determined}$$

Replace in (54):

$$\epsilon\frac{r_0^2}{T_0}\left(\frac{q}{r} + \frac{C}{r_0} + \epsilon\tilde{\phi}_1(\frac{r}{r_0})\right) = \phi_{ext}$$

$$\left(\sum_{n=0}^{\infty} B_n(\tilde{t})\,P_n(\cos\theta)\,\frac{1}{r^{n+1}}(1 + (\frac{r}{2l_0})^{n+1}) + \frac{\epsilon}{l_0}\tilde{\phi}_1(\frac{r}{l_0}) + \cdots\right) \quad (54)$$

At leading order we then have:

$$C = 0 \quad (55)$$

$$\phi_{ext} = \epsilon\frac{r_0^2}{T_0} \quad (56)$$

$$B_n(\tilde{t}) = \delta_{n,0}\,q(\tilde{t}) \quad (57)$$

To obtain the limit condition on $\tilde{\phi}_1$, we must continue the expansion.

$$\tilde{\phi}_1(\frac{r}{r_0}) + \epsilon\tilde{\phi}_{11}(\frac{r}{r_0}) + O(\epsilon^2) = \frac{q}{2} + \frac{q}{4}\frac{r}{l_0}\cos\theta + \epsilon\tilde{\phi}_1(\frac{r}{r_0}) +$$

$$+O\left((\frac{r}{r_0})^2\right) \quad (58)$$

r/l_0 is of order $\epsilon(1)$ so equating terms at leading order give us:

$$\lim_{r\to\infty}\tilde{\phi}_1 = \frac{q}{2} \quad (59)$$

Order ϵ

Inner problem at order ϵ

Since $\dot{R}_0$ and $\dot{\phi}_0$ only depend on time, at order ϵ the equations of the problem become:

$$\Delta\tilde{\phi}_1 = 0 \quad (60)$$

$$\lim_{r\to\infty}\tilde{\phi}_1 = \frac{q}{2} \quad (61)$$

$$\{\frac{\partial\tilde{\phi}_1}{\partial r} + \dot{R}_1\frac{\partial^2\tilde{\phi}_0}{\partial r^2}\}_{r=R_0} = \frac{\partial\dot{R}_1}{\partial r} - G_*\dot{R}_0 \quad (62)$$

$$\{\frac{\partial\dot{\phi}_1}{\partial r} + \dot{R}_1\frac{\partial^2\dot{\phi}_0}{\partial r\partial t} + \frac{\partial\tilde{\phi}_1}{\partial r}\frac{\partial\tilde{\phi}_0}{\partial r} + \dot{R}_1\frac{\partial\dot{\phi}_0}{\partial r}\frac{\partial^2\tilde{\phi}_0}{\partial r^2} + \dot{R}_0G_*\frac{\partial\tilde{\phi}_0}{\partial r} +$$

$$\mu v_s(t)\dot{R}_0\,F(\theta,\psi)\}_{r=R_0} = 3K\mathcal{P}\dot{R}_1\dot{R}_0^{-3K-1} \quad (63)$$

where

$$G_* = 2a_2\cos\theta\sin\theta\cos\psi + a_1(\sin^2\theta\cos^2\psi - \cos^2\theta) \quad (64)$$

$$F = a_1\sin\theta\cos\psi + a_2\cos\theta \quad (65)$$

Resolution of the order ϵ

The general solution of the Laplace equation can be written:

$$\tilde{\phi}_1 = \sum_{j=0}^{\infty}\sum_{m=-j}^{j}(A_{1jm}r^j + \frac{B_{1jm}}{r^{j+1}})Y_{jm}, \quad (66)$$

$$\dot{R}_1 = \sum_{j=0}^{\infty}\sum_{m=-j}^{j}R_{1jm}Y_{jm}. \quad (67)$$

Y_{jm} are the spherical harmonics:

$$Y_{jm} = \begin{cases} P_j^m(\cos\theta)\cos m\psi; & \text{for } m \geq 0 \\ P_j^{|m|}(\cos\theta)\sin|m|\psi; & \text{for } m < 0 \end{cases} \quad (68)$$

The limit condition at infinity on $\tilde{\phi}_1$ leads us to take:

$$A_{1jm} = \delta_{j,0}\frac{q}{2}, \quad (69)$$

Since the problem is symmetrical about the $(Ox\,z)$ plane, there are no terms in $\sin\psi$,and we do not have to consider $m < 0$. Using the fact that

$$\cos\theta\sin\theta\cos\psi = \frac{1}{3}Y_{21}, \quad (70)$$

$$\sin^2\theta\cos^2\psi - \cos^2\theta = -Y_{20} + \frac{Y_{22}}{6} = Y_f, \quad (71)$$

Equation (18) becomes:

$$-\frac{j+1}{\dot{R}_0^{j+2}}B_{1jm}Y_{jm} + \frac{2q}{\dot{R}_0^3}R_{1jm}Y_{jm} = \dot{R}_{1jm}Y_{jm} - \frac{2}{3}\dot{R}_0a_2Y_{21} +$$

$$+a_1\dot{R}_0(Y_{20} - \frac{Y_{22}}{6}) \quad (72)$$

$$\frac{\dot{q}}{2} + \frac{\dot{B}_{1jm}}{\dot{R}_0^{j+1}}Y_{jm} - \frac{\dot{q}}{\dot{R}_0^3}R_{1jm}Y_{jm} + q\frac{j+1}{\dot{R}_0^{j+4}}B_{1jm}Y_{jm} -$$

$$-2\frac{q^2}{\dot{R}_0^3}R_{1jm}Y_{jm} - \frac{2}{3\dot{R}_0}qa_2Y_{21} - \frac{q}{\dot{R}_0}a_1(-Y_{20} + \frac{Y_{22}}{6}) +$$

$$\mu\dot{R}_0v_s(a_1Y_{11} + a_2Y_{10}) = \dot{R}_{100}Y_{00}3K\mathcal{P}\dot{R}_0^{-3K-1} \quad (73)$$

For $j > 2$ we have a homogeneous linear differential system where the initial conditions are zero. The solution is therefore $R_{1jm} = B_{1jm} = 0;\ \forall j > 2$.

Resolution for $m = j = 0$

We have to solve the following differential system:

$$-\frac{B_{100}}{\dot{R}_0^2} + 2q\frac{\dot{R}_{100}}{\dot{R}_0^3} = \dot{R}_{100} \quad (74)$$

$$\frac{\dot{q}}{2} + \frac{\dot{B}_{100}}{\dot{R}_0} + \frac{q}{\dot{R}_0^2}B_{100} - (\frac{2q^2}{\dot{R}_0^3} + \frac{\dot{q}}{\dot{R}_0^2})\dot{R}_{100} =$$

$$= \dot{R}_{100}\{3K\mathcal{P}\dot{R}_0^{-3K-1} + \frac{1}{\mathcal{W}}(3K\dot{R}_0^{-3K-1} - \frac{1}{\dot{R}_0^3})\} \quad (75)$$

$\dot{R}_{100}$ is the solution of the linear differential equation:

$$\ddot{R}_0\ddot{R}_{100} + 3\dot{R}_0\dot{R}_{100} + \dddot{R}_0R_{100} = -\ddot{R}_0\dot{R}_0^2 - \frac{1}{2}\dot{R}_0^2\ddot{R}_0 -$$

$$-\dot{R}_{100}\{3K\mathcal{P}\dot{R}_0^{-3K-1} + \frac{1}{\mathcal{W}}(3K\dot{R}_0^{-3K-1} - \frac{1}{\dot{R}_0^3})\} \quad (76)$$

and B_{100} is computed using

$$B_{100} = -(\ddot{R}_0\dot{R}_{100} + 2\dot{R}_0\dot{R}_0\dot{R}_{100}) \quad (77)$$

Resolution for $j = 1$

We have the same differential system to solve for R_{I10} and R_{I11}. The only difference is α_1 instead of α_2.

Resolution for $m = 0$ We have to solve the following differential system:

$$-2\frac{B_{I10}}{\dot{R}_0^3} + 2q\frac{\dot{R}_{I10}}{\dot{R}_0^3} = \dot{\bar{R}}_{I10} \tag{78}$$

$$\frac{\dot{B}_{I10}}{\dot{R}_0^2} + 2\frac{q}{\dot{R}_0^3}B_{I10} - (\frac{2q^2}{\dot{R}_0^3} + \frac{\dot{q}}{\dot{R}_0^2})\dot{R}_{I10} - \mu\dot{R}_0 v_x \alpha_1 = 0 \tag{79}$$

$\dot{R}_{I10}$ is the solution of the linear differential equation:

$$\ddot{R}_0\ddot{\bar{R}}_{I10} + 3\dot{R}_0\dot{\bar{R}}_{I10} = 2\mu\dot{R}_0\alpha_1 v_x \tag{80}$$

$$\dot{\bar{R}}_{I10} = \frac{1}{\dot{R}_0^3}\int_0^t 2\mu\dot{R}_0^3 v_x \alpha_1 dt \tag{81}$$

and B_{I10} is computed using:

$$B_{I10} = -\frac{1}{2}\dot{R}_0^3\dot{\bar{R}}_{I10} - 2\dot{R}_0^2\ddot{R}_0\dot{R}_{I10} \tag{82}$$

Resolution for $m = 1$ $\dot{R}_{I11}$ and B_{I11} are computed using:

$$\dot{\bar{R}}_{I11} = \frac{1}{\dot{R}_0^3}\int_0^t 2\mu\dot{R}_0^3 v_x \alpha_2 dt \tag{83}$$

$$B_{I11} = -\frac{1}{2}\dot{R}_0^3\dot{\bar{R}}_{I11} - 2\dot{R}_0^2\ddot{R}_0\dot{R}_{I11} \tag{84}$$

Resolution for $j = 2$

We have the same differential system to solve for R_{I21} and R_f. The only difference is that we have $\frac{2}{3}\alpha_2$ instead of α_1 .

Resolution for $m = 1$ We have to solve the following differential system:

$$-3\frac{B_{I21}}{\dot{R}_0^4} + 2q\frac{\dot{R}_{I00}}{\dot{R}_0^3} = \dot{\bar{R}}_{I21} - \frac{2}{3}\dot{R}_0\alpha_2 \tag{85}$$

$$\frac{\dot{B}_{I21}}{\dot{R}_0^3} + 3\frac{q}{\dot{R}_0^4}B_{I21} - (\frac{2q^2}{\dot{R}_0^3} + \frac{\dot{q}}{\dot{R}_0^2})\dot{R}_{I21} - \frac{2q}{3\dot{R}_0}\alpha_2 = 0 \tag{86}$$

$\dot{R}_{I21}$ is the solution of the linear differential equation:

$$\ddot{R}_0\ddot{\bar{R}}_{I21} + 3\dot{R}_0\dot{\bar{R}}_{I21} - \ddot{\bar{R}}_0\dot{R}_{I21} = \frac{10}{3}\dot{R}_0\ddot{R}_0\alpha_2 + \frac{2}{3}\dot{R}_0^2\dot{\alpha}_2 \tag{87}$$

and B_{I21} is computed using:

$$B_{I21} = -\frac{\dot{R}_0^4}{3}\dot{\bar{R}}_{I21} - \frac{2}{3}\dot{R}_0^3\ddot{R}_0\dot{R}_{I21} + \frac{2}{9}\dot{R}_0^4\alpha_2 \tag{88}$$

Resolution of the coefficient in front of Y_f $\dot{R}_{If}$ is the solution of the linear differential equation:

$$\ddot{R}_0\ddot{\bar{R}}_{If} + 3\dot{R}_0\dot{\bar{R}}_{If} - \ddot{\bar{R}}_0\dot{R}_{If} = 3\dot{R}_0\ddot{R}_0\alpha_1 + \dot{R}_0^2\dot{\alpha}_1 \tag{89}$$

and B_{If} is computed using:

$$B_{If} = -\frac{\dot{R}_0^4}{3}\dot{\bar{R}}_{If} - \frac{2}{3}\dot{R}_0^3\ddot{R}_0\dot{R}_{If} + \frac{1}{3}\dot{R}_0^4\alpha_1 \tag{90}$$

The potential and radius at order ϵ are:

$$\tilde{\phi}_1 = \frac{q}{2} + \frac{B_{I00}}{\tilde{r}} + \frac{1}{\tilde{r}^2}(B_{I10}\cos\theta + B_{I11}\sin\theta\cos\psi) + \frac{1}{\tilde{r}^3}(3B_{I21}\sin\theta\cos\theta\cos\psi + B_{If}(\sin^2\theta\cos^2\psi - \cos^2\theta)) \tag{91}$$

$$\dot{\bar{R}}_1 = \dot{\bar{R}}_{I00} + \dot{\bar{R}}_{I10}\cos\theta + \dot{\bar{R}}_{I11}\sin\theta\cos\psi + 3\dot{\bar{R}}_{I21}\sin\theta\cos\theta\cos\psi + \dot{\bar{R}}_{If}(\sin^2\theta\cos^2\psi - \cos^2\theta) \tag{92}$$

Outer problem at order ϵ

At this order the outer problem sees a singularity at the origin due to the presence and behavior of the bubble, and also the curvature of the body (see Figure 2). The solution can again be obtained by placing an identical singularity symmetrically about the wall and by adding a distribution of sources on the body. The singularity distribution will induce a change, L, in the velocity potential at the origin. The outer problem's solution at order ϵ is then:

$$\tilde{\phi}_1 = C(\frac{1}{\tilde{r}} + \frac{1}{\tilde{r}'}) + L(\vec{r}) \quad with \quad L(O) = L \tag{93}$$

Order ϵ^2

To continue the asymptotic expansions, we need to evaluate the bi-gradient of the velocity field.

Matching condition at order ϵ

Using the solution of the outer problem at order ϵ, (94), where the constant C has been evaluated

$$\tilde{\phi}_1 = \frac{q}{2} + \frac{B_{I00}}{\tilde{r}}, \tag{94}$$

we obtain::

$$B_{I00} + \frac{r}{l_0}\tilde{\phi}_{I1}(\frac{r}{r_0}) + O(\epsilon\frac{r}{r_0}) = C(1 + \frac{1}{2}\frac{r}{l_0}) + \frac{q}{4}\frac{r^2}{r_0 l_0}\cos\theta + L\frac{r}{l_0} \tag{95}$$

which leads to $C = B_{I00}$.

$$\tilde{\phi}_{I1}(\frac{r}{r_0}) + O(\epsilon) = \frac{B_{I00}}{2} + L + \frac{q}{4}\frac{r}{r_0}\cos\theta + O(\frac{r^2}{r_0 l_0}) \tag{96}$$

$$\Rightarrow \lim_{\tilde{r}\to\infty}(\tilde{\phi}_{I1}(\tilde{r}) - \frac{B_{I00}}{2} - L - \frac{q}{4}\tilde{r}\cos\theta) = 0 \tag{97}$$

Resolution of the inner problem at order ϵ^2

For the following order we need to calculate the terms of order ϵ^2 for the following expressions:

$$\{\frac{\partial\tilde{\phi}}{\partial\tilde{r}}\}_{\tilde{r}=\tilde{R}} : \frac{\partial\tilde{\phi}_{I1}}{\partial\tilde{r}} + \dot{\bar{R}}_1\frac{\partial^2\tilde{\phi}_1}{\partial\tilde{r}^2} + \ddot{\bar{R}}_{I1}\frac{\partial^2\tilde{\phi}_0}{\partial\tilde{r}^2} + \frac{1}{2}\dot{\bar{R}}_1^2\frac{\partial^3\tilde{\phi}_0}{\partial\tilde{r}^3} \tag{98}$$

$$\{-\frac{1}{\tilde{R}^2}\frac{\partial\tilde{\phi}}{\partial\theta}\frac{\partial\tilde{R}}{\partial\theta}\}_{\tilde{r}=\tilde{R}} : -\frac{1}{\dot{R}_0^2}\frac{\partial\tilde{\phi}_1}{\partial\theta}\frac{\partial\tilde{R}_1}{\partial\theta} \tag{99}$$

$$\{-\frac{1}{\tilde{R}^2\sin^2\theta}\frac{\partial\tilde{\phi}}{\partial\psi}\frac{\partial\tilde{R}}{\partial\psi}\}_{\tilde{r}=\tilde{R}} : -\frac{1}{\dot{R}_0^2\sin^2\theta}\frac{\partial\tilde{\phi}_1}{\partial\psi}\frac{\partial\tilde{R}_1}{\partial\psi} \tag{100}$$

$$\{(\vec{V}_c - \vec{V}_O)\cdot\vec{n}\}_{\tilde{r}=\tilde{R}} : -\frac{1}{2}\dot{R}_0^2 H_r - G_r\dot{\bar{R}}_1 + G_\theta\frac{\partial\dot{R}_1}{\partial\theta} + \frac{G_\psi}{\sin\theta}\frac{\partial\dot{R}_1}{\partial\psi} \tag{101}$$

$$\{\vec{\omega}\times\vec{OM}\cdot\vec{n}\}_{\tilde{r}=\tilde{R}} : \tilde{\omega}(\cos\psi\frac{\partial\dot{R}_1}{\partial\theta} - \frac{\sin\psi\cos\theta}{\sin\theta}\frac{\partial\dot{R}_1}{\partial\psi}) \tag{102}$$

$$\{\frac{\partial\tilde{\phi}}{\partial\tilde{t}}\}_{\tilde{r}=\tilde{R}} : \frac{\partial\tilde{\phi}_{I1}}{\partial\tilde{t}} + \dot{\bar{R}}_1\frac{\partial^2\tilde{\phi}_1}{\partial\tilde{t}\partial\tilde{r}} + \ddot{\bar{R}}_{I1}\frac{\partial^2\tilde{\phi}_0}{\partial\tilde{t}\partial\tilde{r}} + \frac{1}{2}\dot{\bar{R}}_1^2\frac{\partial^3\tilde{\phi}_0}{\partial\tilde{t}\partial\tilde{r}^2} \tag{103}$$

$$\{\frac{1}{2}\left(\frac{\partial\tilde{\phi}}{\partial\tilde{r}}\right)^2\}_{\tilde{r}=\tilde{R}} : \frac{\partial\tilde{\phi}_0}{\partial\tilde{r}}\left(\frac{\partial\tilde{\phi}_{I1}}{\partial\tilde{r}} + \dot{\bar{R}}_1\frac{\partial^2\tilde{\phi}_1}{\partial\tilde{r}^2} + \ddot{\bar{R}}_{I1}\frac{\partial^2\tilde{\phi}_0}{\partial\tilde{r}^2} + \right.$$

$$+\frac{1}{2}\dot{R}_0^3\frac{\partial^3\dot{\phi}_0}{\partial\dot{r}^3}\Big)+\frac{1}{2}(\frac{\partial\dot{\phi}_1}{\partial\dot{r}})^2+\frac{1}{2}\dot{R}_0^3(\frac{\partial^2\dot{\phi}_0}{\partial\dot{r}^2})^2+\dot{R}_1\frac{\partial\dot{\phi}_1}{\partial\dot{r}}\cdot\frac{\partial^2\dot{\phi}_0}{\partial\dot{r}^2} \quad (104)$$

$$\{\frac{1}{2\dot{R}^2}\left(\frac{\partial\dot{\phi}}{\partial\theta}\right)^2\}_{\dot{r}=\dot{R}} : \frac{1}{2\dot{R}_0^2}\left(\frac{\partial\dot{\phi}_1}{\partial\theta}\right)^2 \quad (105)$$

$$\{\frac{1}{2\dot{R}^2\sin^2\theta}\left(\frac{\partial\dot{\phi}}{\partial\psi}\right)^2\}_{\dot{r}=\dot{R}} : \frac{1}{2\dot{R}_0^2\sin^2\theta}\left(\frac{\partial\dot{\phi}_1}{\partial\psi}\right)^2 \quad (106)$$

$$\{(\vec{V}_O-\vec{V}_c)\cdot\nabla\dot{\phi}\}_{\dot{r}=\dot{R}} : \frac{1}{2}\dot{R}_0^2H_r\frac{\partial\dot{\phi}_0}{\partial\dot{r}}+G_r$$

$$\left(\dot{R}_1\frac{\partial\dot{\phi}_0}{\partial\dot{r}}+\dot{R}_0\frac{\partial\dot{\phi}_1}{\partial\dot{r}}\right)-\ G_\theta\frac{\partial\dot{\phi}_1}{\partial\theta}-G_\psi\frac{\partial\dot{\phi}_1}{\partial\psi} \quad (107)$$

$$\frac{1}{2}\left(V_O^2-V_O^2(O,t)\right) : \mu v_x(t)\dot{R}_1(a_2\cos\theta+a_1\sin\theta\cos\psi)+$$

$$\dot{R}_0^2(G_r^2+G_\theta^2+\psi^2)+\frac{1}{2}\mu v_x(t)\dot{R}_0^2(\gamma_1\cos^2\theta+\gamma_3\sin\theta\cos\theta\cos\psi) \quad (108)$$

$$\{\vec{\omega}\times\vec{OM}\cdot\nabla\dot{\phi}\}_{\dot{r}=\dot{R}} : \dot{\omega}(\cos\psi\frac{\partial\dot{\phi}_1}{\partial\theta}-\frac{\sin\psi\cos\theta}{\sin\theta}\frac{\partial\dot{\phi}_1}{\partial\psi}) \quad (109)$$

The system becomes:

$$\Delta\dot{\phi}_{11}=0 \quad (110)$$

$$\lim_{\dot{r}\to\infty}(\dot{\phi}_{11}(\vec{r})-\frac{B_{100}}{2}-L-\frac{q}{4}\dot{r}\cos\theta)=0 \quad (111)$$

$$\{\frac{\partial\dot{\phi}_{11}}{\partial\dot{r}}+\dot{R}_1\frac{\partial^2\dot{\phi}_1}{\partial\dot{r}^2}+\dot{R}_{11}\frac{\partial^2\dot{\phi}_0}{\partial\dot{r}^2}+\frac{1}{2}\dot{R}_0^3\frac{\partial^3\dot{\phi}_0}{\partial\dot{r}^3}-\frac{1}{\dot{R}_0^2}\frac{\partial\dot{\phi}_1}{\partial\theta}\frac{\partial\dot{R}_1}{\partial\theta}-$$
$$-\frac{1}{\dot{R}_0^2\sin^2\theta}\frac{\partial\dot{\phi}_1}{\partial\psi}\frac{\partial\dot{R}_1}{\partial\psi}\}_{\dot{r}=\dot{R}_0}=\{\frac{\partial\dot{R}_{11}}{\partial\dot{t}}-\frac{1}{2}\dot{R}_0^2H_r-G_r\dot{R}_1+$$
$$G_\theta\frac{\partial\dot{R}_1}{\partial\theta}+\frac{G_\psi}{\sin\theta}\frac{\partial\dot{R}_1}{\partial\psi}-$$
$$-\dot{\omega}(\cos\psi\frac{\partial\dot{R}_1}{\partial\theta}-\frac{\sin\psi\cos\theta}{\sin\theta}\frac{\partial\dot{R}_1}{\partial\psi})\}_{\dot{r}=\dot{R}_0} \quad (112)$$

$$\frac{\partial\dot{\phi}_{11}}{\partial\dot{t}}+\dot{R}_1\frac{\partial^2\dot{\phi}_1}{\partial\dot{t}\partial\dot{r}}+\dot{R}_{11}\frac{\partial^2\dot{\phi}_0}{\partial\dot{t}\partial\dot{r}}+\frac{1}{2}\dot{R}_0^3\frac{\partial^3\dot{\phi}_0}{\partial\dot{t}\partial\dot{r}^2}+\frac{\partial\dot{\phi}_0}{\partial\dot{r}}\cdot\frac{\partial\dot{\phi}_{11}}{\partial\dot{r}}+$$
$$+\dot{R}_1\frac{\partial\dot{\phi}_0}{\partial\dot{r}}\cdot\frac{\partial^2\dot{\phi}_1}{\partial\dot{r}^2}+\dot{R}_{11}\frac{\partial\dot{\phi}_0}{\partial\dot{r}}\cdot\frac{\partial^2\dot{\phi}_0}{\partial\dot{r}^2}+\frac{1}{2}\dot{R}_0^3\frac{\partial\dot{\phi}_0}{\partial\dot{r}}\cdot\frac{\partial^3\dot{\phi}_0}{\partial\dot{r}^3}+$$
$$+\frac{1}{2}(\frac{\partial\dot{\phi}_1}{\partial\dot{r}})^2+\frac{1}{2}\dot{R}_0^3(\frac{\partial^2\dot{\phi}_0}{\partial\dot{r}^2})^2+\dot{R}_1\frac{\partial\dot{\phi}_1}{\partial\dot{r}}\cdot\frac{\partial^2\dot{\phi}_0}{\partial\dot{r}^2}+\frac{1}{2\dot{R}_0^2}\left(\frac{\partial\dot{\phi}_1}{\partial\theta}\right)^2$$
$$\frac{1}{2\dot{R}_0^2\sin^2\theta}\left(\frac{\partial\dot{\phi}_1}{\partial\psi}\right)^2+\frac{1}{2}\dot{R}_0^2H_r\frac{\partial\dot{\phi}_0}{\partial\dot{r}}+G_r\left(\dot{R}_1\frac{\partial\dot{\phi}_0}{\partial\dot{r}}+\dot{R}_0\frac{\partial\dot{\phi}_1}{\partial\dot{r}}\right)-$$
$$-G_\theta\frac{\partial\dot{\phi}_1}{\partial\theta}-G_\psi\frac{\partial\dot{\phi}_1}{\partial\psi}+\mu v_x(t)\dot{R}_1(a_2\cos\theta+a_1\sin\theta\cos\psi)+$$
$$+\dot{R}_0^2(G_r^2+G_\theta^2+G_\psi^2)+\frac{1}{2}\mu v_x(t)\dot{R}_0^2(\gamma_1\cos^2\theta+$$
$$\gamma_3\sin\theta\cos\theta\cos\psi)+\dot{\omega}(\cos\psi\frac{\partial\dot{\phi}_1}{\partial\theta}-\frac{\sin\psi\cos\theta}{\sin\theta}\frac{\partial\dot{\phi}_1}{\partial\psi})\}_{\dot{r}=\dot{R}_0}$$
$$=3K\mathcal{P}\left(K_1\dot{R}_{100}^2\dot{R}_0^{-3K-2}+\dot{R}_0^{-3K-1}\dot{R}_{110}\right) \quad (113)$$

The limit condition at infinity leads us to take $\dot{\phi}_{11}$ as:

$$\dot{\phi}_{11}=\frac{B_{100}}{2}+L+\frac{q}{4}\dot{r}\cos\theta+\sum_{j,m}\frac{B_{11jm}}{\dot{r}^{j+1}}Y_{jm} \quad (114)$$

$\dot{R}_1$ and $\dot{\phi}_1$ are functions of spherical harmonics up to the order Y_{2j}. The products of these functions give us harmonics up to the order 4, which leads to 15 independent linear differential equations to solve.

Application to Bubble Dynamics near a Headform

In this section, we put into application the asymptotic expansion by studying the collapse of a bubble near a semi-infinite bluff body. The velocity potential considered is that due to a superposition of a uniform flow and a source of intensity Q:

$$\phi_0=V_\infty X+\frac{Q}{r} \quad (115)$$

It simulates the flow around the Rankine ogive of radius R at infinity:

$$R=\sqrt{\frac{Q}{\pi V_\infty}} \quad (116)$$

The stagnation point occurs for $X=-R/2$.

At order ϵ^0, the outside pressure $\Delta p(t)$ is taken to be the pressure in the fluid in absence of the bubble along the trajectory of a fluid particle. At higher orders of ϵ, the gradient and bigradient are also taken into account while following a fluid particle. Figure 3 shows the streamlines around the headform.

A fourth order Runge-Kutta procedure is used to solve the differential equations presented earlier. To illustrate the method, a Rankine body with a radius of 10 centimeters advancing at a constant velocity of 1 m/s was selected . Figures 4 through 7 show some results obtained on bubble behavior near the Rankine body. Figures 4a through 4d show a case where the interaction between the bubble and the ogive's flow field is significant. The initial bubble radius is r_0 = 1 cm. and its distance, l_0, from the wall is such that $\epsilon = r_0/l_0$ is equal to 0.3.

Figure 4b shows the trajectory of the bubble center along the body, and figure 4c shows the variations of the pressure in time imposed on the bubble. In the initial phase $t < 1.7$ the bubble sees a pressure drop and as a results it grows, later on, the pressure rises back towards the ambient pressure and the bubble collapse. Figure 4d. shows the velocity of the fluid along the bubble trajectory. This velocity is also that chosen for translating the origin of coordinates in which the bubble shape is prescribed. Figure 4a shows, overlaid on each other, the bubble contours at different times during the bubble growth and collapse. The orientation of the bubble relative to the body is the same as illustrated in Figure 4b which shows bubble positions versus time. It is apparent from the contour plots that the bubble moves toward the body wall during its collapse. Due to the velocity and pressure gradient around the body the bubble elongates and in fact rotates around its center of mass. Initially, the side of the bubble surface facing an intermediary direction between the downstream direction and the wall direction flattens out. A reentrant jet is then produced perpendicular to that face. The direction of the jet appears to change with time in a fashion indicating increased influence of the presence of the wall with time. The computations shown in the figure stopped when the bubble wall touched the origin of coordinates. This moment can be delayed in future computations by adding a component to the translation of the origin of coordinates that is perpendicular to the wall.

Figure 5 shows the influence of the distance of the bubble to the wall, or ϵ, on its shape history. In all three cases shown, ϵ = 0.1, 0.3 and 0.7 only bubble collapse contours are shown. As expected, deviation from sphericity is enhanced with the proximity to the wall. Due to stronger shearing action closer to the body approaching the wall has the effect of increasing bubble stretching and elongation during its growth, then reinforcing the reentrant jet formation during the collapse. For ϵ = 0.3 and ϵ = 0.7 the computation stopped when the bubble surface touched the origin of coordinates. However due the weak nature of the interaction for ϵ = 0.1 the collapse is completed with no reentrant jet and is followed by a bubble rebound or second growth that is not shown on the figure.

Also, as expected, a similar effect as in figure 5 is obtained if the distance to the body is maintained constant while the bubble size is changed. Figure 6 shows such a case where the distance between the bubble center and the wall is maintained at 10/3 cm., while the bubble

size is changed from 0.5 cm ($\epsilon = 0.15$), to 1 cm ($\epsilon = 0.3$), to 2 cm ($\epsilon = 0.6$). Here too the jet is seen to rotate to become closer and closer to a perpendicular to the wall.

Conclusions and suggested improvements

We have presented in this paper an analytical approach based on a matched asymptotic method to study the behavior of a bubble in a nonuniform potential flow field. The analysis was conducted up to order ϵ^2 where ϵ is the ratio initial bubble size to initial bubble distance to the nearby wall generating the nonuniform flow field. Numerical results calculated up to the order ϵ show the formation of a jet moving opposite to the bubble trajectory and towards the wall on a curved trajectory which approaches a perpendicular to the wall with time. A lengthening effect on the bubble period is observed as well as an imparted rotation of the bubble.

Improvements on the numerical approach should include using a motion of the frame of reference which incorporates,in addition to the motion parallel to the fluid particle trajectory, a component perpendicular to this trajectory so as to account for the bubble motion towards the wall and retard as much as possible crossing of the origin of coordinates by the bubble surface. This will enable the description of the bubble dynamics for a longer period of time in the latest phases of the collapse. The results of this approximate analytical method should also be compared with those obtained with the available three dimensional boundary element method 3DynaFS.

Acknowledgments

The work described in this report was partially funded by the Office of Naval Research, Contract N00014-89-C-0025. The authors would like to thank Dr. Alain Bovis professor at the Ecole Polytechnique, Palaiseau France, who has made the stay of the first author at DYNAFLOW possible.

References

Blake, J. R., Taib, B. B., and Doherty, G., *"Transient Cavities Near Boundaries,"* Journal of Fluid Mechanics, Vol. 170, pp. 479-497, 1986.

Blake, J. R, and Gibson, D. C., *"Cavitation Bubbles Near Boundaries,"* Annual Review Fluid Mechanics, Vol. 19, pp. 99-123, 1987.

Chahine, G. L., *"Experimental and Asymptotic Study of Nonspherical Bubble Collapse,"* Applied Scientific Research, 38, pp. 187-197, 1982.

Chahine, G. L. and Bovis, A. G., *"Pressure Field Generated by Nonspherical Bubble Collapse,"* ASME Journal of Fluids Engineering, Vol. 105, No. 3, pp. 356-364, September 1983.

Chahine, G.L., *"A Numerical Model for Three-Dimensional Bubble Dynamics in Complex Configurations,"* 22nd. American Towing Tank Conference, St. Johns, Newfoundland, Canada, Aug. 1989.

Chahine, G.L., *"Numerical Modelling of the Dynamic Behavior of Bubbles in Nonuniform Flow Fields,"* ASME Symposium on Numerical Methods for Multiphase Flows, Toronto, Canada, June 1990.

Chahine, G.L., *"Dynamics of the Interaction of Non-Spherical Cavities"*, Mathematical Approaches in Hydrodynamics, Editor Touvia Miloh, SIAM Publications, 1991.

Duncan, J.H. ,and Zhang S., *"Numerical Calculations of the Interaction of a Collapsing Cavity and a Compliant Wall,"*, Journal of Fluid Mechanics, 1990.

Guerri, L., Lucca, G., and Prosperetti, A., *"A Numerical Method for the Dynamics of Non-Spherical Cavitation Bubbles,"* Proceedings 2nd International Colloquium on Drops and Bubbles, JPL Publ. 82-7, Monterey CA, Nov 1981.

Shima, A. and Nakajima, K, *"The Collapse of a Non- Hemispherical Bubble Attached to Solid Wall,"* Journal of Fluid Mechanics, 80, Part 2, pp 369-391, 1977.

Wilkerson, S., *"Boundary Integral Technique for Explosion Bubble Collapse Analysis,"* ASME Energy Sources Tech. Conference and Exhibition, Houston Tx. Jan. 1989.

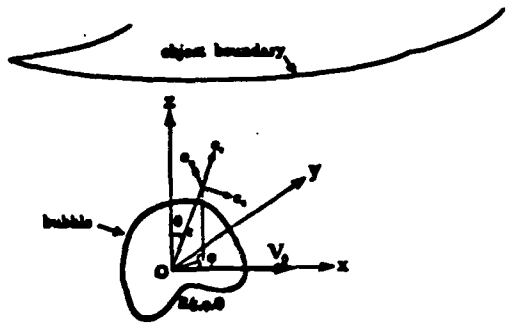

Figure 1: Coordinate systems of the moving frame R

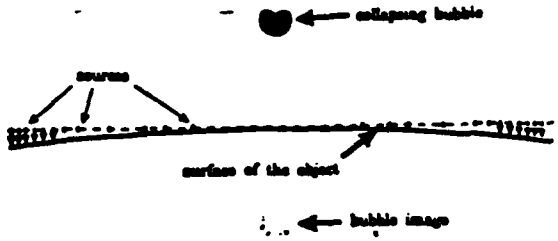

Figure 2: Representation of the object surface by means of a distribution of sources.

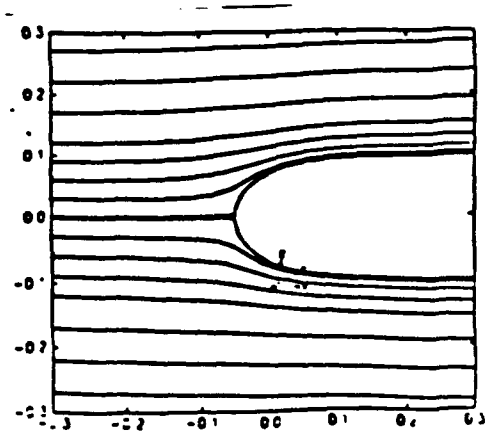

Figure 3: Streamlines around the Rankine body considered in the numerical application.

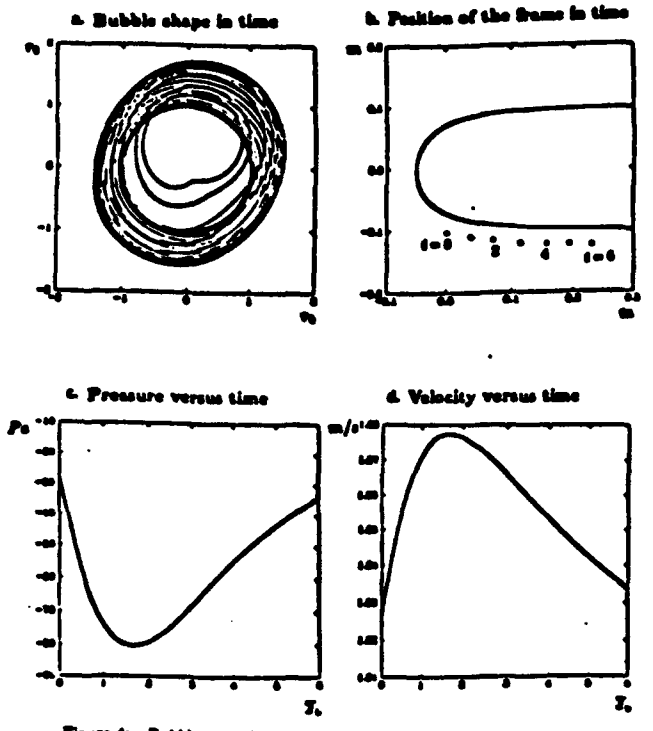

Figure 4: Bubble growth and collapse in the vicinity of a Rankine body. Bubble contours and position versus time. Flow pressure and velocity along bubble trajectory.

Bubble shape in time for different values of ε

$V_\infty = 1\,m/s$ $\quad r_0 = 1cm$ $\quad \mathcal{P} = 1.5$

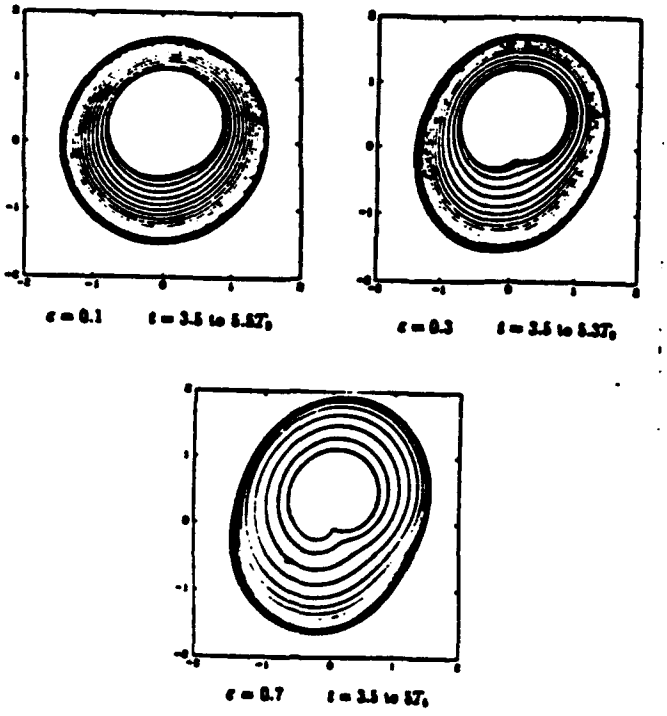

Figure 5: Influence of the bubble distance from the Rankine body on its dynamics. Bubble contours versus time.

Bubble shape in time for different values of the initial bubble radius

$V_\infty = 1\,m/s$ $\quad \Delta p = 98Pa$ $\quad \mathcal{P} = 1.5$

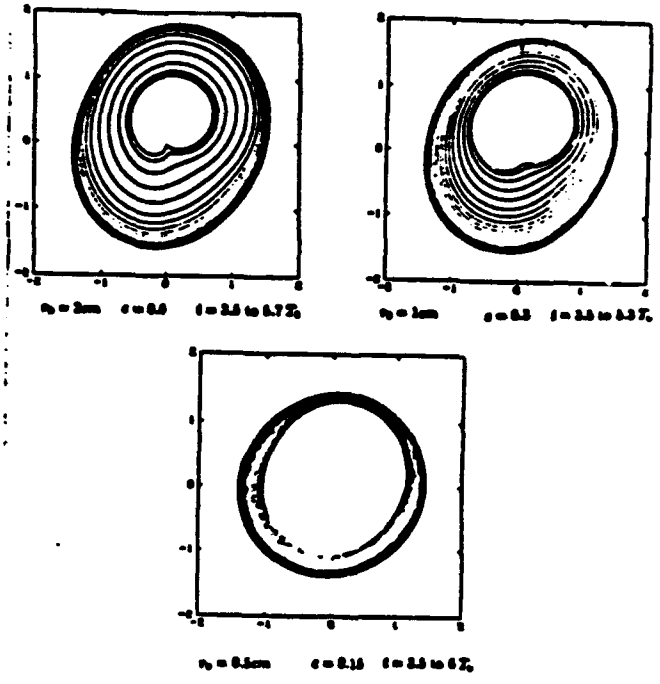

Figure 6: Influence of the bubble size on its dynamics near a Rankine body. Bubble contours versus time.

Proceedings, ASME *Cavitation and Multiphase Flow Forum*, Los Angeles, 1992.

Analytical study of a gas bubble in the flow field of a line vortex.

RAMANI DURAISWAMI AND GEORGES L. CHAHINE[1]
DYNAFLOW, Inc.
7210 Pindell School Road
Fulton, MD 20759

abstract

The flow surrounding a bubble in the flow field of a line vortex is investigated by means of an asymptotic analysis. The flow is potential, and the length scale characteristic of the bubble is assumed to be much smaller than the distance from the bubble to the vortex. The analysis is performed in a coordinate system moving with the bubble. Preliminary results show that the bubble moves with the flow, at a rate faster than the regular flow, and that a jet on the side away from its direction of motion, directed towards the vortex axis is formed.

1 Introduction

The problem of the interaction between bubbles and vortical flows is of relevance to several fluid engineering problems. Important examples include cavitation in shear layers, tip vortex cavitation, bubbles in regions of flow separation, and bubbles in boundary layers. In these flows it has been postulated that the bubbles cause several dramatic effects (e.g. noise generation, material erosion, drag reduction) (Young 1989, Rood 1991, Hammit 1980, Blake and Gibson 1987). However, the mechanisms by which the bubbles play a role have not been fully understood. While a number of studies in the past have elucidated important mechanisms in acoustic cavitation, in the field of flow/vortex cavitation not much progress has been made. In this paper we hope to obtain some understanding of the interaction of bubbles and vortex structures by studying a relatively simple problem — the interaction between a Rankine line vortex and a gas bubble.

When a bubble approaches a region of high vorticity in a fluid, it is accelerated towards the center of the vortex structure because of the pressure gradient it sees. The bubble undergoes a corresponding increase in volume and may split because of the dynamics of its motion. Explosive growth may occur if the bubble pressure drops below its critical pressure. This phenomenon was recently numerically simulated by Chahine (1990) using a boundary element method. This study is intended to complement that work.

We present preliminary results from an analytical study of this problem. The study assumes that the bubble is outside the viscous core of the vortex. Consequently the flow may be assumed potential - an assumption standard in cavitation bubble dynamics. The assumption that the ratio of the bubble radius to its distance from the line vortex is a small quantity (ϵ) then allows us to treat the problem using an asymptotic technique. The results are accurate to $O(\epsilon^2)$.

The novel feature of our analysis is that it represents one of the first analytical studies of the motion of a deforming bubble in a flow field where the velocity is not negligible. Indeed in our scaling the velocity of the flow and the bubble collapse velocity are of the same order. The crucial part of the analysis is in performing the analysis in a coordinate system which approximates the bubble motion. This is in contrast to earlier studies which relied on an approximate model, e.g. Bovis (1980), where the Rayleigh Plesset equation was combined with a model of a spherical bubble in the flow field of a vortex. Preliminary results are presented, which qualitatively agree with observations and the simulations of Chahine (1990).

2 Problem formulation

Consider an initially spherical bubble in an incompressible, inviscid liquid of density ρ_l in an infinite domain at a distance d from a line vortex of strength Γ. The bubble is initially at rest with a radius R_0 and has gas at pressure p_{g_0}. The pressure at infinity is p_∞ and the fluid is at rest there. The velocity due to the vortex alone (i.e. excluding any bubble effects) is denoted $\mathbf{V}$.

Figure 1 indicates the situation considered. The size of the bubble is assumed small compared to the distance d. To perform the calculations we shall consider two coordinate frames. The first is the *fixed frame* which is convenient for describing the overall flow, and through the origin of which the vortex passes, while the second is the *moving frame* which has its origin initially at the center of the bubble and moves at the rate the liquid would in the absence of the bubble. We denote the location of the moving origin by b.

We choose a cylindrical coordinate system, (ϱ, ϑ, z), with the vortex axis along the z axis, and the origin in an orthogonal plane containing the initial bubble center. Since the motion is irrotational we may define a potential $\phi(\mathbf{x}, t)$ so that:

[1] Asst. Research Professor: Department of Mechanical Engineering, The Johns Hopkins University, Baltimore, MD 21218

$$\mathbf{u} = \nabla\phi. \tag{1}$$

The equations of motion are

$$\nabla \cdot \mathbf{u} = \nabla^2\phi = 0, \tag{2}$$

and

$$\frac{\partial\phi}{\partial t} + \frac{1}{2}\nabla\phi \cdot \nabla\phi = \frac{p_\infty - p}{\rho}. \tag{3}$$

These equations are subject to the conditions that

$$\lim_{|\mathbf{x}|\to\infty} p \to p_\infty \qquad \lim_{|\mathbf{x}|\to\infty} \mathbf{u} = \nabla\phi \to 0 \tag{4}$$

The equation of the surface of the bubble may be assumed to be represented in the form $\mathcal{B}(\mathbf{x},t) = 0$. Determining this function is an objective of this study.

The bubble is assumed to undergo deformations according to a polytropic law. Thus

$$pV^k = \text{constant}, \tag{5}$$

where V is the volume of the bubble, and k the polytropic exponent. The mass of the gas in the bubble is assumed to remain constant and equal to m. The kinematic boundary condition requires that the bubble surface be a material surface

$$\frac{D\mathcal{B}}{Dt} = 0. \tag{6}$$

The balance of the normal stresses at the interface yields

$$p|_{\mathcal{B}} = p_g + p_v - \sigma C, \tag{7}$$

where p_g represents the pressure of the gas inside the bubble, p_v the vapor pressure, σ the surface tension coefficient and C the curvature of the surface $\mathcal{B}$. The normal to the surface $\mathcal{B}$ is given by

$$\mathbf{n} = \frac{\nabla\mathcal{B}}{|\nabla\mathcal{B}|}. \tag{8}$$

The curvature may then be computed from the formula

$$C = \nabla \cdot \mathbf{n} = \nabla \cdot \frac{\nabla\mathcal{B}}{|\nabla\mathcal{B}|} = \frac{1}{|\nabla\mathcal{B}|}\nabla^2\mathcal{B} + \nabla\frac{1}{|\nabla\mathcal{B}|} \cdot \nabla\mathcal{B}. \tag{9}$$

Since we are interested in the modification in the flow caused by the presence of the bubble it is convenient to introduce the reduced potential ψ, defined by

$$\psi = \phi - \frac{\Gamma}{2\pi}\beta = \phi - \phi_v, \tag{10}$$

where β is the angular cylindrical coordinate in the fixed frame. The quantity ψ represents the change to the potential of the flow because of the presence of the bubble. Because of linearity, the function ψ also satisfies Laplace's equation. The boundary conditions it is subject to on the bubble surface are

$$\mathbf{n} \cdot \nabla\psi|_{\mathcal{B}} = \left[\dot{\mathcal{B}}\mathbf{e}_r - \mathbf{V}|_{\mathcal{B}}\right] \cdot \mathbf{n}, \tag{11}$$

which is a restatement of the kinematic boundary condition, and

$$\left[\frac{\partial\psi}{\partial t} + \frac{1}{2}|\nabla\psi|^2 + \mathbf{V} \cdot \nabla\psi + \frac{1}{2}\mathbf{V}^2\right] = p_\infty - p_g - p_v + \sigma C, \tag{12}$$

which is a restatement of the dynamic boundary condition. Here we have used the symbol $\mathbf{V}$ to indicate the quantity $\nabla\phi_v$. Additionally, far from the bubble, the potential is expected to reduce to that of the vortex, and so we require

$$\lim_{|\mathbf{x}|\to\infty} \psi = 0 \tag{13}$$

We now consider a moving system of coordinates. The coordinates are initially coincident with the bubble center, and move at the rate the flow at that location would have in the absence of the bubble. In the moving frame we let the Cartesian axes remain parallel to those in the fixed frame. Let $\mathbf{x}$ denote a vector referred to the fixed frame and $\mathbf{x}'$ the same vector referred to the moving frame. Then

$$\mathbf{x} = \mathbf{x}' + \mathbf{b}(t), \tag{14}$$

with the new coordinates changing with time. We may thus write a given function $\psi(\mathbf{x},t)$ as

$$\psi(\mathbf{x},t) = \psi(\mathbf{x}' + \mathbf{b},t) = \Psi(\mathbf{x}',t) \tag{15}$$

where the functions ψ and Ψ have the same values at a given physical location, but have different functional form (and are hence indicated with different symbols). To clarify the behavior of this representation of the potential we note

$$\mathbf{u} - \mathbf{V} = \frac{\partial\psi}{\partial x_i}\mathbf{e}_i = \frac{\partial\Psi}{\partial x_i'}\mathbf{e}_i, \tag{16}$$

and

$$\frac{\partial\psi}{\partial t} = \frac{\partial\Psi}{\partial t} + \frac{\partial\Psi}{\partial x_i}\frac{\partial x_i}{\partial t} = \frac{\partial\Psi}{\partial t} - \frac{\partial\Psi}{\partial x_i}\frac{\partial b_i}{\partial t} \tag{17}$$

Thus in what follows all conservation equations are written in an inertial system of coordinates, but the scalar representation of the problem (in terms of the potential) may be expressed in terms of coordinates belonging to a moving system. In particular this implies that inertial accelerations (such as centrifugal or Coriolis forces etc.) will *not* have to be considered. The potential Ψ may be called a "mixed" potential, and we must be careful to reverse the transformations while interpreting results.

The velocity $\mathbf{V}$ is expressed in the moving frame as

$$\mathbf{V} = \frac{\Gamma}{2\pi l}\mathbf{e}_{z'} \times \mathbf{e}_l, \tag{18}$$

where $\mathbf{e}_l$ is a unit vector along the shortest line joining the point at which the velocity is to be measured and the z axis of the fixed system, and l the length of this line. This quantity is evaluated explicitly in the appendix. At the origin of the moving system it is

$$\mathbf{V}_O = \frac{\Gamma}{2\pi d}\{-\sin\omega t\,\mathbf{e}_{1'} + \cos\omega t\,\mathbf{e}_{2'}\},$$

where we denote the Velocity of the basic flow at the origin of the moving coordinate system by $\mathbf{V}_O$. The advantage of defining the moving system is, of course, that the equation of the bubble surface may be represented in a single-valued closed form more conveniently. Ideally such a system should be centered at the bubble centroid. However for this asymptotic study it is sufficient to let the origin of the moving system be initially at the bubble center, and let it move with the velocity a liquid particle at that location would have had in the absence of the bubble. This restriction could perhaps be lifted at the expense of more complicated analysis. Let $F(\mathbf{x}',t)$ represent the equation of the bubble in the moving system. In the fixed system the equation of the bubble may then be written as $F(\mathbf{x} - \mathbf{b},t)$. Thus the condition that the bubble surface is a material surface requires

$$\frac{DF}{Dt} = 0,$$

which may be written as

$$\frac{\partial F}{\partial t} + \frac{\partial F}{\partial b_i}\frac{\partial b_i}{\partial t} + \nabla'\phi \cdot \nabla' F = \frac{\partial F}{\partial t} + (\nabla'\Psi + \mathbf{V} - \mathbf{V}_O)|_F \cdot \nabla' F = 0. \tag{19}$$

In the moving frame we introduce a spherical coordinate system (r,θ,φ), centered at the point $\mathbf{b}$. The equation of the bubble free surface may then be written as

$$r = \mathcal{R}(\theta,\varphi,t). \tag{20}$$

The governing equations may then be written as

$$\nabla'^2\Psi = 0, \qquad \text{subject to}$$

$$\nabla'\Psi \cdot \mathbf{n}|_{r=\mathcal{R}} = \left(\frac{\partial\mathcal{R}}{\partial t}\right)\mathbf{e}_r + (\mathbf{V}|_{r=\mathcal{R}} - \mathbf{V}_O) \cdot \mathbf{n}, \tag{21}$$

$$\left[\frac{\partial\Psi}{\partial t} + \frac{1}{2}|\nabla'\Psi|^2 + (\mathbf{V} - \mathbf{V}_O) \cdot \nabla\Psi + \frac{1}{2}\mathbf{V}^2\right]_{r=\mathcal{R}} = \frac{p_\infty}{\rho_l}\left[1 - \frac{p_v}{p_\infty}\left(\frac{V_0}{V}\right)^k - \frac{p_1}{p_\infty} + \frac{\sigma C}{p_\infty}\right].$$

$$\lim_{r\to\infty} \Psi = 0$$

3 Dimensional Analysis

The flow is assumed to be divided into two regions, an external region where the effects of the vortex dominate, while the region close to the bubble is dominated by its dynamics. The length scale characteristic of the bubble region is R_0, the initial bubble radius. The time scale is taken as T_0 (to be determined), and the scale of the pressure is taken to be the initial value of the imposed pressure field at infinity. The idea is to exploit the fact that the bubble size is much smaller than the length scale associated with the vortex flow, by using perturbation techniques.

The physical quantities entering the problem are p_{g0} and R_0 (from the bubble), and p_∞, Γ, and ρ_l from the liquid. The distance between the bubble and the vortex, d is taken to be the length scale of the "outer" problem, while the initial bubble radius is characteristic of the "inner" one. We define

$$\epsilon = \frac{R_0}{d} \ll 1, \tag{22}$$

and will use it as the small parameter in the asymptotic treatment.

3.1 The inner problem

We non-dimensionalize the inner problem first, using

$$\mathbf{x}' = R_0\tilde{\mathbf{x}}' \quad t = T_0\tilde{t} \quad p = p_\infty\tilde{p} \quad \Psi = \phi_0\tilde{\Psi}. \tag{23}$$

In what follows, primes denoting relative variables will be dropped when we are concerned with the inner problem. Upon substitution in the equations of motion we have

$$\tilde{\nabla}^2\tilde{\Psi} = 0. \tag{24}$$

The problem scaling is determined by the boundary conditions. The kinematic boundary condition leads to

$$\frac{\phi_0}{R_0}\mathbf{n}\cdot\tilde{\nabla}\tilde{\Psi} = (\mathbf{V} - \mathbf{V}_O)\cdot\mathbf{n} + \frac{R_0}{T_0}\tilde{R}\mathbf{e}_r\cdot\mathbf{n}.$$

We are interested here in situations where the initial bubble nucleus grows quite rapidly. Consequently the proper scaling is

$$\phi_0 = \frac{R_0^2}{T_0}.$$

We shall return to the scaling of the velocity difference term on the right hand side after determining the proper time scale. Upon using the above scaling for the potential the dynamic boundary condition yields

$$\frac{\partial\tilde{\Psi}}{\partial\tilde{t}} + \frac{1}{2}|\tilde{\nabla}\tilde{\Psi}|^2 + \frac{T_0}{R_0}(\mathbf{V} - \mathbf{V}_O)\cdot\tilde{\nabla}\tilde{\Psi} + \left(\frac{T_0}{R_0}\right)^2\frac{1}{2}\mathbf{V}^2\Big|_{r=\tilde{R}} = \frac{p_\infty T_0^2}{\rho_l R_0^2}\left(1 - \frac{p_{g0}}{p_\infty}\left(\frac{V_0}{V}\right)^k - \frac{p_v}{p_\infty} + \frac{\sigma}{R_0 p_\infty}\tilde{C}\right) \tag{25}$$

Balancing terms,

$$T_0 = R_0\sqrt{\frac{\rho_l}{p_\infty}}, \tag{26}$$

which is the Rayleigh scaling for the time. The principle of least degeneracy leads to the condition that the scaling for the velocity $\mathbf{V}$ be such that it is of the same order as the bubble deformation velocity

$$|\mathbf{V}| \sim \frac{\Gamma}{2\pi d} \sim \frac{R_0}{T_0}. \tag{27}$$

We denote

$$\Omega = \frac{\Gamma/2\pi d}{\sqrt{p_\infty/\rho_l}}. \tag{28}$$

The nondimensional velocity is then defined by

$$\mathbf{V} = \Omega\tilde{\mathbf{V}}\frac{R_0}{T_0} \tag{29}$$

Returning to the kinematic boundary condition, since the velocity is assumed to be regular, and the bubble size small in comparison to its scale of variation, the velocity difference term is seen to be $O(\epsilon)$. Formally this imposes the following restriction the gradient of the vortex velocity field

$$(\mathbf{V}|_{\tilde{\mathbf{x}}} - \mathbf{V}_O) \sim R_0|\nabla\mathbf{V}| \sim \epsilon\frac{R_0}{T_0}. \tag{30}$$

Denoting

$$\mathbf{V} - \mathbf{V}_O = \epsilon\frac{R_0}{T_0}\Omega\tilde{\mathbf{V}}_d, \tag{31}$$

where we have used the symbol $\tilde{\mathbf{V}}_d$ to denote the nondimensional velocity difference term, and

$$\mathcal{W} = \frac{\sigma}{p_\infty R_0} \qquad \mathcal{P}_g = \frac{p_{g0}}{p_\infty} \qquad \mathcal{P}_v = \frac{p_v}{p_\infty}, \tag{32}$$

(where $\mathcal{W}$ is a Weber number), the complete inner problem may be written as

$$\tilde{\nabla}^2\tilde{\Psi} = 0 \tag{33}$$

$$\left[\frac{\partial\tilde{\Psi}}{\partial\tilde{t}} + \frac{1}{2}\tilde{\nabla}\tilde{\Psi}\cdot\tilde{\nabla}\tilde{\Psi} + \epsilon\Omega\tilde{\mathbf{V}}_d\cdot\tilde{\nabla}\tilde{\Psi} + \frac{1}{2}\Omega^2\tilde{\mathbf{V}}^2\right]_{r=\tilde{R}} = \left(1 - \mathcal{P}_g\left(\frac{\tilde{V}_0}{\tilde{V}}\right)^k - \mathcal{P}_v + \mathcal{W}\tilde{C}\right) \tag{34}$$

$$\left[\mathbf{n}\cdot\tilde{\nabla}\tilde{\Psi}\right]_{r=\tilde{R}} = \mathbf{n}\cdot\left(\frac{\partial\tilde{R}}{\partial\tilde{t}}\mathbf{e}_r + \epsilon\mathbf{V}_d\right) \tag{35}$$

An important quantity is the rotation frequency of a particle around the vortex line. This is given by

$$\omega = \frac{2\pi}{(2\pi)/(\Gamma/2\pi d)} = \frac{\Gamma}{2\pi d^2}. \tag{36}$$

In the current scaling the ratio of this frequency and the Rayleigh frequency is seen to be

$$\omega T_0 = \frac{R_0}{d}\frac{\Gamma/2\pi d}{\sqrt{p_\infty/\rho_l}} \sim O(\epsilon). \tag{37}$$

3.2 The outer problem

Since the outer problem for Ψ has no boundary conditions except regularity at infinity and matching with the inner solution, the solution can be obtained easily by replacing the inner variable with the outer one, and retaining terms of appropriate order. Thus it need not be considered separately. To enforce regularity we just add the condition

$$\lim_{|\tilde{\mathbf{x}}|\to\infty}\tilde{\Psi} = 0, \tag{38}$$

to the inner problem. With this in view, and for ease of expression, the tildes indicating non-dimensional variables are dropped in what follows.

4 Asymptotic expansions

The above equations are solved up to and including terms of $O(\epsilon)$ though some of the work for the $O(\epsilon^2)$ problem has been done, and these results are also given where available. We write the potential and the expression for the bubble surface as

$$\Psi = \Psi_0 + \epsilon\Psi_1 + \epsilon^2\Psi_2 + o(\epsilon^2) \tag{39}$$

$$r = a(t) + \epsilon\mathcal{R}_1(\theta,\varphi,t) + \epsilon^2\mathcal{R}_2(\theta,\varphi,t) + o(\epsilon^2). \tag{40}$$

It has been assumed here that the leading order term in the expansion for the bubble radius is independent of the angular variables, as will be justified *a posteriori*. Additionally we suppose that the functions $\mathcal{R}_1$ and $\mathcal{R}_2$ are regular so that we may expand them as

$$\mathcal{R}_i(\theta,\varphi,t) = r_{i0} + \sum_{l=1}^{\infty}\sum_{m=-l}^{l} r_{ilm}(\theta,\varphi)Y_l^m(\theta,\varphi), \quad i = 1,2 \tag{41}$$

with $Y_l^m(\theta,\varphi)$ the surface spherical harmonics (see the appendix for details).

Order ϵ^0

Upon introducing the expansions, the leading order problem at this order is

$$\nabla^2\Psi_0 = 0, \tag{42}$$

subject to

$$\left.\frac{\partial\Psi_0}{\partial r}\right|_{r=a} = -\dot{a}, \tag{43}$$

and

$$\lim_{r\to\infty}\Psi_0 = 0. \tag{44}$$

The spherical symmetry of the problem is obvious, and this justifies our previous expansion for the bubble shape function.

This problem has solution

$$\Psi_0 = \frac{\varphi_0}{r}. \tag{45}$$

Application of the kinematic boundary condition yields

$$\varphi_0 = -a^2\dot{a}, \tag{46}$$

where the dot indicates a time derivative. Substituting the above solution in the dynamic boundary condition

$$\frac{\partial\Psi_0}{\partial t} + \frac{1}{2}\left(\frac{\partial\Psi_0}{\partial r}\right)^2 + \Omega^2 = 1 - \mathcal{P}_g a^{-3k} - \mathcal{P}_v + \frac{2\mathcal{W}}{a}, \tag{47}$$

yields the following equation for a

$$a\ddot{a} + \frac{3}{2}\dot{a}^2 = \mathcal{P}_g a^{-3k} - \frac{2\mathcal{W}}{a} + \left(\mathcal{P}_v + \Omega^2 - 1\right). \tag{48}$$

This may be recognized as a variation on the conventional Rayleigh-Plesset equation (Plesset and Prosperetti, 1977) for spherical bubble dynamics.

Order ϵ^1

The equations at $O(\epsilon)$ are

$$\nabla^2\Psi_1 = 0 \tag{49}$$

subject to

$$\frac{\partial\Psi_1}{\partial r} - 2\frac{\dot{a}}{a}\mathcal{R}_1\Big|_{r=a} = \frac{\partial\mathcal{R}_1}{\partial t} + \Omega\mathbf{V}_d\cdot\mathbf{e}_\theta, \tag{50}$$

and

$$\frac{\partial\Psi_1}{\partial t} + \dot{a}\frac{\partial\Psi_1}{\partial r} + \mathcal{R}_1\left(2\frac{\dot{a}^2}{a} + \ddot{a}\right) + \dot{a}\Omega\mathbf{V}_d\cdot\mathbf{e}_r + \mathbf{V}_0\cdot\mathbf{V}_1\Big|_{r=a}$$
$$= 3k\mathcal{P}_g\frac{r_{100}}{a^{3k+1}} - \frac{2\mathcal{W}}{a}\sum_{l=1}^{\infty}\sum_{m=-l}^{l}\frac{r_{1lm}}{a}\left(1 - \frac{(l-1)(l+2)}{2}\right) \tag{51}$$

Introducing the expansion for the function $\mathcal{R}_1$, setting

$$\Psi_1 = \sum_{l=0}^{\infty}\sum_{m=-l}^{l}\frac{b_{1lm}}{r^{l+1}}Y_l^m(\theta,\varphi), \tag{52}$$

and taking scalar products with a generic spherical harmonic, the kinematic boundary condition may be written as

$$-(l+1)\frac{b_{1lm}}{a^{l+2}} - 2\frac{\dot{a}}{a}r_{1lm} = \dot{r}_{1lm} + \Omega(A\delta_{12}^{m2} + A^*\delta_{12}^{m,-2}). \tag{53}$$

Here A and A^* are complex constants (functions of time), given in the appendix, and δ_{ij}^{mn} is the Kronecker delta in two indices, with value unity if $m = n$ and $i = j$, and is zero otherwise. From this equation we get

$$b_{1lm} = -\frac{a^{l+2}}{l+1}\left(\dot{r}_{1lm} + 2\frac{\dot{a}}{a}r_{1lm} + \Omega(A\delta_{12}^{m2} + A^*\delta_{12}^{m,-2})\right). \tag{54}$$

Substituting in the dynamic boundary condition we get

$$\frac{a}{l+1}\left\{\ddot{r}_{1lm} + 2\left(\frac{\dot{a}}{a}\dot{r}_{1lm} - \left(\frac{\dot{a}}{a}\right)^2 r_{1lm} + \frac{\ddot{a}}{a}r_{1lm}\right) + \Omega\left(\dot{A}\delta_{12}^{m2} + \right.\right.$$
$$\left.\left. + \dot{A}^*\delta_{12}^{m,-2}\right)\right\} + \frac{\dot{a}}{l+1}\left(\dot{r}_{1lm} + 2\frac{\dot{a}}{a}r_{1lm} + \Omega(A\delta_{12}^{m2} + A^*\delta_{12}^{m,-2})\right) \tag{55}$$
$$-\left(2\frac{\dot{a}^2}{a} + \ddot{a}\right)r_{1lm} = -3k\mathcal{P}_g\frac{r_{100}\delta_{l0}^{m0}}{a^{3k+1}} + \frac{2\mathcal{W}}{a}\frac{r_{1lm}}{a}(1 -$$
$$\left.\frac{(l-1)(l+1)}{2}\right) + \Omega(A\delta_{12}^{m2} + A^*\delta_{12}^{m,-2}) + \Omega^2(a\delta_{11}^{m1} + a^*\delta_{11}^{m,-1}),$$

where the coefficients A, A^*, a, a^* are given in the appendix. Here * indicates complex conjugation.

Examination of the above equation reveals that, except for $(l, m) = (2,2), (2,-2), (1,1)$, and $(1,-1)$ the equations are homogeneous second order linear differential equations (initial value problems). Since we have assumed the bubble starts from a spherical shape, and is initially at rest, the solutions to these equations will vanish identically. For the four non-trivial cases, the differential equation satisfied by the particular radial component may be written as follows

$$a\ddot{r}_{111} + 3\dot{a}\dot{r}_{111} - 4\frac{\dot{a}^2}{a}r_{111} = 4\frac{\mathcal{W}r_{111}}{a^2} + 2\Omega^2 a \tag{56}$$

$$a\ddot{r}_{11,-1} + 3\dot{a}\dot{r}_{11,-1} - 4\frac{\dot{a}^2}{a}r_{11,-1} = 4\frac{\mathcal{W}r_{11,-1}}{a^2} + 2\Omega^2 a^* \tag{57}$$

$$\frac{a}{3}\ddot{r}_{122} + \dot{a}\dot{r}_{122} - \left(2\frac{\dot{a}^2}{a} + \frac{1}{3}\ddot{a}\right)r_{122} = -\frac{\mathcal{W}r_{122}}{a^2} + \Omega\left(\frac{2}{3}A\dot{a} - \frac{1}{3}\dot{A}a\right) \tag{58}$$

$$\frac{a}{3}\ddot{r}_{12,-2} + \dot{a}\dot{r}_{12,-2} - \left(2\frac{\dot{a}^2}{a} + \frac{1}{3}\ddot{a}\right)r_{12,-2} = -\frac{\mathcal{W}r_{12,-2}}{a^2} +$$
$$+\Omega\left(\frac{2}{3}A^*\dot{a} - \frac{1}{3}\dot{A}^*a\right) \tag{59}$$

The coefficients A, A^*, a, a^* are complex numbers, and it would be convenient instead to seek solutions of real combinations of them. An examination of the differential equations satisfied by r_{122} and $r_{12,-2}$ reveals that they are complex conjugates. Similarly the equations for r_{111} and $r_{11,-1}$ indicate that they too are complex conjugates. Consequently if we define instead the new variables

$$R_{111} = r_{111} + r_{11,-1} \qquad R_{11,-1} = \frac{r_{111} - r_{11,-1}}{i}, \tag{60}$$

$$R_{122} = r_{122} + r_{12,-2} \qquad R_{12,-2} = \frac{r_{122} - r_{12,-2}}{i}, \tag{61}$$

we obtain four equations in real quantities. These are given by

$$a\ddot{R}_{111} + 3\dot{a}\dot{R}_{111} - 4\frac{\dot{a}^2}{a}R_{111} = 4\frac{\mathcal{W}R_{111}}{a^2} - 2\sqrt{2}\Omega^2 a\cos\omega t \tag{62}$$

$$a\ddot{R}_{11,-1} + 3\dot{a}\dot{R}_{11,-1} - 4\frac{\dot{a}^2}{a}R_{11,-1} = 4\frac{\mathcal{W}R_{11,-1}}{a^2} + 2\sqrt{2}\Omega^2 a\sin\omega t \tag{63}$$

$$\frac{a}{3}\ddot{R}_{122} + \dot{a}\dot{R}_{122} - \left(2\frac{\dot{a}^2}{a} + \frac{1}{3}\ddot{a}\right)R_{122} = -\frac{\mathcal{W}R_{122}}{a^2} +$$
$$2\sqrt{2}\Omega\left(\frac{a\dot{a}}{3}\sin 2\omega t - \frac{2\omega a^2}{3}\cos 2\omega t\right) \tag{64}$$

$$\frac{a}{3}\ddot{R}_{12,-2} + \dot{a}\dot{R}_{12,-2} - \left(2\frac{\dot{a}^2}{a} + \frac{1}{3}\ddot{a}\right)R_{12,-2} = -\frac{\mathcal{W}R_{12,-2}}{a^2} +$$
$$2\sqrt{2}\Omega\left(\frac{a\dot{a}}{3}\cos 2\omega t + \frac{2\omega a^2}{3}\sin 2\omega t\right) \tag{65}$$

In terms of these new coefficients the surface of the bubble (in the moving coordinate system) is given by

$$r = a + \epsilon\left[(R_{111}\cos\varphi - R_{11,-1}\sin\varphi)\sin\theta\right. \tag{66}$$
$$\left. + (R_{122}\cos 2\varphi - R_{12,-2}\sin 2\varphi)\sin^2\theta\right]_1^1 + O(\epsilon^2).$$

5 Results and Conclusions

We present here some results from a numerical study using the above equations. The equations involve 4 parameters - $\mathcal{P}_g, \mathcal{P}_v, \Omega, \mathcal{W}$ and the perturbation parameter ϵ. In the following we have not attempted to map the parameter space of the above equations, but rather demonstrate the characteristics of their solutions for a particular choice of the parameters and show that they make physical sense. We choose the following for the physical parameters:

$$P_\infty = 1.03 \times 10^5 Pa, \qquad R_0 = 10^{-3} m, \qquad d = 5 \times 10^{-2} m$$

$$\Gamma = 1.2 m^2/s, \qquad P_v = 2 \times 10^3 Pa, \qquad \sigma = 7 \times 10^{-3} N/m,$$

$$P_{g0} = 3 \times 10^4 Pa \qquad \rho = 10^3 \qquad k = 1.4.$$

This yields the following for the non-dimensional parameters

$$\mathcal{P}_g = 2.9126 \times 10^{-1} \qquad \mathcal{P}_v = 1.9417 \times 10^{-2} \qquad \mathcal{W} = 6.7961 \times 10^{-4}$$

$$\Omega = 3.764 \times 10^{-1} \qquad T_0 = 9.85 \times 10^{-5} \qquad \epsilon = 7.53 \times 10^{-3}.$$

The equation systems at $O(1)$ and $O(\epsilon)$ are integrated using a simple fourth-order accurate Runge-Kutta scheme (Press *et al*, 1989). The equations at $O(\epsilon)$ are linear, and consequently do not pose a difficult numerical task to integrate.

The results from this trial run are shown in Figures 2-7. The results indicated that the expression for the bubble becomes multivalued for times after $4.6T_0$, i.e. the origin of the local coordinates lies outside the bubble after this time. Thus results of the integration to this time are shown. Figures 2-4 show the behavior of the radius coefficients $a, R_{1,1}, R_{1,-1}, R_{2,2}$ and $R_{2,-2}$ as functions of time. The growth of the nonspherical modes with time indicates the asymmetric nature of the bubble behavior.

Figure 5 shows a cross-sectional view of the bubble in the x, y plane. The bubble motion and deformation, and the formation of the jet are clearly seen. The bubble initially collapses almost spherically (while moving with the vortex flow), and reaches a minimum at approximately $1.55T_0$, and grows till it reaches a maximum size at $2.97T_0$. It subsequently collapses and shows the formation of a jet on the side opposite to its direction of motion, and directed towards the vortex axis. The computations are stopped at $4.6T_0$ when the bubble no longer contains the origin of coordinates. Figure 6 shows the motion of the $\varphi = 0$ and $\varphi = \pi$ points in this cross-section. Finally Figure 7 shows cross-sectional views of the bubble at the same times, but in a normal plane. This plane contains the z axis and the line connecting the moving coordinate origin and the vortex. The fact that the jet is directed towards the vortex axis becomes apparent in this view.

Quite obviously a more systematic study of the parameter space is required. Also, as in Chahine and Duraiswami (1992) the results of the asymptotic analysis and of the 3D boundary element program 3DynaFS must be compared. Qualitatively the same type of results are observed. The expression used for the motion of the moving coordinate system must be refined to prevent bubble function becoming multi-valued so early in the collapse. These and related aspects are items of current research.

Acknowledgments

This study was supported by the Office of Naval Research under contract N00014-89-C-0025.

References

[1] Blake, J. R. and Gibson, D. C., (1987). "Cavitation Bubbles Near Boundaries," Annual Review Fluid Mechanics, **19**, pp. 99-123.

[2] A Bovis. (1980). "Etude Asymptotique du Phenomene de Cavitation non Spheriques." *These Docteur-Ingenieur: L' Universite Pierre et Marie Curie, Paris VI.*

[3] G.L Chahine. (1990.) "Nonspherical bubble dynamics in a line vortex." Proceedings of ASME Cavitation and Multiphase Flow Forum, Toronto 1990.(ed. O Furuya) *ASME*. 121-126.

[4] G L Chahine and H L Liu. (1985 "A Singular Perturbation Theory of the Growth of a Bubble Cluster in a Super-heated Liquid." *J. Fluid Mech.*, **156**, 257-274.

[5] G.L. Chahine, (1991)."Dynamics of the interaction of nonspherical cavities," in "Mathematical approaches in hydrodynamics," ed. T. Miloh, *SIAM, Philadelphia.*

[6] G.L. Chahine and R. Duraiswami, (1992). "Dynamical Interactions in a multi-bubble cloud. " to appear in *ASME J. Fluids Engineering.*

[7] L. Greengard (1988.) "The Rapid Evaluation of Potential Fields in Particle Systems," *MIT Press, Cambridge.*

[8] T.M. McRobert, (1967.) "Spherical Harmonics," *3rd ed. Pergammon, Oxford.*

[9] A.H. Nayfeh, (1973). "Perturbation Methods." *Wiley, New York.*

[10] M.S. Plesset and A. Prosperetti, (1977). "Bubble Dynamics and Cavitation," *Ann. Rev. Fluid Mech.*, **9**, 145-185.

[11] W.H. Press, B.P. Flannery, S.A. Teukolsky, and W T. Vetterling, (1989), "Numerical Recipes," *Cambridge University Press, Cambridge.*

[12] E.P. Rood, (1991.) "Review - Mechanics of cavitation inception," *ASME J. Fluids Eng.*, **113**, 163-175.

[13] F.R. Young, (1989). "Cavitation," *McGraw-Hill, London.*

Appendix

The presence of the non uniform flow field makes the analysis a little involved. Here we present a summary of the relations used to perform the analysis. McRobert (1967) and Greengard (1988) were useful for material regarding the spherical harmonics.

Spherical Harmonics

Laplace's equation in spherical coordinates (r, θ, φ) may be written as

$$\nabla^2 \Phi = \frac{1}{r^2}\left(r^2 \frac{\partial \Phi}{\partial r}\right) + \frac{1}{r^2 \sin\theta}\frac{\partial}{\partial \theta}\left(\sin\theta\left(\frac{\partial \Phi}{\partial \theta}\right)\right) + \frac{1}{r^2 \sin^2\theta}\frac{\partial^2 \Phi}{\partial \varphi^2} = 0 \tag{67}$$

The finite solutions of Laplace equations in an unbounded region may be represented as

$$\Phi = A + \sum_{l=0}^{\infty}\sum_{l=-m}^{m} A_n^m \frac{Y_l^m(\theta,\varphi)}{r^{l+1}}, \tag{68}$$

where the coefficients A_n^m are constant, and $Y_l^m(\theta,\varphi)$ are the spherical harmonics. These are defined by

$$Y_l^m(\theta,\varphi) = \sqrt{\frac{(n-|m|)!}{(n+|m|)!}} P_n^{|m|}(\cos\theta)\exp(im\varphi). \tag{69}$$

We note that $Y_l^m(\theta,\varphi)$ and $Y_l^{-m}(\theta,\varphi)$ are complex conjugates.

The part of the Laplacian operator with differentiation over the angular variables is denoted ∇_S^2, i.e

$$\nabla_S^2 : \frac{1}{r^2 \sin\theta}\frac{\partial}{\partial \theta}\left(\sin\theta\left(\frac{\partial}{\partial \theta}\right)\right) + \frac{1}{r^2 \sin^2\theta}\frac{\partial^2}{\partial \varphi^2}. \tag{70}$$

Because of the form of Laplace's equation, the spherical harmonics satisfy the following identity

$$\nabla_S^2 Y_l^m(\theta,\varphi) = -(n+1)(n+2). \tag{71}$$

Any regular function can be expanded on the surface of the unit sphere in terms of the spherical harmonics. In particular the expressions for the vortex velocity field involve expressions in the cartesian coordinates x, y.

Expression for the normal

The Taylor series for the expression for the normal to the surface S given by

$$r - a(t) - \epsilon\mathcal{R}_1(\theta,\varphi) - \epsilon\mathcal{R}_2(\theta,\varphi) = 0 \tag{72}$$

about the surface $r = a$ is

$$\mathbf{n} = \mathbf{e}_r + \epsilon\left[\frac{1}{a}\frac{\partial\mathcal{R}_1}{\partial\theta}\mathbf{e}_\theta + \frac{1}{a\sin\theta}\frac{\partial\mathcal{R}_1}{\partial\varphi}\mathbf{e}_\varphi\right] + O(\epsilon^2) \tag{73}$$

Expression for the Curvature

Consider the equation of the surface given by

$$S: \qquad r = a + \epsilon\mathcal{R}_1(\theta,\varphi) + \epsilon^2\mathcal{R}_2(\theta,\varphi) + o(\epsilon^2) \tag{74}$$

The expression for the curvature of the surface is

$$C = \nabla\cdot\mathbf{n} = \nabla\cdot\left[\frac{\nabla S}{|\nabla S|}\right] = \frac{1}{A}\nabla^2 S + \nabla\left(\frac{1}{A}\right)\cdot\nabla S;$$

$$\text{where} \qquad A = |\nabla S| \tag{75}$$

We estimate the terms in the above equation upto $o(\epsilon^2)$. The gradient of the surface is

$$\nabla S = \left[1, -\frac{1}{r}\frac{\partial}{\partial\theta}\left(\epsilon\mathcal{R}_1 + \epsilon^2\mathcal{R}_2\right), -\frac{1}{r\sin\theta}\frac{\partial}{\partial\varphi}\left(\epsilon\mathcal{R}_1 + \epsilon^2\mathcal{R}_2\right)\right] \tag{76}$$

The quantity $A = |\nabla S|$ may be estimated as

$$A = \left[1 + \frac{\epsilon^2}{r^2}\left(\mathcal{R}_{1\theta}^2 + \frac{\mathcal{R}_{1\varphi}^2}{\sin^2\theta}\right)\right]^{1/2} + o(\epsilon^2) =$$

$$\left[1 + \frac{\epsilon^2}{2r^2}\left(\mathcal{R}_{1\theta}^2 + \frac{\mathcal{R}_{1\varphi}^2}{\sin^2\theta}\right)\right] + o(\epsilon^2). \tag{77}$$

Thus

$$\frac{1}{A} = 1 - \frac{\epsilon^2}{2r^2}\left(\mathcal{R}_{1\theta}^2 + \frac{\mathcal{R}_{1\varphi}^2}{\sin^2\theta}\right) + o(\epsilon^2). \tag{78}$$

Consequently,

$$\nabla\left(\frac{1}{A}\right) = \frac{\epsilon^2}{r^2}\left[\frac{1}{r}\left(\mathcal{R}_{1\theta}^2 + \frac{\mathcal{R}_{1\varphi}^2}{\sin^2\theta}\right), \ldots, \ldots\right] \tag{79}$$

The second term on the right hand side of eq. (75), denoted C_{II}, may be estimated as

$$C_{II} = \nabla\left(\frac{1}{A}\right)\cdot\nabla S = \frac{\epsilon^2}{r^3}\left(\mathcal{R}_{1\theta}^2 + \frac{\mathcal{R}_{1\varphi}^2}{\sin^2\theta}\right) \tag{80}$$

The first term in eq. (75), denoted C_I, may be written as

$$C_I = \frac{1}{A}\left(\frac{2}{r} - \frac{\epsilon}{r^2}\nabla_S^2\mathcal{R}_1 - \frac{\epsilon^2}{r^2}\nabla_S^2\mathcal{R}_2\right), \tag{81}$$

where ∇_S^2 denotes the part of the spherical Laplacian operator containing derivatives with respect to the angular variables, and is defined in Eq. (70). Combining the expressions for C_I and C_{II}, we get

$$C = C_I + C_{II} = \left[1 - \frac{\epsilon}{r^2}\nabla_S^2\mathcal{R}_1 - \frac{\epsilon^2}{r^2}\nabla_S^2\mathcal{R}_2\right] \tag{82}$$

The above expression is to be expanded in Taylor series about $r = a$. The final formula for the curvature then is

$$C = \frac{2}{a}\left\{1 - \epsilon\left[\frac{1}{2}\nabla_S^2\frac{\mathcal{R}_1}{a} + \frac{\mathcal{R}_1}{a}\right]\right.$$

$$\left.+\epsilon^2\left[-\frac{1}{2}\nabla_S^2\frac{\mathcal{R}_2}{a} + \frac{\mathcal{R}_1}{a}\nabla_S^2\frac{\mathcal{R}_1}{a} + \left(\frac{\mathcal{R}_1}{a}\right)\right]\right\} + o(\epsilon^2). \tag{83}$$

The terms involving the spherical surface Laplacian may be simplified by use of the identity (71).

Bubble volume

The radius is expanded as

$$r = a + \epsilon\mathcal{R}_1(\theta,\varphi) + \epsilon^2\mathcal{R}_2(\theta,\varphi) + o(\epsilon^2) \tag{84}$$

The volume of the bubble may be written as

$$V = \int_0^{2\pi} d\varphi \int_0^{\pi} \sin\theta d\theta \int_0^{a+\epsilon\mathcal{R}_1+\epsilon^2\mathcal{R}_2} r^2 dr = a^3\left\{\frac{4\pi}{3} + \right. \tag{85}$$

$$\left.\epsilon\frac{1}{a}\int_0^{2\pi} d\varphi\int_0^{\pi}\sin\theta d\theta\mathcal{R}_1 + \epsilon^2\int_0^{2\pi} d\varphi\int_0^{\pi}\sin\theta d\theta\left[\frac{\mathcal{R}_1^2}{a^2} + \frac{\mathcal{R}_2}{a}\right]\right\}$$

If the functions $\mathcal{R}_i, i = 1,2$ are expanded in terms of spherical harmonics as

$$\mathcal{R}_i = r_{i00} + \sum_{l=1}^{\infty}\sum_{m=-l}^{l} r_{ilm}Y_l^m(\theta,\varphi), \tag{86}$$

then, using the orthogonality of the harmonics, we may write

$$V = a^3\left[\frac{4\pi}{3} + 4\pi\epsilon\frac{r_{100}}{a} + 4\pi\epsilon^2\frac{r_{200}}{a} + \epsilon^2\sum_{l=1}^{\infty}\sum_{m=-l}^{l}\left(N_l^m\frac{r_{1lm}}{a}\right)^2\right] \tag{87}$$

where

$$N_l^m = \sqrt{\frac{4\pi}{2l+1}}. \tag{88}$$

Asymptotic development of the basic flow velocity

The equations (33) involve several expressions for the vortex induced velocity expressed in the moving system of coordinates. These expressions are developed in asymptotic series here.

In the fixed system of coordinates

$$\mathbf{V} = \frac{\Gamma}{2\pi\rho}\mathbf{e}_\beta. \tag{89}$$

To express this in the moving system at a point P, we denote the intersection of the xy plane through P with the x axis as O. Then

$$\mathbf{V} = \frac{\Gamma}{2\pi|OP|^2}\mathbf{e}_z\times\mathbf{e}_{OP} = \frac{\Gamma}{2\pi|OP|^2}\mathbf{e}_{z'}\times\mathbf{e}_{OP}.$$

Performing the indicated cross-product

$$\mathbf{V} = \frac{\Gamma}{2\pi d}\frac{-(\bar{r}\sin\theta\cos\varphi + \sin\omega t)\mathbf{e}_x + (\bar{r}\sin\theta\sin\varphi + \cos\omega t)\mathbf{e}_y}{1 + 2\bar{r}\sin\theta\cos(\omega t - \varphi) + \bar{r}^2\sin^2\theta}$$

We introduce the non-dimensionalization of §3.1, but drop the tilde notation for the non-dimensional variables.

$$\mathbf{V} = \frac{-(\epsilon r\sin\theta\cos\varphi + \sin\omega t)\mathbf{e}_x + (\epsilon r\sin\theta\sin\varphi + \cos\omega t)\mathbf{e}_y}{1 + 2\epsilon r\sin\theta\cos(\omega t - \varphi) + \epsilon^2 r^2\sin^2\theta}$$

Expanding the denominator binomially

$$\mathbf{V} = [-(\sin\omega t + \epsilon r\sin\theta\sin\varphi)\mathbf{e}_x + (\cos\omega t + \epsilon r\sin\theta\cos\varphi)\mathbf{e}_y](90)$$

$$\left[1 - 2\epsilon r\sin\theta\cos(\omega t - \varphi) + \epsilon^2\left\{-r^2\sin^2\theta + r^2\sin^2\theta\cos^2(\omega t - \varphi)\right\}\right].$$

This expression has to be expanded in Taylor series about the surface $|\mathbf{x}| = a + \epsilon\mathcal{R}_1 + \epsilon^2\mathcal{R}_2$. Such vectorial manipulations are most easily done in a Cartesian representation, and accordingly we express the above as

$$\mathbf{V} = [-(\sin\omega t + \epsilon y)\mathbf{e}_x + (\cos\omega t + \epsilon x)\mathbf{e}_y] \tag{91}$$

$$\times\left[1 - 2\epsilon(x\cos\omega t + y\sin\omega t) - \epsilon^2(x\sin\omega t - y\cos\omega t)^2\right] + o(\epsilon^2).$$

Expressing the above to consistent order

$$\mathbf{V} = \{[-\sin\omega t\mathbf{e}_x + \cos\omega t\mathbf{e}_y] + \epsilon[(-y + 2\sin\omega t(x\cos\omega t + y\sin\omega t))\mathbf{e}_x$$

$$+(x - 2\cos\omega t(x\cos\omega t + y\sin\omega t))\mathbf{e}_y] + \epsilon^2\left[\left(\sin\omega t(x\sin\omega t - y\cos\omega t)^2\right.\right.$$

$$2y(x\cos\omega t + y\sin\omega t))\mathbf{e}_x - \left(\cos\omega t(x\sin\omega t - y\cos\omega t)^2\right. \tag{92}$$

$$\left.\left.+2x(x\cos\omega t + y\sin\omega t))\mathbf{e}_y\right]\right\} + o(\epsilon^2).$$

Evaluation at $O(\epsilon)$

At $O(\epsilon)$ the expressions for the quantities required are

$$\begin{aligned}(\mathbf{V}-\mathbf{V}_O)\cdot\mathbf{e}_r &= (-y+2\sin\omega t(x\cos\omega t+y\sin\omega t))\frac{x}{r}+\\ &\quad (x-2\cos\omega t(x\cos\omega t+y\sin\omega t))\frac{y}{r}\\ &= \frac{x^2-y^2}{r}\sin(2\omega t)-\frac{2xy}{r}\cos(2\omega t). \qquad (93)\end{aligned}$$

This can be expressed in terms of the spherical harmonics by using the relations given previously as

$$(\mathbf{V}-\mathbf{V}_O)|_{r=a}\cdot\mathbf{e}_r = AY_2^2(\theta,\varphi)+A^*Y_2^{-2}(\theta,\varphi), \qquad (94)$$

where

$$A = a\sqrt{\frac{2}{3}}(\sin 2\omega t+i\cos 2\omega t), \qquad (95)$$

and the superscript $*$ indicates complex conjugation.

The other expression requiring evaluation at this order is:

$$\begin{aligned}\mathbf{V}_0\cdot\mathbf{V}_1|_{r=a} &= -x\cos\omega t+y\sin\omega t|_a\\ &= -a\left[\frac{Y_1^1+Y_1^{-1}}{\sqrt{2}}\cos\omega t-i\frac{Y_1^1-Y_1^{-1}}{\sqrt{2}}\sin\omega t\right]\\ &= \frac{-a}{\sqrt{2}}\left[(\cos\omega t-i\sin\omega t)Y_1^1(\theta,\varphi)+(\cos\omega t+i\sin\omega t)Y_1^{-1}(\theta,\varphi)\right] \qquad (96)\end{aligned}$$

This may be written in the form

$$\mathbf{V}_0\cdot\mathbf{V}_1|_{r=a} = \left(\alpha Y_1^1(\theta,\varphi)+\alpha^*Y_1^{-1}(\theta,\varphi)\right),$$

where

$$\alpha = \frac{-a}{\sqrt{2}}(\cos\omega t-i\sin\omega t). \qquad (97)$$

$\lim_{|x|\to\infty}\mathbf{u}\to 0$

$\lim_{|x|\to\infty}p\to p_\infty$

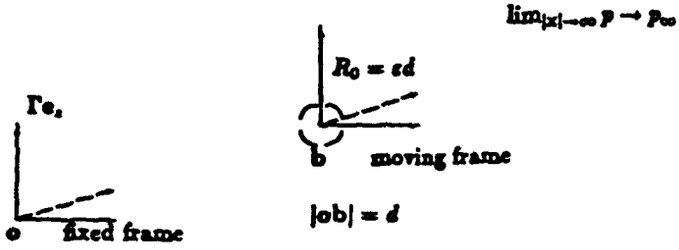

Figure 1: Problem Geometry

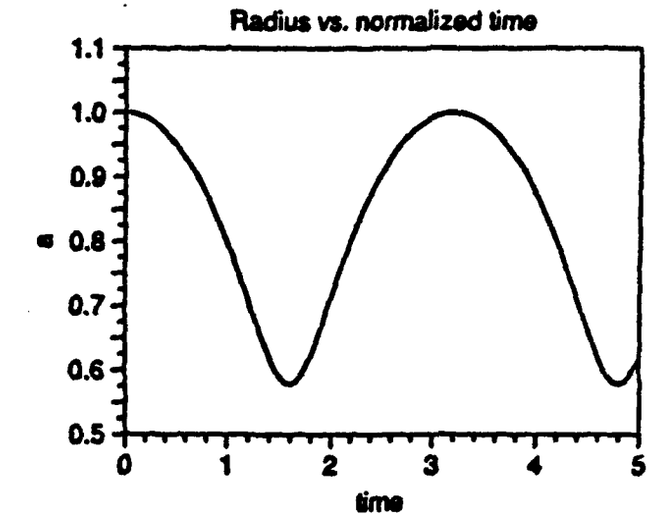

Figure 2: Radius component a at $O(\epsilon^0)$ plotted vs. normalized time.

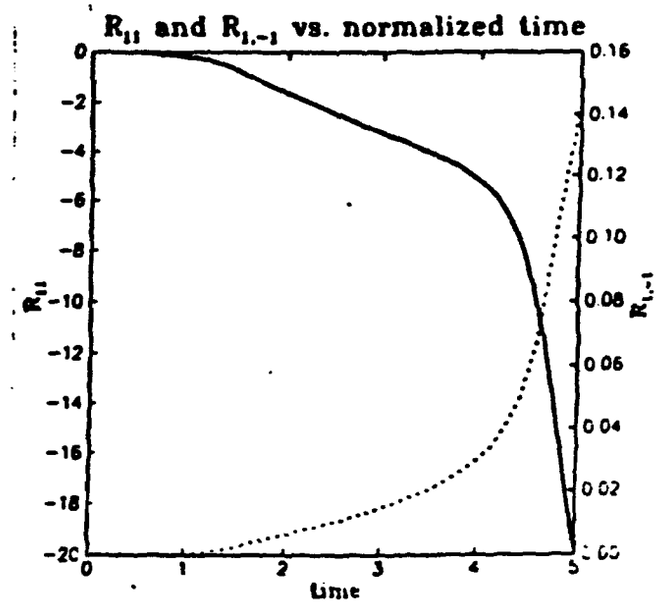

Figure 3: Radius components at $O(\epsilon)$, $R_{1,1}$ (solid line) and $R_{1,-1}$ (dotted line) vs. normalized time.

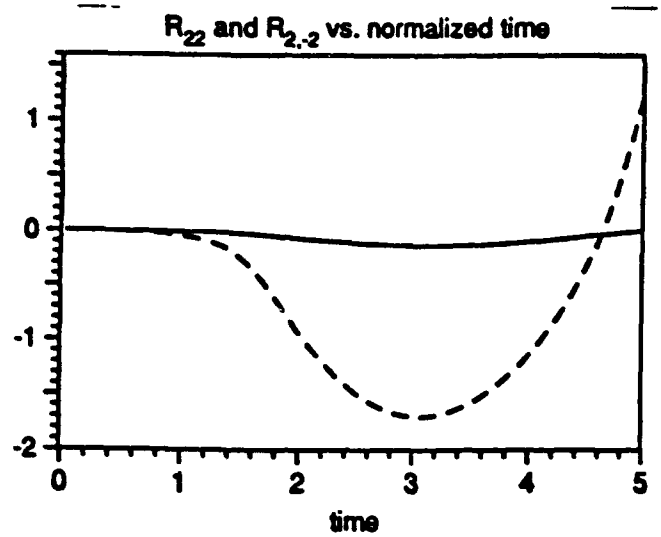

Figure4: Radius components at $O(\epsilon)$, $R_{2,2}$ (solid line) and $R_{2,-2}$ (dotted line) vs. normalized time.

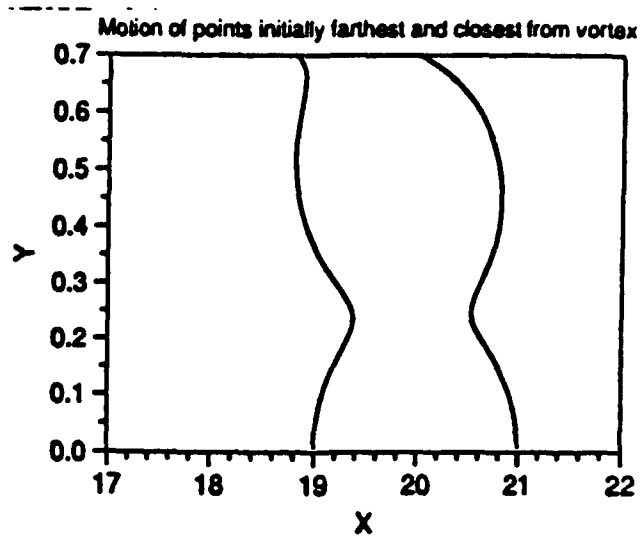

Figure 6: Motion of the points initially farthest from and closest to the vortex axis. The vortex passes through $(x, y) = (0, 0)$ along the z axis.

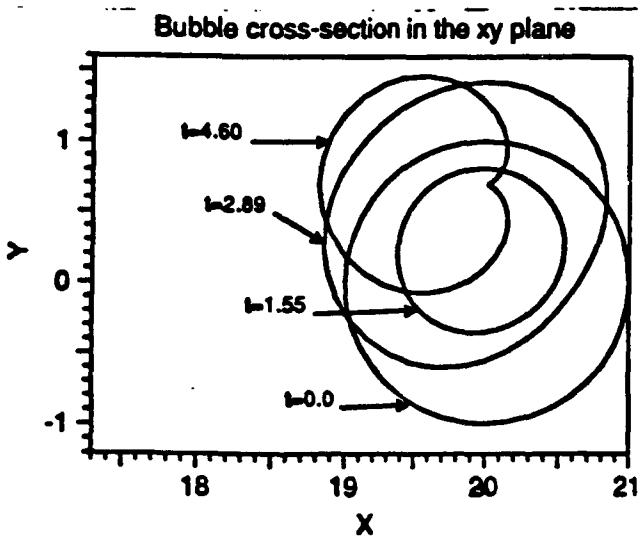

Figure 5: Cross-section of the predicted bubble shape in the $x - y$ plane (normal to the vortex axis). The vortex passes through $(x, y) = (0, 0)$ along the z axis (normal to the plane of the paper).

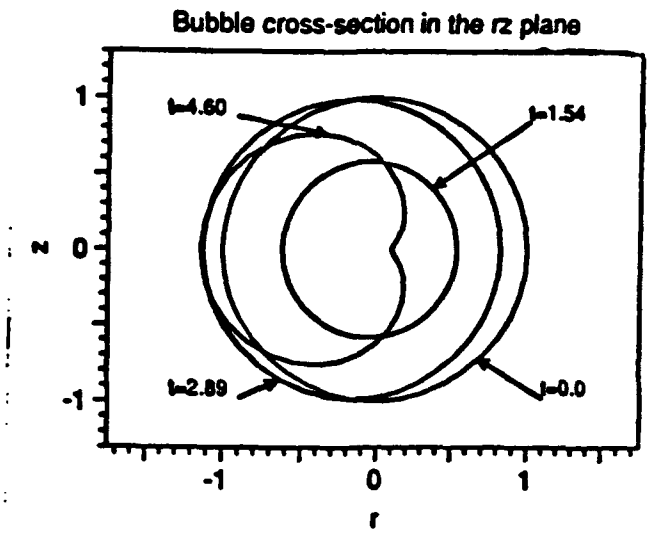

Figure 7: Cross-section of the predicted bubble shape in a plane containing the vortex line and the center of the moving coordinate system. The vortex axis is at -20, on the abscissa.

Nineteenth ONR Symposium on Naval Hydrodynamics, Seoul, S. Korea, 1992.

ANALYTICAL AND NUMERICAL STUDY OF LARGE BUBBLE/BUBBLE AND BUBBLE/FLOW INTERACTIONS

by

Georges L. CHAHINE*
Ramani DURAISWAMI
Mathieu REBUT

DYNAFLOW, Inc.
7210 Pindell School Road
Fulton, MD 20759

Abstract

The presence of cavities in a liquid can have significant effects on its behavior and its flow characteristics. In practical flow situations, these effects cannot be fully understood or predicted without addressing complicated, but nonetheless fundamental phenomena associated with the dynamics, interactions, and deformation of bubbles. The importance of these phenomena has long been recognized, but has largely been neglected due to the difficulty of the associated mathematical problems. In this contribution, bubble shape oscillations in response to nonuniform flow fields and/or due to their interaction with other bubbles are considered using both a matched asymptotic expansions technique and a fully three-dimensional boundary integral method.

Results from both approaches in a few particular cases are compared, and the limits of application of these methods for these cases is assessed.

Nomenclature

- r_{b0}, characteristic bubble size,
- τ_{b0}, characteristic bubble time scale
- L_0, *outermost* characteristic flow length scale
- τ_0, characteristic flow time scale
- l_0, bubble/boundary distance scale
- T_0, interaction time scale,
- ϵ, ratio between r_{b0} and l_0
- t, time
- ϕ, bubble velocity potential in moving frame
- ϕ_b, bubble velocity potential $= \phi' - \phi_0$
- ϕ', total velocity potential
- ϕ_0, basic velocity potential
- $\mathcal{G}$, velocity gradient scale
- $\mathcal{H}$, velocity bigradient scale
- R_i, ith component of the bubble radius

*also Research Professor The Johns Hopkins University, Baltimore MD

Introduction

The presence and dynamics of bubbles and cavities in a flow field can have significant effects of relevance to engineering applications. These effects include erosion, noise generation, damping of acoustic signals, degradation of performance...etc [1, 2, 3, 4]. This has instigated a great interest in the study of the problem, and thousands of publications have been devoted to the study of cavity flows since the early work of Rayleigh [5] and Besant [6]. Due to the complexity of the general mathematical and physical problem, most approaches have, however, been limited to the study of spherical, isolated bubbles, or to elongated linearized two-dimensional cavities. More recently, with the advent of new mathematical and computational tools, increasing attention has been given to the study of more practical cavity configurations: namely nonspherical bubbles and bubble clouds. Nonspherical axisymmetric bubble dynamics, such as in the vicinity of a solid wall or a free surface were most particularly studied [7, 8, 9, 4]. All these studies were restricted to the simplified case where the bubble is in a quiescent fluid and where external forces, if any are potential, and act in a direction perpendicular to any nearby rigid or free boundary. Advantage was taken of the axisymmetry of the resulting problem. Deviations from these simplifying assumptions could significantly influence the results. In fact, in most practical cases bubbles are neither isolated, nor in a uniform flow or in a quiescent fluid. Common examples include cavitation bubbles near propeller blades, large cavity dynamics near complex geometries in a gravity field, dynamics of bubble clouds, and bubble dynamics in a shear or boundary layers.

The dynamics of bubble clouds have also recently received a lot of attention [10, 11, 12, 13], especially since they have been observed to produce dramatic deleterious effects, which cannot be explained with approaches based on single bubble dynamics.

All these studies but [9, 11], have considered only the contribution of the bubble volume change on the cloud dynamics, and have either neglected bubble fluid relative motion and bubble deformation, or restricted their approach to acoustic perturbations.

In a first approach, based on the method of matched asymptotic expansions, we consider these effects in the limiting configuration where the bubble size is small compared to inter-bubble distance (small void fraction), or where the bubble size is much smaller than some characteristic length scale of the surrounding flow.

These include problems of bubble dynamics in nonuniform flow fields (bubble dynamics in the flow field of a vortex or near a headform) and the inclusion of compressibility. In these cases, the small perturbation is chosen to express small but not negligible interactions.

This limitation is removed in a second parallel approach where a fully three dimensional numerical method is developed. This method has been tested for bubble dynamics in a quiescent fluid [14, 15], and has been recently used for the investigation of bubble dynamics in complex flow fields such as vortical, boundary and shear flows [16, 17].

In this contribution we will present first the model used for the bubble dynamics (Section 1). We will highlight effects taken into account and attempt to describe the limits of validity of the model. We will then describe in general terms the asymptotic approach used (Section 2). In Sections 3 to 5 bubble behavior in nonuniform flow fields, particularly the flow about a headform and in a vortex flow are described. In Section 6 the same method is used to describe the particular configurations of multibubble clouds with a particular note on the extension of the method to the case where the bubbly medium is slightly compressible. In the following sections the studies described above will be extended to very large deformations and interactions. The numerical method used will be described in Section 7 while Sections 8 will consider the particular cases of bubble behavior in a sheared flow field near a solid wall, in a vortex flow, and for a multibubble configuration. Finally some conclusions are drawn from the results.

1 Bubble Dynamics Model

We will consider mostly cavitation bubbles where relatively large bubble wall velocities are involved and where, as a result, viscosity has no appreciable effect on the growth and collapse of the bubbles. The study will also be restricted to the case where the flow velocities remain small compared to the speed of sound in water, and as a result, we can neglect or approximately account for compressibility effects. This is usually valid until the latest collapse phase. The above two assumptions, classical in cavitation bubble dynamics studies, result in a flow *due to bubble dynamics* that is potential (velocity potential, $\phi_b(\mathbf{x},t)$) so that $\mathbf{u}_b = \nabla\phi_b$, and which satisfies the Laplace equation,

$$\nabla^2\phi_b = 0. \tag{1}$$

In our numerical work this assumption is not imposed on the "basic flow," i.e. to the underlying flow existing in absence of the bubble, . In addition, compressibility of the liquid, or of the bubbly medium in the case of a bubble cloud, can be considered in an "ad-hoc" fashion through a delay time for the propagation of information between the source and a field point, as well as through a compressible model for the *spherical component* of the bubble oscillations. The solution must in addition satisfy boundary conditions at infinity, at the bubble walls and at the boundaries of any nearby bodies. At all moving or fixed surfaces (such as a bubble surface or a nearby boundary) an identity between fluid velocities normal to the boundary and the normal velocity of the boundary itself is to be satisfied. For instance, at the bubble-liquid interface, the normal velocity of the moving bubble wall must equal the normal velocity of the fluid, or,

$$\nabla\phi_b \cdot \mathbf{n} = \mathbf{V}_s \cdot \mathbf{n}, \tag{2}$$

where $\mathbf{n}$ is the local unit vector normal to the bubble surface and $\mathbf{V}_s$ is the local velocity vector of the moving surface. This equation expresses the fact that the bubble surface, $\mathcal{B}(r,\theta,\phi,t)$, is a material surface of the liquid

$$\frac{D\mathcal{B}}{Dt} = 0. \tag{3}$$

The bubble is assumed to contain noncondensible gas as well as vapor of the surrounding liquid. The pressure within the bubble at any given time is considered to be the sum of the partial pressures of the noncondensible gases, P_g, and that of the vapor, P_v. Vaporization of the liquid is assumed to occur at a fast enough rate so that the vapor pressure remains constant throughout the simulation and equal to the equilibrium vapor pressure at the liquid ambient temperature. In contrast, since time scales associated with gas diffusion are much larger, the amount of noncondensible gas inside the bubbles is assumed to remain constant and the gas is assumed to satisfy the polytropic relation, $P_g\mathcal{V}^k = constant$, where $\mathcal{V}$ is the bubble volume and k the polytropic constant, with $k = 1$ for isothermal behavior and $k = c_p/c_v$ for adiabatic conditions. In previous studies the influence of heat transfer [18], and gas diffusion [19] on the dynamics of a bubble cloud was considered. We will neglect these effects in this presentation.

The pressure in the liquid at the bubble surface, P_L, is obtained at any time from the following pressure balance equation:

$$P_L = P_v + P_{g_0}\left(\frac{\mathcal{V}_0}{\mathcal{V}}\right)^k - C\sigma, \tag{4}$$

where P_{g_0} and $\mathcal{V}_0$ are the initial gas pressure and volume respectively, σ is the surface tension, C the local curvature of the bubble, and $\mathcal{V}$ the instantaneous value

of the bubble volume. Here P_{g_0} and $\mathcal{V}_0$ are known quantities at $t = 0$. The curvature and the normal, n, to the surface $\mathcal{B}$ are given by:

$$\mathcal{C} = \nabla \cdot \mathbf{n} \qquad \mathbf{n} = \frac{\nabla \mathcal{B}}{|\nabla \mathcal{B}|}. \tag{5}$$

2 Asymptotic Theory for Bubble Flow Interactions

The asymptotic method that we have developed is centered on the following approach. Whether the problem considered is that of bubble interactions in a cloud or that of the interaction between bubbles and a nonuniform complex flow, the problem is addressed by a decomposition of both time and space domains into multiple scales. For instance, the dynamics of any bubble is obtained by considering an *inner* problem of scales r_{b0}, a characteristic bubble size, and τ_{b0}, a characteristic bubble time scale. The overall flow field, on the other hand is addressed by considering an *outermost* problem with scales L_0, a characteristic flow length scale, and T_0, a characteristic flow time scale. Using the same procedure, an intermediate *outer* problem is introduced with *outer* scales such as a characteristic length scale of interbubble distances or bubble/boundary distances, l_0, and an interaction time scale, τ_0. Finally, a *far-field* acoustic field scale can be introduced based on the length, $c\tau_{b0}$, where c is the sound speed in the liquid.

An asymptotic analysis of the problem can be developed when these various scales are of different orders of magnitude. For instance, for bubble/bubble interactions in a cloud or for bubble/flow interactions near a boundary an asymptotic approach can be introduced when r_{b0} is much smaller than l_0, in which case one could use the ratio between r_{b0} and l_0 as the small perturbation parameter, ϵ.

$$\epsilon = \frac{r_{b0}}{l_0} \tag{6}$$

The *outer problem* is associated with the macroscopic behavior of the bubbles in a bubble cloud or in a complex flow geometry. A bubble then appears as a superposition of singularities of various orders. If more then one bubble is involved, the summation is to be carried out over all the bubbles. The *inner problem* obtained when the lengths are normalized by r_{b0}, provides the microscopic details of the behavior of the flow in the vicinity of an individual bubble center (B_i). The presence of the other bubbles or boundaries, all considered to be at infinity in the *inner problem*, is sensed only by means of the matching condition with the *outer problem*. The boundary conditions at infinity for the *inner problem* are therefore obtained at each order of approximation by the asymptotic behavior of the outer solution in the vicinity of B_i. Thus, if one knows the behavior of all bubbles except B_i, the motion, deformation and pressure field due to this cavity can be determined by solving linearized forms of the equations presented in the previous section. At the lowest order, $\epsilon = 0$, each bubble (of index i) behaves spherically as if in an infinite medium and the time dependence of its radius, $a_0^i(t)$, is given by the Rayleigh-Plesset equation if the medium compressibility is neglected, [20], or by the Keller-Herring equation [21, 24] for example if a slight compressibility of the medium is taken into account (see section 6).

The combination of all these first approximations of each *inner* problem provides a description of the whole first order flow field (i.e. a distribution of sources or sinks representing all bubble oscillations). The behavior of this *outer* flow field in the vicinity of each bubble sets the boundary conditions at infinity at the following order of approximation, ϵ, for the corresponding *inner* problem. The same process is then repeated for the successive orders.

At all orders solutions of the Laplace equation are expanded in general form as spherical harmonics and the bubble radius equation is expanded in surface harmonics:

$$\phi(r,\theta,\varphi,t) = \sum_{j=0}^{\infty} \sum_{m=-j}^{j} (A_{ljm} r^j + \frac{B_{ljm}}{r^{j+1}}) Y_{jm}(\theta,\varphi), \tag{7}$$

$$r = \mathcal{R}(\theta,\varphi,t) = \sum_{j=0}^{\infty} \sum_{m=-j}^{j} R_{ljm}(t) Y_{jm}(\theta,\varphi), \tag{8}$$

In what follows, quantities indicated with a superscript $\tilde{}$ are inner variables, while those with a superscript $\bar{}$ refer to outer variables. The Y_{jm} are given by:

$$Y_{jm} = \begin{cases} P_j^m(\cos\theta)\cos m\varphi; & \text{for } m \geq 0 \\ P_j^{|m|}(\cos\theta)\sin |m|\varphi; & \text{for } m < 0 \end{cases} \tag{9}$$

Then all quantities, χ, particularly $\tilde{\phi}, \bar{\phi}, and \tilde{R}$, are expanded in powers of ϵ as follows:

$$\chi = \chi_0 + \epsilon\chi_1(r,\theta,\varphi,t) + \epsilon^2\chi_2(r,\theta,\varphi,t) + O(\epsilon^3). \tag{10}$$

3 Bubble Behavior in a Nonuniform Flow Field

Let us consider a *basic* flow field (flow in absence of the bubble) that is potential and steady, with a velocity vector $\mathbf{V_0}$ deriving from the potential ϕ_0. Let the pressure be p_0 and the liquid density ρ. The velocity potential satisfies the Laplace equation and the Bernoulli equation:

$$\nabla^2\phi_0 = 0, \qquad \frac{1}{2}(\nabla\phi_0)^2 + \frac{p_0}{\rho} = \text{constant}. \tag{11}$$

Let ϕ' and p' be the potential, the speed and pressure in presence of the bubble. We now have similar equations as (11-12) with these complete flow variables. In addition, far away from the bubble, we have

$$\phi' = \phi_0,$$

and the continuity of the normal velocities at the bubble wall can be written:

$$\{\nabla\phi' \cdot \mathrm{n}\}_{r=\mathcal{R}} = \left\{\frac{\partial \mathcal{R}}{\partial t}\mathbf{e}'_r \cdot \mathrm{n}\right\}_{r=\mathcal{R}}, \tag{12}$$

We will consider now the ***bubble potential***, ϕ_b, difference of the potentials ϕ' and ϕ_0.

$$\phi_b = \phi' - \phi_0. \tag{13}$$

Since at infinity V_b and ϕ_b decay to zero, and the pressure is p_0, the Bernoulli equation becomes:

$$\{\frac{\partial \phi_b}{\partial t} + \frac{1}{2}(\nabla\phi_b)^2 + \frac{1}{2}V_0^2 \;+\; \nabla\phi_b \cdot V_0 + \frac{p'}{\rho}\}_{r=\mathcal{R}} = \\ = \left\{\frac{1}{2}V_0^2 + \frac{p_0}{\rho}\right\}_{M=\infty}, \tag{14}$$

where we have limited ourselves to the case where the *basic* flow is steady. The right hand side of the equation is a constant of the *basic* flow field.

At this time we can transform the above equations to those in a coordinate system with origin o moving with a velocity *prescribed* V_M, and decompose this velocity as

$$\mathrm{V}_M = \mathrm{V}_e x + \vec{\omega} \times \mathrm{oM}, \tag{15}$$

where V_e is the translation velocity of o, and $\vec{\omega}$ is the rotation velocity with respect to the fixed frame.

Making the transformation, the system of equations of the problem becomes, ϕ being the velocity potential of the ***bubble flow*** in the moving frame:

$$\Delta\phi = 0; \quad \lim_{\infty}\phi = 0; \quad \{\nabla\phi \cdot \mathrm{n}\}_{wall} = 0,$$

$$\left\{\nabla\phi \cdot \mathrm{n} = \frac{\partial R}{\partial t} + (\mathrm{V}_e - \mathrm{V}_0) + \vec{\omega} \times \mathrm{oM} \cdot \mathrm{n}\right\}_{r=\mathcal{R}},$$

$$\left\{\frac{\partial \phi}{\partial t} + \frac{1}{2}(\nabla\phi)^2 + (\mathrm{V}_0 - \mathrm{V}_e - \vec{\omega} \times \mathrm{oM}) \cdot \nabla\phi + \right.$$

$$\left. + \frac{1}{2}(V_0^2 - V_e^2) + \frac{p}{\rho}\right\}_{r=R} = \frac{p_0(\mathrm{o})}{\rho}. \tag{16}$$

The pressure at the bubble wall and the pressure inside the bubble are related through Equation (4).

Nondimensionalizations

All equations can be normalized using the following scales. In the *outer* problem:

r	$= l_0 \tilde{r}$	l_0 : the initial bubble wall distance
ϕ	$= \phi_{ext}\,\tilde{\phi}$	ϕ_{ext} : outer velocity potential scale

In the *inner* problem:

R	$= r_0 \tilde{R}$	r_0 : the initial bubble radius
p	$= \Delta p\, \tilde{p}$	Δp : pressure change scale
t	$= T_0 \tilde{t}$	T_0 : characteristic collapse time
ϕ	$= r_0^2\tilde{\phi}/T_0$	r_0^2/T_0 : inner velocity potential scale
V_0	$= v_0\tilde{V}_0$	v_0 : basic flow velocity scale
∇V_0	$= \mathcal{G}\,\tilde{\nabla}V_0$	$\mathcal{G}$: basic velocity gradient scale

The matching conditions between the *inner* and the *outer* solutions is obtained by formally writing that there exists an intermediate region characterized by r^*, $r_0 \ll r^* \ll l_0$ where both solutions are valid. This leads to:

$$\frac{r_0^2}{T_0}\,\tilde{\phi}(\frac{r}{r_0}) = \phi_{ext}\,\bar{\phi}(\frac{r}{l_0}). \tag{17}$$

Taylor series expansions of the basic velocity

Since we are considering the case where the size of the *inner* region is small compared to the characteristic length of the *basic* flow, we can express the velocity field in the *inner* region as a Taylor series expansion about the moving origin o.

$$\mathrm{V}_0(\tilde{\mathrm{r}}) = \mathrm{V}_0|_{\mathrm{o}} + \tilde{\mathrm{r}} \cdot \tilde{\nabla}\mathrm{V}_0\Big|_{\mathrm{o}} + \frac{1}{2}\tilde{\mathrm{r}} \cdot \tilde{\nabla}\tilde{\nabla}\mathrm{V}_0\Big|_{\mathrm{o}} \cdot \tilde{\mathrm{r}} + O(\epsilon^3)$$

In order to compute the various terms in Equation (16) we need the following quantities:

$$\mathrm{V}_0(\mathrm{r}) - \mathrm{V}_e \;=\; \mathcal{G}\, r_0\, \tilde{\mathrm{r}} \cdot \tilde{\nabla}\mathrm{V}_0(\mathrm{o}) + \\ \frac{1}{2} r_0^2\, \mathcal{H}\, \tilde{\mathrm{r}} \cdot \tilde{\nabla}\tilde{\nabla}\mathrm{V}_0(\mathrm{o}) \cdot \tilde{\mathrm{r}} + \cdots \tag{18}$$

$$(\mathrm{V}_0(\mathrm{r}) - \mathrm{V}_e) \cdot \tilde{\nabla}\phi \;=\; \frac{r_0^2}{T_0^2}\,\tilde{\nabla}\tilde{\phi} \cdot (\mathcal{G} T_0 \tilde{\mathrm{r}} \cdot \tilde{\nabla}\mathrm{V}_0(\mathrm{o}) + \\ \frac{1}{2}\,\mathcal{H} T_0^2 r_0\, \tilde{\mathrm{r}} \cdot \tilde{\nabla}\tilde{\nabla}\mathrm{V}_0(\mathrm{o}) \cdot \tilde{\mathrm{r}} + \cdots$$

$$\frac{1}{2}(\mathrm{V}_0^2(\mathrm{r}) - \mathrm{V}_e^2) \;=\; \frac{r_0^2}{T_0^2}(\mathcal{G}\, T_0^2 \frac{v_0}{r_0}\, \tilde{\mathrm{r}} \cdot \tilde{\nabla}V_0(\mathrm{o}) \cdot \mathrm{V}_0(\mathrm{o}) + \\ \frac{1}{2}\;\; T_0^2 v_0\, \mathcal{H}\, \tilde{\mathrm{r}} \cdot \tilde{\nabla}\tilde{\nabla}\mathrm{V}_0(\mathrm{o}) \cdot \tilde{\mathrm{r}} \cdot \mathrm{V}_0(\mathrm{o}) + \\ \frac{1}{2}\;\; \left(\mathcal{G}\, T_0\, \tilde{\mathrm{r}} \cdot \tilde{\nabla}\mathrm{V}_0(\mathrm{o})\right)^2 + \cdots \tag{19}$$

where v_0 is the characteristic velocity of the flow field, $\mathcal{G}$ the characteristic dimension of the velocity gradient and $\mathcal{H}$ the characteristic dimension of the velocity bigradient.

4 Problems with a Plane of Symmetry

We now consider the problem of a bubble in a flow in the case where there is a plane of symmetry. This assumption is not fundamental and has been made to simplify the analysis. The general theory is first developed, and is then applied to the problem of a bubble collapsing near a semi-infinite bluff axisymmetric body in a uniform flow field.

Problem formulation

We will choose a coordinate system $Oxyz$ fixed to a streamline, $\mathrm{V}_e = \mathrm{V}_0(\mathrm{o}(t))$, so that the x-axis is parallel to $V_0(\mathrm{o})$; $\tilde{\mathrm{V}}_0 = v_x(t)\mathbf{e}_x$. If we consider the case where

the problem is symmetrical about the (Oxz) plane then

$$\tilde{\nabla}\mathbf{V}_0(\mathbf{o}) = \begin{bmatrix} \alpha_1 & 0 & \alpha_2 \\ 0 & 0 & 0 \\ \alpha_2 & 0 & -\alpha_1 \end{bmatrix}_{\mathbf{e_x},\mathbf{e_y},\mathbf{e_z}} \tag{20}$$

As a result $\tilde{\mathbf{r}}\cdot\nabla\mathbf{V}_0(\mathbf{o})$ and $\tilde{\mathbf{r}}\cdot\nabla\nabla\mathbf{V}_0(\mathbf{o})\cdot\tilde{\mathbf{r}}$ can be written:

$$\tilde{\nabla}\mathbf{V}_0(\mathbf{o})\cdot\begin{bmatrix} x \\ y \\ z \end{bmatrix}_{\mathbf{e_x},\mathbf{e_y},\mathbf{e_z}} = \begin{bmatrix} \alpha_1 x + \alpha_2 z \\ 0 \\ -\alpha_1 z + \alpha_2 x \end{bmatrix}_{\mathbf{e_x},\mathbf{e_y},\mathbf{e_z}}$$

$$= r\begin{bmatrix} G_r(\theta,\psi) \\ G_\theta(\theta,\psi) \\ G_\psi(\theta,\psi) \end{bmatrix}_{\mathbf{e_r},\mathbf{e_\theta},\mathbf{e_\psi}}$$

$$\begin{bmatrix} x \\ y \\ z \end{bmatrix}_{\mathbf{e_x},\mathbf{e_y},\mathbf{e_z}} \cdot\nabla\nabla\vec{V}_0(O)\begin{bmatrix} x \\ y \\ z \end{bmatrix}_{\mathbf{e_x},\mathbf{e_y},\mathbf{e_z}} =$$

$$\begin{bmatrix} \gamma_1 z^2 + 2\gamma_3 xz \\ 0 \\ \gamma_4 x^2 + 2\gamma_3 xz \end{bmatrix}_{\mathbf{e_x},\mathbf{e_y},\mathbf{e_z}} = r^2\begin{bmatrix} H_r \\ H_\theta \\ H_\psi \end{bmatrix}_{\mathbf{e_r},\mathbf{e_\theta},\mathbf{e_\psi}}$$

where we have transformed the quantities from cartesian coordinates (x,y,z) to spherical coordinates (r,θ,ψ) with the polar axis along the z axis. In the above equations:

$$\gamma_1 = \frac{\partial\alpha_2}{\partial z}, \qquad \gamma_2 = \frac{\partial\alpha_2}{\partial x},$$
$$\gamma_3 = \frac{\partial\alpha_1}{\partial z}, \qquad \gamma_4 = \frac{\partial\alpha_1}{\partial x}. \tag{21}$$

Since the problem has a plane of symmetry, we shall take $\vec{\omega} = \omega(t)\mathbf{e}_Y$,

$$\vec{\omega}\times\mathbf{oM} = \omega\, r\,(\mathbf{e}_Y\times\mathbf{e}_r). \tag{22}$$

We nondimensionalize ω as $\omega = \Omega\tilde{\omega}$, where Ω is the characteristic rotation speed of the frame.

Domain of validity of the asymptotic solution

The choice of the relative sizes of the six nondimensional parameters of the problem to consider was determined first by application of the least degeneracy principle. This was then relaxed in order to obtain solutions in some practical physical configurations. The analytical and numerical solutions presented below are based on the following sizes of these parameters relative to ϵ.

1. The characteristic length of the *inner* problem is smaller than that of the *outer* problem, $r_0/l_0 << 1$.
2. The characteristic velocity of the initial flow, v_0, is of same order as the characteristic collapse velocity, $v_0 = O(r_0/T_0)$.
3. The characteristic basic velocity gradient is of the order of ϵ in the *inner* problem: $\mathcal{G}T_0 = O(\epsilon)$.
4. The characteristic velocity bigradient at the scale of the *inner* problem is far smaller than that of the *inner* problem: $\mathcal{H}T_0 r_0 = O(\epsilon^2)$.
5. The characteristic rotation speed at the scale of the *inner* problem is smaller than the collapse velocity: $\Omega T_0 = O(\epsilon)$.
6. The collapse velocity is directly related to the local pressure by $\rho v_{collapse}^2/\Delta p = O(1)$.

The bubble is considered to be close enough to the submerged body so that at leading order, ϵ^0, in the *outer* problem, the body appears as an infinite flat wall. At subsequent orders, the curvature is taken into account. This means that the ratio of the bubble standoff distance to the local radius of curvature of the body is of order ϵ. In the *inner* problem, the effect of the wall is seen first at order ϵ for the potential and at order ϵ^2 for the bubble radius. The effect of the curvature only intervenes at order ϵ^2 on the potential and only adds a constant to the equations.

Order ϵ^0

The system of equations described above reduces at order ϵ^0 in the *inner problem* to that of an oscillating spherical bubble:

$$\tilde{\phi}_0 = q/\tilde{r} \quad \text{with} \quad q = -\tilde{R}_0{}^2\dot{\tilde{R}}_0, \tag{23}$$

where $\tilde{R}_0$ is determined by the Rayleigh-Plesset equation

$$\tilde{R}_0\ddot{\tilde{R}}_0 + \frac{3}{2}\dot{\tilde{R}}_0^2 = \mathcal{P}\left(\tilde{R}_0{}^{-3K} - 1\right) - 2W^{-1}\left(\frac{1}{\tilde{R}_0} - \tilde{R}_0{}^{-3K}\right) - \Delta\tilde{p}, \tag{24}$$

where $W = \Delta P R_0/\sigma$ and $\mathcal{P} = (p_\infty - p_v)/\Delta P$, with the initial conditions: $\tilde{R}_0 = 1$ and $\dot{\tilde{R}}_0 = 0$. In the *outer problem* the general solution (7) reduces to

$$\tilde{\phi}_0 = B_0(\tilde{t})\,P_0(\cos\theta)\,(\frac{1}{\tilde{r}^{n+1}} + \frac{1}{\tilde{r}^{n+1}}) \tag{25}$$

The matching condition between the two problems can be written

$$\frac{r_0^2}{T_0}\left[\tilde{\phi}_0(\tilde{r}) + \epsilon\tilde{\phi}_I(\tilde{r}) + \epsilon^2\tilde{\phi}_{II}(\tilde{r}) + O(\epsilon^3)\right] = \phi_{ext}\left[\tilde{\phi}_0(\tilde{r}) + \epsilon\tilde{\phi}_I(\tilde{r}) + \epsilon^2\tilde{\phi}_{II}(\tilde{r}) + O(\epsilon^3)\right] \tag{26}$$

which leads to:

$$\phi_{ext} = \epsilon\frac{r_0^2}{T_0}; \quad B_0(\tilde{t}) = q(\tilde{t}); \quad \lim_{\tilde{r}\to\infty}\tilde{\phi}_I = \frac{q}{2} \tag{27}$$

Order ϵ

After accounting for the solution at $O(\epsilon^0)$ the equations of the problem at $O(\epsilon)$ become:

$$\Delta\tilde{\phi}_1 = 0; \qquad \lim_{\tilde{r}\to\infty}\tilde{\phi}_1 = \frac{q}{2}$$

$$\left\{\frac{\partial\tilde{\phi}_1}{\partial\tilde{r}} + \tilde{\phi}_1\frac{\partial^2\tilde{\phi}_0}{\partial\tilde{r}^2}\right\}_{\tilde{r}=\tilde{R}_O} = \frac{\partial\tilde{\phi}_1}{\partial\tilde{r}} - G_r\tilde{R}_O$$

$$\left\{ \frac{\partial \phi_1}{\partial \tilde{t}} + \phi_1 \frac{\partial^2 \tilde{\phi}_0}{\partial \tilde{t} \partial \tilde{r}} + \frac{\partial \phi_1}{\partial \tilde{r}} \frac{\partial \tilde{\phi}_0}{\partial \tilde{r}} + \phi_1 \frac{\partial \tilde{\phi}_0}{\partial \tilde{r}} \frac{\partial^2 \tilde{\phi}_0}{\partial \tilde{r}^2} + \right. \quad (28)$$

$$\left. \tilde{R}_O G_r \frac{\partial \tilde{\phi}_0}{\partial \tilde{r}} + \mu v_x(t) \tilde{R}_O F(\theta, \psi) \right\}_{r=R_O} = 3K\mathcal{P}\phi_1 \tilde{R}_O^{-3K-1}$$

where

$$\begin{aligned} G_r &= 2\alpha_2 \cos\theta \sin\theta \cos\psi + \alpha_1(\sin^2\theta \cos^2\psi - \cos^2\theta) \\ F &= \alpha_1 \sin\theta \cos\psi + \alpha_2 \cos\theta \end{aligned} \quad (29)$$

Resolution of the order ϵ

Using the general solution of the Laplace equation, the limit condition at infinity on ϕ_1 leads us to take:

$$A_{1jm} = \delta_{j,0}\, q/2, \quad (30)$$

Since the problem is symmetrical about the (Oxz) plane, there are no terms in $\sin\psi$,and we do not have to consider $m < 0$. Equation (16) becomes:

$$\begin{aligned} -\frac{j+1}{\tilde{R}_O^{j+2}} B_{1jm} Y_{jm} &+ \frac{2q}{\tilde{R}_O^3} R_{1jm} Y_{jm} = \dot{R}_{1jm} Y_{jm} + \\ &- \frac{2}{3} \tilde{R}_O \alpha_2 Y_{21} + \alpha_1 \tilde{R}_O (Y_{20} - \frac{Y_{22}}{6}), \\ \frac{\dot{q}}{2} + \frac{\dot{B}_{1jm}}{\tilde{R}_O^{j+1}} Y_{jm} &- \frac{\dot{q}}{\tilde{R}_O^2} R_{1jm} Y_{jm} + q \frac{j+1}{\tilde{R}_O^{j+4}} B_{1jm} Y_{jm} + \\ &- 2\frac{q^2}{\tilde{R}_O^5} R_{1jm} Y_{jm} - \frac{2}{3\tilde{R}_O} q\alpha_2 Y_{21} + \\ -\frac{q}{\tilde{R}_O} \alpha_1 (\frac{Y_{22}}{6} - Y_{20}) &+ \mu \tilde{R}_O v_x (\alpha_1 Y_{11} + \alpha_2 Y_{10}) \\ &= \dot{R}_{100} Y_{00} 3K\mathcal{P} \tilde{R}_0^{-3K-1} \end{aligned} \quad (31)$$

For $j > 2$ we have a homogeneous linear differential system where the initial conditions are zero. The solution is therefore $R_{1jm} = B_{1jm} = 0;\ \forall j > 2$.

The equations for the non-zero terms at order ϵ as well as all equations obtained at order ϵ^2 can be found in Reference [22]. At order ϵ the bubble behavior is modified by both the presence of the wall, which at this order only appears as a flat plate, and the presence of a pressure gradient. At the following order ϵ^2 the curvature of the wall comes into play as well as the velocity bigradient.

Application to Bubble Dynamics near a Headform

We consider now the dynamics of a bubble near a semi-infinite bluff body. The velocity potential considered is that due to a superposition of a uniform flow and a source of intensity Q located at the origin:

$$\phi_0 = V_\infty x + \frac{Q}{r} \quad (32)$$

This simulates the flow field about a Rankine body of radius, $R = \sqrt{\frac{Q}{\pi V_\infty}}$ and stagnation point at $X = -R/2$.

At order ϵ^0, the outside pressure $\Delta p(t)$ is taken to be the pressure in the fluid in absence of the bubble along the trajectory of a fluid particle. At higher orders of ϵ, the gradient and bigradient are also taken into account while following a fluid particle.

A fourth order Runge-Kutta procedure is used to solve the ordinary differential equations presented earlier. To illustrate the method, a Rankine body with a radius of 10 centimeters with flow at infinity advancing at a velocity of 1.15 m/s was selected. Figures 1 through 4 show some results obtained on bubble behavior near the Rankine body. Figures 1a through 1c show a case where the interaction between the bubble and the flow field is significant. The initial bubble radius is $r_0 = 1$ cm. and its distance, l_0, from the wall is such that $\varepsilon = r_0/l_0$ is equal to 0.3.

Figure 1b shows the trajectory of the bubble center along the body, and Figure 1c shows the pressure and velocity variations with time. In the initial phase $t < 2.0$ the bubble sees a pressure drop. Later, the pressure rises back towards the ambient pressure. This velocity is also that chosen for translating the origin of coordinates in which the bubble shape is prescribed. Figure 1a shows, overlaid on each other, the bubble contours at different times (from $t = 0.1T_0$ to $2T_0$ during the bubble growth and collapse. The orientation of the bubble relative to the body is the same as illustrated in Figure 1b which shows bubble positions versus time. It is apparent from the contour plots that the bubble moves toward the body wall during its collapse. Due to the velocity and pressure gradient around the body the bubble elongates and in fact rotates around its center of mass. Initially, the side of the bubble surface facing an intermediary direction between the downstream direction and the wall direction flattens out. A reentrant jet is then produced perpendicular to that face. The direction of the jet appears to change with time in a fashion indicating increased influence of the presence of the wall. The computations shown in the figure stopped when the bubble wall touched the origin of coordinates. This moment will be delayed in future computations by selecting an adequate translation of the origin of coordinates that is perpendicular to the wall.

Figure 2 shows the influence of the distance of the bubble to the wall, or ε, on its shape history. Bubble collapse contours are shown for $\varepsilon = 0.15, 0.3$ and 0.6. As expected, deviation from sphericity increases with the proximity to the wall. Due to stronger shearing action closer to the body approaching the wall has the effect of increasing bubble stretching and elongation during its growth, then reinforcing the reentrant jet formation during the collapse. For $\varepsilon = 0.3$ and $\varepsilon = 0.6$ the computation stopped when the bubble surface touched the origin of coordinates. However, due to the weak nature of the interaction for $\varepsilon = 0.15$ the collapse is completed with no reentrant jet and is followed by a bubble re-

bound or second growth that is not shown on the figure.

Also, as expected, a similar effect as in figure 2 is obtained if the distance to the body is maintained constant while the bubble size is changed. Figure 3 shows such a case, where the distance between the bubble center and the wall is maintained at 3.333 cm, while the bubble size is varied from 0.5 cm ($\epsilon = 0.15$), to 1 cm ($\epsilon = 0.3$), to 2 cm ($\epsilon = 0.6$). Here too the jet is seen to rotate to become closer and closer to perpendicular to the wall.

5 Bubble/Vortex Interaction

One of the most fundamental phenomena observed in flow cavitation is the capture of bubbles/nuclei by vortices. The problem of the interaction of a single gas bubble and a Rankine line vortex is amenable to treatment via analytical techniques. Here we also apply to this problem the method of matched asymptotic expansions described above. To do so we assume that the length scale characteristic of the bubble, r_{bo} is small compared to the initial distance from the bubble to the vortex, d.

The analytical results have been tested for a plausible set of parameters, and yield physically reasonable solutions. The solution shows that the bubbles are attracted towards the vortex center, and that a jet appears on the side of the bubble opposite to the flow direction. Further investigation of the parameter space and computation of higher order corrections are currently underway.

Problem formulation

Consider a spherical bubble initially at rest in an incompressible, inviscid liquid at a distance d from a line vortex of strength Γ. The pressure at infinity is p_∞ and the velocity due to the vortex alone (i.e. excluding any bubble effects) is$\mathbf{V}_0$. To perform the calculations we consider, as in the previous section, two coordinate frames. The first is a *fixed frame* which is convenient for describing the overall flow, one axis of which coincides with the vortex axis. The second is a *moving frame* which has its origin initially at the center of the bubble and moves at the liquid velocity in the absence of the bubble. We denote the location of the moving origin by o.

With the same assumptions as in the previous section the equations of the problem, both for the flow and the boundary conditions on the bubble are the ones presented in Section 1. Since we are interested in the modification in the flow caused by the presence of the bubble, it is convenient to introduce as in Section 3 the *reduced* or *bubble potential* ϕ_b, defined by

$$\phi_b = \phi' - \frac{\Gamma}{2\pi}\beta = \phi' - \phi_v, \tag{33}$$

where ϕ_v is the velocity potential due to the isolated vortex and β is the angular cylindrical coordinate in the fixed frame. The quantity ϕ_b represents the change to the potential of the flow because of the presence of the bubble. Because of linearity, the function ϕ_b also satisfies Laplace's equation and conditions described in Section 3.

We now consider the moving system of coordinates. The coordinates are initially coincident with the bubble center, and move with the flow at that location in the absence of the bubble while the Cartesian axes remain parallel to those in the fixed frame. Let ϕ denote the *bubble velocity potential* in the moving frame.

$$\phi_b(\mathbf{x}, t) = \phi_b(\mathbf{x}' + \mathbf{o}, t) = \phi(\mathbf{x}', t) \tag{34}$$

where $\mathbf{x}'$ is $\mathbf{x}$ referred to the moving frame. The velocity $\mathbf{V}$ is expressed in the moving frame as

$$\mathbf{V} = \frac{\Gamma}{2\pi l}\mathbf{e}_{z'} \times \mathbf{e}_l, \tag{35}$$

where $\mathbf{e}_l$ is a unit vector along the shortest line joining the point at which the velocity is to be measured and the z axis of the fixed system, and l the length of this line. The velocity of the moving coordinate system is then:

$$\mathbf{V}_O = \frac{\Gamma}{2\pi d}\left[-\sin\omega t\ \mathbf{e}_{1'} + \cos\omega t\ \mathbf{e}_{2'}\right], \tag{36}$$

By maintaining the moving cartesian axis parallel to the fixed frame axis we obtain the same equations for ϕ as in Section 3, with $\omega \equiv 0$.

Dimensional Analysis

As in the previous section the flow is assumed to be divided into two regions, an external region where the effects of the vortex dominate, while the region close to the bubble is dominated by its dynamics. The length scale characteristic of the bubble region is r_{bo}, the initial bubble radius, while the *outer problem* has as scale d. We will consider the case where $\epsilon = r_{bo}/d$ is small. The physical quantities entering the problem are p_{g0} and r_{bo} (from the bubble), and p_∞, Γ, and ρ_l from the liquid.

The matching between the *inner* and *outer* problem and the application of the principle of least degeneracy leads to the condition that the scaling for the velocity $\mathbf{V}$ be such that it is of the same order as the bubble deformation velocity

$$|\mathbf{V}| \sim \frac{\Gamma}{2\pi d} \sim \frac{r_{bo}}{T_0}. \tag{37}$$

The nondimensional velocity is then defined by

$$\mathbf{V} = \Omega\tilde{\mathbf{V}}\frac{r_{bo}}{T_0} \text{ with } \Omega = \frac{\Gamma/2\pi d}{\sqrt{p_\infty/\rho}}. \tag{38}$$

This imposes the following restriction on the gradient of the vortex velocity field

$$(\mathbf{V}|_{\mathcal{R}} - \mathbf{V}_O) \sim r_{bo}|\nabla\mathbf{V}| \sim \epsilon\frac{r_{bo}}{T_0}. \tag{39}$$

We will denote

$$\mathbf{V} - \mathbf{V}_O = \epsilon\frac{r_{bo}}{T_0}\Omega\tilde{\mathbf{V}}_d, \tag{40}$$

An important quantity is the rotation frequency of a particle around the vortex line. This is given by

$$\omega = \frac{\Gamma}{2\pi d^2}. \tag{41}$$

The ratio of this frequency and the Rayleigh frequency is seen to be

$$\omega T_0 = \frac{r_{b_0}}{d}\frac{\Gamma/2\pi d}{\sqrt{p_\infty/\rho_l}} \sim O(\varepsilon). \tag{42}$$

Asymptotic expansions

After expanding the equations of the problem described earlier as indicated in Section 2 these are solved up to and including terms of $O(\varepsilon)$. As in the previous section problem upon introducing the expansions, the leading order problem ϵ^0 reduces to the spherical oscillating bubble problem. This problem has solution

$$\phi_0 = q_0/r = -R_0^2\dot{R}_0/r, \tag{43}$$

which yields the following Rayleigh-Plesset equation for R_0

$$R_0\ddot{R}_0 + \frac{3}{2}\dot{R}_0{}^2 = \mathcal{P}_g R_0^{-3k} - \frac{2\mathcal{W}^{-1}}{R_0} + \left(\mathcal{P}_v + \Omega^2 - 1\right), \tag{44}$$

where

$$\mathcal{P}_g = \frac{p_{g0}}{p_\infty}; \qquad \mathcal{P}_v = \frac{p_v}{p_\infty}, \tag{45}$$

Order ε^1

The equations at $O(\varepsilon)$ are

$$\nabla^2\phi_1 = 0 \tag{46}$$

subject to

$$\frac{\partial\phi_1}{\partial r} - 2\frac{\dot{R}_0}{R_0}R_1\bigg|_{r=R_0} = \frac{\partial R_1}{\partial t} + \Omega\mathbf{V}_d\cdot\mathbf{e}_r, \tag{47}$$

and

$$\frac{\partial\phi_1}{\partial t} + \dot{R}_0\frac{\partial\phi_1}{\partial r} + R_1\left(2\frac{\dot{R}_0{}^2}{R_0} + \ddot{R}_0\right) + +51$$
$$+\dot{R}_0\Omega\mathbf{V}_d\cdot\mathbf{e}_r + \mathbf{V}_0\cdot\mathbf{V}_1\big|_{r=R_0} = 3k\mathcal{P}_g\frac{r_{100}}{R_0^{3k+1}} +$$
$$-\frac{2\mathcal{W}}{R_0}\sum_{l=1}^{\infty}\sum_{m=-l}^{l}\frac{r_{1lm}}{R_0}\left(1 - \frac{(l-1)(l+2)}{2}\right) \tag{48}$$

Introducing the expansion for the function R_1 and ϕ_1 similar to that in Section 2, with the difference that the $Y_{lm}(\theta,\varphi)$ are defined here as

$$Y_l^m(\theta,\varphi) = \sqrt{\frac{(n-|m|)!}{(n+|m|)!}}P_n^{|m|}(\cos\theta)\exp(im\varphi).$$

the dynamic boundary condition becomes:

$$\frac{R_0}{l+1}\left\{\ddot{r}_{1lm} + 2\left(\frac{\dot{R}_0}{R_0}\dot{r}_{1lm} - \left(\frac{\dot{R}_0}{R_0}\right)^2 r_{1lm} + \frac{\ddot{R}_0}{R_0}r_{1lm}\right) +\right.$$
$$\left.+\Omega(\dot{A}\delta_{l2}^{m2} + \dot{A}^*\delta_{l2}^{m,-2})\right\} + \frac{\dot{R}_0}{l+1}\left(\dot{r}_{1lm} + 2\frac{\dot{R}_0}{R_0}r_{1lm} +\right.$$
$$\left.+\Omega(A\delta_{l2}^{m2} + A^*\delta_{l2}^{m,-2})\right) - \left(2\frac{\dot{R}_0^2}{R_0} + \ddot{R}_0\right)r_{1lm} =$$
$$-3k\mathcal{P}_g\frac{r_{100}\delta_{l0}^{m0}}{R_0^{3k+1}} + \frac{2\mathcal{W}}{R_0}\frac{r_{1lm}}{R_0}\left(1 - \frac{(l-1)(l+1)}{2}\right) +$$
$$+\Omega(A\delta_{l2}^{m2} + A^*\delta_{l2}^{m,-2}) + \Omega^2(R_{0l}\delta_{l1}^{m1} + R_{0l}^*\delta_{l1}^{m,-1}),$$

where

$$\alpha = \frac{-R_0}{\sqrt{2}}(\cos\omega t - i\sin\omega t). \tag{49}$$

Examination of the above equation reveals that, except for $(l,m) = (2,2)$, $(2,-2)$, $(1,1)$, and $(1,-1)$ the equations are homogeneous second order linear differential equations (initial value problems). Since we have assumed the bubble starts from a spherical shape, and is initially at rest, the solutions to these equations will vanish identically. For the four non-trivial cases, the differential equation satisfied by the particular radial component may be written as follows:

$$R_0\ddot{R}_{111} + 3\dot{R}_0\dot{R}_{111} - 4\frac{\dot{R}_0^2}{R_0}R_{111} =$$
$$4\frac{\mathcal{W}R_{111}}{R_0^2} - 2\sqrt{2}\Omega^2 R_0\cos\omega t; \tag{50}$$

$$R_0\ddot{R}_{11,-1} + 3\dot{R}_0\dot{R}_{11,-1} - 4\frac{\dot{R}_0^2}{R_0}R_{11,-1} =$$
$$1\frac{\mathcal{W}R_{11,-1}}{R_0^2} + 2\sqrt{2}\Omega^2 R_0\sin\omega t; \tag{51}$$

$$\frac{R_0}{3}\ddot{R}_{122} + \dot{R}_0\dot{R}_{122} - \left(2\frac{\dot{R}_0^2}{R_0} + \frac{1}{3}\ddot{R}_0\right)R_{122} =$$
$$-\frac{\mathcal{W}R_{122}}{R_0^2} + 2\sqrt{\frac{2}{3}}\Omega\left(\frac{R_0\dot{R}_0}{3}\sin 2\omega t - \frac{2\omega R_0^2}{3}\cos 2\omega t\right); \tag{52}$$

$$\frac{R_0}{3}\ddot{R}_{12,-2} + \dot{R}_0\dot{R}_{12,-2} - \left(2\frac{\dot{R}_0^2}{R_0} + \frac{1}{3}\ddot{R}_0\right)R_{12,-2} =$$
$$-\frac{\mathcal{W}R_{12,-2}}{R_0^2} + 2\sqrt{\frac{2}{3}}\Omega\left(\frac{R_0\dot{R}_0}{3}\cos 2\omega t + \frac{2\omega R_0^2}{3}\sin 2\omega t\right), \tag{53}$$

where

$$R_{111} = r_{111} + r_{11,-1} \qquad R_{11,-1} = \frac{r_{111} - r_{11,-1}}{i},$$
$$R_{122} = r_{122} + r_{12,-2} \qquad R_{12,-2} = \frac{r_{122} - r_{12,-2}}{i}, \tag{54}$$

In terms of these new coefficients the surface of the bubble (in the moving coordinate system) is given by

$$r = R_0 + \varepsilon\left[(R_{111}\cos\varphi - R_{11,-1}\sin\varphi)\sin\theta +\right.$$
$$\left.(R_{122}\cos 2\varphi - R_{12,-2}\sin 2\varphi)\sin^2\theta\right] + O(\varepsilon^2). \tag{55}$$

Results and Conclusions

We present here some results from a numerical study using the above equations. The equations involve 4 parameters - $\mathcal{P}_g, \mathcal{P}_v, \Omega, \mathcal{W}$ and the perturbation parameter ϵ. In the following we have not attempted to map the parameter space of the above equations, but rather demonstrate the characteristics of their solutions for a particular choice of the parameters and show that they make physical sense. We choose the following for the physical parameters: $P_\infty = 1.03 \times 10^5 Pa$, $R_0 = 10^{-3} m$, $d = 5 \times 10^{-2} m$, $\Gamma = 1.2 m^2/s$, $P_v = 2 \times 10^3 Pa$, $\sigma = 7 \times 10^{-2} N/m$, $P_{g0} = 3 \times 10^4 Pa$, $\rho = 10^3 kg/m^3$, $k = 1.4$.

This yields the following for the non-dimensional parameters: $\mathcal{P}_g = 2.9126 \times 10^{-1}$, $\mathcal{P}_v = 1.94174 \times 10^{-2}$, $\mathcal{W}^{-1} = 6.7961158 \times 10^{-4}$, $\Omega = 3.764 \times 10^{-1}$, $T_0 = 9.85 \times 10^{-5}$, $\epsilon = 0.05\omega = 7.53 \times 10^{-3}$.

The equation systems at $O(1)$ and $O(\epsilon)$ are integrated using a simple fourth-order accurate Runge-Kutta scheme. The results from this trial run are shown in Figures 4-6. The results indicate that the expression for the bubble becomes multivalued for times after $4.6T_0$, i.e. the origin of the local coordinates lies outside the bubble after this time. Thus results of the integration up to this time are shown. Figure 4 shows a cross-sectional view of the bubble in the x, y plane at various times. The bubble motion and deformation, and the formation of the jet are clearly seen. The bubble initially collapses almost spherically (while moving with the vortex flow), and reaches a minimum at approximately $1.55T_0$, and grows till it reaches a maximum size at $2.9T_0$. It subsequently collapses and shows the formation of a jet on the side opposite to its direction of motion, and directed towards the vortex axis. The computations are stopped at $4.6T_0$ when the bubble no longer contains the origin of coordinates. Figure 5 shows the trajectory of the $\varphi = 0$ and $\varphi = \pi$ points in this cross-section. Finally Figure 6 shows cross-sectional views of the bubble at the same times, but in a normal plane. This plane contains the z axis and the line connecting the moving coordinate origin and the vortex. The fact that the jet is directed towards the vortex axis becomes apparent in this view.

Quite obviously a more systematic study of the parameter space is required. Also, as in Reference [28] the results of the asymptotic analysis and of the 3D boundary element program **3DynaFS** must be compared. Qualitatively the same types of results are observed. The expression used for the motion of the moving coordinate system must be refined to prevent bubble function becoming multi-valued so early in the collapse. These and related aspects are items of current research.

6 Bubble Cloud Study

Consider a cloud of N bubbles of radius r_b^i, $i = 1, \cdots, N$ immersed in a liquid. The bubbles are initially assumed to be at rest and at equilibrium with the surrounding fluid. The characteristic radius of the bubbles is r_{b0}. We denote the distance between bubbles i and j as l_{ij}, which we take to be of the order of the characteristic distance l_0. We define as before ϵ as r_{b0}/l_0.

The matched asymptotic expansions method described in the previous sections was implemented earlier in [11, 25] to study the behavior of such a bubble cloud. Here we will only sketch an outline of the model. We assume that the characteristic geometric scale of the cloud (l_0), is small compared to the outside driving pressure field scale (L_0), but is much larger than the typical bubble radius r_{b0}. Therefore, to first approximation, the same driving pressure is assumed to be felt at the same time by all bubbles in the cloud. Variations of this pressure due to the position of each bubble are only seen at the higher orders. In a more general case, the pressure felt by each bubble is dependent on the bubble location and on the modification of the outside flow field by the presence of the bubble cloud. We are presently implementing such an approach which accounts for the compressibility of the two-phase bubbly medium.

Since ϵ is the ratio r_{b0}/l_0, it is directly related to the void fraction here assumed to be low. At the lowest order, $\epsilon = 0$, each bubble (of index i) behaves spherically as if in an infinite medium and the time dependence of its radius, $a_0^i(t)$, is given by the Rayleigh Plesset equation, [20]. If the compressibility of the medium is to be included, then an equivalent equation such as in [24] can be used. This first approximation of the whole flow field (a distribution of sources or sinks representing all bubble oscillations) sets the boundary conditions at infinity at the following order of approximation. The same process is then repeated for the successive orders. *Up to the order* $O(\epsilon^3)$, one can show, [11, 25], that the influence of the remaining bubbles on each bubble B_i, can be schematically replaced by the influence of a single equivalent bubble centered at G_i. The growth rate and position of this equivalent bubble are determined by the distribution and the growth rate of the other cavities. In general, this fictitious bubble equivalent to the "rest-of-the-cloud" and the corresponding "cloud center" and "equivalent bubble intensity" are different for each bubble. If θ_{ig} is the angle between the centers' direction $\mathbf{B_iG_i}$ and the direction of a field point $\mathbf{B_iM}$, the equation of the surface of the axisymmetric bubble B_i can be written in the form:

$$R(\theta_{ig}, \varphi, t) = a_0^i(t) + \epsilon a_1^i(t) + \epsilon^2[a_2^i(t) + f_2^i(t).\cos\theta_{ig}] + \epsilon^3[a_3^i(t) + f_3^i(t).\cos\theta_{ig} + g_3^i(t)\mathcal{P}_2(\cos\theta_{ig})] + o(\epsilon^3),$$

where $\mathcal{P}_2$ is the Legendre polynomial of order 2, and argument $\cos\theta_{ij}$. The components, a_n^i, f_n^i and g_n^i, satisfy

linear second order differential equations which can be written in symbolic form as follows:

$$\mathcal{D}_2(y_n^i) = \sum_j^i \left(\frac{l_0}{l_0^{ij}}\right)^m \mathcal{F}_j^i(y_0^i, \ldots, y_{n-1}^i)\mathcal{P}_m(\cos\theta_{ij}). \quad (56)$$

Here $\mathcal{D}_2(y_n^i)$ represents a differential operator of the second order in time acting on the radius component y_n^i (one of a_n^i, f_n^i, g_n^i) of the bubble i ; l_0^{ij} is the initial distance between the bubbles B_i and B_j; $\mathcal{F}_j^i(y_0^i, \ldots, y_{n-1}^i)$ is a known function of the terms (y_k^i), determined at the preceding orders; m is an integer indicating the order of the spherical harmonic; θ_{ij} is the polar angle measured wth respect to the line connecting the center of the bubble i and the center of the equivalent bubble B_j; and n is an integer indicating the order of the approximation.

The detailed expressions can be found in Reference [11]. The behavior of B_i can then be computed by integration of the obtained system of differential equations using a multi-Runge-Kutta procedure. The behavior of the whole cloud is thus obtained. Earlier studies [11, 25, 18] have shown that collective bubble behavior can have a dramatic effect on both bubble growth and implosion. Specifically, bubble growth is inhibited by bubble interactions, while bubble collapse is enhanced. This cumulative effect comes from the fact that the interaction reduces any driving pressure drop as a result of the other bubble growth, while it increases the collapse driving pressure as a result of the other bubble collapse. Due to the cumulative effects of the collapse of all the bubbles in the cloud, each bubble ends its collapse under the influence of a pressure which is orders of magnitude higher than that for an isolated bubble (see Figure 9 described below and corresponding discussion)

Extension to a slightly compressible liquid

The incompressibility approximation assumed above can be relaxed. In this section we extend our asymptotic treatment of a bubble cloud to the case of a slightly compressible liquid. Briefly the method followed is that of expansion in two parameters - the Mach number $\mathcal{M}$, and the parameter ϵ introduced earlier. We derive $O(\mathcal{M})$ corrections to the incompressible equations (valid till $O(\epsilon^3)$ discussed above.

To consider the effect of compressibility we consider the following equations of motion:

$$\frac{1}{\rho}\left(\frac{\partial\rho}{\partial t} + (\mathbf{u}\cdot\nabla)\rho\right) + \nabla\cdot\mathbf{u} = 0 \quad (57)$$

$$\left(\frac{\partial\mathbf{u}}{\partial t} + (\mathbf{u}\cdot\nabla)\mathbf{u}\right) + \frac{1}{\rho}\nabla p = 0 \quad (58)$$

$$\frac{dp}{d\rho} = c_\infty^2 \qquad h = \int_{p_\infty}^{p}\frac{dp}{\rho} \quad (59)$$

The flow is assumed irrotational, so that we can define a velocity potential

$$\mathbf{u} = \nabla\phi. \quad (60)$$

Substituting from (59) for the velocity in the equations of motion we obtain

$$\nabla^2\phi + \frac{1}{\rho c_\infty^2}\left[\frac{\partial h}{\partial t} + (\nabla\phi\cdot\nabla)h\right] = 0, \quad (61)$$

and

$$\frac{\partial\phi}{\partial t} + \frac{1}{2}|\nabla\phi|^2 + h = 0 \quad (62)$$

We now consider the cases where the length scale $L_0 = c_\infty\tau_{b0}$ is much larger than the length scales l_0 and r_{b0}, so that

$$r_{b0} \ll l_0 \ll L, \quad (63)$$

and define a new parameter $\mathcal{M}$ such that

$$\mathcal{M} = \frac{r_{b0}}{L} = \frac{r_{b0}/\tau_0}{c_\infty}. \quad (64)$$

We can identify $\mathcal{M}$ with the Mach number, and use it as a perturbation parameter. The details of this calculation will be demonstrated in a later paper [29], and we only outline the approach here, and present some preliminary results.

The problem can be decomposed into an acoustic part and a hydrodynamic part. The acoustic part consists of the "far" field corresponding to the pure liquid far away from the cloud region, while the "near" field is that in the neighbourhood of the bubbles, and corresponds to the hydrodynamic part of the problem. The near field can be decomposed, as before, into an "inner" (corresponding to the neighborhood of a bubble) and "outer" field (corresponding to the rest of the cloud).

It turns out that if we take $\mathcal{M} \sim \epsilon^3$ the inner equations are almost identical to the incompressible ones until $O(\mathcal{M})$, except that they account for the time retardation due to the compressibility of the medium.

Performing the analysis with this assumption yields that the preceding equations hold, with the equation of the bubble radius at $O(\epsilon^0)$ modified from a Rayleigh-Plesset form to a Keller-Herring form [21]

This equation can be written as

$$\rho\left[\left(1-\frac{\dot a}{c}\right)a\ddot a + \frac{3}{2}\left(1-\frac{\dot a}{3c}\right)\dot a^2\right] = \frac{1}{\rho}\left(1+\frac{\dot a}{c}+\frac{a}{c}\frac{d}{dt}\right)[p_B - p_\infty], \quad (65)$$

where

$$p_B = p_{g0}\left(\frac{V_0}{V}\right)^k + p_v - \frac{2\sigma}{a}, \quad (66)$$

and c is the sound speed.

This model is being used in in combination with the bubble interaction model to extend the study to the case where a slight compressibility of the liquid is taken into account. Figure 7, for instance shows the influence of a finite sound speed on the behavior of a bubble in a 6-bubble configuration.

7 Boundary Element Method for Three-Dimensional Bubble Dynamics

In order to enable the simulation of bubble behavior in complex geometry and flow configurations including the full non-linear boundary conditions, a three-dimensional Boundary Element Method was developed. This method uses Green's identity to solve Laplace's equation. If the velocity potential, ϕ, or its normal derivative is known on the fluid boundaries (points M), and ϕ satisfies the Laplace equation, then ϕ can be determined anywhere in the domain of the fluid (field points P) using the identity:

$$\int\int_s \left[-\frac{\partial \phi}{\partial n} \frac{1}{|\,\mathbf{MP}\,|} + \phi \frac{\partial}{\partial n}\left(\frac{1}{|\,\mathbf{MP}\,|} \right) \right] ds = a\pi\phi(P), \quad (67)$$

where $a\pi = \Omega$ is the solid angle under which P sees the fluid.

$a = 4$, if P is a point in the fluid

$a = 2$, if P is a point on a smooth surface

$a < 4$, if P is at a corner of the discretized surface.

The advantage of this integral representation is that it effectively reduces the dimension of the problem by one. If the field point P is selected to be on the boundary of the fluid domain (a bubble surface or on any other boundary), then a closed system of equations can be obtained and used at each time step to solve for values of $\partial\phi/\partial n$ (or ϕ) assuming that all values of ϕ (or $\partial\phi/\partial n$) are known at the preceding step.

To solve Equation (66) numerically, it is necessary to discretize the bubble into panels, perform the integration over each panel, and then sum up the contributions to complete the integration over the entire bubble surface. To do this, the initially spherical bubble is discretized into a geodesic shape using flat, triangular panels. After discretizing the surface, Equation (66) becomes a set of N equations (N is the number of discretization nodes) of index i of the type:

$$\sum_{j=1}^{N} \left(A_{ij} \cdot \frac{\partial \phi_j}{\partial n} \right) = \sum_j (B_{ij} \cdot \phi_j) - a\pi\phi_i, \quad (68)$$

where A_{ij} and B_{ij} are elements of matrices which are the discrete equivalent of the integrals given in Equation (66). To evaluate the integrals in (66) over any particular panel, a linear variation of the potential and its normal derivative over the panel is assumed. In this manner, both ϕ and $\partial\phi/\partial n$ are continuous over the bubble surface, and are expressed as a function of the values at the three nodes which delimit a particular panel. Obviously higher order expansions are conceivable, and would probably improve accuracy at the expense of additional analytical effort and numerical computation time. The two integrals in (66) are then evaluated analytically. The resulting expressions, too long to present here, can be found in [27]. In order to proceed with the computation of the bubble dynamics several quantities appearing in the above boundary conditions need to be evaluated at each time step. The bubble volume presents no particular difficulty, while the unit normal vector, the local surface curvature, and the local tangential velocity at the bubble interface need further development. In order to compute the curvature of the bubble surface a local bubble surface three-dimensional fit, $f(x,y,z) = 0$, is first computed. The unit normal at a node and the local curvature can then be expressed using Equations (5).

To obtain the total fluid velocity at any point on the surface of the bubble, the tangential velocity, $\mathbf{V_t}$, must be computed at each node in addition to the normal velocity, $\mathbf{V_n} = \partial\phi/\partial n\ \mathbf{n}$. This is also done using a local surface fit to the velocity potential, $\phi_l = h(x,y,z)$. Taking the gradient of this function at the considered node, and eliminating any normal component of velocity appearing in this gradient gives a good approximation for the tangential velocity

$$\mathbf{V_t} = \mathbf{n} \times (\nabla\phi_l \times \mathbf{n}). \quad (69)$$

With the problem initialized and the velocity potential known over the surface of the bubble, an updated value of $\partial\phi/\partial n$ can be obtained by performing the integrations outlined above, and solving the corresponding matrix equation. The unsteady Bernoulli equation can then be used to solve for $D\phi/Dt$, the total material derivative of ϕ,

$$\frac{D\phi}{Dt} = \frac{\partial\phi}{\partial t} + |\,\nabla\phi\,|^2 = \frac{P_\infty - P_L}{\rho} - gz + \frac{1}{2}|\,\nabla\phi\,|^2 . \quad (70)$$

$D\phi/Dt$ provides the total time variations of ϕ at any node during its motion with the fluid. The second term on the right hand side is the hydrostatic pressure and is introduced to account for cases where the influence of the gravitational acceleration is not negligible. Using an appropriate time step, all values of ϕ on the bubble surface can be updated using ϕ at the preceding time step and $D\phi/Dt$. In the results presented below the time step was based on the ratio between the length of the smaller panel side, l_{min} and the highest node velocity, V_{max}. This choice limits the motion of any node to a fraction of the smallest panel side. It has the great advantage of constantly adapting the time step, by refining it at the end of the collapse – where l_{min} becomes very small and V_{max} very large – and by increasing it during the slow bubble size variation period. New coordinate positions of the nodes are then obtained using the position at the previous time step and the displacement,

$$d\mathbf{M} = \left(\frac{\partial\phi}{\partial n}\mathbf{n} + \mathbf{V_t} \right) dt. \quad (71)$$

This time stepping procedure is repeated throughout the bubble oscillation period, resulting in a shape history of the bubbles.

8 Presence of a Viscous Basic Flow

Cavitation bubbles seldom grow and collapse in a quiescent fluid or in a uniform flow field. To the contrary, cavities are most commonly observed in shear layers, boundary layers and vortical structures. To study bubble dynamics in a nonuniform flow field, let us consider the case where the "basic flow" of velocity $\mathbf{V_0}$ is known and satisfies the Navier Stokes equations:

$$\frac{\partial \mathbf{V_0}}{\partial t} + \mathbf{V_0} \cdot \nabla \mathbf{V_0} = -\frac{1}{\rho}\nabla P_0 + \nu \nabla^2 \mathbf{V_0} \ . \tag{72}$$

If the basic flow is potential the application of the Boundary Element Method is straightforward and there is no need for any additional assumptions.

In the presence of the oscillating bubbles, the velocity field is given by $\mathbf{V}$ which also satisfies the Navier Stokes equation:

$$\frac{\partial \mathbf{V}}{\partial t} + \mathbf{V} \cdot \nabla \mathbf{V} = -\frac{1}{\rho}\nabla P + \nu \nabla^2 \mathbf{V} \ . \tag{73}$$

Both $\mathbf{V}$ and $\mathbf{V_0}$ also satisfy the continuity equation. We can now define bubble flow velocity and pressure variables, $\mathbf{V_b}$ and P_b, as follows:

$$\mathbf{V_b} = \mathbf{V} - \mathbf{V_0}, \qquad P_b = P - P_0. \tag{74}$$

If we assume that this bubble flow field ($\mathbf{V_b}$ and P_b) is potential, we can use a method similar to the one described in the previous section to study the dynamics. This assumption implies that, even though the basic flow is allowed to interact with the bubble dynamics and be modified by it, no new vorticity is allowed to be generated by the bubble behavior. Within this restriction, we have

$$\mathbf{V_b} = \nabla \phi_b, \qquad \nabla^2 \phi_b = 0. \tag{75}$$

By subtracting (72) from (71), and accounting for (74) we obtain

$$\nabla \left[\frac{\partial \phi_b}{\partial t} + \frac{1}{2}\mathbf{V_b}^2 + \mathbf{V_0} \cdot \mathbf{V_b} + \frac{P_b}{\rho} \right] = \mathbf{V_b} \times (\nabla \times \mathbf{V_0}). \tag{76}$$

This equation, once integrated, may be considered the equivalent of the classical unsteady Bernoulli equation in potential flow. As an illustration consider the case where the basic flow field is that of a two-dimensional Rankine vortex, $\mathbf{V_0} = V_\theta \mathbf{e_\theta}$, with

$$V_\theta = \frac{\Gamma}{2\pi r}; \qquad r \geq a_c;$$

$$V_\theta = \omega r = \frac{\Gamma r}{2\pi a_c^2}; \qquad r \leq a_c, \tag{77}$$

where a_c is the radius of the viscous core, Γ the vortex circulation and V_θ the tangential velocity. In that case the Bernoulli equation can be replaced by:

$$\frac{\partial \phi_b}{\partial t} + \frac{1}{2}|\mathbf{V_b}|^2 + \frac{P_b}{\rho} = \text{constant along radial direction.} \tag{78}$$

Accounting for at-infinity conditions, the pressure at the bubble wall, P_L, is related to the pressure field in the Rankine vortex, P_0, by:

$$\left[\frac{P_L}{\rho} = \frac{P_O}{\rho} - \frac{\partial \phi_b}{\partial t} - \frac{1}{2}|\mathbf{V_b}|^2 \right]_{at\ bubble\ wall} \tag{79}$$

The nondimensional basic flow pressure, $\overline{P}_0$, normalized with the ambient pressure, P_∞, is known and is given by:

$$\overline{P}_O(\overline{r}) = 1 - \Omega\left[1 - \frac{1}{2}\left(\frac{\overline{r}}{\overline{a}_c}\right)^2\right]; \qquad \overline{r} \leq \overline{a}_c$$

$$\overline{P}_O(\overline{r}) = 1 - \frac{\Omega}{2}\left(\frac{\overline{a}_c}{\overline{r}}\right)^2; \qquad \overline{r} \geq \overline{a}_c,$$

where lengths are normalized by R_{max}, the maximum radius the bubble would achieve in an infinite medium if the pressure drops to the value on the vortex axis. The swirl parameter Ω, defined as,

$$\Omega = \frac{\rho}{P_\infty}\left(\frac{\Gamma}{2\pi a_c}\right)^2, \tag{80}$$

characterizes the intensity of the rotation-generated pressure drop relative to the ambient pressure. The pressure on the vortex axis is $(1 - \Omega)$ and goes to zero if $\Omega = 1$.

9 Computational Results and Discussion

We present in this section some results obtained with the Boundary Element Method code (3DynaFS), and compare them with results from the asymptotic expansion method. The accuracy of the numerical code was evaluated by using simple test cases known in the literature such as the collapse of spherical and axisymmetric bubbles. For spherical bubbles, comparison with the Rayleigh-Plesset "exact" solution revealed that numerical errors were less than 0.14 percent for a discretized bubble of 162 nodes. The error dropped to 0.05 percent for 252 nodes. The two discretizations - 162 nodes (320 triangular panels) or 252 nodes (500 panels) - are usually selected for most of our nonspherical bubble dynamics runs. However, for the purpose of studying multibubble interactions we were limited to 102 node bubbles (200 panels) due to the limitations of our 32 MBytes MIPS RC3240 computer. For an 8-bubble configuration the code uses about 30 MBytes for 102-node bubbles. With this "coarse" discretization the error is about 2 percent on the achieved maximum radius, but is very small, 0.03 percent, on the bubble period. (This can be seen in figure 9). Comparisons were also made with studies of axisymmetric bubble collapse available in the literature [8, 4], and have shown, for the coarse discretization, differences with these stud-

ies on the bubble period of the order of 1 percent. Finally, comparison with actual test results of the complex three-dimensional behavior of a large bubble collapse in a gravity field near a cylinder shows very satisfactory results, [15] (see Figure 8). The observed difference in the period was shown to be related to the confinement of the experimental bubble in a cylindrical container [27].

Figure 9 compares the results obtained with the 3D code with those given by the asymptotic approach. The bubble cloud is subjected to a sudden pressure drop, and for ease of interpretation, only symmetric cloud configurations are considered. Results for one, two, four and eight-bubble symmetric configurations are shown. For the two-bubble case the bubble centers are separated by a distance l_0, and the initial gas pressure in each bubble is such that the bubble would achieve a maximum radius $R_{max} = R_{b0} = 0.07 l_0$ if isolated. The four-bubble configuration considers similar bubbles centered on the corners of a square with sides of dimension l_0. Finally, the eight bubbles are located on the corners of a cube of side l_0. The figure presents the variations with time of the distance between an initial bubble center and both the point closest to (< 0), and the point farthest (> 0) from the "cloud center". These points are selected because they lie along the direction of development of the reentrant jet the farthest point becoming the tip of the jet which penetrates the bubble during the collapse. As we can see from the figure, the BEM method clearly shows that for bubbles *oscillating in phase* the period of oscillation increases with the number of interacting bubbles. The maximum bubble size along the jet axis is however not significantly modified. The jet advancement towards the "cloud center" increases with the number of bubbles. This is seen by the crossing of the $r = 0$ line by the upper curves on the graph which becomes more and more pronounced with an increase in the number of bubbles. This effect is more pronounced for larger values of ϵ (see Figure 10).

Figure 9 also compares the results of the BEM code with the asymptotic approach. It illustrates the limitations of the incompressible asymptotic approach as it stands now. When the number of bubbles increases the method diverges towards the end of the collapse and predicts either a much faster collapse than obtained with the more accurate BEM method (N=2 and 4), or an unexplained early bubble rebound ($N = 8$). This behavior occurs earlier when either the number of bubbles or the value of ϵ increases.

Figure 10 shows the influence of ϵ on the bubble dynamics for a 4-bubble configuration. Using the BEM 3D results enables one to study the influence of reducing bubble inter-distance on the dynamics of each bubble. Increasing the proximity between the bubbles, or increasing the number of bubbles is seen to increase the lengthening effect on the bubble period, while enhancing the reentrant jet formation, as in the more classical case of bubble collapse near a solid wall. In all cases, the reentrant jet formed is directed towards the center of the bubble cloud, or here, the center of the square. As expected, the asymptotic approach gives a very good approximation at low values of ϵ, but fairs poorly for high values of ϵ (note that for $\epsilon = 0.5$ the bubbles touch at their maximum size). The above conclusions on the asymptotic approach have to be tempered by the fact that all cases presented addressed relatively intense bubble collapse (with a strong reentrant jet formation). The relevant nondimensional parameter to characterize the collapse intensity is the ratio, $\mathcal{P}_{gm}$, of the gas pressure to the outside pressure at maximum bubble size. This ratio is about 0.06 for the cases shown above. For higher values of $\mathcal{P}_{gm}$ a smoother collapse followed by a rebound occurs, and the asymptotic approach fairs much better [28]. Figures 11 and 12 illustrate further the three-dimensional behavior of the bubble, using 198-node bubbles. Figure 11 shows two cross-sectional views of the bubble shapes at various times during the collapse for a strong interaction case ($\epsilon = 0.498$), for a 4-bubble configuration. The first view shows bubble contours in the $Z = 0$ plane, plane of the four bubble centers. In this plane all four bubbles can be seen, and the reentrant jet appears very wide giving the bubble at the end of the collapse the appearance of a "deflated balloon". The second view is a diagonal cut though the centers of two of the bubbles. In this view, the reentrant jet appears much more pronounced. The combination of the two views illustrates very clearly the reentrant jet formation, its direction towards the center of the square, and gives a qualitative idea about the intensity of the collapse. In this case, due the geometry of the configuration, the jet has a two-dimensional flat shape, rather than a conical axisymmetric shape. This clearly provides one reason for the failure of the asymptotic approach for this case, since the expansions in that approach were stopped to an order (ϵ^3) which does not allow the description of any azimuthal bubble shape variations. Figure 12 presents a 3D view of the bubbles towards the end of a relatively weak collapse of a 4-bubble configuration ($\epsilon = 0.185$). Since the case shown is symmetrical and all bubbles have the same shape, this diagonal view can be interpreted as showing the shape of the same bubble from different view angles. The reentrant jet is here again seen to be wide, pointed, and well advanced towards the other side of the bubble. A complete history of the advancement of the jet in the bubble can be deduced from figure 10. Figures 13 through 17 illustrate various important effects due to either asymmetries in the bubble configuration, or due to the presence of an underlying nonuniform flow. Figure 13 shows the case of an asymmetric five bubble configuration. All bubbles have the same initial radius and internal pressure, and are initially spherical and located in the same plane. The most visible effect observed is that on the center bubble. Its growth is initially similar to that of the other bubbles, but it ends up being

the least deformed. Later on, as the collapse phase advances with the development of a reentrant jet directed towards the central bubble, this bubble appears to be shielded by the rest of the cloud. Its period appears to be at least double that of the other bubbles. Unfortunately, the code cannot presently follow the dynamics beyond this point since it fails following the touchdown of the first reentrant jet on the other bubble side. Here, this occurs before any significant progress of the collapse of the central bubble is observed. The issue of continuing the computations beyond this point is clearly important and is presently the subject of an ongoing research at DYNAFLOW. Reference [30] gives results of our first attempt towards solving this problem. Figure 14 shows a 4-bubble configuration where the bubbles are centered on the corners of a square. All bubbles were chosen so that they would behave identically if in an infinite medium. However, a time delay between the bubble oscillations was imposed. As a result, at $t = 0$ the bubbles had relative initial sizes in the ratios $2, 1, 3, 1$ counter-clockwise starting from the bubble centered at the origin. This results in a very asymmetric behavior of the cloud configuration. The bubble periods appear to be lengthened the most for the larger bubbles at $t = 0$. The "delayed" bubbles (the smaller at $t = 0$) are prevented by the other bubbles from growing significantly, and end up collapsing very early in their history. These bubbles on the other hand significantly influence the "earlier" ones by increasing at some point the pressure drop these bubbles sense and then by preventing them later on from collapsing. Since the code presently breaks down before a significant collapse, we can only speculate that a very strong collapse of the larger bubbles would ensue, because of the large pressure produced by the collapse of the smaller bubbles. This can be illustrated by observing the modification of the imposed pressure drop by the behavior of an individual bubble. As shown in figure 15, the bubble growth initially reduces the effective pressure drop that would be felt by a second bubble at the distance l_0, this trend is later reversed, and is followed by a significant pressure rise during the bubble collapse.

Figure 16 shows the three-dimensional behavior of a bubble in a line vortex. The bubble is initially positioned at a distance of $2R_{max}$ from the vortex axis located at $\overline{X} = 2$. The normalized core size is 4 in this case. Figure 16*a* gives a view in the XOY plan of the bubble at different instants. The bubble is seen spiraling around the vortex axis (perpendicular to the figure) while approaching it. At the same time, due to the presence of the pressure gradient, the bubble strongly deforms and a reentrant jet is formed directed towards the axis of the vortex. Figure 16*b* shows the same bubble seen from the OX axis. Here some elongation is observed along the axis of the vortex as well as a very distinct side view of the re-entrant jet. This result is totally contrary to the usually held belief that bubbles constantly grow during their capture until they reach the axis and elongate along it. Finally, Figure 17 shows in the XOY plane perpendicular to the vortex axis the motion of two particular points on the bubble, A and B, initially along OY. Also shown is the motion of the mid point, C. While C seems to follows a path similar to the classical logarithmic spiral, A and B follow more complicated paths, even moving away from the vortex axis at some point in time.

Figures 18 and 19 , address the behavior of a bubble near a solid wall in the presence of a nonuniform flow field and as a result of a relative velocity between the bubble and the flow. In the example shown a simple linear velocity profile is used to simulate the the boundary layer flow near the wall in which the bubble dynamics is considered. The *basic* flow velocity varies from a value, V_{shear} at a distance r_{b0} from the wall to zero at the wall. The *basic* pressure is assumed constant across the shear layer and is an input of the problem, P_{amb}, as is the initial gas pressure inside the bubble, P_{g0}. The bubble center is located at a distance l_0 from the wall, the ratio r_{b0}/l_0 being a key parameter characterizing the bubble / wall interaction. Here, another important parameter is the ratio between the characteristic *shear velocity* and a characteristic bubble dynamics velocity [16], for instance $\chi = V_{shear}/\sqrt{\Delta P/\rho}$. Figure 18 shows an example of bubble growth and collapse shape contours obtained with **3DynaFS** near a solid wall in the absence of shear. Figure 19 shows for the same conditions the bubble collpase in the presence of the nonuniform flow. A very significant effect of the wall flow is seen on the development of the reentrant jet. The jet is seen to be much weakened and delayed. Since we have made these *numerical* observations in 1990 in [16], tests conducted by other researchers in the Large Cavitation Channel appears to confirm experimentally at least some aspects of these observations.

Figure 20 shows the strong interaction between a growing and collapsing bubble and a vortex ring. Figure 20a shows a high speed movie sequence where the vortex ring, the axis of which is on the left edge of the successive pictures, was generated using the impulsive motion of a piston in a tank where a reduced ambient pressure was imposed [45]. The bubble was spark-generated using submerged electrodes positionned where the initial bubble center is sought. The figure shows that the bubble grows initially almost spherically, then the shear flow due to the vortex ring becomes very important leading to a stretching and elongation of the bubble along a stream line of the vortex flow. The bubble then collapses in a very unusual manner producing a constriction along the vortex flow line, then decomposing into two bubble clouds. A set of various bubble / vortex interaction intensities is presented in [45]. Figure 20b is a direct numerical simulation of the experimental case shown in figure 20a. The vortex ring flow was simulated assuming a Rankine model and a viscous core size as observed from other tests where microbubble motion inthe vortex flow were visualized. Given such a crude

model of the vortex ring and given that the modification of the vortex flow by the bubble dynamics neglected, the similitude between the numerical simulation and the experimental result is quite satisfactory and is able to capture most of the feature of the bubble behavior. An improved viscous model and the inclusion of the *basic* flow modification will enable an even better correspondence. The study of such an interaction is essential to the understanding of the the interaction between microbubble and large organized viscous structures which occur in boundary layers. These interactions are expected to be much more significant at full scale than in the laboratory, particularily due to a significant increase of the ratio between hydrodynamics scales and bubble scales.

10 Conclusions

In this contribution the dynamics of the interaction between bubbles and nearby boundaries (other bubbles or complex geometries) or nonuniform flows was considered using an asymptotic method and a three-dimensional Boundary Element model. Both approaches enabled us to address aspects of the bubble dynamics that have been ignored to date due to their mathematical difficulty. The asymptotic approach, valid for the case of *weak* interactions, enables a better understanding of the general trends without recourse to an extensive analysis of test cases, since it provides analytical expressions from parts of the solutions. On the other hand direct 3D simulation have the advantage of enabling the study of *strong* interactions where the asymptotic expansion metod fails. Comparison of the two methods provides a means of mutual validation of the methods.

From the application of both methods the following conclusions can be drawn from the study:

1. When compared to the dynamics of a single bubble, significant modification of the bubble dynamics and shape is observed for multibubble interaction. For identical bubbles acting in concert, an increase in the bubble period is observed without significant modification of the bubble maximum size when the number of bubbles increase or when their separation distance decreases.

2. A shielding effect of the bubbles was observed leading to an increased period and maximum size of the bubbles in the center of the cloud.

3. While very large pressures are computed using the asymptotic method with bubble clouds composed of the same size bubbles, more moderate pressures are obtained when the bubbles are not exactly in phase and when large deformations are taken into account.

4. Bubble collapse near a solid wall and in the presence of a nonuniform flow field is seen to be significantly modified by the presence of this flow field. Reentrant jet formation is seen to be delayed and weakened when not eliminated.

5. Bubble capture, growth and collapse in a line vortex flow field is seen to involve significantly non spherical effects which have been systematically neglected by previous studies. For instance, noise generation at the inception of tip vortex cavitation can probably be explained by the deformation, collapse and splitting of the bubble while being captured.

6. The study of the interaction between bubbles and large organized structures provides some hints about the complexity of bubble dyanmics in real full scale flow fields.

On-going areas of improvement of this study include extension of the asymptotic approach to the case of a compressible fluid and coupling of the multibubble approach to a two-phase medium model. The Boundary Element Method approach is being improved to include the full description of the reentrant jet piercing of the bubble and its subsequent advancement in the fluid. The 3D code **3DynaFS** is also being exercised on a Cray Y-MP and implemented on a parallel Connection Machine in order to significantly improve computation time, and to allow practical consideration of a much larger number of elements than at present.

Acknowledgments

We would like to acknowledge the support of the Office of Naval Research, Contract N00014-89-C-0025, and the interest and technical discussions with Dr. Edwin Rood. The authors would like to acknowledge the many contributions and significant discussions of several colleagues at DYNAFLOW, INC.

References

[1] YOUNG, F.R., "Cavitation," *McGraw-Hill, London.* 1989.

[2] ROOD, E.P., "Review - Mechanics of cavitation inception," *ASME Journal of Fluids Engineering*, Vol. 113, 163-175, 1991.

[3] HAMMITT, F.G., *Cavitation and Multiphase Flow Phenomena*, McGraw-Hill, New York, 1980.

[4] BLAKE, J. R, AND GIBSON, D. C., "Cavitation Bubbles Near Boundaries," *Annual Review of Fluid Mechanics*, Vol. 19, pp. 99-123, 1987.

[5] RAYLEIGH LORD,"On the Pressure Developed in a Liquid During Collapse of a Spherical Cavity," *Phil. Mag.*, pp. 34, 94-98, 1917

[6] BESANT, W., "A Treatise on Hydrodynamics", *Cambridge University Press*, pp. 198, 1859.

[7] SHIMA, A. AND NAKAJIMA, K., "The Collapse of a Non-Hemispherical Bubble Attached to Solid Wall," *Journal of Fluid Mechanics*, Vol. 80, pp. 369-391, 1977.

[8] GUERRI, L., LUCCA, G., AND PROSPERETTI, A., "A Numerical Method for the Dynamics of Non-Spherical Cavitation Bubbles," *Proceedings 2nd International Colloquium on Drops and Bubbles, JPL Publication 82-7, Monterey CA*, Nov 1981.

[9] CHAHINE, G. L., "Experimental and Asymptotic Study of Nonspherical Bubble Collapse," *Applied Scientific Research*,38, pp. 187-197, 1982.

[10] VAN WIJNGAARDEN, L. , "On the Collective Collapse of a Large Number of Gas Bubbles in Water," *Proceedings of the 11th International Congress of Applied Mechanics, Springer, Berlin*, pp. 854-865, 1964.

[11] CHAHINE, G.L., "Cloud Cavitation: Theory," *14th Symposium on Naval Hydrodynamics, Ann Arbor, Michigan, National Academy Press, Washington, D.C.*, pp. 165-195. 1983.

[12] D'AGOSTINO, L. AND BRENNEN, C.E.,"On the Acoustical Dynamics of Bubble Clouds," *ASME Cavitation and Polyphase Flow Forum, Houston, Texas*, pp. 72-76. 1983.

[13] KUMAR, S. AND BRENNEN, C.E., "Some nonlinear interactive effects in bubbly cavitation clouds," submitted to *Journal of Fluid Mechanics*.

[14] CHAHINE, G.L. AND PERDUE, T.O., "Simulation of the Three-Dimensional Behavior of an Unsteady Large Bubble Near a Structure," *Proc. 3rd Int. Coll. on Drops and Bubbles, Monterey CA, Sept. 1988.*

[15] CHAHINE, G.L., "A Numerical Model for Three-Dimensional Bubble Dynamics in Complex Geometries," *22nd American Towing Tank Conference, St. Johns, Newfoundland, Canada, August 1989.*

[16] CHAHINE, G.L., "Numerical Modelling of the Dynamic Behavior of Bubbles in Nonuniform Flow Fields," *ASME 1990 Cavitation and Multiphase Flow Forum, Toronto, Canada*, 1990.

[17] CHAHINE, G.L., "Nonspherical bubble dynamics in a line vortex," Proceedings of ASME Cavitation and Multiphase Flow Forum, Toronto 1990,(ed. O. FURUYA) *ASME*, pp. 121-126, 1990.

[18] CHAHINE, G. L. AND LIU, H. L.,"A Singular Perturbation Theory of the Growth of a Bubble Cluster in a Super-heated Liquid," *Journal of Fluid Mechanics*, Vol. 156, pp. 257-274, 1985.

[19] KALUMUCK, K.M. AND CHAHINE, G.L, "The Influence of Gas Diffusion on the Growth of a Bubble Cloud," *ASME Cavitation and Multiphase Flow Forum, Cincinnati, Ohio*, pp. 17-21, June 1987.

[20] PLESSET, M.S. AND PROSPERETTI, A., "Bubble Dynamics and Cavitation," *Annual Review of Fluid Mechanics*, Vol. 9, pp. 145-185, 1977.

[21] PROSPERETTI, A. AND LEZZI, A.M., "Bubble Dynamics in a Compressible Liquid. Part 1. First Order Theory." *Journal of Fluid Mechanics* 168, pp. 457-478, 1986.

[22] REBUT, M. AND CHAHINE, G.L., "Asymptotic Study of Bubble Dynamics in a Nonuniform Potential Flow", ASME Cavitation and Multiphase Flow Forum, Los Angeles 1992.

[23] DURAISWAMI, R. AND CHAHINE G.L., "Analytical study of a gas bubble in the flow field of a line vortex," *ASME Cavitation and Multiphase Flow Forum, Los Angeles 1992.*

[24] HERRING, C., "Theory of the Pulsations of the Gas Bubble Produced by an Underwater Explosion" *Columbia University NDRC Reo. C-4 SR 20-010*, 1941.

[25] CHAHINE, G. L., "Pressure Field Generated by the Collective Collapse of Cavitation Bubbles," *Proceedings, IAHR Symposium on Operating Problems of Pump Stations and Power Plants, Amsterdam, Holland*, 2-1, pp. 1-12., 1982.

[26] G.L. CHAHINE, K.M. KALUMUCK, AND T.O. PERDUE, "Cloud Cavitation and Collective Bubble Dynamics," *Tracor Hydronautics, Technical Report 83017-1*, 1986.

[27] CHAHINE, G. L., PERDUE, T. O. AND TUCKER, C.B., "Interaction Between an Underwater Explosion Bubble and a Solid Submerged Body," *DYNAFLOW, Inc. Technical Report 89006-1*, 1989.

[28] CHAHINE, G.L. AND DURAISWAMI, R. "Dynamical Interactions in a multi-bubble cloud." in "Proceedings of the ASME Cavitation and Multiphase Flow Forum, Portland 1991" (ed. O. FURUYA) *ASME*, 49-54, (also *To appear in the Journal of Fluids Engineering*), 1991.

[29] DURAISWAMI, R. AND CHAHINE, G.L., "Multiple bubble dynamics in a slightly compressible liquid," *in preparation.*

[30] ZHANG, S., DUNCAN, J., AND CHAHINE, G.L., "Dynamics of a bubble past the point of collapse," *Asme Cavitation and Multiphase Flow Forum, Los Angeles, 1992.*

[31] SNAY, H.G., GOERTNER J.F., AND PRICE, R.S.,, "Small Scale Experiments to Determine Migration of Explosion Bubbles Towards Submarines," *Navord Rep. 2280*, 1952.

[32] CHAHINE, G.L,"Dynamics of the interaction of nonspherical cavities," in "Mathematical approaches in hydrodynamics," ed. T. MILOH, *SIAM, Philadelphia*, 1991.

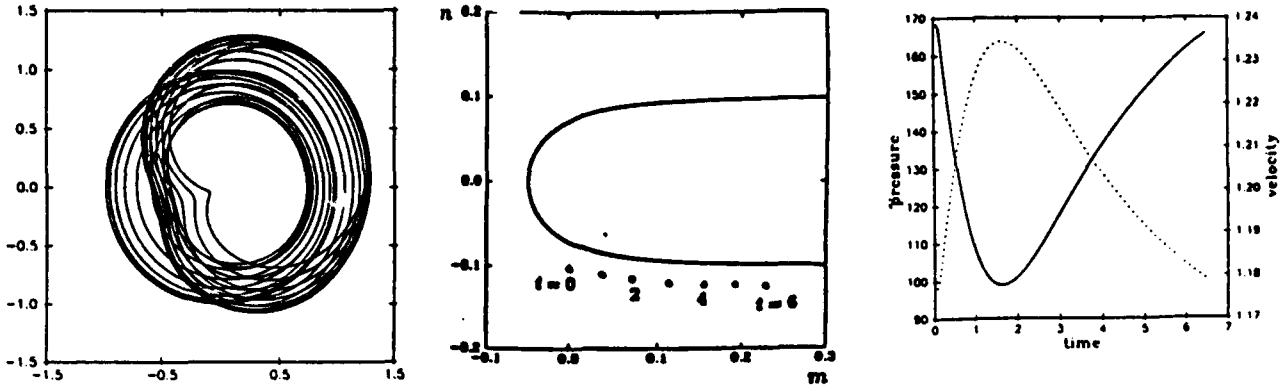

a b c

Figure 1a-c: Fig. 1b and Fig. 1c show the geometry and flow field of the problem considered. The trajectory of the bubble center along the headform (of radius 10 cm) is indicated in Fig. 1b. The pressure (in Pa - y axis) and the velocity (in ms^{-1} - right y axis) of the basic flow along this streamline, are plotted against the non-dimensional time. The free stream velocity is 1.15 ms^{-1}. Fig. 1a shows the computed bubble contours for $\epsilon = 0.3$, and time between $0.1T_0$ to $2T_0$. Bubble translation, rotation and re-entrant jet formation are clearly seen.

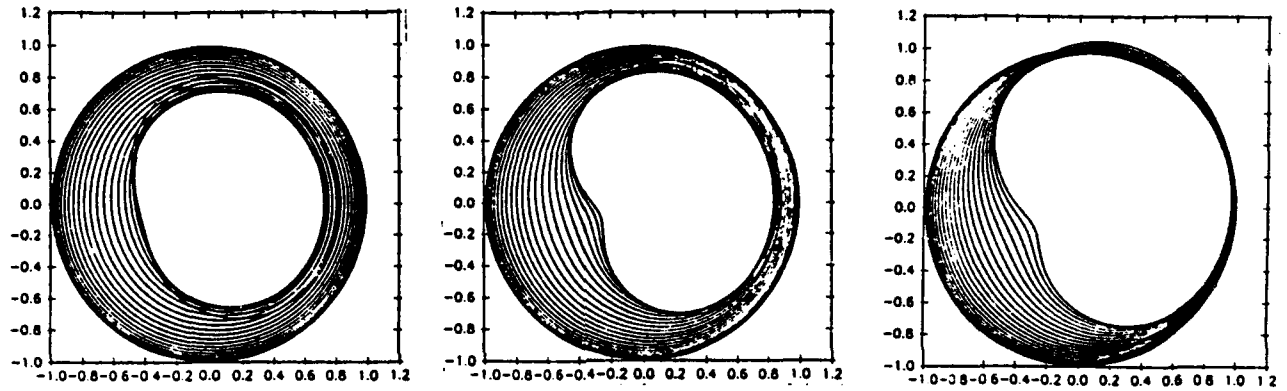

a b c

Figure 2a-c: Bubble contours at various times for $\epsilon = 0.15, 0.3$ and 0.6. Here the initial bubble radius was kept constant at 1 cm, while the initial standoff from the head form was varied to change ϵ. Increasing interaction is seen with decreasing standoff.

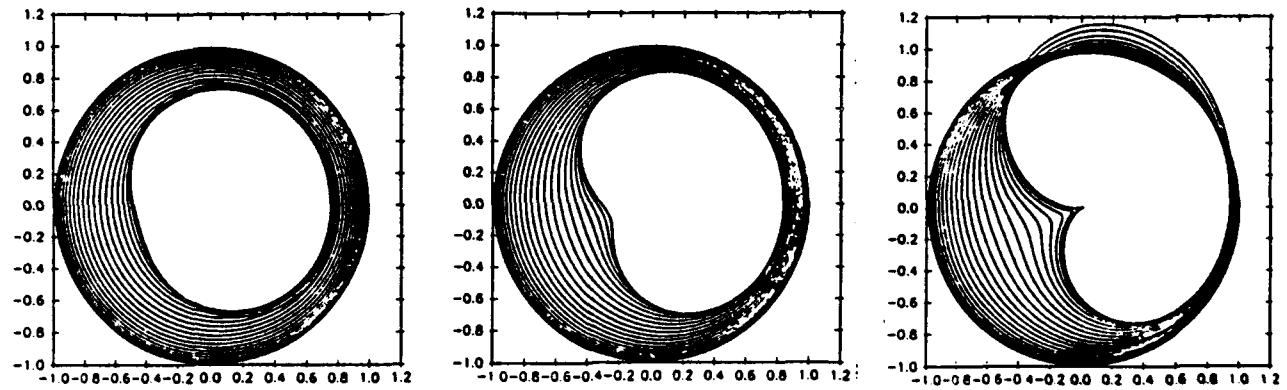

a b c

Figure 3a-c: Bubble contours at various times for $\epsilon = 0.15, 0.3$ and 0.6. Here the initial standoff distance l_0 was kept constant at 3.333 cm, while the initial radius was varied to change ϵ. Increasing interaction is seen with increasing initial bubble size.

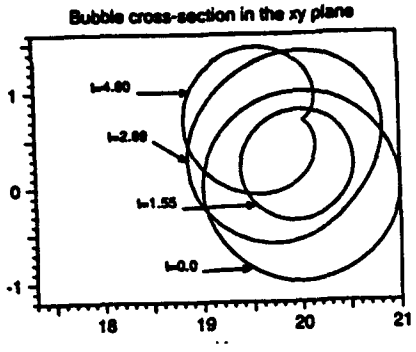

Figure 4:

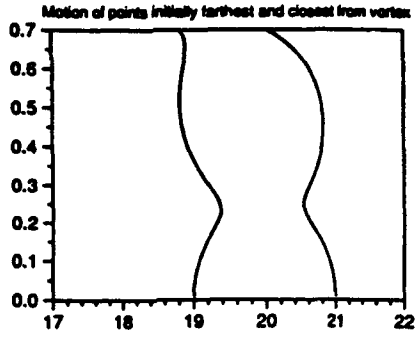

Figure 5:

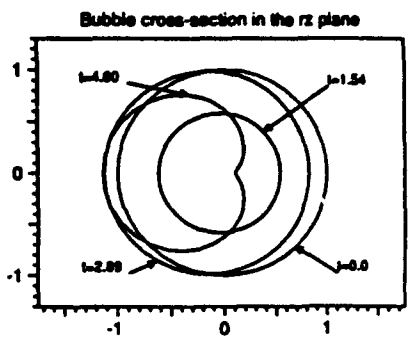

Figure 6:

Figures 4-6: The interaction of the bubble with a line vortex is shown in these figures (see Section 5). Fig. 4 shows the cross-section of the predicted bubble shape in the $x-y$ plane (normal to the vortex axis). The vortex passes through $(x,y)=(0,0)$ along the z axis (normal to the plane of the paper). Fig. 5 indicates the motion of the points initially farthest from and closest to the vortex axis in Fig. 4. Fig. 6 shows the cross-section of the predicted bubble shape in a plane containing the vortex line and the center of the moving coordinate system. The vortex axis is at -20, on the abscissa.

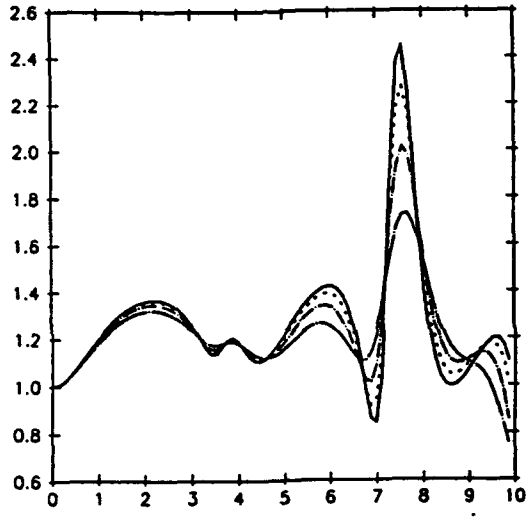

Figure 7: Influence of compressibility on the dynamics of a 6-bubble cloud. The figure shows $R(\theta_{ij}=0,t)$ vs. time for one bubble. The bubbles have an initial radius of 0.01 cm and are arranged at equal distances from the origin along the coordinate axes, so that $\epsilon=0.07$. The bubbles are at equilibrium at $t=0$ when they are subjected to a sudden pressure drop. Here $\mathcal{P}=2.0$, and $\mathcal{W}=679$. The solid line indicates the incompressible solution. Also plotted is the corresponding curve for $\mathcal{M}$ =0.01 (small dashes), $\mathcal{M}$ =0.03 (small dash-dot), and $\mathcal{M}$ =0.07 (dash-dot). The strong effect of increasing compressibility can be seen.

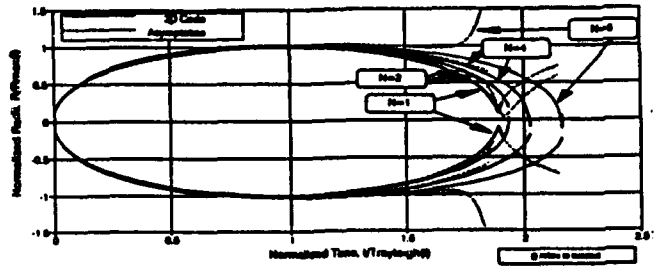

Figure 9: Motion of the bubble points farthest and closest to the cloud center versus time for 1,2,4 and 8-bubble symmetric configurations. Comparison between 3D code results and the asymptotic analysis. $\epsilon=0.07$, $P_{g0}/P_{amb}=283$.

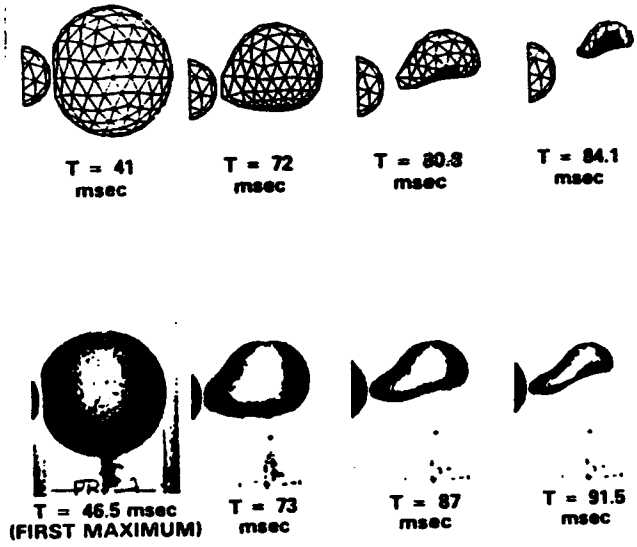

Figure 8: Large bubble collapse near a cylinder. Comparison between our three-dimensional BEM code and the experimental results of Goertner *et al.*

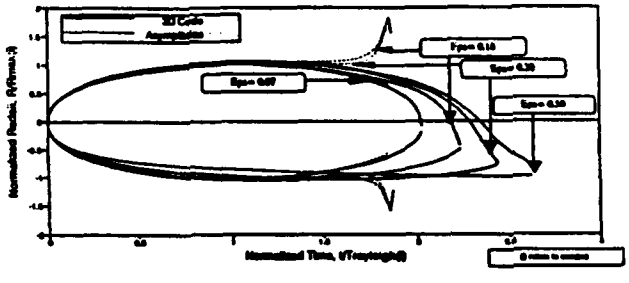

Figure 10: Motion of the bubble points farthest and closest to the cloud center versus time for a 4-bubble symmetric configuration. Comparison between 3D code results and the asymptotic analysis. Influence of bubble proximity or ϵ. $P_{g0}/P_{amb}=283$.

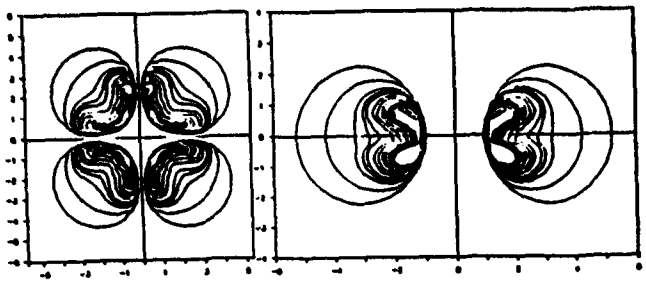

Figure 11: Bubble contours during collapse of a 4-bubble configuration. a) Cross sectional view in the plane $Z = 0$. b) Cross sectional view in the plane $Y = X$. $\epsilon = 0.498$ based on the maximum radius. Note the non-axisymmetric shape of the jet during collapse.

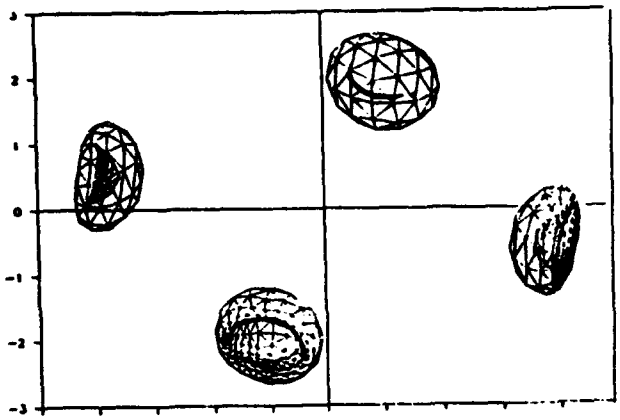

Figure 12: Bubble Contours for the collapse of a 4-bubble cloud for $\epsilon = 0.185$. Since the case shown is symmetrical and all bubbles have the same shape, this diagonal view can be interpreted as showing the shape of the same bubble from different view angles.

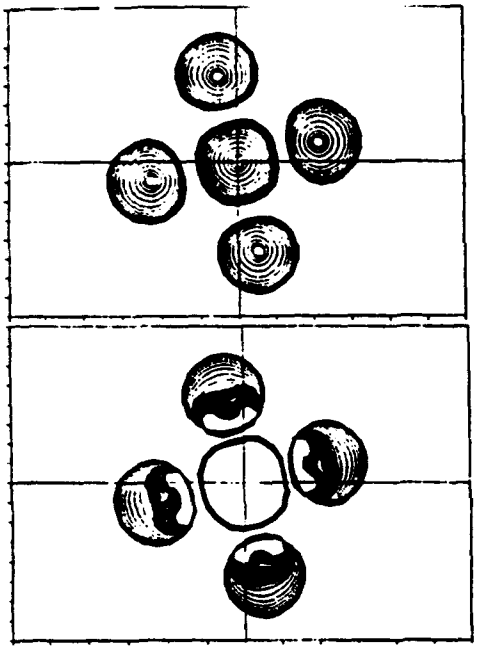

Figure 13: Growth and collapse of 5 bubbles having the same initial size and internal pressure. Influence of the initial bubble geometry on dynamics. $\epsilon = 0.474$ based on the maximum radius. The center bubble is seen to have a remarkably different behavior.

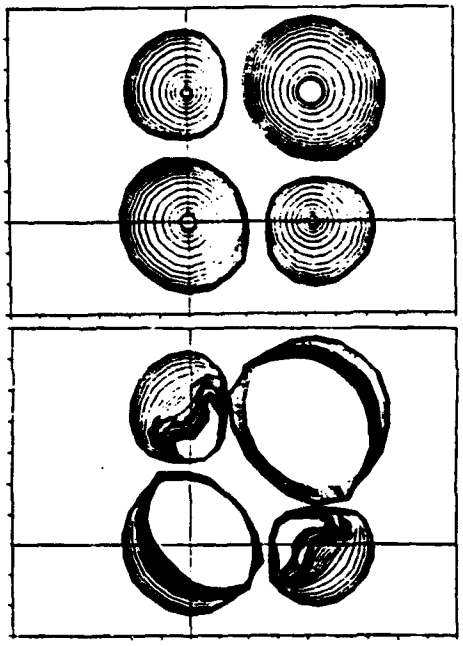

Figure 14: Growth and collapse of 4 identical bubbles initially symmetrically distributed but with different initial radii (2,1,3,1 clockwise starting from origin). The figure shows the influence of 'phasing' on the dynamics.

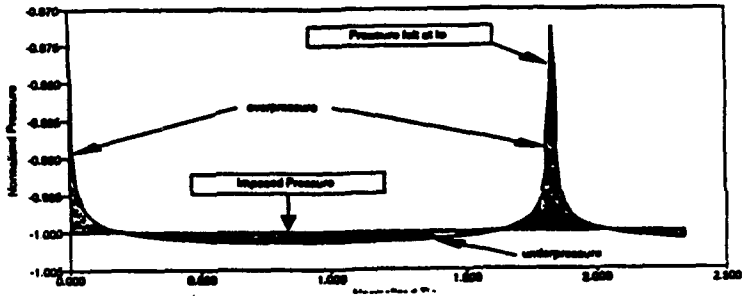

Figure 15: Pressure at distance l_0 from a bubble following a sudden pressure drop. $\epsilon = 0.3$, $P_{g0}/P_{amb} = 283$.

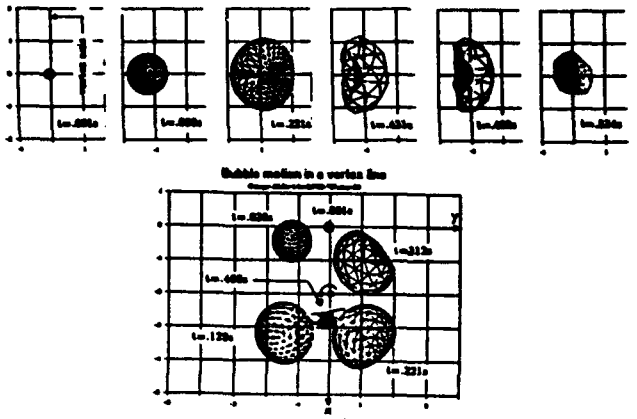

Figure 16:

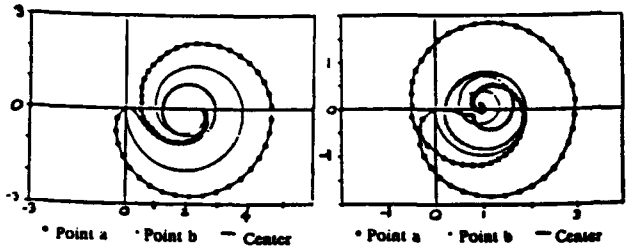

Figure 17:

Figure 16-17: These figures show bubble vortex interaction for $\Omega = 0.948$, $a_c = 4R_{max}$, and $P_{g0}/P_{amb} = 584$. Figure 16 shows three dimensional bubble shapes at various times during bubble capture in a vortex line. a) View in the XOY plane. b) View in the XOZ plane. Figure 17 shows the motion of the two bubble points initially on axis OY and their mid-point vs. time. a) Vortex at $X = 2$. b) Vortex at $X = 1$.

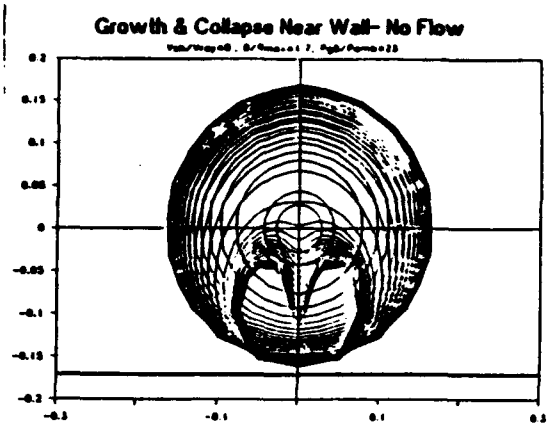

Figure 18:

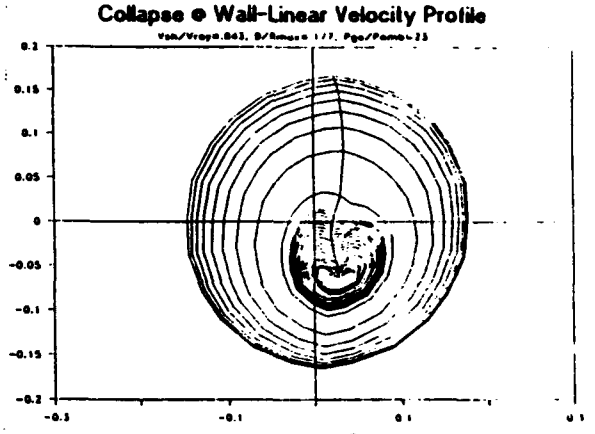

Figure 19:

Figure 18-19: These figures show the influence of a shear flow in the growth and collapse of a bubble in the vicinity of a wall. $P_{g0}/P_{amb} = 23$. $L/R_{max} = 1.77$ Fig. 18 shows a case where and there is no shear flow. Fig. 19 shows the same case for $V_{shear}/V_{Rayleigh}$=0.042.

STRONG INTERACTION BETWEEN A BUBBLE AND A VORTEX STRUCTURE

Figure 20: Comparison of 3D BEM simulation and high speed movie sequence for the interaction between a bubble and a vortex ring. The bubble is spark generated and the vortex ring piston generated.

ASME *J. Fluids Engg.*, vol. 114, 1992.

Dynamical Interactions in a Bubble Cloud

GEORGES L. CHAHINE,[1] RAMANI DURAISWAMI, A.N. LAKSHMINARASIMHA
DYNAFLOW, Inc.
10422 Mountain Quail Road
Silver Spring, MD 20901.

1 Introduction

Practical liquid flows contain many microscopic bubbles which respond dynamically to the flow. These bubbles can grow explosively and collapse, leading to cavitation and all its deleterious effects [1,2]. These bubbles seldom occur singly, and their mutual interaction is likely to play an important part in the fluid dynamics. However, most previous studies consider only the problem of single bubbles (including only spherical or axisymmetric deformations in their models), or consider highly simplified models of multiple bubble interactions. To study cavitation in practical flows one needs to be able to properly model these interactions. Mathematically the problem is a difficult one, as it is intrinsically three-dimensional, and involves multiple free surfaces (with the associated non-linearity). Purely analytical progress into the problem is clearly out of reach presently.

Our studies into this subject have proceeded along two different paths. In the first, [3-7,13,14], an asymptotic approach was employed, using the assumption that the characteristic inter-bubble distance was large compared to characteristic bubble size. Solutions valid to the third order in this parameter were obtained. Our more recent efforts have been devoted to the development of a completely three-dimensional boundary element method capable of handling multiple free-surfaces, and rigid surfaces and particles. A computer program (3DynaFS) implementing the method has been developed. It has been applied to problems involving single bubbles in a variety of configurations, and more recently to problems involving several bubbles and where the bubbles are in either a shear flow or in the flow field of a Rankine vortex [8-12].

In this paper we present some preliminary results from numerical experiments with the code 3DynaFS. We study a number of flows involving a few bubbles, with particular emphasis on the effects of various parameters on bubble growth and collapse. Additionally the "exact" numerical solutions from the boundary element technique are used to obtain a domain of validity for the asymptotic studies.

2 Mathematical Formulation

Consider an incompressible liquid in an infinite domain (this restriction can be relaxed to allow rigid boundaries or other free surfaces within the domain). Distributed in this liquid are N bubbles, numbered $1, \ldots N$. Since we shall be concerned with cavitation bubbles where relatively large wall velocities are involved, viscosity has no appreciable effect on the dynamics of the bubble. Additionally we restrict the case to flows where the Mach number is small enough so that the incompressibility assumption holds. (We are currently working to relax this assumption).These two assumptions are classical in cavitation bubble studies, and with suitable initial conditions the flow is irrotational. Following standard procedure we introduce a velocity potential ϕ, in terms of which the conservation laws in the liquid may be stated in the form

$$\nabla^2 \phi = 0 \tag{1}$$

and

$$P + \rho \left(\frac{\partial \phi}{\partial t} + \frac{1}{2} |\nabla \phi|^2 \right) = \text{constant} \tag{2}$$

Here (2) is the Bernoulli integral of the momentum equation. We shall study the reaction of this system to a prescribed pressure field at infinity, $P_\infty(t)$. These equations are subject to initial conditions for the potential, and boundary conditions on the surfaces of the bubbles (and on any rigid surfaces in the domain). At all boundaries we impose the condition that the surface is a material surface and moves with the flow, so that

$$\mathbf{n} \cdot \nabla \phi = \mathbf{n} \cdot \mathbf{V}_s, \tag{3}$$

where $\mathbf{V}_s$ is the velocity of the surface, and $\mathbf{n}$ is the local unit vector normal to the surface. In addition on the surface of the bubble we must balance the normal stresses in the liquid and the gas. The bubble is assumed to contain both non-condensible gas and vapor. Within the bubble the pressure is assumed not to vary spatially, and to be given by the sum of the partial pressures of the noncondensible gases, P_g, and that of the vapor, P_v. Vaporization of the liquid is assumed to occur at a fast enough rate so that the vapor pressure can be assumed constant throughout the simulation and equal to the equilibrium vapor pressure at the liquid ambient temperature. Since time scales associated with gas diffusion are much larger than those of interest, the amount of non-condensible gas inside the bubble is assumed to remain constant. This gas is assumed to satisfy the polytropic relation, $PV^k = constant$, where V is the bubble volume, and k the polytropic index, with $k = 1$ representing isothermal behavior and $k = C_p/C_v$ adiabatic behavior. With these assumptions the condition of normal stress balance, at any time t, on any point $\mathbf{x}_c$ on the surface, may be stated as

[1] Also Research Professor, Department of Mechanical Engineering, The Johns Hopkins University, Baltimore, MD 21218.

$$P_L(\mathbf{x}_S,t) = P_v + P_{g_0}\left(\frac{\mathcal{V}_0}{\mathcal{V}(t)}\right)^k - \sigma C(\mathbf{x}_S,t), \qquad (4)$$

where P_L is the liquid pressure at the bubble wall, P_{g_0} and $\mathcal{V}_0$ are the initial gas pressure and volume respectively, σ is the surface tension coefficient, C the local curvature of the bubble, and $\mathcal{V}$ the instantaneous value of the bubble volume. Here P_{g_0} and $\mathcal{V}_0$ are known quantities at $t = 0$. The curvature of the bubble can be computed using the relation $C = \nabla \cdot \mathbf{n}$. The pressure at the bubble surfaces can be related to the potential using Bernoulli's equation, to give

$$\rho\left[\frac{\partial\phi}{\partial t} + \frac{1}{2}|\nabla\phi|^2\right]_S = P_\infty(t) - P_v - P_{g0}\left(\frac{\mathcal{V}_0}{\mathcal{V}}\right)^k + \sigma\nabla\cdot\mathbf{n}(5)$$

On any moving rigid surfaces, we need an equation similar to (5) relating the velocity of the surface to the pressure. Equations (1-5), along with prescribed initial conditions, form a complete system of equations for the variables $\phi, \mathbf{x}_S, P_l$, and determine the location and geometry of the bubbles, and the pressure and velocity in the domain. The two methods used to solve this non-linear problem are described briefly in what follows. For more complete descriptions see [5,8,9].

Boundary element solution

The boundary element method (BEM) uses Green's identity to solve Laplace's equation. If the velocity potential, ϕ (or its normal derivative, $\partial\phi/\partial n$) is known on the boundaries of the domain, and ϕ satisfies the Laplace equation, then ϕ can be determined anywhere in the domain of the fluid by using the identity:

$$\int_S\left[-\frac{\partial\phi(\mathbf{y})}{\partial n_\mathbf{y}}\frac{1}{|\mathbf{x}-\mathbf{y}|} + \phi(\mathbf{y})\frac{\partial}{\partial n_\mathbf{y}}\left(\frac{1}{|\mathbf{x}-\mathbf{y}|}\right)\right]dS_\mathbf{y} = a\pi\phi(\mathbf{x}).(6)$$

We first select $\mathbf{x}$ on the boundary to determine $\partial\phi/\partial n$ (or ϕ) on the boundary, and then using the known values on the boundary determine ϕ at the required point in the domain. Here $a\pi = \Omega$ is the solid angle under which the point $\mathbf{x}$ sees the fluid, with
$a = 4$ if $\mathbf{x}$ is a point in the fluid
$a = 2$ if $\mathbf{x}$ is a point on a smooth surface
$a < 4$ if $\mathbf{x}$ is a point at a sharp corner on the boundary.

The advantage of this representation is that it reduces the dimension of the problem by one. If the point $\mathbf{x}$ is selected to be on the boundary of the fluid domain (a bubble surface or on any other boundary), then a closed system of equations can be obtained and used at *each time step* to solve for values of $\partial\phi/\partial n$ (or ϕ). The points on the moving boundaries (bubble surfaces) are advanced in a Lagrangian fashion using the calculated velocities, while the potential at the subsequent times is obtained by integrating (5).

To solve (6) numerically, we discretize the bubble surfaces as well as other boundaries into panels. A local linear basis for ϕ and $\partial\phi/\partial n$ is assumed over each panel. Integration is performed over each panel, and the results summed up to complete the integration over the complete boundary. The initially spherical bubble is discretized into a geodesic shape using flat, triangular panels. Equation (6) then becomes a set of M linear equations (M is the total number of discretization nodes) of index i of the type:

$$\sum_{j=1}^{M}\left(A_{ij}\cdot\frac{\partial\phi_j}{\partial n}\right) = \sum_{j=1}^{M}(B_{ij}\cdot\phi_j) - a\pi\phi_i, \qquad (7)$$

where A_{ij} and B_{ij} are elements of matrices which are the discrete equivalent of the integral operators given in Equation (6). Details of the calculation of these matrices, of the geometrical quantities needed (normal, curvature, volume), the other physical variables (tangential and normal velocities, pressure) the adaptive time integration scheme can be found in [8,9,11]. Results of the validation of this code may be found in [9,7,12].

If the potential at a point within the domain is needed, (6) (or its discrete equivalent (7)) can be used. The known values of ϕ and $\partial\phi/\partial n$ on the boundary are used to compute the integrals on the left hand side. To calculate velocities at an interior point the potential in a neighborhood of the point is obtained and local finite-differencing used, while the pressure is obtained via the Bernoulli equation (2).

Asymptotic solutions

We seek asymptotically valid solutions to Equations (1-5), under the assumption that the characteristic size, r_{b0}, of the bubbles is small compared with a characteristic inter- bubble distance l_0. The small parameter used to linearize the system is the ratio between r_{b0} and l_0 denoted ϵ. The zero order approximation ($\epsilon = 0$) reduces to the case of a single bubble in an infinite medium. In the absence of relative motion with respect to the surrounding fluid, each of the bubbles reacts to the local pressure variations spherically, as if isolated.

At higher orders of approximation ($\epsilon \neq 0$), mutual bubble interactions and individual bubble motion and deformation come into play. These approximations are obtained by means of the method of matched asymptotic expansions. The "outer problem" is that obtained when the reference length is chosen to be l_0. This problem is associated with the macroscopic behavior of the cloud, and each bubble appear in it only as the summation of singularities of various orders. The "inner problem" is that obtained when the lengths are normalized by r_{b0}. The solution of this problem provides the microscopic details of the behavior of the cloud, i.e., in the vicinity of an individual bubble center (B_i). The presence of the other bubbles, all considered to be at infinity in the "inner problem," is sensed only by means of the matching condition with the "outer problem." The boundary conditions at infinity for the "inner problem" are obtained, at each order of approximation by the asymptotic behavior of the outer solution in the vicinity of B_i. Thus, if one knows the behavior of all bubbles except B_i, the motion, deformation and pressure field due to this cavity can be determined by solving linearized, non-dimensional versions of Equations (1-5). The non-dimensionalization yields the following parameters $\epsilon, \mathcal{P}, \mathcal{W}, \nu, N$. These are defined by

$$\epsilon = \frac{r_{b0}}{l_0} \qquad \mathcal{P} = \frac{P_\infty(0) - P_v}{\Delta P}$$
$$\mathcal{W} = \frac{r_{b0}\Delta P}{\sigma} \qquad \nu = \omega r_{b0}\sqrt{\frac{\rho}{\Delta p}}. \qquad (8)$$

Here ϵ is a measure of the void fraction in the bubble cloud, $\mathcal{P}$ is a 'cavitation number,' $\mathcal{W}$ is a Weber number, ν is the ratio of the forcing frequency ω and the natural frequency of a bubble with radius r_{b0}, while Δp is the characteristic pressure variation associated with the forcing P_∞.

At the lowest order, $\epsilon = 0$, each bubble, B_i, behaves spherically as if in an infinite medium and the time dependence of its radius, $a_0^i(t)$, is given by the Rayleigh-Plesset equation,[1]. This first approximation of the whole flow field (a distribution of sources or sinks representing all bubble oscillations) sets the boundary conditions at infinity at the following order of approximation. The same process is then repeated for the successive orders. One can show, [5,6], that *up to the order* $O(\epsilon^3)$, the influence of the remaining bubbles on each bubble B_i, can be schematically replaced by the influence of a single equivalent bubble centered at G_i (see Figure 1). The growth rate and position of this equivalent bubble are determined by the distribution and the growth rate of the other cavities. In general, this fictitious bubble equivalent to the "rest-of-the-cloud" and

the corresponding "cloud center" and "equivalent bubble intensity" are different for each bubble. If θ_{ij} is the angle between the direction of the center, $\underline{B_iG_i}$, and the direction of a field point $\underline{B_iM}$, the equation of the surface of the axisymmetric bubble B_i can be written in the form:

$$R(\theta_{ij},\varphi,t) = a_0^i(t) + \epsilon a_1^i(t) + \epsilon^2[a_2^i(t) + f_2^i(t).\cos\theta_{ij}] + \\ +\epsilon^3[a_3^i(t) + f_3^i(t).\cos\theta_{ij} + g_3^i(t)P_2(\cos\theta_{ij})] + o(\epsilon^3), \quad (9)$$

where P_2 is the Legendre polynomial of order 2, and argument $\cos\theta_{ij}$, while the φ dependence is not seen till the order of the included terms.

The first component, $a_0^i(t)$, is given by the Rayleigh-Plesset equation, while the other components, a_n^i, f_n^i and g_n^i, are given by similar second order differential equations which can be written in symbolic form as follows:

$$\mathcal{D}_2(y_n^i) = \sum_j \left(\frac{l_0}{l_0^{ij}}\right)^m \mathcal{F}_j^i(y_0^i,....,y_{n-1}^i)P_m(\cos\theta^{ij}). \quad (10)$$

Here $\mathcal{D}_2(y_n^i)$ represents a second order, non-linear, differential operator in time, acting on the radius component y_n^i (one of a_n^i, f_n^i, g_n^i) of the bubble i; l_0^{ij} is the initial distance between the bubbles B_i and B_j; $\mathcal{F}_j^i(y_0^i,....,y_{n-1}^i)$ is known (it is a function of the terms (y_k^i), determined at the preceding orders); m indicates the order of the spherical harmonic; θ_{ij} is the angle between the direction $\underline{B_iB_j}$ connecting the bubble centers and the direction of motion of bubble i toward the cloud center, B_g; and n indicates the order of approximation. The detailed expressions can be found in [5]. The behavior of B_i can then be computed by integration of the obtained system of differential equations using a Runge-Kutta procedure. The behavior of the whole cloud thus obtained.

Earlier studies [3,5,6] have shown that collective bubble behavior can have a dramatic effect on both bubble growth and implosion. Specifically, bubble growth is inhibited by bubble interactions, while bubble collapse is enhanced. This cumulative effect comes from the fact that the interaction reduces any driving pressure drop as a result of the other bubble growth, while it increases the collapse driving pressure as a result of the other bubble collapse. Due to the cumulative effects of the collapse of all the bubbles in the cloud, each bubble ends its collapse under the influence of a pressure which is orders of magnitude higher than that for an isolated bubble (see Figures 6 and 7).

3 Numerical Experiments

Comparison of the two methods

While the BEM code represents a significant advance in that it allows us to simulate flows with very strong bubble interactions in a relatively accurate way, it is computationally intensive compared to the asymptotic code. While the latter requires $O(N)$ floating point operations per time step, where N is the number of bubbles, the BEM code requires $O(M^2)$ operations per time step where M is the total number of nodes in the discretization. It is thus a matter of some interest to determine the region in the parameter space (see (8)) for which the asymptotic analysis holds. A complete map of the parameter space is a matter of current study. Here a few preliminary results are presented.

In all cases presented for comparison here the ratio ϵ is the ratio of the *initial* radius of the bubble, and the minimum distance (at $t = 0$) between any two bubbles in the configuration. The study was restricted to one particular form of the driving pressure field-a drop in the pressure field at time $t = 0$. Thus the influence of the parameter ν is not studied. Two values of the initial pressure drop were chosen corresponding to values for $\mathcal{P}$of 1.004 (a very large drop) and 2.508 (a relatively milder drop). The number of bubbles varied from 2 to 8, while the value of epsilon was also varied. The studies were performed for large $\mathcal{W}$ (corresponding to large bubbles). Symmetric bubble configurations were chosen for ease of visualization, and efficiency in computation. The bubbles were arranged respectively at the edges of a line, a square, and a cube. In each case the bubble oscillations caused "collapse" of the bubble in the direction towards the center of the cloud. The data for the "radii" reported are for points on a bubble which are closest to the cloud center initially (the positive radii in Figure 2) and that which are farthest from the cloud center (the negative radii).

As can be seen (Figure 2) the BEM code shows that the time period of the oscillation of the bubbles increases with the number of interacting bubbles. The maximum bubble size along the jet axis is however not much modified. The jet advancement towards the cloud center increases with N. This is seen from the fact that the upper curves in the graph cross the $r = 0$ axis earlier as N increases. This effect is more pronounced as ϵ is increased (Figure 3). The asymptotic code predicts substantially the same curves for small N (Figure 2) and low ϵ (Figure 3), but begins to diverge at higher values. The method predicts either a much faster collapse for $N = 2, 4$ or an unexpected early rebound for $N = 8$ in Figure 2.

In the cases addressed in Figure 2 and 3 the collapse of the bubbles was relatively intense. This may be seen that the value of $\mathcal{P}$ =1.001, corresponds to a pressure drop of 240 times the original. Thus it is unreasonable to expect good agreement from the asymptotic analysis. To check if the method fares better in case the pressure drop is milder, a case where P_∞ is reduced to approximately 40% of its original value was studied, corresponding to $\mathcal{P}$ =2.508. Results from such a study are shown figures 4 and 5. The agreement between the asymptotic method and the BEM code is seen to be quite good at low ϵ. Figure 4 presents the influence of changing N while figure 5 presents results for a four bubble study where ϵ is varied from 0.05404 to 0.386. (Note that the bubbles would touch for $\epsilon = 0.5$, as the scaling is based on the radius.)

The relative influence the dynamics of an individual bubble has on its neighbors may be best understood by examining the pressure at a point and compare it with its value in the absence of the bubbles. Figures 6 and 7 show the pressure at the center of the cloud, non- dimensionalized with respect to the maximum pressure that would have been induced by a "Rayleigh-Plesset bubble" (i.e. an isolated bubble at a distance $l_0/2$ away. The pressure predicted by the asymptotic analysis is seen to be much higher during collapse. This high value is explained by the much higher values of the velocity during collapse predicted by the asymptotic analysis (see Figure 2,3,4) than by the BEM code. Again the influence of increasing N or increasing ϵ is to make the asymptotic analysis less accurate.

An explanation of why the predictions of the asymptotic method are in error during the collapse phase is provided by Figure 8, which shows the collapse of a 4 bubble cloud. Here the value of $\epsilon = 0.4$. Here two cross-sectional cuts of the cloud are shown, the first being a top-view, while the second is a view from the plane of the bubbles with the viewing angle perpendicular to an edge. The fact that the bubbles are distributed in a plane is clearly visible from the appearance of the jet, which is seen to have a two-dimensional flat appearance, rather than a conical axisymmetric shape. Since the asymptotic method, to the order we have solved for $(O(\epsilon^3))$, only allows for deformations expressible in terms of the first two Legendre modes, it becomes inaccurate during the final stages of the collapse. The error made in the pressure is much higher since it depends on the time derivative of the shape (the velocity).

From these experiments we may conclude that, as expected,

the asymptotic method is good for relatively large inter bubble separation, for a small number of bubbles, and when the bubble collapse is weak.

Other Experiments

Here we report the results of some numerical experiments performed with 3DynaFS on some asymmetric bubble configurations. The effects of phasing (i.e. the introduction of differences in the temporal response), and the screening effect of the outer bubbles in a cloud on their inner members are studied.

Figure 9 shows a 4-bubble configuration where the bubbles are centered on the corners of a square. All bubbles were chosen so that they would behave identically if in an infinite medium. However, a time delay between the bubble oscillations was imposed. As a result, at $t = 0$ the bubbles had relative initial sizes in the ratios $2, 1, 3, 1$ counter- clockwise starting from the bubble centered at the origin. A dramatic modification in the behavior of the cloud is seen. The bubble periods appear to be increased for the larger bubbles at $t = 0$. The "delayed" bubbles (the smaller ones at $t = 0$) are prevented by the other bubbles from growing too much, and end up collapsing very early in their history. These bubbles on the other hand significantly influence the "earlier" ones by increasing at some point the pressure drop these bubbles sense and then by preventing them later on from collapsing. Since the code presently breaks down during the last stages of a violent collapse, we can only speculate that a very strong collapse of the larger bubbles would ensue, because of the large pressure produced by the collapse of the smaller bubbles. This can be illustrated by observing the modification of the imposed pressure drop by the behavior of an individual bubble. As shown in figure 8, the bubble growth initially reduces the effective pressure drop that would be felt by a second bubble at the distance l_0, this trend is later reversed, and is followed by a significant pressure rise during the bubble collapse.

Figure 10 shows the case of an asymmetric five bubble configuration. All bubbles have the same initial radius and internal pressure, and are initially spherical and located in the same plane. The most visible effect is observed on the center bubble. Its growth is initially similar to that of the other bubbles, but it ends up being the least deformed. Later on, as the collapse phase advances with the development of a reentrant jet directed towards the central bubble, this bubble appears to be shielded by the rest of the cloud. Its period appears to be at least double that of the other bubbles. Unfortunately, the code cannot presently follow the dynamics beyond this point since it fails following the touchdown of the first reentrant jet on the other bubble side. Here, this occurs before much progress of the collapse of the central bubble is observed. The issue of continuing the computations beyond this point is clearly important and is presently the subject of an ongoing research program at DYNAFLOW. Figure 11 shows a similar computation for a 16 bubble cloud. Here due to memory limitations the discretization is coarser. However the same qualitative features as the 5 bubble cloud can be observed.

4 Conclusion

In this contribution the dynamics of a multi-bubble system was considered using an asymptotic method and a three-dimensional Boundary Element model. While the asymptotic method is simple and satisfactory for relatively weak interactions and non-violent bubble oscillations, the 3D numerical approach is more involved computationally, but allows one to study both very large deformations and very intense oscillations. For multibubble interaction the 3D code shows significant modifications of the bubble dynamics and shape. For identical bubbles acting in concert, an increase in the bubble period is observed without significant modification of the bubble maximum size when the number of bubbles increase or when their separation distance decreases. For violent interaction the asymptotic approach allows one to follow the dynamics only partially during the collapse. The pressures that it predicts during the collapse increase tremendously at the "cloud center" with the number of bubbles. Comparisons with the BEM code results show that the asymptotic approach can significantly overpredict the velocities at the end of the collapse, which implies that the conclusions on the pressures, while still correct, need to be tempered. Similarly, other real fluid flow conditions, such as the presence in the cloud of various bubble sizes, the presence of a velocity or pressure gradient, etc., moderate the conclusions drawn from simplified symmetric models. These various effects can be considered and analyzed using the 3D code.

The phasing study indicates that the influence of compressibility on the dynamics of multiple bubbles is likely to be significant. Similarly the screening effect observed in the multiple bubble simulations shows that the dynamics of a cloud of bubbles is very different from that of a single bubble.

We are presently attempting to repeat our asymptotic analysis by including compressibility. The results from the phasing study indicate that the compressibility of the medium is likely to play an important role, as identical bubbles would receive pressure information at different times, and consequently could have very different behavior. The large reduction of the sound speed (from its value in pure water) in a bubbly medium makes it important that such an effect be included.

While the BEM code 3DynaFS represents a significant advancement in our ability to computationally treat problems hitherto impossible in an efficient way, its application to more realistic problems requires much further work. In a current study at DYNAFLOW we are attempting to take advantage the inherent parallelizability of the BEM technique by implementing it on a Connection Machine.

Acknowledgments

This study was supported by the Office of Naval Research, Contract N00014-89-C-0025.

References

[1] Plesset, M.S., and Prosperetti, A., "Bubble Dynamics and Cavitation," *Ann. Rev. Fluid Mech.*, 9, 145-185, 1977.

[2] Blake, J. R, and Gibson, D. C., "Cavitation Bubbles Near Boundaries," Annual Review Fluid Mechanics, 19, pp. 99-123, 1987.

[3] Chahine, G. L., "Pressure Field Generated by the Collective Collapse of Cavitation Bubbles," Proceedings, IAHR Symposium on Operating Problems of Pump Stations and Power Plants, Amsterdam, Holland, 2-1, 1-12, 1982.

[4] Chahine, G. L., "Experimental and Asymptotic Study of Non- spherical Bubble Collapse," Applied Scientific Research, 38, 187-197, 1982.

[5] Chahine, G.L.,"Cloud Cavitation: Theory," *14th Symposium on Naval Hydrodynamics, Ann Arbor, Michigan, National Academy Press, Washington, D.C.*,165-195, 1983.

[6] Chahine, G. L. and Liu, H. L., "A Singular Perturbation Theory of the Growth of a Bubble Cluster in a Super-heated Liquid," *J. Fluid Mech.*, 156, 257-274, 1985.

[7] Chahine, G.L., "Dynamics of the interaction of non-spherical cavities," to appear in "Mathematical approaches in hydrodynamics," ed. T. Miloh, *SIAM, Philadelphia*, 1991.

[8] Chahine, G.L. and Perdue, T.O., "Simulation of the Three- Dimensional Behavior of an Unsteady Large Bubble Near a Structure," in "A.I.P. Conference Proceedings 197: Drops and Bubbles. Third International Colloquium," ed. Wang, T.G., *American Institute of Physics, New York*, 188-199, 1989.

[9] Chahine, G. L., Perdue, T. O. and Tucker, C. B., "Interaction Between an Underwater Explosion Bubble and a Solid Submerged Body," *DYNAFLOW, Inc. Technical Report #9006-1*, 1989.

[10] Chahine, G.L., "A Numerical Model for Three-Dimensional Bubble Dynamics in Complex Geometries," 22nd American Towing Tank Conference, St. Johns, Newfoundland, Canada, August 1989.

[11] Chahine, G.L., "Nonspherical Bubble Dynamics in a Line Vortex" ASME 1990 Cavitation and Multiphase Flow Forum, Toronto, Canada, 1990.

[12] Chahine, G.L., "Numerical Modelling of the Dynamic Behavior of Bubbles in Nonuniform Flow Fields" *ASME 1990 Cavitation and Multiphase Flow Forum, Toronto, Canada, 1990.*

[13] Van Wijngaarden, L. "On the Collective Collapse of a Large Number of Gas Bubbles in Water," Proc. 11th International Cong. of Appl. Mechanics, Springer, Berlin, 854-865, 1964.

[14] D'Agostino, L. and Brennen, C. E., "On the Acoustical Dynamics of Bubble Clouds," ASME Cavitation and Polyphase Flow Forum, Houston, Texas, 72-76, 1983.

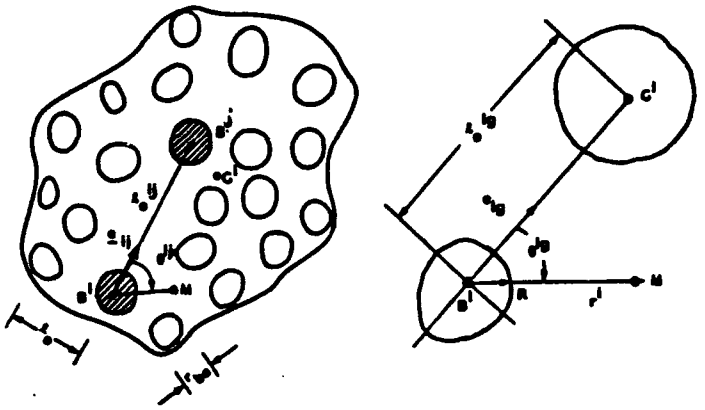

Figure 1: Geometry of the bubble cloud. The influence of the bubble cloud (bubbles B^j) on a bubble B^i may be replaced by the action of a single bubble placed at G^i.

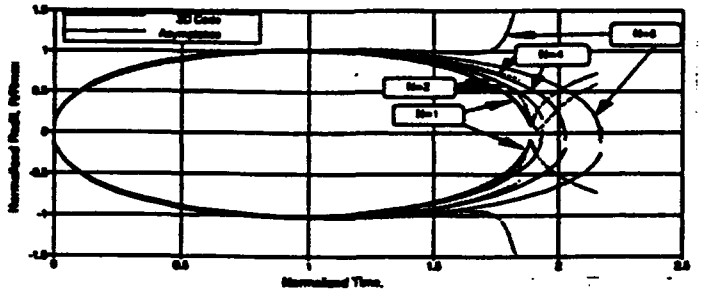

Figure 2: Motion of the bubble points farthest and closest to the "cloud center" versus time for 1, 2, 4 and 8-bubble symmetric configurations. Comparison between 3DynaFS and the asymptotic code results. $\epsilon = 0.0076, \mathcal{P} = 1.0014, \mathcal{W} = 2.4 \times 10^9$. Note $\epsilon = 0.07$ if it were calculated at maximum bubble size.

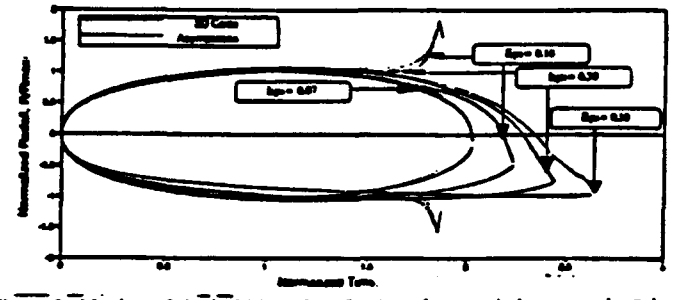

Figure 3: Motion of the bubble points farthest from and closest to the "cloud center" versus time for a 4-bubble symmetric configuration. Comparison between 3DynaFS code results and the asymptotic code results. Influence of bubble proximity or $\epsilon = R_{max}/l_0$. $\mathcal{P} = 1.0014, \mathcal{W} = 2.4 \times 10^9$. The values of ϵ used in the asymptotic calculations is based on the initial radius, and are 0.076, 0.02, 0.0323, and 0.0543, respectively for the cases shown.

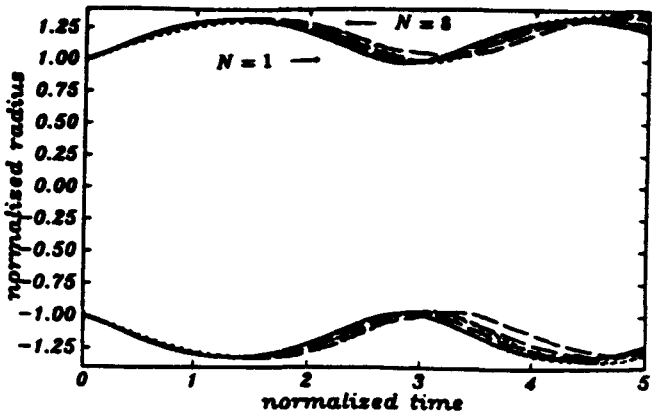

Figure 4: The effect of changing the number of bubbles. $\epsilon = 0.047, \mathcal{P} = 2.508, \mathcal{W} = 6.7^6$. This case is one where the collapse is less violent. Not the substantial improvement in the agreement of the asymptotic analysis an the results from 3DynaFS. The solid line indicates the Rayleigh-Plesset solu tion, the short dashes the BEM solution, while the long dashes the asymptoti results.

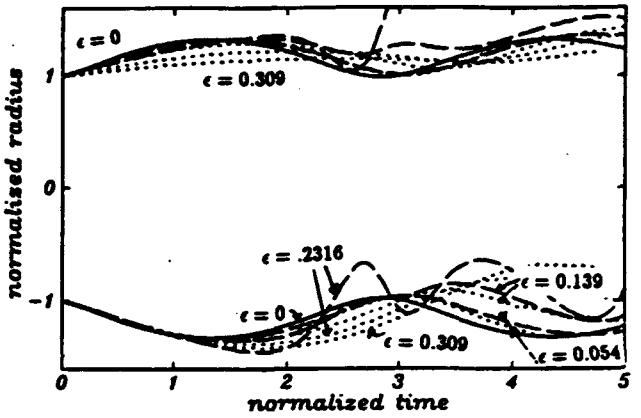

Figure 5: The effect of changing ϵ. $N = 4$, $\mathcal{P}$ =2.508, $\mathcal{W}$ =6.7 $\times 10^5$. The asymptotic results are indicated with long dashes, and the BEM results with short dashes. The solid line indicates the Rayleigh-Plesset solution. Asymptotic results for $\epsilon = 0.309$ are not shown.

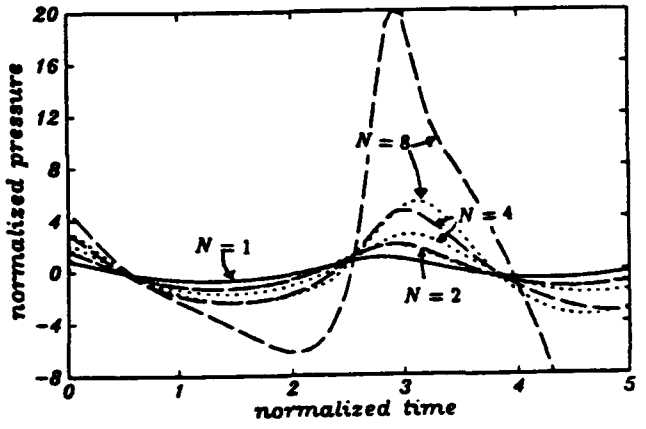

Figure 6: Comparison of the pressure predicted by 3DynaFS and the asymptotic analysis at the center of the bubble cloud for Figure 4. The pressure is non-dimensionalized by the max. pressure that would be felt in the field of an isolated bubble at a distance $l_0/2$ from the center. This scaling was chosen to highlight any relationship between N and the increase in the pressure. The agreement for $N = 2$ is good, but worsens for other cases for reasons cited in the text.

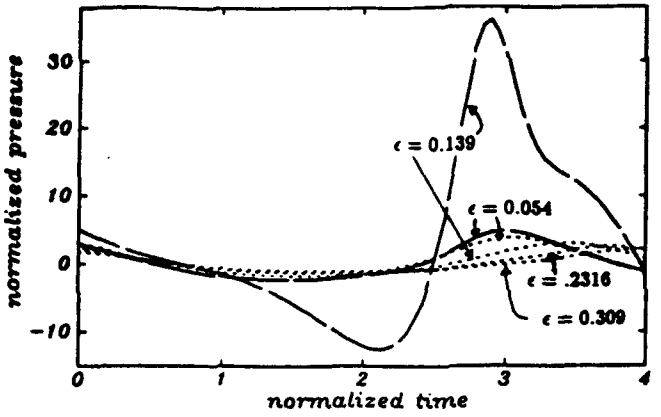

Figure 7: Comparison of the pressure predicted by **3DynaFS** and the asymptotic analysis for Figure 5. The results from the asymptotic analysis are shown only for the $\epsilon = 0.054$ and $\epsilon = 0.139$ cases.

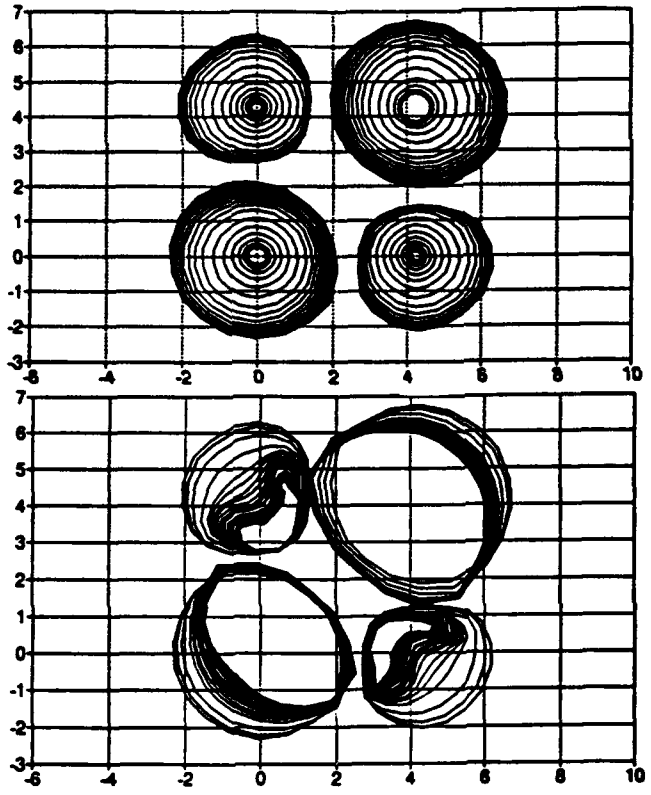

Figure 9: Growth and collapse of 4 identical bubbles initially symmetrically distributed but with different initial radii (2,1,3,1 clockwise starting from origin). The figure shows the influence of 'phasing' (see discussion in §3) on the dynamics.

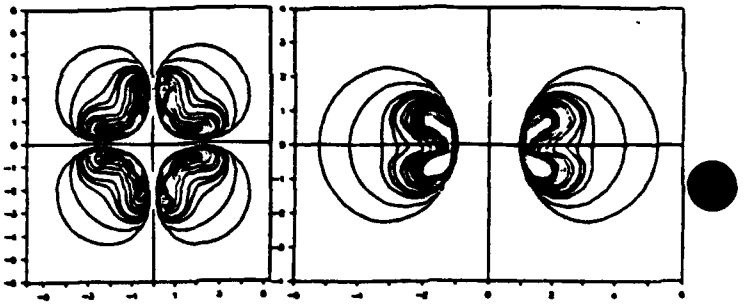

Figure 8: Bubble contours during collapse of a 4-bubble configuration. a) Cross sectional view in the plane $Z = 0$. b) Cross sectional view in the plane $Y = X$. $\epsilon = 0.498$ based on the maximum radius. Note the non-axisymmetric shape of the jet during collapse.

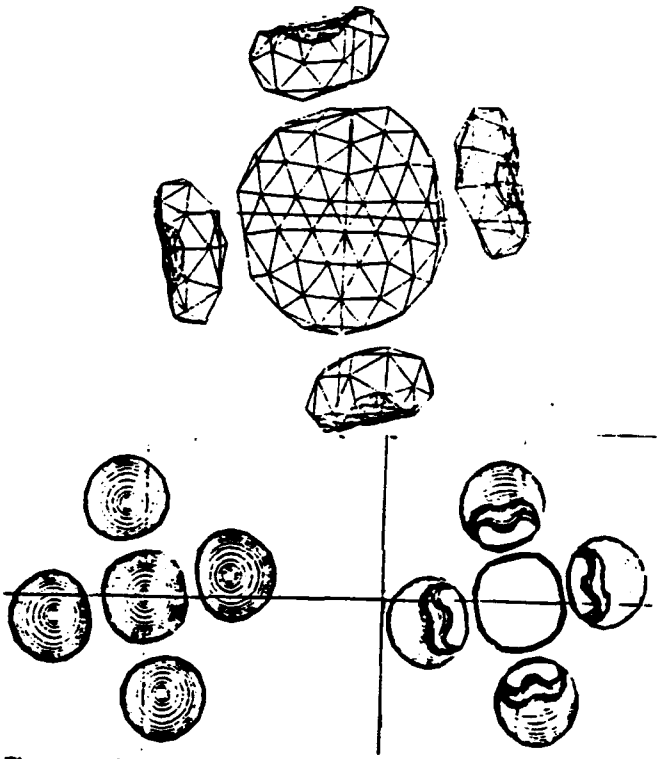

Figure 10: Growth and collapse of 5 bubbles having the same initial size and internal pressure. Influence of the initial bubble geometry on dynamics. $\epsilon = 0.474$ based on the maximum radius. The center bubble is seen to have a remarkably different behavior.

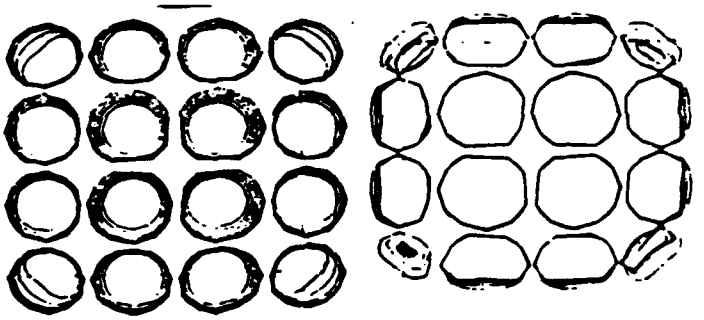

Figure 11: Contours of the collapse of a sixteen bubble cloud. The bubbles are arranged initially on a regular grid in a plane. Again the central bubbles show different behavior than the outer bubbles. Contours from the growth phase are on the left while those from the collapse phase are on the right.

From "MATHEMATICAL APPROACHES IN HYDRODYNAMICS," ed. TOUVIA MILOH, SIAM, Philadelphia, 1991.

Chapter 4

Dynamics of the Interaction of Non-Spherical Cavities

Georges L. Chahine

Abstract

The presence of cavities in a liquid can have significant effects on its behavior and its flow characteristics. In practical flow situations, these effects cannot either be fully understood or predicted without addressing complicated, but nonetheless fundamental phenomena associated with the dynamics, interactions, and deformation of bubbles. The importance of these phenomena has long been recognized, but has largely been neglected due to the difficulty of the associated mathematical problems. In this contribution, bubble shape oscillations in response to nonuniform flow fields and/or due to their interaction with other bubbles are considered using both a fully three- dimensional boundary integral method and a previously developed matched asymptotic expansions technique. Results from both approaches in a few particular cases are compared, and the limits of application of these methods for these cases is assessed.

4.1. Introduction

The understanding of bubble and cavity dynamics has preoccupied researchers and engineers over the past several decades. Since the early work of Rayleigh [1] and Besant [2], numerous papers and books have been devoted to the study of cavity flows. However, due to the complexity of the general mathematical problem, most approaches have been limited to the study of spherical bubbles, or elongated linearized two-dimensional cavities. More recently, with the advent of new mathematical and computational tools, increasing attention has been given to the study of more practical cavity configurations: namely nonspherical bubbles and bubble clouds. This contribution presents a recently developed three-dimensional nonlinear numerical approach whose results will be compared with an earlier contribution, presently being improved, which uses an asymptotic approach.

Since the late seventies considerable attention has been given to the study of nonspherical bubble dynamics, but restricted to the axisymmetric cases in the vicinity of a solid wall or a free surface [3,4,5,6]. All these studies were constrained to the simplified case where external forces act in the same direction as the nearby rigid or free boundary and took advantage of the axisymmetry of the resulting problem. Deviations from this simplifying assumption were not considered, even though such deviations can be expected to have significant influence on the results. Examples of where this assumption fails include large cavity dynamics near complex geometries in a gravity field, the dynamics of a cloud of bubbles, and bubble dynamics in a shear or boundary layer. The study presented here differs from all previous investigations

in that it considers both the fully three-dimensional dynamics of the bubble and that it accounts for the strong interaction between bubbles in a "cloud" or multi-bubble system.

The dynamics of bubble clouds have also recently received a lot of attention [8,9,10], as they have been observed to produce dramatic deleterious effects (erosion, noise, .. etc.), which cannot be explained with approaches based on single bubble dynamics. All these studies but [5,9], have considered only the contribution of the bubble volume change on the cloud dynamics, and have neglected bubble/fluid relative motion and bubble deformation. Our own previous contributions considered these effects in the limiting configurations where bubble size is small compared to inter-bubble distance (small void fraction).

In the numerical method presented here this limitation is removed. A more complete three-dimensional dynamic behavior of the bubbles including the fully nonlinear boundary conditions of the problem is considered. The method, already well tested for bubble dynamics in a quiescent fluid [11,12], is presently being extended to the investigation of bubble dynamics in complex flow fields such as vortical, boundary and shear flows [13,14]. Some of these results are shown below. The use of the method for the study of multiple bubble dynamics is here illustrated and the results compared with the results of the matched asymptotic expansion method.

In the following sections we present the general model used for the bubble dynamics. The assumptions needed for the asymptotic approach are then presented, and the steps needed to expand the various orders of approximation are outlined. The following two sections are devoted to the numerical approach and describe its implementation for nonspherical bubble dynamics in the presence or absence of an underlying base flow. This is followed by a section presenting and discussing some particular results using both the asymptotic and the numerical methods.

4.2. Bubble Dynamics Model

This study will consider cavitation bubbles where relatively large bubble wall velocities are involved, and where, as a result, viscosity has no appreciable effect on the growth and collapse of the bubbles. The study will also be restricted to the case where the flow velocities remain small compared to the speed of sound in water, and as a result, compressibility effects are neglected. This is valid until the last phases of bubble collapse. The above two assumptions, classical in cavitation bubble dynamics studies, result in a flow due to the bubble wall motion that is potential (velocity potential, ϕ) and which satisfies the Laplace equation,

$$\nabla^2\phi = 0. \tag{4.1}$$

The solution must in addition satisfy initial conditions and boundary conditions at infinity, at the bubble walls and at the boundaries of any nearby bodies.

At all moving or fixed surfaces (such as a bubble surface or a nearby boundary) an identity between fluid velocities normal to the boundary and the normal velocity of the boundary itself is to be satisfied. For instance, at the bubble-liquid interface, the normal velocity of the moving bubble wall must equal the normal velocity of the fluid, or,

$$\nabla\phi \cdot \mathbf{n} = \mathbf{V_S} \cdot \mathbf{n}, \tag{4.2}$$

where $\mathbf{n}$ is the local unit vector normal to the bubble surface and $\mathbf{V_S}$ is the local velocity vector of the moving surface.

The bubble is assumed to contain noncondensible gas as well as vapor of the surrounding liquid. The pressure within the bubble at any given time is considered to be the sum of the partial pressures of the noncondensible gases, P_g , and that of the vapor, P_v. Vaporization of the liquid is assumed to occur at a fast enough rate so that the vapor pressure may be assumed to remain constant throughout the simulation and equal to the equilibrium vapor pressure at the liquid ambient temperature. In contrast, since time scales associated with gas diffusion are much larger, the amount of noncondensible gas inside the bubbles is assumed to remain constant and the gas is assumed to satisfy the polytropic relation, $PV^k = constant$, where V is the bubble volume and k the polytropic constant, with $k = 1$ for isothermal behavior and $k = c_p/c_v$ for adiabatic conditions.

The pressure in the liquid at the bubble surface, P_L , is obtained at any time from the following pressure balance equation:

$$P_L = P_v + P_{g_0}(\frac{V_0}{V})^k - C\sigma, \tag{4.3}$$

where P_{g_0} and V_0 are the initial gas pressure and volume respectively, σ is the surface tension, C the local curvature of the bubble, and V the instantaneous value of the bubble volume. Here P_{g_0} and V_0 are known quantities at $t = 0$.

4.3. Asymptotic Theory for Multiple Bubble Dynamics

Let us consider a finite number of bubbles clustered in a cloud. If the characteristic size, r_{b0}, of the bubbles in the cloud is small compared with a characteristic inter-bubble distance l_0, then an asymptotic analysis of the bubble dynamics can be developed using the ratio between r_{b0} and l_0 as the small parameter, ϵ. Thus, the first order approximation ($\epsilon = 0$) consists in neglecting interactions between the bubbles. In the absence of relative motion with respect to the surrounding fluid, each of the individual bubbles reacts to the local pressure variations spherically, as if isolated.

At higher orders of approximation ($\epsilon \neq 0$), mutual bubble interactions and individual bubble motion and deformation come into play. These approximations are obtained by means of the method of matched asymptotic expansions. The "outer problem" is that obtained when the reference length is chosen to be l_0. This problem is associated with the macroscopic behavior of the cloud, and each bubble appear in it only as the summation of singularities of various orders. The "inner problem" is that obtained when the lengths are normalized by r_{b0}. The solution of this problem provides the microscopic details of the behavior of the cloud, i.e., in the vicinity of an individual bubble center (B_i). The presence of the other bubbles, all considered to be at infinity in the "inner problem," is sensed only by means of the matching condition with the "outer problem." The boundary conditions at infinity for the "inner problem" are obtained, at each order of approximation by the asymptotic behavior of the outer solution in the vicinity of B_i. Thus, if one knows the behavior of all bubbles except B_i, the motion, deformation and pressure field due to this cavity can be determined by solving linearized forms of the equations presented in the previous section.

The following assumption was adopted for the numerical examples presented below. The characteristic geometric scale of the cloud is small compared to the outside driving pressure field scale. Therefore, to first approximation, the same driving pressure is assumed to be felt at the same time by all bubbles in the cloud. Variations of this pressure due to the position of each bubble are only seen at the higher orders. In a more general case, the pressure felt by each bubble is dependent on the bubble location and on the modification of the outside flow field by the presence of the

bubble cloud. We are presently implementing such an approach which accounts for the compressibility of the two-phase bubbly medium.

At the lowest order, $\epsilon = 0$, each bubble (of index i) behaves spherically as if in an infinite medium and the time dependence of its radius, $a_0^i(t)$, is given by the Rayleigh-Plesset equation, [15]. If the compressibility of the medium is to be included, then an equivalent equation such as in [7] can be used. This first approximation of the whole flow field (a distribution of sources or sinks representing all bubble oscillations) sets the boundary conditions at infinity at the following order of approximation. The same process is then repeated for the successive orders. One can show, [9,16], that *up to the order* $O(\epsilon^3)$, the influence of the remaining bubbles on each bubble B_i, can be schematically replaced by the influence of a single equivalent bubble centered at G_i. The growth rate and position of this equivalent bubble are determined by the distribution and the growth rate of the other cavities. In general, this fictitious bubble equivalent to the "rest-of-the-cloud" and the corresponding "cloud center" and "equivalent bubble intensity" are different for each bubble. If θ_{ig} is the angle between the centers' direction $\underline{B_iG_i}$ and the direction of a field point $\underline{B_iM}$, the equation of the surface of the axisymmetric bubble B_i can be written in the form:

$$\begin{aligned} R(\theta_{ij},\varphi,t) = a_0^i(t) \quad &+ \quad \epsilon a_1^i(t) + \epsilon^2[a_2^i(t) + f_2^i(t).\cos\theta_{ij}] + \\ &+ \quad \epsilon^3[a_3^i(t) + f_3^i(t).\cos\theta_{ij} + g_3^i(t)\mathcal{P}_2(\cos\theta_{ij})] + o(\epsilon^3), \end{aligned} \tag{4.4}$$

where $\mathcal{P}_2$ is the Legendre polynomial of order 2, and argument $\cos\theta_{ij}$.

The first component, $a_0^i(t)$, is given by the Rayleigh-Plesset equation, while the other components, a_n^i, f_n^i and g_n^i, are given by similar second order differential equations which can be written in symbolic form as follows:

$$\mathcal{D}_2(y_n^i) = \sum_j \left(\frac{l_0}{l_0^{ij}}\right)^m \mathcal{F}_j^i(y_0^i, ..., y_{n-1}^i)\mathcal{P}_m(\cos\theta^{ij}). \tag{4.5}$$

Here $\mathcal{D}_2(y_n^i)$ represents a differential operator of the second order in time acting on the radius component y_n^i (one of a_n^i, f_n^i, g_n^i) of the bubble i ; l_0^{ij} is the initial distance between the bubbles B_i and B_j; $\mathcal{F}_j^i(y_0^i, ..., y_{n-1}^i)$ is a known function of the terms (y_k^i), determined at the preceding orders; m is an integer indicating the order of the spherical harmonic; θ_{ij} is the angle between the direction $\underline{B_iB_j}$ connecting the bubble centers and the direction of motion of bubble i toward the cloud center, B_g; and n is an integer indicating the order of approximation. The detailed expressions can be found in reference [9]

The behavior of B_i can then be computed by integration of the obtained system of differential equations using a multi-Runge-Kutta procedure. The behavior of the whole cloud is thus obtained.

Earlier studies [9,16,17] have shown that collective bubble behavior can have a dramatic effect on both bubble growth and implosion. Specifically, bubble growth is inhibited by bubble interactions, while bubble collapse is enhanced. This cumulative effect comes from the fact that the interaction reduces any driving pressure drop as a result of the other bubble growth. while it increases the collapse driving pressure as a result of the other bubble collapse. Due to the cumulative effects of the collapse of all the bubbles in the cloud. each bubble ends its collapse under the influence of a pressure which is orders of magnitude higher than that for an isolated bubble (see Figure 4.8 and corresponding discussion).

4.4. Boundary Element Method for Three-Dimensional Bubble Dynamics

In order to enable the simulation of bubble behavior in complex geometry and flow configurations including the full non-linear boundary conditions, a three-dimensional Boundary Element Method was developed. This method uses Green's identity to solve Laplace's equation. If the velocity potential, ϕ , or its normal derivative is known on the fluid boundaries (points M), and ϕ satisfies the Laplace equation, then ϕ can be determined anywhere in the domain of the fluid (field points P) using the identity:

$$\int\int_s [-\frac{\partial \phi}{\partial n}\frac{1}{|\,\mathbf{MP}\,|} + \phi\frac{\partial}{\partial n}(\frac{1}{|\,\mathbf{MP}\,|})]ds = a\pi\phi(p), \tag{4.6}$$

where $a\pi = \Omega$ is the solid angle under which P sees the fluid.

a = 4, if P is a point in the fluid,

a = 2, if P is a point on a smooth surface, and

a < 4, if P is a point at a sharp corner of the discretized surface.

The advantage of this integral representation is that it effectively reduces the dimension of the problem by one. If the field point P is selected to be on the boundary of the fluid domain (a bubble surface or on any other boundary), then a closed system of equations can be obtained and used at each timestep to solve for values of $\partial\phi/\partial n$ (or ϕ) assuming that all values of ϕ (or $\partial\phi/\partial n$) are known at the preceding step.

To solve Equation (4.6) numerically, it is necessary to discretize the bubble into panels, perform the integration over each panel, and then sum up the contributions to complete the integration over the entire bubble surface. To do this, the initially spherical bubble is discretized into a geodesic shape using flat, triangular panels. After discretizing the surface, Equation (4.6) becomes a set of N equations (N is the number of discretization nodes) of index i of the type:

$$\sum_{j=1}^{N}(A_{ij}\cdot\frac{\partial\phi_j}{\partial n}) = \sum_{j}(B_{ij}\cdot\phi_j) - a\pi\phi_i, \tag{4.7}$$

where A_{ij} and B_{ij} are elements of matrices which are the discrete equivalent of the integrals given in Equation (4.6).

To evaluate the integrals in (4.6) over any particular panel, a linear variation of the potential and its normal derivative over the panel is assumed. In this manner, both ϕ and $\partial\phi/\partial n$ are continuous over the bubble surface, and are expressed as a function of the values at the three nodes which delimit a particular panel. Obviously higher order expansions are conceivable, and would probably improve accuracy at the expense of additional analytical effort and numerical computation time. The two integrals in (4.6) are then evaluated analytically. The resulting expressions, too long to present here, can be found in [18].

In order to proceed with the computation of the bubble dynamics several quantities appearing in the above boundary conditions need to be evaluated at each time step. The bubble volume presents no particular difficulty, while the unit normal vector, the local surface curvature, and the local tangential velocity at the bubble interface need further development. In order to compute the curvature of the bubble surface a local bubble surface three-dimensional fit, $f(x,y,z) = 0$, is first computed. The unit normal at a node can then be expressed as:

$$\mathbf{n} = \pm\frac{\nabla\mathbf{f}}{|\,\nabla\mathbf{f}\,|}\ , \tag{4.8}$$

with the appropriate sign chosen to insure that the normal is always directed towards the fluid. The local curvature is then computed using

$$C = \nabla \cdot \mathbf{n}. \tag{4.9}$$

To obtain the total fluid velocity at any point on the surface of the bubble, the tangential velocity, $\mathbf{V_t}$, must be computed at each node in addition to the normal velocity, $\mathbf{V_n} = \partial\phi/\partial n\ \mathbf{n}$. This is also done using a local surface fit to the velocity potential, $\phi_l = h(x, y, z)$. Taking the gradient of this function at the considered node, and eliminating any normal component of velocity appearing in this gradient gives a good approximation for the tangential velocity

$$\mathbf{V_t} = \mathbf{n} \times (\nabla\phi_l \times \mathbf{n}). \tag{4.10}$$

With the problem initialized and the velocity potential known over the surface of the bubble, an updated value of $\partial\phi/\partial n$ can be obtained by performing the integrations outlined above, and solving the corresponding matrix equation. The unsteady Bernoulli equation can then be used to solve for $D\phi/Dt$, the total material derivative of ϕ,

$$\frac{D\phi}{Dt} = \frac{\partial\phi}{\partial t} + \mid \nabla\phi \mid^2 = \frac{P_a - P_L}{\rho} - gz + \frac{1}{2} \mid \nabla\phi \mid^2 . \tag{4.11}$$

$D\phi/Dt$ provides the total time variations of ϕ at any node during its motion with the fluid. The second term on the right hand side is the hydrostatic pressure and is introduced to account for cases where the influence of the gravitational acceleration is not negligible.

Using an appropriate timestep, all values of ϕ on the bubble surface can be updated using ϕ at the preceding time step and $D\phi/Dt$. In the results presented below the timestep was based on the ratio between the length of the smaller panel side, l_{min} and the highest node velocity, V_{max}. This choice limits the motion of any node to a fraction of the smallest panel side. It has the great advantage of constantly adapting the timestep, by refining it at the end of the collapse – where l_{min} becomes very small and V_{max} very large – and by increasing it during the slow bubble size variation period. New coordinate positions of the nodes are then obtained using the position at the previous time step and the displacement,

$$d\mathbf{M} = (\partial\phi/\partial n.\mathbf{n} + \mathbf{V_t})dt. \tag{4.12}$$

This time stepping procedure is repeated throughout the bubble oscillation period, resulting in a shape history of the bubbles.

4.5. Presence of a Basic Flow

Cavitation bubbles seldom grow and collapse in a quiescent fluid or in a uniform flow field. To the contrary, cavities are most commonly observed in shear layers, boundary layers and vortical structures. To study bubble dynamics in a nonuniform flow field, let us consider the case where the "basic flow" of velocity $\mathbf{V_0}$ is known and satisfies the Navier Stokes equations [1] :

$$\frac{\partial\mathbf{V_0}}{\partial t} + \mathbf{V_0} \cdot \nabla\mathbf{V_0} = -\frac{1}{\rho}\nabla P_0 + \nu\nabla^2\mathbf{V_0} . \tag{4.13}$$

[1] If the basic flow is potential the application of the Boundary Element Method is straightforward and there is no need for any additional assumptions

In the presence of the oscillating bubbles, the velocity field is given by $\mathbf{V}$ which also satisfies the Navier Stokes equation:

$$\frac{\partial \mathbf{V}}{\partial t} + \mathbf{V} \cdot \nabla \mathbf{V} = -\frac{1}{\rho} \nabla P + \nu \nabla^2 \mathbf{V} \,. \tag{4.14}$$

Both $\mathbf{V}$ and $\mathbf{V_0}$ also satisfy the continuity equation. We can now define bubble flow velocity and pressure variables, $\mathbf{V_b}$ and P_b, as follows:

$$\mathbf{V_b} = \mathbf{V} - \mathbf{V_0}, \qquad P_b = P - P_0. \tag{4.15}$$

If we assume that this bubble flow field ($\mathbf{V_b}$ and P_b) is potential, we can use a method similar to the one described in the previous section to study the dynamics. This assumption implies that, even though the basic flow is allowed to interact with the bubble dynamics and be modified by it, no new vorticity is allowed to be generated by the bubble behavior. Within this restriction, we have

$$\mathbf{V_b} = \nabla \phi_b, \qquad \nabla^2 \phi_b = 0. \tag{4.16}$$

By subtracting (4.14) from (4.13), and accounting for (4.16) we obtain

$$\nabla \left[\frac{\partial \phi_b}{\partial t} + \frac{1}{2} \mid \mathbf{V_b} \mid^2 + \mathbf{V_0} \cdot \mathbf{V_b} + \frac{P_b}{\rho} \right] = \mathbf{V_b} \times (\nabla \times \mathbf{V_0}). \tag{4.17}$$

This equation, once integrated, may be considered the equivalent of the classical unsteady Bernoulli equation in potential flow.

As an illustration consider the case where the basic flow field is that of a two-dimensional Rankine vortex, $\mathbf{V_0} = V_\theta . \mathbf{e_\theta}$, with

$$V_\theta = \frac{\Gamma}{2\pi r}; \qquad r \geq a_c;$$

$$V_\theta = \omega r = \frac{\Gamma r}{2\pi a_c^2}; \qquad r \leq a_c, \tag{4.18}$$

where a_c is the radius of the viscous core, Γ the vortex circulation and V_θ the tangential velocity. In that case the Bernoulli equation can be replaced by:

$$\frac{\partial \phi_b}{\partial t} + \frac{1}{2} \mid \mathbf{V_b}^2 \mid + \frac{P_b}{\rho} = \textit{constant along radial directions}. \tag{4.19}$$

Accounting for at-infinity conditions, the pressure at the bubble wall, P_L, is related to the pressure field in the Rankine vortex, P_0, by:

$$\left[\frac{P_L}{\rho} = \frac{P_O}{\rho} - \frac{\partial \phi_b}{\partial t} - \frac{1}{2} \mid \mathbf{V_b} \mid^2 \right]_{\textit{at bubble wall}} \tag{4.20}$$

The nondimensional basic flow pressure, $\overline{P}_0$, normalized with the ambient pressure, P_∞, is known and is given by:

$$\overline{P}_O(\overline{r}) = 1 - \Omega \left[1 - \frac{1}{2} (\frac{\overline{r}}{\overline{a}_c})^2 \right]; \qquad \overline{r} \leq \overline{a}_c$$

$$\overline{P}_O(\overline{r}) = 1 - \frac{\Omega}{2} (\frac{\overline{r}}{\overline{a}_c})^2; \qquad \overline{r} \geq \overline{a}_c,$$

where lengths are normalized by R_{max}, the maximum radius the bubble would achieve in an infinite medium if the pressure drops to the value on the vortex axis. The swirl parameter Ω, defined as,

$$\Omega = \frac{\rho}{P_\infty}\left(\frac{\Gamma}{2\pi a_c}\right)^2, \tag{4.21}$$

characterizes the intensity of the rotation-generated pressure drop relative to the ambient pressure. The pressure on the vortex axis is $(1 - \Omega)$ and goes to zero if $\Omega = 1$.

4.6. Computational Results and Discussion

We present in this section some results obtained with the Boundary Element Method code (**3DynaFS**), and compare them with results from the asymptotic expansion method. The accuracy of the numerical code was evaluated by using simple test cases known in the literature such as the collapse of spherical and axisymmetric bubbles. For spherical bubbles, comparison with the Rayleigh-Plesset "exact" solution revealed that numerical errors were less than 0.14 percent for a discretized bubble of 162 nodes. The error dropped to 0.05 percent for 252 nodes. The two discretizations – 162 nodes (320 triangular panels) or 252 nodes (500 panels) – are usually selected for most of our nonspherical bubble dynamics runs. However, for the purpose of studying multibubble interactions we were limited to 102 node bubbles (200 panels) due to the limitations on our 32 Mbytes MIPS RS3240 computer. For an 8-bubble configuration the code uses about 30 Mbytes for 102-node bubbles. With this "coarse" discretization the error is about 2 percent on the achieved maximum radius, but is very small, 0.03 percent, on the bubble period. (This can be seen in figure 4.2). Comparisons were also made with studies of axisymmetric bubble collapse available in the literature [4,6], and have shown, for the coarse discretization, differences with these studies on the bubble period of the order of 1 percent . Finally, comparison with actual test results of the complex three-dimensional behavior of a large bubble collapse in a gravity field near a cylinder shows very satisfactory results, [12] (see Figure 4.1). The observed difference in the period was shown to be related to the confinement of the experimental bubble in a cylindrical container [18].

Figure 4.2 compares the results obtained with the 3D code with those given by the asymptotic approach. The bubble cloud is subjected to a sudden pressure drop, and for ease of interpretation, only symmetric cloud configurations are considered. Results for one, two, four and eight-bubble symmetric configurations are shown. For the two-bubble case the bubble centers are separated by a distance l_0, and the initial gas pressure in each bubble is such that the bubble would achieve a maximum radius $R_{max} = R_{b0} = 0.07 l_0$ if isolated. The four-bubble configuration considers similar bubbles centered on the corners of a square with sides of dimension l_0. Finally, the eight bubbles are located on the corners of a cube of side l_0. The figure presents the variations with time of the distance between an initial bubble center and both the point closest to (< 0), and the point farthest (> 0) from the "cloud center". These points are selected because they lie along the direction of development of the reentrant jet the farthest point becoming the tip of the jet which penetrates the bubble during the collapse.

As we can see from the figure, the BEM method clearly shows that for bubbles *oscillating in phase* the period of oscillation increases with the number of interacting bubbles. The maximum bubble size along the jet axis is however not significantly

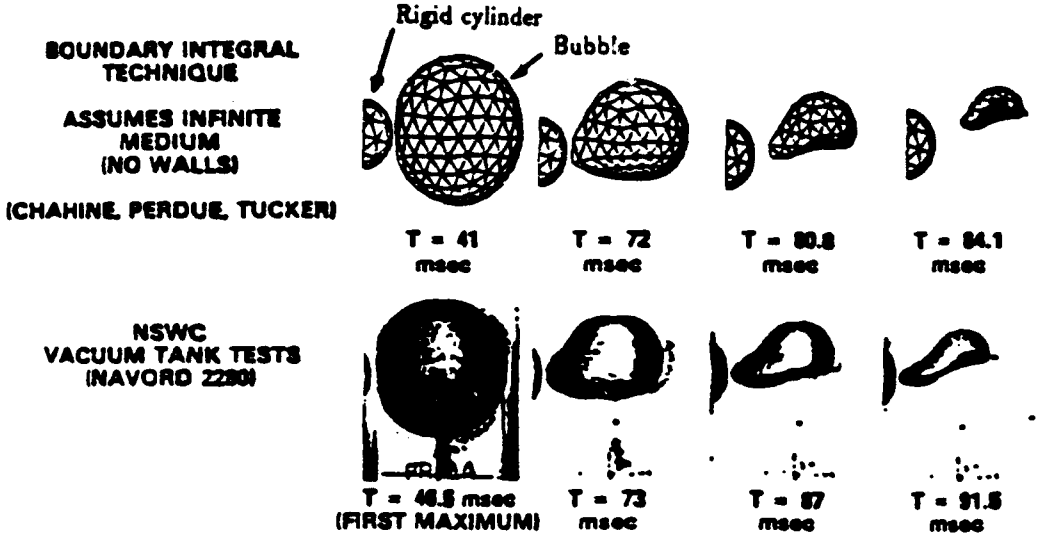

Fig. 4.1. *Large bubble collapse near a cylinder. Comparison between the three-dimensional BEM code results [18] and experimental results of reference 19.*

modified. The jet advancement towards the "cloud center" increases with the number of bubbles. This is seen by the crossing of the $r = 0$ line by the upper curves on the graph which becomes more and more pronounced with an increase in the number of bubbles. This effect is more pronounced for larger values of ϵ (see Figure 4.3).

Figure 4.2 also compares the results of the BEM code with the asymptotic approach. It illustrates the limitations of the incompressible asymptotic approach as it stands now. When the number of bubbles increases the method diverges towards the end of the collapse and predicts either a much faster collapse than obtained with the more accurate BEM method (N=2 and 4), or an unexplained early bubble rebound (N=8). This behavior occurs earlier when either the number of bubbles or the value of ϵ increases.

Figure 4.3 shows the influence of ϵ on the bubble dynamics for a 4-bubble configuration. Using the BEM 3D results enables one to study the influence of reducing bubble inter-distance on the dynamics of each bubble. Increasing the proximity between the bubbles, or increasing the number of bubbles is seen to increase the lengthening effect on the bubble period, while enhancing the reentrant jet formation, as in the more classical case of bubble collapse near a solid wall. In all cases, the reentrant jet formed is directed towards the center of the bubble cloud, or here, the center of the square. As expected, the asymptotic approach gives a very good approximation at low values of ϵ, but fairs poorly for high values of ϵ (note that for $\epsilon = 0.5$ the bubbles touch at their maximum size).

The above conclusions on the asymptotic approach have to be tempered by the fact that all cases presented addressed relatively intense bubble collapse (with a strong reentrant jet formation). The relevant nondimensional parameter to characterize the collapse intensity is the ratio, $\overline{P}_{gm}$, of the gas pressure to the outside pressure at maximum bubble size. This ratio is about 0.06 for the cases shown above. For higher values of $\overline{P}_{gm}$ a smoother collapse followed by a rebound occurs, and the asymptotic approach fairs much better [5].

Figures 4.4 and 4.5 illustrate further the three-dimensional behavior of the bubble, using 198-node bubbles. Figure 4.4 shows two cross-sectional views of the bubble

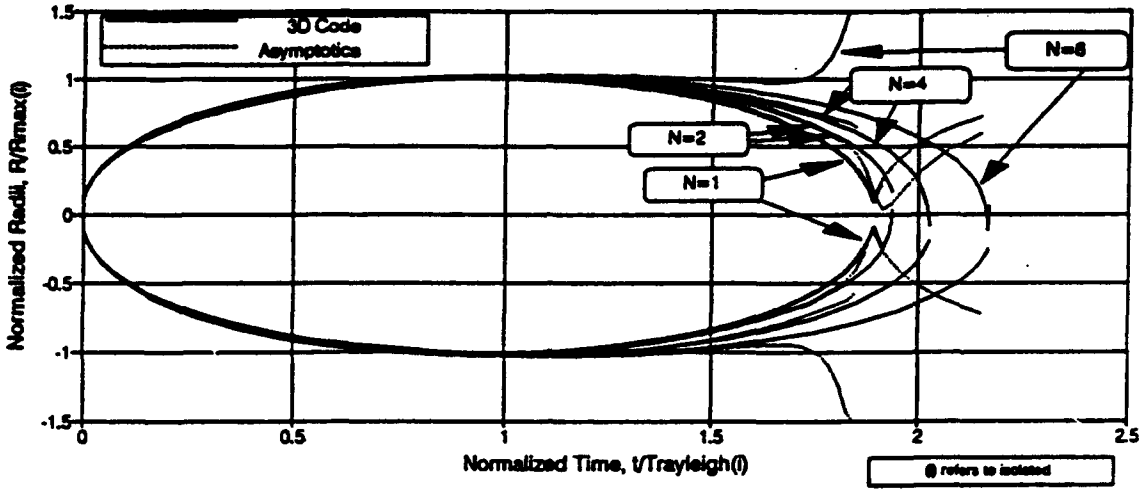

Fig. 4.2. *Motion of the bubble points farthest and closest to the "cloud center" versus time for* $1, 2, 4$ *and* 8*-bubble symmetric configurations. Comparison between 3D code results and the asymptotic code results.* $\epsilon = 0.07, P_{g0}/P_{amb} = 283$.

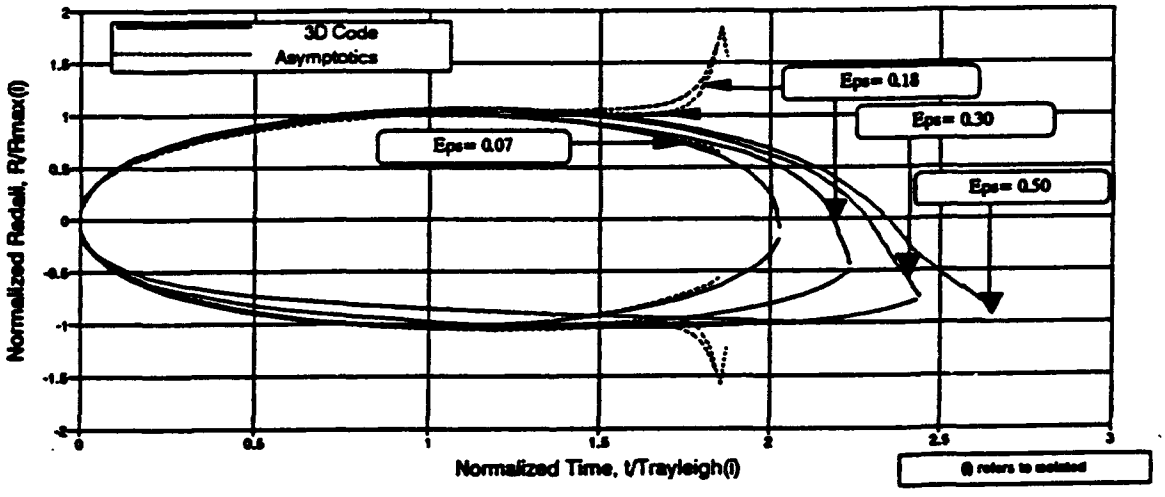

Fig. 4.3. *Motion of the bubble points farthest from and closest to the "cloud center" versus time for a* 4*-bubble symmetric configuration. Comparison between* 3DynaFS *code results and the asymptotic code results. Influence of bubble proximity or* $\epsilon = R_{max}/l_0$, $P_{g0}/P_{amb} = 283$.

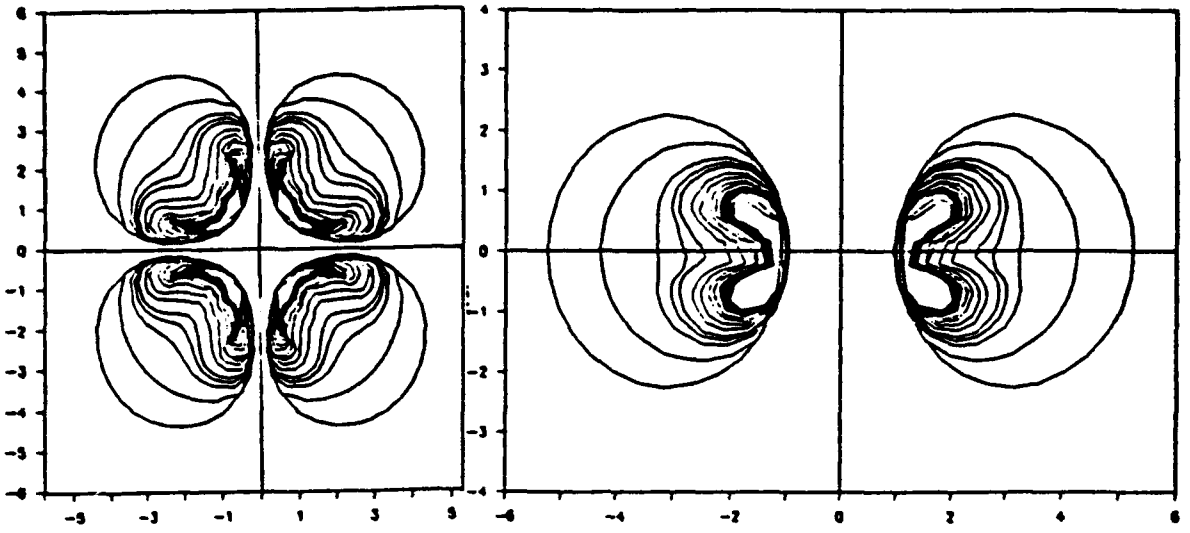

Fig. 4.4. *Bubble contours during collapse of a 4-bubble configuration. a) Cross sectional view in the plane Z=0. b) Cross sectional view in the plane Y=X.* $\epsilon = 0.498$, $P_{g0}/P_{amb} = 283$.

shapes at various times during the collapse for a strong interaction case ($\epsilon = 0.498$), for a 4-bubble configuration. The first view shows bubble contours in the $Z = 0$ plane, plane of the four bubble centers. In this plane all four bubbles can be seen, and the reentrant jet appears very wide giving the bubble at the end of the collapse the appearance of a "deflated balloon". The second view is a diagonal cut though the centers of two of the bubbles. In this view, the reentrant jet appears much more pronounced. The combination of the two views illustrates very clearly the reentrant jet formation, its direction towards the center of the square, and gives a qualitative idea about the intensity of the collapse. In this case, due the geometry of the configuration, the jet has a two-dimensional flat shape, rather than a conical axisymmetric shape. This clearly provides one reason for the failure of the asymptotic approach for this case, since the expansions in that approach were stopped to an order (ϵ^3) which does not allow the description of any azimuthal bubble shape variations.

Figure 4.5 presents a 3D view of the bubbles towards the end of a relatively weak collapse of a 4-bubble configuration ($\epsilon = 0.185$). Since the case shown is symmetrical and all bubbles have the same shape, this diagonal view can be interpreted as showing the shape of the same bubble from different view angles. The reentrant jet is here again seen to be wide, pointed, and well advanced towards the other side of the bubble. A complete history of the advancement of the jet in the bubble can be deduced from figure 4.3.

Figures 4.6 through 4.10 illustrate various important effects due to either asymmetries in the bubble configuration, or due to the presence of an underlying nonuniform flow. Figure 4.6 shows the case of an asymmetric five bubble configuration. All bubbles have the same initial radius and internal pressure, and are initially spherical and located in the same plane. The most visible effect observed is that the center bubble. Its growth is initially similar to that of the other bubbles, but it ends up being the least deformed. Later on, as the collapse phase advances with the development of a reentrant jet directed towards the central bubble, this bubble appears to be shielded by the rest of the cloud. Its period appears to be at least double that of the other bubbles. Unfortunately, the code cannot presently follow the dynamics

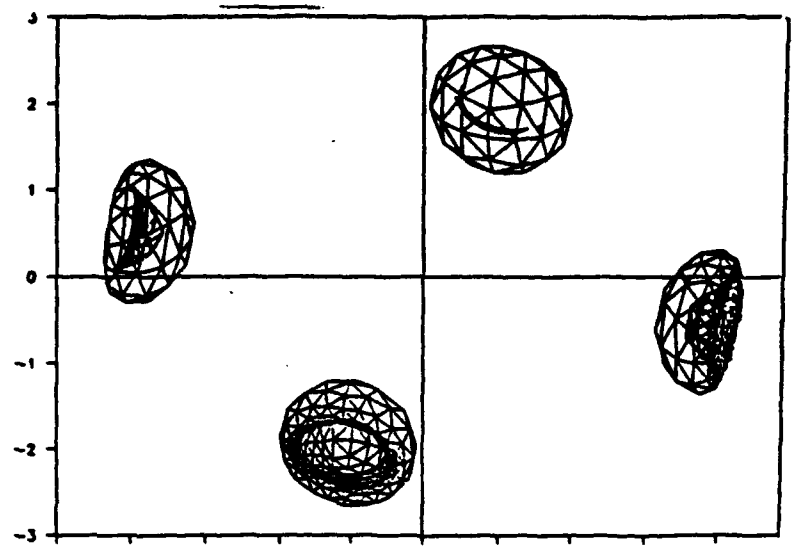

Fig. 4.5. *Three-dimensional view of bubble shape at* $\bar{t} = 1.8$ *during collapse of a 4-bubble configuration.* $\epsilon = 0.184$, $P_{g0}/P_{amb} = 283$.

beyond this point since it fails following the touchdown of the first reentrant jet on the other bubble side. Here, this occurs before any significant progress of the collapse of the central bubble is observed. The issue of continuing the computations beyond this point is clearly important and is presently the subject of an ongoing research at DYNAFLOW.

Figure 4.7 shows a 4-bubble configuration where the bubbles are centered on the corners of a square. All bubbles were chosen so that they would behave identically if in an infinite medium. However, a time delay between the bubble oscillations was imposed. As a result, at $t = 0$ the bubbles had relative initial sizes in the ratios 2, 1, 3, 1 counter-clockwise starting from the bubble centered at the origin. This results in a very asymmetric behavior of the cloud configuration. The bubble periods appear to be lengthened the most for the larger bubbles at $t = 0$. The "delayed" bubbles (the smaller at $t = 0$) are prevented by the other bubbles from growing significantly, and end up collapsing very early in their history. These bubbles on the other hand significantly influence the "earlier" ones by increasing at some point the pressure drop these bubbles sense and then by preventing them later on from collapsing. Since the code presently breaks down before a significant collapse, we can only speculate that a very strong collapse of the larger bubbles would ensue, because of the large pressure produced by the collapse of the smaller bubbles. This can be illustrated by observing the modification of the imposed pressure drop by the behavior of an individual bubble. As shown in figure 4.8, the bubble growth initially reduces the effective pressure drop that would be felt by a second bubble at the distance l_0, this trend is later reversed, and is followed by a significant pressure rise during the bubble collapse.

Figure 4.9 shows the three-dimensional behavior of a bubble in a line vortex. The bubble is initially positioned at a distance of $2R_{max}$ from the vortex axis located at $\overline{X} = 2$. The normalized core size is 4 in this case. Figure 4.9*a* gives a view in the XOY plan of the bubble at different instants. The bubble is seen spiraling around the vortex axis (perpendicular to the figure) while approaching it. At the same time, due to the presence of the pressure gradient, the bubble strongly deforms and a reentrant jet is formed directed towards the axis of the vortex.

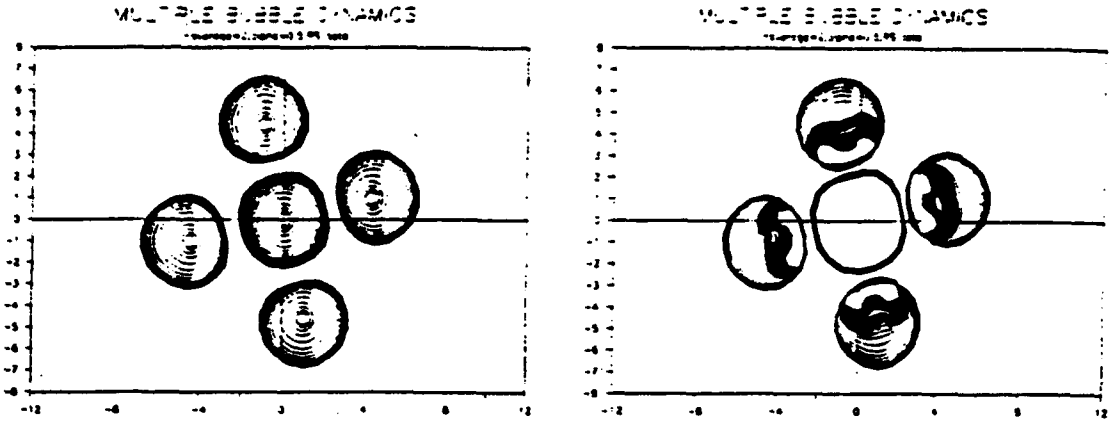

Fig. 4.6. *Growth and collapse of 5 bubbles having the same initial size and internal pressure. Influence of the initial bubble geometry distribution on dynamics.* $\epsilon = 0.474$, $P_{g0}/P_{amb} = 283$.

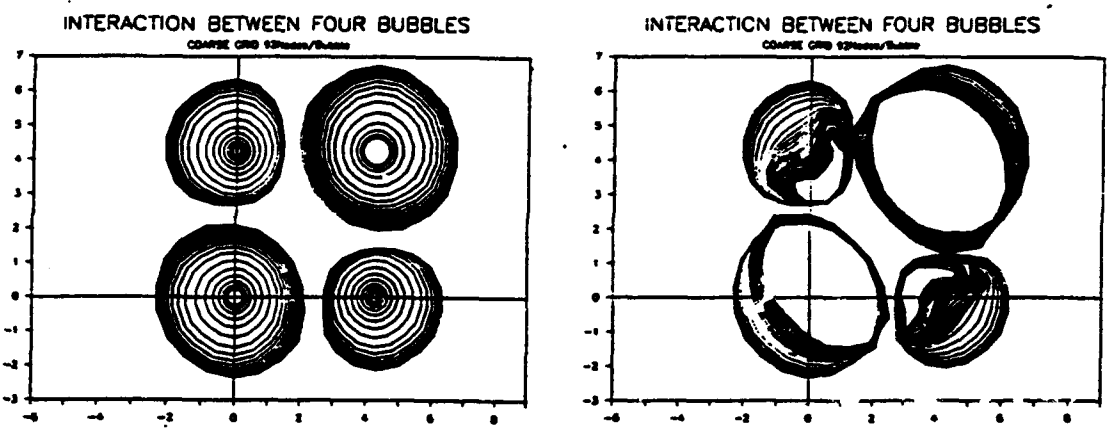

Fig. 4.7. *Growth and collapse of 4 identical bubbles initially symmetrically distributed but with different initial radii (2,1,3,1 clockwise starting from origin). Influence of phasing on dynamics.* $P_{g0}/P_{amb} = 283$.

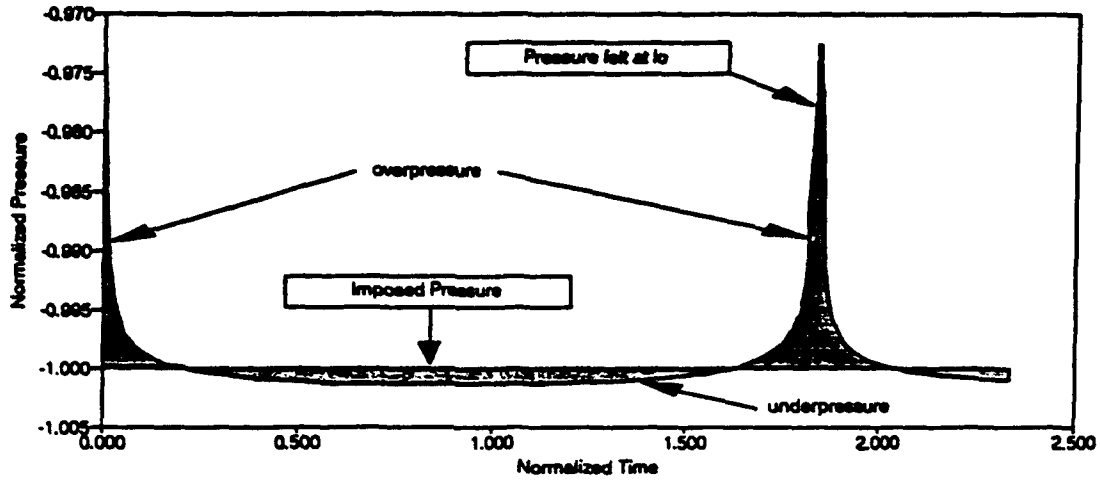

Fig. 4.8. *Pressure at a distance l_0 from a bubble following a sudden pressure drop.* $\epsilon = R_{max}/l_0 = 0.3$, $P_{g0}/P_{amb} = 283$.

Figure 4.9*b* shows the same bubble seen from the OX axis. Here some elongation is observed along the axis of the vortex as well as a very distinct side view of the re-entrant jet. This result is totally contrary to the usually held belief that bubbles constantly grow during their capture until they reach the axis and elongate along it.

Finally, Figure 4.10 shows in the XOY plane perpendicular to the vortex axis the motion of two particular points on the bubble, A and B, initially along OY. Also shown is the motion of the mid point, C. While C seems to follows a path similar to the classical logarithmic spiral, A and B follow more complicated paths, even moving away from the vortex axis at some point in time.

4.7. Conclusions

In this contribution the dynamics of a multi-bubble system was considered using an asymptotic method and a three-dimensional Boundary Element model. The emphasis in the presentation was placed on the 3D BEM results since they are both more accurate and constitute a more recent development in our efforts. While the asymptotic method is simple and satisfactory for relatively weak interactions and non-violent bubble oscillations, the 3D numerical approach is more involved computationally, but allows one to study both very large deformations and very intense oscillations. For multibubble interaction the 3D code shows significant modifications of the bubble dynamics and shape. For identical bubbles acting in concert, an increase in the bubble period is observed without significant modification of the bubble maximum size when the number of bubbles increase or when their separation distance decreases. For violent interaction the asymptotic approach allows one to follow the dynamics only partially during the collapse. The pressures that it predicts during the collapse increase tremendously at the "cloud center" with the number of bubbles. Comparisons with the BEM code results show that the asymptotic approach can significantly overpredicts the velocities at the end of the collapse, which implies that the conclusions on the pressures, while still correct, need to be tempered. Similarly, other real fluid flow conditions, such as the presence in the cloud of various bubble sizes, the presence of a velocity or pressure gradient, ..etc. moderate the conclusions drawn from simplified symmetric models. These various effects can be considered and analyzed using the 3D

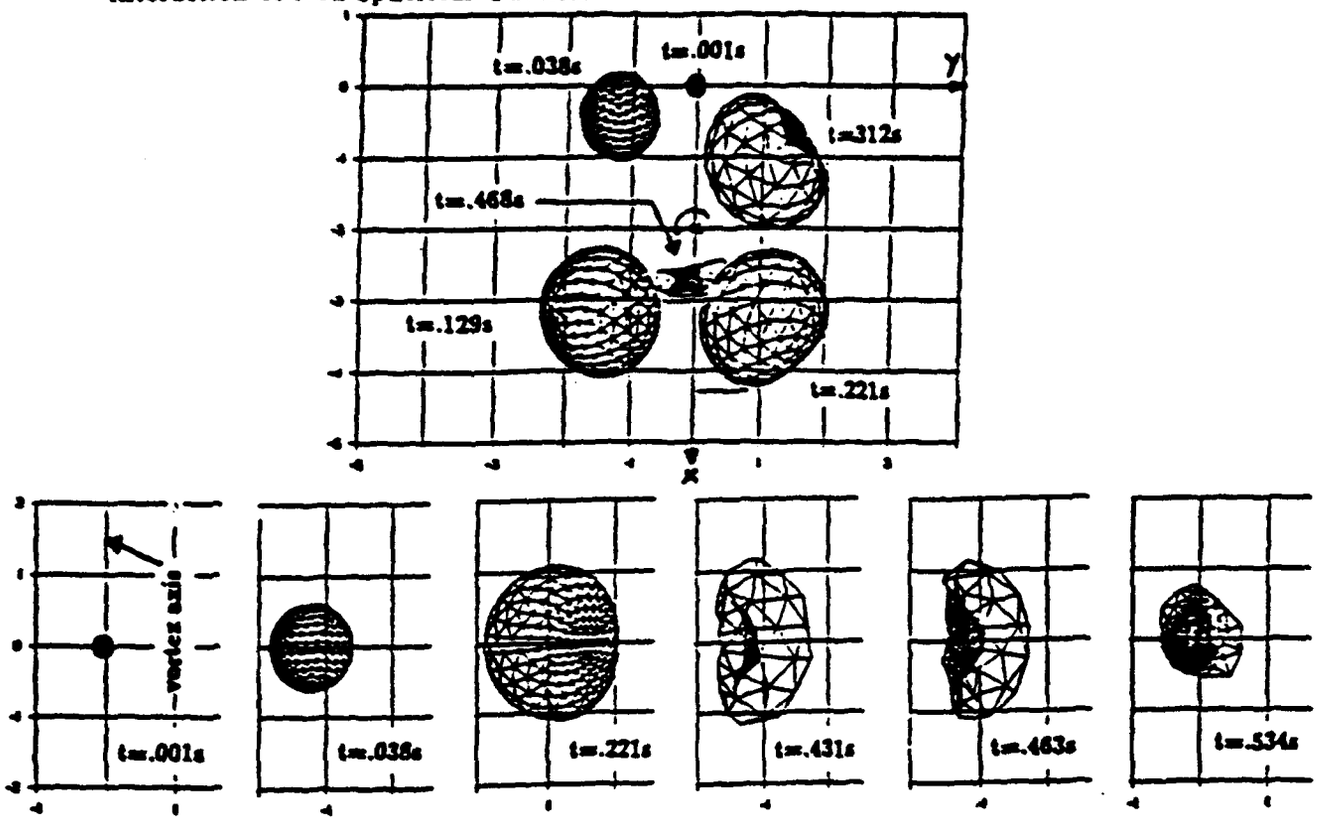

Fig. 4.9. Three-dimensional bubble shapes at various times during bubble capture in a vortex line. $\omega = 0.948$, $a_c = 4R_{max}$, $P_{g0}/P_{amb} = 584$. a) View in XOY plan, b) View in XOZ plan.

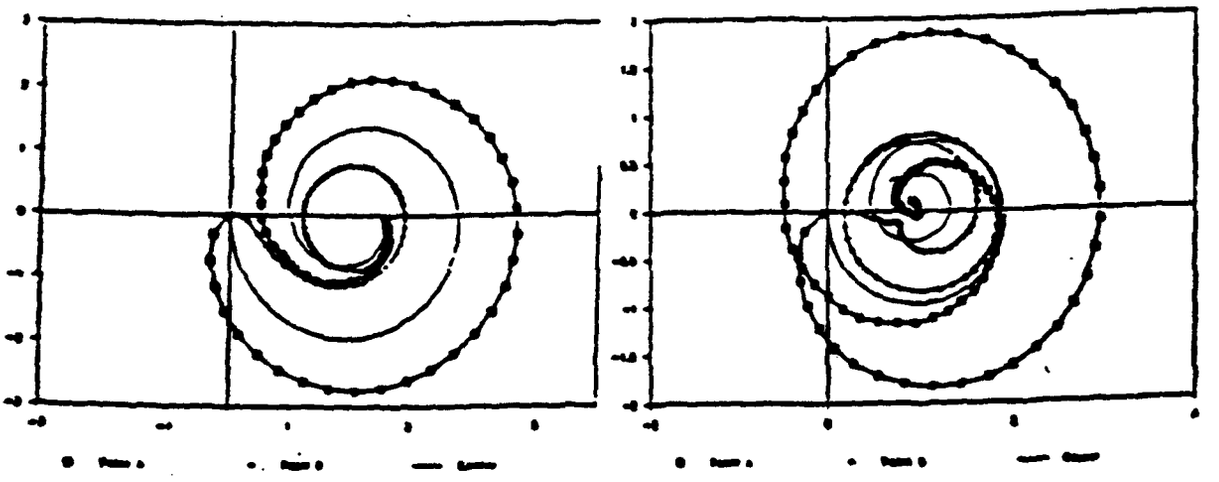

Fig. 4.10. Motion of two bubble points initially on axis OY and their mid point versus time. $\omega = 0.948$, $a_c = 4R_{max}$, $P_{g0}/P_{amb} = 584$. a) Vortex at X=2, b) Vortex at X=1.

code. In this communication, an example of these effects related to the problem of bubble capture, growth and collapse in a line vortex flow field was presented. Nonspherical effects, commonly neglected, were shown to significantly modify our understanding of the phenomenon. As a result, noise generation at the inception of tip vortex cavitation can now be explained by the deformation, collapse and splitting of the bubble while being captured.

On-going areas of improvement of this study include extension of the asymptotic approach to the case of a compressible fluid and coupling of the multibubble approach to a two-phase medium model. The Boundary Element Method approach is being improved to include the full description of the reentrant jet piercing of the bubble and its subsequent advancement in the fluid. The 3D code is also being implemented on a parallel Connection Machine in order to significantly improve computation time, and to allow practical consideration of a much larger number of elements than at present.

4.8. Acknowledgments

This study was supported by the Office of Naval Research, Contract N00014-89-C-0025. The author would like to thank Marshall P. Tulin whom we honor in this volume for suggesting the cloud cavitation problem. The many contributions of several colleagues at DYNAFLOW, Inc. are also greatly appreciated.

References

[1] Rayleigh Lord, "On the Pressure Developed in a Liquid During Collapse of a Spherical Cavity" Phil. Mag., pp. 34, 94-98, 1917

[2] Besant, W., "A Treatise on Hydrodynamics", Cambridge University Press, pp. 198, 1859

[3] Shima, A. and Nakajima, K., "The Collapse of a Non-Hemispherical Bubble Attached to Solid Wall," Journal of Fluid Mechanics, 80, Part 2, pp. 369-391, 1977.

[4] Guerri, L., Lucca, G., and Prosperetti, A., "A Numerical Method for the Dynamics of Non-Spherical Cavitation Bubbles," Proc. 2nd Int. Coll. on Drops and Bubbles, JPL Publication 82-7, Monterey CA, Nov 1981.

[5] Chahine, G. L., "Experimental and Asymptotic Study of Nonspherical Bubble Collapse," Applied Scientific Research, 38, pp. 187-197, 1982.

[6] Blake, J. R, and Gibson, D. C., "Cavitation Bubbles Near Boundaries," Annual Review Fluid Mechanics, Vol. 19, pp. 99-123, 1987.

[7] Herring, C., "Theory of the Pulsations of the Gas Bubble Produced by an Underwater Explosion" Columbia University NDRC Reo. C-4 SR 20-010, 1941

[8] Van Wijngaarden, L. "On the Collective Collapse of a Large Number of Gas Bubbles in Water," Proc. 11th International Cong. of Appl. Mechanics, Springer, Berlin, pp. 854-865, 1964.

[9] Chahine, G.L.,"Cloud Cavitation: Theory," 14th Symposium on Naval Hydrodynamics, Ann Arbor, Michigan, National Academy Press, pp.165- 195, Washington, D.C. 1983.

[10] D'Agostino, L. and Brennen, C. E., "On the Acoustical Dynamics of Bubble Clouds," ASME Cavitation and Polyphase Flow Forum, Houston, Texas, pp. 72-76, 1983

[11] Chahine, G.L. and Perdue, T.O., "Simulation of the Three- Dimensional Behavior of an Unsteady Large Bubble Near a Structure," Proc. 3rd Int. Coll. on Drops and Bubbles, Monterey CA, Sept. 1988.

[12] Chahine, G.L., "A Numerical Model for Three-Dimensional Bubble Dynamics in Complex Geometries," 22nd American Towing Tank Conference, St. Johns, Newfoundland, Canada, August 1989.

[13] Chahine, G.L., "Nonspherical Bubble Dynamics in a Line Vortex" ASME 1990 Cavitation and Multiphase Flow Forum, Toronto, Canada, 1990

[14] Chahine, G.L., "Numerical Modelling of the Dynamic Behavior of Bubbles in Nonuni-

form Flow Fields" ASME 1990 Cavitation and Multiphase Flow Forum, Toronto, Canada, 1990

[15] Plesset, M.S., "Dynamics of Cavitation Bubbles", Trans. ASME J. Appl. Mechan. 16, pp. 228-231, 1948

[16] Chahine, G. L. "Pressure Field Generated by the Collective Collapse of Cavitation Bubbles," Proceedings, IAHR Symposium on Operating Problems of Pump Stations and Power Plants, Amsterdam, Holland, pp. 2-1, 1-12, 1982

[17] Chahine, G. L. and Liu, H. L. "A Singular Perturbation Theory of the Growth of a Bubble Cluster in a Super-heated Liquid," Journal of Fluid Mechanics, 156, pp. 257-274, 1985

[18] Chahine, G. L., Perdue, T. O. and Tucker, C. B., "Interaction Between an Underwater Explosion Bubble and a Solid Submerged Body" DYNAFLOW, Inc. Technical Report 89006-1; 1989

[19] Snay, H.G., Goertner J.F., and Price, R.S., "Small Scale Experiments to Determine Migration of Explosion Bubbles Towards Submarines," Navord Rep. 2280, July 1952.